Modeling of impact and surface processes on small bodies : interpretation of observations, implications for their physical properties and support to space mission operations

Florian Thuillet

UNIVERSITÉ CÔTE D'AZUR

ÉCOLE DOCTORALE
SCIENCES FONDAMENTALES ET APPLIQUÉES

THÈSE DE DOCTORAT

Modélisation des processus d'impact et de surface des petits corps

Interprétation des observations, implications sur leurs propriétés physiques, et support aux opérations des missions spatiales

Florian THUILLET

Laboratoire J.-L. Lagrange (UMR 7293), Observatoire de la Côte d'Azur

Présentée en vue de l'obtention du grade de docteur en
Science de la Planète et de l'Univers
de l'Université Côte d'Azur

Thèse dirigée par Patrick MICHEL

Soutenue le : 29 octobre 2019

Devant le jury composé de :

Rapporteurs :	M. Olivier BARNOUIN
	M. Sébastien CHARNOZ
Directeur :	M. Patrick MICHEL
Examinateurs :	Mme Elena LEGA
	M. Hirdy MIYAMOTO
	Mme Aurélie MOUSSI

Modélisation des processus d'impact et de surface des petits corps

Interprétation des observations, implications sur leurs propriétés physiques, et support aux opérations des missions spatiales

Jury:

Directeur de thèse

M. Patrick MICHEL	-	Directeur de Recherche	-	Université Côte d'Azur

Rapporteurs

M. Olivier BARNOUIN	-	Professeur	-	Johns Hopkins University APL
M. Sébastien CHARNOZ	-	Professeur	-	Université Paris VII

Examinateurs

Mme Elena LEGA	-	Ingénieur de recherche	-	Université Côte d'Azur
M. Hideaki MIYAMOTO	-	Professeur	-	Université de Tokyo
Mme Aurélie MOUSSI	-	Docteur en Astrophysique	-	CNES

Abstract

This thesis aims for a better understanding of the dynamics of regolith in a low-gravity environment through numerical simulations. It is incorporated within the framework and operations of two sample-return missions towards near-Earth asteroids, JAXA's Hayabusa2 and NASA's OSIRIS-REx.

The simulations were performed with the numerical *N*-body code `pkdgrav` adapted to model the interactions with granular medium. Comparing the results of low-speed impact experiments in glass beads with numerical simulations, great agreements were found, demonstrating the validity of these simulations to this application. The form of the Coulomb force (friction force opposing the penetration) was also derived and seems to go from constant to proportional to penetration depth for an increasing size or impactor-grain size ratio. Moreover, inclined plane simulations were also conducted to investigate the relations between parameters of `pkdgrav` and the continuum approach using a constitutive law $\mu(I)$ relating the friction parameter and inertial number. For a moderate friction, such a relation can be established; however, the discrepancies between methods in the velocity profiles are too large for high-friction materials such as gravel.

Concerning the Hayabusa2 mission, after a brief analysis of Ryugu's geophysics are presented the studies on CNES-DLR MASCOT lander and on the sampling mechanism. MASCOT simulations were performed in order to better understand the impact response of the lander on assumed surface granular materials, and to support the engineering team in the landing site selection and the interpretation of landing outcome. Among the results is the increase in the distance traveled after impact for shallower beds, more-grazing impacts, higher-friction materials, and with MASCOT landing on its back corner. It is also shown that the post-impact traces left by MASCOT depend on the lander's attitude and the surface friction properties. Furthermore, additional simulations were performed with a boulder and a side wall, to model the actual landing context. These lead to the realization that outgoing-to-incoming speed ratios as low as 0.3 could be due to microbounces (quick succession of contacts), and not necessarily to a soft surface/boulder.

Then is presented a numerical study of Hayabusa2 sampling, firstly without the modeling of the structure of the sampler, to derive general results on impact cratering in low gravity on a granular material and compare them to the literature. For instance, it was found that streamlines in the bed are well represented by the analytical Z-model, and that the ejecta quantity seems to scale with the impact velocity. With the horn, the majority of simulations fulfill the scientific objective of collecting at least 100 mg.

Finally are introduced the OSIRIS-REx mission and its target (101955) Bennu. Two phenomena observed on the asteroid, i.e., particle ejections and terraces, are

treated as applications of previous chapters. Some particle ejections can potentially be explained by re-impacts of particles after a first ejection, modeled with an adaptation of MASCOT simulations. In addition, using inclined planes, a preliminary study aims at understanding the formation of terraces on Bennu.

To conclude, a large range of simulations of granular material dynamics in different conditions were performed and applied to Hayabusa2 and OSIRIS-REx results and devices. However, the results and associated developed numerical tools are general enough to be applied to future missions devoted to small body exploration and interaction, such as the JAXA MMX mission to Phobos and ESA Hera/NASA DART asteroid deflection missions.

Keywords: Numerical Simulations - Granular Material - Asteroid - Hayabusa2 - OSIRIS-REx

Résumé (français)

Cette thèse a pour but d'améliorer notre compréhension de la dynamique du régolithe en faible gravité grâce à des simulations numériques. Elle s'inscrit dans le cadre de deux missions de retour d'échantillon, Hayabusa2 (JAXA) et OSIRIS-REx (NASA).

Les simulations ont été réalisées grâce au code numérique N-corps `pkdgrav`, adapté pour modéliser les interactions avec un milieu granulaire. Des simulations numériques sont comparées aux résultats d'expériences d'impact à faible vitesse et valident les simulations dans ce contexte. La forme de la force de Coulomb (force de friction s'opposant à la pénétration) semble évoluer de constante à proportionnelle à la profondeur de pénétration, lorsque la taille ou le rapport de taille impacteur/grain augmente. De plus, des simulations de plans inclinés ont été réalisées pour étudier les relations entre les paramètres de `pkdgrav` et l'approche continue utilisant la loi constitutive $\mu(I)$ reliant le paramètre de friction et le nombre inertiel. Pour une friction modérée, une telle relation peut être établie; cependant, les divergences dans les profils de vitesse entre les deux méthodes sont trop grandes avec des matériaux à haute friction tels que du gravier.

Sur la mission Hayabusa2, après une brève analyse de la géophysique de Ryugu sont présentés des travaux sur l'atterrisseur MASCOT (CNES-DLR) et sur le mécanisme de récolte. Les simulations concernant MASCOT ont été réalisées pour mieux comprendre la réponse de l'impact de l'atterrisseur sur la surface granulaire supposée, et pour aider l'équipe d'ingénieurs pour le choix du site d'atterrissage et l'interprétation des résultats. Parmi les résultats, la distance parcourue après impact augmente pour des lits moins profonds, des impacts plus rasants, des matériaux avec de plus hautes frictions et lorsque MASCOT atterrit sur son coin arrière. Il est aussi montré que les traces laissées par MASCOT après l'impact dépendent de son attitude et des propriétés de friction de la surface. En outre, des simulations additionnelles ont été réalisées avec un rocher et un mur vertical, pour modéliser le véritable contexte de l'atterrissage. Celles-ci montrent que des ratios de vitesse avant et après impact peuvent être aussi faibles que 0.3 à cause de micro-rebonds (rapide succession de contacts), et non pas nécessairement à cause d'une surface ou d'un rocher ductile.

Une étude numérique de la récolte de Hayabusa2 est ensuite présentée, d'abord sans la modélisation de la structure du collecteur pour en extraire des résultats généraux sur le processus de cratérisation en faible gravité dans un milieu granulaire, et les comparer à la littérature. Par exemple, les lignes de courant dans le milieu sont bien représentées par le modèle analytique appelé Z-model, et la quantité d'ejecta semble dépendre directement de la vitesse d'impact. Avec le collecteur, l'objectif scientifique de collecter au moins 100 mg est rempli dans la majorité des simulations.

Enfin, la mission OSIRIS-REx et sa cible (101955) Bennu sont présentées. Deux phénomènes observés sur l'astéroïde, l'éjection de particules et la formation de terrasses, sont traités en tant qu'applications des chapitres précédents. Certaines éjections de particules peuvent potentiellement être expliquées par la retombée de particules déjà éjectées, modélisée par une adaptation des simulations sur MAS-

COT. De plus, en utilisant des simulations de plans inclinés, une étude préliminaire cherche à comprendre la formation de terrasses sur Bennu.

En conclusion, un grand éventail de simulations de dynamiques de milieux granulaires, dans différentes conditions, ont été réalisées et appliquées au cadre des missions Hayabusa2 et OSIRIS-REx. Cependant, les résultats et les outils numériques développés dans ce but sont suffisamment généraux pour pouvoir être appliqués à des futures missions vers des petits corps, telles que la mission MMX (JAXA) vers Phobos et les missions de déviation d'astéroïde Hera (ESA) et DART (NASA).

Mots clés : Simulations Numériques - Milieu Granulaire - Astéroïde - Hayabusa2 - OSIRIS-REx

Acknowledgement

La thèse se termine et voici venue l'heure des remerciements. Je tiens à m'excuser par avance pour tous ceux que je vais oublier de citer, ou sur lesquels je ne vais pas suffisamment m'étendre, mais n'oubliez pas que ce n'est qu'un petit texte sur une feuille de papier (que 4 personnes liront), et qu'il ne peut pas refléter toute ma reconnaissance envers tout le monde. En tout cas, sachez que c'est grâce à vous tous que je suis arrivé jusque là, et je vous en remercie grandement.

Tout d'abord merci infiniment Patrick. C'est presque par hasard que je me suis retrouvé avec toi en thèse à l'Observatoire (merci Clara au passage), mais ce n'est pas du hasard si ça s'est si bien passé : tu m'as tant appris d'un point de vue scientifique, tu m'as poussé à présenter à la moindre occasion et à combattre ma timidité (même s'il y a encore du boulot), mais tu as aussi été un formidable compagnon de visite à travers le globe. Je crois qu'on a discuté au cours des trois ans de tous les sujets possibles et inimaginables, et c'était toujours passionnant. Avec ton agenda aussi chargé, je te remercie de m'avoir pris en thèse, car seul toi connaît autant d'anecdotes sur tout (du CNES à Brian May en passant par Jacques Chirac) et m'a permis de comprendre le fonctionnement de la recherche et du spatial comme je n'aurais jamais pu le faire par moi-même. Merci aussi d'avoir été patient, car j'ai parfois la mémoire d'un poisson rouge. Et enfin merci pour la relecture du manuscrit, qu'il a fallu faire dans un temps très court et pour lequel toi et ton anglais clairement meilleur que le mien avez été au rendez-vous.

Merci aux deux relecteurs Sébastien et Olivier pour avoir accepté de relire cette thèse et me donner les clés pour l'améliorer. Merci aussi aux membres du Jury, Aurélie, Elena et Hirdy, quelque soit votre décision finale, merci d'avoir accepté de prendre part à cette aventure et de m'écouter présenter pendant 45 min.

Many thanks to Ron, Steve, Yun, Derek, and Yang, I did not know anything about pkdgrav and SSDEM before this thesis, and you taught me so much, you were always there to answer my numerous questions, even if they could sometimes be naive.

Also many thanks to two wonderful teams, Hayabusa2 and OSIRIS-REx for accepting me in the teams even if I did not have the renown of so many other members. Even if I was a simple PhD student, you let me present my results, listened to my presentations with interest, and always helped me going further with great questions and suggestions. Thanks to the ONC team, and particularly Seiji, Eri, and Shogo, for your interest; you made me feel included in the Hayabusa2 team, and above all useful.

Merci Laurence, Aurélie, Romain et tous ceux du CNES qui ont montré de l'intérêt dans mes recherches, et qui m'ont fait suffisamment confiance pour utiliser mes résultats. J'espère vous revoir bientôt et avoir la chance de travailler avec vous !

Merci à Lucas, Rudy et Elie de l'Ecole des Mines pour m'avoir permis d'élargir mon champ de connaissances en m'initiant à vos simus, et en montrant votre intérêt. J'espère que ces collaborations pourront continuer dans le futur !

Mais tout bon doctorant sait que la réussite des trois années de thèse ne tient pas qu'au travail, qu'à toutes ces rencontres professionnelles. Merci à tous les gens du labo que j'ai côtoyé et qui m'ont très souvent bien aidé (le Conseil, les gestionnaires, les membres de l'équipe TOP, et j'en passe). Merci aux doctorants du labo pour votre gentillesse et votre bonne humeur, malheureusement les trois ans sont passés bien vite et il y en a beaucoup que je n'ai pas eu le temps de mieux connaître ou voir plus régulièrement. En tout cas, je vous souhaite bien de la réussite.

Et parmi ces doctorants, merci à la Dream Team avec qui j'ai passé des journées et des soirées mémorables (sauf une), Antho, le pro du Lego, le Marveliste convaincu et qui a parcouru plus de 16 000 km juste pour venir à ma thèse, Kévin, le bro de l'ortho, le vrai amateur de vraie musique (quelque chose de suffisamment bourrin mais délicat quand-même), exilé trop tôt à Meudon, et Clément le survivant, le seul à avoir pu me tenir compagnie à la fin au labo, le king of Python (et tous les autres trucs pour lesquels j'ai pu te demander mille fois de l'aide), à la rationalité implacable et qui aura presque réussi à me convertir au café (presque). Merci d'avoir été là, pendant les trois ans comme le jour J, mais quelques lignes ne suffisent pas pour vous remercier assez. Bonne chance en tout cas aux deux derniers pour la fin de vos thèses, vous allez tout déchirer. Merci bien sûr aussi à Jerem, qui a partagé nombre d'aventures avec nous (merci pour nous avoir supporté quand on parlait de trucs inintéressants) et qui lui aussi a décidé de faire 16 000 km pour s'infliger 45 min de soutenance elle aussi certainement que partiellement intéressante. Merci à Spip pour avoir accepté sans trop râler qu'on reste chez lui jusqu'à des heures indues.

Merci aussi à tous mes autres amis qui ont suivi mes aventures à distance. Merci à Quentin et Romain les toulousains, qui auraient été à ma soutenance s'ils n'avaient pas des yeux aussi pourris que les miens (et si elle avait été à Toulouse), et merci au binôme, un jour tu trouveras des extraterrestres.

Merci au CRD de Mont de Marsan et à sa bibliothécaire, qui pourrait concurrencer Sebastien Loeb sur les routes escarpées vers Cilaos.

Merci à ma famille bien sûr, particulièrement, merci à Maman Léonie, Papa, et Phiphi, c'est grâce à vous si j'ai réussi jusque là et si j'ai pu me concentrer autant dans mes études. Même si je ne vous le dis pas régulièrement, vous comptez beaucoup pour moi et je sais que sans vous je serais moins. Merci à Swann pour toutes les années qu'on a pu passer ensemble, à tant partager, et je souhaite du fond du coeur que tu trouves quelque chose que tu adores. Même si c'est le grand-frère qui est censé montrer l'exemple, tu m'as beaucoup appris. Et merci à Nastia avec ton grand coeur, la mordue du sport, je suis sûr que tu iras aussi loin que tu le veux. Et c'est grâce à toi si j'ai Steph (bien sûr...). Merci à toutes les autres personnes de ma famille, dont mes grand-parents, mes cousins et cousines, Tango, etc.

Et le meilleur pour la fin, comme on dit, milles mercis à toi Steph. Merci pour avoir été à mes côtés pendant ces années, de près ou par téléphone quand la distance nous séparait (mais pas le coeur) et pour m'avoir soutenu quand c'était plus dur et que le moral était au plus bas, pour m'avoir même aidé jusque dans les derniers moments. Merci à toi la reine de la planification de rédaction et de manuscrit, cette thèse existe aussi grâce à toi. Merci pour m'avoir défendu et soutenu à chaque fois que quelqu'un critiquait mon travail, même si clairement souvent ils avaient raison. Sans toi ces années auraient été bien plus tristes, merci pour m'avoir tant apporté. Et merci pour m'avoir supporté parce que j'imagine que c'est pas tous les jours facile avec un énergumène pareil, surtout pendant une thèse. Un paragraphe n'est pas assez pour te remercier suffisamment, mais l'exercice l'impose. Merci pour tout.

Contents

1 Introduction

> *Did you ever hear the tragedy of Darth Plagueis the Wise?*
>
> — **Preface to Asteroids IV**

1.1 Asteroids

Vestiges of the Solar System formation, space wanderers (even if not considered as "planets"), at the same time heralds of Armageddon and promising refueling point for the future of human space exploration, asteroids never stopped to intrigue both researchers and engineers. The purpose of this section is to introduce them, the interest in studying them and the different ways to enable such studies.

1.1.1 Asteroids in the Solar System

According to the International Astronomical Union, a small Solar System body (SSSB) is a celestial object that is neither a planet, a dwarf planet nor a natural satellite, namely an object orbiting the Sun, not massive enough to assume hydrostatic equilibrium, and that has not cleared its neighborhood. The most famous among the ranks of the SSSBs are classical asteroids and comets, but one can also find hybrid centaurs, with semi-major axes between the ones of the outer planets and presenting characteristics from both asteroids an comets, and the faraway trans-Neptunian objects small enough to not be considered as dwarf planets, and mainly located after Neptune's orbit. Only one asteroid is not considered as a small body, because of its size making it a dwarf planet: (1) Ceres, the first asteroid to be discovered, in 1801, by the Italian monk Giuseppe Piazzi.

Most of SSSBs are located in relatively stable regions, in particular in two circumstellar discs: the asteroid belt, between Mars' and Jupiter's orbits, and the much larger Kuiper belt, approximately from Neptune's orbit to 50 AU from the Sun (see Fig. 1.1). However, small bodies can be found almost everywhere in the Solar System, and even very close to the Earth; these are called near-Earth objects (NEOs), and most are asteroids (NEAs), and will be described later in more detail.

Since the two missions closely linked to my PhD (Hayabusa2 and OSIRIS-REx) target asteroids, I will focus more on this kind of small bodies than on others, although most results are applicable to all kinds of small bodies, as they all present low-gravity environments.

Asteroids are SSSBs different from comets as they are thought to be mainly composed of minerals and rocks, and not of ice and dust. However, the recent discovery of ice in the asteroid belt and of active asteroids suggests that the frontier between the two populations is not as sharp as previously thought, and that there is rather a continuum between the two populations. Most of the asteroids are located in the asteroid belt, which is thought to contain about 5×10^{-4} Earth masses (Krasinsky et al., 2002). It mostly goes from about 2.1 to 3.3 AU, but asteroids are not uniformly distributed along this distance, as they are several gaps, firstly noticed by Kirkwood in 1867 (Kirkwood, 1867), and therefore called *Kirkwood gaps*. They correspond to mean motion resonances with Jupiter, which increase the orbital eccentricity of a small body residing into it, so that it is transported in only a few million years in the near-Earth space (e.g. Gladman et al. (1997) and Granvik et al. (2018)). The biggest gaps are linked to the 4:1, 3:1, 5:2, 7:3 and 2:1 resonances. An a:b orbital resonance with Jupiter means that the ratio between the two orbital periods involves two integers a and b (a/b), which means that the celestial body performs *a* periods, Jupiter completes *b* periods.

1.1.2 Earth-based observations

Apart from a small list of asteroids that have been closely observed during flybys (see Section 1.2.2), only limited information is known for the major part of Solar System asteroids, and this information comes from Earth-based observations. As of August 2019, there were roughly 800,000 asteroids detected for which we knew the orbit, and we had enough data for more than 540,000 asteroids to give them numbered designations, according to the IAU Minor Planet Center (IAU Minor Planet Center, 2019). For 100,000 asteroids, measurements about their surface compositions through ground- or space-based spectral observations were available (Ivezić et al., 2001; Szabó et al., 2004; Nesvorný et al., 2005; Carvano et al., 2010). The future of asteroid

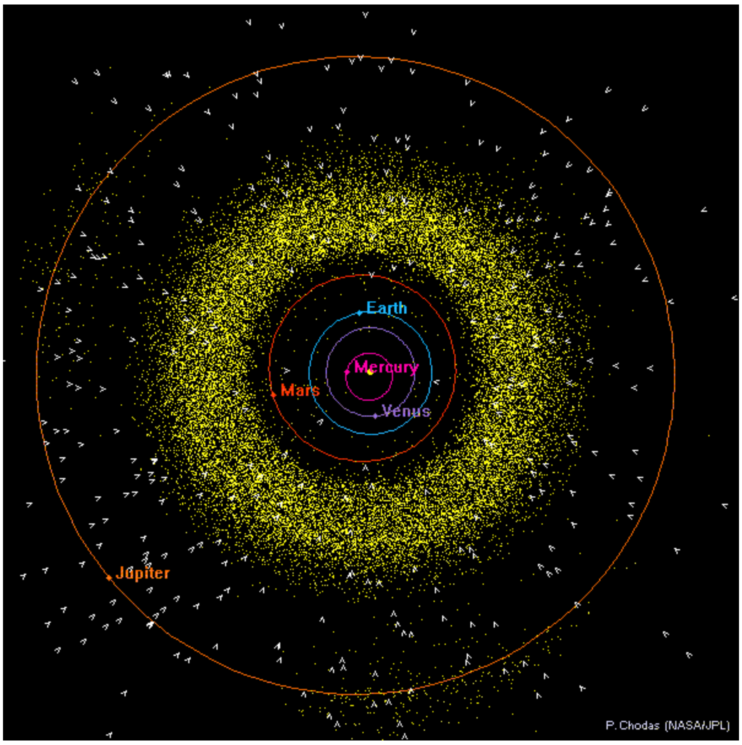

(a) Inner Solar System

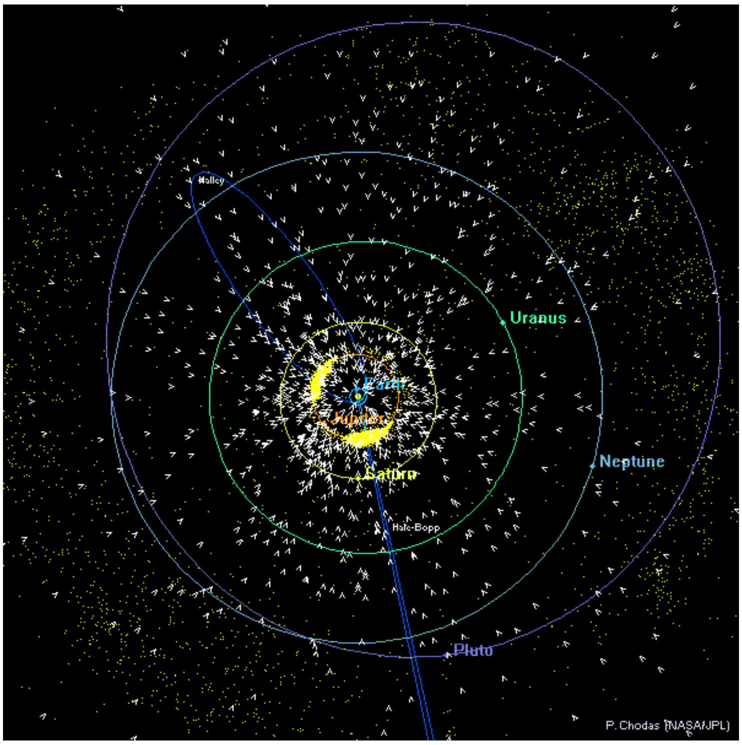

(b) Outer Solar System

Fig. 1.1.: Inner and outer solar system orbit diagrams. Numbered asteroids are yellow dots, and comets are sunward-pointing wedges. The orbits of planets and Pluto are also shown. Image credit: Courtesy NASA/JPL-Caltech.

detection and characterization is assured from Earth by large telescopes such as the LSST (Large Synoptic Survey Telescope) (Ivezić et al., 2007; Jones et al., 2009), and from space observatories such as Gaia (Mignard et al., 2007), which has already provided two data releases.

Several properties are accessible from Earth or from near-Earth space, for example we can measure in infrared the thermal emission of the asteroid, linked to the albedo and the surface area. Combinations of both visible and infrared observations, in a technique we call radiometry, enable to determine both albedo and mean radius.

Concerning their shape, the standard method for asteroids is lightcurve analysis. The changes in the photometric intensity of an asteroid as a function of time can give us hints about its shape and its rotation axis and sense. Another technique, using radar observation, is more precise but requires close enough objects, and therefore is more often used for near-Earth objects, as described later. However, lightcurve inversions can sometimes give reliable shape estimates, as demonstrated by the good comparison of the shape obtain for NEA 6489 Golevka by radar and lightcurve inversion techniques (Kaasalainen et al., 2002). Since a few years, the instrument SPHERE (Spectro-Polarimetric High-contrast Exoplanet REsearch) (Beuzit et al., 2008), initially developed to characterize extra-solar planetary systems with the VLT (Very Large Telescope), has been also used for solar system objects such as main-belt asteroids. Fétick et al. (2019) shows for example that from lightcurves captured by VLT/SPHERE/ZIMPOL (Zurich Imaging Polarimeter) (Schmid et al., 2018), the shape and the biggest surface features of large main-belt asteroids such as Vesta can be reconstructed very accurately. With the incoming new Earth-based telescopes (like the Extremely Large Telescope, or ELT) (ESO, 2019), the resolution will be even higher, dramatically extending our sample of asteroidal shapes and surface features and increasing our knowledge in this field.

1.1.3 Taxonomic complexes

From Earth-based measurements, asteroids were divided, according to their observed properties, into three major taxonomic complexes: the S-complex ("stony", supposedly with a silicaceous composition, with moderate silicate absorption features, and linked to ordinary chondrite meteorites), the C-complex ("carbonaceous", connected to carbonaceous chondrite meteorites, with low-albedo surfaces) and the X-complex (a degenerate complex with very low- or high-albedo surfaces). Complexes are again divided into taxonomic types depending on the spectral features observed from Earth. A detailed description of the spectral features of the three complexes and the different types can be found in Bus et al. (2002), DeMeo et al. (2009), and DeMeo et al. (2015). The spectral features could possibly give us information about the asteroid's surface composition, but the interpretation of spectral data can be difficult and information is limited to the first micrometers of the asteroid surface. Their composition tell us about the history of the Solar system and contain the record of the original composition of the Solar nebula. The age of the Solar System is currently estimated to be 4.567 billion years (Bouvier et al., 2010), thanks to meteoritic calcium-aluminium-rich inclusions (CAIs) which represent the oldest material that we have at our disposal. The age of the Solar System and the composition of the nebula where the Sun formed can be obtained by measuring the composition of asteroids and meteorites. Most of them, called chondrites, contain refractory inclusions (like CAIs) and chondrules, round grains that are believed to have been created 1-3 million years after inclusions in brief, but still not yet understood, heating events (Heide et al., 1995). Among chondrites, there are special meteorites, named CI chondrites, that do not contain any chondrule and are expected to represent the oldest solid materials within the Solar System, and therefore to be representative of the composition of the Solar photosphere (DeMeo et al., 2015). This explains the quest to link meteorite and asteroid compositions through spectral observations and ideally sample return space missions.

1.1.4 Near-Earth Asteroids

All asteroids are not constrained to the asteroid belt, and this is particularly due to a combination of collisions, a thermal process called the Yarkovsky effect (Bottke et al., 2002b; Bottke et al., 2006) and dynamical resonances. Every celestial body in the Solar System is subject to the influence of the Sun: through the gravitational attraction obviously, but also through solar radiation, and the reemission of the absorbed solar radiation by asteroids creates a small but continuous force leading to steady drifts of their orbital semi-major axes. This drift is called Yarkovsky effect, and depends on many factors, such as the size of the asteroid, its distance to the Sun and other properties. As its orbit drifts, the asteroid may reach an orbital resonance (Nesvorný et al., 2002) increasing its eccentricity and leading to possible interactions with terrestrial planets. Some of these asteroids have an orbit very close to Earth's one, and are therefore called Near-Earth asteroids (NEAs).

There are two types of resonances, the mean motion resonances (associated with Kirkwood gaps, as explained previously), and secular resonances. Numerical computations estimate that around $35-40\%$ of the near-Earth asteroids went through the secular resonance ν_6, and that $20-25\%$ came from Jupiter's 3:1 mean motion resonance (Gladman et al., 1997). Most of NEOs are either ejected from the Solar System, collide with the Sun, or are disrupted by it, by tidal or thermal forces. The rest collides with the Moon and the inner planets, such as the Earth, creating shooting stars, delivering meteorites, or producing massive extinctions, smaller damages and/or craters.

Properties and origins of Near-Earth Objects (NEOs, i.e., NEAs and other bodies, like comets, whose orbits bring them close to Earth's orbit) are described in Binzel et al. (2002), Morbidelli et al. (2002), and Morbidelli et al. (2015). Among NEOs are present the whole range of taxonomic classes observed in the Main Belt, which is an argument in favor of this region being the main supplier of the near-Earth population.

Craters on the Moon tell us that the impactor flux in the Solar System has been on average in a steady state number during the last 4 billion years. Since NEAs have a limited lifetime, they must thus be replenished. In fact, collisions continuously occur in the main belt. They generate new fragments that can either be directly injected in a resonance or drift into one through the Yarkovsky effect, feeding the NEA population and keeping it in a steady state.

Another source of NEAs are Jupiter-family comets, which represent only a small fraction (6%) of the whole NEO population (Bottke et al., 2002b).

Near-Earth asteroids are subdivided in several groups depending on their current orbit's semi-major axis and eccentricity, and accounting for Earth's aphelion (the point where Earth is the furthest from the Sun, i.e., 1.017 AU) (Shoemaker et al., 1979). For example, Amor asteroids have perihelia (points of their orbits closest to the Sun) greater than Earth's aphelion (but less than 1.3 AU), and therefore approach but never cross Earth's orbit. On the other hand, Apollo asteroids have semi-major axes greater than 1 AU but perihelia smaller than Earth's aphelion, and do intersect Earth's orbit. Most of the discovered NEOs (about 90%) belong to Amor or Apollo categories (Pater et al., 2015). Typical orbits for inner solar system asteroids are shown in Fig. 1.2.

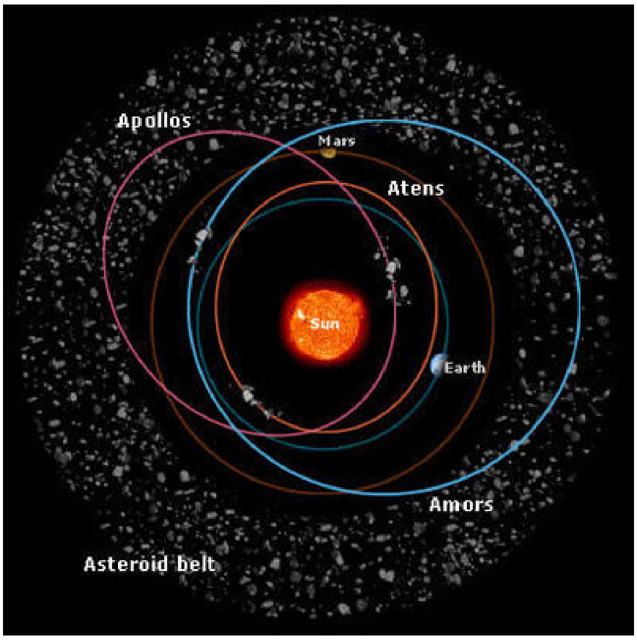

Fig. 1.2.: Typical orbits for inner solar system asteroids, with the orbits of Earth and Mars. Apollo and Aten asteroids cross Earth's orbit, contrarily to Amor asteroids. Image credit: ESA.

If an incoming NEA is at least several tens of meters in size, it can be a threat to cities, civilizations or even humanity, as one of them did 66 million years ago, leading to Cretaceous-Tertiary extinction (Renne et al., 2013). Indeed, the theory of a large bolide (10-15 km wide) impacting Earth and leading to the mass extinction was reinforced by the discovery of the Chicxulub crater underneath the Yucatán Peninsula in Mexico in the 1990s (Hildebrand et al., 1991). The impactor caused the quasi-instantaneous extinction of about 75% of all plant and animal species on Earth, among them the famous dinosaurs (Schulte et al., 2010). Such asteroids whose orbit can come within 0.01 AU of Earth's one are called Potentially Hazardous Asteroids (or PHAs). Making the inventory of NEOs and PHAs, characterizing them and validating deflection techniques will allow us to prevent future possibly catastrophic events. The latter is one of the primary goals of the DART mission (Double Asteroid Redirection Test, Cheng et al. (2018)), which goal is to strike with a kinetic impactor the moon of the binary NEA (65803) Didymos. DART should be followed by Hera (Michel et al., 2018), which should observe the result of the impact, such as the crater, the momentum transferred by the impact, the internal structure, and other dynamical and physical properties of the target.

Another motivation for studying NEOs is their potential future role in space exploration (Abell et al., 2015), as they could be used as refueling or resting bases during long journeys towards the outer Solar System, or in a shorter term as low-gravity laboratories to study the effects of low gravity and radiations on living forms of life (the human body, crops, etc.). Indeed, although it is still a challenge, it is less difficult to land and take off from an asteroid than on a planet with gravity and a poor atmosphere such as Mars, and they are thought to be rich in minerals that can potentially be used to generate propellant.

Furthermore, their proximity to Earth enables many ground-based observational techniques that cannot be used for Main Belt asteroids. Their shapes, some of their surface properties, their spin axis and other characteristics can be estimated from the ground with less but still existing difficulties than for Main Belt asteroids, much further away from the Earth. When they come close enough to Earth, observations using radar techniques can be performed. Planetary radar astronomy is a measurement method to learn about the shape and the surface of a close-enough celestial object by illuminating the object with radio waves and measuring the reflected signal. Radar telescopes can detect asteroids from a large range of size, from meter-scale 2006 RH120 to 33 km-diameter 1036 Ganymed, but also impact craters (4183 Cuno, 33342 1998 WT24 by Busch et al. (2008), 53319 1999 JM8 by Benner et al. (2002) and 185851 2000 DP107 by Naidu et al. (2015)) and boulders (Toutatis, comparison between radar images by Hudson et al. (2003) and Chang'e-2 spacecraft images by Huang et al. (2013)). The radar analyses also allow performing very high accuracy astrometry, which often allows eliminating collision solutions for NEAs with originally ambiguous trajectories. Radar astrometry has for example been used to estimate the shapes of 101955 Bennu, the target asteroid of the OSIRIS-REx (Lauretta et al., 2015; Lauretta et al., 2017) missions.

1.2 Asteroid surfaces

1.2.1 Regolith

Fly-by and even better rendezvous mission to asteroids lead to a better understanding and new discoveries. Indeed, information provided by ground-based observations (see Sec. 1.1.2) does not allow accessing detailed properties of an asteroid, specially concerning its surface and interior, or its boulder and crater distribution. In fact, one of the most essential characteristics of asteroids when we need to interact with them, whether for scientific purposes, for deviation or for asteroid mining, is their surface, and in some cases their subsurface. Yet, the surface, at least currently, can only be determined by close observations using flybys, rendezvous, or landings. Since only a few missions provided images of an asteroid from close enough to learn about their surface features, our knowledge about the asteroidal surfaces still presents several deficiencies. However, after each mission, our understanding of the surface properties and the different processes asteroids undergo strongly increases. A lot of characteristics and interpretations that came from those observations (and from comparisons with Earth) are detailed in this section. This increasing knowledge is for instance clearly visible in the *Asteroids* book series, which purpose is to describe new developments in this field on timescales of the order of a decade (Gehrels, 1979; Binzel et al., 1989; Bottke et al., 2002a; Michel et al., 2015a).

One of the realizations that came from close flybys and orbiting or hovering spacecraft is that all the small asteroids are not monolithic rocks but can also be rubble piles, i.e., they consist of many pieces of rock, which agglomerated and hold together thanks to self-gravity and sometimes a small amount of cohesion. There is now strong evidence that most of asteroids between a few hundred meters and 10 km, and maybe larger, are rubble piles (Pater et al., 2015; Walsh, 2018), as measured densities are much lower than the ones of meteorite analogues.

Even though we had direct evidence of a regolith layer on the Moon from images of the surface taken by first Apollo missions (Shoemaker et al., 1967; Shoemaker et al., 1969), it was believed that asteroids could not keep any loose material on their surface due to their low-gravity and to the assumed high ejection speeds of ejecta produced by impacts (Chapman, 1976; Pater et al., 2015). However, missions such as NASA's Galileo (in 1991 and 1993), NASA's NEAR-Shoemaker (in 2000-2001) and JAXA's Hayabusa (in 2005) found the presence of regolith on the surfaces of, respectively, (951) Gaspra and (243) Ida (Veverka et al., 1994; Belton et al., 1996), (433) Eros (Sullivan et al., 2002; Robinson et al., 2002), and (25143) Itokawa (Fujiwara et al., 2006).

Even if we already had different examples of granular media on Earth (see Section 1.3.2), such low gravities and completely different environments could mean different ways to react to external stimulations (e.g., impacting meteoroids, solar wind, cosmic rays or even man-made landers). Despite these direct observations of regolith, the structural properties, the contact forces, and the dynamics of the grains are still poorly understood, especially in these low-gravity environments. Yet, a better understanding of the nature of the regolith on the surface of asteroids as well as its physical properties is essential in order to perform any operation on the surface of asteroids leading to interactions with the grains, even more considering the cost of space missions (about US \$300 million for Hayabusa2 without civil service staff and university professors salaries, and \$1 billion for OSIRIS-REx including all salaries) and the possibility of future mining.

One of the most recent definitions of regolith was given by Robinson et al. (2002) as “loose unconsolidated material that comprises the upper portions of the asteroid”. Since it is believed to occupy the top layers of the asteroid, and thus the surface and sub-surface, the regolith has several effects on asteroid observations. It was therefore possible to infer from Earth-based observations the presence of a granular medium before the first asteroid flybys. However, the surface properties cannot be completely determined from Earth, and to be certain of a significant amount of regolith as well as to characterized its detailed properties, flybys and even closer observations were necessary. Nonetheless, observational features due to the presence of regolith are now detectable from Earth. One of them is the opposition effect, or opposition surge, which results in a change in asteroid brightness as a function of the phase angle Φ, i.e., the angle between the Sun, the object and the observer. This effect was first discovered by Gehrels (1956), who found that when the phase angle decreases and goes closer to $0°$, the intensity strongly increases. Indeed, the asteroid brightness corresponds to reflected sunlight by particles on the surface. When the phase angle is high, the irregularity of the terrain, as well as in a microscopic scale the granularity and porosity of the regolith, create shadows on the surface (sometimes imperceptible), and coherent backscattering (representative of a granular medium). When the incoming sunlight is normal to the surface, there are no or less shadows and coherent backscattering, and the albedo of the asteroid increases. The smaller the irregularities, the smaller the phase angles corresponding to drastic changes of intensity. For example, Buratti et al. (1996) showed that, for the Moon, a change from $4°$ to $0°$ in the phase angle implies an increase of 40% in brightness. Muinonen et al. (2002) also described the opposition effect for different asteroids such as (4) Vesta, the second largest asteroid in the Main Belt and the brightest one.

Another effect of the presence of regolith on the surface of asteroid is their polarization, and the way it changes as a function of the phase angle. These changes are usually the indication of porous material or particulate surfaces. C-type asteroids (like Ryugu and Bennu) show for example the steepest slopes, meaning the polarization of the observed objects changes faster with the phase angle. This slope is directly linked to the albedo of the asteroid, and not to the nature of the surface, and therefore the albedo can be determined by polarimetry. As the influences of albedo and radius can be difficult to discern from direct observations, this method is an alternative to provide only the albedo, hence splitting the two properties.

To summarize, regolith seems ubiquitous on all asteroid surfaces, as evidenced by close and remote observations. However, regolith is not necessarily as homogeneously distributed on the surface as one could think, and is not always the unique component. This will be demonstrated by the description of asteroid surfaces observed by spacecraft in the following section.

1.2.2 Visited asteroids

Up to now, a total of 16 minor planets have been visited by spacecraft. Since the targets of OSIRIS-REx and Hayabusa2, which are the two missions to which I participated during my PhD, are small asteroids (diameter of the order of the kilometer or less), I do not present here our knowledge on the surface of the largest asteroids (1) Ceres and (4) Vesta, visited by Dawn (Russell et al., 2013; Russell et al., 2016), but rather a quick chronological overview of the knowledge regarding the other asteroids visited by spacecraft, by insisting on the NEAs visited with rendezvous and therefore on (433) Eros and (25143) Itokawa. Further details can be found in the articles mentioned in respective subsections, as well as in Barucci et al. (2015) and Murdoch et al. (2015).

Images of all visited asteroids show evidence of the presence of regolith as well as linear structures, that can be decomposed into four basic types according to Thomas et al. (2010): troughs, grooves, ridges and modifications of crater shapes. These linear structures are evoked in the coming descriptions. Asteroids are first introduced with their full names as defined by the International Astronomical Union, and then only the names without the number.

Asteroids visited by flybys

Several asteroids were visited by flybys, but the brevity of the observations and the relative speeds between objects do not enable observations and measurements as high-resolved as for a rendezvous. Nevertheless, we learned a lot from these flybys about the asteroids and, above all, on their surfaces. I concentrate here on the detection of regolith or of signs suggesting the presence of granular material on the surface. I do not consider here (9969) Braille (Buratti et al., 2004) and (5535) Annefrank (Hillier et al., 2011), because their surfaces could not be resolved.

Asteroid (951) Gaspra

The first asteroid visited by a spacecraft was S-type, main-belt asteroid, (951) Gaspra, by NASA Galileo on its way to Jupiter in 1991. Its geology is described in Carr et al. (1994). Grooves were observed on the surface and suggest the presence of a regolith layer on the surface, supposedly with a thickness of several tens of meter.

Asteroid (243) Ida and its satellite Dactyl

In 1993, the Galileo spacecraft also crossed path with main-belt (243) Ida, an irregularly-shaped S-type asteroid, and discovered a small natural satellite later called Dactyl. Ida's geology is described in Sullivan et al. (1996). Both bodies present distinct spectral properties and composition (Pater et al., 2015). Massive rocks from 45 to 150 m were detected, and the impact-dominated surface suggests a 50 m thick layer of potentially mobile material on the surface (Sullivan et al., 1996).

Asteroid (253) Mathilde

On its way to (433) Eros, NASA NEAR-Shoemaker (Cheng et al., 1997; Cheng, 2002) performed a flyby of the very dark main belt asteroid (253) Mathilde in 1997, providing the first images from spacecraft of a C-type asteroid (Veverka et al., 1999). Mathilde's low density (1.3 ± 0.3 g cm^{-3}) and its spectral similarities with CM chondrites suggest a high fraction of porosity, between 40 and 60% (Veverka et al., 1999). There was no detection of ejection blocks larger than 300 m across (detection limit), or no evidence of surface modifications due to impact ejecta, contrarily to Ida (Geissler et al., 1996).

Asteroid (2867) Šteins

E-typed (2867) Šteins was observed by ESA's Rosetta on its way to comet 67P/Churyumov-Gerasimenko (Keller et al., 2010) in September 2008. It is a irregular, oblate, body, with an average diameter of 5.3 km. A gigantic crater, whose diameter has been estimated to 2.1 km, has been identified in its south pole, as well as 23 other craters. Linear structures are also visible on the surface, such as linear faults and an apparent crater chain. It is believed to be a rubble pile, probably shaped by the YORP effect (Keller et al., 2010).

Asteroid (21) Lutetia

After flying by Šteins, Rosetta was also able to visit another main belt asteroid, (21) Lutetia, in July 2010, before reaching its comet target (Sierks et al., 2011). Lutetia is a M-type asteroid, an unusual spectral type. M-type asteroids are believed to be the source of iron meteorites and the remnants of metallic cores of former differentiated asteroids. Lutetia's density was measured to 3.4 ± 0.3 g cm^{-3}, i.e., one of the highest densities measured so far (Sierks et al., 2011). An image of Lutetia taken by OSIRIS camera onboard Rosetta is shown in Fig. 1.3.

Lutetia shows a very complex surface, with regions much older than others (and much more cratered), a high ridge, and many lineaments. Thorough descriptions of Lutetia surface, and descriptions of the regions can be found in Sierks et al. (2011), Massironi et al. (2012), and Thomas et al. (2012). Baetica contains a cluster of craters, shown in Fig. 1.3, that have certainly been formed by a succession of impacts (Massironi et al., 2012). These impacts may have caused the covering or filling up of smaller craters, explaining the shortage of craters in this region (Sierks et al., 2011; Vincent et al., 2012). The global shortage of small craters on Lutetia can be explained by the presence of a regolith layer, whose thickness was estimated from ejecta blankets as about 600 m (Vincent et al., 2012), and by seismic shaking inducing crater covering or degradation. However, the shortage of craters with diameters up to 8 km should be explained differently.

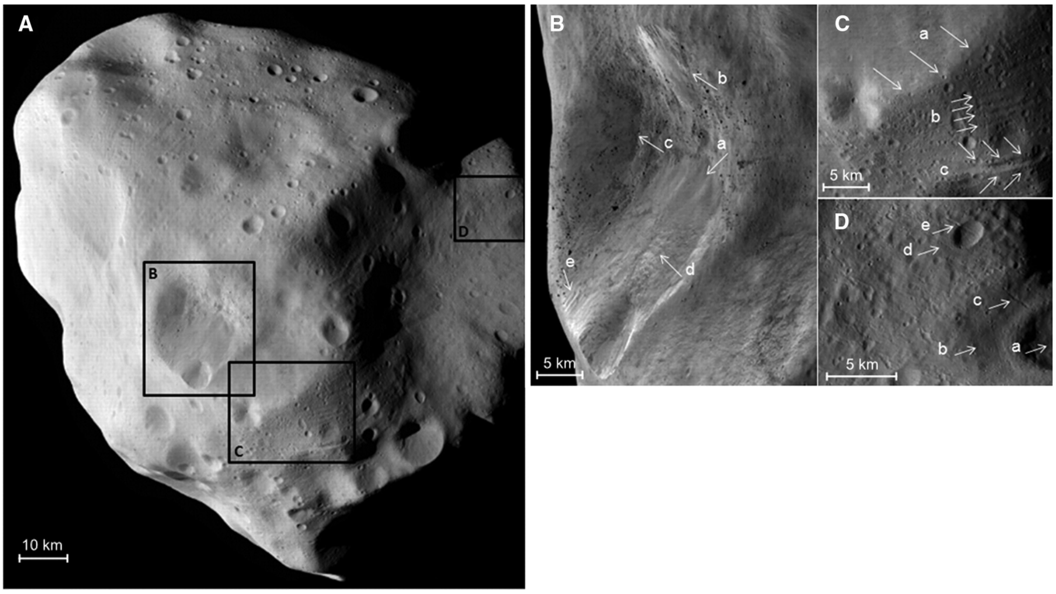

Fig. 1.3.: Closest approach image of Lutetia **(A)** with details shown under different illumination conditions in **(B)** to **(D)**. In **(B)** is shown the 21 km-diameter central crater cluster (in Baetica), with arrows pointing landslides. In **(C)** is the boundary between Baetica (young terrain) and Noricum (old terrain), and in **(D)** arrows show curvilinear features in Narbonensis. Image credit: Sierks et al. (2011)

Asteroid (4179) Toutatis

After having fulfilled its mission to orbit the Moon, Chinese Chang'E-2 mission was extended to visit S-type near-Earth asteroid (4179) Toutatis, and was able to take close images of the asteroid in December 2012 (Zhu et al., 2014). Descriptions of the surface can be found in Huang et al. (2013) and Zhu et al. (2014). Images of Toutatis and its surface morphology are shown in Fig. 1.4. Its actual shape is strikingly similar to that predicted by radar observations from Earth (Hudson et al., 2003). Toutatis' porosity, as well as its morphology and its surface, are very similar to (25143) Itokawa (see Section 1.2.2), and it is thought to be a rubble pile too (Huang et al., 2013).

A regolith layer was detected from crater blankets made of fine grains, and from smaller (smaller than $30-50$ m), less degraded, bowl-shaped, craters, its thickness was estimated to at least several meters, even if it is still uncertain. The shortage of observed small craters could be due to illumination bias or to relatively recent large impacts that could have erased the smallest craters (Zhu et al., 2014).

I now describe the only (before 2018) near-Earth asteroids visited by rendezvous, namely (433) Eros and (25143) Itokawa. Thanks to the rendezvous,

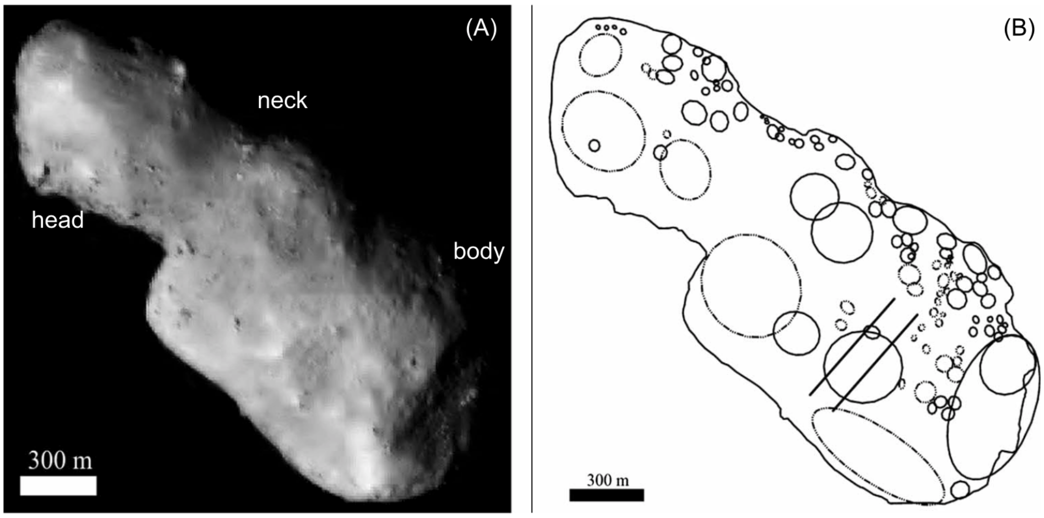

Fig. 1.4.: Images of Toutatis and its surface morphology. In **(A)**, the spatial resolution is 8.3 m/pixel. In **(B)** are shown grooves (straight lines), confirmed craters (solid circles), and unconfirmed ones (dashed circles). Image credit: Zhu et al. (2014)

the resolution of images is much higher than for flybys, and the quasi-totality of the asteroid can be observed.

Asteroid (433) Eros

(433) Eros was the first asteroid to be orbited by a spacecraft and to witness the first interaction of an artificial satellite with an asteroid surface, since it was decided to land (crash) the spacecraft on Eros at the end of the mission. NEAR-Shoemaker (Cheng et al., 1997) did a close fly-by of Eros in December 1998 and then began its orbit around it in February 2000, to finally end on its surface in February 2001 (Cheng, 2002). Therefore, images of Eros surpass all previous asteroid ones, and the proximity enabled resolutions from orbit as low as meters. A picture of Eros is shown in Fig. 1.5.

Eros is an S-type asteroid, with a mean radius of about 8.4 km (Yeomans et al., 2000). Thanks to the orbit of NEAR, studies of its surface could be much more thorough than for previous visited asteroids. Its surface features are described in Veverka et al. (2000), Veverka et al. (2001a), Veverka et al. (2001b), Thomas et al. (2002), Robinson et al. (2002), Prockter et al. (2002), and Buczkowski et al. (2008), and several other papers. A substantial summary of in situ observations of Eros surface can be found in Murdoch et al. (2015).

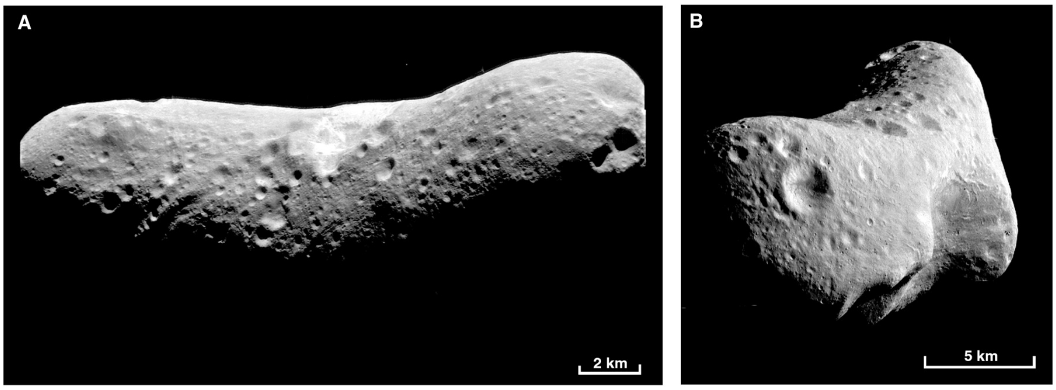

Fig. 1.5.: Mosaic of images taken from 190 km for **(A)** showing the densely cratered area, and from 230 km for **(B)** showing the sparsely cratered area. Image credit: Veverka et al. (2000)

Eros has an irregular shape, as shown in Fig. 1.5, and is covered with a regolith layer. It is scattered with craters, ejecta blocks and other geological features. Two major features on Eros surface are the titanic saddle-like depression Himeros, larger than 10 km, looking like a highly-degraded crater, and the bowl-shaped crater, 5.3 km-diameter, Psyche. Eros' density was measured to be 2.67 ± 0.03 g cm-3 (Yeomans et al., 2000), and its internal porosity was estimated to be about 20%, i.e., much less than Mathilde.

Regolith motion

In a general way, Eros has quite uniform color and albedo. Nonetheless, bright (particularly on steep slopes) and dark (on the bottom of topographic lows) features were observed. Since composition is the same, these variations are believed to be due to the freshness of the material. Bright material could thus be newly uncovered material that space weathering had not altered yet, following downslope movement of regolith (Robinson et al., 2002; Thomas et al., 2002). Such indicators of downslope motion are also observed for slopes gentler than what is believed to be the angle of repose of the material. A trigger mechanism could therefore be at the origin of the motion, for example impact-induced seismic shaking, but that is still under discussion. Two craters on Eros are shown in Fig. 1.6, and exemplify the differences of albedo inside larger craters: dark material at the bottom of the crater, and bright material on the slopes.

The layer of regolith observed on Eros is believed to have an average thickness of about several tens of meters (Barnouin-Jha et al., 2001; Veverka et al., 2001a; Robinson et al., 2002). This regolith layer is not uniform over the surface of Eros; this heterogeneity could be due to the ejecta blankets

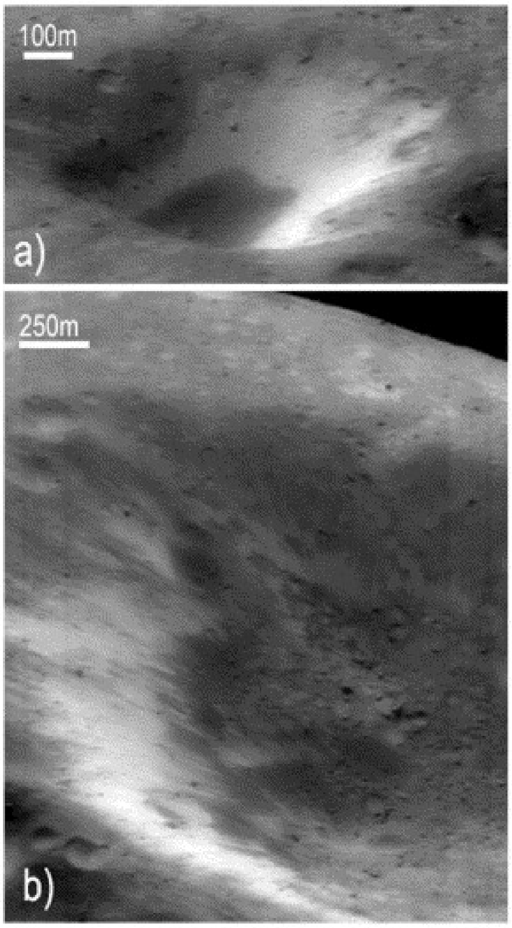

Fig. 1.6.: Two craters on Eros: Valentine Crater in **(a)** (1.4 km-diameter) and Selene Crater in **(b)** (3 km-diameter), whose albedo pattern is similar to Psyche. Image credit: Mantz et al. (2004)

created by impacts on the surface, amplified by the fact that craters are also irregularly distributed on Eros surface, as shown in Fig. 1.5. The regolith layer is made of particles of various sizes, from centimeter-sized dust particles filling topographic lows in what are called "ponds", to ejecta blocks larger than 8 m (about a million of boulders with diameter between 8 and 100 m) (Thomas et al., 2002).

Craters

A large number of craters were observed on Eros, but they are not homogeneously distributed, as shown in Fig. 1.5. Fresher craters show larger depth-to-diameter ratios than older ones, meaning that craters are degraded with time, and there is a lack of small craters (with diameter smaller than 2 km) (Veverka et al., 2000; Veverka et al., 2001b). This is another sign of regolith motion, that could be due to seismic shaking, microcratering, or alternations of thermal cycles weakening structures (Veverka et al., 2001b; Cheng, 2002).

Linear features

Linear structures, such as depressions, ridges, scarps, crater chains were also observed on Eros (Veverka et al., 2000). In order for these features to exist in such an environment, Eros needs a cohesive strength so high that it should be a coherent body, and its irregular shape and relatively low internal porosity also advocate for a high strength. The diversity in the orientation of these features suggests that they were formed during separate events (Veverka et al., 2000; Robinson et al., 2002; Thomas et al., 2002; Prockter et al., 2002). These linear features were observed on a global scale on Eros but also at smaller scales with observed structures ranging from kilometers to tens of meters (Prockter et al., 2002).

Moreover, linear features are usually associated with craters and are ubiquitous on all larger asteroids except maybe on Mathilde.

Asteroid (25143) Itokawa

Several space milestone were reached with (25143) Itokawa: it was the smallest visited asteroid and the first one not visited by NASA, and above all it was the first target of a successful asteroid sample return mission, namely Hayabusa (Yoshikawa et al., 2015).

Hayabusa mission

Hayabusa was a Japanese mission launched by the Institute of Space and Astronautical Science (ISAS), which merged in 2003 with two other Japanese space centers to form the Japan Aerospace eXploration Agency (JAXA). In addition to being the first mission to go to an asteroid and return back to Earth with an asteroid sample, as well as the first spacecraft to visit a sub-kilometer-sized asteroid (Yoshikawa et al., 2015), it also made the demonstration of Electric Delta-V Earth Gravity Assist (EDVEGA) technology with ion engines (Kawaguchi et al., 2004).

The spacecraft was launch on May 9, 2003 and, in May 19, 2004, performed a Earth swingby (Kawaguchi et al., 2004), to finally reach the asteroid (25143)

Itokawa on September 12, 2005. However, everything did not work as planned and the spacecraft experienced several difficulties. Firstly, it suffered the largest solar flare on record, which resulted in solar panels' degradation, and therefore a reduced amount of energy dedicated to the ion engines (Yoshikawa et al., 2015). Then, during the touchdown practice maneuvers, it released the surface robot MINERVA (MIcro/Nano Experimental Robot Vehicle Asteroid), but it missed its target and went wandering into space.

On November 20, 2005, the spacecraft attempted its first touchdown in order to collect samples. It reached its target marker on the surface and was ready to shoot, but the obstruction detection sensor malfunctioned and no projectile was shot. The spacecraft bounced on the surface and waited 30 minutes to finally receive the emergency lift command sent from ground control. Five days later, a second touchdown was attempted. All on board sensors seemed to claim it was a success; however, the projectile trigger was in safe mode due to the first attempt and did not shoot. Fortunately, probably due to static electricity and the several contacts with the surface during the two touchdown attempts, several particles made their way into the sampling capsule (Tsuchiyama et al., 2011).

Other incidents kept on happening during the way back to Earth, like a RCS (reaction control system) fuel leak causing a loss of attitude control, and a seven-week loss of communication with ground control, but Hayabusa's team finally managed to overcome these incidents and recovered the capsule in Australia (Kawaguchi et al., 2010). Despite all these incidents, the Hayabusa mission, from the on-board cameras and the collected particles, brought insightful information about Itokawa and more generally about NEAs.

Itokawa global properties

From Earth, Itokawa was determined to be a S-type near-Earth asteroid, a 500 m-diameter slightly flattened ellipsoid (Sekiguchi et al., 2003; Ostro et al., 2004; Müller et al., 2005). When Hayabusa reached the asteroid, accurate measurements could be done, for example concerning its bulk density and its spectra, leading to a small object whose size is $535 \times 294 \times 209$ m, close to what was expected from ground-based observations, with a spin period of about 12 h, a bulk density of 1.9 g cm^{-3} (Fujiwara et al., 2006) and no satellites (Fuse et al., 2008). The bulk density and its similarity in spectra with LL ordinary chondrites suggested a porosity of about 40%, in agreement with the asteroid being a rubble pile. It has a bifurcated shape, with a "head" and a “body”, as shown in Fig. 1.7 from (Saito et al., 2006). Itokawa had a shape and a surface different from any other observed so far. The spacecraft landed near MUSES-C region, indicated in Fig. 1.7.

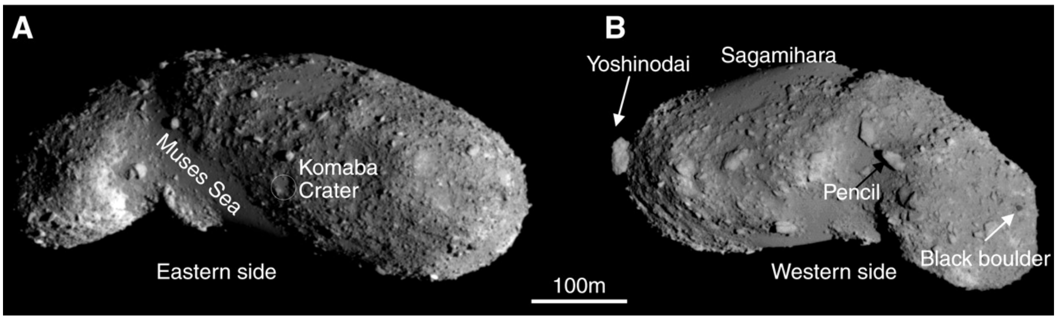

Fig. 1.7.: Eastern (left) and western (right) sides of asteroid Itokawa from Hayabusa spacecraft. Image credit: Saito et al. (2006)

Regolith and boulders

The surface of Itokawa can be divided in two types: rough terrains, with numerous boulders, and smooth terrains, covered with a layer of regolith. In the rough terrain, the average density of boulders larger than 5 m is 10^{-3} km^{-2} (Michikami et al., 2008), which is slightly higher than the density on Eros (Thomas et al., 2001), the largest boulder Yoshinodai being as large as $50 \times 30 \times 20$ m (a tenth of Itokawa) (Saito et al., 2006). In principle, if boulders originate from an impact cratering event, once can estimate the crater radius from the boulder sizes (Gault et al., 1963; Lee et al., 1996; Thomas et al., 2001). The boulder sizes on Itokawa would then imply a much larger crater than the ones detected on its surface. A better scenario is then that those boulders are part of the reaccumulation process that formed Itokawa during the disruption of its parent body, also in favor of a rubble pile structure (Michel et al., 2001; Yoshikawa et al., 2015). Michikami et al. (2008) found that the cumulative size distribution of boulders shows a slope index of -3.1 ± 0.1, similar to the value found by Thomas et al. (2001) for $15 - 80$ m-boulders on Eros.

Concerning the regolith on the surface of Itokawa, it is interesting to notice that there are locations where the ground appears very rough and boulder-studded, and therefore is not favorable for a landing. In these regions, the topographic level can increase by 4 m over several meters, and no particles smaller than 1 cm are expected to be present (Barnouin-Jha et al., 2008).

The sampling site was rather chosen to be in the “Muses Sea”, one of the two fine-regolith regions, alongside with “Sagamihara”. There, the regolith is expected to be centimeter- to millimeter- particles (Yano et al., 2006). Interestingly, the particles that were brought back to Earth are much smaller than the ones covering the surface (most collected particles are smaller than $10\ \mu$m). Nevertheless, the apparent absence of fines can be explained by the possibility that they left the surface due to electric-charge-induced levitation (Lee, 1996; Kimura et al., 2014), or could have migrated inwards (Asphaug, 2007; Miyamoto et al., 2007), or may be due to the fact that small ejecta from cratering have ejection speeds that are systematically larger than the escape speed of Itokawa and consequently never fall back on the surface (Nakamura et al., 1994). Regolith motion is supported by the round shape of some particles collected, possibly due to friction between grains (Tsuchiyama et al., 2011). The fine-regolith regions are globally homogeneous, roughly flat, and correspond to low gravitational potentials. It is believed that the smaller particles in these regions left the actual boulder-filled regions and were transported to gravitational lows, creating a 2.5 m regolith layer (Miyamoto et al., 2007; Cheng et al., 2007; Barnouin-Jha et al., 2008).

Craters

The number of craters found on Itokawa was much lower than on Eros, and no small crater (diameter smaller than 1 m) was distinctly detected by Hayabusa (Saito et al., 2006; Fujiwara et al., 2006). The absence of small craters and the lack of larger ones could be explained by regolith motion, probably due to impact-induced seismic shaking (Richardson et al., 2004; Michel et al., 2009). Observed craters in the transitional areas between smooth and coarse regions confirm this theory as they have low depth-to-diameter ratios and their floors are filled with fine regolith (Saito et al., 2006; Barnouin-Jha et al., 2008).

Linear features

No linear structures as global as the ones on Eros were found on Itokawa (Fujiwara et al., 2006). However, smaller ones, identifiable as alignments of boulders (Cheng et al., 2007) were found in “the body”. A ridge in particular, about 2.5 m high and hundreds of meters long, was identified (Barnouin-Jha et al., 2008). In general, lineaments (linear structures) on Itokawa have considerable lateral extent compared to their small heights, and may have a major role in Itokawa topography (Barnouin-Jha et al., 2008).

1.2.3 Current missions

During my PhD, our knowledge of asteroid surfaces significantly increased due to the first images and close observations of two asteroids of the C complex, (162173) Ryugu and (101955) Bennu, respectively by sample return missions Hayabusa2 (JAXA) and OSIRIS-REx (NASA). I had the privilege of being part of both teams, and I present in the dedicated chapters the missions, as well as the first interpretations of the surface images and associated publications to which I contributed in the scope of my PhD. Hayabusa2 and its target asteroid Ryugu are treated in Chapter 3, and OSIRIS-REx and its target asteroid Bennu are treated in Chapter 6.

As we have seen, depending on their size, their composition, and their history, observed surfaces of visited asteroids can be very different. However, many mechanisms are recurrent, as well as the presence of granular material (which can be very coarse such as on Ryugu, or much finer like in Itokawa smooth regions). Since, during my PhD, I concentrated on granular asteroid surfaces, I present in the following section a brief and non-exhaustive presentation of our knowledge on granular matter.

1.3 Granular Matter

In Section 1.2, I described the latest discoveries about asteroid surfaces, and defined regolith as granular matter. Here, I briefly review our current knowledge of granular matter, focusing on aspects that are relevant for our applications.

1.3.1 General introduction

First of all, granular matter deals with large numbers of macroscopic solid particles, dissipating energy through contact forces between each other associated with various kinds of friction (Jaeger et al., 1996; Duran, 2000; Richard et al., 2005). Granular matter is not a phase of matter, but shares attributes of several phases: depending on the energy of each grains and the fraction of space occupied by grains in the material (called packing fraction), granular matter can behave like a solid, a liquid or a gas, making it thixotropic.

When the energy per grain is very low and grains have small speeds relative to each other, for example in a heap, the material is "quasistatic" and behaves like a solid state. In this solid-like state, stress and forces are not distributed uniformly but along networks called force chains, linking particles in contact resting on one another. Force chains are where the highest stresses are experienced, shielding the other particles at rest that are not part of these chains with mechanisms similar to the ones in vaults and arches. An example of force chains is shown in Fig. 1.8, from Zhang et al. (2008).

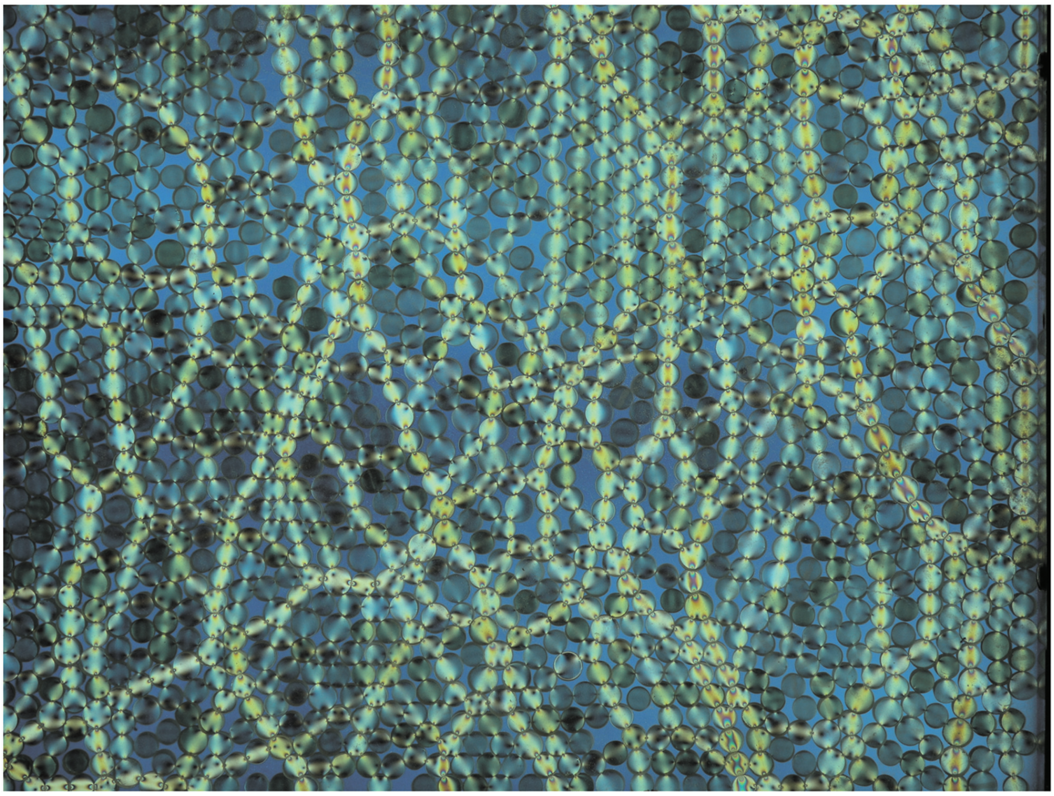

Fig. 1.8.: Snapshot of a granular shear experiment with photoelastic disks. The higher the contact forces, the brighter the disk. Image credit: Zhang et al. (2008)

Due to the presence of force chains, the force transmission is nonlinear and depends on the position of these chains. As a consequence, effects are not necessarily confined at the contact point and propagate through the granular material along the force chains. For example, during grain silos or hoppers discharges, the containers can experience high stresses and the sides can break before the bottom (Jaeger et al., 1996; Schwartz et al., 2012).

When the energy per grain increases, the granular material behaves more and more like a fluid, leading to dense flows. Particles still have many neighbors and there are many interactions between particles, but they are not stuck together like in the solid-like state described previously. Liquid state behaviors are then discernible in the granular flow: Nichol et al. (2010) fluidized a granular medium, and observed high-density probes sinking, low-density probes floating at height dictated by Archimedes law, and drag forces scaled linearly with the velocity. This confirms that granular matter, under certain conditions, can behave like a fluid.

If the energy per grains keeps increasing, the number of particles in contact with each other decreases and the contacts last less time. Granular matter then behaves like a gas. The granular material can be defined as granular gas when the time between collisions is much larger than the duration of a collision, meaning particles do not often directly interact with each other, or at least much less than for the previous described states. In these more dilute flows, the root mean square of grain velocity fluctuations can be compared to a gas thermodynamic temperature. However, there are still behaviors that differ between a granular gas and a gas: since the collisions between grains are dissipative, particles forming the granular gas tend to cluster and therefore will not be as spread as they would be for a gas. These states and the transitions from one to another are thoroughly described in Andreotti et al. (2013), and an example including the three regimes of a granular material is shown in Fig. 1.9.

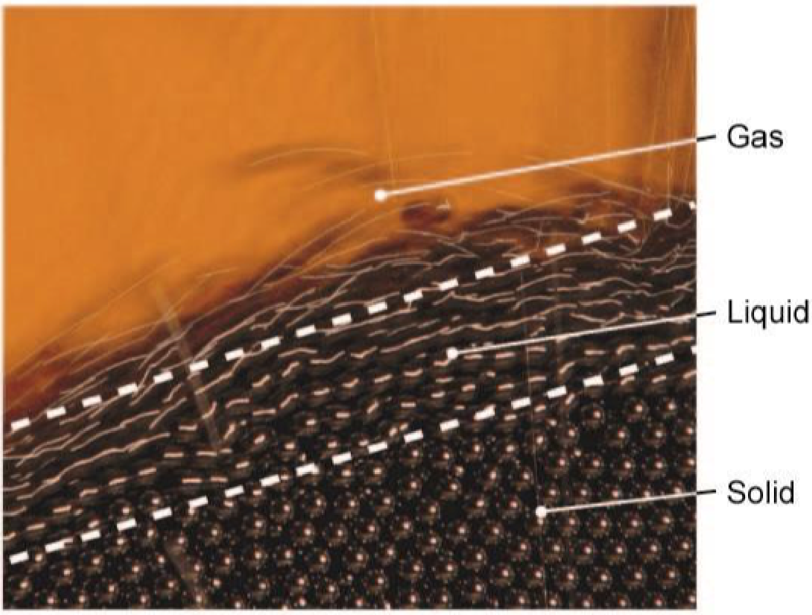

Fig. 1.9.: Illustration of the three flow regimes with the pouring of steel beads on a pile: ballistic grains on top behave like a gas, bouncing over the denser flow of beads, similar to a liquid. This liquid-like phase flows over static beads in the pile, representative of a solid-like regime. Image credit: Forterre et al. (2008)

Thus, the model chosen to represent a granular material depends on the considered regime. For a quasistatic case, models coming from continuum and solid mechanics, are adapted, for example if the grains are very small compared to characteristic length scales, and if the deformations are small enough (Holsapple et al., 2006). Classic continuum mechanics models can use perfect elasticity, meaning that a deformed material return to its original shape once the applied stress is removed. In theory, this is true as long as the applied stress is smaller than the yield stress; beyond that point, plasticity has to be considered (changes due to an applied stress are non-reversible anymore). The yield criterion, defining the elasticity limit under any combination of stresses, can be defined by many different theories, such as the Mohr-Coulomb yield criterion (using cohesion and angle of internal friction) or the Drucker-Prager yield criterion, a smooth version of the Mohr-Coulomb one.

For a liquid-like state, such as dense granular flows, fluid mechanics can be used to model granular material (Forterre et al., 2008). Usually, in this case, a set of four equations can be established: a continuity equation (from conservation of mass), a momentum equation (from conservation of momentum), an energy equation (from conservation of energy), and an equation of state (describing the state of matter under defined physical conditions).

Finally, for a gas-like phase, when the medium is very diluted and collisions between particles are uncommon (at least much less common than in previously cited states), models from kinetic theory can be used (Jenkins et al., 2002). If collisions are instantaneous and the density is low enough, a "granular temperature" can be defined, depending on the differences of translational and rotational velocities of the grains and the average values for both velocities. This temperature is comparable to the thermodynamic temperature, but is a different quantity.

1.3.2 Granular material on Earth

A lot of studies have already been devoted to granular matter: it is no surprise as it is very common to find granular material on Earth. The first example that comes in mind is sand. However, granular material on Earth is not reduced to sand. They are "the second-most manipulated material in industry" according to Richard et al. (2005); among them can be found nuts, rice, coffee, corn flakes and fertilizer. Many industries are therefore interested in granular matter physics, and they are plenty of applications. Hopper discharges and induced stresses have been studied as previously mentioned, and are interesting for the design of silos and hoppers, for example to size the cylinder or the neck. Rockslides observed for example in mountains are also considered as granular material processes.

Another phenomenon characteristic of granular materials observed with everyday life's objects is granular convection. When assorted nuts of different sizes are together in a container, largest particles (in this case Brazil nuts) will end up on the surface. Granular convection is, for this reason, also called "Brazil nut effect" (Rosato et al., 1987). There are different theories concerning the reasons of Brazil nut effect with possible implications for asteroid surfaces, and more details can be found in Section 1.3.5.

Different examples of granular material found on Earth are shown in Fig. 1.10; among them are ball pit balls in playgrounds, stone fragments near lakes, assorted beans, and pharmaceutical pills. This figure shows the diversity of granular media on Earth.

Fig. 1.10.: Images of granular materials found on Earth. From top to bottom and from left to right, a ball pit, stone fragments, beans in brown sacks, and pills.

1.3.3 Granular material in the Solar System

Granular material are widespread all over the Solar System.

As previously stated, extraterrestrial regolith was first discovered on the Moon by Shoemaker et al. (1967), following the landings of the Surveyors landers, and lunar regolith is now the most studied and best understood surface on an airless body (Heiken et al., 1991). Astronauts and rovers on the Moon also confirmed the presence of a very fine granular material on the surface (see image from Apollo 11 in Fig. 1.11a). Regolith layers on the Moon are believed to expand from $4-5$ m on the mare to 20 m in the highlands, and the density increases very fast with depth, following a power-law fit given by $\rho = 1799z^{0.056}$ kg m^{-3}, where ρ is the bulk density and z is the depth in m.

Granular material was also found on other small bodies, such as Martian moons Phobos and Deimos. They are both irregularly shaped, with respective average radii of 11 km and 6 km. Their surfaces are very smooth, and the in-filled craters suggest the presence of a regolith layer. A description of Phobos and Deimos surface topographies can be found in Thomas (1993), and part of Phobos surface is shown in Fig. 1.11b. Phobos has spectral characteristics similar to low-albedo D-type asteroids, and two scenarios have been proposed for their origin: a giant impact with Mars or captured asteroids (Burns, 1992; Barlow, 2008).

Saturn's rings, first discovered by Galileo Galilei in 1610 and identified as rings by Christian Huygens in 1655, are one of the most remarkable features of the Solar System. The rings are very thin compared to their size, as their thickness ranges from 10 m to 1 km, whereas the main rings extend from $7,000$ km to $80,000$ km. The observed spectra are dominated by water ice particles (and partly rocky material, like silicates or tholins), with a grain radius of $5-20$ μm (Nicholson et al., 2008), certainly covering the largest ring particles making up the visible rings, of sizes estimated between a few centimeters to several meters (Marouf et al., 1983; French et al., 2000). An image of Saturn rings taken from the Voyager probe is shown in Fig. 1.11c.

The origin of Saturn's moons, such as Enceladus, could be the gravitational accumulation of the granular material forming the rings beyond Saturn's Roche limit (inside the Roche limit, a body disintegrates due to tidal forces of Saturn, and disperses, forming rings) (Charnoz et al., 2010; Charnoz et al., 2011). Enceladus itself is covered with fine particles, partly coming from impact and plume debris reaccreting on the surface (Schenk et al., 2011). An image taken by Cassini-Huygens is shown in Fig. 1.11d.

Granular media seems ubiquitous on the surface of small bodies in the Solar System, of different sizes and compositions. Detailed studies of granular physics and dynamics are required to understand how granular materials shape and modify the surface of these bodies, how they respond to external

(a) A step on the lunar regolith surface from Apollo 11

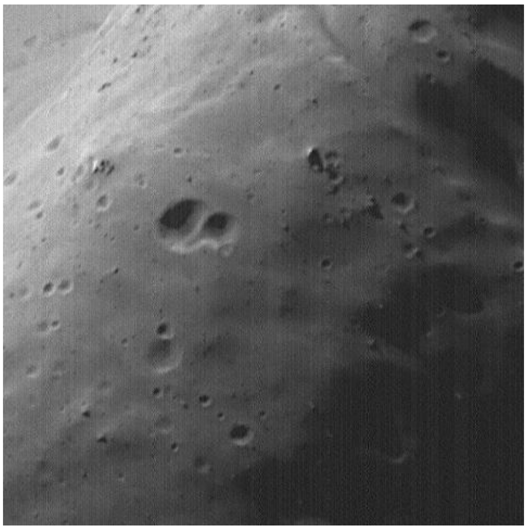

(b) Phobos surface from Mars Global Surveyor

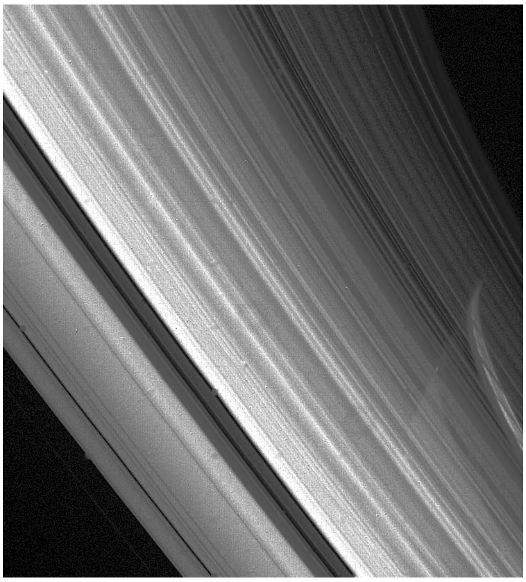

(c) Saturn rings from Voyager

(d) Enceladus surface from Cassini-Huygens

Fig. 1.11.: Images of granular materials found in the Solar System. Image credits: NASA/JSC and NASA/JPL

actions and what are their detailed properties. A perfect example is the upcoming JAXA mission Martian Moons eXploration (MMX), whose objective is a round trip to Phobos and Deimos and a sample return from Phobos (Kuramoto et al., 2018). The main spacecraft, as well as the potential rover that will take part of the mission, will be exposed to the fine granular material covering Phobos surface.

1.3.4 Granular material in an asteroid environment

Even though granular material can be found on Earth, and in many locations in the Solar System, this does not mean that they behave in an exactly similar manner. Indeed, the asteroid environment is very different from the Earth's one, because of the differences in size, and therefore mass and gravity, composition, etc. Here, I describe the main characteristics of asteroidal granular matter, and the specificities of such an environment.

Origin

On large asteroids, the principal origin of granular material is meteorite impacts. Impacts are very frequent in the Solar System, and micrometeorites constantly impact planetary bodies. For example, the Apollo astronauts were only a few hours on the Moon's surface, and their suits recorded a large amount of micrometeorite impacts.

An asteroid surface is regularly impacted and, as time goes by, the virgin, fresh, rock on the surface is broken by new impacts. Therefore, more and more debris occupy the surface. Each new impact generates a crater and, provided that gravity is high enough to cause the fall back of a substantial amount of ejecta, it also generates an ejecta blanket, and these ejecta are part of the regolith layer that forms on the surface. Repeated impacts also overturn material, as, at each impact, material is ejected further from the diameter of the crater (and may end up in other craters). Since the depth of the rock being broken depends on the projectile's size, the larger the impactor, the deeper the exposed region. Small impactors are much more numerous than large ones, and therefore the upper layers are overturned more frequently than deeper regions. This process is called "gardening", and implies a more or less regular recycling of surface material, and regolith mixing, both vertically and horizontally (Melosh, 2011).

Concerning the formation of fine particles, analyses of the particles brought back from Itokawa by Hayabusa suggested that they were formed by meteoroid impacts, and then that a seismic-induced grain motion wore them away (Tsuchiyama et al., 2011).

Concerning small asteroids whose gravity may not be high enough to cause the fall back of crater ejecta, a possible dominant source of regolith is thermal fatigue. Due to the succession of thermal cycles, rocks can fragment and generate fresh regolith grains. It was shown to be effective by numerical simulations and laboratory experiments, and even more effective than micrometeoroid impacts for breaking up rocks larger than a few centimeters (Delbo et al., 2014).

Composition

The composition of asteroid surfaces is mainly deduced from albedo, thermal, and spectral measurements. For example, Masiero et al. (2009) showed that the polarization of light reflected from an asteroid is defined by the mineralogical and chemical composition of surface particles.

The analysis of particles brought back by Hayabusa from asteroid Itokawa delivered also precious information on the composition of the surface. It was found that they were mainly composed of olivine, pyroxene, and plagioclase, and that their composition was similar to the one of LL ordinary chondrites, even if the abundance of troilite was a little lower in Itokawa's samples (Tsuchiyama et al., 2011). In a more general way, it is believed that the surface of Itokawa is generally composed of these three types of minerals. Interestingly, spectral observations from Earth predicted the relationship between Itokawa and LL chondrites, which demonstrates that for this type of asteroid, the analysis of the samples could confirm this prediction, and showing that for this kind of asteroids, there is a direct link between remote spectra and known meteorites.

Reduced gravity

Asteroid surface gravities are much smaller than on Earth, affecting the granular material behavior on asteroids. Examples of surface gravities calculated for Itokawa, (66391) 1999 KW4, Ryugu, and Bennu (Yoshikawa et al., 2015; Scheeres et al., 2015; Scheeres et al., 2010; Watanabe et al., 2019; Scheeres et al., 2019) show that the gravitational accelerations on small bodies are not comparable even with the Moon's one. Indeed, for example on Ryugu the GM constant is about 30.0 m^3 s^{-2}, meaning that at the equator ($R = 502$ m), the gravitational acceleration is about $1.19 \cdot 10^{-4}$ m s^{-2}, or about $1.2 \cdot 10^{-5} g_{\mathrm{Earth}}$. Such small surface gravities also mean very low escape velocities, and therefore only particles ejected with speeds lower than these small values stay on the asteroid.

Moreover, the terrain is usually uneven, leading to brutal changes in the gravitational acceleration over small distances, as well as non-perpendicular gravitational fields.

Strength and friction

Strength is necessary to support relief. From a simple calculation, Sir Harold Jeffreys showed in *The Earth* in 1952 (Jeffreys, 1952) that, without strength, a mountain (or any other topographic feature) with a width w and an infinite length in the other horizontal dimension, would survive only a certain given time t_{collapse} before collapsing and disappearing on the surface of a strengthless body, given by:

$$t_{\text{collapse}} = \sqrt{\frac{\pi}{8}\frac{w}{g}}, \tag{1.1}$$

where g is the gravitational acceleration on the body. For example, a 100 km wide mountain on Earth would disappear in about one minute, and in two and a half minute on the Moon. Without strength, the topographies observed in numerous Solar System bodies would not exist, and yet they do! Strength is what allows a body to resist deformation forces. The measure of these forces per unit area is called "stress", and the deformation produced by these forces is called "strain" (strain is dimensionless so the deformation has to be normalized by the length itself). If a force per unit area is applied to stretch or compress, we talk about "normal" stress and "longitudinal" strain, whereas if the solid is deformed in a parallel direction to the opposite side, or by "shear", the terms are shear stress and strain. In a three-dimensional environment, there are three stresses and three strains.

In 1665, Robert Hooke found a relation linking longitudinal strain ε_{l} and normal stress σ_{n}, that will be called later *Hooke's law*:

$$\sigma_{\text{n}} = E\varepsilon_{\text{l}}, \tag{1.2}$$

where E is the Young's modulus. In the 1800s was defined a second constant relating shear stress and shear strain, the shear modulus μ, such as:

$$\sigma_{\text{s}} = 2\mu\varepsilon_{\text{s}}. \tag{1.3}$$

These two constants depend on the material, but can also depends on the temperature (for metals for example). The two equations previously presented are usually called constitutive relations, and we call “rheology” the study of the relation between deformation and stress (Melosh, 2011).

However, Hooke’s law considers a perfect solid, i.e. perfectly elastic, meaning that it will come back to its original state after removing the stress. Real solids have a limit stress (or strain) that, if exceeded, removes the linearity of the relationship. The deformation can then be reversible (non-linear elasticity) or irreversible (plasticity). When strain becomes even higher, the material can either lose strength and brittle, or continue to deform even after significant plastic deformation (ductility). If we consider ideal plasticity, the material does not undergo any strain if the stress is below the limit considered as the strength of a material. Even if simple laws such as Hooke’s law were defined several centuries ago, a full understanding of the strength of a material is very recent, and rheology is still a very active field.

Previous results concern solids, but now we consider a broken rock, in the perspective of a granular material. Such a material does not have a tensile strength, meaning that it has no capacity to resist loads tending to elongate it. For a granular material, its ability to resist deformations comes from the frictional forces between contacts. Charles-Augustin de Coulomb, in Coulomb (1776), was the first to formulate a law ruling the mechanics of a broken rock or a pile of sand, and introduce a macroscopic friction coefficient. This coefficient of friction is the ratio between shear and normal stress in a granular pile, and is equal to the tangent of the angle of internal friction (close to the angle of repose, i.e., the steepest angle of the slope of a granular pile with a given material).

Later, in the end of the 19$^{\text{th}}$ century, Christian Otto Mohr generalized the theory developed by Coulomb, and lead to a failure criterion called the Mohr-Coulomb yield criterion:

$$\tau_{\mathrm{s}} = \sigma_{\mathrm{n}} \tan\phi + c, \tag{1.4}$$

where τ_{s} is the shear strength, σ_{n} the normal stress, ϕ the angle of internal friction ($\tan\phi$ is called coefficient of friction), and c the cohesion. The shear strength corresponds to the maximum shear stress before failure, and then the Mohr-Coulomb yield criterion defines an envelope of possible values for the normal stress without failure. The sole coefficient of friction depends on a multitude of parameters, such as the grain-to-grain friction, the grains’ shape, the packing of the granular material, and the size distribution, and is supposed to represent all these characteristics. The cohesion term influences the angle of repose, but not the angle of internal friction. If, in a theoretical consideration, the cohesion term is equal to zero, both angles are the same. If the angle of internal friction is equal to zero, the criterion is called the Tresca criterion, and if $\phi = 90°$ the model is equivalent to the Rankine model.

Based on Earth experiments, cohesionless granular materials have angles of internal friction ranging from $25°$ to $45°$ depending on the shape of particles and their microscopic frictions (Carrigy, 1970; Pohlman et al., 2006; Kleinhans et al., 2011).

Usually, it is easier to measure the angle of repose, but it can either be the static angle of repose or the dynamic one. The static angle of repose is the maximum steepness before the formation of an avalanche, and can be measured either by tilting a box filled with granular material until sliding of the top layers occurs, or by pouring material through a funnel and measuring the angle formed by the slopes. On the other hand, the dynamic angle of repose is the slope of the material resulting from the avalanche, and can be measured for example by the slope taken by the granular material inside a slowly rotating tumbler.

The static and dynamic angles of repose are generally close to each other. However, experiments from parabolic flights showed that the dynamic angle of repose decreases with a decreasing gravity, whereas the static one increases (Kleinhans et al., 2011). A description of landslides in granular material, with and without cohesion, can be found in (Melosh, 2011).

Many other yield criteria were defined, such as the von Mises criterion, or the Drucker-Prager yield criterion, a smooth version of the Mohr-Coulomb criterion usually used for concrete or rocks, and that can also have as parameters angle of internal friction and cohesion.

Cohesive forces

There is a cohesion term in the Mohr-Coulomb yield criterion, and we describe here the different sources of cohesion. Cohesion increases the angle of repose, and represents the attractive forces between molecules of a material. Without cohesion, no vertical scarp could exist, not even the small vertical formations around the bootprint of the Apollo 11 astronaut on the Moon (see Fig. 1.11a).

Van der Waals forces are intermolecular forces different from covalent or ionic bonding (McNaught et al., 1997), and are usually the weakest chemical forces. However, when there are a multitude of interactions, the sum of forces can be much higher.

Heinrich Hertz (1857-1894) was a precursor in the field of contact mechanics (Hertz, 1896). From its early analysis and from the elastic Hertzian pressure were derived two major theories for adhesion: the JKR model (Johnson, Kendall, and Roberts) for which were added attractive surface forces over the contact area (Johnson et al., 1971), and the DMT model (Derjaguin, Muller, and Toporov) for which even non-contact forces in the vicinity were added to the model (Derjaguin et al., 1975).

The pull-off force between two spherical particles can be written for both models as:

$$F_{\mathrm{JKR}} = 3\pi\gamma \frac{R_1 R_2}{R_1 + R_2}, \tag{1.5}$$

$$F_{\mathrm{DMT}} = 4\pi\gamma \frac{R_1 R_2}{R_1 + R_2}, \tag{1.6}$$

where γ is the effective solid surface energy and R_1 and R_2 are the radii of the particles. The JKR model is more adapted to large soft bodies, whereas the DMT model is more accurate for small hard solid particles. Other theoretical and experimental studies were conducted on adhesive forces (Heim et al., 1999; Israelachvili, 2011).

According to Castellanos (2005), Perko et al. (2001), and Rognon et al. (2008) and explained in Scheeres et al. (2010), the Van der Waals cohesive force between two spherical particles can be written as:

$$F_c = \frac{A}{48(t+d)^2} \frac{R_1 R_2}{R_1 + R_2}, \tag{1.7}$$

where A is the Hamaker constant ($A = 4.3 \cdot 10^{-20}$ J for lunar regolith), t is the minimum interparticle distance between the surfaces (usually nonzero because of adsorbed molecules on the surface), and d is the distance between particles (zero for particles in contact).

Since there is no water vapor or atmospheric gases on asteroids (or on the Moon), the minimum distance between particles can be much smaller than on Earth, and a surface cleanliness ratio can be introduced as the fraction of Ω, the diameter of an oxygen ion O^{2-} over the minimum interparticle distance t (Perko et al., 2001; Scheeres et al., 2010). With this notation, for asteroid particles in contact, Eq. 1.7 becomes:

$$F_c = \frac{AS^2}{48\Omega^2} \frac{R_1 R_2}{R_1 + R_2}. \tag{1.8}$$

The cleanliness ratio tends to 1 for a clean surface, for example for Sun-exposed regolith, and closer to 0.1 in an Earth-like environment with atmosphere and water vapor (Perko et al., 2001).

Asperities on the surface and inclusions of smaller particles between the two considered particles can be modeled by (Castellanos, 2005; Scheeres et al., 2010):

$$F_c a \approx \frac{r_a}{r} F_c \approx S^2 F_c, \tag{1.9}$$

if the particles are covered with smaller particles with a radius r_a, and if we consider $S \approx \sqrt{\frac{r_a}{r}}$.

To compare the influence of cohesion to other forces present on the surface of an asteroid, we use what is called a bond number B. This bond number represents the ratio of the considered force over the the gravitational force exerted by the asteroid on the particle. The bond numbers give a valuable information to understand which forces are to be considered to explain observations and measurements. For example, the bond number for cohesion B_c is equal to:

$$B_c = \frac{F_c}{F_g}. \tag{1.10}$$

On asteroids, the gravitational forces are much smaller than on Earth, which usually allows cohesion to play a larger role. For example, particularly highly porous structures on the Moon, called “fairy castles” (Hapke et al., 1963), were suggested to explain the strong opposition surge, and would require a high cohesion to exist.

An example of computation of the cohesion bond number applied to Ryugu can be found in Section 3.2.2.

Since the cohesive bond number depends on both gravity and radius, experiments were conducted on Earth with very small fine powders to compensate the higher gravity, and try to reproduce asteroidal mechanisms (Mériaux et al., 2008; Durda et al., 2013). Many numerical simulations also showed that small cohesive forces (about 100 Pa) are enough to play a role in the spin rates of asteroids, or in the possibility of motion on asteroid surfaces (Sánchez et al., 2014; Hirabayashi, 2014; Rozitis et al., 2014; Hirabayashi et al., 2014; Scheeres, 2014).

Electrostatic forces

Due to solar wind depositing electrons on the surface of asteroids and photoemission producing the loss of electrons, asteroid surfaces are usually electrically charged. The incidence angle of the Sun, the shape of the asteroid, the rotation rate, etc. result in different charges on the surface, and therefore influence the charges on particles as well as the plasma environment, which can lead to electrostatic lofting or hovering.

Electrostatic lofting was first observed by the Surveyor spacecrafts (Rennilson et al., 1974): a line of light along the lunar horizon, corresponding to the limit of the local sunset (i.e., the terminator zone, or twilight zone), was detected and explained by levitation of electrically charged grains. Then, an explanation proposed for the existence of ponds on Eros (see Section 1.2.2) was the electrostatic lofting and levitation of dust grains (Robinson et al., 2001; Colwell et al., 2005; Hughes et al., 2008).

Moreover, another potential evidence of electrical forces on the surface of asteroids is the very small particles brought back by Hayabusa, even if the sampling mechanism did not work as planned (Yano et al., 2006). A possibility is that they could have stuck to the sampling horn due to opposite charging of the horn and the particles (Tsuchiyama et al., 2011). Still about Itokawa, Kimura et al. (2014) proposed that single grains ranging from 100 μm to 1 m, and aggregates with a volume-equivalent-sphere radius larger than 10 μm could be lofted off Itokawa.

According to Colwell et al. (2005) and Scheeres et al. (2010), the electrostatic force for lofting is:

$$F_{\mathrm{es}} = QE = \varepsilon_0 E^2 \Lambda = 4\pi\varepsilon_0 E^2 r^2, \tag{1.11}$$

with E the eletrical field, $Q = \varepsilon_0 E\Lambda$ the total charge on a particle, ε_0 the vacuum permittivity, and $\Lambda = 4\pi r^2$ the particle surface. A bond number for electrostatic forces can also be defined similarly to the cohesive one, i.e., the ratio of the electrostatic force over the gravitational force, and an example of computation can be found in Scheeres et al. (2010).

1.3.5 Granular processes on asteroids

Several granular processes visible on asteroids were already described with the observations of asteroid surfaces in Section 1.2.2, such as mass wasting, and here we concentrate on two particular processes: seismic shaking and regolith size segregation.

Seismic shaking

Seismic shaking has already been mentioned several times, and is believed to have a significant influence on the surface of small asteroids. When a projectile impacts the surface of an asteroid, it generates a shock wave that propagates through the asteroid and can provoke local downslope movements on the surface (Richardson Jr. et al., 2005).

Usually, a granular pile or the slope of a crater is stable if the slope is smaller than the angle of repose. However, this can be relaxed due to perturbations such as seismic waves. The only true stable state is a horizontally flat surface, and thus under perturbations a pile or a crater will tend to relax toward a horizontal plane. Granular surfaces on asteroids are governed by this relaxation, which can be the cause of crater erasure (Richardson et al., 2004), for example on Eros (Thomas et al., 2005) and Itokawa (Michel et al., 2009). A schematic illustration is shown in Fig. 1.12.

Analytical formulas can be derived to represent the effect of seismic shaking on asteroids. According to (Miyamoto et al., 2007), the average seismic strain energy per unit volume of rock e can be defined as:

$$e = \rho_a \pi^2 f^2 A^2, \tag{1.12}$$

where ρ_a is the bulk density of the asteroid, f the seismic frequency, and A the maximum half-cycle amplitude. Moreover, the maximum acceleration magnitude for the rock is:

$$a = 4\pi^2 f^2 A. \tag{1.13}$$

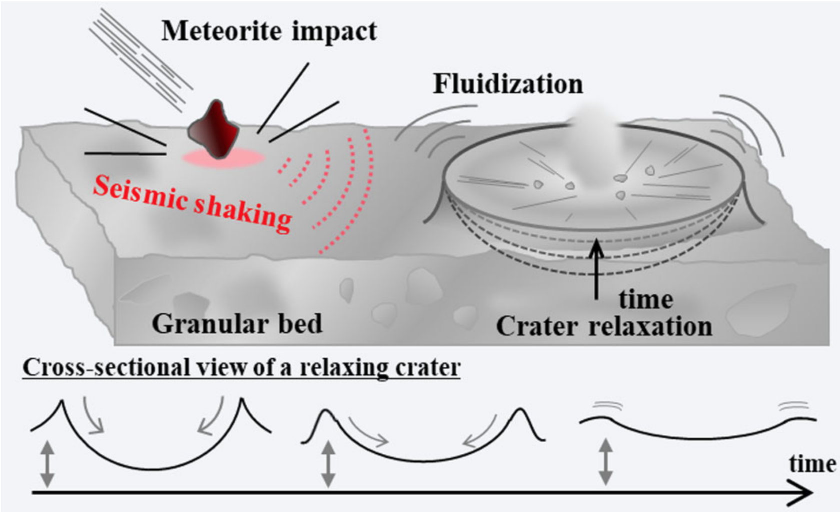

Fig. 1.12.: Crater relaxation caused by impact-induced seismic shaking on a small body. Image credit: Tsuji et al. (2018)

According to Lay et al. (1995), the total energy density in the system is $2e$; thus the total seismic energy E_s of the spherical asteroid with a diameter D_a is:

$$E_s = \frac{1}{6}\pi D_a^3 \times 2e = \frac{\rho_a D_a^3 a^2}{48\pi f^2}. \tag{1.14}$$

Only a fraction of the kinetic energy of an impactor E_i is transformed into seismic energy at impact, and we call η the seismic efficiency factor representing this loss of energy. Thus:

$$E_s = \eta E_i = \frac{1}{12}\eta\pi\rho_i D_i^3 v_i^2, \tag{1.15}$$

where D_i and v_i are the diameter and the speed of the impactor.

By combining Eq. 1.14 and 1.15:

$$a = 2\pi v_i f \sqrt{\eta \frac{\rho_i}{\rho_a}\left(\frac{D_i}{D_a}\right)^3}. \tag{1.16}$$

Moreover, the gravitational acceleration on the surface of the asteroid can be written as:

$$g = \frac{2}{3}\pi G D_a \rho_a, \tag{1.17}$$

where G is the gravitational constant. Therefore, the maximum acceleration relative to the gravity is:

$$\frac{a}{g} = \frac{3fv_i}{G}\sqrt{\eta\frac{\rho_i}{\rho_a^3}\frac{D_i^3}{D_a^5}}. \tag{1.18}$$

This equation is valid for monolithic asteroids. However, we have seen in Section 1.2 that most small asteroids are possibly rubble piles, with a significant volume of void spaces inside of them. Therefore, we must expect the seismic waves to be attenuated inside the body, between boulder/boulder or boulder/void transitions. By applying diffusive scattering theory (Richardson Jr. et al., 2005), the seismic attenuation A_t of a wave propagating through the body can be written as:

$$A_t = \exp\left(\frac{-fD_a^2}{K\pi Q}\right), \tag{1.19}$$

where K is the seismic diffusivity and Q the seismic quality factor. The maximum acceleration relative to the gravity expressed in Eq. 1.18 has to be multiplied by the factor A_t to represent the diffusion through a rubble pile. Properties of asteroids are not determined well enough to be able to accurately compute such a ratio. However, Eq. 1.18 can give hints about the internal structure of an asteroid from observations. Also, it can give an idea of the possibility of mechanisms such as granular convection on relatively known asteroids. According to Lambe et al. (1969), the ratio of the surface acceleration over gravity has to be higher than 0.2 to destabilize the surface (and potentially partly erase craters), and, according to Jaeger et al. (1996), the ratio has to be higher than 1 to drive granular convection. Granular convection will be described more in details in Section 1.3.5.

Finally, this is still a field under study, as recent simulations of seismic wave propagation for different asteroid interiors carried out by Garcia et al. (2015) showed that simple computations such as the one presented here could underestimate the accelerations by a factor of about 50, and that the frequency of impacts inducing shakings is even higher than anticipated.

Size segregation

Size segregation can take different forms for a polydispersed granular material. One example is size segregation in granular flows or avalanches. When grains flow down along a slope, due to a void-filling mechanism, small particles go to the bottom of the flow, whereas larger particles are oppositely pushed upwards. This process is called kinetic sieving, and is believed to be the main cause of size segregation, compared to diffusive remixing, or particle-density differences (Bridgwater, 1976; Thomas et al., 2000; Gray et al., 2006).

Another example of size segregation is the "Brazil-nut effect", that different theories tried to explain (Kudrolli, 2004). It was first proposed that local rearrangements could lead to size segregation, when the granular material is submitted to vibrations such as impact-induced seismic shaking (Williams, 1976; Rosato et al., 1987). However, some experiments show that the size separation is due to fluid-like convection processes, rather than from local rearrangements (Knight et al., 1993). Nevertheless, the mechanism at the origin of this process of size segregation on small bodies is still incompletely understood. Models and simulations from Gray et al. (2005) and Maurel et al. (2017) suggest that larger particles elevate in the granular material submitted to shaking or vibrations thanks to a void-filling process by the smallest particles.

Recent numerical simulations and experiments show that convection efficiency is much weaker in low-gravity environments, and therefore that, on asteroids, size segregation induced by Brazil-nut effect could need long timescales to happen (Tancredi et al., 2012; Güttler et al., 2013; Murdoch et al., 2013a; Matsumura et al., 2014). On the other hand, models from Yamada et al. (2016) investigating the timescale of asteroid resurfacing due to regolith convection lead to the conclusion that this process should be possible within the mean collisional lifetime of the asteroid.

Even if the processes governing the Brazil nut effect are not perfectly understood for the moment, this effect is characteristic of granular media, and is sometimes chosen as an explanation for many geological observations on the surface of asteroids (see Section 1.2.2).

Now that I have introduced granular matter in a general context and the application on the surface of asteroids, I describe here the different methods at our disposal to investigate regolith dynamics.

1.4 Investigating regolith dynamics

Even if observations of asteroid surfaces teach us a lot about different granular processes in asteroidal environments, space missions allowing us to study or observe these processes in situ are rare. Therefore, different ways to investigate regolith properties have been developed on Earth, or in a low-Earth orbit such as the International Space Station. Classic granular experiments had to be adapted in order to be relevant for comparisons, and numerical simulations were developed as a proxy. For example, Section 5.1.4 describes experiments and simulations aimed at a better understanding of the cratering process in a granular material in the low-gravity environment of an asteroid.

1.4.1 Experiments

Most experiments dealing with granular material on Earth are done under a 1 g environment, for practical reasons. However, recent experiments performed under reduced gravities showed the influence of gravity. An example is the decrease of granular convection efficiency identified with lower gravities (see Section 1.3.5).

One approach for simulating low gravity is to make use of a drop-tower. During a drop-tower experiment, the granular material is in free fall, allowing a low relative gravity. For example, Sunday et al. (2016) describes the functioning of an Atwood machine, a system of pulleys and counterweights, used to obtain reduced gravities. Drop-tower experiments can be used either to better understand granular flow (Hofmeister et al., 2009) or low-velocity collisions (Beitz et al., 2011; Schräpler et al., 2012; Murdoch et al., 2017). With this experimental setup, gravities as low as $8 \cdot 10^{-4}$ g (i.e., 8 mm s^{-2}) can be reached (Beitz et al., 2011).

The use of parabolic flights is another method to obtain conditions of reduced gravity. When the thrust is reduced to only counter air drag, the granular material is in free fall during dozens of seconds. This method allows microgravity, and therefore smaller gravities than drop-tower experiments, but it needs to mobilize a plane (usually commercial) and a whole crew to pilot the plane, assure the safety, and oversee the smooth running of the experiment. Another drawback is the increased-gravity period (up to 2 g) preceding the microgravity one, which could compress the granular material.

However, this method remains one of the most convenient methods to have access to reduced-gravity environments on Earth. Using parabolic flights, experiments of granular shear were performed by Murdoch et al. (2013b), while granular convection was investigated by Murdoch et al. (2013a) and Güttler et al. (2013). Moreover, Colwell et al. (2008) and Colwell et al. (2015) studied impact experiments (PRIME) and Dove et al. (2013) charged particle motion.

However, these are not the only solutions, and other reduced-gravity experiments were done using sounding rockets (Krause et al., 2004) or the International Space Station, such as COLLIDE (Colwell, 2003). CubeSats such as AOSAT (Schwartz et al., 2018) could also be a future opportunity for the investigation of regolith dynamics under reduced gravity.

All these methods require specific material or opportunities that are not available to every researcher. Numerical modeling is the best alternative to cover wider parameter space and conditions than those available in experiments, provided that they are valid. I present the different approaches using in numerical modeling in the following section. Note that numerical models necessarily work with simplifications and assumptions that have to be kept in mind when considering the results. Moreover, numerical simulations cannot be totally decorrelated from experiments, as comparisons between experiments and simulations are required to prove the reliability of a numerical model. With these limitations in mind, numerical simulations are extremely precious to understand granular processes and behaviors, and guide experiments.

1.4.2 Numerical simulations

Numerical approaches can be divided into two categories: continuum and discrete. A presentation of both categories can be found in the following sections, as well as a comparison between the different methods and approaches.

Continuum approach

Continuum approach represents quantities in a granular material by averaging the physics across many particles, and using smooth transitions to account for variance. They are usually based on a Navier-Stokes framework and consider conservation laws such as mass, momentum, and energy conservations.

They can either use an Eulerian specification of the flow field or a Lagrangian one. The Eulerian specification uses a fixed mesh, and focuses on a material flow in specific locations, whereas the Lagrangian one follows individual parcels of material as they flow, and features nodes that may move with the velocity field. Both have advantages and drawbacks: for example, the numerical diffusion issue associated to computer simulations of continua and known since VonNeumann et al. (1950), is easier to mitigate with an Eulerian approach. On the other hand, since Lagrangian approaches do not use a fixed mesh, the resolution can adapt depending on the scale of any process (Benz et al., 1994). Hybrids of Eulerian and Lagrangian specifications have also been developed, for example AMR methods (Adaptive Mesh Refinement) that enable an increase of local resolutions and that are used in shock-physics codes such as CTH (McGlaun et al., 1990).

Continuum approaches have been used for many years in planetary science. For example, scaling laws for impacts were investigated by Holsapple (1993) using the continuum approach, as did Benz et al. (1994) in their work on two-body collisions.

For granular media, the material is usually considered as a deformable solid, and in order to treat stability problems, a yield criterion has to be chosen (for example the Mohr-Coulomb yield criterion described in Section 1.3.4).

A continuum approach, based on Jop et al. (2006) and defining the friction as a direct function of inertia, was also developed by Coupez et al. (2013) and Valette et al. (2019) and is presented in Section 2.3.

Since granular material is by definition composed of individual grains, it could be natural to model it not by averaging the physics in some areas but by representing each grain separately. This corresponds to the discrete approach I describe below.

Discrete approach

In the discrete-element method (or DEM), each grain is explicitly treated as an individual particle, and large particles can also serve as proxies for collections of smaller ones. Therefore, each individual interaction between grains has to be computed explicitly. In order to do this, physical parameters need to be defined, and these parameters are usually taken from continuum mechanics. Such parameters can for example represent Young's modulus, Poisson's ratio, and the shear modulus, used in Hooke's law, or friction coefficients, used in Mohr-Coulomb criterion, and spring constants.

Since discrete-element methods usually need to handle a large number of particles, they are generally built off N-body codes. They offer efficient algorithms to treat interactions between many particles, as well as exterior forces exerted on them. The high number of particles and the computation of each interaction already require significant computational resources, and to accelerate the running time of simulations, a spherical shape is assumed for all grains. However, coefficients in DEM codes can be defined to mimic the behavior of non-spherical grains, such as the shape factor in `pkdgrav` described in Chapter 2.1 and introduced by Zhang et al. (2017). Moreover, new simulations also cope with nonspherical particles, such as the ones presented by Ferrari et al. (2018).

It is notable that there are other methods using a discrete approach than DEM, and among them is the Smoothed Particle Hydrodynamics (SPH) method, which uses numerical particles that do not necessary directly represent actual grains. An introduction can be found in Monaghan (1988) and a more recent review in Monaghan (2012). SPH methods are particularly used in shock-physics codes (Sirono, 2004; Jutzi et al., 2008; Jutzi et al., 2013), but have also recently been used for modeling cliff collapse (Jutzi, 2015).

DEM simulations can be separated into two categories: hard-sphere DEM (or HSDEM) or soft-sphere DEM (SSDEM). Both are described in the coming paragraphs.

Hard-sphere discrete-element method

With HSDEM, collisions between particles are predicted in advance, and treated instantaneously. For each considered timestep, each particle's motion is analyzed, and its trajectory is interpolated to check if any collision with another particle could occur before the next timestep. If so, the collision is resolved analytically with solid, non-deformable, particles (Richardson, 1994; Richardson, 1995).

Soft-sphere discrete-element method

Contrarily to HDSEM, grains are deformable and, to account for this deformation, overlaps between grains are allowed. Collisions are not predicted and instantaneously resolved like with HDSEM, but are treated by computing contact forces between overlapping grains. An introduction to SSDEM can be found in Cundall et al. (1979), and an overview of the different types of SSDEM codes is presented in Radjaï et al. (2011). Depending on the code, contact forces such as friction and resistance to penetration between grains are resolved for each timestep, and a contact lasts usually at least several timesteps. The resistance to overlap is generally spring-like or Hertzian, i.e., the repulsive force is either proportional to the penetration depth or with a $3/2$ power law.

Both methods could be described much more in detail, but since many reviews of these methods exist, I rather describe them by comparing each other, as well as comparing them with the continuum method.

Comparison between the different approaches

Each approach obviously has its advantages and its drawbacks. Depending on the context and the granular matter regime, one method could be more adapted than the others. Since SSDEM is the only method that computes explicitly all interactions and treats each grain as an individual particle, ideally, one should use it in all cases. However, given its computational cost, one often has to choose the best compromise between the required degree of realism and its expense. A thorough comparison can be found in Murdoch et al. (2015), with more examples of authors and solutions to mitigate the issues associated to each method.

Nevertheless, HSDEM have been used in planetary science before SSDEM, because it requires less computational power. For example, HSDEM was used by Richardson et al. (1998) to investigate tidal distortion and disruption of asteroids passing close to the Earth, and by Michel et al. (2013) to study the formation of the asteroid Itokawa by catastrophic disruption of a parent body and subsequent reaccumulation. It was also used in dilute regimes, where the granular material behaves like a gas (Richardson et al., 2011; Murdoch et al., 2012), and by Walsh et al. (2008) and Walsh et al. (2012) for the study of rotational break-ups and disruptions of rubble-pile asteroids, as well as grain displacements due to YORP-induced rotations. When the number of particles is very high, SSDEM requires a large computational power and HSDEM can be preferred to SSDEM. Still, since modern CPUs and GPUs become more and more powerful, modern SSDEM codes exceed HSDEM codes in number.

Since HDSEM needs to detect collisions in advance, collisions need to be computed one at a time, and parallelization is limited, whereas true parallelization can be reached for SSDEM and continuum codes. Therefore, even with large simulations involving a lot of particles or a significant volume, SSDEM and continuum codes can be more efficient than HDSEM ones by parallelizing the tasks (Schwartz et al., 2012). Moreover, with the development of codes using GPUs rather than CPUs (Cheng et al., 2019), the high computational power required for simulations is compensated by a decrease in computation time.

Since particles/grains in DEM are usually spherical, some codes introduced walls or objects that can have different geometries, and that can react or not to particles (Schwartz et al., 2012; Ballouz, 2017). Since looking for contact in SSDEM consists only at checking intersections between particles at a given time, it is much simpler than for HSDEM that has to take into account the future positions of particles. Therefore, it becomes a four dimension problem in HSDEM, and it is much more difficult to introduce special geometries than for SSDEM.

SSDEM is thus commonly used to model granular material dynamics, not only in industries, but also for planetary science applications. For example, it is used to model subsonic impacts on granular surfaces (Wada et al., 2006; Schwartz et al., 2014), to investigate the origin and characteristics of the Brazil-nut effect in asteroids (Tancredi et al., 2012; Matsumura et al., 2014; Maurel et al., 2017), to analyze the effects of tidal forces on asteroid surfaces (Yu et al., 2014), or to examine the creep stability of asteroids (Zhang et al., 2017).

In extreme cases, for example if the number of particles is significantly high, or if the speeds at stakes imply very low timesteps in dilute environments, other approaches can still be better solutions. In some cases such as very high impact velocities leading to a shock wave in the material, shock physics codes such as those relying on the SPH (Smoothed Particle Hydrodynamics) techniques are preferred over SSDEM codes. New continuum approaches, such as `CIMLIB-CFD` presented in Section 2.3, could also in some cases dramatically reduce the computation time, and could even be associated with SSDEM codes, in order to create an hybrid code that could switch between approaches inside a simulation run. Since in my PhD I did not study very high speed impacts, I decided to use a SSDEM code called `pkdgrav`, extensively described in Section 2, and I tried to establish a comparison of the parameters of the two codes `pkdgrav` and `CIMLIB-CFD`.

1.5 Presentation of my thesis

During my PhD, I had the opportunity to be a member of the science teams of two sample return missions, JAXA's Hayabusa2 and NASA's OSIRIS-REx, from near-Earth asteroids (162173) Ryugu and (101955) Bennu, and I worked on better understanding granular material mechanics on the surface of such small asteroids. I worked on different parts of both missions, but all of them concern the dynamics of granular material. In order to model granular matter, I chose to use and adapt to the considered problems the SSDEM numerical code `pkdgrav`. It had already been used in the past for diverse applications and had been proven conform to experimental results.

The manuscript is split into seven chapters, this introduction being the first one. Chapter 2 describes the version of the numerical code `pkdgrav` I used for all my simulations. Since comparisons with experiments are always useful, I helped analyzing the results of low-speed impact experiments conducted at ISAE-Supaero, in Toulouse, by Gautier Nguyen and Naomi Murdoch, and developed numerical simulations of these experiments to perform a comparison. Moreover, in order to compare `pkdgrav` parameters with the much fewer parameters of the continuum code `CIMLIB-CFD`, I performed inclined plane simulations, established the velocity profiles obtained with `pkdgrav`, and extracted from these corresponding coefficients in `CIMLIB-CFD`.

Then, in Chapter 3 I present the first observations and interpretations of Ryugu's surface, focusing on the results related to the presence of regolith. In Hayabusa2, I mainly focused on the modeling of the dynamics of the impact of the CNES-DLRS lander MASCOT with the granular surface of Ryugu and of the sampling mechanism and its outcome.

My work on MASCOT is presented in Chapter 4. My first simulations of MASCOT interaction with the surface were done before arrival to Ryugu, in order to support the landing operation, and I had to choose the different parameters representing the surface, such as the grain sizes and distribution, from Earth-based observations and previous knowledge of asteroids. Then I was able to consider new observations to adapt my simulations, and interpret the actual landing.

In Chapter 5, concerning the sampling of the surface, I modeled the Hayabusa2 sampling mechanism and, since it involves the impact of a small projectile at 300 m s^{-1}, I studied more generally the cratering process and crater formation in this impact speed regime and in this reduced-gravity environment.

During my PhD, the OSIRIS-REx spacecraft also arrived to its target asteroid Bennu (on December 3, 2018), and I present in Chapter 6 the first observations and interpretations, focusing on granular material, like for Ryugu.

Finally, in Chapter 7, I apply to Bennu several of my results to the understanding and origins of two phenomena observed on the asteroid, i.e., particle ejection and the formation of terraces.

pkdgrav and applications

2

> *I find your lack of faith disturbing.*
>
> — **When asked for a pkdgrav validation**

Contents

The purpose of this chapter is first to present the numerical code that I adapted to run the diverse simulations presented in this chapter and the following ones. Then, I show comparisons between this code and an actual experiment, consisting of a low-speed impact of a steel sphere into a bucket filled with glass beads. Finally, I present angle-of-repose simulations that I performed, to verify that the free parameters that I adopt correspond to the desired angles of repose. From these angles of repose, I compare pkdgrav parameters to the coefficients of another numerical code using the continuum approach to represent granular material, the code Cimlib-CFD (Coupez et al., 2013) using the $\mu(I)$ law where the friction coefficient μ depends only on the inertial number I (Jop et al., 2006).

2.1 Numerical code pkdgrav

2.1.1 Description of the code

For my PhD thesis, I adapted the parallel N-body tree code `pkdgrav` to the considered problems to simulate. A N-body code computes at each timestep the forces and torques applied to each body by other bodies or fields (e.g., a gravity or a magnetic field), and solves the equations of motion to advance to the next timestep. This code was firstly used for large cosmological simulations (Stadel, 2001) and then adapted for granular dynamics by treating collisions and computing particles trajectories by Richardson et al. (2000), Richardson et al. (2009), and Richardson et al. (2011). The numerical method was then a discrete-element method, meaning that it treats actual regolith grains by representing them explicitely with particles (the bodies of the N-body code). Originally, `pkdgrav` used a hard-sphere discrete-element method (HSDEM), and therefore collisions between particles were considered as instantaneous, with rigid spheres (i.e., no overlap was allowed between different particles). In hard-sphere methods, collisions are predicted in advance and thus can be quickly computed analytically, by using the positions and moments of the particles before collision and a few parameters, in particular the coefficients of restitution, describing the behavior of the considered material for basic collisions.

However, HSDEM shows some limits. Indeed, due to the predictive resolution of collisions, HSDEM cannot treat simultaneously collisions with more than two particles, and therefore multiple contact effects cannot be taken into account. In dense regimes where particles are in contact with several others, this is a major limitation. Moreover, collisions with fast-rotating particles, depending on the material properties, could not be treated adequately (Müller et al., 2012a). Even if attempts have been made to rectify this by adding analytic corrections to consider pre-collision rotation (Müller et al., 2013), HSDEM still presents some drawbacks. One of them is when two deformable grains experience a grazing impact between each other: the real collision may cause a weak interaction and a slight deviation whereas HSDEM involves high amounts of energy and moments whatever the type of collision. More details about the different methods for modeling granular material can be found in Section 1.4.2.

In order to model asteroid surfaces, which can be rather dense environments, an improved version of `pkdgrav` has been developed by Schwartz et al. (2012), by implementing the soft-sphere discrete-element method (SSDEM) (Cundall et al., 1979). With SSDEM, particles are considered as deformable spheres and overlaps between particles are allowed to mimic these deformations. Collisions are usually treated during several timesteps as long as particles are overlapping, and a repulsive force (linear in `pkdgrav`) depending on penetration depth limits the percentage of overlapping. Due to the computation of every force and every overlap step by step, SSDEM enables multiple contacts as well as any collision setup if the timestep is small enough. Therefore, it is particularly useful for dense environments like asteroid surfaces. However, since it usually requires several timesteps to correctly treat collisions, the timestep may need to be very small, in particular with high energy collisions, leading to high computation time. Comparisons between HSDEM and SSDEM, as well as continuous methods, are more deeply detailed in Murdoch et al. (2015). An example of comparison between HSDEM and SSDEM can also be found in Richardson et al. (2012), where low-speed rubble-pile collisions are simulated with both methods.

The version used during my PhD is the SSDEM one, developed by Schwartz et al. (2012), and modified to add new features by Zhang et al. (2017), Ballouz (2017) and Maurel et al. (2018). As it has already been said, in SSDEM particles are allowed to penetrate into each other and, when it occurs, particles are subject to a repulsive force depending on their relative velocities and spins, on the overlap depth, and on the material properties. The repulsive restoring spring force vector is composed of a normal component computed from Hooke's law,

$$\mathbf{F}_{N,\text{restoring}} = -k_n\, x\, \hat{\mathbf{n}}, \tag{2.1}$$

where k_n is the normal spring constant, x the overlap depth and $\hat{\mathbf{n}}$ a unit vector giving the direction of the main particle's center to the neighbor particle, and a tangential component

$$\mathbf{F}_{T,\text{restoring}} = k_t\, \mathbf{S}, \tag{2.2}$$

where k_t is the tangential spring constant and $\mathbf{S}$ is the tangential displacement from the equilibrium contact point.

Kinetic friction is also to be taken into account, modeled in `pkdgrav` by damping forces. The normal and tangential components of the SSDEM force become

$$\mathbf{F}_N = \mathbf{F}_{N,\text{restoring}} + \mathbf{F}_{N,\text{damping}} = -k_n\, x\, \hat{\mathbf{n}} + C_n\, \mathbf{u}_n, \tag{2.3}$$
$$\mathbf{F}_T = \mathbf{F}_{T,\text{restoring}} + \mathbf{F}_{T,\text{damping}} = k_t\, \mathbf{S} + C_t\, \mathbf{u}_t, \tag{2.4}$$

where C_n and C_t are the damping coefficients respectively along the normal unit vector $\hat{\mathbf{n}}$ and the tangential one $\hat{\mathbf{t}}$ (direction of the tangential relative velocity), and $\mathbf{u}_n$ and $\mathbf{u}_t$ the normal and tangential components of the total relative velocity (sum of relative translational and rotational velocities). Moreover, due to the possibility of slippage between particles, static friction has to be introduced to compute the highest tangential force supported by the contact:

$$\mathbf{F}_T = \min\left\{\mu_s|\mathbf{F}_N|\hat{\mathbf{S}};\ k_t\,\mathbf{S} + C_t\,\mathbf{u}_t\right\}. \tag{2.5}$$

The tangential spring constant k_t is conventionally taken equal to $\frac{2}{7}k_n$ (as it has been taken in Schwartz et al. (2014), Zhang et al. (2017) and Maurel et al. (2018) for example). The normal spring constant k_n largely depends on the simulations; usually, k_n is chosen to limit the maximum overlap depth to about 1% of the smallest particle radius (Schwartz et al., 2012). The higher the k_n, the smaller the overlaps, the larger the repulsive forces and thus the smaller the timestep required to correctly process the interactions during contacts or collisions. The chosen k_n needs therefore to be high enough to forbid too large overlaps, but not so high that it would require too much computation time to fully run simulations. A subroutine in `pkdgrav` helps finding a suitable value for k_n, from the typical mass of a particle m_p, the maximum particle expected speed $v_{p,\text{max}}$, and the maximum overlap allowed in the simulation x_{max}. From this value of k_n can also be derived a suitable timestep Δt, thanks to the desired number of steps per overlap $\text{nb}_{\text{steps/overlap}}$ (estimated here at 30 steps), if we consider equal masses and zero damping coefficients.

$$k_n = m_p\left(\frac{v_{p,\text{max}}}{x_{\text{max}}}\right) \tag{2.6}$$

$$\Delta t = \frac{\pi\sqrt{\frac{1}{2}\frac{m_p}{k_n}}}{\text{nb}_{\text{steps/overlap}}} \tag{2.7}$$

The coefficients of restitution between grains need to be chosen as inputs for the simulations. The normal coefficient of restitution is usually defined by

$$\varepsilon_n = \frac{|\mathbf{u}_{n,\text{final}}|}{|\mathbf{u}_{n,\text{initial}}|}, \tag{2.8}$$

and the normal damping coefficient C_n can be directly linked to the normal coefficient of restitution ε_n by

$$C_n = -2 \ln \varepsilon_n \sqrt{\frac{k_n \mu}{\pi^2 + (\ln \varepsilon_n)^2}}, \tag{2.9}$$

where μ is the reduced mass $\mu = m_i m_j / (m_i + m_j)$ of the colliding pair of particles whose masses are m_i and m_j. Unfortunately, there is no relation as direct as Eq. 2.9 between C_t and the usual tangential coefficient of restitution, and a new tangential coefficient of restitution ε_t has been introduced and defined analogously to ε_n as

$$C_t = -2 \ln \varepsilon_t \sqrt{\frac{k_t \mu}{\pi^2 + (\ln \varepsilon_t)^2}}. \tag{2.10}$$

The coefficients of restitution $(\varepsilon_n, \varepsilon_t)$ are thus used instead of the damping coefficients (C_n, C_t), and both sets are directly linked by Eqs. 2.9 and 2.10.

In addition to these normal and tangential forces, a rotational resistance model was implemented, considering rolling and twisting frictions. Firstly, a model best suited for dynamic flows (Ai et al., 2011) was implemented by Schwartz et al. (2012). However, when we consider a rubble-pile that remains in a quasi-static state until structural failure occurs or a bed of regolith almost at rest, this model has to be modified. Thus, Zhang et al. (2017) implemented an elastic-plastic spring-dashpot rotational resistance model. In this model, twisting and rolling resistances are computed as torques thanks to similar formulas:

$$\mathbf{M}_T = \begin{cases} k_T \boldsymbol{\delta}_T + C_T \boldsymbol{\omega}_T & \text{if } |k_T \boldsymbol{\delta}_T| < M_{T,\text{max}} \\ M_{T,\text{max}} \boldsymbol{\delta}_T / |\boldsymbol{\delta}_T| & \text{if } |k_T \boldsymbol{\delta}_T| \geq M_{T,\text{max}} \end{cases}, \tag{2.11}$$

$$\mathbf{M}_R = \begin{cases} k_R \boldsymbol{\delta}_R + C_R \boldsymbol{\omega}_R & \text{if } |k_R \boldsymbol{\delta}_R| < M_{R,\text{max}} \\ M_{R,\text{max}} \boldsymbol{\delta}_R / |\boldsymbol{\delta}_R| & \text{if } |k_R \boldsymbol{\delta}_R| \geq M_{R,\text{max}} \end{cases}, \tag{2.12}$$

where k_T, k_R, C_R and C_T are, respectively, the twisting and rolling stiffness and viscous damping coefficients, $\boldsymbol{\delta}_T$, $\boldsymbol{\delta}_R$, $\boldsymbol{\omega}_T$ and $\boldsymbol{\omega}_R$ are the twisting and rolling angular displacements and relative motions, and $M_{T,\text{max}}$ and $M_{R,\text{max}}$ are the critical twisting and rolling torques. These two equations introduce six new parameters that are in `pkdgrav` expressed thanks to the previous coefficients and three new ones, the shape parameter β representing the non-sphericity of real grains or particles, and the rolling and twisting static friction coefficients μ_T and μ_R, by:

$$\begin{array}{rcl} k_T = 2k_t\left(\beta R\right)^2 & , & C_T = 2C_t\left(\beta R\right)^2 \\ k_R = k_n\left(\beta R\right)^2 & , & C_R = C_n\left(\beta R\right)^2 \\ M_{T,\max} & = & \mu_T \beta R \mu_s \left|\mathbf{F}_N\right| \\ M_{R,\max} & = & \mu_R \beta R \left|\mathbf{F}_N\right| \end{array} , \tag{2.13}$$

where $R = r_i r_j / \left(r_i + r_j\right)$ is the effective radius of the two spherical particles whose radii are r_i and r_j. From the twisting and rolling resistance model are therefore three new parameters, the shape parameter β and the rolling and twisting friction coefficients μ_R and μ_T representing the hardness of the particle material. The shape factor β is linked to the angle of repose and it represents the effect of the angularity of the particles: the higher it is, the more the particles behave like angular ones, and therefore particles will slide less effectively on each other, resulting in a steeper angle of repose.

A material is thus defined in `pkdgrav` by a set of five parameters $(\varepsilon_n, \varepsilon_t, \mu_s, \mu_T, \mu_R, \beta)$. We particularly studied two types of regolith, defined by two different angles of repose, i.e., two different sets of parameters. There are described in Table 2.1.

Tab. 2.1.: Characteristics and properties of the two material types considered in our simulations

Material type	Angle of repose (°)	ε_n	ε_t	μ_s	μ_R	μ_T	β
Gravel-like friction	38.5	0.5	0.5	1.0	1.05	1.3	1.0
Moderate friction	28						0.2

We notice that the considered material types in Table 2.1 differ only by their shape parameter β. These values come from simulations by Y. Zhang (2017, personal communication) who determined the correlation between the shape parameter β and the angle of repose. The values used for the coefficients of restitution are similar to the ones found by Chau et al. (2002) for terrestrial rocks. These two material types were the same as the one used by Maurel et al. (2018).

In `pkdgrav`, in addition to spheres (here representing the regolith grains), infinite-mass barriers dedicated to confine particles, called “walls”, are also implemented. They exert forces on the particles, and therefore affect their motions, but are not affected by the particles, due to their infinite inertia. They can have diverse shapes, like disks, rectangles, or cylinders. In our simulations, these confinement walls have the same friction coefficients as those of the particles, but have low coefficients of restitution to damp wave propagation and avoid strong boundary effects caused by reflection on these outer walls.

Usually, to contain the regolith bed, we use a cylinder that allows us, contrarily to a parallelepipedic container, to have in all the directions of the horizontal plane a unique fixed distance from the impact point and minimize the number of grains to consider (and thus the computation time).

However, in order to model spacecrafts and Cubesats interactions with regolith soils, a new type of wall was implemented: the "reactive wall". A reactive wall is an assembly made of one or several walls that have, together, a finite mass, and therefore react to particle forces, like an inertial body. The dynamics of an assembly is defined by a center of gravity, an inertia matrix and three principal axes.

When a collision happens between a wall and a particle, the resulting accelerations are treated with a leap-frog integrator as it is for a standard particle-particle interaction. However, for a reactive wall, spin and orientation of the wall have to be determined after the impact, governed by Equations 2.14:

$$
\begin{aligned}
I_1\dot{\omega}_1 - \omega_2\omega_3\left(I_2 - I_3\right) &= \mathbf{N_1} \\
I_2\dot{\omega}_2 - \omega_3\omega_1\left(I_3 - I_1\right) &= \mathbf{N_2} \\
I_3\dot{\omega}_3 - \omega_1\omega_2\left(I_1 - I_2\right) &= \mathbf{N_3}
\end{aligned}
\tag{2.14}
$$

where, for $k \in \{1, 2, 3\}$, I_k is the principal moment of inertia of the wall assembly along the axis k, ω_k is the spin component along this axis, and $\mathbf{N_k}$ is the net torque component along the same axis, sum of the individual torques from each particle-wall collision. The changes of orientation of the principal axes of the wall assembly are computed using Equations 2.15:

$$
\begin{aligned}
\dot{\hat{\mathbf{p}}}_\mathbf{1} &= \omega_3\hat{\mathbf{p}}_\mathbf{2} - \omega_2\hat{\mathbf{p}}_\mathbf{3} \\
\dot{\hat{\mathbf{p}}}_\mathbf{2} &= \omega_1\hat{\mathbf{p}}_\mathbf{3} - \omega_3\hat{\mathbf{p}}_\mathbf{1} \\
\dot{\hat{\mathbf{p}}}_\mathbf{3} &= \omega_2\hat{\mathbf{p}}_\mathbf{1} - \omega_1\hat{\mathbf{p}}_\mathbf{2}
\end{aligned}
\tag{2.15}
$$

where $\hat{\mathbf{p}}_\mathbf{k}$ represents the k-th principal axis and $\dot{\hat{\mathbf{p}}}_\mathbf{k}$ its time derivative. Equations 2.14 and 2.15 are solved thanks to a 5-th order time-adaptive Runge-Kutta integrator. The method is more deeply described in Maurel et al. (2018).

In practice, I used reactive walls to model Hayabusa2 lander MASCOT (see Chapter 4) and the projectile of Hayabusa2 sampling mechanism (see Chapter 5). In the case of MASCOT, I used an assembly.

2.1.2 Previous validations and uses of the SSDEM version

The SSDEM version of `pkdgrav` was implemented by Schwartz et al. (2012) and validated for hopper discharges. In that paper, empirical relations between several parameters, such as the discharge rate with the aperture radius or the density, were established from experiments, and similar relations could be found with the modeled hopper, validating the numerical method.

Concerning medium-speed impacts, Schwartz et al. (2013) ran numerical simulations of impacts on cohesive glass beads agglomerates, in order to reproduce the experimental results of Machii et al. (2011). Target's grains were linked together thanks to cohesion, and a first version of cohesion, represented by springs connecting particles, was developed for `pkdgrav`. Results show that the numerical code reproduced well the actual impacts, and that the cohesion model was satisfying, at least for this kind of application.

With the same order of magnitude of impact speed, Schwartz et al. (2014) modeled a 11 m s^{-1} impact on a cohesionless granular medium, in order to compare their results with the experiments conducted in Makabe et al. (2008). The goal of the experiments and the numerical simulations was to support the design of the Hayabusa2 sampling mechanism, even if the actual projectile speed is higher, and to see which projectile shape leads to the highest amount of ejected particles. In the simulations, inertial walls were not implemented yet and the projectile could only move vertically. Moreover, larger glass beads than those used in the experiments had to be used due to computation time. However, concerning both the most efficient shape and the amount of mass ejected, simulations matched up well the experiments.

Ballouz (2017) also studied low-speed impacts, from 0.5 to about 7 m s^{-1}, into granular material with diverse physical properties. The purpose was there to compare penetration depths and drag forces to experiments (cited as personnal communication in Ballouz (2017)) and look at the influence of the gravitational acceleration. Comparisons with experiments showed that the code can well reproduce the penetration depth for impacts in this range of speeds. It was also found that the penetration depth should depend on gravitational acceleration, as $\log g$, which explains why Earth-based experiments would not detect this dependency with 10^{-1} g experiments (Nakamura et al., 2013; Altshuler et al., 2014).

In order to establish equivalences between actual granular materials and parameters defined in `pkdgrav`, comparisons have also been made with experiments. Yu et al. (2014) modeled sandpiles and avalanches to be able to get the right parameters in order to represent the behaviors of gravel, glass beads, and smooth material. Ballouz (2017) performed angle-of-repose simulations to determine the equivalence of friction parameters with actual material, as well as uni-axial compression tests. The aim of these latter tests was to measure the Young's modulus, representative of the stiffness of a granular medium, and the Poisson's ratio, ruling the transversal expansion relatively to the amount of axial compression.

When the new rotational resistance model and the shape coefficient β were introduced by Zhang et al. (2017), new comparisons were required. They were made through avalanches to link angles of repose to all the parameters in use in `pkdgrav`, and are partly presented in Maurel et al. (2018) for two different types of material, even if a much wider parameter space was covered but had not been published yet (Zhang, personal communication). The main results were that the angle of repose usually increases with the friction coefficients and β, and that it depends less on the coefficients of restitution than on the aforementioned coefficients. Furthermore, the new twisting friction implemented in Zhang et al. (2017) has a small influence on the angle of repose, and therefore the equivalence between `pkdgrav` coefficients and angles of repose are not far from what was found in previous studies. Obviously, the equivalence between `pkdgrav` parameters and the angle of repose is degenerate, and several sets of numerical coefficients lead to the same angle of repose.

As an additional check of the validity of the new version of `pkdgrav`, I performed comparisons between low-speed impacts into a bucket filled with glass beads and numerical simulations modeling the same impacts. In general, most comparisons for low-speed impacts are not done with similar grain sizes, as experiments are usually done with small glass beads or sand, implying a very high number of particles that, once modeled, leads to very high computation times (for example, see Schwartz et al. (2014)). In the comparison I present here, the sizes of the experimental glass beads are the same as the ones we considered in our simulations. This ensures that any discrepancy does not come from the grain size difference, and is an added value to this comparison.

2.2 Comparisons pkdgrav / low-speed impact experiment

In this section, I describe the setup of the bucket experiments conducted in Nguyen et al. (2019) and then my numerical setup, and finally compare simulations I ran to the actual experiments. I also compared the numerical and experimental results to literature.

2.2.1 Presentation of the setups

Experimental setup

The purpose of the experiments conducted in Nguyen et al. (2019) was to measure the acceleration of an impactor into a granular material, and to compare with previous theories the drag force of the medium. The considered experiments consisted of an aluminium sphere (the one used in Murdoch et al. (2017)), with two accelerometers inside, being released without any initial speed at various heights above the surface of the granular medium. The latter is either made of quartz sand or soda lime glass beads of several sizes, and fills a cylindrical bucket whose bottom diameter is 31.5 cm and upper diameter 35 cm. In order to reproduce the experiments with a $1:1$ scale ratio, we consider only the trials done with large enough glass beads: the 5 mm and 10 mm ones.

The aluminium sphere has a diameter of 10 cm and a total mass of about 1 kg, with a center of mass being the geometric center of the sphere. It is dropped from heights smaller than 5 cm, resulting under Earth gravity to impact speeds up to 1 m s-1. The release is operated thanks to an electromagnet. An example of a trial is shown in Fig. 2.1.

A more thorough description of the experimental setups can be found in Nguyen et al. (2019).

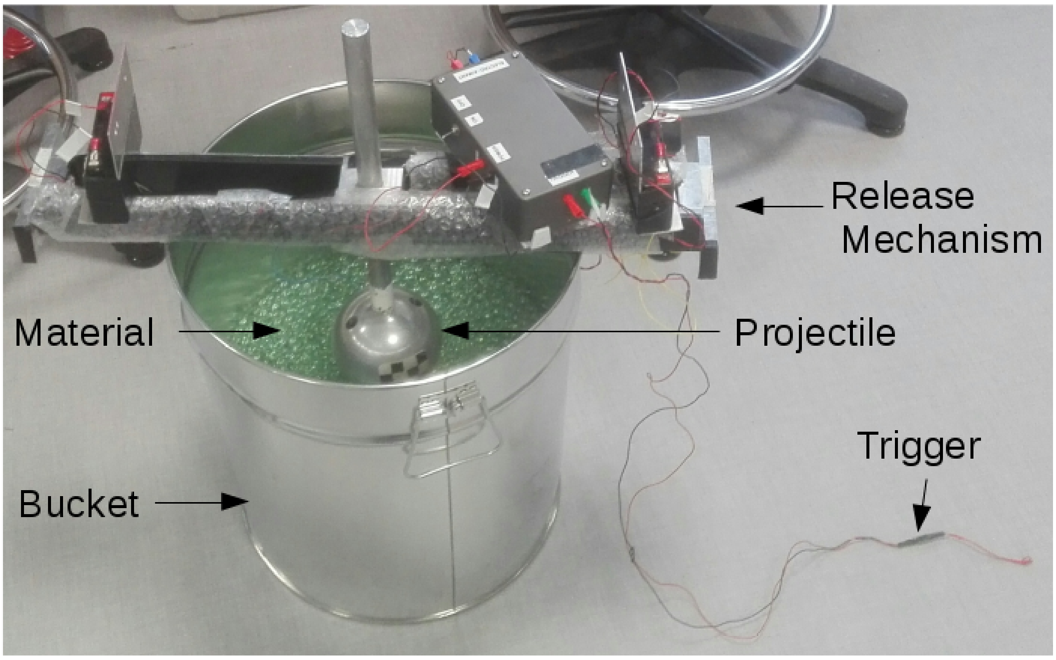

Fig. 2.1.: Picture of the Earth-gravity experiment that I simulated numerically. The bucket is filled with glass beads, and the sphere is initially located 5 cm above the surface. Image credit: Nguyen et al. (2019)

Numerical setup

I reproduced the experimental setup in pkdgrav. Since only the bottom part of the bucket is filled with glass beads, I modeled a cylinder wall with a constant diameter equal to 31.5 cm to represent the bucket, and a disk at the bottom. The bucket is filled with monodisperse particles, with a diameter of either 5 mm or 10 mm. The impactor is a shell wall, with the actual mass of 1 kg.

Normal and tangential coefficients of restitution ε_n and ε_t for the walls (bucket and sphere) were respectively set to 0.5 and 1.0, as it was done in Schwartz et al. (2014). Concerning the particles, I chose a normal coefficient of restitution of 0.9, as Schwartz et al. (2014) showed that a very high ε_n better matches low-speed impact experiments with glass beads. The same ε_n was chosen by Ballouz (2017). The tangential coefficient of restitution for glass beads was measured by Yu et al. (2014) at about 1.0, and Ballouz (2017) used the same tangential coefficient of restitution to model glass beads.

Concerning the friction coefficients, I could use the angles of repose given in Nguyen et al. (2019), and the conversion into pkdgrav parameters could be done from angle-of-repose tables given by Zhang (personal communication).

However, there is no unique equivalence as there are several parameters that could correspond to the desired angle of repose. Thus, to decrease the degrees of unknowns, I decided to set the coefficients of static and twisting frictions respectively to $\mu_s = 1.0$ and $\mu_T = 1.3$, which are the ones with most data concerning the angles of repose by Zhang (personnal communication) and are standard coefficients taken by Maurel et al. (2018) and Thuillet et al. (2018) for modeling several types of granular material. For the coefficient of rolling friction μ_R and the shape parameter β, I considered several sets to study their influence on the results and find the ones that best match the experiments. In a general way, increasing μ_R and β increases the global friction of the granular material. Angles of repose corresponding to the parameters provided by Zhang (personal communication) considered in this study are shown in Table 2.2.

Tab. 2.2.: Friction properties of the material types considered in the simulations

μ_s	μ_T	μ_R	β	Angle of repose ($^\circ$)
1.0	1.3	1.05	0.1	25
			0.2	28
			0.3	31
		2.0	0.1	26.5
			0.2	31
			0.3	33

The grain density in the simulations was determined by weighting actual 1 cm grains used for the experiments. The density was found to be about 2.48 g cm^{-3} and this value was chosen for 1 cm and 5 mm numerical grains.

I generated the bed by letting particles fall into the bucket, and cutting particles higher than a certain level, depending on the bed height considered. I chose three different bed heights (8, 10, and 12 cm), larger than 6 cm as it was the threshold for not observing any boundary effect according to Nguyen et al. (2019). The influence of the bed height is approached in Section 2.2.3. At the end of the settling phase, and the beginning of the impact simulations, the average (root-mean-squared, or RMS) speed of grains is always smaller than $1 \cdot 10^{-3}$ cm $\mathrm{s}{-1}$ and the individual maximum speeds are smaller than 0.1 cm $\mathrm{s}{-1}$, which is much lower than the impacting speeds considered in this study, and therefore the bed can be considered as settled.

The bulk density can be computed as the total mass of grains inside the simulation over the considered volume for the bed (bed height times area of the bottom disk), or without taking into account the bottom and the surface, where volume is lost due to the bottom disk and the rough cut for flattening the surface. The latter corresponds to a more precise “inner” bulk density, but values given in Nguyen et al. (2019) correspond more to the rough one, for practical reasons. Values are gathered in Table 2.3, as well as measurements from Nguyen et al. (2019).

Tab. 2.3.: Different properties of the beds used in the numerical simulations. $\mathrm{nb_{parts}}$ represents the number of particles in the simulation. ρ_1 corresponds to the rough bulk density, and ρ_2 to the more precise one; they are to be compared with the bulk density given in Nguyen et al. (2019) ρ_{exp}

Grain size	Bed height	$\mathrm{nb_{parts}}$	ρ_1 (g cm^{-3})	ρ_2 (g cm^{-3})	ρ_{exp} (g cm^{-3})
1 cm	8 cm	6274	1.31	1.48	1.53
	10 cm	7987	1.33	1.47	
	12 cm	9682	1.34	1.46	
5 mm	8 cm	53527	1.39	1.46	1.55
	10 cm	67420	1.40	1.46	
	12 cm	79623	1.38	1.45	

I also experimentally measured the bulk density of the glass beads used in Nguyen et al. (2019) in a smaller bucket. By filling the small bucket with water and weighing it, I estimated its volume. Once filled with glass beads, weighing it leads to the bulk density. For 1 cm glass beads, I found 1.47 g cm^{-3}, and for 5 mm glass beads, 1.52 g cm^{-3}. The value is close to the one given by Nguyen et al. (2019) for the small beads, but closer to the one computed in our simulations for the large beads, meaning that the method for filling the bucket leads to different packing fractions, that the size and shape of the buckets have a non-negligible influence on the packing fraction, or that the bed in the experiments could have been more compacted than in the simulations.

2.2.2 Analytical developments

The stopping depth (penetration depth of the projectile once settled) has extensively been studied in the past, for various granular media and projectiles. Some results are presented here and will be compared to the experimental and numerical results, to check their validity or adjust them. A relation between the stopping depth z_{stop} and the total drop height $H = h + z_{\mathrm{stop}}$, where h is the drop height, was found that was approximately verified by previous experiments (Uehara et al., 2003; Ambroso et al., 2005; Katsuragi et al., 2007):

$$z_{\mathrm{stop}} = (z_{\mathrm{stop},0}^2 H)^{\frac{1}{3}}. \tag{2.16}$$

In Eq. 2.16, $z_{\mathrm{stop},0}$ represents the penetration depth for $h = 0$, when a projectile is lying on the bed with no initial speed.

In a more general way, the analysis of the drag force felt by the impactor has been studied in the past. According to Tsimring et al. (2005), the total force on a penetrating projectile is:

$$\sum F = -mg + F_C(z) + \frac{mv^2}{d_1}, \tag{2.17}$$

where $F_C(z)$ is the Coulomb force, function of the penetration z of the bottom of the projectile (z is a function of time before the sphere settles) and $\frac{mv^2}{d_1}$ is an inertial drag force (with d_1 a collision characteristic length). The value of $F_C(z)$ is source of many studies: from numerical simulations, Tsimring et al. (2005) stated that it could vary from quadratic to constant, depending on the shape of the impactor and the crater formation stage; Katsuragi et al. (2007) found from a series of experiments with glass beads that best matches were obtained with a linear term $F_C(z) = k|z|$, where k depends on the granular medium (friction coefficient and density), on the projectile's diameter, and on the gravity, whereas d_1 depends on the projectile's diameter and mass, and on the density of the granular medium. Clark et al. (2013) even considered non constant $F_C(z)$ and $d_1(z)$, and found that $d_1(z)$ is roughly constant when not close to the surface.

In this study, we consider $F_C(z) = f_0 + kz$ and d_1 constant, as it is usually assumed (Clark et al., 2013). As done in Clark et al. (2013), a way to express the velocity as a function of depth from Eq. 2.17 is to use the kinetic energy $K = \frac{1}{2}m\dot{z}^2$: Eq. 2.17 then becomes a linear ordinary differential equation (ODE), and from this equation the velocity can be expressed as a function of depth:

$$v(z) = \sqrt{\frac{2}{m}\left[\left(\frac{1}{2}mV_c^2 - c_1\right)\mathrm{e}^{-c_2 z} + c_1 - c_3 z\right]}, \tag{2.18}$$

where V_c is the collision speed, c_1, c_2, c_3 are constant defined as:

$$c_1 = \frac{(mg - f_0)\,c_2 + k}{c_2^2}, \tag{2.19}$$

$$c_2 = \frac{2}{d_1}, \tag{2.20}$$

$$c_3 = \frac{kd_1}{2}. \tag{2.21}$$

From Eq. 2.18 can be extracted the collision speed as a function of the stopping depth (or final depth) z_{stop}, by considering $v(z_{\text{stop}}) = 0$:

$$V_c = \sqrt{\frac{d_1}{m}\left[e^{\frac{2z_{\text{stop}}}{d_1}}\left(f_0 + kz_{\text{stop}} - \frac{kd_1}{2} - mg\right) - f_0 + \frac{kd_1}{2} + mg\right]}. \tag{2.22}$$

Nguyen et al. (2019) chose to consider Eq. 2.17 with a constant Coulomb force $F_C(z) = f_0$, and $k = 0$. From Eq. 2.22 can therefore be extracted z_{stop} as a function of the collision speed:

$$z_{\text{stop}} = \frac{d_1}{2}\ln\left(1 + \frac{mV_c^2}{(f_0 - mg)\, d_1}\right). \tag{2.23}$$

Still in the same approximation, by making the substitution $v = \frac{d_1 \dot{u}}{u}$ in 2.17, the equation becomes:

$$\ddot{u} + \frac{f_0 - mg}{md_1}u = 0, \tag{2.24}$$

for which the solution is $u = a\cos\left(\sqrt{\frac{f_0 - mg}{md_1}}t + b\right)$, where a and b are constants. This leads to:

$$v = -\sqrt{\frac{d_1}{m}(f_0 - mg)}\tan\left(\sqrt{\frac{f_0 - mg}{md_1}}t + b\right). \tag{2.25}$$

If we consider the stopping time t_{stop} as the time between the impact ($v(t_0) = V_c$) and the time when the sphere stops ($v(t_1) = 0$), thanks to Eq. 2.25, we get:

$$t_{\text{stop}} = \sqrt{\frac{md_1}{f_0 - mg}}\arctan\left(V_c\sqrt{\frac{m}{d_1(f_0 - mg)}}\right). \tag{2.26}$$

2.2.3 Comparisons with bucket experiments

Profiles of position, speed, and acceleration

An example of the beginning and the end of a simulation is shown in Fig. 2.2. A simulation covers a time of about 0.5 s, as the sphere always settles before. It takes usually less than 0.1 s for the sphere to settle, and to this has to be added the duration of the fall. 0.5 s is a conservative duration to ensure the total settlement of the sphere.

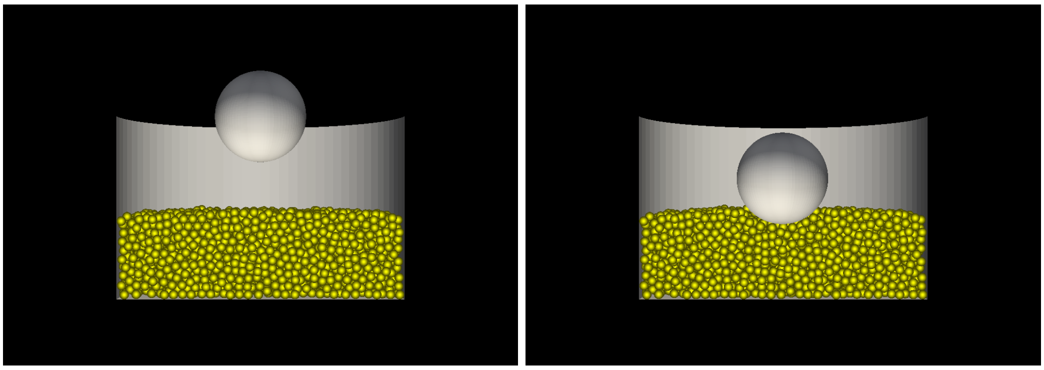

(a) Beginning of simulation: t = 0 s (b) End of simulation: t = 0.5 s

Fig. 2.2.: Snapshots of a simulation of a sphere impacting a bed of glass beads, at the beginning and at the end. Only half of the whole setup is shown for clarity purposes. In this case, the sphere is dropped motionless 5 cm above the surface, and the bed height is about 10 cm.

From simulations can be extracted the position and the speed of the sphere as a function of time. They are shown in Fig. 2.3, and are very similar to the position and speed profiles observed by Nguyen et al. (2019). From these profiles can be extracted the final depth, the collision speed, and the collision duration. The final depth corresponds to the final value of the position of the sphere's bottom (and to the penetration depth since the sphere never bounces) relatively to the surface, and the collision duration is computed as the time between the beginning of the collision, i.e., when the z-component of the velocity increases, and the end when the speed is small enough and the sphere is considered settled.

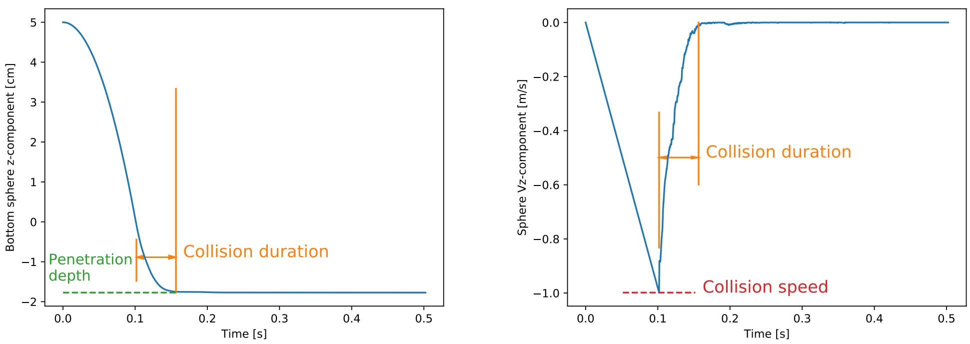

Fig. 2.3.: Vertical components of position and velocity of the impacting sphere as a function of time. The position corresponds to the bottom of the sphere relatively to the surface. In this case, the sphere is dropped motionless 5 cm above the surface, and the bed height is about 10 cm. "data" corresponds to the raw data obtained from numerical simulations, and the other curves correspond to the results of the treatment of the data (TMA and central difference) using different values for the parameters n.

The acceleration of the impactor in the simulations is difficult to use, since variations of acceleration can be very sudden. This makes the peak acceleration very difficult to estimate. Moreover, the acceleration is computed from the speed, and is not directly a simulation output. I used a triangular moving average (TMA) to smoothen the acceleration, and I find that in general the acceleration profiles are similar to the ones obtained in Nguyen et al. (2019). A triangular moving average is a method that, for each point, takes into account a certain number of previous and next points to average the current value. This repeated to every point makes the whole curve smoother.

The triangular moving average derives from the simple moving average (SMA). If we call y_i the i-th point of a curve to be smoothened, and n the parameter of the SMA, describing the number of points to consider before and after the i-th for the smoothing, the SMA for y_i can be defined as:

$$\mathrm{SMA}_{i,n} = \frac{\sum\limits_{j=-n}^{n} y_{i+j}}{2n+1} \tag{2.27}$$

From the SMA can be computed the TMA for y_i, which averages the SMAs by varying the number of considered neighbors up to n.

$$\mathrm{TMA}_{i,n} = \frac{\sum\limits_{k=0}^{n} \mathrm{SMA}_{i,k}}{n+1} \tag{2.28}$$

To derive the z-component of the acceleration of the sphere a_{z_i} from its velocity, we use central finite difference, defined by:

$$a_{z_i} = \frac{v_{z_{i+1}} - v_{z_{i-1}}}{2h} + O(h^2), \tag{2.29}$$

where $v_{z_{i-1}}$ and $v_{z_{i+1}}$ are respectively the z-component of the velocity one iteration before and after the i-th point, and h the constant time between two points. Doing first the TMA on the velocity and then the central finite difference, or with the inverse order the central finite difference to get the acceleration and then smoothen it with the TMA does not change anything, as h is a constant and does not depend on the considered points. An example of an acceleration computed with this method (TMA and central finite difference) is shown on Fig. 2.4.

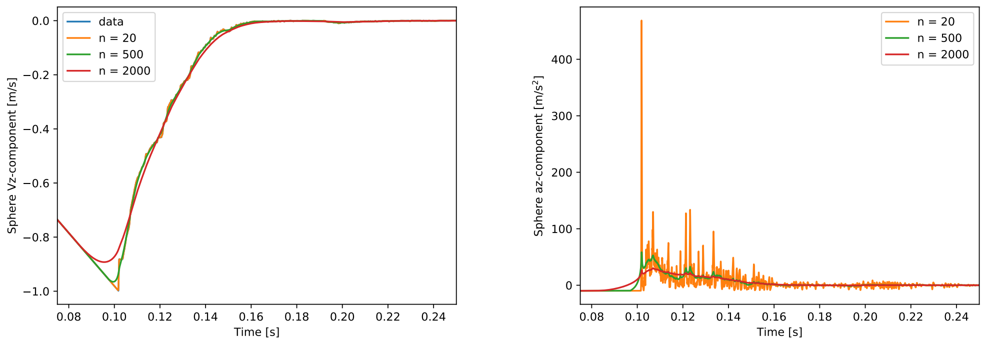

Fig. 2.4.: Vertical components of velocity and acceleration of the impacting sphere as a function of time. In this case, the sphere is dropped motionless 5 cm above the surface, and the bed height is about 10 cm.

The peak acceleration depends on the parameter n ruling the smoothing: the higher the n, the lower the peak acceleration. It is therefore difficult to decide which of them should be the value corresponding to actual experiments. The velocity for high n does not seem to represent well the impact moment, and the real acceleration of the simulations is closer to actual measurements for high n.

Using a slightly modified version of `pkdgrav` provided by Ronald-Louis Ballouz to return the acceleration in the output file, I was able to directly get the acceleration without having to derive it from the velocity. The acceleration is still very irregular and close to the one we get from the central finite difference, meaning that the irregularity of the acceleration is not due to the derivation from the velocity, but is inherent to the simulation. Therefore, the acceleration is not considered for most of the comparisons, and I first focus on the final depth and the collision duration, that are not subject to these uncertainties on the value of the acceleration. However, after the TMA, acceleration can still be used, with caution, because essential information on the drag force can be determined from acceleration data. I use the post-TMA acceleration in Section 2.2.3.

Bed height

Nguyen et al. (2019) considered bed heights ranging from 1 to 12 cm to show that, for a bed height larger than about 6 cm, the vertical boundary conditions do not seem to play a role anymore on the outcomes of the impact, whereas we observe an increase of the peak acceleration for shallower beds. I also ran some simulations with different bed heights to see if a similar trend could be detected. In order to check that, I considered bed heights of 3, 6, 8, 10, and 12 cm. As stated previously, it is difficult to get the exact peak acceleration from the simulations, or at least an acceleration comparable to the actual one. Therefore, it is not the acceleration but the final depth and the collision time that are shown in Fig. 2.5.

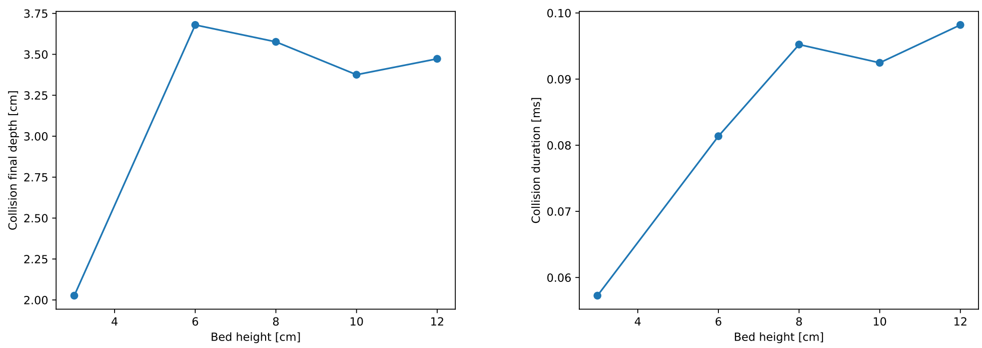

Fig. 2.5.: Final depth and collision duration as a function of the bed height. The final depth corresponds to the bottom of the sphere at the end of the simulation. In this case, the sphere is dropped motionless 5 cm above the surface, and the bed height is about 10 cm.

There are fluctuations due to the variety of surfaces encountered by the sphere, but it can nevertheless be noticed that the final depth and the collision duration seem more or less constant for heights larger than 8 cm, which justifies the choice of considering the three heights 8, 10, and 12 cm in the simulations. It is difficult to know with certainty from Fig. 2.5 if the 6 cm-height simulation is influenced by boundary effect: the final depth does not seem to indicate that, but the collision duration is a little far from the other points with larger heights, and this could be due to a boundary effect. Since the collision duration is very stochastic (as shown in Nguyen et al. (2019)), the 6 cm-height bed may be deep enough to avoid boundary effects, but I conservatively considered only higher beds.

Stopping depth

First, simulation data can be compared to Eq. 2.16, by showing the stopping depth as a function of the total drop height (drop height plus stopping depth). The penetration depth was calculated and the exact drop height was deduced from the speed at impact by $h = V_c^2/(2g)$. In order to verify Eq. 2.16, a linear regression (using logarithmic scales) was performed to determine the coefficient α in

$$z_{\text{stop}} = \left(z_0^{\frac{1}{\alpha}-1} H \right)^{\alpha} . \tag{2.30}$$

thanks to the `numpy.polyfit` routine in `Python` and compare it to $\alpha = 1/3$ shown in Eq. 2.16 and found in previous literature. The result is shown in Fig. 2.6 for 10 mm glass beads, and in Fig. 2.7 for 5 mm glass beads. Coefficients are indicated in the legend.

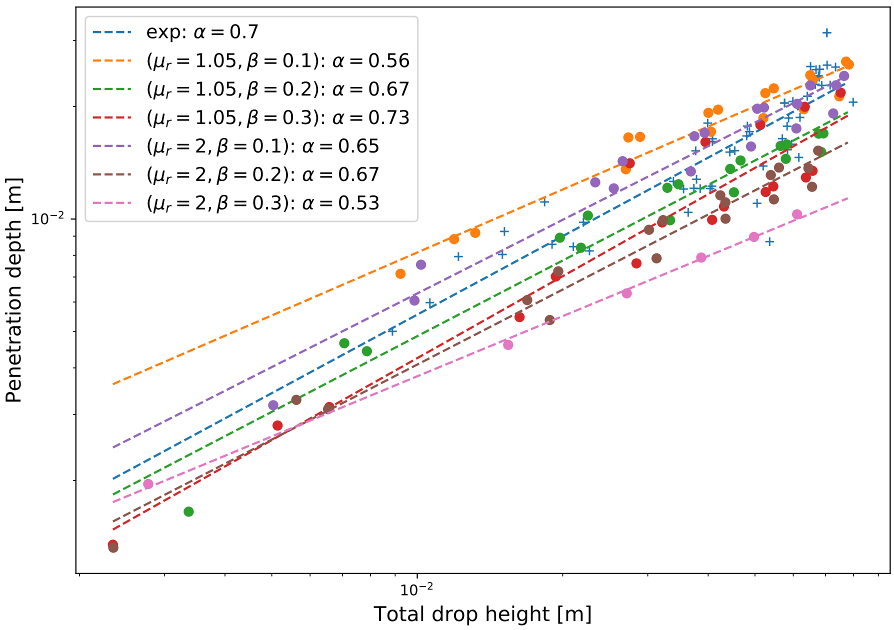

Fig. 2.6.: Stopping depth as a function of the total drop height for 10 mm beads, and for different values of the rolling friction coefficient μ_R and shape parameter β. Coefficient α introduced in Eq. 2.30 is shown in the legend. Results from experiments (Nguyen et al., 2019) are also shown as "exp" with crosses, whereas numerical results are showed as dots.

From Fig. 2.6 and 2.7, it seems that an expression such as Eq. 2.30 is verified by both experimental and numerical data, and that they have similar coefficients, above all for small beads, when surfaces are flatter and therefore stochasticity is lower. However, all the α coefficients found for the best fits are much higher than what was previously observed, i.e., $\alpha = 1/3$ in Eq. 2.16. Indeed, we find that, for 10 mm glass beads, α goes from 0.53 to 0.73, and from 0.61 to 0.64 for 5 mm beads. It is also interesting to notice that α does not seem to increase with the rolling friction coefficient μ_R or β, and therefore the discrepancies found in the α coefficient between this study and previous ones do not seem to be due to the friction of the considered material.

Moreover, comparing numerical data to experiments, pairs of coefficients $(\mu_R = 1.05, \beta = 0.2)$ and $(\mu_R = 2, \beta = 0.1)$ seem to best fit experimental data for 10 mm beads. These coefficients correspond to angles of repose of,

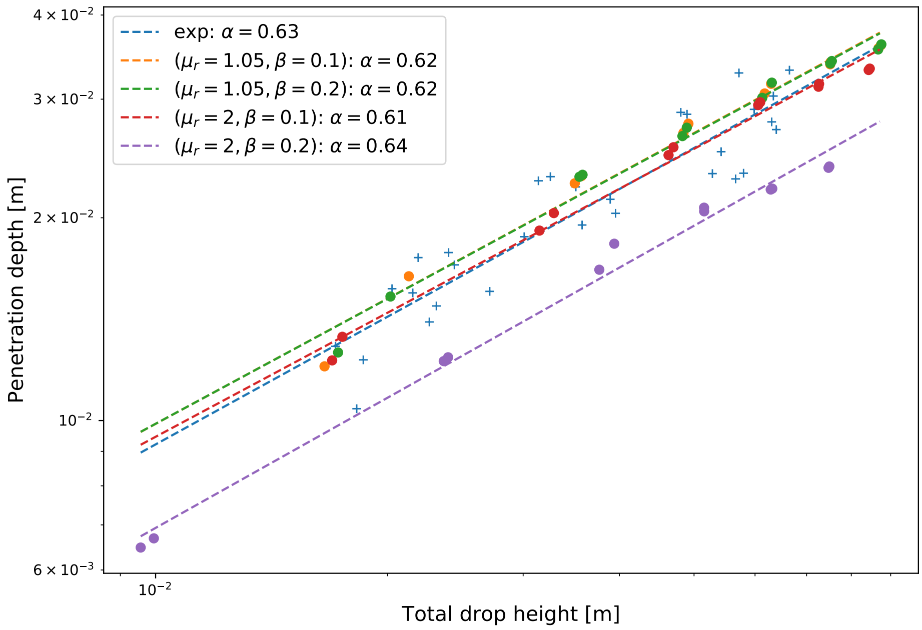

Fig. 2.7.: Stopping depth as a function of the total drop height for 5 mm beads, and for different values of the rolling friction coefficient μ_R and shape parameter β. Coefficient α introduced in Eq. 2.30 is shown in the legend. Results from experiments (Nguyen et al., 2019) are also shown as "exp" with crosses, whereas numerical results are showed as dots. Fits for pairs $(\mu_R = 1.05, \beta = 0.1)$ and $(\mu_R = 1.05, \beta = 0.2)$ are almost exactly equal.

respectively, $28°$ and $26.5°$ (see Table 2.2), which are a little higher than the angles of repose measured in the experiments, i.e., $23.6 \pm 1.2°$. Concerning the 5 mm beads, the pair $(\mu_R = 2, \beta = 0.1)$ presents a response very similar to the one of the experiments. The angle of repose, $26.5°$ is this time very close to the experimental one, $26.2 \pm 2.5°$.

Another way to compare the results between both numerical simulations and experiments and previous work is to represent the stopping depth as a function of collision speed. Data of my simulations can be found in Fig. 2.8 for the 1 cm beads, and in Fig. 2.9 for the 5 mm beads. It is noticeable that results from simulations and experiments are very close to each other, and that best fits correspond to the pairs $(\mu_R = 1.05, \beta = 0.2)$ and $(\mu_R = 2, \beta = 0.1)$ for both beads.

In this case, I consider the Coulomb force in Eq. 2.17 as a linear function of depth, and this leads to Eq. 2.22 relating stopping depth to collision speed. Thanks to the `scipy.optimize.curve_fit` routine in `Python`, the best coefficients f_0, k, and d_1 can be determined for the data to fit Eq. 2.22.

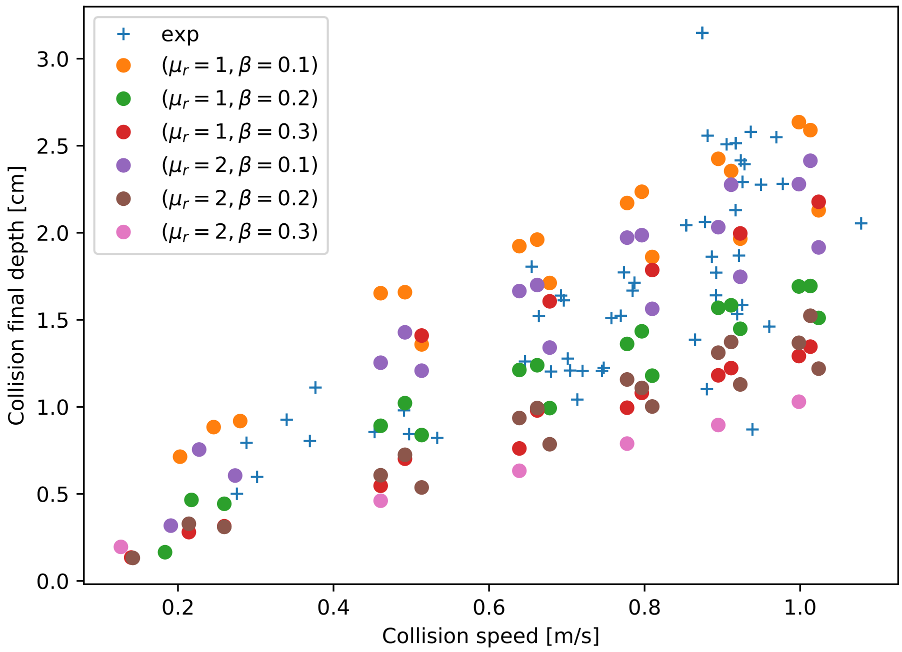

Fig. 2.8.: Collision final depth as a function of the collision speed for 1 cm beads, and for different values of the rolling friction coefficient μ_R and shape parameter β. Results from experiments (Nguyen et al., 2019) are also shown as "exp".

I considered three cases, where the Coulomb force is $F_C(z) = f_0$ as it was done in Nguyen et al. (2019), $F_C(z) = kz$ as it was found to be the best fit in Katsuragi et al. (2007), and a more general case, where $F_C(z) = f_0 + kz$ (even if $F_C(z)$ could be much more complex). The purpose of also trying simplified expressions for the Coulomb force is that reducing the number of variables drastically decreases the values of the estimated covariance, and therefore the error on the values found.

Best matches seem to be obtained for $k = 0$, meaning that the Coulomb force seems to be constant with penetration depth. However, when a proportional function is considered with $f_0 = 0$, satisfying matches are also found, which means that a linear Coulomb force cannot be totally ruled out. However, the function `scipy.optimize.curve_fit` gives relatively large errors and different results in the case considered here. Therefore, I also implemented, for the simplified cases $k = 0$ and $f_0 = 0$, a routine to find the local minima of the χ^2 function, used in the method of least squares. The χ^2 function is either $\chi^2 = \sum_{\text{simus}} (z_i - z_{\text{stop}}(v_i, f_0, d_1))^2$ if Eq. 2.23 is considered ($k = 0$), or $\chi^2 = \sum_{\text{simus}} (v_i - V_c(z_i, d_1, k))^2$ if Eq. 2.22 is considered with $f_0 = 0$. Several local minima with low χ^2 values are found, which means there are several pairs of parameters that correspond to good matches with numerical

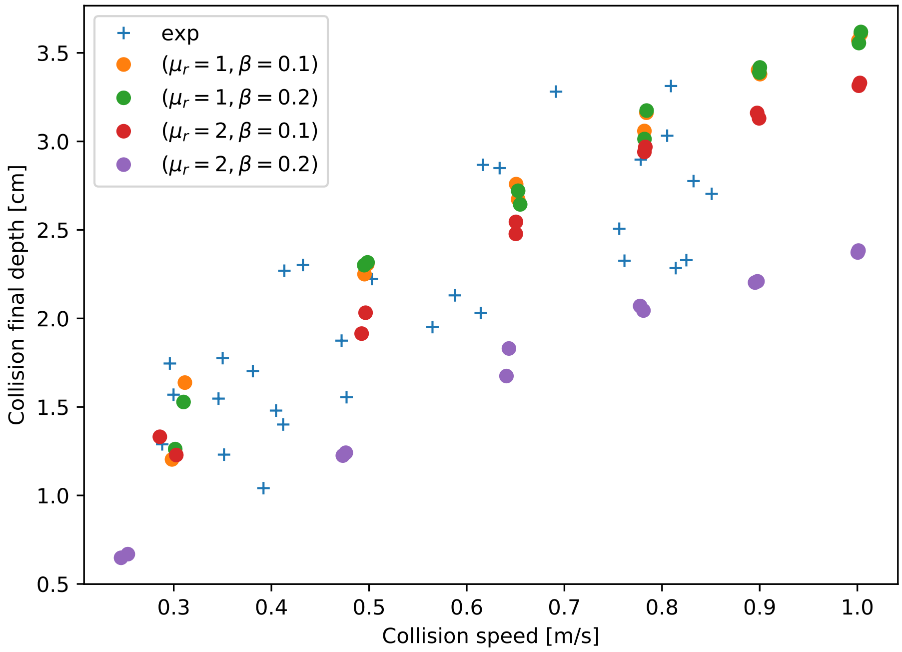

Fig. 2.9.: Collision final depth as a function of the collision speed for 5 mm beads, and for different values of the rolling friction coefficient μ_R and shape parameter β. Results from experiments (Nguyen et al., 2019) are also shown as "exp".

data. Among these fits (or local minima), there is one better than the others, corresponding to the global minimum. The pairs of coefficients corresponding to these best fits, as well as the further pairs related to local minima are shown in Table 2.4 for the 1 cm glass beads, and in Table 2.5. I showed the results only for $k = 0$ since it provides the best fits.

Tab. 2.4.: Best fits for 1 cm glass beads (local minima of the χ^2 function) (SI units)

μ_R	β	Best fit $(f_0, 1/d_1)$	Extreme local minima $(f_0, 1/d_1)$
	0.1	(11.44, 83.0)	(9.84, 214.6), (13.07, 60.3)
1.05	0.2	(15.10, 90.4)	(9.89, 300.4), (19.74, 64.0)
	0.3	(17.13, 76.3)	(9.91, 392.1), (18.5, 59.6)
	0.1	(12.83, 76.4)	(9.87, 223.5), (14.87, 56.7)
2.0	0.2	(19.82, 82.7)	(9.85, 436.3), (19.82, 82.7)
	0.3	(19.68, 139.8)	(10.07, 449.69), (19.68, 139.8)

Tab. 2.5.: Best fits for 5 mm glass beads (local minima of the χ^2 function) (SI units)

μ_R	β	Best fit $(f_0, 1/d_1)$	Extreme local minima $(f_0, 1/d_1)$
1.05	0.1	(11.28, 49.5)	(9.85, 130.5), (11.98, 40.6)
	0.2	(11.29, 49.5)	(9.93, 105.6), (11.99, 40.6)
2.0	0.1	(11.63, 49.98)	(9.84, 150.1), (12.30, 42.3)
	0.2	(13.20, 62.0)	(9.85, 217.5), (14.8, 48.5)

The relatively large range of possible values with good fits to the data shows that it is difficult to precisely determine the values of the coefficients from the penetration depth. However, it is noticeable that the pairs of coefficients corresponding to local minima roughly form a line in the 2-D parameter space. For example, for $k = 0$, the local minima for $(f0, d1)$ are roughly $(f_{0_i}, af_{0_i} + b)$ where a and b are constants depending on the size of the grains, and the material properties.

In Fig. 2.10 are shown the final depths for both bead sizes, as well as the corresponding best fits presented in Tables 2.4 and 2.5 and the experimental data.

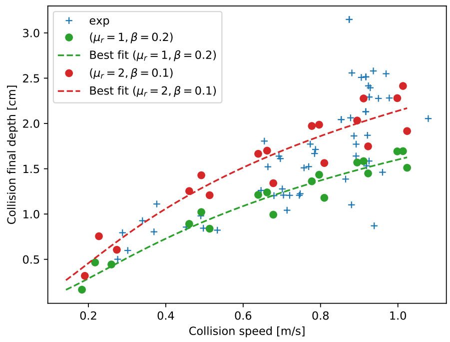

(a) 1 cm glass beads

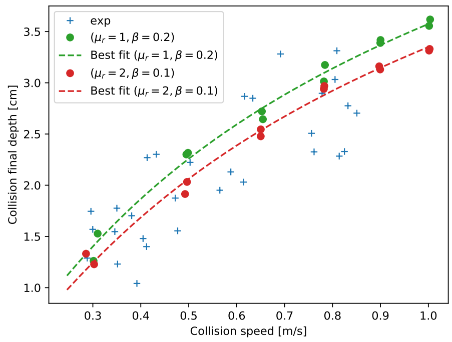

(b) 5 mm glass beads

Fig. 2.10.: Collision final depth as a function of the collision speed for 1 cm and 5 mm beads, and for different values of the rolling friction coefficient μ_R and shape parameter β. Corresponding best fits are also shown in the same color with dashed lines. Results from experiments (Nguyen et al., 2019) are also shown as "exp".

Collision duration

I also computed the duration of the impact for the different pairs of parameters previously considered. As previously stated, the collision duration corresponds to the time between impact and settling. In practice, a condition has to be established to define settling, because reaching a speed exactly equal to zero is theoretical. Depending on this condition, the collision duration may vary a little. In Nguyen et al. (2019), the collision was considered as ended when the acceleration was smaller than $0.1g$. I considered two conditions for my simulations: the collision stops either when the vertical velocity is smaller than 1 cm s^{-1}, or smaller than 1 mm s^{-1}. The collision duration for my simulations and for the experiments are shown in Fig. 2.11 for 1 cm glass beads, and in Fig. 2.12 for 5 mm glass beads. In these figures, both stop conditions are represented: plain bullets correspond to the condition $v_z < 1$ cm s^{-1}, and the other endpoint of the line segment correspond to $v_z < 1$ mm s^{-1}.

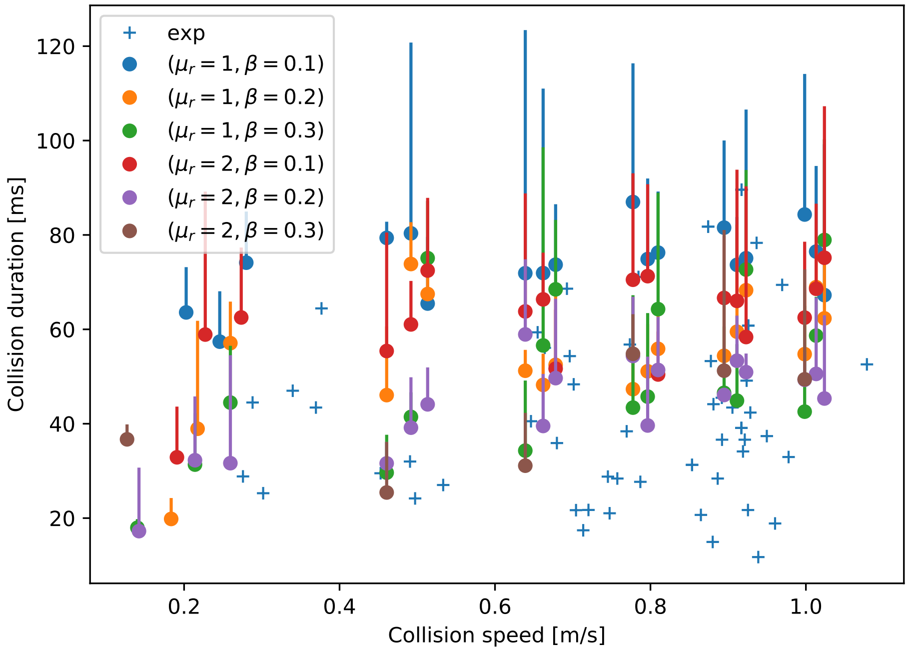

Fig. 2.11.: Collision duration as a function of the bed height for 1 cm beads, and for different values of the rolling friction coefficient μ_R and shape parameter β. Plain bullets correspond to the end-of-collision condition $v_z < 1$ cm s^{-1}, and the other endpoints of the line segments correspond to $v_z < 1$ mm s^{-1} Results from experiments (Nguyen et al., 2019) are also shown as "exp".

Both experimental and numerical data appear scattered, and this may be due to the very small quantities measured, to the precision of the instruments, to the stop condition, and to the influence of the exact local surface. Nevertheless, trends can still be established. For the 1 cm beads, experimental results seem to be smaller on average than numerical ones, whereas, for the 5 mm beads, results are closer to each other, and once again the best fits correspond to the pairs $(\mu_R = 1.05, \beta = 0.2)$ and $(\mu_R = 2, \beta = 0.1)$.

According to theory, if the Coulomb force is supposed constant ($k = 0$), the collision duration can be computed from coefficients (f_0, d_1) using Eq. 2.26. Using the best fits of the (f_0, d_1) coefficients determined from collision depths, for the best pairs $(\mu_R = 1.05, \beta = 0.2)$ and $(\mu_R = 2, \beta = 0.1)$, we find that the theory of constant Coulomb force does not predict the collision duration as well as the collision depth (see Fig. 2.13). Indeed, in our simulations and in experiments, the collision duration seems to be almost constant, with no

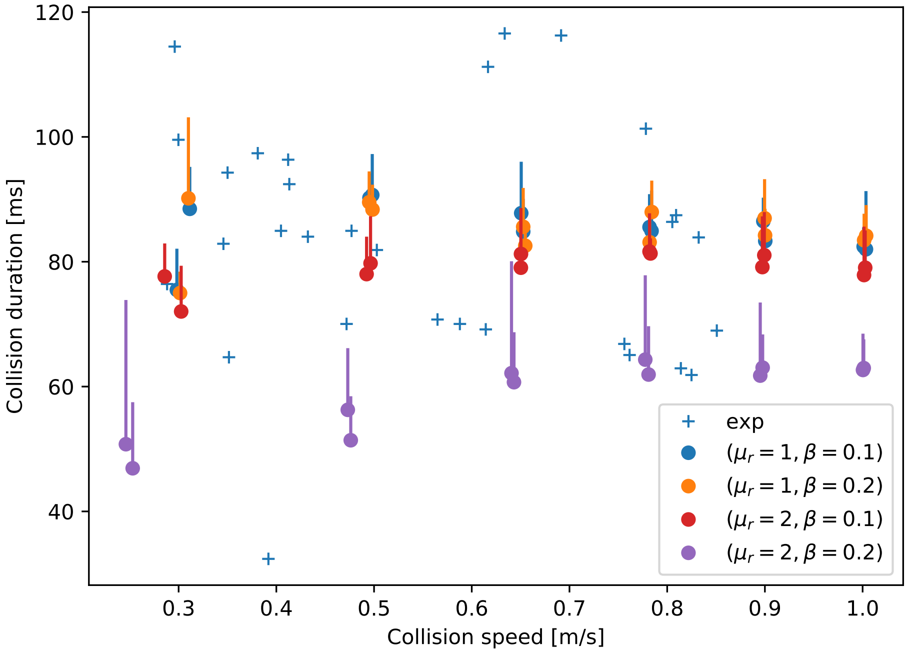

Fig. 2.12.: Collision duration as a function of the bed height for 5 mm beads, and for different values of the rolling friction coefficient μ_R and shape parameter β. Plain bullets correspond to the end-of-collision condition $v_z < 1$ cm s^{-1}, and the other endpoints of the line segments correspond to $v_z < 1$ mm s^{-1}. Results from experiments (Nguyen et al., 2019) are also shown as "exp".

clear increase for increasing impact speeds. Moreover, for the 5 mm beads, the computed durations according to the best fits are much larger than the actual numerical values. They are as well larger than the experimental ones, even if collision depths were correctly represented by the theory. This means that the theory of a constant Coulomb force is not valid with our simulations, or at least that the collision duration cannot be computed from this theory.

Acceleration

In Section 2.2.2, I presented the total force on a projectile, i.e., the sum of the weight, the Coulomb force, and the inertial drag force. For a given material, the Coulomb force is supposed to depend only on the depth (and could even be constant), whereas the inertial drag force $\frac{mv^2}{d_1}$ should depend only on the velocity, if d_1 is considered as a constant. For example, in their glass bead experiments, Katsuragi et al. (2007) verified that d_1 was a constant, and their best fits were obtained with a Coulomb force proportional to the depth.

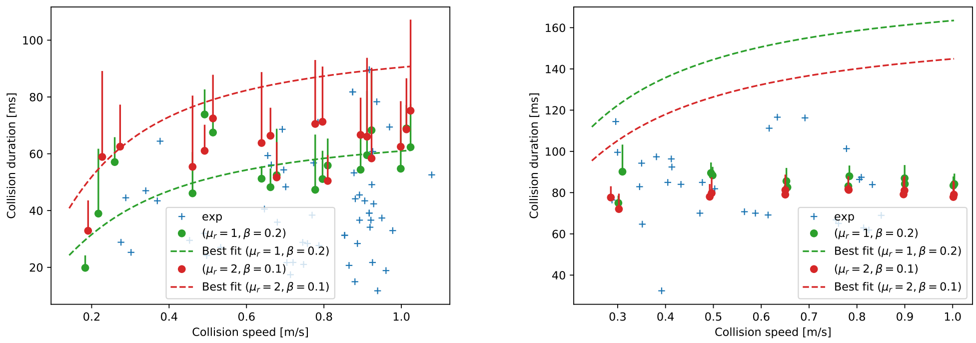

(a) 1 cm glass beads **(b)** 5 mm glass beads

Fig. 2.13.: Collision final depth as a function of the bed height for 1 cm and 5 mm beads, and for different values of the rolling friction coefficient μ_R and shape parameter β. Corresponding best fits are also shown in the same color with dashed lines. Plain bullets correspond to the end-of-collision condition $v_z < 1$ cm s^{-1}, and the other endpoints of the line segments correspond to $v_z < 1$ mm s^{-1}. Results from experiments (Nguyen et al., 2019) are also shown as "exp".

Clark et al. (2013) also investigated the variation of the inertial force as a function of the depth. They defined a more general inertial force, $h(z)v^2$ and found that h was constant, but only for large enough depths. Indeed, for values smaller than 5 cm, the function h decreases with the depth for a circular impactor. Concerning the Coulomb force, they found it was roughly linear, but dominated by the offset and therefore close to a constant.

In Section 2.2.3, I presented how the acceleration is treated with a TMA to "smooth" it and make the acceleration profile closer to a theoretical one. Since the result can depend on the parameter n used in the TMA, the results presented below have to be taken with caution. Nevertheless, they can give us a global idea of the variations of the inertial drag term (and maybe also of the Coulomb force) with depth. In this section, I used a TMA with a parameter $n = 1000$ because I found empirically that this was a good compromise because it enables to get a relatively smooth acceleration profile that still seems faithful to the original acceleration.

From this acceleration, I start from a more general expression of the Coulomb and inertial drag forces, defined in Clark et al. (2013):

$$ma = -mg + f(z) + h(z)v^2, \tag{2.31}$$

where f and h are functions that possibly depend on the depth z.

For one type of grain, i.e., for a given pair (μ_R, β), and for different impact speeds, I express the net acceleration $a + g$ as a function of v^2 for different depths. Since the functions f and h do not depend theoretically on the velocity, if we look at a certain depth z_i, $a + g$ should be a linear function of v^2, where the slope is $h(z_i)$ and the y-intercept is $f(z_i)$. By considering several depths, it is possible to evaluate the functions f and h in different points and therefore reproduce the functions.

First of all, what I noticed is that the values of the functions f and h, and therefore of the forces exerted by the granular bed on a penetrating sphere, depend on the layout of the grains. In my simulations, I considered three different bed heights, and since they are made by cutting grains higher than a certain value, the layout on the surface can be different. For example, the sphere could impact directly the middle of a grain, or the space between grains. This diversity of responses is thus larger for the 1 cm glass beads than for the 5 mm ones, and this is observed in the functions f and h, particularly for depths as low as a few centimeters. Therefore, I computed the values of the functions f and h by separating the different bed heights considered, and therefore the surface.

Moreover, the deeper the depth considered, the fewer the data, since only a few spheres reach large depths. Due to this lack of data for the largest depths, the interpolation of the linear function is less accurate, and therefore I considered above all the shallowest part of the bed. This part usually corresponds to the first centimeter for the 1 cm grains, and $1.5 - 2$ cm for the 5 mm grains.

Examples of the net acceleration as a function of v^2 are shown in Fig. 2.14, for 10 cm height bed setups, and for 1 cm and 5 mm grains with $(\mu_R, \beta) = (1.05, 0.2)$. It is noticeable that the distributions of points for a given height seems to correspond well to a straight line, and therefore that the assumption that f and h do not depend on the velocity seems to be valid.

Inertial drag

The h function can be determined by considering a high number of depths. The function is shown in Fig. 2.15, for the pairs $(\mu_R, \beta) = (1.05, 0.2)$ and $(\mu_R, \beta) = (2, 0.1)$ and for 1 cm grains.

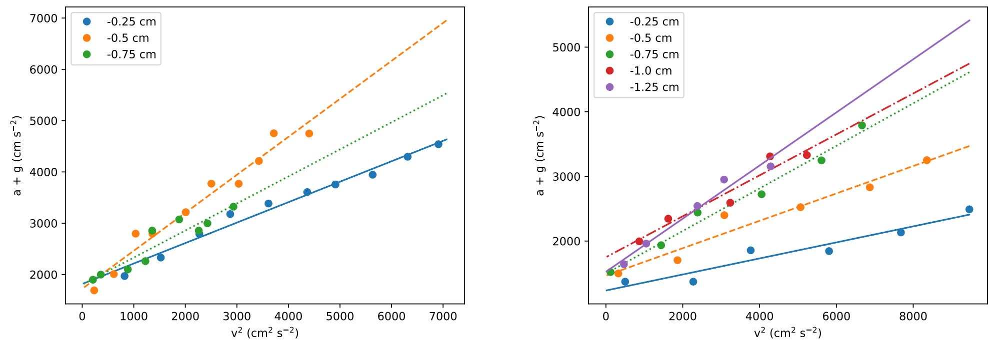

(a) 1 cm grains

(b) 5 mm grains

Fig. 2.14.: Net acceleration as a function of the squared velocity, for a 10 cm height bed, and different depths. The grain parameters are $(\mu_R, \beta) = (1.05, 0.2)$.

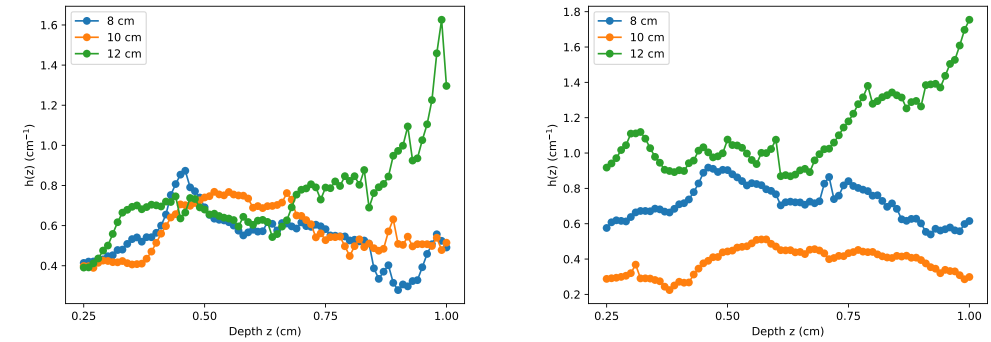

(a) $(\mu_R, \beta) = (1.05, 0.2)$

(b) $(\mu_R, \beta) = (2, 0.1)$

Fig. 2.15.: $h(z)$ as a function of depth z, for two pairs of friction parameters, and 1 cm grains.

We can notice that h seems on average to increase for the smaller depths, but can be considered as almost constant. This corresponds to the choice of a d_1 constant by Nguyen et al. (2019). The three different beds have similar variations, except for the largest depths. In this case, h for the 12 cm bed increases with depth, whereas the function stays more or less constant for other beds. This trend is verified for other friction parameters' pairs, and this could be due to the 12 cm case leading to slightly lower penetrations in general, and therefore for a 1 cm depth, the sphere is already almost settled, contrarily to other layouts. In this case, the trend for larger depths could be an increase of h. However, due to the uncertainties on the computation of the acceleration, this should be taken with caution.

Whether it is increasing or constant, this trend is different from the results of Clark et al. (2013), which found that h decreases with depth for shallow depths. If we consider that h is almost constant and that variations are mostly due to the uncertainties in the computations of the acceleration, the trend is similar to what Katsuragi et al. (2007) found and to the assumption by Nguyen et al. (2019).

Since the absolute value of the acceleration could depend on chosen value of the parameter n, we do not necessary expect to find d_1 from h. However, the average h would correspond to about $0.6 - 0.7$ cm^{-1}, meaning that $1/d_1$ would be in the range $60 - 70$ m. This interval is in the interval of best fits for $1/d1$ (see Table 2.4).

Concerning the 5 mm grains, the functions h are shown in Fig. 2.16 for $(\mu_R, \beta) = (1.05, 0.2)$ and $(\mu_R, \beta) = (2, 0.1)$. This time, the increase in h seems to be clearer for small depths, and therefore could be a true trend but, otherwise, the function h can be considered as relatively constant, or at least not monotonously increasing nor decreasing. The value found for h is this time a little lower than $1/d_1$, and this could be due to the uncertainty on d_1 in the fitting of data, or in the n parameter for the TMA.

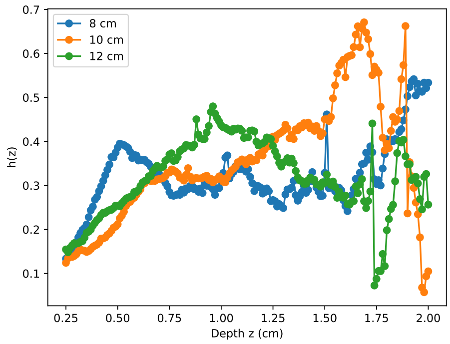

(a) $(\mu_R, \beta) = (1.05, 0.2)$

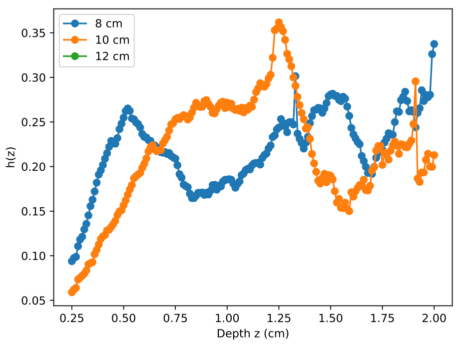

(b) $(\mu_R, \beta) = (2, 0.1)$

Fig. 2.16.: $h(z)$ as a function of depth z, for two pairs of friction parameters, and 5 mm grains.

Coulomb force

The Coulomb force can also be determined as the y-intercept of the $a + g$ function of v^2 curve. However, since the TMA parameter can have a more direct influence on the value of a than on its variation, I was more interested in the variations of f than on the actual value.

Results for 1 cm and 5 mm beads are respectively shown in Fig. 2.17 and 2.18. Considering the 1 cm beads, f is on average constant for most of the simulations, or at least does not generally show any monotonous increase or decrease. However, some data show a slight decrease in f, which is opposite to what was found by Clark et al. (2013) and Katsuragi et al. (2007). They indeed found that f was increasing with the depth: in the case of Katsuragi et al. (2007) f is proportional to depth, and in the case of Clark et al. (2013), f is linear and almost constant. Concerning the 5 mm beads, we see a general increase of f with the depth and a non-zero y-intercept, which suggests a better agreement with the work of Clark et al. (2013) than with Katsuragi et al. (2007).

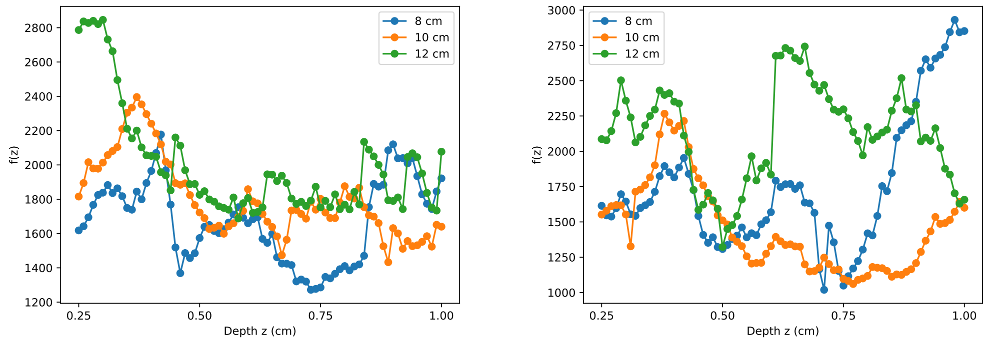

(a) $(\mu_R, \beta) = (1.05, 0.2)$ **(b)** $(\mu_R, \beta) = (2, 0.1)$

Fig. 2.17.: $f(z)$ as a function of depth z, for two pairs of friction parameters, and 1 cm grains.

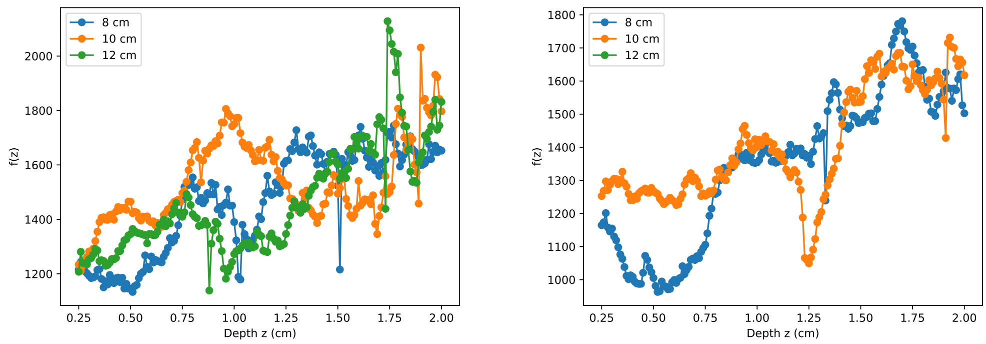

(a) $(\mu_R, \beta) = (1.05, 0.2)$ **(b)** $(\mu_R, \beta) = (2, 0.1)$

Fig. 2.18.: $f(z)$ as a function of depth z, for two pairs of friction parameters, and 5 mm grains.

The decrease observed in some simulations could either be due to the smaller accuracy of the computations of acceleration with the largest grains, or to the larger variations of the results with these grains, and therefore it may not be representative of the actual behavior. However, this could also mean that larger beads do not behave exactly the same as smaller beads. Clark et al. (2013) used 4.3 mm and 6 mm disks in their experiments, and found similar results to mine (with 5 mm beads) for the variation of the Coulomb force, a slight increase with depth. Katsuragi et al. (2013), with smaller glass beads (about $0.25 - 0.3$ mm diameter) found a larger proportional increase of f with depth. On the other hand, I found that f is roughly constant, or could even decrease with depth with larger beads. By summing all these results, we would have a linear Coulomb force $F_c = f_0 + kz$, where the magnitude of k would depend on the size of the grains. k would be slightly negative or equal to zero for 1 cm beads (my work), slightly positive for 5 mm beads (my work and Clark et al. (2013), and even larger with smaller grains (for example Katsuragi et al. (2007) with submillimeter grains). f_0 also seems to depend on the grain size, in an opposite trend, as it decreases with smaller grains (my work), and was evaluated to be about zero with very small grains (Katsuragi et al., 2007). If this were true, the form of the Coulomb force would directly depend on the grain size.

The size ratio between the impactor and the grains is about $70 - 100$ for experiments by Katsuragi et al. (2007), $21 - 30$ for experiments by Clark et al. (2013), 20 for my simulations and experiments by Nguyen et al. (2019) with 5 mm grains, and 10 for the same simulations and experiments with 1 cm grains. This means that, instead of depending on the absolute grain size, the Coulomb force could depend on the impactor/grain size ratio.

2.2.4 Conclusion of the bucket experiments

By modeling the glass beads of the bucket experiments performed by Nguyen et al. (2019), I found great agreements between both results, especially for `pkdgrav` parameters previously considered as good representative of glass beads. This means that `pkdgrav` seems to be correctly adapted to simulate granular material in this context. Parameters that seem to correctly represent the glass beads used in the experiments are the sets ($\mu_s = 1.05, \mu_T = 1.3, \mu_R = 1.05, \beta = 0.2$) and ($\mu_s = 1.05, \mu_T = 1.3, \mu_R = 2.0, \beta = 0.1$). In order to better constrain these coefficients, other comparisons such as compression tests could also be considered.

Moreover, by analyzing the forces on the sphere, I compared my simulations to previous experimental studies, and possibly found a trend on the qualitative form of the Coulomb force for glass beads: $F_c = f_0 + kz$ with f_0 increasing and k decreasing with an increasing particle size. As previously stated, the results should be taken with caution as the acceleration needs to be smoothed before analysis. However, the same trends are observed for all simulations, which reinforces the results I found.

2.3 Inclined planes

In this section, I present inclined plane simulations I performed in order to find corresponding parameters between the DEM code `pkdgrav` and the $\mu(I)$ rheology used in the code `CIMLIB-CFD` of Ecole des Mines ParisTech, by analyzing the velocity profiles. I first briefly present the $\mu(I)$ rheology and `CIMLIB-CFD`, and then present my inclined plane simulations.

2.3.1 $\mu(I)$ rheology

The $\mu(I)$ rheology is a constitutive law for dense granular flows, and is based on a continuum description. It is presented in Cruz et al. (2005) and Jop et al. (2006).

It was introduced to model dense flows between sidewalls. If a granular material is confined under a normal stress P, the shear stress τ is proportional to the normal stress, and the coefficient of proportionality is the friction coefficient μ, function of a dimensionless number called the inertial number I:

$$\tau = \mu(I)P, \tag{2.32}$$

where I is function of the shear rate $\dot{\gamma}$:

$$I = \frac{\dot{\gamma}d}{\sqrt{\frac{P}{\rho_s}}}, \tag{2.33}$$

where d is the particle diameter and ρ_s is the particle density. The inertial number corresponds to the square root of previously introduced Savage number (Savage, 1984) or Coulomb number (Ancey et al., 1999).

From numerical simulations and inclined plane experiments, it was shown that the friction μ, function of the inertial number I, can be written as:

$$\mu(I) = \mu_s + \frac{\mu_2 - \mu_s}{\frac{I_0}{I} + 1}, \tag{2.34}$$

where μ_s and μ_2 correspond to the two extrema of the friction coefficient, and I_0 is a constant representing $\mu(I_0) = \frac{\mu_s+\mu_2}{2}$. An example of the friction coefficient function is shown in Fig. 2.19.

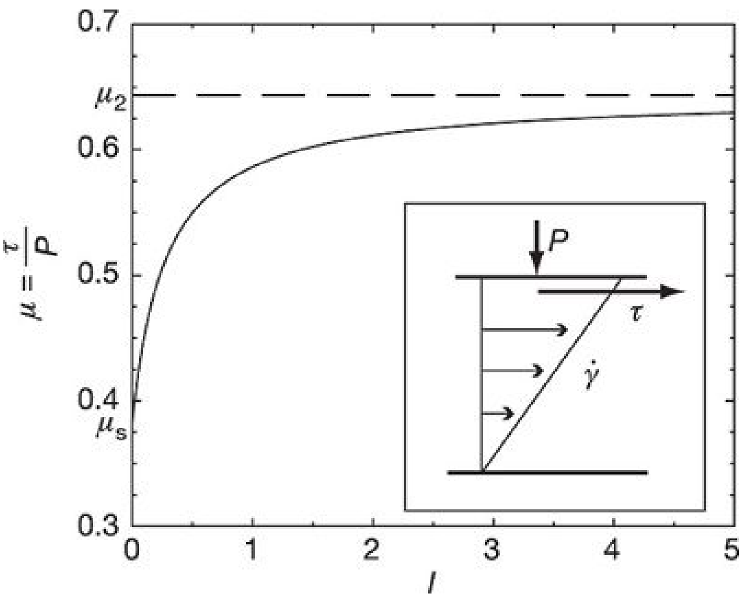

Fig. 2.19.: Friction coefficient μ as a function of the inertial number I with $\mu_s = \tan(20°)$, $\mu_2 = \tan(32.76°)$, and $I_0 = 0.279$. The inset shows, in a plane shear configuration, the pressure P, the shear stress τ, and the shear rate $\dot{\gamma}$. Image credit: Jop et al. (2006)

It was generalized in 3D by Jop et al. (2006), by considering that the packing fraction inside the flow is only affected by small variations, and thus that the material can be represented as an incompressible fluid. The internal stress tensor $\boldsymbol{\sigma}$ is described by the following equations:

$$\sigma_{ij} = -P\delta_{ij} + \tau_{ij}, \tag{2.35}$$

$$\tau_{ij} = \eta(|\dot{\boldsymbol{\gamma}}|, P)\dot{\gamma}_{ij}, \tag{2.36}$$

$$\eta(|\dot{\boldsymbol{\gamma}}|, P) = \frac{\mu(I)P}{|\dot{\boldsymbol{\gamma}}|}, \tag{2.37}$$

$$I = \frac{|\dot{\boldsymbol{\gamma}}|d}{\sqrt{\frac{P}{\rho_s}}}, \tag{2.38}$$

$$\dot{\gamma}_{ij} = \frac{\partial v_i}{\partial x_j} + \frac{\partial v_j}{\partial x_i}, \tag{2.39}$$

$$|\dot{\boldsymbol{\gamma}}| = \sqrt{0.5\dot{\gamma}_{ij}\dot{\gamma}_{ij}}, \tag{2.40}$$

where P is an isotropic pressure, $\eta(|\dot{\boldsymbol{\gamma}}|, P)$ is an effective viscosity, $\boldsymbol{v}$ is the velocity vector, and $\dot{\boldsymbol{\gamma}}$ is the shear rate tensor.

The $\mu(I)$ function is the one defined in Eq. 2.34. As the material gets closer to rest, the shear rate and thus the inertial number tend to 0, and therefore the friction coefficient tends to μ_s. This corresponds to the yield criterion:

$$|\boldsymbol{\tau}| > \mu_s P, \tag{2.41}$$

where $|\boldsymbol{\tau}| = \sqrt{0.5\tau_{ij}\tau_{ij}}$. The material behaves like a rigid body below the threshold, and like a fluid above it.

The main advantage of the $\mu(I)$ rheology is its simplicity, and the extreme speed of execution of numerical codes using this rheology, compared for example to much heavier DEM codes. The $\mu(I)$ rheology was found to be quantitative for 1D steady flows (Midi, 2004), and was compared to a Drucker-Prager continuum model by Ionescu et al. (2015). It was validated by DEM codes for 2D granular column collapses by Lacaze et al. (2009) and Lagrée et al. (2011).

It is currently developed in 3D by Rudy Valette, Lucas Sardo, and the Ecole des Mines ParisTech team, based on the `CIMLIB-CFD` general solver, a parallel, finite element library (Coupez et al., 2013), with first results for granular column collapses by Valette et al. (2017). The model is also adapted for low-speed impacts, and the first results were presented in the 13^{th} World Congress on Computational Mechanics (Sardo et al., 2018).

In this presentation was also evoked the preliminary results of a comparison between the numerical code `pkdgrav`, and `CIMLIB-CFD`. The purpose is to eventually develop a new code, inspired by and taking advantage of both methods. The DEM part is very useful when one wants to reproduce with precision dilute regimes and at a small scale the behavior of the granular material. However, it requires a high computation time. On the other hand, the continuum part with the $\mu(I)$ gives results for larger scales, and the computation time is much shorter. Switching between both methods in a single simulation could therefore strongly reduce the global computation of a DEM code without losing too much accuracy.

One of the milestones to achieve this is to find a relation between the parameters of both methods. Indeed, the $\mu(I)$ rheology requires the knowledge of three parameters to describe the behavior of the granular material, μ_s, μ_2, and I_0, whereas the DEM code `pkdgrav` requires a much greater number of parameters concerning the friction ($\mu_s, \mu_R, \mu_T, \beta$) and additional ones for the coefficients of restitution ($\varepsilon_n, \varepsilon_t$). Since there are more parameters for the DEM part than for the continuum part, we can expect a degenerate dependency between the two sets, i.e., that several sets of DEM parameters correspond to the same behavior of a sole continuum parameter set. Nevertheless, finding an equivalence between parameters (or at least an implication) is necessary to merge the codes and make sure that they represent similar materials.

In order to initiate this work, I performed inclined plane simulations with the types of material I used for MASCOT and Hayabusa2 sampling mechanism (see respectively Chapters 4 and 5), namely one with a gravel-like friction and one with a moderate friction. The velocity profiles in granular flows along inclined planes are well determined by the $\mu(I)$ rheology (Jop et al., 2006), and therefore continuum equivalent parameters can be derived from the outputs of my simulations.

2.3.2 Inclined plane simulations

In this section, I describe the setup of my inclined plane simulations with the numerical code `pkdgrav`, then the application of the $\mu(I)$ rheology applied to inclined planes, and finally the results of my simulations.

Setup

I consider a 3D inclined plane, where grains are stuck to the bottom plane, and on both lateral sides of the slope are periodic boundary conditions instead of walls, which leads to a 2D flow. Uphill and downhill are also periodic boundary conditions, and particles that go through the downhill boundary are reintroduced uphill, which assures a steady flow and no shortage of particle with time.

The initial setup of grains consists of randomly distributed grains above the horizontal bottom plane, initially tilted to the desired angle. Grains fall under Earth's gravity and first grains get stuck against the bottom wall. The flow is therefore created gradually as grains fall and the average particle speed increases. If the angle is smaller than the angle of repose, grains do not flow and form an inert column.

The slope is modeled by a change in the gravity vector. Therefore, the z-axis (and therefore the definition of the height or altitude) is considered perpendicular to the "horizontal" bottom plane, and not parallel to the gravity vector. Likewise, the x- and y-axes are defined from the bottom plane. The x-axis corresponds to the direction of the slope. The inclination θ is defined as the positive angle between the gravity vector and $-\boldsymbol{e}_z$, where $\boldsymbol{e}_z$ is the upward unit vector associated with the z-axis. θ also corresponds to the angle between the bottom plane and the plane normal to the gravity vector. The setup is presented in Fig. 2.20.

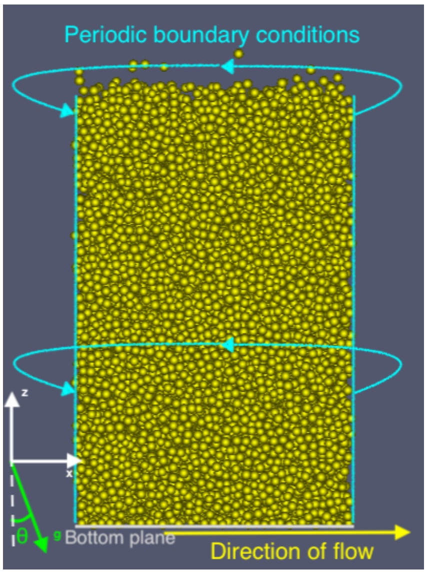

Fig. 2.20.: Schematic view of an inclined plane simulation. Gravity vector $\boldsymbol{g}$ and inclination θ are indicated, as well as the periodic boundary conditions that enable the re-injection of grains uphill after they crossed the limit downhill.

Grains in the simulations have a Gaussian size distribution, with a mean radius of 0.5 cm, a standard deviation $\sigma = 10\%$, and a cut-off at 1σ. I first considered a monodisperse distribution, but I noticed that in some simulations, even when the flow is almost steady, particular re-arrangements can appear that jam the flow and lead to sudden decrease of global kinetic energy. A way to avoid this is to consider a slightly polydisperse distribution, such as the one I eventually opted for.

The two materials I considered in my simulations are a gravel-like material and a moderate-friction one. Their properties are presented in Table 2.1 in Section 2.1. They are the same material types as the ones used for MASCOT's simulations in Chapter 4 and for Hayabusa2 sampler's simulations in Chapter 5.

The steady state is usually reached after about $100 - 200$ s for a gravel-like material, but this time significantly decreases for a moderate-friction material and increases with a larger inclination. The evolution of the column for a gravel-like material is shown in Fig. 2.21. At the beginning, the `pkdgrav` routine for the random generation of grains requires a low density packing, and thus a high column. The fall increases the packing fraction until a maximum, and then the motion stops being vertical and becomes mostly parallel to the bottom plane (in the direction of the slope). In the flow, grains collide with each others, creating more void between them and increasing the porosity and the height of the column. After reaching the steady state, the height becomes roughly constant.

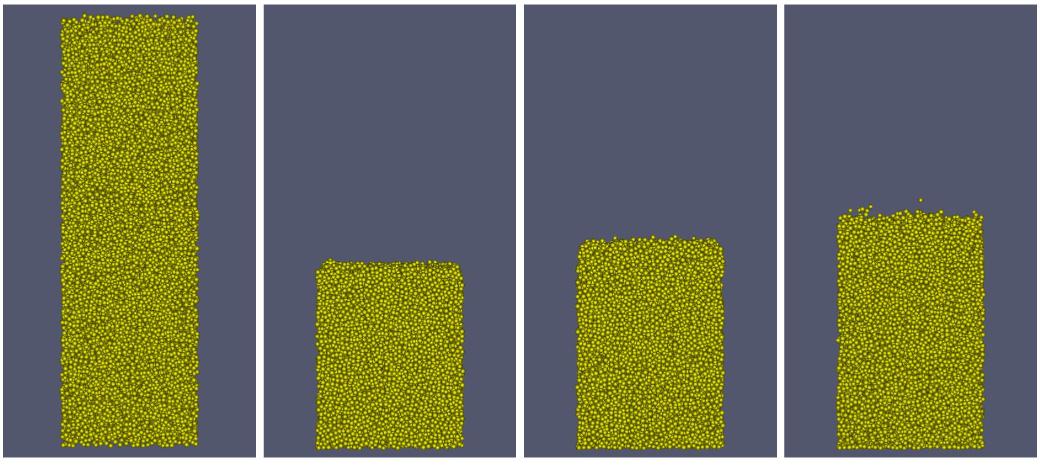

(a) 0 s (b) 1.26 s (c) 11.3 s (d) 61.5 s

Fig. 2.21.: Snapshots of the fall of the grains and the beginning of the flow, for a gravel-like material and an angle of 43°.

The global kinetic energy for different inclinations as a function of time is shown in Fig. 2.22. When the kinetic energy becomes more or less constant, I considered that a steady state was reached. For the gravel-like material, a peak in kinetic energy can be noticed before reaching the steady state.

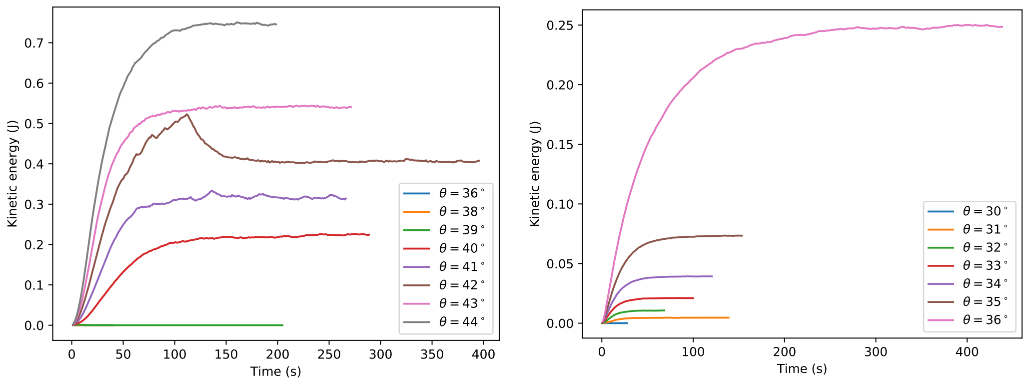

(a) Gravel-like friction (b) Moderate friction

Fig. 2.22.: Global kinetic energy as a function of time for two types of friction, and for several inclinations.

The porosity can also be an indicator of the state of the flow, and is shown as a function of time for two different inclinations and materials in Fig. 2.23. If the inclination is smaller than the angle of repose, the porosity is roughly constant with time and height, up to the top of the pile. In Fig. 2.23, both inclinations are larger than the respective angles of repose, and a flow is observed. With a gravel-like material, the porosity depends on the height, with local minima and maxima, whereas it is mostly constant with a moderate-friction material. I previously said that, in the $\mu(I)$ rheology, the medium is considered as incompressible. Even if grains are incompressible, the relatively large variations of porosity with height could explain potential discrepancies between the $\mu(I)$ model and the numerical results obtained with gravel-like material. However, for a moderate-friction material, the porosity being much more constant with height, we can expect better similarities with an incompressible model.

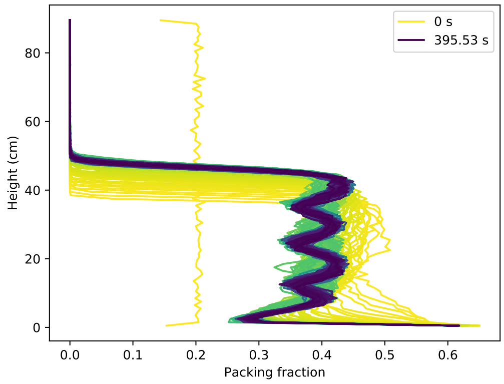

(a) Gravel-like friction, $42°$ inclination

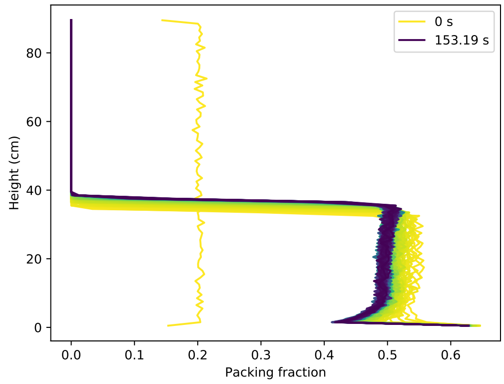

(b) Moderate friction, $35°$ inclination

Fig. 2.23.: Height as a function of packing fraction, for a gravel-like material and a $42°$ inclination (left panel), and for a moderate-friction material and a $35°$ inclination (right panel). Both inclinations are higher than the respective angles of repose. The darker the color, the further in time.

The porosity is computed by considering 1 cm-wide horizontal layers. The velocity of the grains, in the direction of the flow, can also be computed as a function of time to check the convergence to a steady state. The average x-component of the grain velocity for each 1 cm layer is shown in Fig. 2.24, for two different simulations. The left panel corresponds to the simulation for which a peak in kinetic energy was observed, and this peak is clearly visible, as the velocity increased higher than the final one and then decreased to the steady state velocity.

Because of the periodic boundary conditions on both sides of the flow, the flow can be considered as two-dimensional. This is verified by looking at the y- and z-components of the velocity of the grains, and by comparing them to the x-component of the velocity. The ratios of the velocity components are shown in Fig. 2.25 for a gravel-like material. Since most of the ratios are smaller than 1%, we can consider that the flow was mostly two-dimensional (small $\frac{v_y}{v_x}$ ratio) and is parallel to the x-axis (small $\frac{v_z}{v_x}$ ratio).

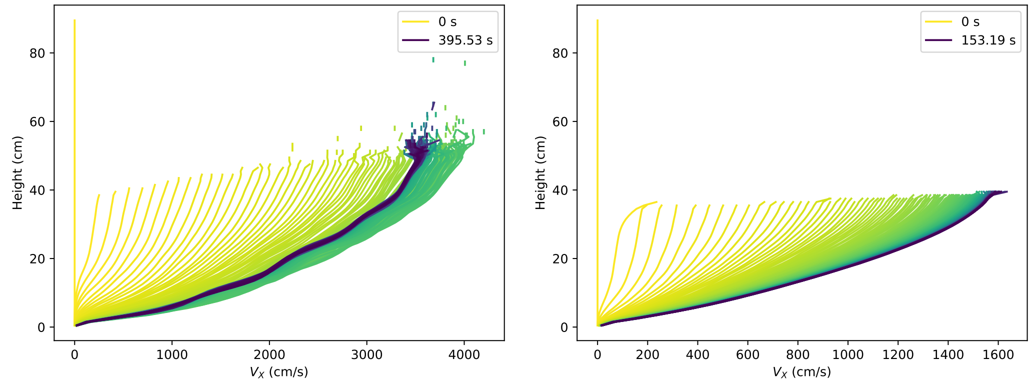

(a) Gravel-like friction, 42° inclination **(b)** Moderate friction, 35° inclination

Fig. 2.24.: Height as a function of average x-component of the velocity, for a gravel-like material and 42° inclination (left panel), and for a moderate-friction material and 35° inclination (right panel). Both inclinations are higher than the respective angles of repose. The darker the color, the further in time.

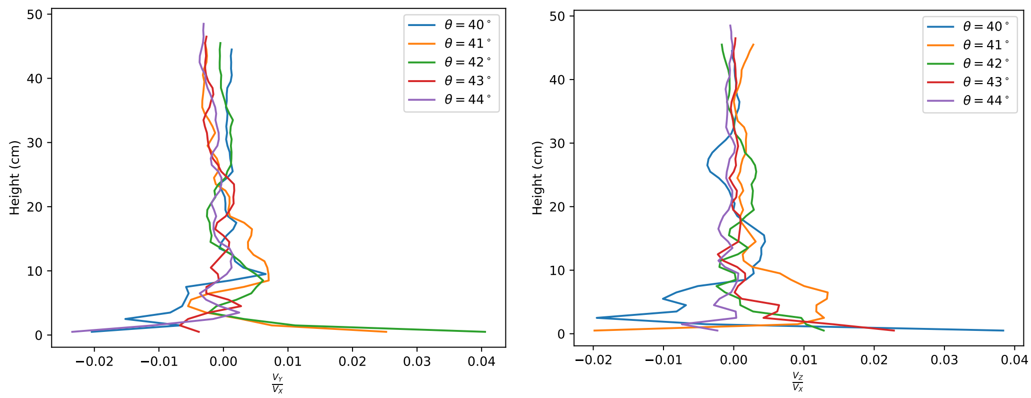

Fig. 2.25.: Height as a function of velocity ratios, for a gravel-like material and several inclinations. The left panel shows the $\frac{v_y}{v_x}$ ratio, and the right panel shows the $\frac{v_z}{v_x}$ ratio.

Application of theory to inclined planes

I previously stated that I consider a two-dimensional problem, which means that the velocity vector $\boldsymbol{v}$ and the internal stress tensor $\boldsymbol{\sigma}$ do not have y-components. Moreover, the flow is parallel to the x-axis (shown from data in the previous section), and I consider $\boldsymbol{v} = v_x(x,z)\boldsymbol{e}_x$, where $\boldsymbol{e}_x$ is the unit vector associated with the x-axis. Since I consider an incompressible medium and a steady state flow, the mass conservation equation gives:

$$\frac{\partial \rho}{\partial t} + \nabla \cdot (\rho \boldsymbol{v}) = 0 \implies \frac{\partial v_x}{\partial x} = 0, \tag{2.42}$$

meaning that $\boldsymbol{v} = v_x(z)\boldsymbol{e}_x$. This was expected as the velocity profile should be the same whatever the value of x, with the periodic boundary conditions ensuring the durability of the flow. Likewise, the internal stress tensor does not depend on x.

The Cauchy momentum equation gives:

$$\frac{\mathrm{D}\boldsymbol{v}}{\mathrm{D}t} = \frac{\partial \boldsymbol{v}}{\partial t} + \boldsymbol{v} \cdot \nabla \boldsymbol{v} = \frac{1}{\rho} \nabla \cdot \boldsymbol{\sigma} + \boldsymbol{g}. \tag{2.43}$$

$\boldsymbol{v} = v_x(z)\boldsymbol{e}_x$ leads to $\frac{\mathrm{D}\boldsymbol{v}}{\mathrm{D}t} = 0$. $\boldsymbol{g}$ is the gravity field and, in our case:

$$\boldsymbol{g} = g(\sin\theta \boldsymbol{e}_x - \cos\theta \boldsymbol{e}_z). \tag{2.44}$$

By projecting Eq. 2.43 on $\boldsymbol{e}_x$ and on $\boldsymbol{e}_z$, we find:

$$\frac{\partial \sigma_{zx}}{\partial z} = -\rho g \sin\theta, \tag{2.45}$$

$$\frac{\partial \sigma_{zz}}{\partial z} = \rho g \cos\theta, \tag{2.46}$$

and, thus, by integrating between h (the height of the flowing pile) and z, and considering there is no stress on the top surface:

$$\sigma_{zx} = \rho g \sin\theta (h - z), \tag{2.47}$$

$$\sigma_{zz} = -\rho g \cos\theta (h - z). \tag{2.48}$$

By taking into account the set of equations from Eq. 2.35 to Eq. 2.40, we have:

$$P = -\sigma_{zz} = \rho g \cos\theta (h - z), \tag{2.49}$$

$$\tau_{zx} = \sigma_{zx} = \frac{\mu(I) P \frac{\partial v_x}{\partial z}}{|\frac{\partial v_x}{\partial z}|} = \rho g \sin\theta (h - z), \tag{2.50}$$

since v_x increases with z.

This leads to $\mu(I) = \tan\theta$, meaning that the friction, and therefore the inertial number, are uniform and directly depend on the inclination. Thus, the inertial number can be directly linked to the inclination θ:

$$\mu(I) = \tan\theta = \mu_s + \frac{\mu_2 - \mu_s}{\frac{I_0}{I} + 1} \implies I = \frac{\tan\theta - \mu_s}{\mu_2 - \tan\theta} I_0. \tag{2.51}$$

Finally, the inertial number can be expressed as a function of the shear rate tensor:

$$I = \frac{|\dot{\gamma}|d}{\sqrt{\frac{P}{\rho_s}}} = \frac{|\dot{\gamma}|d}{\sqrt{g\cos\theta(h-z)}} \implies |\dot{\gamma}| = \frac{\partial v_x}{\partial z} = \frac{I\sqrt{g\cos\theta(h-z)}}{d}. \tag{2.52}$$

Thus, the velocity profile for an inclined plane is given by

$$v_x = \int_0^z \frac{\partial v_x}{\partial z'}\,\mathrm{d}z' = \frac{2Ih^{3/2}}{3d}\sqrt{g\cos\theta}\left(1-\left(1-\frac{z}{h}\right)^{3/2}\right). \tag{2.53}$$

In my simulations, g, θ, and d are known, and I needs to be determined, in order to find μ (i.e., $\tan\theta$ here) as a function of I and also find the parameters of the $\mu(I)$ rheology. h can be determined by two methods. Firstly, it can be directly measured from results. For example, I considered that the flowing pile ends when the packing fraction is smaller than 0.2, and the maximum altitude with a packing fraction higher than 0.2 is considered as the height of the flowing pile. Here, I call h_0 such pile height. Secondly, h can be considered as a free parameter, determined by fitting the theoretical profile to the data, and the values of h can be compared to the actual height of the pile.

The inertial number for each flow, i.e., for each inclination and material, can then be determined from the velocity. If h is directly computed from data, the relation between I and v_x is straightforward:

$$I = \frac{3dv_x(z)}{2\sqrt{g\cos\theta}h^{3/2}(1-(1-\frac{z}{h})^{3/2})} \tag{2.54}$$

However, since the flow is not perfect (among other reasons because the medium is actually not incompressible), Eq. 2.54 leads to a non-constant inertial number in the flow. A solution is to only consider the inertial number from the top of the pile, and this solution is called “top” in the following figures. Another solution (“mean”) is to consider the mean value of the inertial number for all altitudes lower than the pile height.

A third solution is to find the inertial number and the pile height that best fit the velocity profile, by using the method of least squares. This method offers the advantage of not setting an arbitrary value for the minimum packing fraction to define the top of the pile. However, it cannot be directly applied to this problem since one of the parameters has an influence on the size of the available data. Concretely, if the current pile height h is smaller than h_0, we cannot consider all the data, as velocities corresponding to a higher altitude than h are not predicted by the model (since there should not be any material) and thus should not be considered. Therefore, the number of used data values has to be taken into account, otherwise the minimization would lead to very low heights. The function to be minimized, representing the squared residuals, can thus be defined as:

$$\operatorname{res}(I,h) = \frac{\sum_{z_i=0}^{\min(h_0,h)} \left[v_{x_i} - v_x(z_i,I,h)\right]^2}{\min(h_0,h)+1} \tag{2.55}$$

where v_{x_i} corresponds to the x-component of the velocity for an altitude of z_i, and v_x is computed from Eq. 2.53. This third solution is called “min(res)” in the following figures.

For the three methods, the two computed parameters I and h are used to compute the theoretical velocity profile associated with these parameters, to check if it corresponds to the simulation velocity profile.

The velocity profiles for the first two methods, as well as the inertial numbers, are shown for a gravel-like material in Fig. 2.26, and in Fig. 2.27 for a moderate-friction material.

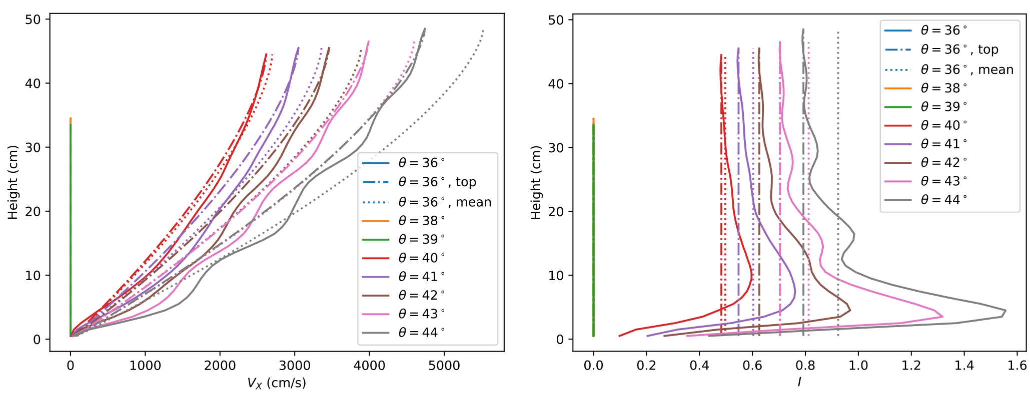

Fig. 2.26.: Velocity profiles and inertial numbers for a gravel-like material and several inclinations. Here, the height of the pile is directly computed from the porosity of the column. Different colors correspond to different inclinations θ, and the line styles correspond to the methods used to compute the inertial number, as indicated for the first inclination. In the left figure, solid lines represent the numerical data, and dashed lines interpolations. In the right figure, solid lines represent the direct computation of I from V_x, and dashed lines computation from two methods described in the text.

First of all, if the inclination is lower than the angle of repose, there is no flow. This means that the angle of repose for a gravel-like material is between $39°$

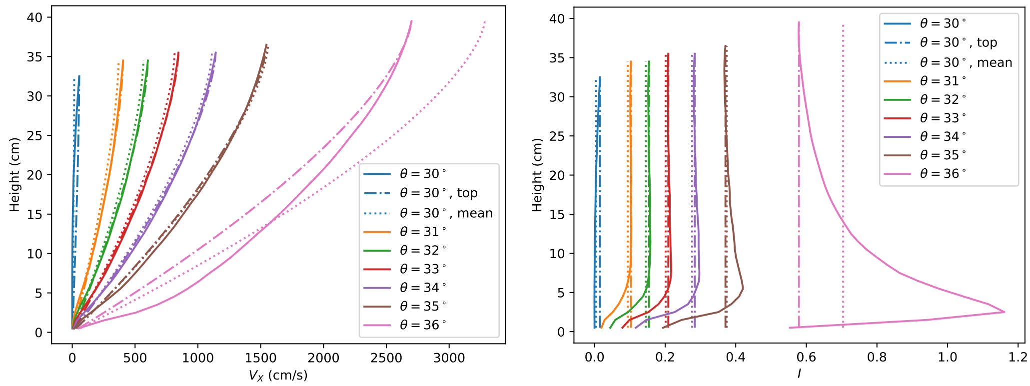

Fig. 2.27.: Velocity profiles and inertial numbers for a moderate-friction material and several inclinations. Here, the height of the pile is directly computed from the porosity of the column. Different colors correspond to different inclinations θ, and the line styles correspond to the methods used to compute the inertial number, as indicated for the first inclination. In the left figure, solid lines represent the numerical data, and dashed lines interpolations. In the right figure, solid lines represent the direct computation of I from V_x, and dashed lines computation from two methods described in the text.

and $40°$, whereas it is between $30°$ and $31°$ for a moderate-friction material. It was previously found that the angles of repose were respectively $38.5°$ and $28°$, which are close to the values found here. The discrepancies can be explained by the method used for measuring the angle of repose. Indeed, depending on the method, the measured angle of repose measured can either be the static one or the dynamic one.

Concerning the simulations for which a flow exists, the best fits seem to correspond to the ones obtained with the “top” method. Indeed, the bottom of the flow does not seem to behave as the theory predicts, especially for large inclinations. It can partially be explained by the material forming the flow not being an incompressible medium (for example, the higher the inclination, the larger the grain velocities, the higher the column, and the smaller the packing fraction). Moreover, compared for example to the 0.53 mm grains used by Jop et al. (2006), the grains I used are larger and fewer, and we expect a behavior more different from a fluid-like behavior with fewer, larger grains in the flow.

It can also be noticed that the theory works better with a moderate-friction material. This is because such a material behaves more like a fluid than a gravel-like material, a behavior I also found in other applications such as MASCOT landing simulations (see Chapter 4).

Now we also consider the third method, with the minimization of the squared residuals' function. In this case, as previously stated, the pile height is also a parameter to be determined. For the minimization, I only consider inclinations for which a flow exists. Results for best fits are shown in Fig. 2.28 for both materials.

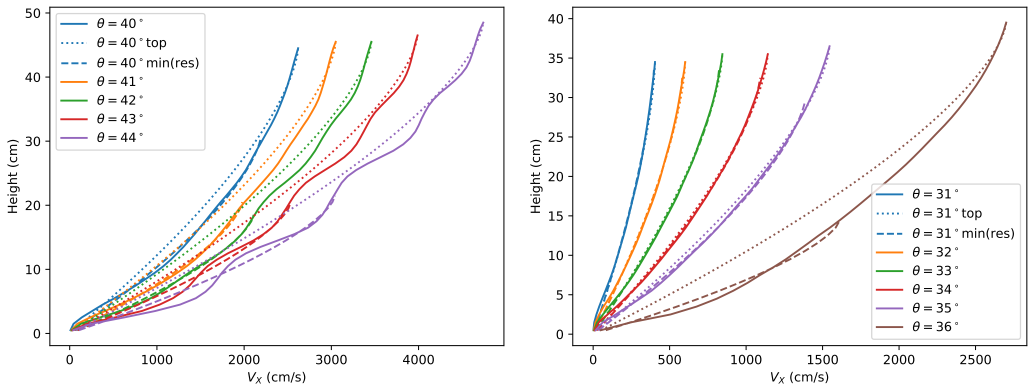

(a) Gravel-like material

(b) Moderate-friction material

Fig. 2.28.: Velocity profiles for a gravel-like and a moderate-friction materials and several inclinations. Different colors correspond to different inclinations θ, and the line styles correspond to the methods used to compute the inertial number, as indicated for the first inclination.

We can see that best fits with the minimization method give good fits for a moderate-friction material. For high inclinations and gravel-like material, the best fits correspond to low pile heights. This confirms what was said previously, i.e., that high inclinations lead to higher piles but with a much smaller grain density and therefore much less contacts between grains. Since the higher regions are much more porous, they contribute less to the weight of the pile, and then the total gravity force on the flow is smaller, leading to a smaller "equivalent" pile height.

Even if the bottom of the flows do not always correspond to the theory, we can compute the friction coefficient μ as a function of the inertial number. It has to be noticed that I considered in Eq. 2.52 that the "fluid" density ρ and the grain density ρ_s were equal. Even if we see variations of the packing fraction with altitude (see Fig. 2.23), we can define an average packing fraction Φ, equal for example to about 0.4 and 0.5 in Fig. 2.23. Thus, we would have $\rho = \Phi\rho_s$. If we consider Φ as constant, the values I found for the inertial number have to be divided by $\sqrt{\Phi}$.

In Fig. 2.29 is presented the friction coefficient as a function of the inertial number, for the "top" and "min(res)" methods, considering or not the Φ factor, and for both materials. The optimal values determined by the fitting (with the `scipy.optimize.curve_fit` routine in `Python`) are presented in Table 2.6. Results for the "min(res)" method are not shown for the gravel-like material, because the determined values were not consistent with realistic values (μ_2 and I_0 higher than 10^6) and with standard deviations too high (larger than 10^{12}).

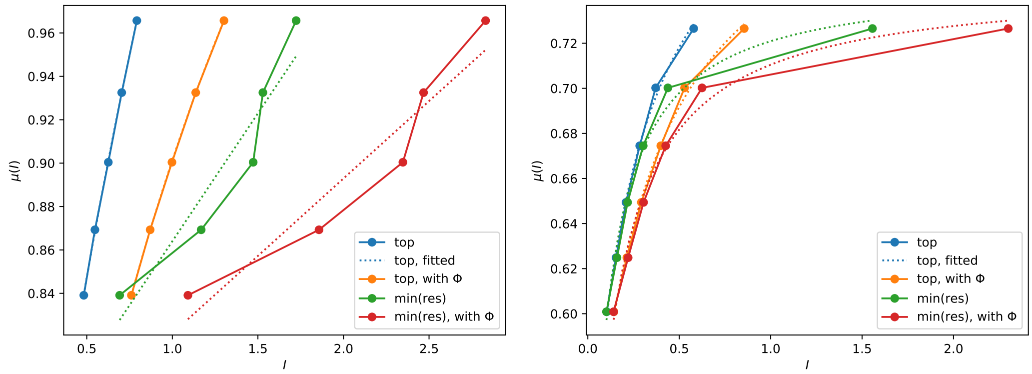

(a) Gravel-like material

(b) Moderate-friction material

Fig. 2.29.: Friction coefficient μ as a function of the inertial number I, for different material types. Different colors correspond to different methods, and the line styles correspond to the best fits with Eq. 2.34 for the three parameters μ_s, μ_2, and I_0, as indicated for the first method. When a method is indicated "with Φ", this means I considered $\rho \neq \rho_s$ and took into account the Φ factor.

Tab. 2.6.: Parameters of the friction coefficient function $\mu(I)$ for the two material types considered, and obtained with different methods. The standard deviations corresponding to the determination of these parameters are indicated. When a method is indicated "with Φ", this means I considered $\rho \neq \rho_s$ and took into account the Φ factor.

Material type	Method	μ_s	μ_2	I_0
Gravel-like	Top	0.573 ± 0.027	2.067 ± 0.347	2.223 ± 0.851
	Top, with Φ	0.527 ± 0.015	1.549 ± 0.045	1.732 ± 0.191
Moderate friction	Top	0.508 ± 0.018	0.827 ± 0.020	0.259 ± 0.065
	Top, with Φ	0.506 ± 0.019	0.815 ± 0.017	0.332 ± 0.081
	min(res)	0.438 ± 0.075	0.748 ± 0.010	0.097 ± 0.045
	min(res), with Φ	0.444 ± 0.069	0.747 ± 0.010	0.137 ± 0.061

Since, for an inclined plane experiment such as this one, μ is supposed to represent the tangent of the inclination angle, the values of μ_s and μ_2 can be expressed as limit inclination angles, respectively θ_s and θ_2. They are presented in Table 2.7. We can see that taking into account or not the Φ factor has only a small influence on the friction parameters and the associated angles.

Tab. 2.7.: Inclination angles corresponding to the parameters μ_s and μ_2 presented in Table 2.6. The angles presented correspond to the limit angles given by the standard deviations.

Material type	Method	θ_s (°)	θ_2 (°)
Gravel-like	Top	$28.6 - 31.0$	$59.8 - 67.5$
	Top, with Φ	$27.1 - 28.5$	$56.4 - 57.9$
Moderate friction	Top	$26.1 - 27.7$	$38.9 - 40.3$
	Top, with Φ	$26.0 - 27.7$	$38.6 - 39.8$
	min(res)	$20.0 - 27.2$	$36.4 - 37.2$
	min(res), with Φ	$20.6 - 27.2$	$36.4 - 37.1$

2.3.3 Conclusion of the inclined plane simulations

In this section, simulations of inclined planes were performed in order to compare the DEM results to the $\mu(I)$ rheology, and to extract corresponding (or adapted) friction parameters. These friction parameters can be used in codes based on the $\mu(I)$ rheology. My inclined plane DEM simulations showed velocity profiles that could either be in agreement with the $\mu(I)$ rheology (for moderate-friction material and inclinations low enough) or be very different (when the inclination is too high, or with a gravel-like material).

The coefficients that best represent the moderate-friction material, in the investigated range, are roughly $\mu_s = 0.51$, $\mu_2 = 0.82 - 0.83$, and $I = 0.26 - 0.33$.

This could mean that the $\mu(I)$ rheology is not adapted for high-friction materials and highly-diluted granular material flows. However, for moderate-friction material, the velocity profiles correspond very well to the predictions of this rheology. In this case, the friction parameters (μ_s, μ_2, and I_0) used in the friction coefficient function can thus be determined from inclined plane DEM simulations, as shown in this section.

A better estimation of these parameters would require a much larger number of simulations, not necessarily covering a larger range of inclinations, but a finer one to have more data on the interval close to the angle of repose.

Hayabusa2 and (162173) Ryugu 3

What's your story, Roundy?

— **Arrival at Ryugu**

Contents

During my PhD, I was a member of the Hayabusa2 science team and co-Investigator on the ONC camera and on the sampling mechanism. Consequently, I had direct access to the first images and contributed to their interpretations. I also attended all meetings of the Hayabusa2 science team. In this chapter, I begin by briefly introducing the Hayabusa2 mission. Then, I continue with a small analysis of the paper published in the journal Science in which I am a co-author about our interpretations of the geology of (162173) Ryugu, by emphasizing the parts concerning the granular material on the surface, in close relation with the applications treated in my PhD (lander MASCOT and sampling mechanism). Finally the paper itself is reproduced in its integrality: Sugita et al. (2019).

3.1 Hayabusa2

Hayabusa2 is the direct heir of the first asteroid sample-return mission Hayabusa, led by JAXA. It was launched in December 3, 2014 from Japan to the C-type NEA (162173) Ryugu (formerly 1999 JU_3). Like its predecessor, its first goal is to bring asteroid samples back to Earth; nevertheless, there are also several other instruments on board that will be described later in this section.

While Hayabusa was a technological demonstrator, Hayabusa2 is a scientific mission. Nevertheless, Hayabusa2 spacecraft has a similar framework as Hayabusa's one, which enabled a fast development. The description of the whole system design of the spacecraft can be found in Tsuda et al. (2013).

Concerning the scientific instruments, the spacecraft carries four remote-sensing systems: the Optical Navigation Camera (ONC) system (Kameda et al., 2017; Suzuki et al., 2018), the LIght Detection And Ranging (LIDAR) laser altimeter (Mizuno et al., 2017; Yamada et al., 2017; Senshu et al., 2017), that are both also used for navigation, the Near-InfraRed Spectrometer NIRS3 (Iwata et al., 2017), and the Thermal Infrared Imager TIR (Okada et al., 2017; Arai et al., 2017). It also carries three mini-rovers/hoppers named MINERVA-II, developed by JAXA and Japanese universities (Watanabe et al., 2017), successors of the first unsuccessful MINERVA experiment on board Hayabusa (Yoshimitsu et al., 2006). Moreover, Hayabusa2 spacecraft carries (CNES-DLR) MASCOT (Ho et al., 2017), presented in more details in Chapter 4.

The main objective of the mission is to bring samples back to Earth, thanks to three touchdowns and a similar sampling mechanism as the one used on Hayabusa spacecraft (Sawada et al., 2017b), detailed later in Chapter 5. In order to have access to fresher material, possibly less altered by space weathering, one of the planed touchdown is preceded by the release of the Small Carry-on Impactor (SCI) (Saiki et al., 2017). The SCI is part of a box which, exploding, is supposed to give to a 2-kg projectile a high speed of about 2 km/s. The impact should then produce a crater in the asteroid surface, where the spacecraft can then perform a touchdown and collect samples originally in the sub-surface. Because of the possibly hazardous ejecta created by the impact, the spacecraft cannot observe directly the impact but instead releases a deployable camera (DCAM3) to observe the ejecta and localize the crater, while it goes at distance and behind the asteroid to be protected (Sawada et al., 2017a; Ogawa et al., 2017; Ishibashi et al., 2017).

Concerning the asteroid Ryugu, there were some data prior to the encounter. Ryugu, formerly 1999 JU_3, is a C-type asteroid (part of the C complex) discovered by the LINEAR survey on May 10, 1999, and is a Potentially Hazardous Asteroid (PHA) classified as an Apollo, because of its semi-major axis of 1.1896 AU and its perihelion of 0.96328 AU (Binzel et al., 2001). Ground-based observations determined that its rotation period is about 7.63

h (Kim et al., 2013; Müller et al., 2017; Perna et al., 2017), its diameter 865 ± 15 m (Müller et al., 2017) and its thermal inertia $150 - 300$ J m^{-2} s$^{-1/2}$ K^{-1} (Müller et al., 2017). Prior to the arrival, the only images of a C-type asteroid were the ones of Mathilde (see Section 1.2.2), but were obtained from a fly-by at high distance and therefore with limited resolution and not regarding the entire body. Thus, Hayabusa2 would provide the first detailed images of a C-type asteroid and its estimated thermal inertia would suggest a boulder/cm-sized, gravel-dominated surface similar to the one of Itokawa. One of the main goals for the sampling was to seek for organic materials and aqueous alteration processes (Watanabe et al., 2017), in order to learn more about the role of asteroids in the emergence of life on Earth.

3.2 Ryugu

3.2.1 General properties

Hayabusa2 spacecraft arrived to Ryugu in June 2018, and provided the first detailed information on an asteroid of this type. Global observations of Ryugu are described in Watanabe et al. (2019). Ryugu's shape revealed to be oblate and similar to a "spinning top", with a prominent equatorial ridge, as shown in Fig. 3.1, an equatorial radius of about 502 m, and a polar-to-equatorial axis ratio of about 0.872 (Watanabe et al., 2019).

Ryugu's spectral type was confirmed as a Cb-type, with a very low geometric albedo of $4.5 \pm 0.2\%$ (Sugita et al., 2019; Kitazato et al., 2019) comparable to the one of Mathilde (see Section 1.2.2). Its rotation is almost perfectly retrograde, like Venus.

From observations from orbit and gravity measurement (Watanabe et al., 2019), its mass and volume could be estimated with accuracy, leading to a bulk density of 1.19 ± 0.02 g cm^{-3}, which is very low, even compared to the visited rubble piles such as Itokawa (Section 1.2.2) but consistent with the estimated bulk density of other dark-type asteroids, including Mathilde. If Ryugu has a similar grain density as carbonaceous chondrites, its porosity is higher than 50%, which is also higher than Itokawa's porosity, which suggests that it is a rubble pile (Watanabe et al., 2019). Other surface features are in agreement with a rubble pile structure, such as the numerous large boulders (Sugita et al., 2019).

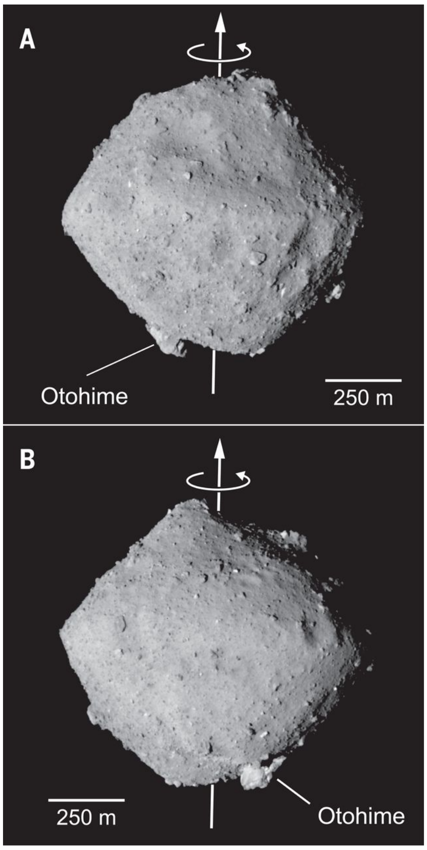

Fig. 3.1.: Visible light images of Ryugu, taken from a 20 km-altitude orbit. The spin axis is shown as a white arrow, and giant boulder Otohime (approx. 140 meter wide) is indicated. Image credit: Watanabe et al. (2019)

The analysis of Ryugu's surface can be found in the article in Section 3.3, but here I concentrate on the potential indicators of granular material on the surface of Ryugu in the craters, the possible grain size (through cohesion), the ridge, the thermal inertia and color observations, and the boulders. This is motivated by the two applications I treated, namely the landing of MASCOT (Chapter 4) and the sampling (Chapter 5).

3.2.2 Regolith on the surface

The main features on Ryugu's surface are impact craters, boulders, troughs, and the equatorial ridge surrounding the asteroid. A geologic map of Ryugu can be seen in Fig. 1A in the article (Section 3.3).

Impact craters

Bowl-shaped depressions that are crater candidates were sorted with different confidence level (CL) values: a lower confidence level means that they are more likely to be impact craters. CL1 depressions are circular with rims, CL2 ones are circular without rims, and CL3 ones are quasi-circular. About 30 CL1 and CL2 depressions larger than 20 m were found, with at least half of them being CL1 (with raised rims). The presence of rims, which is characteristic of impact craters, favors an impact origin.

Among the candidate craters detected on Ryugu, some have shallow floors, such as the one presented in Fig. 3.2. Regolith could have filled the bottom of these craters, as it was observed on (433) Eros (Veverka et al., 2001a). Moreover, fresh bowl-shaped craters can have depth-to-diameter ratios as low as 0.14, comparable to the values found on other asteroids such as Eros, (21) Lutetia, and (4) Vesta, for which the ratio is around 0.15 (Marchi et al., 2015). We know that these surfaces are covered with regolith, thus a comparable depth-to-diameter ratio could suggest the presence of regolith also on the surface of Ryugu, even if it could also be due to other causes.

Nevertheless, in some craters such as Urashima, the largest crater on Ryugu, were observed signs of mass wasting, in this case of wall slumping (shown in Fig. 2A&C in Section 3.3, indicated by arrows, and in Fig. 3.3). This means that there is a layer of unconsolidated material on the surface of Ryugu, and it is the definition of regolith given by Robinson et al. (2002). Since the bump in the LIDAR measurements seems to be of the order of a meter, this means that the regolith could be made of submetric grains.

Mass wasting on craters can also be seen in Fig. 3.3 for two other craters than Urashima, as well as a stereo image of Urashima. We can see that Momotaro (white arrows) has a floor covered with boulders and unconsolidated material.

We also observed a depletion of craters smaller than 100 m, as it was observed on Eros and Itokawa (see Sections 1.2.2 and 1.2.2). The usual interpretation for a shortage of small craters is crater erasure processes such as seismic shaking (see Section 1.3.5) (Richardson et al., 2004; Richardson Jr. et al., 2005; Michel et al., 2009), which is in agreement with a layer of unconsolidated material, and seems to be representative of a surface with no cohesion.

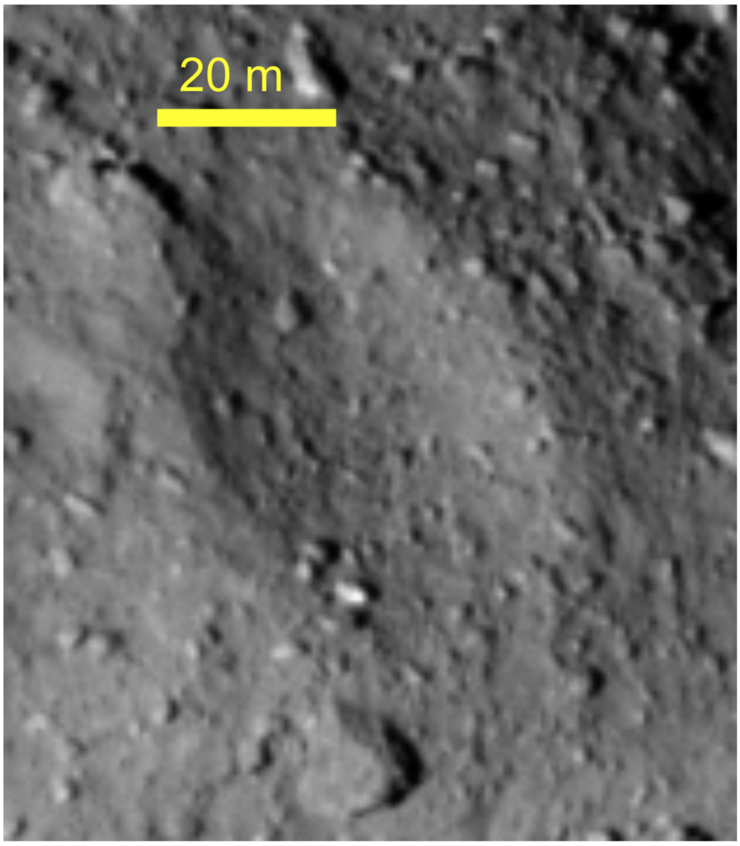

Fig. 3.2.: Shallow-floored crater with a raised rim. Its location is (6.0°N, 308.7°E). Image credit: supplementary material of Sugita et al. (2019)

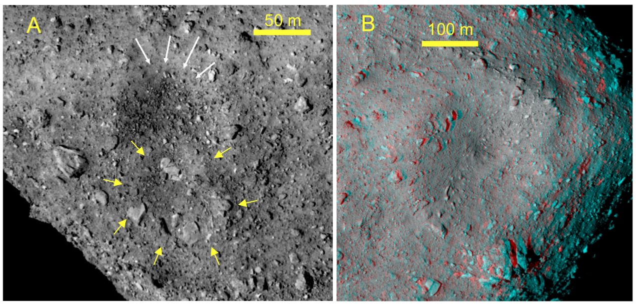

Fig. 3.3.: **(A)** Momotaro (white arrows) and Kibidango (yellow arrows) craters. Momotaro is located near the equatorial ridge. **(B)** Red-blue stereo image of Urashima crater. Image credit: supplementary material of Sugita et al. (2019)

Cohesion

Crater formation on Ryugu seems to be controlled by gravity and weak cohesion strength. Finally, current observations of the crater formed by the Small Carry-on Impactor show a crater diameter which can be matched by conventional cratering scaling laws only if cohesion is assumed to be zero. This suggests that the grains composing the regolith are larger than the size for each Van der Waals force to be effective. Assuming that cohesion is governed by Van der Waals forces, we try to find the smallest possible particle radius for a weak cohesion compared to gravity. According to what is presented in Section 1.3.4 (Scheeres et al., 2010), the cohesion force between two identical particles in contact can be written as:

$$F_c = \frac{AS^2}{48\Omega^2}\frac{r}{2} = 1.99 \cdot 10^{-2} S^2 r, \tag{3.1}$$

with a radius r in m for the particles, and assuming a Hamaker constant A equal to the lunar one: $A = 4.3 \cdot 10^{-20}$ J, and an interparticle distance Ω of $1.5 \cdot 10^{-10}$ m (Perko et al., 2001). S is the cleanliness ratio introduced by Perko et al. (2001), which tends towards 1 for a clean surface, and is closer to 0.1 with atmosphere and water vapor. This force should be compared to the gravity force applied to a particle of radius r on Ryugu. For a weak cohesion, we should have a bond number for cohesion B_c (ratio of cohesive force and weight) smaller than 1 (or even much smaller than 1).

If we consider Ryugu's mass as $4.50 \cdot 10^{11}$ kg (Watanabe et al., 2019), we have a gravitational acceleration g on the equator equal to $1.19 \cdot 10^{-4}$ m s^{-2}, and on the poles equal to $1.57 \cdot 10^{-4}$ m s^{-2}. However, the net surface gravitational acceleration g_A has to take into account the inertial force due to the rotation of the asteroid (Scheeres et al., 2010). If we call the latitude δ and the rotation rate ω, g_A is defined as:

$$g_A = \|\omega * *2 \cos^2 \delta R - g\|. \tag{3.2}$$

For the poles, $\cos\delta$ is equal to 0, whereas it is equal to 1 for the equator, meaning that the difference in the net gravitational acceleration between equator and poles is even larger than for the standard gravitational acceleration. From the period given by Watanabe et al. (2019), we have $\omega = 2.287 \cdot 10^{-4}$ rad s^{-1}. This leads to $g_A = 9.27 \cdot 10^{-5}$ m s^{-2} on the equator, and $g_A = 1.57 \cdot 10^{-4}$ m s^{-2} on the poles.

We consider that the grains on Ryugu are similar to the ones in CM/CI chondrites (even if it is not certain), and from Macke et al. (2011), the average measured grain density of CI chondrites is $2,430$ kg m^{-3}, and for CM chondrites is $2,920$ kg m^{-3}. As a simplification, we take a grain density of $\rho_g = 2,700$ kg m^{-3}.

We therefore have a bond number equal to:

$$B_c = \frac{F_c}{F_g} = 1.76 \cdot 10^{-6} \frac{S^2}{g_A r^2}. \tag{3.3}$$

If we decide that the bond number has to be smaller than 1 to consider that the cohesion is weak, we find that, on the equator, the smallest grain radius is equal to $r_{\min} = 0.14$ m for a cleanliness ratio of 1, and $r_{\min} = 1.4$ cm for a cleanliness ratio of 0.1. On the poles, the smallest radius is $r_{\min} = 0.11$ m for $S = 1$ and $r_{\min} = 1.1$ cm for $S = 0.1$.

Due to friction between grains, the Itokawa particles observed by Tsuchiyama et al. (2011) had a round shape, meaning that the cleanliness ratio for small particles could be close to 1. However, for particles as large as a centimeter or larger, we do not expect perfectly smooth particles. Castellanos (2005) even considers that asperities could be present on the surface between two particles, and these asperities can be represented by smaller particles with a radius r_a. Then, the new cohesion force becomes, according to Scheeres et al. (2010):

$$F_c a = \frac{r_a}{r} F_c \sim S^2 F_c, \tag{3.4}$$

and the minimum radius is 1.4 mm for $S = 0.1$ on the equator.

In these calculations, we used some approximations. We used a grain density for the particles' density, whereas centimer-sized or larger particles or boulders could be porous, and the density could be lower, increasing the minimum radius. On the other hand, the Hamaker coefficient or the interparticle distance could be different for an asteroidal regolith. In any case, this means that, if we see no cohesion on Ryugu, which is the current interpretation of the observations (after the Small Carry-on Impactor experiment for instance), this means that particles have to be large enough. With this simple computation, particles' size on the surface could be of the millimeter scale or centimeter scale. It is also possible that the laws ruling cohesion on asteroids are not completely understood yet, and that the approximated equations are not exactly adapted to their case.

As a comparison, the bond number for self-gravity is:

$$B_{\text{sg}} = G \frac{\pi \rho_g}{3 g_A} r, \tag{3.5}$$

leading to:

$$B_{\text{sg,equator}} = 2.03 \cdot 10^{-3} r, \tag{3.6}$$

$$B_{\text{sg,poles}} = 1.20 \cdot 10^{-3} r, \tag{3.7}$$

meaning that at the considered sizes (centimeter or smaller), the self-gravity is negligible.

Mass wasting

Evidence of mass wasting can clearly be seen on Fig. 1C in Section 3.3. On a slope of the equatorial ridge are visible clear asymmetric regolith deposits uphill of the boulders, and almost none downhill, meaning that the surface is composed of relatively small particles that are moved from geopotential highs towards lows, i.e. in the direction of the current slope. This process has to be younger than the formation of the ridge, the new geopotential field, and the positioning of the boulders.

As already stated, mass wasting is also observed on the walls of large craters.

Thermal inertia and color observations

Hayabusa2 carries the instrument TIR (Okada et al., 2017; Arai et al., 2017) that measured uniform thermal inertia on the surface, with a value in the range $200 - 500$ J m^{-2} s$^{-0.5}$ K^{-1}. It is known that grain size has an influence on the thermal inertia of a surface. According to the theory, it was thought that such thermal inertia corresponded to a grain size ranging from subcentimetric to 10 cm (Okada et al., 2017; Sakatani et al., 2017), and that areas with smaller grains (smaller than 1 mm) were very small. However, measurements of the thermal inertia of a big boulder by MARA (on MASCOT) also gave a low value, meaning that a low thermal inertia could be due to a high porosity and not only to small grains. Therefore, the usual relationship between grain size and thermal inertia could be misleading, because the porosity of a rock can have the same effect as the presence of small grains, and it is difficult to infer the average grain size from thermal inertia measurements.

Concerning the color of Ryugu, the surface has bluer spectral slopes on the equatorial ridge, at the poles, and in large troughs, and this could be due to erosion, for example induced by thermal fatigue (Delbo et al., 2014). Additionally to crater formation, this erosion could be one of the sources of creation of centimeter-sized regolith. Boulders with sharp surfaces also show bluer and brighter surfaces, and could be eroded. On the other hand, areas that are susceptible to accumulate regolith deposits, such as topographic lows and crater bottoms, are darker and redder. Red and dark particles could be due to either space weathering or other processes such as coating of the surface by redder and darker dust. The darkness of the ejecta blanket and the crater observed after the SCI experiment, corresponding to fresh material, could indicate that the red color and the darkness is not due to space weathering but rather to dust coating on topographic lows.

Boulders

The cumulative size distribution of boulders on Ryugu follows a power law with an exponent ranging from -3 and -2.5 (shown in Fig. 4B in Section 3.3), for boulders larger than 10 m. This power law was confirmed around -2.5 for smaller grains or boulders with sizes larger than 0.2 m, by higher resolution images taken during gravity measurement maneuvers, and deployment maneuvers for MINERVA-II and MASCOT. This is similar to other asteroids, such as Eros (Thomas et al., 2001), Itokawa (Mazrouei et al., 2014), and Toutatis (Jiang et al., 2015b). These comparisons could suggest that there is also a high quantity of smaller grains on Ryugu. However, at smaller sizes, the slope becomes shallower, i.e., there is an apparent shortage in small grains. The slope is shown in Fig. 3.4, as well as an image taken during MASCOT deployment maneuver.

This shows that there seems to be less small particles on Ryugu than on previously visited asteroids, and this is in agreement with the observation of a weak cohesion between Ryugu's components. However, the left edge of the curve (smallest particles) could be due to the limited resolution, as we see that each image at a higher resolution shows a higher density for the same boulder size. Near MASCOT's landing site, the image in Fig. 3.4 shows a meter-sized boulder with angular fragments and differences in brightness, which could be caused by eroded parts (maybe due to thermal fatigue) or armoring (the boulder could be the target of impacts and protect the surface). This would mean the presence of smaller particles is not necessarily visible at this resolution. However, this could also mean that some boulders, such as the bright spots in close-up observations, are made of different materials, and that this mixture of materials comes from as far as Ryugu's parent body.

The four types of boulders observed from orbit can be described as: dark and rugged (type 1), bright and smooth (type 2), bright and mottled (type

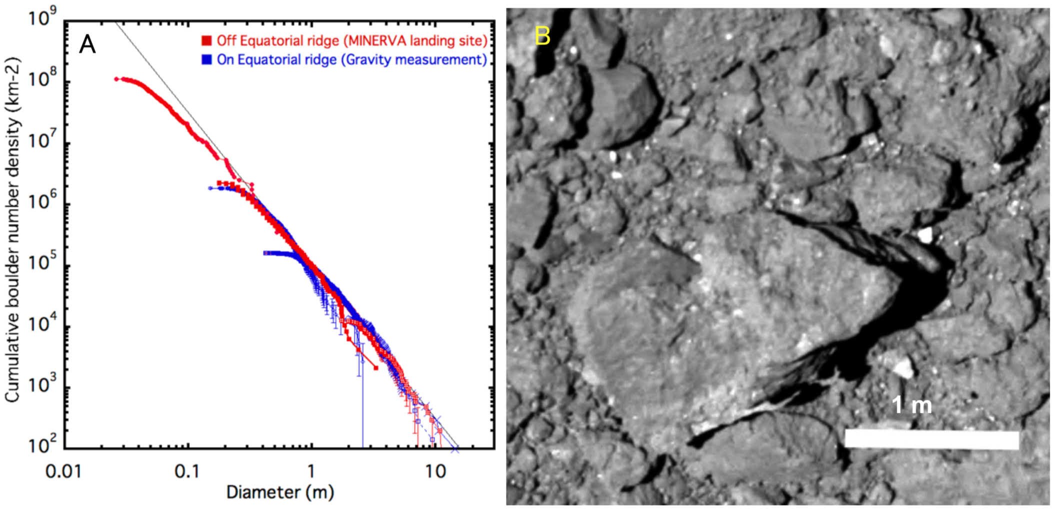

Fig. 3.4.: Close-up observation results of Ryugu surfaces. In **(A)** is shown the size distribution of small boulders, observed outside the ridge during MINERVA-II deployment descent to 67 m (red) and on the ridge during the gravity measurement descent to 0.9 km (in blue). The black line corresponds to an exponent of -2.5. In **(B)** is shown an image near MASCOT landing site with a resolution of 6 mm per pixel; the largest boulder in the image presents angular fragments and slightly differences in brightness. Image credit: supplementary material of Sugita et al. (2019)

3), and Otohime Saxum, with sharp edges and smooth surfaces (type 4). In the high-resolution images, heterogeneities in brightness were found on boulders similar to the lowly-resolved dark and rugged boulders, with layered structured. These could be impact breccias, i.e., rocks composed of broken fragments embedded in a finer matrix, formed during the process of impact cratering. The heterogeneity can then be explained by the mixture of different depths of the parent body during its catastrophic disruption and re-accumulation (Michel et al., 2015b).

Impact breccias are usually porous, and a possible explanation for the low thermal inertias measured from Earth and from TIR is that they could be more due to the porosity of the boulders than to the presence of a fine regolith covering the surface. A combination of micro- and macroporosity would explain the low bulk density of Ryugu still considering carbonaceous chondrite material as the constituent. Even so, boulders require a certain strength to have survived the disruption, the re-accumulation, and the latest impacts on Ryugu.

3.3 Article Ryugu

The geomorphology, color, and thermal properties of Ryugu: Implications for parent-body processes

by

S. Sugita, R. Honda, T. Morota, . . . , F. Thuillet et al.

2019, *Science*, **364**, pp. 252-252

Abstract

The near-Earth carbonaceous asteroid 162173 Ryugu is thought to have been produced from a parent body that contained water ice and organic molecules. The Hayabusa2 spacecraft has obtained global multicolor images of Ryugu. Geomorphological features present include a circum-equatorial ridge, east/west dichotomy, high boulder abundances across the entire surface, and impact craters. Age estimates from the craters indicate a resurfacing age of $\lesssim 10^6$ years for the top 1-meter layer. Ryugu is among the darkest known bodies in the Solar System. The high abundance and spectral properties of boulders are consistent with moderately dehydrated materials, analogous to thermally metamorphosed meteorites found on Earth. The general uniformity in color across Ryugu's surface supports partial dehydration due to internal heating of the asteroid's parent body.

RESEARCH ARTICLE

ASTEROIDS

The geomorphology, color, and thermal properties of Ryugu: Implications for parent-body processes

S. Sugita[1,2]*, R. Honda[3], T. Morota[4], S. Kameda[5], H. Sawada[6], E. Tatsumi[1], M. Yamada[2], C. Honda[7], Y. Yokota[6,3], T. Kouyama[8], N. Sakatani[6], K. Ogawa[9], H. Suzuki[10], T. Okada[6,1], N. Namiki[11,12], S. Tanaka[6,12], Y. Iijima[6]†, K. Yoshioka[1], M. Hayakawa[6], Y. Cho[1], M. Matsuoka[6], N. Hirata[7], N. Hirata[9], H. Miyamoto[1], D. Domingue[13], M. Hirabayashi[14], T. Nakamura[15], T. Hiroi[16], T. Michikami[17], P. Michel[18], R.-L. Ballouz[6,19], O. S. Barnouin[20], C. M. Ernst[20], S. E. Schröder[21], H. Kikuchi[1], R. Hemmi[1], G. Komatsu[22,2], T. Fukuhara[5], M. Taguchi[5], T. Arai[23], H. Senshu[2], H. Demura[7], Y. Ogawa[7], Y. Shimaki[6], T. Sekiguchi[24], T. G. Müller[25], A. Hagermann[26], T. Mizuno[6], H. Noda[11], K. Matsumoto[11,12], R. Yamada[7], Y. Ishihara[6]‡, H. Ikeda[27], H. Araki[11], K. Yamamoto[11], S. Abe[28], F. Yoshida[2], A. Higuchi[11], S. Sasaki[29], S. Oshigami[11], S. Tsuruta[11], K. Asari[11], S. Tazawa[11], M. Shizugami[11], J. Kimura[29], T. Otsubo[30], H. Yabuta[31], S. Hasegawa[6], M. Ishiguro[32], S. Tachibana[1], E. Palmer[13], R. Gaskell[13], L. Le Corre[13], R. Jaumann[21], K. Otto[21], N. Schmitz[21], P. A. Abell[33], M. A. Barucci[34], M. E. Zolensky[33], F. Vilas[13], F. Thuillet[18], C. Sugimoto[1], N. Takaki[1], Y. Suzuki[1], H. Kamiyoshihara[1], M. Okada[1], K. Nagata[8], M. Fujimoto[6], M. Yoshikawa[6,12], Y. Yamamoto[6,12], K. Shirai[6], R. Noguchi[6], N. Ogawa[6], F. Terui[6], S. Kikuchi[6], T. Yamaguchi[6]§, Y. Oki[1], Y. Takao[1], H. Takeuchi[6], G. Ono[27], Y. Mimasu[6], K. Yoshikawa[27], T. Takahashi[6], Y. Takei[6,27], A. Fujii[6], C. Hirose[27], S. Nakazawa[6], S. Hosoda[6], O. Mori[6], T. Shimada[6], S. Soldini[6], T. Iwata[6,12], M. Abe[6,12], H. Yano[6,12], R. Tsukizaki[6], M. Ozaki[6,12], K. Nishiyama[6], T. Saiki[6], S. Watanabe[4,6], Y. Tsuda[6,12]

The near-Earth carbonaceous asteroid 162173 Ryugu is thought to have been produced from a parent body that contained water ice and organic molecules. The Hayabusa2 spacecraft has obtained global multicolor images of Ryugu. Geomorphological features present include a circum-equatorial ridge, east-west dichotomy, high boulder abundances across the entire surface, and impact craters. Age estimates from the craters indicate a resurfacing age of $\lesssim 10^6$ years for the top 1-meter layer. Ryugu is among the darkest known bodies in the Solar System. The high abundance and spectral properties of boulders are consistent with moderately dehydrated materials, analogous to thermally metamorphosed meteorites found on Earth. The general uniformity in color across Ryugu's surface supports partial dehydration due to internal heating of the asteroid's parent body.

The asteroid 162173 Ryugu is the target of the Japan Aerospace Exploration Agency's (JAXA's) Hayabusa2 mission, which arrived in June 2018. Small asteroids, such as Ryugu, are thought to have been born from much older parent bodies through catastrophic disruption and reaccumulation of fragments during evolution of the Solar System (*1*, *2*). We seek to understand the properties of both Ryugu and its parent body. Deciphering the geologic record of an asteroid requires identification and characterization of the geological features on its surface. Detailed global observations of Ryugu were conducted with Hayabusa2's remote-sensing instruments, including the optical navigation cameras (ONCs), one of which is the nadir-viewing telescopic camera (ONC-T), with seven narrow-band filters [0.40 μm (ul), 0.48 μm (b), 0.55 μm (v), 0.59 μm (Na), 0.70 μm (w), 0.86 μm (x), and 0.95 μm (p)] (*3*–*5*); a laser altimeter [light detection and ranging (LIDAR) altimeter] (*6*); and a thermal infrared camera (TIR) (*7*), sensitive to wavelengths from 8 to 12 μm (*8*).

Global images were obtained from the home position located 20 km above the asteroid (*9*), from which we constructed a 0.55-μm map of Ryugu (Fig. 1A). Major geomorphologic features visible in this map include impact craters, boulders, troughs, and an equatorial ridge (Fig. 1B and table S3).

Impact craters

Impact crater morphologies, including rim and floor characteristics, provide indicators of surface age and mechanical properties. Approximately 30 circular depressions ≥20 m in diameter have been identified on Ryugu, many (at least half) with raised rims (Fig. 1A). Several craters also exhibit bowl-like shapes (Fig. 2, A and B), whereas others have shallow floors (fig. S10). The bowl-shaped depressions are classified on the basis of rim morphology and shape, providing confidence levels (CLs) to their identification as impact craters. CL1 features are circular with a clearly identifiable rim, CL2 depressions are circular but exhibit no rim, CL3 depressions are quasi-circular, and CL4 features are circular patterns of boulders with no clear topography. CL1 and CL2 depressions are most likely impact craters. The group of CL3 and CL4 features may include a few craters. Different levels of confidence are used in the statistical analyses to examine the robustness of the results. Laser-altimeter measurements indicate that fresh bowl-shaped depressions have depth/diameter ratios ranging from 0.14 to 0.2 (Fig. 2, C and D) (*8*). Although recent numerical calculations (*10*) show that large cavities may be formed in fast-spinning asteroids via the release of large boulders due to centrifugal force, raised rims are not expected to be generated in such a process. Thus, large equatorial craters on Ryugu are unlikely to have been formed by asteroid spin and are most likely of impact origin.

Some craters show evidence for motion of a loosely consolidated mass of materials on the

[1]The University of Tokyo, Tokyo 113-0033, Japan. [2]Planetary Exploration Research Center, Chiba Institute of Technology, Narashino 275-0016, Japan. [3]Kochi University, Kochi 780-8520, Japan. [4]Nagoya University, Nagoya 464-8601, Japan. [5]Rikkyo University, Tokyo 171-8501, Japan. [6]Institute of Space and Astronautical Science (ISAS), Japan Aerospace Exploration Agency (JAXA), Sagamihara 252-5210, Japan. [7]University of Aizu, Aizu-Wakamatsu 965-8580, Japan. [8]National Institute of Advanced Industrial Science and Technology, Tokyo 135-0064 Japan. [9]Kobe University, Kobe 657-8501, Japan. [10]Meiji University, Kawasaki 214-8571, Japan. [11]National Astronomical Observatory of Japan, Mitaka 181-8588, Japan. [12]SOKENDAI (The Graduate University for Advanced Studies), Hayama 240-0193, Japan. [13]Planetary Science Institute, Tucson, AZ 85719, USA. [14]Auburn University, Auburn, AL 36849, USA. [15]Tohoku University, Sendai 980-8578, Japan. [16]Brown University, Providence, RI 02912, USA. [17]Kindai University, Higashi-Hiroshima 739-2116, Japan. [18]Université Côte d'Azur, Observatoire de la Côte d'Azur, Centre National de le Recherche Scientifique (CNRS), Laboratoire Lagrange, 06304 Nice, France. [19]University of Arizona, Tucson, AZ 85705, USA. [20]Johns Hopkins University Applied Physics Laboratory, Laurel, MD 20723, USA. [21]German Aerospace Center (DLR), Institute of Planetary Research, 12489 Berlin, Germany. [22]International Research School of Planetary Sciences, Università d'Annunzio, 65127 Pescara, Italy. [23]Ashikaga University, Ashikaga 326-8558, Japan. [24]Hokkaido University of Education, Asahikawa 070-8621, Japan. [25]Max-Planck-Institut für Extraterrestrische Physik, 85748 Garching, Germany. [26]University of Stirling, FK9 4LA, Scotland, UK. [27]Research and Development Directorate, JAXA, Sagamihara 252-5210, Japan. [28]Nihon University, Funabashi 274-8501, Japan. [29]Osaka University, Toyonaka 560-0043, Japan. [30]Hitotsubashi University, Tokyo 186-8601, Japan. [31]Hiroshima University, Higashi-Hiroshima 739-8526, Japan. [32]Seoul National University, Seoul 08826, Korea. [33]NASA Johnson Space Center, Houston, TX 77058, USA. [34]Laboratoire d'Etudes Spatiales et d'Instrumentation en Astrophysique (LESIA)–Observatoire de Paris, Paris Sciences et Lettres (PSL), Centre National de le Recherche Scientifique (CNRS), Sorbonne Université, Université Paris-Diderot, 92195 Meudon Principal Cedex, France.
***Corresponding author: Email: sugita@eps.s.u-tokyo.ac.jp** †Deceased. ‡Present address: National Institute for Environmental Studies, Tsukuba 305-8506, Japan. §Present address: Mitsubishi Electric Corporation, Kamakura 247-8520, Japan.

inner walls (i.e., wall slumping; Fig. 2A). This phenomenon was not observed on another subkilometer asteroid, Itokawa (*11*), and indicates the presence of an unconsolidated surface layer. No crater has been found to have a floor with terrace structure, which would form if there was a large strength contrast between the surface and near-surface interior (*12*). These floor morphologies and the high fraction of raised rims indicate that the craters formed in an unconsolidated target, not dominated by pristine mechanical strength of the constituent surface material. Therefore, both gravity and weak cohesion strength controlled the crater formation. The individual boulders in the surface

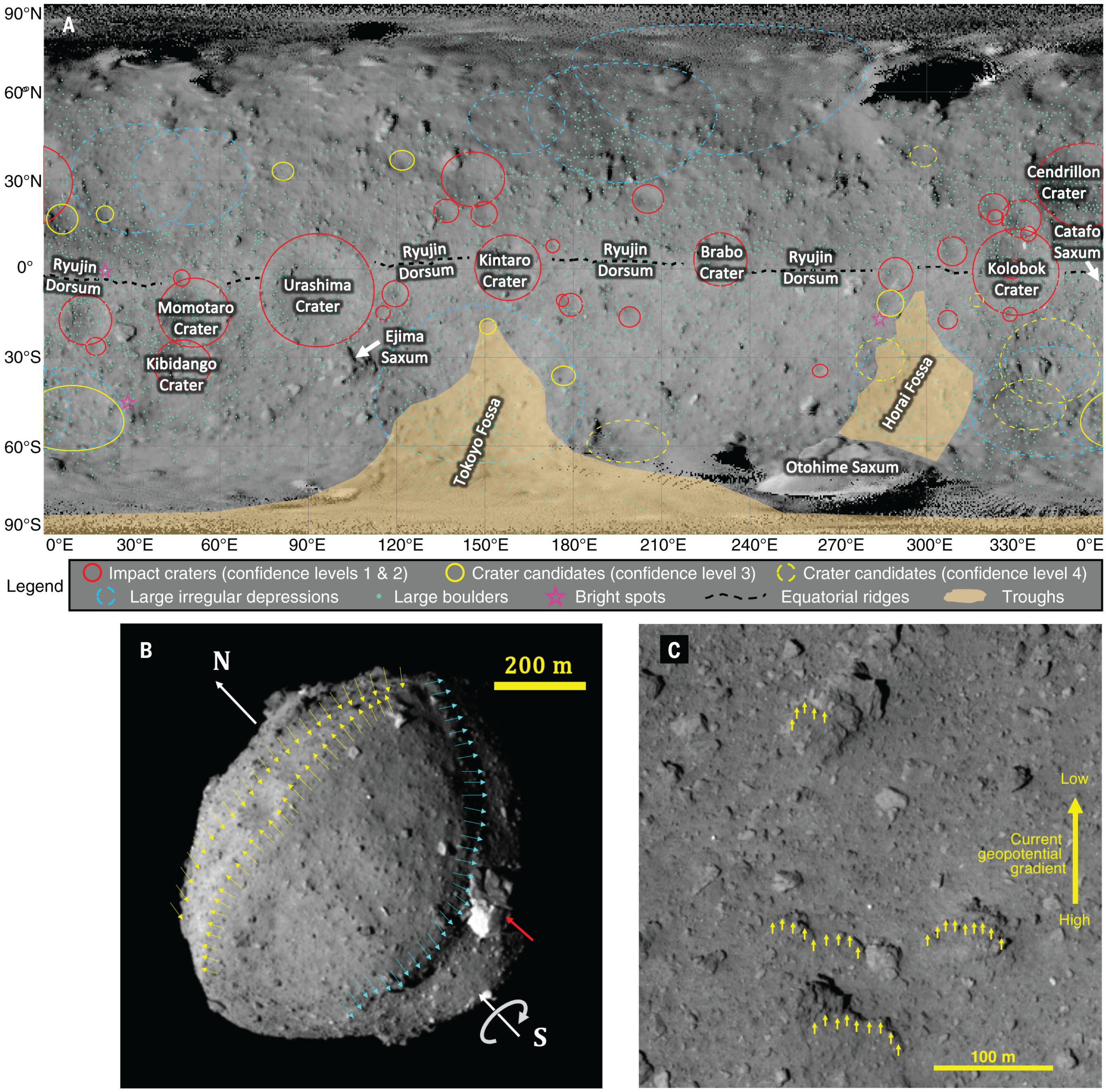

Fig. 1. Global map and images of Ryugu. (**A**) Geologic map of Ryugu based on mosaicked v-band (0.55 μm) images. Impact craters and crater candidates are indicated with circles, color coded by confidence level (see text). There is greater latitudinal exaggeration of map-projected surface area on Ryugu than for a sphere, because of its diamond-like cross section. This leads to the apparent higher crater number density in the equatorial region of this map. (**B**) Oblique view of Ryugu (image hyb2_onc_20180824_102748_tvf_l2b), showing the circum-equatorial ridge (yellow arrows), trough (blue arrows) extending from the equatorial region through the south polar region to the other side of Ryugu, and the large and bright Otohime Saxum (red arrow) near the south pole. The location of the poles and the spin direction are indicated with white arrows. (**C**) Asymmetric regolith deposits on imbricated flat boulders on the northern slope of the circum-equatorial ridge of Ryugu (hyb2_onc_20181003_222509_tvf_l2b). Small yellow arrows at the edges of regolith deposits indicate the direction of mass wasting. The large yellow arrow indicates the current geopotential gradient from high to low (*17*). The direction of geopotential gradient is consistent with the mass wasting.

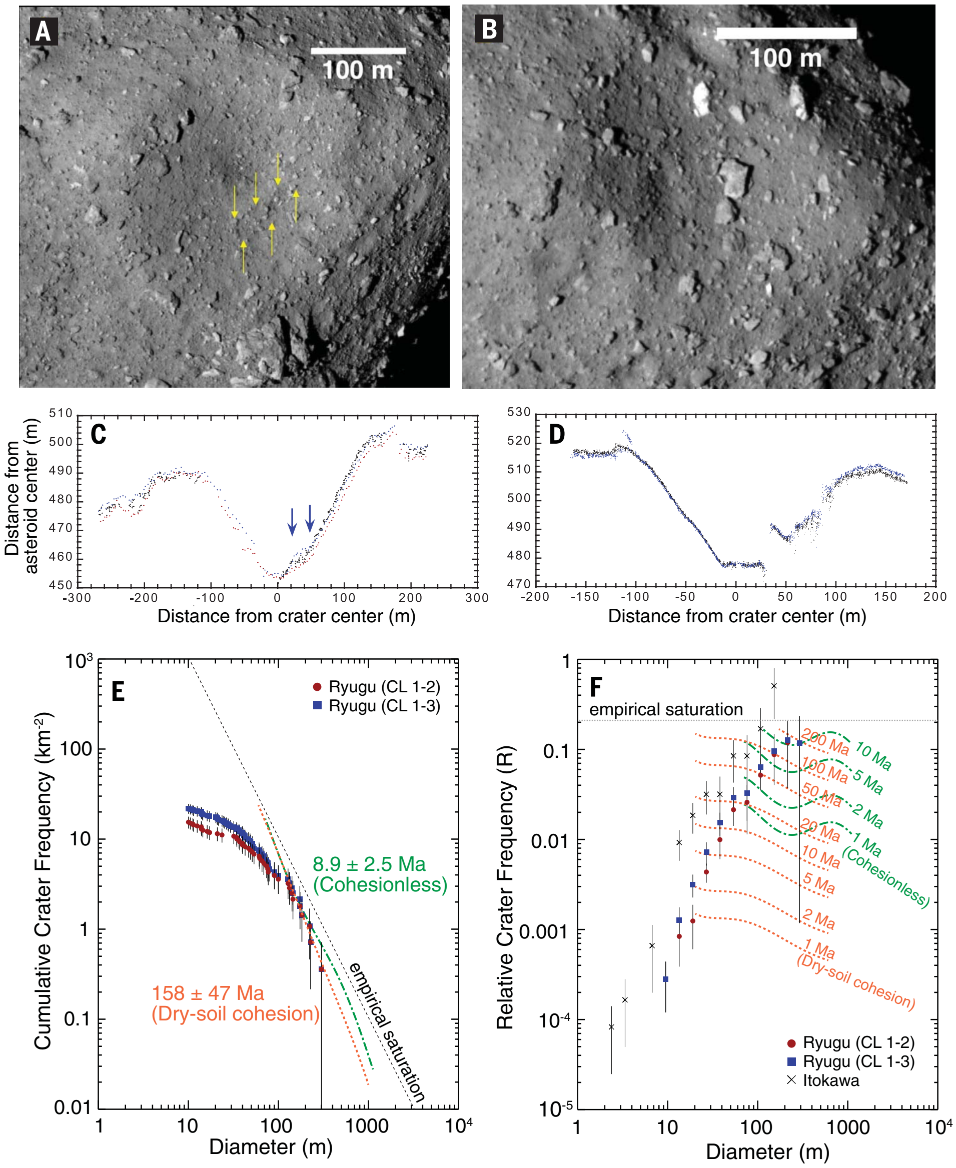

Fig. 2. Craters on Ryugu. (**A**) The largest crater, Urashima (290 m in diameter, 8.3°S, 92.5°E), on Ryugu (hyb2_onc_20180720_071230_tvf_l2b). Wall slumping is indicated with yellow arrows. (**B**) Kolobok crater (240 m, 1.5°S, 333.5°E), which has a deep floor, bowl-like shape, and a raised rim (hyb2_onc_20180720_100057_tvf_l2b). (**C**) LIDAR profiles of Urashima crater. Wall slumping is indicated with blue arrows. (**D**) LIDAR profiles of Kolobok crater. (**E**) CSFD on Ryugu and Itokawa and empirical saturation and crater production curves (*54*) with (orange) and without (green) dry-soil cohesion. Black crosses in (F) represent Itokawa crater candidates (*11*). Red and blue points indicate Ryugu craters with different crater CLs. (**F**) An R-plot (the CSFD normalized by D^{-2}, where D is diameter) for Ryugu (circles and squares) and Itokawa (crosses). The relative crater frequency R is defined as the differential crater frequency in a diameter range between D/k and kD, divided by D^3, where k is $2^{1/4}$. Saturation and crater production curves are the same as in (E). Ma, million years.

layer are large (~3 m in diameter) and are similar to the sizes of the projectiles (~0.1 to 1 m) that formed craters (~1 to 30 m) on Ryugu (*8*). Therefore, these large boulders may reduce crater size via armoring, in which a large fraction of impact energy is lost into the crushing or cratering of the first-contact boulder instead of forming a granular crater on the asteroid (*13*). Impact experiments using targets with constituent boulder sizes similar to the projectile's size indicate that armoring effects influence crater size and that a scaling relation for such targets must include a term for the breakup energy of the first-contact target boulder (*14*).

We estimated the surface crater retention age on the basis of the number density of craters 100 to 200 m in diameter, using a scaling rule with armoring effect (*14*), both with and without a dry-soil cohesion factor, obtaining surface ages of 10^8 and 10^7 years, respectively (Fig. 2E) (*8*). This large (i.e., a factor of 10) uncertainty in surface age comes from the influence of a small amount of cohesion, which controls the excavation flow near the crater rim. On a high-gravity planet, such as Earth, small cohesive forces do not influence crater size, but on microgravity bodies, such as Ryugu, crater size is influenced by the presence or absence of small cohesive forces, which is difficult to simulate in laboratory experiments on Earth. Despite these uncertainties, the observed crater size-frequency distribution (CSFD) indicates that the surface age of Ryugu is equal to or younger than the collisional lifetime (the mean time for an asteroid to experience a collision-induced catastrophic disruption) of kilometer-sized objects in the main asteroid belt [(3 to 5) × 10^8 years (*1*, *2*)] and equal to or older than the expected time (~4 × 10^7 years) Ryugu has stayed in a near-Earth orbit (*9*). Different collision frequencies must be considered for different scales of surface ages, because Ryugu is thought to have migrated from the main belt to its current near-Earth orbit, most likely through ν_6, the innermost resonance zone of the main belt (*9*, *15*). Because the collision frequency is far greater in the main belt, the majority of the craters ≥100 m probably formed while Ryugu was still resident in the main asteroid belt.

Ryugu's CSFD shows a dearth of small craters (<100 m; Fig. 2F). The deficit of small craters on Ryugu as a function of crater size is similar to that found for both Itokawa and Eros (*16*). Because craters in this size range on Ryugu are not greatly influenced by crater size reduction [owing to armoring effects (*14*)], these depletion patterns are more likely to be due to crater erasure processes, such as seismic shaking (*16*). The reduced number of small craters (<100 m) indicates that the crater retention time in this size range is very brief. The number density of craters ~10 m indicates that the average resurfacing of the top ~1-meter layer on Ryugu is <10^6 years for the main-belt impact flux (Fig. 2F) and <2 × 10^6 years for near-Earth impact flux (fig. S3). Because impact cratering is a stochastic process, some of these small craters must have formed more recently, exposing fresh material.

Mass wasting

There is abundant evidence for mass movement along slopes (i.e., mass wasting) on Ryugu, particularly around the equatorial ridge and several craters, such as Urashima crater (Fig. 2A). Some groups of boulders observed along the equatorial ridge overlap one another with preferred orientations (i.e., imbrication) away from the ridge, and they are accompanied by asymmetrically distributed fragmental debris deposits (i.e., regolith). The edges of these boulders display little to no regolith deposits along the downhill sides of the ridge (Fig. 1C). Such imbrication typically occurs during landslides. The asymmetric regolith deposits along these boulders indicate that the direction of recent mass wasting is from the top of the equatorial ridge toward higher latitudes, consistent with Ryugu's current geopotential (*9*, *17*). Wall slumping is observed along crater walls, as discussed above (e.g., Fig. 2A). Some craters, such as Momotaro (12.5°N, 51.9°E) near the equatorial ridge, exhibit a higher concentration of large boulders on their floors than on their rims and walls (fig. S8). Such preferential concentration of larger boulders in topographic lows also occurs as a result of mass wasting. These observations suggest that the equatorial ridge is made of mechanically unconsolidated materials and may have formed during a period of rapid spin (*17*), as material flowed toward an equatorial topographic low. An unconsolidated nature would have allowed Ryugu to reshape, perhaps in response to a change in spin rate. When Ryugu was established in its current geopotential configuration, the ridge experienced mass wasting as some of the unconsolidated materials flowed toward new topographic lows at higher latitudes. Furthermore, interior walls in large craters, such as Urashima, exhibit evidence for mass wasting, such as imbricated boulders and run-up deposits (fig. S8B). This indicates that mass wasting postdates these large craters, which must have formed after the equatorial ridge.

Disk-averaged color

During Hayabusa2's approach phase (before arrival and parking at the home position), a series of disk-averaged photometric observations were acquired in each of the seven ONC filters over 12 different rotational phases. We used these data to examine the accuracy of the radiometric calibrations of ONC-T for each filter. Global reflectance values from the ONC-T images based on preflight and in-flight calibrations (*3*–*5*) were compared with ground-based photometric and spectral observations at 0.55 μm (*18*). The results were consistent within the uncertainties, validating that ONC-T is appropriately calibrated over all filters (*5*, *8*).

The disk-averaged seven-band color measurements exhibit little variation (<0.5%) over the different rotational phases observed (Fig. 3A). The color properties are consistent with the classification of Ryugu as a Cb-type asteroid, on the basis of the Bus taxonomy (*19*). This spectral type establishes connections with potential main-belt asteroid families and Ruygu's parent body. Some ground-based spectral observations have suggested the presence of hydrated minerals, owing to spectral features observed at 0.7 μm and <0.55 μm (*20*–*22*). This would imply that Ryugu's parent body could be a Ch-Cgh asteroid, similar to those in the Erigone asteroid family (*23*). However, the ONC-T color observations rule out such a parent body, as do results from Hayabusa2's Near-Infrared Spectrometer (NIRS3), which show that Ryugu's globally averaged near-infrared spectrum does not have any strong OH absorption band signature around 2.8 μm; only a weak absorption band is seen at 2.72 μm (*24*).

The observed visible spectral type is close to that of the asteroids Eulalia and Polana, which are the parent bodies of C-complex asteroid families in the inner main belt (*25*). The asteroid Erigone has a different spectral type (Fig. 3A). Orbital dynamics calculations have shown that the most likely origin of Ryugu is either Eulalia or Polana (*15*). The collisional lifetime of Ryugu [(3 to 5) × 10^8 years] is similar to or less than the breakup time of these families [830^{+370}_{-150} million years and 1400 ± 150 million years for Eulalia and Polana, respectively (*15*)]. Ryugu might not be composed of material directly ejected from one of these large bodies but could be the product of more than one generation of disruption (see below).

The link between Ryugu and Cb asteroids in the inner main belt has implications for possible meteorite analogs. The fraction of Cb- to B-type asteroids in the main asteroid belt is high; fig. S6 indicates that about half of the C-complex asteroids in the main belt are of types Cb, B, and C, which do not display a clear 0.7-μm band. Their populations in the inner main belt, from which the largest fraction of near-Earth asteroids is derived (*2*), contain many large families, such as the Eulalia and Polana families, with these spectral characteristics (*23*). Therefore, the B-Cb-C population comprises a large fraction of the material reaching Earth as meteorites. There are two major candidates for Ryugu meteorite analogs with sufficiently low-albedo materials: thermally metamorphosed carbonaceous chondrites (CCs) (*26*, *27*), or interplanetary dust particles (IDPs). The latter consist of highly primitive material that has experienced no (or only weak) water-rock reaction to form hydrated silicates (*28*, *29*).

Albedo and reflectance

Using the point-source and whole-disk observations of Ryugu, we performed Hapke modeling to characterize the disk-integrated photometric phase behavior in all seven ONC-T filters (table S1) (*8*). On the basis of these photometric measurements, we derived a geometric albedo of 4.5 ± 0.2% at 0.55 μm, similar to albedos of typical comets (*30*) and the darkest asteroids, such as 253 Mathilde, another Cb-type asteroid (*19*, *31*). We derived the disk-integrated surface reflectance at the standard laboratory observation angles (i, e, α = 30°, 0°, 30°; where i, e, and α are incident, emission, and solar phase angles, respectively) for comparison with meteorite samples measured in the laboratory.

The average value of the standard-condition reflectance factor is 1.88 ± 0.17% at 0.55 μm, which is lower than that of any meteorites reported in the literature. The darkest meteorite samples described in the published literature are the thermally metamorphosed CCs (*26*, *32*). Recent measurements show that meteorites of this type (e.g., Jbilet Winselwan, Y-86029, and Y-793321) exhibit reflectance similar to that of Ryugu (Fig. 3B). These meteorite samples are classified in the weakly heated and moderately heated groups (stages II and III, respectively), in which hydrated silicates have been altered into amorphous silicates as a result of dehydration but have not recrystallized into olivine or pyroxene (*33*). Most of these samples are powders; rough slab surfaces, such as Ryugu's surface, generally exhibit lower reflectance and bluer spectra. Although spectral data for slab samples are not as frequently reported as data for powder samples, slab spectra of major CCs from each clan, such as Murchison and Mighei for CM and Ivuna for CI, have been measured (*34*, *35*). These slab samples are not consistent with Ryugu's spectrum.

Local color variation and age–color relation

Surface colors at specific locations on Ryugu span a large range, and all are consistent with the colors of C-complex asteroids (Fig. 3). The color of the majority of Ryugu's surface is characteristic of regolith (denoted "typical regolith"; Fig. 3, C and D). Other colors are found in relatively limited areas and/or geological features on Ryugu, such as distinctive boulders and crater bottoms. Thus, we analyze the color of all pixels on Ryugu with small incidence and emission angles ($i \leq 40°$ and $e \leq 40°$) and use them to define the regolith color variation across the surface.

The general spectral slope from b-band (0.48 μm) to x-band (0.86 μm) exhibits the greatest regional variation; Ryugu's surface has bluer spectral slopes at both poles, on the equatorial ridge, and in large troughs (Fig. 3E). Both polar regions and the equatorial ridge are topographic highs, which may be subject to gradual erosion, leading to the exposure of fresh surface material. Steep boulder surfaces, which may have recently experienced erosion due to thermal fatigue (*36*) or other processes, tend to have brighter and bluer surfaces (Fig. 3, C and D). In contrast, many locations conducive to deposition, such as crater floors, exhibit redder and darker colors. These observations suggest that exposure of Ryugu materials to space leads to their reddening and darkening. However, it is not clear whether this trend occurs because of space weathering or other processes, such as coating with redder and darker dust (*8*). Local-scale heterogeneity suggests that the large-scale uniformity may not be due to pristine materials on

Ryugu's surface, but instead may be the result of a well-mixed surface.

No regolith-covered surface on Ryugu exhibits a strong 0.7-μm absorption in the ONC-T color data. Dynamical calculations have shown that many near-Earth objects (NEOs) experienced dehydration during orbital excursions near the Sun, which may have contributed to the depletion in 0.7-μm absorption in C-complex NEOs (*37*). NEOs with Ryugu-like orbits may experience large orbital excursions on a time scale of 10^7 years, and the skin depth of solar heating during Ryugu's orbital evolution is tens of centimeters (*9*). This time scale is longer than the retention age (<2 × 10^6 years) of 10-m craters,

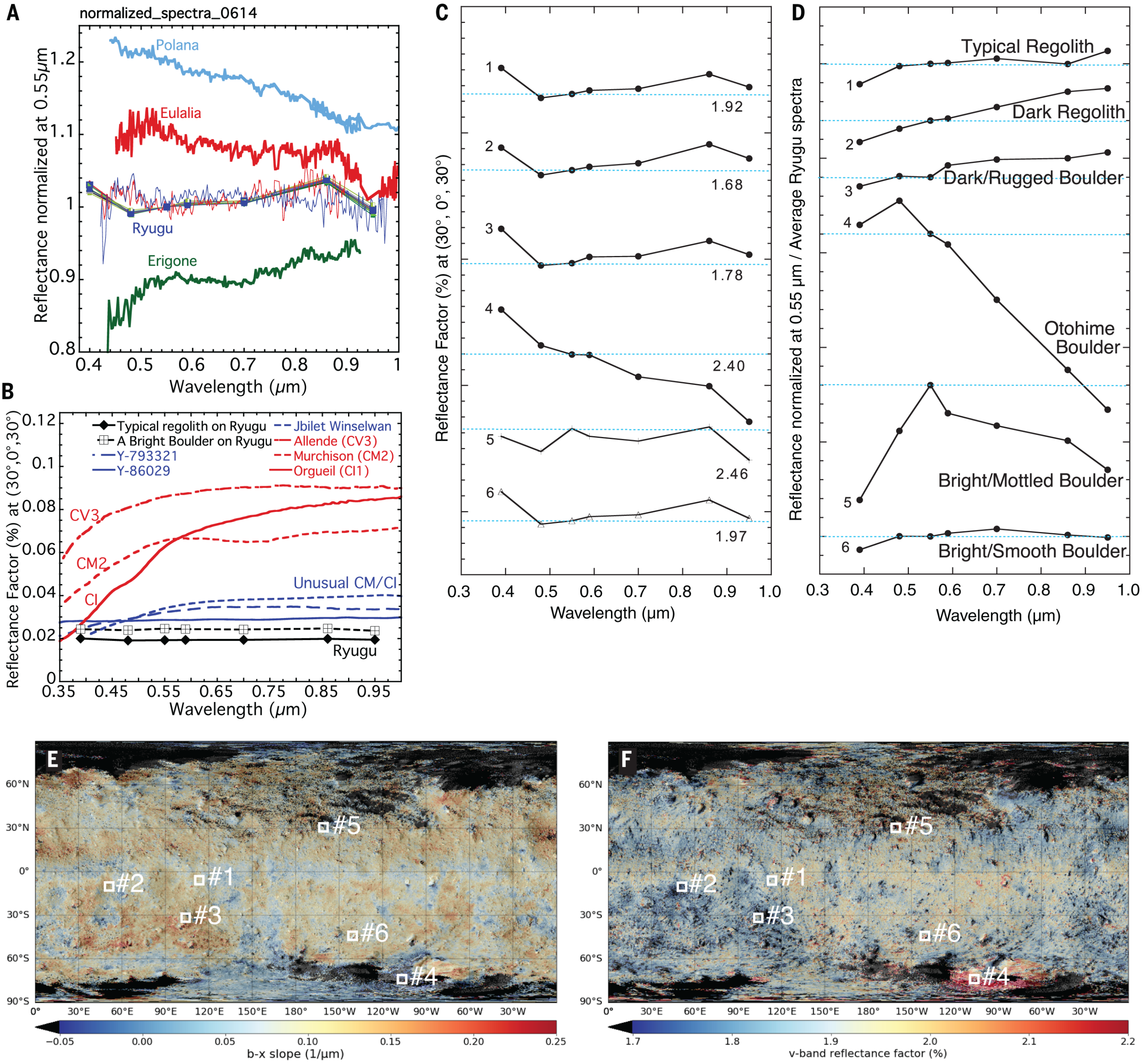

Fig. 3. Multiband colors of Ryugu's surface. (**A**) Comparison between disk-averaged spectra (lines with squares, normalized at 0.55 μm) for Ryugu at 12 different rotational phases and ground-based observations (lines without symbols) of Ryugu from (*55*) (blue) and from (*21*) (red). Data are also shown for the large main-belt asteroids Polana, Eulalia, and Erigone (*56*), each of which is the parent body of an asteroid family. Because of the similarity among the spectra taken at different phases, individual lines for Ryugu overlap. Spectra are offset by 0.1 for clarity. (**B**) Comparison between typical Ryugu surface colors (black) (reflectance factor at 30°, 0°, 30°) and those of dehydrated CCs (blue) and typical CCs (red). Individual meteorite names are indicated. The spectrum of a powder sample (≤155 μm) of Jbilet Winselwan was measured at 30°, 0°, 30° with the spectrometer system at Tohoku University (*57*). The rest of meteorite spectra are from (*58*). (**C**) Reflectance spectra of typical morphologic and color features on Ryugu. Locations of features (labeled 1 to 6) are shown in (E) and (F) and in fig. S12. Individual spectra are shifted vertically for clarity. Vertical-axis tick spacing is 0.05%. (**D**) Same as (C), but normalized by the Ryugu average spectrum. Vertical-axis tick spacing is 0.01. (**E**) b-x slope map (inverse micrometers) and (**F**) v-band reflectance factor map (percent) superposed on a v-band image map. The equatorial ridge and the western side (160°E to 290°E) have slightly higher v-band reflectances than other regions (see fig. S13 for statistical analysis).

which excavate unheated substrate material (crater depths ~1 m). Thus, the lack of a high degree of hydration on Ryugu is unlikely to be due to solar heating during a recent orbital excursion.

East-west dichotomy

Ryugu's western side (160°E to 290°E), which is surrounded by troughs (Fig. 1, A and B), has a v-band albedo higher than that of other areas (Fig. 3F and fig. S13). This western side also has a lower number density of large boulders (Fig. 4A). The topographic highs and bluish b-x spectral slope of the equatorial ridge transect the troughs, suggesting that the equatorial ridge formed more recently than the troughs. Although the equatorial ridge has depressions around 160°E and 290°E, the morphologic characteristics of these features are more consistent with those of impact craters, so we do not consider them to be connected to the mass motion that formed the trough. The formation of the east-west dichotomy probably predates the equatorial ridge formation. However, because there is no difference in b-x spectral slope between the western side and other regions on Ryugu, the nature of its enhanced reflectance is probably not the result of a shorter exposure to the space environment. In contrast, the coincidence between high v-band reflectance and low boulder abundance suggests that this dichotomy may reflect smaller grain size in the western hemisphere. The two hemispheres may have different physical properties, such as grain size and mobility, which could be the result of reaccumulation of two large rubble piles with different grain sizes during the reaccumulation stage immediately after the catastrophic disruption of the parent body (see the "Implications for the evolution of Ryugu's parent body" section below).

Principal components analysis

We conducted a principal components analysis (PCA) of the ONC-T filter data and the second phase of the Small Main-Belt Asteroid Spectroscopic Survey (SMASSII) observations of C-complex main-belt asteroids by ground-based telescopes. This method has been used widely for asteroid spectral analysis and has served as a basis for spectral type definitions (*19*, *38*). Because most reflectance data registered in SMASSII covers only 0.43 to 0.9 μm, we limited the ONC-T data to the b to x bands, excluding the ul and p bands centered at 0.39 and 0.95 μm. Because PCA can expand spectra into orthogonal basis functions, PCA often extracts linear combinations of spectra with physical or mineralogic meanings as the principal components (PCs). Nonorthogonal linear combinations of the second and third PCs produced by our analysis (PC2 and PC3) correspond to the 0.7-μm absorption and drop-off in reflectance shortward of v-band (Fig. 5B and fig. S5). Our results indicate that regolith spectra from ONC-T are consistent with moderately dehydrated CCs (e.g., Y-86029) and reside both near the edge of the B-Cb-C population and the dehydration tracks for CM and CI chondrites (Fig. 5B and fig. S4).

TIR observations provide constraints on surface grain size, which influences the PCA results of colors on Ryugu. TIR observations indicate that the peak temperatures of Ryugu's surface correspond to uniform thermal inertia values between 200 and 500 J m^{-2} s$^{-0.5}$ K^{-1} (Fig. 6). These values are consistent with the disk-averaged value (150 to 300 J m^{-2} s$^{-0.5}$ K^{-1}) estimated on the basis of prearrival telescope observations (*39*) and suggest subcentimeter to 10-cm grains (*7*, *40*); the fraction of surface area covered with grains ≤1 mm

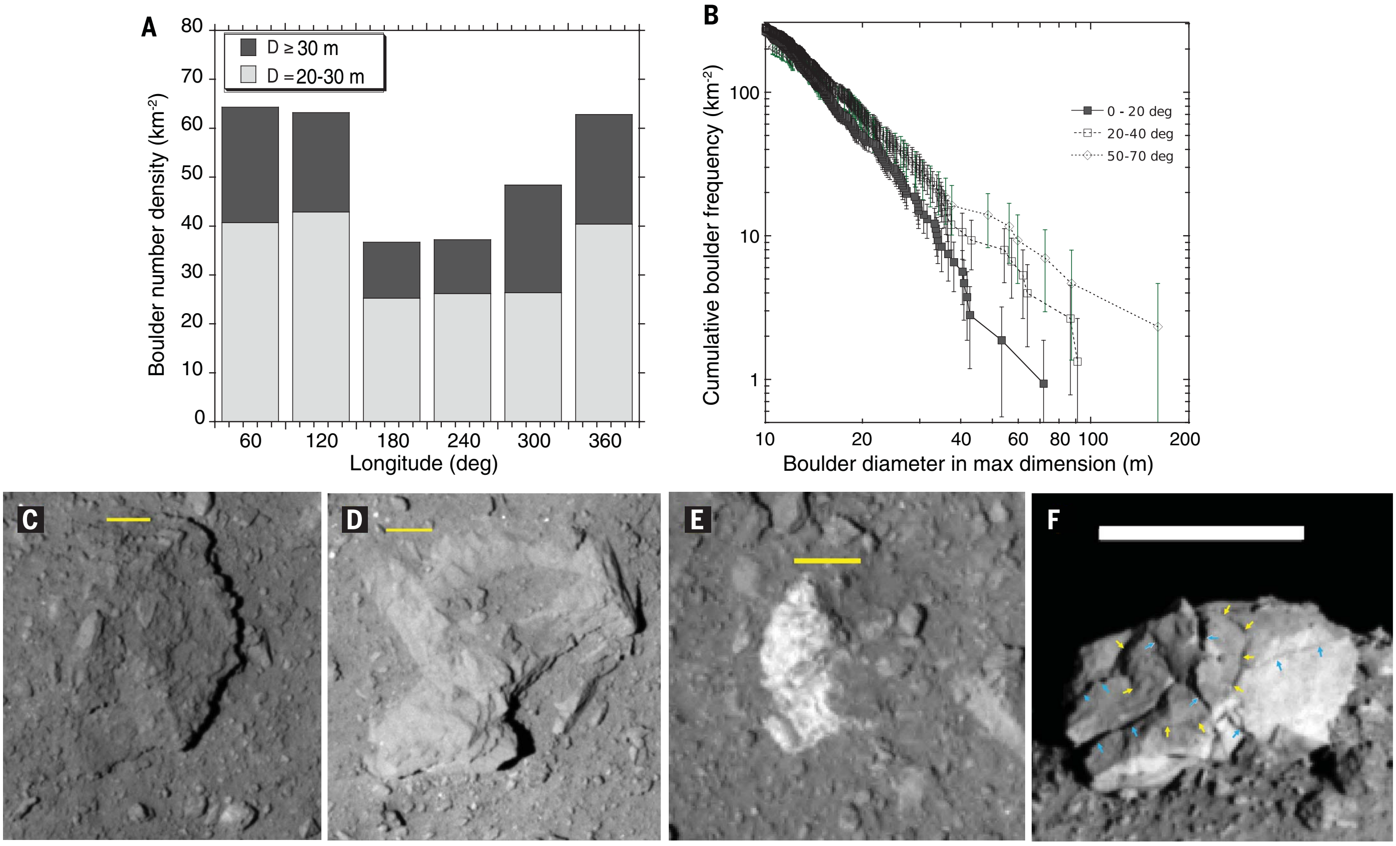

Fig. 4. Statistics and morphologies of boulders on Ryugu. (**A**) Distribution in longitude of boulders with diameters of 20 to 30 m and ≥30 m. (**B**) Cumulative size distribution of large boulders, compared between different latitudinal zones. (**C**) A type 1 boulder, which is dark and rugged (hyb2_onc_20181004_042509_tvf_l2b). A close-up view of its layered structure is shown in fig. S11D. (**D**) A type 2 bright boulder with smooth surfaces and thin layered structure (hyb2_onc_20181004_012509_tvf_l2b). A close-up view of its layered structure is shown in fig. S11E. (**E**) A type 3 bright and mottled boulder (hyb2_onc_20180801_213221_tvf_l2b). (**F**) The sole type 4 boulder, Otohime Saxum, has concentric (yellow arrows) and radial (blue arrows) fractures, consistent with a fracture system generated by an impact (hyb2_onc_20180719_124256_tvf_l2b). In (C) to (F), the brightness of each image is stretched independently. The yellow and white scale bars are 10 and 100 m, respectively.

is very small. Laboratory examination of CC powders of different grain sizes demonstrates that in the visible wavelengths the reflectance and spectral slope do not change markedly for grain sizes larger than ~1 mm, although the effects of compaction and thin coating of fine powers may influence the spectra (*41*). Comparison between the PCA results of Ryugu's surface and the dehydration track for heated coarse-grained samples of the Murchison meteorite shows that the distribution of Ryugu's surface is much narrower than that of the Murchison dehydration track in the PC space (Fig. 5B), suggesting that Ryugu is dominated by materials that experienced similar degrees of dehydration.

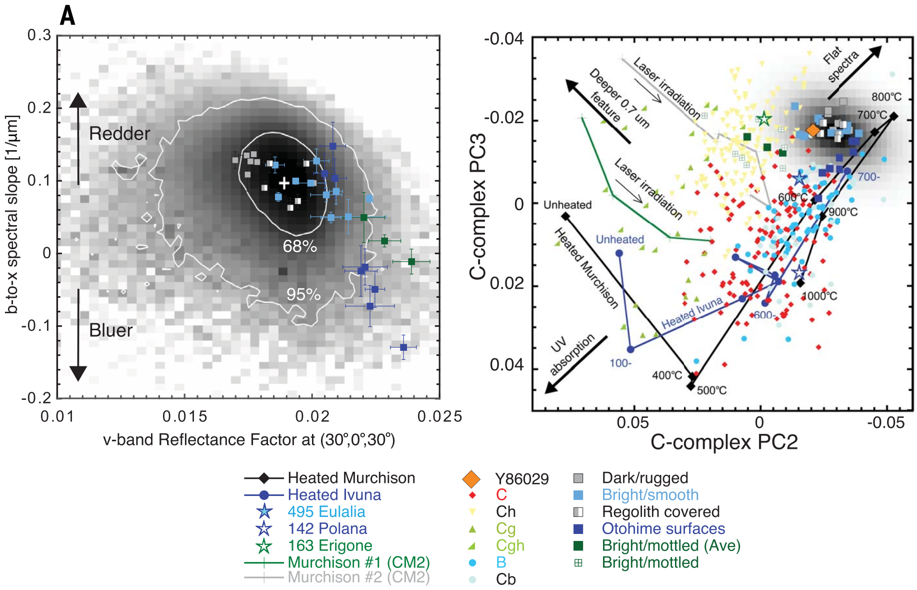

Fig. 5. Colors of surface features on Ryugu. Colors measured from ONC-T images are compared between areas of regolith (gray-black contour) and the four types of boulders (solid, monotone squares) on Ryugu. The legend applies to both panels. (**A**) Comparison of v-reflectance factor and b-x slope distribution. The average value of Ryugu's surface is indicated with a white cross. Contours indicate 95 and 68% of the surface area. (**B**) Comparison of principal component space (PC2-PC3) and main-belt C-complex asteroids (*56*) (colored circles), a moderately dehydrated CC [Y-86029, orange diamond (*58*)], Murchison (CM2) samples with heating [black line (*58*)] and laser irradiation [light green (*59*) and gray lines (*58*)], and heated Ivuna (CI) samples [blue line (*58*)]. Parent bodies of major asteroid families in the inner main belt, Polana (open blue star), Eulalia (solid light blue star), and Erigone (open green star), are also shown (*56*). Images of the four types of boulders are shown in Fig. 4 and fig. S11. Thick black arrows denote locations of end-member spectra (spectra with deep 0.7-µm absorption, flat spectra, and spectra with deep ultraviolet absorption) in this PC space.

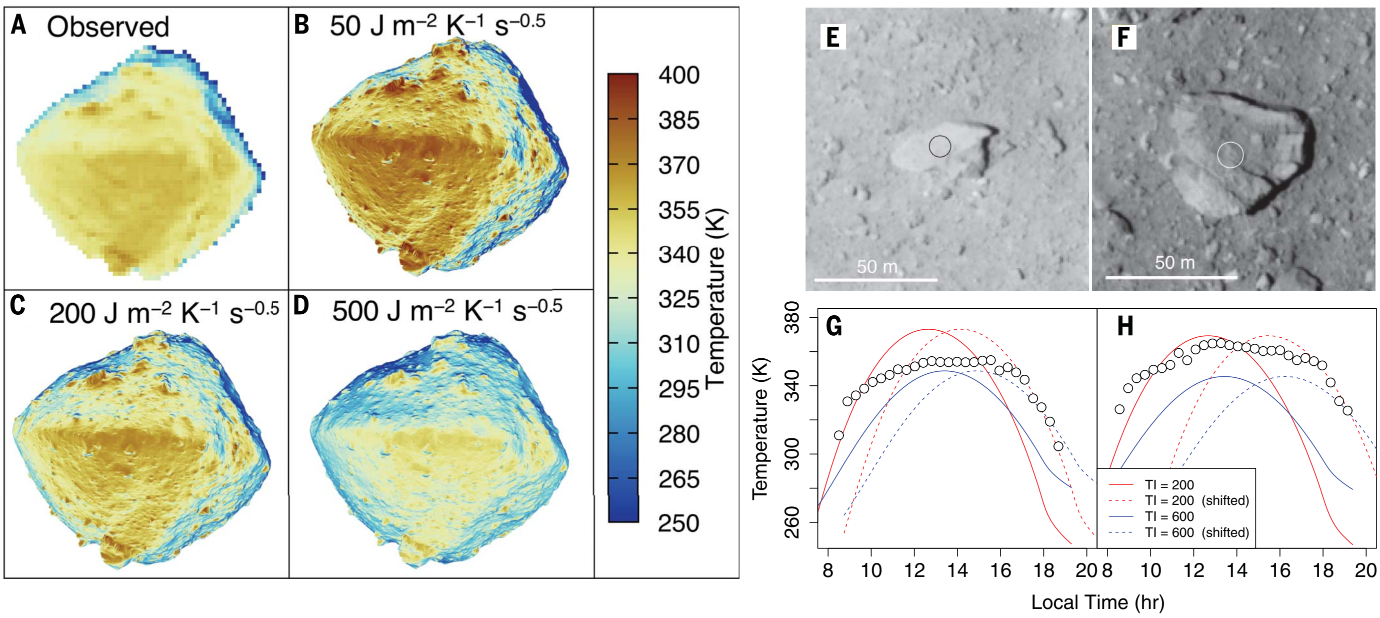

Fig. 6. Thermal infrared camera measurement results. (**A**) Brightness temperature image taken with TIR at 06:07:11 UTC on 10 July 2018 (hyb2_tir_20180710_060711_l2). (**B** to **D**) The image in (A) compared with calculated thermal images by using the structure-from-motion shape model (*17*), assuming uniform thermal inertia of (B) 50, (C) 200, and (D) 500 J m^{-2} s$^{-0.5}$ K^{-1}, respectively. (**E**) An ONC-T image of large boulders (6.4°S, 148.4°E), taken during low-altitude (5 to 7 km) observations (hyb2_onc_20180801_144909_tvf_l2b). Surface area (open circle) not covered with regolith was chosen for temperature analysis. (**F**) As in (E), but for a boulder at (20.9°S, 27.8°E) (hyb2_onc_20180801_174157_tvf_l2b). (**G**) Temperature profile of the location indicated with the circle in (E) observed with TIR at 20 km from the Ryugu center (open circles). Theoretical temperature profiles for uniform thermal inertias of 200 and 600 J m^{-2} K^{-1} s$^{-0.5}$ are shown with curves. Solid curves are for a horizonal plane that starts to receive solar light at local time 7.5 hours; dashed curves represent a tilted plane that receives sunlight at later times. The observed data are largely enclosed by the upper envelopes of time-shifted curves for 200 and 600 J m^{-2} K^{-1} s$^{-0.5}$. (**H**) Same as (G), but for the location indicated by the circle in (F).

Abundance and distribution of boulders

Ryugu's surface contains many boulders that span a wide range of sizes (Fig. 4B). The largest boulders (>20 m) are too large to be ejecta from the observed craters (≤300 m) (42), which suggests that they are instead fragments of Ryugu's parent body. The cumulative distribution of boulder sizes follows a power law with an exponent between −2.5 and −3 (Fig. 4B), similar to that measured for other small asteroids (43–45).

The global average number density of boulders ≥20 m in diameter at latitudes ≤70° is 50 km^{-2} on Ryugu, which exceeds the value for Itokawa by a factor of 2 (39, 41). However, the number density of craters on Ryugu is of the same order of magnitude as that of Itokawa, which suggests that boulders on both asteroids have experienced similar degrees of meteoritic bombardment. Thus, the higher abundance of large boulders on Ryugu suggests that the impact strength of these boulders may be of a similar order of magnitude to that of Itokawa's boulders. Given the apparent high surface mobility, it is possible that many previously existing boulders may have been ejected from Ryugu as macroscopic bodies. If so, fragments from Ryugu may reach Earth as macroscopic meteorites.

The spatial distribution of boulders on Ryugu differs from that on Itokawa and Eros, which have boulder-poor regions, such as smooth terrains (46, 47) and regolith ponds (48). Ryugu does not contain large areas with low boulder abundance, suggesting that the degree of size sorting is much lower on Ryugu. A contributing factor may be the difference in the overall shape of these asteroids: Itokawa and Eros are elongated, whereas Ryugu is spheroidal. However, there is evidence for some global size segregation in the latitudinal variation in boulder size: The boulder number density is lower in the equatorial region than at higher latitudes (Fig. 3A). This may be because of mass flow during the equatorial ridge formation (17). There is also a smaller boulder abundance variation in the longitudinal direction (Fig. 3B), with the boulder abundance in the western hemisphere (160°E to 290°E) systematically lower than at all other longitudes on Ryugu.

Color and morphology of boulders

There is a systematic trend between boulder colors and morphologies on Ryugu. We have identified four distinct morphologic boulder types. (i) Type 1: Dark and rugged boulders. This type possesses rugged surfaces and edges, tends to have uneven layered structures possibly related to inclusion of coarse-grained clasts (Figs. 4C and fig. S11A), and has color properties similar to Ryugu's average color (Fig. 3C). Many boulders of this type are partially buried by regolith; as is the case for Ejima Saxum (Fig. 1A). (ii) Type 2: Bright and smooth boulders. This boulder type displays several thin and parallel layers (Fig. 4D). Many of these boulders are positioned atop the regolith, and some exhibit distinctive striped patterns (fig. S11B). Their typical color ranges from slightly bluer than average to Ryugu's average color (Fig. 3). (ii) Type 3: Bright and mottled boulders. This boulder type does not show clear layers but displays a blocky variegation in albedo (Fig. 4E and fig. S11C). The bright parts exhibit a drop-off in reflectance at short wavelengths (ul and b) (Fig. 3C). (iv) Type 4: The largest boulder on Ryugu, Otohime Saxum, does not match the other types. It is located near the south pole (Figs. 1 and 4F), with sharp edges and smooth surfaces but no obvious layering. Its vertical face is the brightest surface on Ryugu and exhibits a very blue color (Fig. 3). The differences in brightness among these four types of boulders are not very large; the range of their v-band reflectance factors is similar to that of the background regolith (Fig. 5A).

More quantitative examinations of boulder colors were performed using reflectance-slope statistics and PCA. Although the dark, rugged boulders and the bright, smooth boulders are distinct in morphology, they form a single linear trend in reflectance-slope diagrams and PC2-PC3 space (Fig. 5) parallel to the general distribution of PC scores over the entire surface. The range in boulder color variation is similar to the color variation seen over the entire surface; the range of PC2 scores of 27 large boulders encompasses the PC2 score range of more than half of Ryugu's surface. This agreement in PC-score trends between regolith and boulders suggests that the color variation in regolith on Ryugu may be controlled by the color variation of these two types of boulders, from which the regolith may be produced through comminution processes.

In contrast, the different sides or facets of Otohime Saxum form their own trend in the reflectance-slope diagram (Fig. 5A) and PC spaces (Figs. 5B and fig. S7), approximately parallel to the trend for heat-induced dehydrated CC materials (26). The trend observed for Otohime Saxum is also parallel to the distribution trend in the B-Cb-C population (Fig. 5B and fig. S4), which suggests that their color variations may result from the same process, such as dehydration.

In the PC2-PC3 space, the bright, mottled boulders are consistent with the Ch-Cgh asteroid population, closest to Erigone (Fig. 5B). These type 3 boulders extend the trend seen in the regolith and other types of boulders (Fig. 5B and fig. S7). The 0.7-μm absorption—measured as the difference, $(v + x)/2w - 1$, between w-band reflectance and the linear continuum defined by v- and x-band reflectance values—is not stronger than the average Ryugu spectrum. Type 3 boulders are close in PC space to the Ch-Cgh population, owing to their low b-band reflectance.

The linear trend extending through type 3 boulders, the average regolith, and type 1 and 2 boulders is seen in the first three PC values plotted against albedo. This trend cannot be produced by space weathering and/or grain size effects. It also differs from the L-shaped distribution of laboratory dehydration data (Fig. 5B). Although the low-temperature evolution of the dehydration track for CM chondrites is similar to the boulder trend (both cross the dividing gap between Ch-Cgh and B-Cb-C populations and have a large PC2 change), they differ in PC3 change, leading to a very different slope in the PC2-PC3 space. Instead, the trend formed by boulder types 1 to 3 connects the average Ryugu spectrum and the Ch-Cgh population. A simple interpretation of these trends is the mixing between two components in Ch-Cgh and B-Cb-C populations. This trend is consistent with mixing seen not only in the regolith but also in the boulders. This observation based on PCA suggests that these boulders have experienced mixing processes.

Boulder texture and regolith grains

Hayabusa2 carried several landers [encompassed by three MIcro Nano Experimental Robot Vehicles for Asteroid (MINERVA-IIs) and the Mobile Asteroid Surface Scout (MASCOT)]. Deployment of these landers required multiple spacecraft descents to <100-m altitude, which provided opportunities for obtaining close-up images down to a scale of 6 mm per pixel (Fig. 7 and fig. S14).

The higher-resolution images show that the global size distribution of both boulders and pebbles follows a power-law distribution down to decimeter scales; the slope (i.e., power-law index) of their cumulative size distribution is about −2.5 at sizes larger than ~0.2 m, similar that found for large blocks (10 to 160 m) (Fig. 4B). The slope then becomes shallower at smaller sizes (fig. S14A). The shallower slope in the small size range suggests a non-negligible mechanical strength of individual boulders and pebbles on Ryugu. Although such high-resolution measurements have been conducted only in limited areas on Ryugu, no differences have been observed between areas on and off the equatorial ridge.

Many images of Ryugu exhibit bright spots (Fig. 7, A and B, and fig. S14B). Some of these spots are brighter than the average background by a few tens of percent, whereas others are brighter by a factor of 2 or greater. These spots may be impact craters or recent fragments from preexisting boulders, both of which could exhibit higher albedos because of the freshness of their interior, or they may be small fragments of distinct intrinsic composition. Their distinctive brightness and relatively low abundance suggest that they may be composed of materials similar to bright and mottled boulders, whose spectra are consistent with Ch-Cgh populations (Fig. 5). Ryugu's surface material may be a mixture of materials with different lithologies representative of its parent body.

Heterogeneity in brightness can also be found within individual boulders (Fig. 7A). This morphologic characteristic is consistent with coarse-grained clastic rocks (impact breccia), including rock fragments broken by impact. The majority constituent of CCs has been proposed to be impact breccia (49). This suggests material mixing before these boulders were formed, which likely took place on Ryugu's parent body. Because impact breccias can contain multiple components with variable mixing ratios, they can readily account for the mixing trends seen in the PC spaces (fig. S7). Breccia formation on the parent body

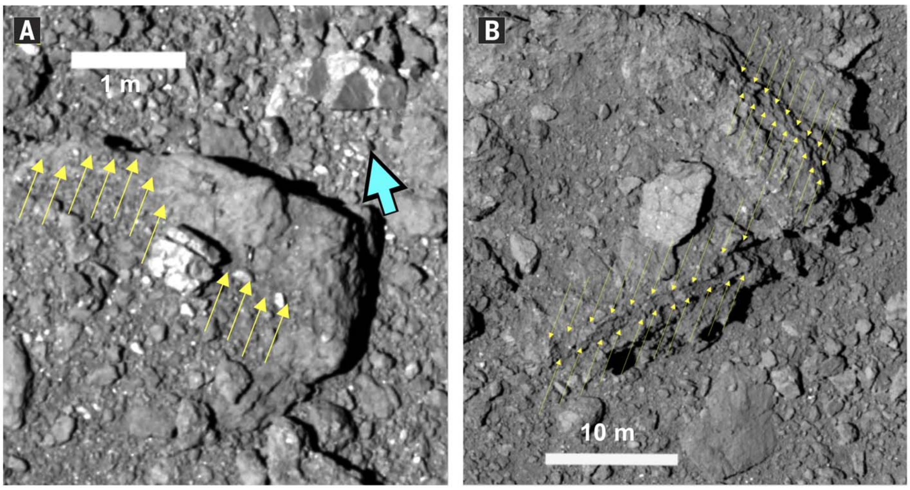

Fig. 7. Close-up observation results of surfaces on Ryugu. (**A**) A boulder partially buried with regolith (yellow arrows) and a smaller boulder with angular fragments having different brightness (blue arrow) near the MINERVA-II landing site (9 mm per pixel, hyb2_onc_20180921_040154_tvf_l2b). (**B**) A rugged boulder with layered structure (yellow arrows) near the MASCOT landing site (6 cm per pixel, hyb2_onc_20181003_003036_tvf_l2b).

can also account for porous textures observed in many dark boulders on Ryugu (Fig. 7B). These porous boulders seen in the high-resolution images have the same morphologies as the dark, rugged boulders observed in lower-resolution global and regional images (Fig. 4C). These boulders often have quasi-parallel layers (Fig. 7B). Thus, if these boulders are impact breccias, they may originate from the sedimentation of multiple ejecta blankets.

Layered structures are seen on boulder surfaces, suggesting that these boulders are not covered with loose regolith, supporting our interpretation that the thermal inertias of boulders measured by TIR (Fig. 6) reflect the bulk properties of the boulders. The presence of rugged grains and pores is also consistent with low thermal conductivity and density.

The porous nature of impact breccias would increase the bulk porosity of Ryugu. The very low bulk density [$(1.19 \pm 0.02) \times 10^3$ kg/m^3] of Ryugu would require very high porosity (~50%) if the grain densities of typical CCs are assumed (*17*). Such a high porosity is substantially greater than that (~40%) for closest packing with a single boulder size. If Ryugu possesses pores within individual boulders (intraboulder pores) in addition to pores between multiple boulders (interboulder pores), such low density can be achieved with typical CC materials.

Implications for the evolution of Ryugu's parent body

Our observations suggest the presence of partially hydrated minerals on Ryugu, though with a low degree of hydration. The low average albedo (Fig. 3B), average spectra lying in the midrange of dehydration tracks of CM and CI chondrites (Fig. 5B), and shortward drop-off in the spectra of some boulders (Fig. 3D) are consistent with moderately dehydrated CCs and/or weakly altered IDPs and are inconsistent with completely dehydrated CCs. In this section, we discuss the origin of these materials on Ryugu.

Recent numerical calculations of large asteroid breakups by collision show that fragments formed by the reaccumulation of material, resulting in a rubble pile structure, can contain materials sampling different depths on the original parent asteroid (~100 km in diameter) (*50*). Mixtures of impact debris with different lithologies from the original parent body could deposit on the reaccumulated fragments, leading to the formation of impact breccias. A subsequent impact on such a reaccumulated fragment would generate boulders with a large heterogeneity in color properties. Using a similar method, we conducted numerical calculations to estimate how much material is collected in reaccumulated bodies from different depths of a 100-km–diameter parent body (*8*) (fig. S9). The results indicate that materials from all depths of the parent body are accumulated in each small reaccumulated body. This could account for both the relatively homogeneous spectral properties of Ryugu and the limited amount of local heterogeneity found in the boulders, if partial dehydration occurred as a result of internal heating (e.g., due to radioactive decay of ^{26}Al). Internal heating can warm a large fraction of the volume of the parent body relatively uniformly, leaving a small volume of outer layer relatively cool (*51*) (Fig. 8).

In contrast, partial dehydration due to a single-shock heating event, such as that induced by the catastrophic impact that disrupted the original parent body, is unlikely because most boulders on Ryugu do not possess a strong 0.7-μm absorption band. To suppress the 0.7-μm band in the majority of a resulting body composed of reaccumulated fragments, the impact must heat the relevant mass to 400°C or higher. However, impact heating is an inefficient global process; efficient heating occurs only around the impact site (fig. S15). Most of the volume does not experience much heating and simply fractures into cold impact fragments. The numerical calculation results (*50*) (fig. S9) indicate that a catastrophic disruption event due to a large impact would sample different portions of the parent body along the excavation streamlines. Thus, any body formed from reaccumulated fragments would be primarily heterogeneous unless the parent body itself was homogeneous—i.e., the large-scale radial heterogeneity in the parent body would be inherited by the boulders comprising the reaccumulated-fragments body. Consequently, the preponderance of materials with little water signature on Ryugu suggests that a dominant part of its original parent body was also water poor. Such global partial dehydration is possible with impacts, but only if many impacts occurred before the catastrophic disruption (Fig. 8). Geochemical analyses of thermally metamorphosed meteorites are consistent with short-term heating (*27*, *52*); thus, this scenario cannot readily be discarded. However, the observation that Ryugu's regolith and boulders are concentrated in a relatively small area in the dehydration track in the PC spaces suggests that a large volume of Ryugu's original parent body was dehydrated to a similar state. Such uniformity is more consistent with internal heating on the parent body than partial dehydration caused by multiple impacts.

An alternative possibility is that Ryugu is covered with materials that experienced only incipient aqueous alteration before forming Fe-rich serpentine, which has 0.7-μm absorption. In this scenario, the closest meteoritic counterpart would be IDPs. If Ryugu is made of such highly primitive materials, the trend connecting regolith and dark boulders in the B-Cb-C population with bright, mottled boulders in the Ch-Cgh population may be a progression of aqueous alteration (*28*, *29*). However, there are insufficient IDP reflectance spectra available to constrain this scenario. It is difficult to distinguish materials that experienced only a low degree of hydration from materials that originally were highly hydrated and subsequently experienced partial dehydration. Nevertheless, the boulders on Ryugu have survived impact processes during catastrophic disruption, the reaccumulation process, and more-recent impacts on Ryugu; they are not dust balls with little cohesion. Thus, this scenario is in conflict with the boulder-rich nature of Ryugu. If Ryugu is composed of IDP-like materials and does not have a macroscopic meteorite counterpart, there must be an additional mechanism to break up boulders and pebbles before they arrive at Earth as meteorites.

Although multiple scenarios for the evolution of Ryugu's parent body remain viable, our comparison between Hayabusa2 remote-sensing data, meteoritic samples, and asteroids leads us to prefer the scenario of parent-body partial dehydration due to internal heating. This scenario suggests that asteroids that accreted materials that condensed at ≤150 K (the H_2O condensation

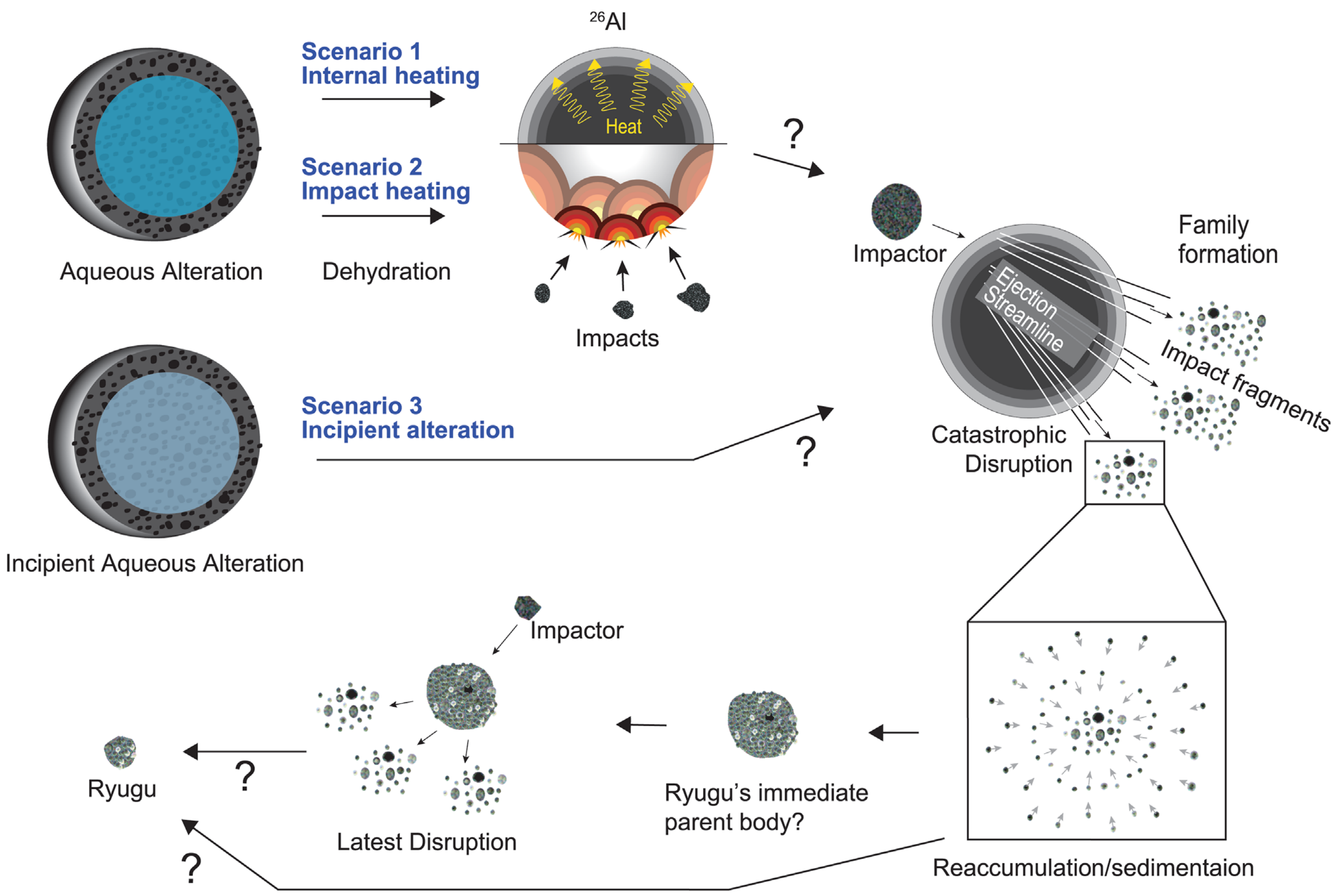

Fig. 8. Schematic illustration of Ryugu's formation. Ryugu formed from the reaccumulation of material ejected from an original parent body by an impact, possibly by way of an intermediate parent body (bottom). Three scenarios to explain Ryugu's low hydration and thermal processing may have occurred before disruption of the original parent body (top).

temperature under typical solar nebula conditions) must have either formed early enough to contain high concentrations of radiogenic species, such as ^{26}Al, or formed close to the Sun, where they experienced other heating mechanisms (*53*). The degree of internal heating would constrain the location and/or timing of the snow line (the dividing line between H_2O condensation and evaporation) in the early Solar System.

REFERENCES AND NOTES

1. D. P. O'Brien, R. Greenberg, The collisional and dynamical evolution of the main-belt and NEA size distributions. *Icarus* **178**, 179–212 (2005). doi: 10.1016/j.icarus.2005.04.001
2. W. F. Bottke Jr. *et al.*, The fossilized size distribution of the main asteroid belt. *Icarus* **175**, 111–140 (2005). doi: 10.1016/j.icarus.2004.10.026
3. S. Kameda *et al.*, Preflight calibration test results for optical navigation camera telescope (ONC-T) onboard the *Hayabusa2* spacecraft. *Space Sci. Rev.* **208**, 17–31 (2017). doi: 10.1007/s11214-015-0227-y
4. H. Suzuki *et al.*, Initial inflight calibration for Hayabusa2 optical navigation camera (ONC) for science observations of asteroid Ryugu. *Icarus* **300**, 341–359 (2018). doi: 10.1016/j.icarus.2017.09.011
5. E. Tatsumi *et al.*, Updated inflight calibration of Hayabusa2's Optical Navigation Camera (ONC) for scientific observations during the cruise phase. *Icarus* **325**, 153–195 (2019). doi: 10.1016/j.icarus.2019.01.015
6. T. Mizuno *et al.*, Development of the laser altimeter (LIDAR) for Hayabusa2. *Space Sci. Rev.* **208**, 33–47 (2016). doi: 10.1007/s11214-015-0231-2
7. T. Okada *et al.*, Thermal Infrared Imaging Experiments of C-Type Asteroid 162173 Ryugu on Hayabusa2. *Space Sci. Rev.* **208**, 255–286 (2017). doi: 10.1007/s11214-016-0286-8
8. Materials and methods are available as supplementary materials.
9. S. Tardivel, P. Sánchez, D. J. Scheeres, Equatorial cavities on asteroids, an evidence of fission events. *Icarus* **304**, 192–208 (2018). doi: 10.1016/j.icarus.2017.06.037
10. P. Michel, M. Delbo, Orbital and thermal evolutions of four potential targets for a sample return space mission to a primitive near-Earth asteroid. *Icarus* **209**, 520–534 (2010). doi: 10.1016/j.icarus.2010.05.013
11. N. Hirata *et al.*, A survey of possible impact structures on 25143 Itokawa. *Icarus* **200**, 486–502 (2009). doi: 10.1016/j.icarus.2008.10.027
12. V. R. Oberbeck, W. L. Quaide, Genetic Implications of Lunar Regolith Thickness Variations. *Icarus* **9**, 446–465 (1968). doi: 10.1016/0019-1035(68)90039-0
13. C. Güttler, N. Hirata, A. M. Nakamura, Cratering experiments on the self armoring of coarse-grained granular targets. *Icarus* **220**, 1040–1049 (2012). doi: 10.1016/j.icarus.2012.06.041
14. E. Tatsumi, S. Sugita, Cratering efficiency on coarse-grain targets: Implications for the dynamical evolution of asteroid 25143 Itokawa. *Icarus* **300**, 227–248 (2018). doi: 10.1016/j.icarus.2017.09.004
15. W. F. Bottke *et al.*, In search of the source of asteroid (101955) Bennu: Applications of the stochastic YORP model. *Icarus* **247**, 191–217 (2015). doi: 10.1016/j.icarus.2014.09.046
16. P. Michel, D. P. O'Brien, S. Abe, N. Hirata, Itokawa's cratering record as observed by Hayabusa: Implications for its age and collisional history. *Icarus* **200**, 503–513 (2009). doi: 10.1016/j.icarus.2008.04.002
17. S. Watanabe *et al.*, Hayabusa2 arrives at the carbonaceous asteroid 162173 Ryugu—A spinning top–shaped rubble pile. *Science* **364**, 268–272 (2019). doi: 10.1126/science.aav8032
18. M. Ishiguro *et al.*, Optical properties of (162173) 1999 JU3: In preparation for the JAXA Hayabusa2 sample return mission. *Astrophys. J.* **792**, 74 (2014). doi: 10.1088/0004-637X/792/1/74
19. S. J. Bus, R. P. Binzel, Phase II of the small main-belt asteroid spectroscopic survey: A feature-based taxonomy. *Icarus* **158**, 146–177 (2002). doi: 10.1006/icar.2002.6856
20. R. P. Binzel *et al.*, Spectral Properties of Near-Earth Objects: Palomar and IRTF Results for 48 Objects Including Spacecraft Targets (9969) Braille and (10302) 1989 ML. *Icarus* **151**, 139–149 (2001). doi: 10.1006/icar.2001.6613
21. F. Vilas, Spectral characteristics of Hayabusa 2 Near-Earth asteroid targets 162173 1999 JU3 and 2001 QC34. *Astron. J.* **135**, 1101–1105 (2008). doi: 10.1088/0004-6256/135/4/1101
22. D. Lazzaro *et al.*, Rotational spectra of (162173) 1999 JU3, the target of the Hayabusa2 mission. *Astron. Astrophys.* **549**, L2 (2013). doi: 10.1051/0004-6361/201220629
23. D. Morate *et al.*, Compositional study of asteroids in the Erigone collisional family using visible spectroscopy at the 10.4 m GTC. *Astron. Astrophys.* **586**, A129 (2016). doi: 10.1051/0004-6361/201527453
24. K. Kitazato *et al.*, The surface composition of asteroid 162173 Ryugu from Hayabusa2 near-infrared spectroscopy. *Science* **364**, 272–275 (2019). doi: 10.1126/science.aav7432
25. J. de León *et al.*, Expected spectral characteristics of (101955) Bennu and (162173) Ryugu, targets of the OSIRIS-REx and Hayabusa2 missions. *Icarus* **313**, 25–37 (2018). doi: 10.1016/j.icarus.2018.05.009
26. T. Hiroi, M. E. Zolensky, C. M. Pieters, M. E. Lipschutz, Thermal metamorphism of the C, G, B, and F asteroids seen from the 0.7 μm, 3 μm, and UV absorption strengths in comparison with carbonaceous chondrites. *Meteorit. Planet. Sci.* **31**, 321–327 (1996). doi: 10.1111/j.1945-5100.1996.tb02068.x

27. E. Tonui *et al*., Petrographic, chemical and spectroscopic evidence for thermal metamorphism in carbonaceous chondrites I: CI and CM chondrites. *Geochim. Cosmochim. Acta* **126**, 284–306 (2014). doi: 10.1016/j.gca.2013.10.053
28. P. Vernazza *et al*., Interplanetary dust particles as samples of icy asteroids. *Astrophys. J.* **806**, 204 (2015). doi: 10.1088/0004-637X/806/2/204
29. S. Fornasier, C. Lantz, M. A. Barucci, M. Lazzarin, Aqueous alteration on main belt primitive asteroids: Results from visible spectroscopy. *Icarus* **233**, 163–178 (2014). doi: 10.1016/j.icarus.2014.01.040
30. J. M. Bauer *et al*., The NEOWISE-Discovered Comet Population and the CO + CO_2, Production Rates. *Astrophys. J.* **814**, 85 (2015). doi: 10.1088/0004-637X/814/2/85
31. B. E. Clark *et al*., NEAR Photometry of asteroid 253 Mathilde. *Icarus* **140**, 53–65 (1999). doi: 10.1006/icar.1999.6124
32. E. A. Cloutis, P. Hudon, T. Hiroi, M. J. Gaffey, Spectral reflectance properties of carbonaceous chondrites 4: Aqueously altered and thermally metamorphosed meteorites. *Icarus* **220**, 586–617 (2012). doi: 10.1016/j.icarus.2012.05.018
33. T. Nakamura, Post-hydration thermal metamorphism of carbonaceous chondrites. *J. Mineral. Petrol. Sci.* **100**, 260–272 (2005). doi: 10.2465/jmps.100.260
34. E. A. Cloutis, T. Hiroi, M. J. Gaffey, C. M. O. D. Alexander, P. Mann, Spectral reflectance properties of carbonaceous chondrites: 1. CI chondrites. *Icarus* **212**, 180–209 (2011). doi: 10.1016/j.icarus.2010.12.009
35. E. A. Cloutis, P. Hudon, T. Hiroi, M. J. Gaffey, P. Mann, Spectral reflectance properties of carbonaceous chondrites: 2. CM chondrites. *Icarus* **216**, 309–346 (2011). doi: 10.1016/j.icarus.2011.09.009
36. M. Delbo *et al*., Thermal fatigue as the origin of regolith on small asteroids. *Nature* **508**, 233–236 (2014). doi: 10.1038/nature13153; pmid: 24695219
37. S. Marchi, M. Delbo', A. Morbidelli, P. Paolicchi, M. Lazzarin, Heating of near-Earth objects and meteoroids due to close approaches to the Sun. *Mon. Not. R. Astron. Soc.* **400**, 147–153 (2009). doi: 10.1111/j.1365-2966.2009.15459.x
38. S. C. Koga *et al*., Spectral decomposition of asteroid Itokawa based on principal component analysis. *Icarus* **299**, 386–395 (2018). doi: 10.1016/j.icarus.2017.08.016
39. T. G. Müller *et al*., Hayabusa-2 mission target asteroid 162173 Ryugu (1999 JU3): Searching for the object's spin-axis orientation. *Astron. Astrophys.* **599**, A103 (2017). doi: 10.1051/0004-6361/201629134
40. N. Sakatani *et al*., Thermal conductivity model for powdered materials under vacuum based on experimental studies. *AIP Adv.* **7**, 015310 (2017). doi: 10.1063/1.4975153
41. E. Cloutis *et al*., Spectral reflectance "deconstruction" of the Murchison CM2 carbonaceous chondrite and implications for spectroscopic investigations of dark asteroids. *Icarus* **305**, 203–224 (2018). doi: 10.1016/j.icarus.2018.01.015
42. T. Michikami *et al*., Size-frequency statistics of boulders on global surface of asteroid 25143 Itokawa. *Earth Planets Space* **60**, 13–20 (2008). doi: 10.1186/BF03352757
43. P. C. Thomas, J. Veverka, M. S. Robinson, S. Murchie, Shoemaker crater as the source of most ejecta blocks on the asteroid 433 Eros. *Nature* **413**, 394–396 (2001). doi: 10.1038/35096513; pmid: 11574880
44. S. Mazrouei, M. G. Daly, O. S. Barnouin, C. M. Ernst, I. DeSouza, Block distribution on Itokawa. *Icarus* **229**, 181–189 (2014). doi: 10.1016/j.icarus.2013.11.010
45. Y. Jiang *et al*., Boulders on asteroid Toutatis as observed by Chang'e-2. *Sci. Rep.* **5**, 16029 (2015). doi: 10.1038/srep16029; pmid: 26522880
46. H. Demura *et al*., Pole and global shape of 25143 Itokawa. *Science* **312**, 1347–1349 (2006). doi: 10.1126/science.1126574; pmid: 16741112
47. H. Miyamoto *et al*., Regolith migration and sorting on asteroid Itokawa. *Science* **316**, 1011–1014 (2007). doi: 10.1126/science.1134390; pmid: 17446355
48. J. Veverka *et al*., Imaging of small-scale features on 433 Eros from NEAR: Evidence for a complex regolith. *Science* **292**, 484–488 (2001). doi: 10.1126/science.1058651; pmid: 11313490
49. A. Bischoff *et al*., "Nature and origins of meteoritic breccias" in *Meteorites and the Early Solar System II*, D. S. Lauretta, H. Y. McSween Jr., Eds. (Univ. of Arizona Press, 2006), pp. 679–712.
50. P. Michel *et al*., Selective sampling during catastrophic disruption: Mapping the location of reaccumulated fragments in the original parent body. *Planet. Space Sci.* **107**, 24–28 (2015). doi: 10.1016/j.pss.2014.08.005
51. S. Wakita, M. Sekiya, Thermal Evolution of Icy Planetesimals in the Solar Nebula. *Earth Planets Space* **63**, 1193–1206 (2011). doi: 10.5047/eps.2011.08.012
52. G. D. Cody *et al*., Organic thermometry for chondritic parent bodies. *Earth Planet. Sci. Lett.* **272**, 446–455 (2008). doi: 10.1016/j.epsl.2008.05.008
53. F. Herbert, C. P. Sonett, M. J. Gaffey, "Protoplanetary thermal metamorphism: The hypothesis of electromagnetic induction in the protosolar wind" in *The Sun in Time* (Univ. of Arizona Press, 1991), pp. 710–739.
54. W. F. Bottke Jr., M. C. Nolan, R. Greenberg, R. A. Kolvoord, Velocity distributions among colliding asteroids. *Icarus* **107**, 255–268 (1994). doi: 10.1006/icar.1994.1021
55. N. A. Moskovitz *et al*., Rotational characterization of Hayabusa II target Asteroid (162173) 1999 JU3. *Icarus* **224**, 24–31 (2013). doi: 10.1016/j.icarus.2013.02.009
56. S. J. Bus, R. P. Binzel, Phase II of the small main-belt asteroid spectroscopic survey: The observations. *Icarus* **158**, 106–145 (2002). doi: 10.1006/icar.2002.6857
57. M. Matsuoka *et al*., An evaluation method of reflectance spectra to be obtained by Hayabusa2 Near-Infrared Spectrometer (NIRS3) based on laboratory measurements of carbonaceous chondrites. *Earth Planets Space* **69**, 120 (2017). doi: 10.1186/s40623-017-0705-4
58. C. M. Pieters, Strength of mineral absorption features in the transmitted component of near-infrared reflected light: First results from RELAB. *J. Geophys. Res.* **88**, 9534–9544 (1983). doi: 10.1029/JB088iB11p09534
59. M. Matsuoka *et al*., Pulse-laser irradiation experiments of Murchison CM2 chondrite for reproducing space weathering on C-type asteroids. *Icarus* **254**, 135–143 (2015). doi: 10.1016/j.icarus.2015.02.029

ACKNOWLEDGMENTS

We thank the anonymous reviewers for their helpful comments. The Hayabusa2 spacecraft was developed and built under the leadership of Japan Aerospace Exploration Agency (JAXA), with contributions from the German Aerospace Center (DLR) and the Centre National d'Études Spatiales (CNES), and in collaboration with NASA, Nagoya University, University of Tokyo, National Astronomical Observatory of Japan (NAOJ), University of Aizu, Kobe University, and other universities, institutes, and companies in Japan. We also thank many engineers, including N. Inaba at JAXA and T. Masuda, S. Yasuda, K. Matsushima, and T. Ohshima at NEC Corp. for their dedicated work on the Hayabusa2 mission; K. Sato at NEC Corp. for ONC development; S. Kashima at NAOJ for optical calculations; and Y. Baba at UTOPS for illustrating Fig. 8. **Funding:** This study was supported by KAKENHI from the Japanese Society for Promotion of Science (JSPS) (grants JP25120006, 17H01175, JP17H06459, JP17K05639, JP16H04059, JP17KK0097, JP26287108, and JP16H04044) and the JSPS Core-to-Core program "International Network of Planetary Sciences." P.M. and M.A.B. acknowledge funding support from the French space agency CNES. P.S. acknowledges funding from the Complex Systems Academy of Excellence and the Space, Environment, Risk, and Resilience Academy of Excellence, part of the IDEX JEDI of the Université Côte d'Azur in connection with its Center for Planetary Origin. T.M. has received funding from the European Union's Horizon 2020 Research and Innovation Programme (Grant 687378). D.D.L., C.M.E., L.L.C., and M.K. acknowledge funding through the NASA Hayabusa2 Participating Scientist Program. **Author contributions:** S.Su. coordinated coauthor contributions; led the ONC data acquisition, analyses, and interpretations; and wrote the paper, with contributions from D.D., T.Ok., N.Na., T.Mo., and R.-L.B. ONC data acquisitions and reductions: R.Ho., T.Mo., Y.Ii., S.Ka. H.Sa., E.T., C.Ho., Y.Yo., M.Ya., T.K., N.Sa., K.Og., H.Su., K.Yoshio., M.Ha., Y.C., M.M., D.D., and H.K. Geomorphology analyses: H.M., T.Mo., E.T., C.Ho., T.Mi., Y.C., M.Hi., P.M., O.S.B., C.M.E., L.L.C., S.E.S., R.J., K.Ot., N.Sc., H.K., R.He., G.K., T.Mic., S.Sa., and P.A.A. Spectral analysis: E.T., D.D., R.Ho., Y.Yo., T.Mo., C.S., N.T., Y.Su., S.Ha., M.I., S.Tac., M.O., K.Na., M.E.Z., F.V., and M.A.B. TIR data acquisitions and analyses: T.Ok., T.F., S.Tan., M.T., T.A., H.Se., H.D., Y.Og., T.K., N.Sa., Y.Sh., T.Se., T.G.M., and A.Ha. LIDAR data acquisitions and analyses: N.Na, T.Miz., H.Se., H.N., K.M., N.H. (Kobe), R.Y., Y.Is., H.I., H.A., K.Ya., S.A., F.Y., A.Hi., S.Sa, S.O., S.Ts., K.A., S.Ta., M.S., H.M., H.D., J.K., T.Ot.; Shape modeling: N.H. (Kobe), N.H. (Aizu), R.N., E.P., R.G., O.S.B., C.M.E., and S.W. 3D numerical calculations: R.-L.B. Interpretation and writing contribution: T.Mo., E.T., D.D., R.Ho, T.Ok., N.Na., T.N., T.H., P.M., O.S.B., C.M.E., S.E.S., H.Yab., M.E.Z., S.W., and M.F. Science operations of spacecraft: S.Tan., M.Yo., T.I., M.A., M.Ha., T.Ok., R.N., Y.Sh., N.Sa., M.M., H.Yan., R.T., M.O., F.T., N.O., H.Sa., T.Y., S.Ki., Y.Ok., Y.Taka., H.T., G.O., Y.Mi., K.Yoshik., T.T., Y.Take., A.F., C.Hi., S.N., S.Ho., O.M., T.Sh., S.So., K.Ni., T.S., and Y.Ts. **Competing interests:** Y.Ya. is also affiliated with Tokyo Metropolitan University. **Data and materials availability:** All images, new software, and input data used in this study are available at the JAXA Data Archives and Transmission System (DARTS) at www.darts.isas.jaxa.jp/pub/hayabusa2/paper/Sugita_2019/. Additional data from the mission will be delivered to the DARTS archive at www.darts.isas.jaxa.jp/planet/project/hayabusa2/, and higher-level data products will be available in the Small Bodies Node of the NASA Planetary Data System (https://pds-smallbodies.astro.umd.edu/) 1 year after mission departure from the asteroid.

SUPPLEMENTARY MATERIALS

science.sciencemag.org/content/364/6437/eaaw0422/suppl/DC1
Materials and Methods
Figs. S1 to S15
Tables S1 to S3
References (*60–87*)

13 November 2018; accepted 12 March 2019
Published online 19 March 2019
10.1126/science.aaw0422

Science

The geomorphology, color, and thermal properties of Ryugu: Implications for parent-body processes

S. Sugita, R. Honda, T. Morota, S. Kameda, H. Sawada, E. Tatsumi, M. Yamada, C. Honda, Y. Yokota, T. Kouyama, N. Sakatani, K. Ogawa, H. Suzuki, T. Okada, N. Namiki, S. Tanaka, Y. Iijima, K. Yoshioka, M. Hayakawa, Y. Cho, M. Matsuoka, N. Hirata, N. Hirata, H. Miyamoto, D. Domingue, M. Hirabayashi, T. Nakamura, T. Hiroi, T. Michikami, P. Michel, R.-L. Ballouz, O. S. Barnouin, C. M. Ernst, S. E. Schröder, H. Kikuchi, R. Hemmi, G. Komatsu, T. Fukuhara, M. Taguchi, T. Arai, H. Senshu, H. Demura, Y. Ogawa, Y. Shimaki, T. Sekiguchi, T. G. Müller, A. Hagermann, T. Mizuno, H. Noda, K. Matsumoto, R. Yamada, Y. Ishihara, H. Ikeda, H. Araki, K. Yamamoto, S. Abe, F. Yoshida, A. Higuchi, S. Sasaki, S. Oshigami, S. Tsuruta, K. Asari, S. Tazawa, M. Shizugami, J. Kimura, T. Otsubo, H. Yabuta, S. Hasegawa, M. Ishiguro, S. Tachibana, E. Palmer, R. Gaskell, L. Le Corre, R. Jaumann, K. Otto, N. Schmitz, P. A. Abell, M. A. Barucci, M. E. Zolensky, F. Vilas, F. Thuillet, C. Sugimoto, N. Takaki, Y. Suzuki, H. Kamiyoshihara, M. Okada, K. Nagata, M. Fujimoto, M. Yoshikawa, Y. Yamamoto, K. Shirai, R. Noguchi, N. Ogawa, F. Terui, S. Kikuchi, T. Yamaguchi, Y. Oki, Y. Takao, H. Takeuchi, G. Ono, Y. Mimasu, K. Yoshikawa, T. Takahashi, Y. Takei, A. Fujii, C. Hirose, S. Nakazawa, S. Hosoda, O. Mori, T. Shimada, S. Soldini, T. Iwata, M. Abe, H. Yano, R. Tsukizaki, M. Ozaki, K. Nishiyama, T. Saiki, S. Watanabe and Y. Tsuda

Science **364** (6437), eaaw0422.
DOI: 10.1126/science.aaw0422originally published online March 19, 2019

Hayabusa2 at the asteroid Ryugu

Asteroids fall to Earth in the form of meteorites, but these provide little information about their origins. The Japanese mission Hayabusa2 is designed to collect samples directly from the surface of an asteroid and return them to Earth for laboratory analysis. Three papers in this issue describe the Hayabusa2 team's study of the near-Earth carbonaceous asteroid 162173 Ryugu, at which the spacecraft arrived in June 2018 (see the Perspective by Wurm). Watanabe *et al.* measured the asteroid's mass, shape, and density, showing that it is a ''rubble pile'' of loose rocks, formed into a spinning-top shape during a prior period of rapid spin. They also identified suitable landing sites for sample collection. Kitazato *et al.* used near-infrared spectroscopy to find ubiquitous hydrated minerals on the surface and compared Ryugu with known types of carbonaceous meteorite. Sugita *et al.* describe Ryugu's geological features and surface colors and combined results from all three papers to constrain the asteroid's formation process. Ryugu probably formed by reaccumulation of rubble ejected by impact from a larger asteroid. These results provide necessary context to understand the samples collected by Hayabusa2, which are expected to arrive on Earth in December 2020.

Science, this issue p. 268, p. 272, p. eaaw0422; see also p. 230

Science (print ISSN 0036-8075; online ISSN 1095-9203) is published by the American Association for the Advancement of Science, 1200 New York Avenue NW, Washington, DC 20005.

4 Hayabusa2 lander MASCOT

> *Hello there.*
>
> — **MASCOT to Ryugu**

Contents

In this chapter, I first present the lander MASCOT, part of the Hayabusa2 mission. Thanks to the numerical code `pkdgrav`, I modeled the landing of MASCOT on asteroid Ryugu, and I present the simulations I performed before Hayabusa2 reached Ryugu, and after arrival. I also present simulations aiming at the reconstruction of the actual landing, taking into account the observations and measurements from MASCOT and Hayabusa2. Finally are reproduced the first paper published in Astronomy & Astrophysics (Thuillet et al., 2018) and the second article accepted under minor revisions, in the same journal.

4.1 Description of MASCOT

4.1.1 The landing package

The JAXA mission Hayabusa2 carried several instruments in order to better understand the asteroid's properties and composition, and among them is the European lander MASCOT (Mobile Asteroid surface SCOuT) (Ho et al., 2017), shown in Fig. 4.1. MASCOT is a 10-kg landing package whose purpose was to study *in situ* the asteroid's surface properties thanks to its four onboard instruments: the camera MasCam (Jaumann et al., 2017), the hyperspectral microscopic imager MicrOmega (Bibring et al., 2017), the magnetometer MasMag (Herčík et al., 2017) and the radiometer MARA (Grott et al., 2017). The German Aerospace Agency DLR (*Deutsches Zentrum för Luft- und Raumfahrt*) was in charge of MASCOT's development and ground segment, as well as planning and conducting operations. The French Space Agency CNES (*Centre National d'Etudes Spatiales*) provided support to flight dynamics analysis, and was also involved in the lander as supplier of antennas, electrical power system, and part of the MicrOmega instrument.

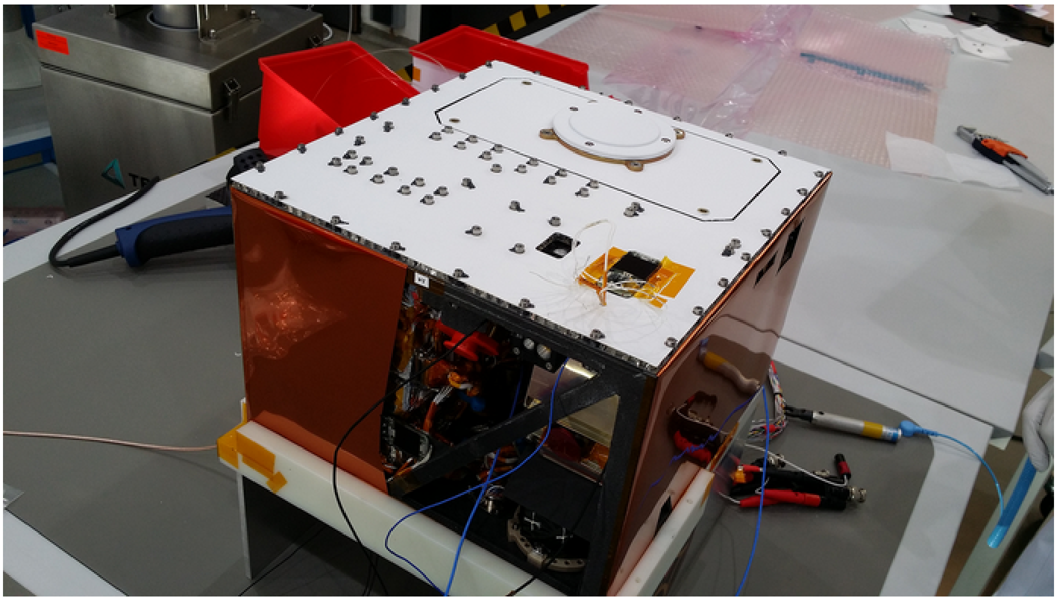

Fig. 4.1.: CNES-DLR lander MASCOT. Image credit: CNES

Hayabusa2 was supposed to release MASCOT in early October 2018. Since the spacecraft was always facing the Earth, only a limited range of latitudes were available for the deployment of the lander. Hayabusa2 would get closer to the asteroid until reaching an altitude lower than a 100 meters above Ryugu's surface. Then, the spacecraft would release MASCOT using a spring mechanism ejecting the lander at a speed of about 5 cm s^{-1} and let it fall toward the asteroid under the influence of Ryugu's weak gravity field. According to simulations done by Lorda et al. (2017), the fall would last around ten minutes, even if the duration clearly depends on the actual gravity field and therefore on the asteroid's mass, only roughly known at the time of these simulations. MASCOT would finally impact the surface at about 19 cm s^{-1}, and potentially bounce once or several times to another location.

Since MASCOT is relatively small compared to the resolution of Hayabusa2 Optical Navigation Camera, it could be detected only from lowest orbits. Once the spacecraft is back to its home position (20 km from the surface), MASCOT is no longer visible. Therefore, it had to be found fast enough, and this is why CNES performed simulations of bounces on Ryugu to find the probable final settling positions, estimate the time needed to settle and establish dispersion ellipses on Ryugu's surface around the first contact point. The requirement to find MASCOT quickly and to prevent that it bounces on a too long timescale is also due to the limited lifetime of its batteries (only about 16h).

There are several ways to model the impact of MASCOT on the asteroid's surface. The objective was to already have good sets of bouncing simulations until rest of MASCOT before the arrival of Hayabusa2 to Ryugu and before the deployment of MASCOT. A completely realistic modeling taking a lot of computation time, Lorda et al. (2017) decided to represent each contact point on Ryugu's surface by three parameters to quickly process each impact. These three parameters consisted of the coefficient of restitution C_R (outgoing-to-incoming normal speed ratio), the coefficient of friction C_F (outgoing-to-incoming tangential speed ratio) and the angle θ between the plane containing the incoming velocity $\mathbf{v}_{in}$ and the local normal, and the plane containing the outgoing velocity $\mathbf{v}_{out}$ and the local normal. These three parameters are enough to compute the evolution of MASCOT from the first impact to its final position at rest. However, the difficulty in this type of approach is to define reasonable values for the coefficients and angle. Since little data are available for the dynamics ruling a landing on small bodies, and none for Ryugu's surface, the coefficients are extremely hard to guess. The coefficients can be chosen from experiments made on Earth with well-known materials like drop-towers using glass beads or sand (Tardivel et al., 2014; Biele et al., 2017), but the gravity field, the actual surface properties, and the topology of Ryugu being poorly known, these parameters are hard to constrain, even more before arrival.

My approach was rather to model the lander and a granular surface only in the vicinity of MASCOT's impact point, using the numerical code `pkdgrav` (see Section 2). Since in this case, all interactions are explicitly computed, between the grains themselves as well as between the grains and the lander, simulations are very expensive computationally. Therefore, only the first impact and its outcome can be computed in a reasonable time. My analysis of the impact outcome focuses on results that can feed the approach of Lorda et al. (2017), i.e. the coefficients of restitution and friction as well as the velocity angle, as a function of the assumed surface (regolith) properties. The results of my simulations could therefore provide constraints to these three inputs; in other words, these parameters are taken from the results of my simulations and fed in the more global and parametrized simulations such those of Lorda et al. (2017).

4.1.2 Landing Site Selection

Various constraints had to be taken into account to choose a proper landing site for MASCOT. The first one was imposed by JAXA, since Hayabusa2 needs to also land two MINERVA-II mini-rovers before MASCOT landing and then make a first sampling after MASCOT landing. The three sites for these three operations needed to be chosen so that there is enough distance separating them. Several areas were chosen for Hayabusa2 touchdown, in mid- and low latitudes (see Section 5.1.2), and another set of areas was available for MASCOT's landing, distant enough from potential collection sites. The strategy was to avoid MASCOT's reflective surface to be considered by Hayabusa2 as a target marker for the touch-down operation.

The selected site also had to enable communication with Hayabusa2, to respect the various constraints imposed by the different instruments (i.e., temperature etc.) and to possibly prevent that MASCOT bounces for a too long time, considering the limited lifetime of the batteries.

A first selection of MASCOT's landing sites was done at CNES center in Toulouse (France) by the MASCOT French-German team on August 14th, 2018. Ryugu's surface and composition being roughly homogeneous, the choice of the landing site was more influenced by the availability of the different sites from celestial mechanics calculations and by the temperature on the surface (Ryugu's surface being very dark, the temperature can reach very high values during local daytime) than by the nature of the surfaces of the sites. Finally, one southern site was chosen, and is shown in Fig. 4.2.

As previously stated, CNES needed coefficients of restitution for MAS-COT/surface interactions. They considered two cases, bouncing on a regolith surface or on a boulder, and ran simulations with different percentages of these two types of surface. For each type of surface, depending on the impact angle, a value for the speed ratio was randomly drawn in the corresponding interval of possible values, which were chosen from my simulations for a

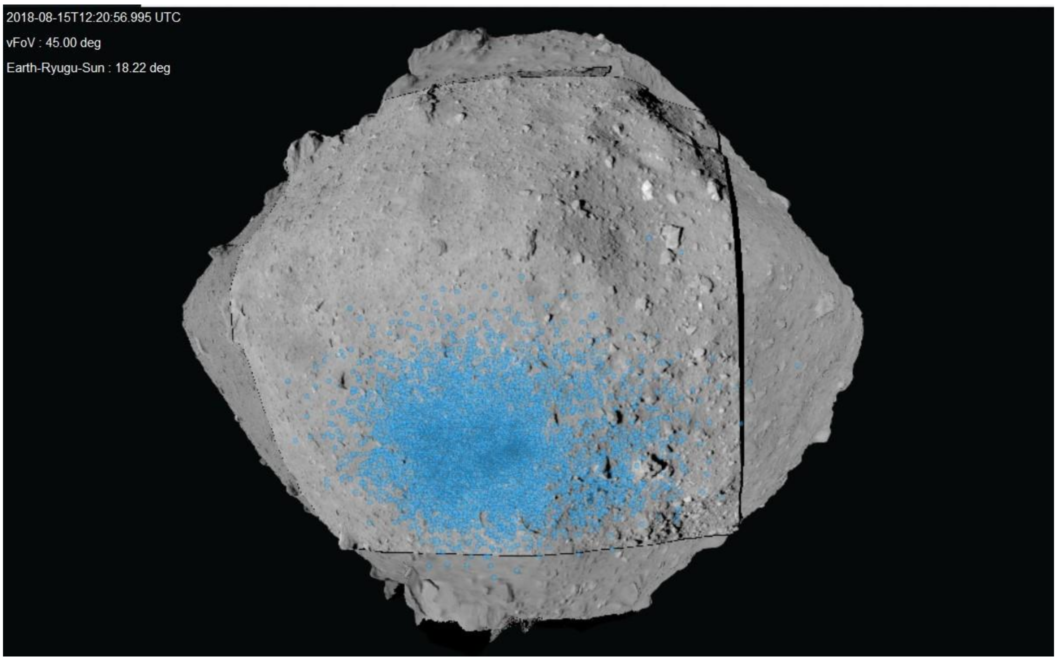

Fig. 4.2.: Selected site for MASCOT's landing, with blue dots corresponding to potential settlement locations resulting from CNES simulations. Image credit: JAXA, University of Tokyo, Kochi University, Rikkyo University, Nagoya University, Chiba Institute of Technology, Meiji University, University of Aizu, AIST, CNES, DLR.

regolith surface. Varying the percentages of surface types, MASCOT's direction resulting from impacts, and other uncertain parameters, results of simulations led to the blue dots in Fig. 4.2.

A second meeting took place in ISAS (Institute of Space and Astronautical Science), in Sagamihara, Japan, in August 17 2018. It was a joint meeting for the selection of Hayabusa2 first touchdown site, MASCOT's landing site, and MINERVA-II's landing site. The first choice in Toulouse was approved by JAXA, in charge of Hayabusa2 operations, and MASCOT's landing was confirmed for October 2-3 2018.

4.2 Pre-landing simulations

In this part, I describe the first simulations I conducted to establish general trends of MASCOT impact outcomes, using assumed surface properties. Before the arrival of Hayabusa2 at Ryugu, there was no knowledge on the surface properties of the asteroid, except the expectation that the surface would not be bare rock and rather covered with some sort of regolith. However, the MASCOT team needed to narrow down the possible range of distances that MASCOT could travel, and thus of the coefficients of restitution of MASCOT on the soil, i.e., the outgoing-to-incoming speed ratio of its impact. Moreover, studying the way granular matter reacts to a landing in a low-gravity environment is also interesting from a scientific point of view, even if the considered environment may be different from the one eventually discovered. This is useful for example for other space missions with segments landing on small bodies in low-gravity environments.

Given the great unknown about the surface properties of Ryugu, the advantage of numerical simulations is that they can cover a much wider parameter space than the one achievable with experiments, and therefore determine the influence of critical parameters and different possible behaviors of MASCOT at first impact.

As already stated in Chapter 1, only a few asteroids have been closely observed so far, and the only images of the surface we had from a C-class one was from (253) Mathilde, taken in 1997, for which the pixels were larger than 200 m. Therefore, we did not know what to exactly expect for the surface of Ryugu. The thermal inertia (Müller et al., 2011) was the only parameter that could give us some estimate of the typical size of grains forming the regolith, but the relation between thermal inertia and grain size is never guaranteed. I thus performed a large set of simulations, covering various possible scenarios, and because there is an observed level of stochasticity in the outcome, due to the sensitivity of the exact impact point and other effects, I looked for general trends that could be drawn from these simulations instead of giving too much attention to each result.

4.2.1 Generating the bed

Simulations of MASCOT impacting Ryugu's surface required the generation of regolith beds to be then used to simulate MASCOT's impact. These beds are contained in a cylinder and several methods exist to numerically fill the cylinders, some more efficient or more random than others. One of them is to directly compute the cylinder filling, letting one particle after another fall into the container. When the current particle encounters another one, it rolls around it until it finds a new particle or the cylinder wall, and it can roll again around this new particle. This can be repeated until it cannot move downward anymore, and the particle is settled at this final position. This method is called the dropping and rolling method, and an example of this kind of method is presented in Hitti et al. (2013).

Another method consists of using Voronoi tessellations to efficiently generate beds with different packing fractions and layouts. A Voronoi tessellation, or Voronoi diagram, is a partitioning of a plane or a volume into cells defined by the distance to specific points called nuclei. The cell $R_{\mathbf{P_i}}$, associated with the nucleus i-th $\mathbf{P_i}$, is defined by Equation 4.1, and an example of partitioning with Voronoi cells is shown in Fig. 4.3.

$$\{R_{\mathbf{P_i}}\} = \left\{\mathbf{x} \in \mathbb{R}^3 \,|\, \forall\, \mathbf{P_j} \neq \mathbf{P_i}, \|\mathbf{x} - \mathbf{P_j}\| \geqslant \|\mathbf{x} - \mathbf{P_i}\|\right\} \tag{4.1}$$

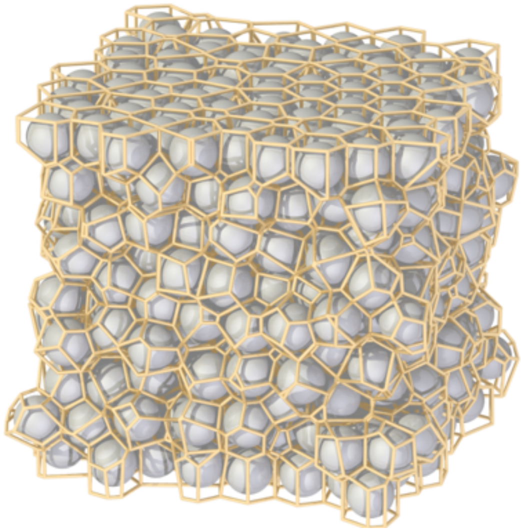

Fig. 4.3.: Region of particles partitioned using Voronoi cells. Image credit: Rycroft (2001)

The metric used in Eq. 4.1 can be any metric, leading to the existence of different methods of packing using Voronoi tessellation. For example, the "power-distance" leads to the Laguerre-Voronoi tessellation, used in many packing methods (Falco et al., 2017).

However, these methods are not implemented yet into `pkdgrav` and developing them would require some additional amount of work. I dedicated part of my time to the dropping and rolling method and worked with Marc Bernacki at the Ecole des Mines ParisTech who developed a container filling algorithm, but we did not manage to have interesting results within my thesis. One of the problems was the relaxing time after the filling, i.e., the required time for particles to be at rest in a nonzero-gravity environment. Indeed, these methods do not always consider an equilibrium with gravity, and turning it on may imply a long time for particles to find their final positions. Moreover, another issue is that these methods consider hard spheres, with no overlaps, and even with particles at equilibrium, uploading such settings into our soft-sphere simulations can break their former apparent equilibrium, increasing the relaxing time.

Finally, the solution I chose was to generate, thanks to a routine already implemented in `pkdgrav`, a certain number of particles in a cylindrical area. The algorithm is not as complex as the ones previously quoted, and leads to particles randomly distributed with a non-controlled porosity. However, by locating the cylinder of particles inside and above the wall cylinder (the particle cylinder being higher because of the higher than required number of particles and the low porosity), and by setting the gravity to 1 g (gravity on Earth, about 9.8 m s^{-2}), the wall cylinder can be quickly filled with randomly distributed particles, as shown in Fig. 4.4. Since the particles form a cone on the top of the surface, there needs to be enough particles to fill even the edge of the cylinder. Then, each particle with an altitude higher than the top of the cylinder is removed to create a flat surface. Finally, the bed has to relax by gradually decreasing the gravity down to the one on Ryugu. One of the advantages of this method, in addition to its versatility (any shape of container can be filled with this method) and its relative speed, is that different friction or cohesion values could lead to different packing ratios. For example, one can expect a lower packing ratio (i.e., a higher porosity) with higher friction and higher cohesion forces. In any case, this method ensures a certain randomness in the position of the grains in the cylinder, whereas other methods, run several times, would lead to same particle positions or at least similar patterns.

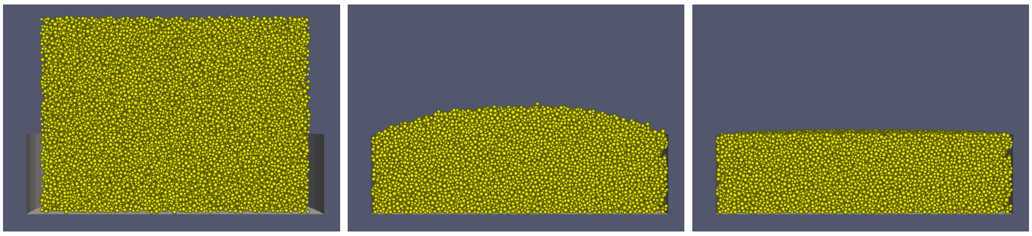

Fig. 4.4.: Snapshots of a filling simulation (showing half of the setup for clarity purposes) presenting three particular steps: random generation of particles in a taller cylinder, filled cylinder after fall of particles, and removal of particles higher than the top of the cylinder.

One drawback however is that the time spent to generate a packing with this method highly depends on the required timestep when particles freefall under 1 g. The more uniform the particle distribution, the lower the timestep. As it is explained in the first article in Section 4.4, I chose a Gaussian distribution to model the size distribution of particles forming the regolith bed because of the high computation time that a power-law size distribution would require. The Gaussian distribution has a mean radius of 1 cm, a standard deviation of 33%, and a cut-off at 1σ. At the beginning of simulations, the bed is considered at rest, since the (root-mean-square) average speed of all particles constituting the bed is always lower than $2 \cdot 10^{-3}$ cm s^{-1}, and the maximum speed is lower than $2.5 \cdot 10^{-1}$ cm s^{-1}.

4.2.2 Results of pre-landing simulations

The setup is described in more detail in the first article in Section 4.4, as well as the choice for the different parameters, which were mostly similar to the ones in Maurel et al. (2018). An example of simulation can be seen in Fig. 4.5. MASCOT impacts the regolith bed at 19 cm s^{-1}.

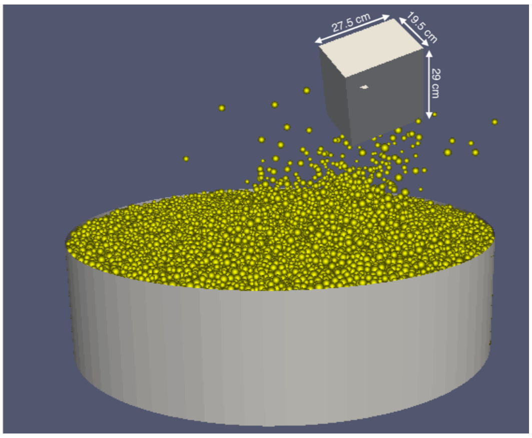

Fig. 4.5.: Example of simulation of MASCOT bouncing on a granular bed. MASCOT's dimensions are indicated in the figure, and the average grain radius is 1 cm.

The aim was to provide speed ratio coefficients to CNES to prepare MASCOT's landing, but also to learn more about low-speed collisions (19 cm s^{-1}) in granular media in a more general way. The particularity of MASCOT is its angular shape, which makes it react differently to a contact with a granular surface than for example a sphere would. Most studies concentrated on penetration of spherical objects (like experiments presented by Brisset et al. (2018)) and/or with much higher speeds (for example numerical simulations by Wada et al. (2006)). In this study, the influence of different impact characteristics and lander's and target's properties was studied regarding the traveled distance, the time of travel, the outgoing-to-incoming speed ratio, the maximum penetration, the spin, and other quantities.

Moreover, the traces left by the lander after the impact were studied as we found that different parameters or geometries led to different traces. As previously stated, finding MASCOT could be an issue. However, the location of MASCOT's first impact was supposed to be known with a relative accuracy, and therefore the traces left by MASCOT on the ground should be observable by Hayabusa2 Optical Navigation Camera on its way up after the release. My simulations showed that different traces could be linked to different materials or orientations of MASCOT at impacts, and therefore to different traveled distances. By imaging the first impact point, an area could be defined in which it would be probable to find the second impact (if MASCOT bounces), giving a useful hint to find MASCOT more quickly.

General results

General results can be found in the first article in Section 4.4. Here is a brief summary of the main results.

We found that the angular shape of MASCOT increases the stochasticity in the results (for reasons explained in the article), but that general trends could still be drawn for the different studied quantities. In most of the simulations, MASCOT bounces after its first impact. The cases when it does not bounce are usually for a vertical impact. The traveled distances and speed ratios increase with the angle from the vertical. More exhaustively, largest traveled distances are obtained for the shallowest regolith beds, the grains with the highest friction (here, gravel-like material), the most grazing impacts, and MASCOT landing on its back-corner first. From the derived impact angles and speed at second impact, we also predict that a second impact should be likely.

In order to be useful for CNES simulations, for each material and for each impact angle, I gathered the different values and computed average values, extrema, as well as standard deviations. Randomly generated speed ratio tables could then be built, taking into account the distribution obtained by my simulations. Values are summarized in Fig. 4.6.

Average speed ratios as functions of impact angles were approximated by third-order polynomials. They are described in Eq. 4.2 for gravel-like material and Eq. 4.3 for a moderate-friction regolith.

$$\left(\frac{V_{\text{out}}}{V_{\text{in}}}\right)_{\text{gravel}} = -5.98 \cdot 10^{-7}\theta^3 + 1.03 \cdot 10^{-4}\theta^2 + 1.26 \cdot 10^{-3}\theta + 1.11 \cdot 10^{-1}, \quad (4.2)$$

$$\left(\frac{V_{\text{out}}}{V_{\text{in}}}\right)_{\text{moderate}} = -8.14 \cdot 10^{-7}\theta^3 + 1.84 \cdot 10^{-4}\theta^2 - 2.54 \cdot 10^{-3}\theta + 1.27 \cdot 10^{-2}. \quad (4.3)$$

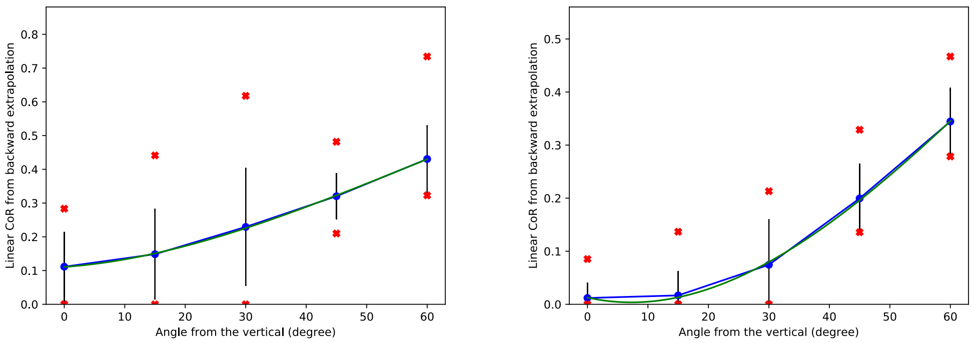

(a) Gravel-like material

(b) Moderate-friction material

Fig. 4.6.: Outgoing-to-incoming speed ratios as a function of the impact angle for two different materials. Extrema, standard deviation, and average values are shown, as well as a third-order polynomial interpolation for the average values.

with θ the impact angle from the vertical in degrees.

The mechanism at the origin of MASCOT bouncing is explained in the first article in Section 4.4, but can be summarized as follows. When a corner impacts the surface, it slightly penetrates but eventually the bottom face of MASCOT comes in contact with the surface too, and is more easily stopped by the grains (the effect is more or less pronounced depending on the material friction). Therefore, MASCOT pivots around the center of the bottom face, and opposite bottom corners penetrate inside the bed. They also are stopped, and from this stop, rotational energy is converted into translational energy, leading to MASCOT bouncing away from the surface.

Regarding the traces left after MASCOT's first bounce, we found that gravel-like and moderate-friction materials did not respond in the same way to the impact. For example, for a back-corner-first impact, gravel-like material is more likely to lead to a two-hole crater, whereas a moderate-friction material can be associated to a single-hole, deeper, crater, with much more ejecta. Since a higher friction usually leads to a larger traveled distance, observations of the crater can gives valuable clues for a possible search of MASCOT.

Finally, a study of the influence of coefficients of restitution (ε_n and ε_t), both of MASCOT and grains, was done. A rather non-intuitive observation was that smaller coefficients of restitution of grains lead to higher speed ratios, because small values decrease the energy transferred from surface particles to the others, and thus their mobility, rigidifying the bed.

In the second article (presented in Section 4.5), we looked at the influence of a slope, and of a slight change in the gravitational acceleration. We find that, certainly because of the already very weak gravity, a change in the slope or in the norm of the gravitational acceleration has no influence, or at least too weak to be detected in our simulations. We also looked at different impact speeds, mostly from 2.5 to 20 cm s^{-1}, and found that if the friction is low enough, the speed ratio does not seem to depend on the impact speed. For higher-friction material, the trend is more difficult to establish, because either there is no similar trend or that the stochasticity is too high.

I also briefly investigated the influence of cohesion on my results, and these results are not in the articles as they are still preliminary. In Chapter 3, I wrote that first observations seem to indicate a weak cohesion. However, we can look at the theoretical cohesive Bond number B_c in our simulations, i.e., the ratio between the cohesive force and the weight of a particle. By using the values used in my simulations and thanks to Eq. 1.7 in Section 1.3.4, I find $B_c = 165\,S^2$, where S is the cleanliness ratio, meaning that the cohesion, for 1 cm particles, may not be negligible.

In `pkdgrav`, the current cohesion model has been implemented by Zhang et al. (2018), and is based on a combination of the cohesion model of Sánchez et al. (2014) and Sánchez et al. (2016) with granular bridges, and the contact model of Jiang et al. (2013) and Jiang et al. (2015a). The magnitude of the normal force can be written as $F_c = cA_{\text{eff}}$, where c is the interparticle cohesive coefficient, $A_{\text{eff}} = 4(\beta R)^2$ the effective contact area, β the shape parameter presented in Section 2.1, and R the effective radius. This attracting force has to be added to the other existing forces.

I performed a few MASCOT landing simulations with different values of the cohesion to check its influence on the trends observed before. Seeing no significant influence of the cohesive coefficient for values smaller than 100 Pa, I increased it up to 300 Pa, where the influence of cohesion is clearly visible on the speed ratio and the time between impacts, and shown in Fig. 4.7. With a 300 Pa cohesion, the penetration depth is smaller as expected, and the post-impact velocities are more vertical. The more vertical post-impact velocities and the higher speeds after impact both lead to much higher times between impacts for the 300 Pa coefficient than for smaller coefficients, whereas this difference is less visible in the distance between impacts. This trend seems to be also true for 100 Pa. However, for coefficients lower than 100 Pa, the influence of cohesion on the outputs is unclear and would require a larger number of simulations.

In our case, the cohesive Bond number can be written as a function of the cohesive coefficient c: $B_c = 331c$. This means that in our simulations, the Bond number has to be very high to see a noticeable difference in the outcomes.

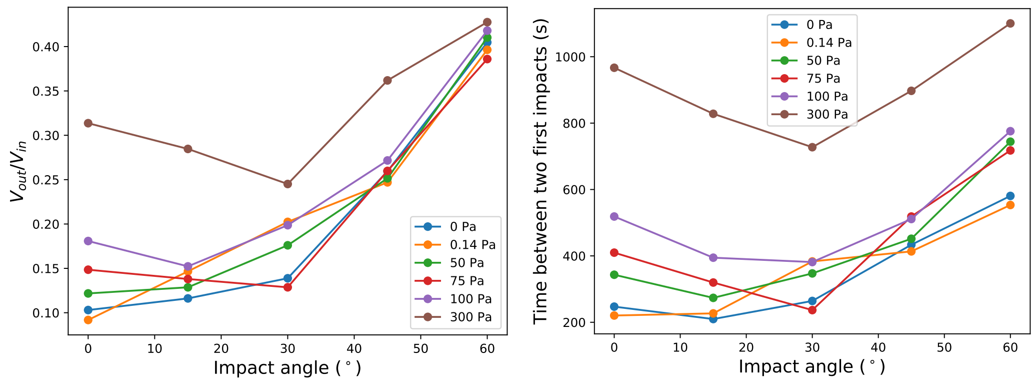

(a) Speed ratio **(b)** Time between impacts

Fig. 4.7.: Outgoing-to-incoming speed ratio and time between impacts for a gravel-like material, a flat impact, and different impact angles and cohesive coefficients.

Presence of a boulder

The closest images of Ryugu's surface MASCOT teams had access to before the release were taken from an altitude of about 1 km, during a maneuver intended to determine Ryugu's gravity, and from MINERVA-II landers on the surface.

The gravity measurement maneuver was done on August, 6 and 7 2018 and proceeded in this way: after having descended to an altitude of 6 km, Hayabusa2 began its free fall until it reached its lowest altitude of 851 m, taking advantage of the unprecedented proximity to the surface to take a series of pictures such as the ones shown in Fig 4.8; then, the thrusters were ignited again without any orbit or attitude control until the altitude of 5 km. Finally, the spacecraft went back to its parking position at about 20 km from the asteroid. Thanks to the free fall, the gravity was precisely measured, to eventually confirm the value estimated from the home position.

From these images, one can see a lot of boulders on the surface, and what seems to be finer grains of regolith between. In our simulations, it became

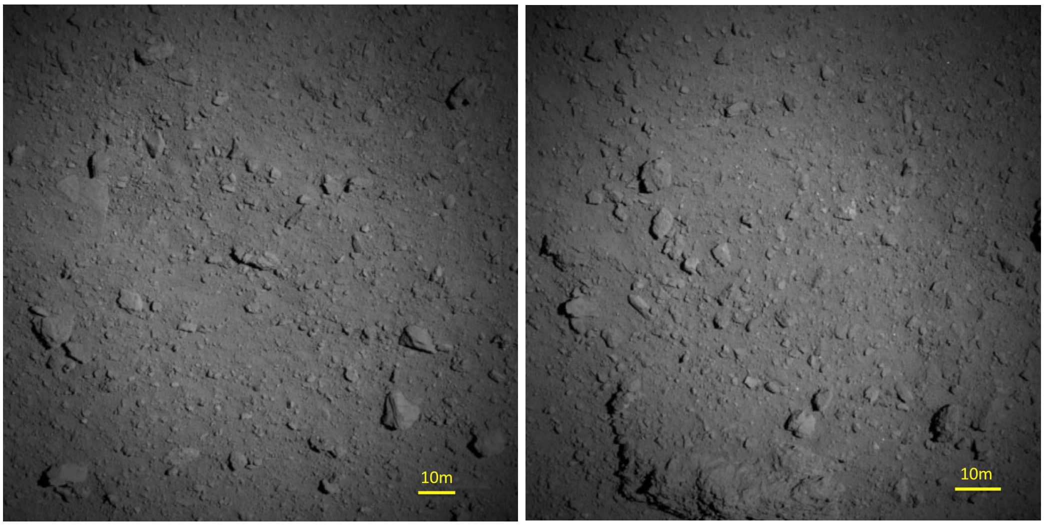

(a) Surface from an altitude of 1.25 km (b) Surface from an altitude of 1 km

Fig. 4.8.: Images of different regions of Ryugu's surface taken with the Optical Navigation Camera - Telescopic (ONC-T), respectively from 1.25 km and 1 km to the surface. Image credit: JAXA, University of Aizu & collaborators (JAXA et al., 2019)

therefore obvious that regolithic surfaces but also boulders, whether buried or on the surface, needed to be considered in the simulations. Indeed, MASCOT had significant chances to land on or at close proximity of one of them. It is impossible however from these images to know the size of the smallest particles existing on Ryugu's surface.

Images from MINERVA-II rovers showed a surface with no fine regolith and numerous boulders, which confirmed the necessity to consider the presence of boulders in the simulations.

New simulations were conducted with the presence of a boulder in the bed, and these simulations are presented in the second article in Section 4.5. We considered ellipsoidal boulders with aspect ratios $\frac{a}{a} : \frac{b}{a} : \frac{c}{a}$ of $1 : 0.74 : 0.43$ similar to what was observed for boulders observed on Itokawa by Hayabusa (Michikami et al., 2016) and particles collected by Hayabusa (Tsuchiyama et al., 2014; Michikami et al., 2018), and with a semi-major axis of 30 cm, comparable to MASCOT's size but not detectable from Hayabusa2. Our boulders are made of aggregates of regular grains that are stuck together.

It was generally found that the presence of a boulder close enough to the impact point increases the stochasticity of the impact. Depending on how MASCOT lands on it, the outcomes can be very diverse. Nonetheless, general trends can be derived from these simulations. First of all, previous trends seem to still be effective, such as larger impact angles from the vertical lead to higher speed ratios. Moreover, it is noticeable that the higher the boulder in the bed, the larger the speed ratio, and the larger the range of possible values for the speed ratio and the spin. If the boulder is under 15 cm of regolith, it has no influence on the outcomes.

We found that, even with a rigid boulder such as our aggregates, the speed ratio could be very low, meaning that a low outgoing speed does not necessary mean a soft medium but could also be the result of the impact geometry, and that therefore direct estimates of surface properties from speed ratio measurements should be considered with caution, in the case of an impactor as angular as MASCOT.

4.3 Landing and post-landing simulations

4.3.1 Landing

MASCOT was safely released during the night of October 2-3 2018 (ECT), and began its descent towards Ryugu. Hayabusa2 Optical Navigation Camera was able to take a photograph of MASCOT shortly after the release, which visually confirmed the deployment.

During MASCOT's downward trajectory, Hayabusa2 Optical Navigation Camera was able to image the lander at different locations on its trajectory. From these images, a first reconstruction of MASCOT's trajectory could be done, and is presented in Fig. 4.9.

The first impact shows a significant change in the orientation of MASCOT, and both images taken just before and after the contact have MASCOT very close to a large rock, located on MASCOT's initial path. Therefore, we can consider as a very probable possibility that MASCOT impacted the large rock. In other pictures, this rock appears much less flat and more steep, and MASCOT seems to have impacted the side of the rock (or cliff).

From the timestep between each image, the position of Hayabusa2 as it took the images, and MASCOT's shadow, visible in most of the images, it seems that the speed ratio of the collision is about 0.3. Moreover, measurements from MASCOT's onboard instruments such as the magnetometer MAG indicate the first contact was a "hard" one.

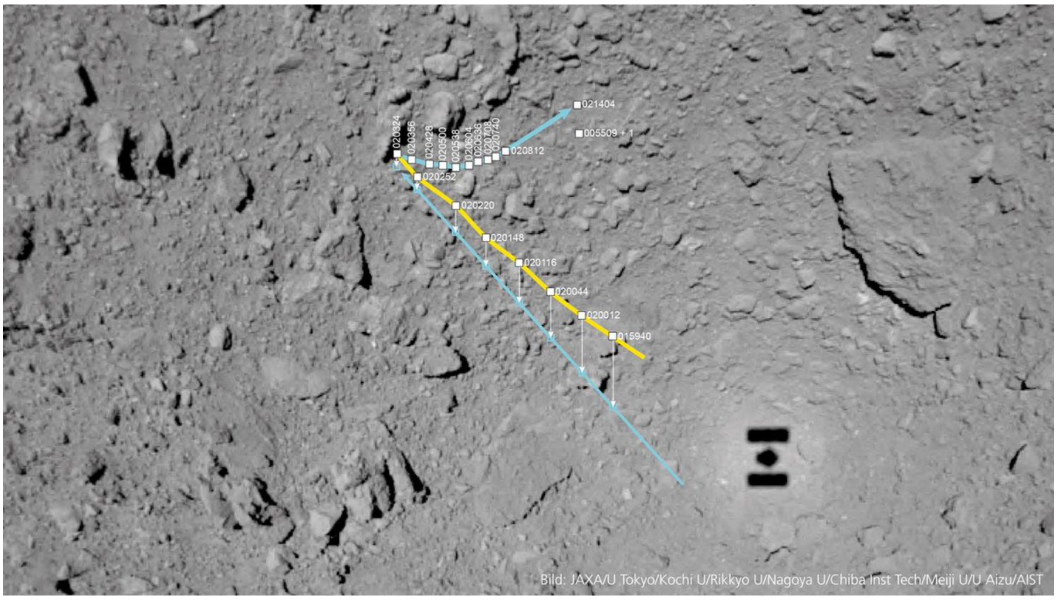

Fig. 4.9.: Locations of MASCOT in the different pictures taken by Hayabusa2 Optical Navigation Camera, and first reconstruction of its trajectory. Image credit: JAXA, University of Tokyo, Kochi University, Rikkyo University, Nagoya University, Chiba Institute of Technology, Meiji University, University of Aizu, AIST, CNES, DLR.

In the second article on MASCOT simulations (see Section 4.5), we show that a speed ratio as low as 0.3 could be obtained even if MASCOT bounces on a rigid boulder. This is due to the presence of "micro-bounces"; the contact between MASCOT and the boulder can be decomposed in a sequence of short contacts, each of them participating in the energy dissipation. By interpreting all of these contacts as a single global one, this can lead to low outgoing-to-incoming speed ratios.

Since from the images no large modification of the rock before and after the contact with the lander can be discerned, an assumption could be that the rock was structurally strong enough to withstand the encounter without crumbling into pieces or even move at all.

Moreover, from the images following the impacts can be observed that MASCOT had an almost horizontal velocity, which encourages us to argue that it first impacted the ground at the bottom of the vertical rock and then the face of the rock. In order to study this possible scenario, we ran simulations of MASCOT bouncing on the regolith bed as previously done in Thuillet et al. (2018) and then impacting the rock, modeled as a unmovable wall with particles stuck on it. Indeed, in `pkdgrav`, walls cannot interact with other walls, and therefore stuck particles on a vertical wall enable an interaction with the walls composing MASCOT. Particles were stuck to the wall by creating a small overlap between particles and wall and setting the normal coefficient of the wall to 0. An example of simulation of MASCOT bouncing on the regolith bed and then on the particle-covered wall is shown on Fig. 4.10.

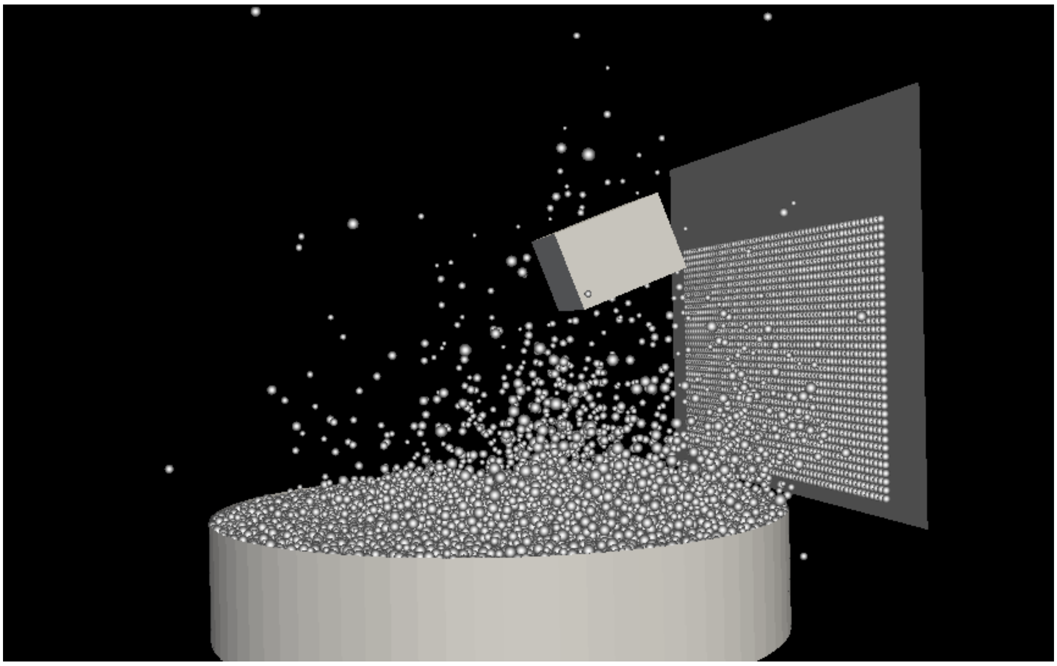

Fig. 4.10.: Snapshot of a simulation of MASCOT impacting the regolith bed and then a particle-covered wall.

We ran simulations with different angles, from $15°$ to $45°$ from the vertical, and with a gravel-like friction. In our simulations, MASCOT can partially penetrate the wall, meaning that our model of a wall is not totally rigid. However, these penetrations are very small. If they become too large, MASCOT goes completely through the wall and we do not consider these cases. In the considered cases, the penetration is very small and does not exceed 0.1% of MASCOT's volume.

Tab. 4.1.: Minimum and maximum values for speed ratios, rotation speed, and energy ratios for MASCOT. The 0 index corresponds to MASCOT before the impact, 1 after the contact with the regolith bed, and 2 after the contact with the wall.

	$\frac{V_1}{V_0}$	$\frac{V_2}{V_1}$	$\frac{V_2}{V_0}$	ω_2 (rad s^{-1})	$\frac{E_1}{E_0}$	$\frac{E_2}{E_1}$	$\frac{E_2}{E_0}$
Minimum value	0.125	0.73	0.09	0.09	0.02	0.6	0.013
Maximum value	0.32	1.11	0.33	0.77	0.15	1.78	0.26

The minimum and maximum values in our simulations for the outgoing-to-incoming speed ratios, rotation speeds, and energy ratios are shown in Table 4.1. The indexes correspond to the considered instant: 0 corresponds to MASCOT prior to the impact, 1 to MASCOT just after the impact on the regolith bed, and 2 to MASCOT after the impact on the wall. If we look specifically at the contact with the wall, we see that the speed ratio can be higher than 1. This is due to MASCOT not being a point or even a sphere, and therefore impacting the wall with a corner increases the rotational energy, which can be transformed, through a second impact, into translational energy. The contact with the wall is not one bounce, but a series of "microbounces", and these microbounces on a wall can lead to high energy ratios.

The total speed ratio can be as high as 0.33 (for the angles considered), which means that speed ratios of about 0.3 can be obtained either when bouncing on the top of a boulder, or on a regolith bed and then hitting a wall.

However, we see simulations for which the bouncing on the wall sometimes result in energy ratios higher than 1. This means that there is certainly an issue in our solution to model the wall with particles stuck on it. The excess of energy could come from the fact that particles interacting with MASCOT cannot move but still exert a force on it. We are currently working on a solution, and these results have to be considered with caution.

Reconstruction of the trajectory is still ongoing, and the grain size distribution assumed for our simulations could be wrong; yet, our simulations provide an important message which is that the derivation of surface properties done from speed ratio measurements should be considered with caution. For example, combining the two articles, it is found that a speed ratio of 0.3 can be obtained for all of these configurations (non-exhaustive list): $30°$ back-corner-first landing in a gravel-like material, $60°$ flat landing in a moderate-friction material, vertical back-corner-first landing in a gravel-like material with a boulder buried under 10 cm of regolith, $15°$ back-corner-first landing in a gravel-like material on a half-buried boulder, and $45°$ flat landing in a moderate-friction material also on a half-buried boulder.

4.4 Article MASCOT I

Numerical modeling of lander interaction with a low-gravity asteroid regolith surface

Application to MASCOT on board Hayabusa2

by

Florian Thuillet, Patrick Michel, Clara Maurel, Ronald-Louis Ballouz, Yun Zhang, Derek C. Richardson, Jens Biele, Eri Tatsumi, and Seiji Sugita

2018, *A&A*, **615**, A41

Abstract

Landing on the surface of small bodies is particularly challenging, as the physical properties of the surface material are not well known and the mechanical response of this material in a low-gravity environment is not well understood. In order to improve our understanding of low-speed impact processes on granular media and their outcome in low-gravity environments, we consider the landing of the package MASCOT, to be released by the JAXA asteroid sample return mission Hayabusa2 on (162173) Ryugu in October 2018. Beyond addressing the theoretical aspects of the mechanical response of granular media in low gravity, this study also supports both engineering and scientific teams of Hayabusa2 in the search for the lander and in the determination of Ryugu's surface properties. A campaign of hundreds of numerical simulations using the soft-sphere discrete element method implemented in the *N*-body code `pkdgrav` were performed to study the interaction between the lander and the low-gravity surface of the asteroid made of a granular medium representing the regolith. Assuming a broad range of regolith properties, and the lander's trajectory and motion, we analyzed the outcomes of the landing (distance traveled by the lander, penetration depth, and shape of the traces left in the regolith surface) to determine the influence of the many parameters defining the properties of MASCOT and of the grains, and the ingoing motion of the lander. We identify well-marked trends for the fate of the lander and the traces left in the granular material. Distances traveled by the lander are greater and penetrations are shallower for gravel-like media than for less frictional material. A similar trend is found

for grazing impacts as opposed to vertical ones. Different regolith properties also generate different traces on the ground after the impact.

A&A 615, A41 (2018)
https://doi.org/10.1051/0004-6361/201832779

Astronomy & Astrophysics

Numerical modeling of lander interaction with a low-gravity asteroid regolith surface

Application to MASCOT on board Hayabusa2

Florian Thuillet[1], Patrick Michel[1], Clara Maurel[2], Ronald-Louis Ballouz[3,4], Yun Zhang[3,5], Derek C. Richardson[3], Jens Biele[6], Eri Tatsumi[7], and Seiji Sugita[7,8]

[1] Lagrange Laboratory, Université Côte d'Azur, Observatoire de la Côte d'Azur, CNRS, CS 34229, 06304 Nice Cedex 4, France
e-mail: fthuille@oca.eu
[2] Department of Earth and Planetary Sciences, Massachusetts Institute of Technology, 77 Massachusetts Avenue, Cambridge, MA 02139, USA
[3] Department of Astronomy, University of Maryland, College Park, MD 20742, USA
[4] Institute for Space and Astronautical Studies, Japanese Aerospace eXploration Agency, Sagamihara, Kanagawa Prefecture 252-5210, Japan
[5] School of Aerospace Engineering, Tsinghua University, Beijing 100084, PR China
[6] DLR German Aerospace Center, Micro-Gravity User Support Center, 51147 Cologne, Germany
[7] Department of Earth and Planetary Science, University of Tokyo, 7-3-1 Hongo, Bunkyo-ku, Tokyo 113-0033, Japan
[8] Research Center for the Early Universe, University of Tokyo, 7-3-1 Hongo, Bunkyo-ku, Tokyo 113-0033, Japan

Received 6 February 2018 / Accepted 6 April 2018

ABSTRACT

Context. Landing on the surface of small bodies is particularly challenging, as the physical properties of the surface material are not well known and the mechanical response of this material in a low-gravity environment is not well understood.

Aims. In order to improve our understanding of low-speed impact processes on granular media and their outcome in low-gravity environments, we consider the landing of the package MASCOT, to be released by the JAXA asteroid sample return mission Hayabusa2 on (162173) Ryugu in October 2018. Beyond addressing the theoretical aspects of the mechanical response of granular media in low gravity, this study also supports both engineering and scientific teams of Hayabusa2 in the search for the lander and in the determination of Ryugu's surface properties.

Methods. A campaign of hundreds of numerical simulations using the soft-sphere discrete element method implemented in the N-body code `pkdgrav` were performed to study the interaction between the lander and the low-gravity surface of the asteroid made of a granular medium representing the regolith. Assuming a broad range of regolith properties, and the lander's trajectory and motion, we analyzed the outcomes of the landing (distance traveled by the lander, penetration depth, and shape of the traces left in the regolith surface) to determine the influence of the many parameters defining the properties of MASCOT and of the grains, and the ingoing motion of the lander.

Results. We identify well-marked trends for the fate of the lander and the traces left in the granular material. Distances traveled by the lander are greater and penetrations are shallower for gravel-like media than for less frictional material. A similar trend is found for grazing impacts as opposed to vertical ones. Different regolith properties also generate different traces on the ground after the impact.

Key words. minor planets, asteroids: individual: (162173) Ryugu – methods: numerical

1. Introduction

The dynamics of granular material, and the material's response to external actions, is an active domain of research with various industrial and scientific applications. Its study in the low-gravity environment of asteroids is very recent and motivated by the realization that asteroids are covered with regolith. Furthermore, asteroids considered as aggregates can be treated entirely as a granular medium. This domain of research is also motivated by the development of asteroid space missions, such as Hayabusa2 (Watanabe et al. 2017) and OSIRIS-REx (Lauretta et al. 2017), which need simulations of the hardware that will interact with the surface, either to collect samples or to perform in situ measurements. In this regard, the aim of this paper is to contribute to the general understanding of the behavior of granular materials in the low-gravity environment of an asteroid's surface when experiencing an external action, in our case the low-speed interaction of the lander MASCOT on board Hayabusa2.

The JAXA asteroid-sample-return mission Hayabusa2 was launched on December 3, 2014, toward the carbonaceous near-Earth asteroid (162173) Ryugu (Binzel et al. 2001). After arriving at the asteroid in June 2018, the spacecraft intends to carry out a two-month characterization of this asteroid followed by several close approaches to collect some samples and return them to Earth in 2020. Before collecting the desired samples, the main spacecraft will release the European (DLR/CNES) lander MASCOT (Mobile Asteroid Surface Scout) that will perform in situ measurements (Ho et al. 2017) with four instruments including an IR imaging spectrometer (MicrOmega), a camera (MASCAM), a radiometer (MARA), and a magnetometer (MASMAG).

The asteroid Ryugu is 870 m in diameter and although its bulk density is not precisely known yet, its surface gravity is expected to be very low (about 2.5×10^{-4} m s^{-2}, Maurel et al. 2017), with an escape speed estimated at about 37 cm s^{-1} (Ho et al. 2017). Such extreme conditions challenge our ability to successfully land a package on the asteroid. The example of Philae, on board the ESA spacecraft Rosetta (Boehnhardt et al. 2017), demonstrated that landing on a low-gravity surface for which we have essentially no a priori information is a great challenge. However, Philae relied on a damping mechanism (which worked) and anchoring (which did not), while MASCOT is designed specifically to bounce. This feature implies that MASCOT's final resting place can be far from the first touchdown point, but operational constraints require keeping that distance small and predicting the area where MASCOT is likely to settle. It is thus important to quantify the outcome of the first impact of the lander as a function of the many parameters of the impact and the environment. Moreover, the traces left by the lander at the impact point can inform us on the surface properties and may also be used to estimate the position and characteristics of the following impact.

This paper addresses these issues with numerical simulations of the interaction between a granular medium (representing the surface of the asteroid) and the lander under expected gravity conditions. The surface of Ryugu is assumed to be covered with a layer of granular material, called regolith, that has been observed on all asteroids for which we have images, and seems to be present on all those that have a thermal inertia estimate (e.g., Delbo et al. 2015). Even if regolith has been observed on asteroids, its actual mechanical properties are poorly known, and we cannot rely on the observations of other asteroids to determine the properties of the Ryugu regolith. For example, even two bodies of the same spectral type, such as the two S-types 433 Eros and 25143 Itokawa, can have very different regolith properties, at least partly due to their very different sizes and therefore gravitational environments. The situation is even worse for C-type asteroids such as Ryugu as to date we have no detailed image of the surface of an asteroid of this type. The only information we have regarding surface properties is an estimate of Ryugu's thermal inertia. According to Müller et al. (2011), the most likely thermal inertia ranges between 200 and 600 J m^{-2} K^{-1} s$^{-\frac{1}{2}}$, about a factor of 2 lower than the value measured for Itokawa. Within this range, the surface state is expected to go from a thick-dust regolith to a boulder/cm-sized, gravel-dominated surface similar to that of 25143 Itokawa. In the absence of the critical parameters necessary to anticipate Ryugu's surface, numerical simulations become a precious resource. Simulations can provide an estimated behavior of the lander for multiple configurations covering a parameter space too large to be experimentally explored in order to be best prepared for the landing phase of the mission.

This study builds on a previous work by Maurel et al. (2017) who performed simulations of MASCOT's landing. Here, we extend the parameter space of those simulations and perform additional data analysis that can help in the interpretation of MASCOT's interaction with the surface and in the search of the lander on the surface if it bounces. Our results could also help the mission's team to infer non-resolved regolith properties from observed ones. The actual landing is scheduled for early October 2018, and this study aims to provide some useful information at the time of landing (on the probable position of MASCOT and on the regolith properties) and also to provide a numerical tool that is already tested and ready to be efficiently used once we are at the asteroid. Moreover, once there, if the actual data on the regolith is out of the range of our present assumptions, new simulations can be run to determine how MASCOT will react on the actual surface.

In Sect. 2, we present the method used to perform the numerical simulations and the considered parameter space for the regolith properties and the impact conditions of the lander. Section 3 presents the results. Conclusions and perspectives are given in Sect. 4.

2. Methodology

2.1. Numerical code: `pkdgrav`

The interaction between MASCOT and a granular medium (representing the asteroid's regolith) was simulated with the parallel *N*-body gravity tree code `pkdgrav` (Richardson et al. 2000, 2009, 2011; Stadel 2001). To capture the dynamics and contacts between grains of a granular material, the soft-sphere discrete element method (SSDEM) was implemented in the code by Schwartz et al. (2012). We also used the implementation of a new rotational resistance model for the grains (Zhang et al. 2017), which considers twisting and rolling spring-dashpot-slider models.

The `pkdgrav` code also computes, under any gravitational environment, the interactions between spherical grains and "walls", whose geometry and physical properties (like the distribution of mass within the walls, i.e., the inertia tensor) can be defined. Walls can be assigned as "reactive", meaning they react to forces from the particles (otherwise they are treated as having infinite mass), and can form an "assembly" of multiple walls to represent a sampling device or a lander.

Various experiments have already been used to validate the SSDEM implementation into `pkdgrav`. For instance, simulation results have been compared with experiments with hopper discharges by Schwartz et al. (2012), low-speed impacts and projectile penetration depths by Schwartz et al. (2014) and Ballouz (2017), and avalanches and angles of repose by Yu et al. (2014) and Maurel et al. (2017). Some preliminary comparisons have also been performed with drop-tower experiments of lander impacts on a regolith bed in low gravity, and show good agreement.

2.2. Setup of the simulation

We considered the landing of MASCOT on a regolith bed with an impact speed of 19 cm s^{-1} (upper limit of what is expected for the impact, Biele et al. 2017). The setup of the regolith bed in our simulations is similar to that used by Maurel et al. (2017): a cylindrical non-reactive wall with its top face open, filled with Gaussian size-distributed, spherical soft particles representing the regolith. The gravity considered in our simulations is the same as that assumed for Ryugu, i.e., 2.5×10^{-4} m s^{-2} (Maurel et al. 2017). It is based on the reasonably well-known effective diameter (Müller et al. 2011, 2017) and inputs from JAXA concerning shape, rotation rate, and an estimate of the uncertainty of the center of gravity, and is computed considering simple rotating sphere approximation.

The granular beds are created by letting the particles free-fall into the cylinder, letting them relax under the desired level of gravity, and removing any that end up higher than the top of the cylinder. This method ensures a randomness in the position of the grains in the cylinder at the expense of large CPU

Table 1. Characteristics and properties of the two material types considered in our simulations.

Material type	Angle of repose (°)	ε_n	ε_t	μ_s	μ_r	μ_t	β
Gravel-like friction	38.5	0.5	0.5	1.0	1.05	1.3	1.0
Moderate friction	28	0.5	0.5	1.0	1.05	1.3	0.2

times. Since we do not know in advance the regolith properties, two different types of regolith grains were considered, one with a gravel-like friction and one with a moderate friction. These two frictions differ in their equivalent angle of repose (Table 1), corresponding in the simulations to two different shape factors β (Zhang et al. 2017). The shape factor β is directly linked to the angle of repose because it represents the angularity of the particles: the higher it is, the more angular the particles are, and therefore particles will slide less effectively on each other, resulting in a steeper angle of repose. The interaction between particles in contact in `pkdgrav` is mainly controlled by six parameters: the normal and tangential coefficients of restitution ε_n and ε_t; the interparticle friction coefficients for sliding, rolling, and twisting, respectively μ_s, μ_r, and μ_t; and the shape factor β. Here ε_n and ε_t dominate the energy dissipation, and the other four parameters describe the frictional strength (see Sect. 2 in Zhang et al. 2017 for details). In Sects. 3.6 and 3.7 we analyze the influence of the coefficients of restitution of MASCOT and the grains, respectively.

Regarding the depth of the regolith (the depth of the cylinder), we consider 15, 30, and 40 cm (Table 2). The depth controls possible boundary effects. If it is shallow enough, the wave produced by MASCOT's impact will reflect at the bottom, representing a situation where a hard surface is covered by a thin layer of regolith. The deeper case (40 cm) represents a surface with a layer of regolith that is thick enough that the wave produced by the impact almost never sees a hard bottom, and when it does, by the time it comes back to the surface, the lander has already bounced away. This has been confirmed by changing the properties of the bottom wall for the different depths considered. For further information about the influence of the bed depth, see Sect. 3.3. The diameter of the cylinder is 150 cm, corresponding to a little more than five times the largest dimension of MASCOT (i.e., 29 cm). When the diameter of the container is less than five times the diameter of the projectile, according to Seguin et al. (2008), some boundary effects may play a role. However, according to Goldman & Umbanhowar (2008), for impact speeds low enough (less than 2 m s^{-1}), the diameter of the cylinder should not have a significant effect on the results. Nonetheless, we used to methods to check that the outermost particles do not feel the impact, or at least do not influence the fate of the lander or the crater attributes. First, throughout the simulations we checked the maximum and root mean square (RMS) speeds of particles contained in the outermost rectangular cross section torus whose width is 5 cm and height is that of the cylinder. The RMS speed never goes higher than 0.06 cm s^{-1}, which is too low to influence the lander's behavior. A lone particle can have a speed of up to 2.5 cm s^{-1}, but does not create feedback on the lander or the crater after the wave bounces on the cylindrical wall. Second, we modified the coefficients of restitution of the cylindrical wall and did not observe any meaningful variations in the results.

In terms of size distribution of the grains, since there are no well-known constraints, we used a Gaussian distribution of particle radii with mean radius of 1 cm, a standard deviation (sigma) of 33%, and a cut-off after 1σ. This assumption represents one of the possible cases derived from the range of thermal inertia estimated for the asteroid (Gundlach & Blum 2013), although we recognize that it is idealized compared with a more realistic power-law size distribution. The influence of a power-law size distribution was succinctly treated by Maurel et al. (2017), who found that it mostly enhances the stochastic aspect of the simulations. However, we did not consider it here because it would significantly increase the computation time of every simulation.

Table 2. Different depths considered in our simulations with the corresponding numbers of particles for the two different material types.

Depth	Gravel-like friction	Moderate friction
15 cm	28 375 particles	31 082 particles
30 cm	58 454 particles	62 551 particles
40 cm	78 176 particles	83 097 particles

The numerical model of MASCOT is described in Maurel et al. (2017). It consists of a 19.5 cm × 27.5 cm × 29 cm cuboid, with a small prominence representing the sensor of the hyperspectral microscopic imager (MicrOmega). MASCOT and MicrOmega form what we called earlier an assembly of reactive walls, and is initially placed about 40 cm above the top of the regolith bed.

The initial (slow) rotation of MASCOT after ejection from the Hayabusa2 spacecraft, which is the result of various non-ideal conditions, has a large dispersion. With the uncertainties on gravity (and thus on the duration of the descent) and on the release height above the actual first contact point, all these dispersions make the attitude at first contact random. However, MASCOT is more likely to land on a corner, and because the impact orientation is just one of the many parameters that can have an effect and that we need to study, we decided to focus on three possible orientations (see Fig. 1): Flat, Back-Corner-First (BCF) and Front-Corner-First (FCF). Indeed, MASCOT is more likely to land on a corner and, since we wanted to study the effect of many different parameters and not only orientation, we considered only these three orientations. Other orientations, for example MASCOT landing on an edge, have been studied by Maurel et al. (2017). A slow spin like that transmitted to the lander during its ejection from the spacecraft (0.1 rad s^{-1}) does not induce any critical change in the outcomes of the impact (Maurel et al. 2017). We therefore considered no initial spin in our simulations.

Since, as we said previously, there are still a lot of uncertainties concerning MASCOT's separation, the landing site, and Ryugu's surface topography, the range of MASCOT's angle of impact is broad. However, to study the influence of the impact angle, we restrained it to five different angles, as done by Maurel et al. (2017): 0°, 15°, 30°, 45°, and 60° (0° means a purely vertical trajectory; larger angles represent more grazing impacts).

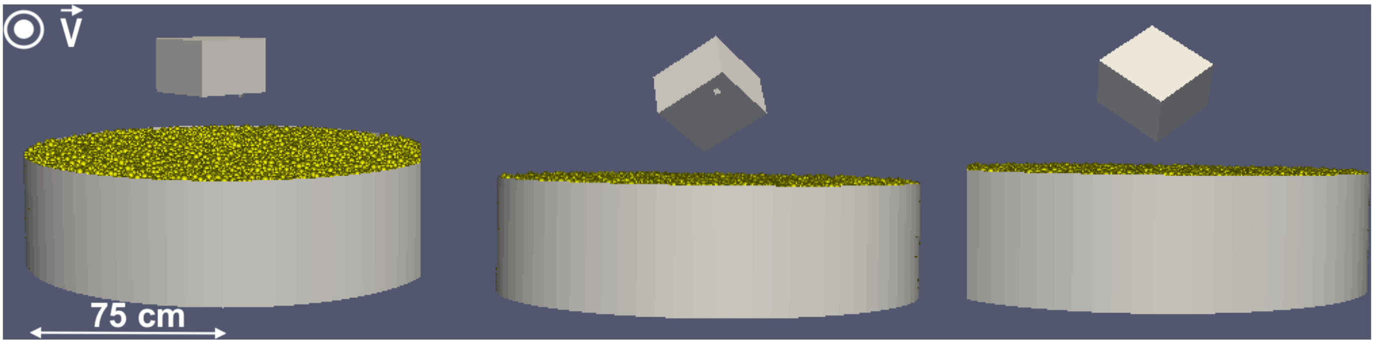

Fig. 1. Different orientations of MASCOT (coming toward the reader in these snapshots) used in our simulations: Flat, Back-Corner-First, and Front-Corner-First

2.3. Investigated output quantities

We can compute several characteristics related to the impact itself: the outgoing-to-incoming speed ratio of MASCOT's center of gravity, the outgoing rotational-to-linear energy ratio, the collision duration, the maximum penetration depth of the lander into the bed, and the outgoing trajectory angle. The maximum penetration depth corresponds to the lowest point reached by any of the corners of MASCOT, and the collision duration the time from MASCOT's first contact with the regolith bed until all its height corners are above the plane at the top of the cylinder. These parameters were chosen because they enable us to describe the collision (duration, penetration of the lander into the regolith bed) as well as MASCOT's state just after the collision (outgoing speed, energies, and trajectory angle).

We also compute the evolution of MASCOT after its first impact. If MASCOT bounces after its first impact, we ballistically extrapolate its future behavior as a free-fall trajectory, using the data from the end of the simulation of the first impact. Doing so, we can determine the distance that MASCOT travels after the first impact, the time between the first and the second impact, and the second impact speed and angle, considering a flat environment. The distance traveled by MASCOT is the distance on the surface (assumed to be flat) between the spot where MASCOT leaves the ground (its height corners are higher than the surface) and the spot where MASCOT touches the ground again (when its equivalent spherical radius reaches the surface). The distance traveled by MASCOT is mostly directed by the outgoing speed and the outgoing angle between MASCOT's motion direction and the horizontal plane, but not necessarily. The ejected particles impacting the bottom of MASCOT when leaving the bed may indeed affect its trajectory. The simulations are long enough to allow a good extrapolation of MASCOT's behavior after the impact.

Furthermore, we studied the properties of the crater resulting from the first impact, particularly its shape and depth. At the end of our simulations, the crater may still be transient, which is the state in which it will probably be observed by the Hayabusa2 team just after the landing of MASCOT. The aim of this analysis is to understand whether the transient crater's properties can be used as a diagnostic of MASCOT's distance from the impact point, provided that the camera on board Hayabusa2 can resolve it and that we find a direct link between those properties and MASCOT's fate in our simulations. As we will see, those properties can also give us some information on the regolith properties, as different properties yield different traces.

The Hayabusa2 optical navigation camera (ONC) system, which consists of a telescope (ONC-T) and two wide-angle cameras (ONC-W1 and -W2) (Kameda et al. 2017; Suzuki et al. 2018) can observe MASCOT while it is descending as well as crater(s) and ejecta deposits resulting from MASCOT's impact. During Hayabusa2's ascending sequence following the release of MASCOT, the slant viewing ONC-W2 camera will obtain images of separation motion of MASCOT from the side panel of the Hayabusa2 main spacecraft. Then, the nadir-viewing ONC-W1 camera will take images of MASCOT's fall. These observations will help estimate MASCOT's trajectory before the first bounce. As shown in Sect. 3.1, the angle and velocity of MASCOT's impact will be determined by MASCOT's descent trajectory and Ryugu's local topography and will provide constraints on Ryugu's surface physical properties. Subsequently, ONC-T will start taking a sequence of images of the surface area around MASCOT's first bounce location. The spatial resolution and field of view (FOV) of the ONC-T camera will change due to the ascent of Hayabusa2, which may depend on many unknown parameters of Ryugu, such as the surface gravity. We note that the nominal spatial resolution and FOV of each ONC-T image are about 3.6–11 cm pix^{-1} and 36–108 m, respectively. This resolution should be good enough to capture and characterize the traces left by MASCOT after its impact on the asteroid because the typical crater diameter in our simulations is between 160 and 200 cm. Also, because the total coverage of the ONC-T images taken during the ascent is 150–200 m in diameter, it should cover the landing ellipsoid of MASCOT's first bounce, which is expected to be of the same order of magnitude as MASCOT's releasing altitude (~60 m). However, the total number of such high-resolution ONC-T images is limited to nine in the current plan; this series of images may end before comes to rest after multiple bounces. Subsequent imaging of MASCOT will be performed from much higher altitudes (~3 km) with lower resolutions (~30 cm pix^{-1}). If it bounces, finding MASCOT on the asteroid may thus become a challenge, as it was for Philae. It may be easier to find MASCOT's first impact site in the ellipse of uncertainty, when the main spacecraft is still at low altitudes, and to image the traces. We therefore also investigated the relations between the distance traveled by the lander and the traces left in the ground.

3. Outcomes of the lander/regolith interaction and sensitive parameters

In this section, we derive general trends from our simulations in terms of traveled distance of the lander after the first impact, traces left on the asteroid surface, and other outcomes, and identify the sensitive parameters that drive these trends.

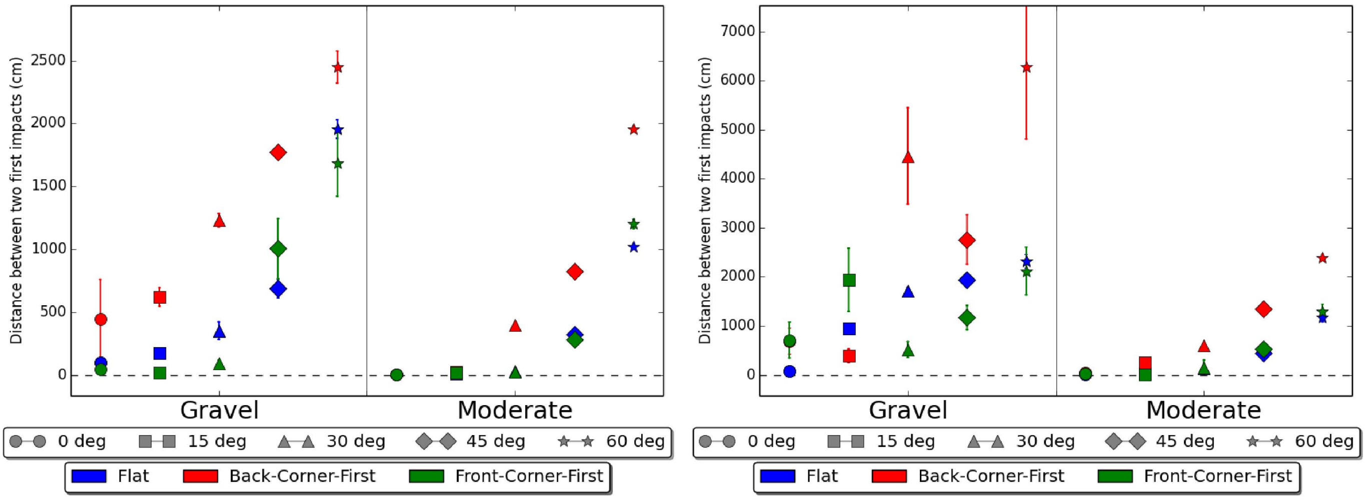

(a) 30 cm deep bed

(b) 15 cm deep bed

Fig. 2. Distance traveled by the lander between the first bounce and the second impact as a function of the impact angle ("0 deg" means a pure vertical trajectory with no lateral motion; larger angles represent more grazing impacts), the material type, and the orientation of MASCOT at impact, for a 30 cm bed (*left*) and a 15 cm bed (*right*). The shapes of the markers represent the five angles considered, while the two columns show the two material types. The color refers to the orientation of MASCOT. The arrows represent error bars (see text for details). When the error bars are not visible, they are smaller than the markers.

Table 3. Average impact characteristics for 54 simulations with three different depths, two material types, and three orientations at impact for each of the five different angles of approach considered in our simulations.

Angle	Traveled distance	Time between impacts	$\frac{V_{out}}{V_{in}}$	$\frac{E_{rot,out}}{E_{lin,in}}$	$\frac{E_{rot,out}}{E_{lin,out}}$	Collision duration	Maximum penetration depth	Incoming angle at second impact	Speed at second impact
0°	1.2 m	84 s	6%	1.9%	359%	11.0 s	9.4 cm	32°	1.2 cm s^{-1}
15°	2.7 m	86 s	11%	1.1%	142%	10.6 s	8.5 cm	48°	1.6 cm s^{-1}
30°	6.0 m	153 s	17%	3.0%	54%	9.5 s	7.9 cm	54°	2.9 cm s^{-1}
45°	10.1 m	231 s	26%	5.0%	58%	6.1 s	5.9 cm	56°	4.9 cm s^{-1}
60°	19.7 m	295 s	41%	7.4%	45%	3.8 s	5.2 cm	61°	7.4 cm s^{-1}

Notes. V, E_{rot}, and E_{lin} correspond respectively to MASCOT's speed, rotational energy and linear energy, and *out* and *in* to outgoing and incoming values.

3.1. Influence of the angle of impact

One of the most influential parameters on the distance traveled by the lander is the angle of impact. In our simulations, we notice an increase in the distance traveled by MASCOT after the first impact correlated with the angle of impact. In other words, the more grazing the impact, the greater the traveled distance. The process governing the impact is described in detail in Sect. 3.2, but the higher the tangential component of the velocity, the higher the tangential speed after the impact, and the higher the bouncing probability, which leads to a greater distance traveled. These results are clearer for regolith beds of 30 cm and 40 cm in depth, as shown in Fig. 2a. For a 15 cm bed (Fig. 2b), due to the boundary effects of the bottom of the bed (see Sect. 3.3 for the influence of depth), the points are more scattered and the trend is less obvious, but it holds in a general way. The error bars correspond to standard deviations obtained for three similar simulations. The stochasticity in the simulations is more thoroughly described in Sect. 3.8, but we note that it does not invalidate the trends established here. Therefore, and for better readability, we do not include error bars in every figure.

Table 3 displays an average of several characteristic output quantities over the different considered bed depths, material types, and orientations of MASCOT (54 simulations for each of the five angles of impact considered here, for a total of 270 simulations). Once again, we note that the more grazing the impact (i.e., the higher impact angle), the greater the distance traveled. When the impact angle is high, the lander spends less time in contact with the soil, the collision is shorter, and less energy is imparted to the bed particles (resulting in a shallower crater, if we consider the maximum penetration depth). However, recalling that the incoming linear energy is the same for all simulations, we note that the outgoing rotational energy increases with the angle of impact, whereas the outgoing rotational-to-linear energy ratio sharply decreases when the impact angle increases. This indicates that for grazing angles, the impact makes MASCOT spin more than for vertical ones, but the increase in rotational energy is less significant than the increase in linear energy when the angle of impact increases. Moreover, the outgoing rotational energy is always much lower than the incoming linear energy, but the outgoing linear energy depends largely on the angle of approach. After the impact, depending on the angle, the linear energy can be either dominant or dominated over the rotational energy: for vertical impact, the rotational energy is higher than the linear energy, whereas it is the opposite for very grazing impacts.

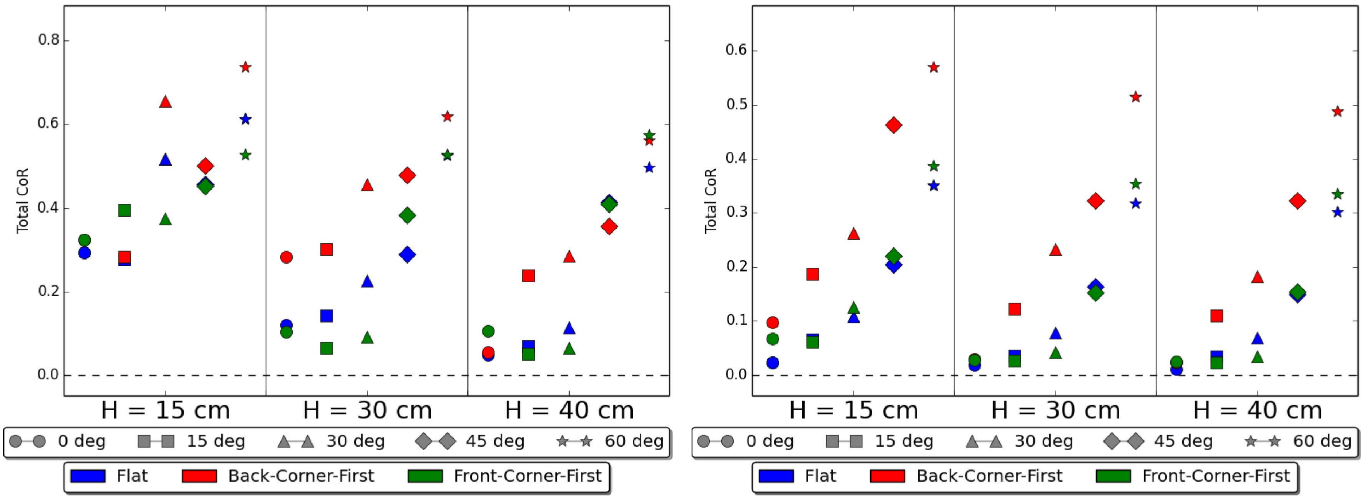

(a) With gravel-like friction

(b) With moderate friction

Fig. 3. Total coefficient of restitution CoR as a function of the impact angle ("0 deg" means a pure vertical trajectory with no lateral motion; larger angles represent more grazing impacts), the bed depth, and the orientation of MASCOT at impact, for a gravel-like friction (*left*) and a moderate friction (*right*). The shapes of the markers represent the five considered angles, while the three columns show the three bed depths. The color refers to the orientation of MASCOT.

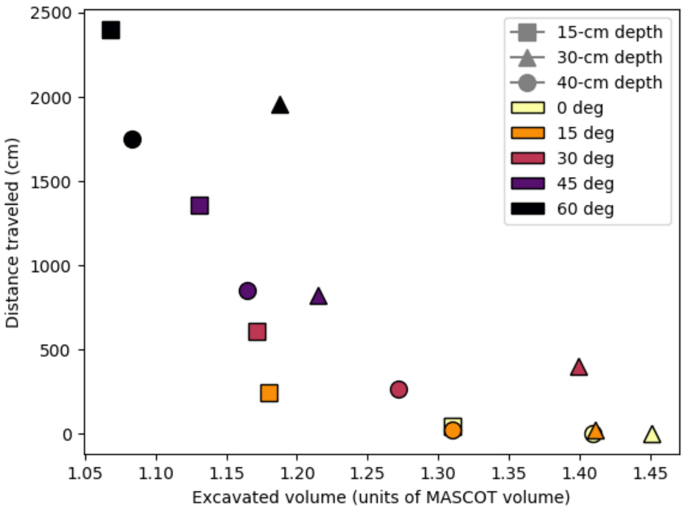

Fig. 4. Excavated volume vs. distance traveled by the lander between the first bounce and the second impact at the end of the simulation as functions of the impact angle and the bed depth. Only the Back-Corner-First MASCOT impact orientation is shown, with a moderate-friction regolith. The shade of gray depends on the impact angle and the symbol shape on the bed depth, as shown in the legend. MASCOT volume is about 1.56×10^4 cm^3.

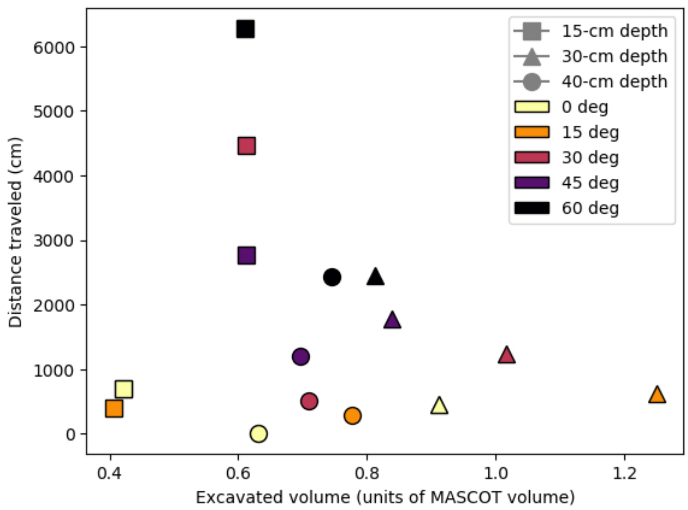

Fig. 5. Excavated volume vs. distance traveled by the lander between the first bounce and the second impact at the end of the simulation as functions of the impact angle and the bed depth. Only the Back-Corner-First MASCOT impact orientation is shown, with a gravel-like regolith. The shade of gray depends on the impact angle and the symbol shape on the bed depth, as shown in the legend. MASCOT volume is about 1.56×10^4 cm^3.

Figure 3 shows MASCOT's outgoing-to-incoming total energy ratio (also called total coefficient of restitution, or total CoR) considering both rotational and linear energies for different bed depths, angles of impact, orientations, and frictions. We note that the total CoR increases when the angle of impact increases (i.e., when the impact is more grazing), as does the traveled distance.

We also analyzed the influence of the angle of impact on the ejected volume of regolith. As shown in Fig. 4, a grazing impact ejects less material, and makes a shallower crater. However, these trends are only present for angles higher than 30° and for a moderate-friction regolith. For gravel-like material, there is no clear trend as the impact angle increases (see Fig. 5) and we show in Sect. 3.2 the differences in the mechanisms of the impact between the different types of regolith considered in this paper. These differences of excavated volume and penetration depth are visible in Fig. 6, where we compare the craters formed after impacts at 15° and 45°. The depth of the crater may give hints to determine the first angle of impact and thus the distance traveled by MASCOT after the first bounce.

In the event of a second impact, the incoming speed as well as the angle of the second impact strongly increase with the angle of the first impact (Table 3). It is mainly due to MASCOT having higher tangential velocities before grazing impacts than before normal ones and therefore having a slightly higher tangential velocity after the impact, leading to higher second impact angles. Peaks of occurrence for the five different considered angles are shown in Fig. 7. Even if we can see a slight increase with the

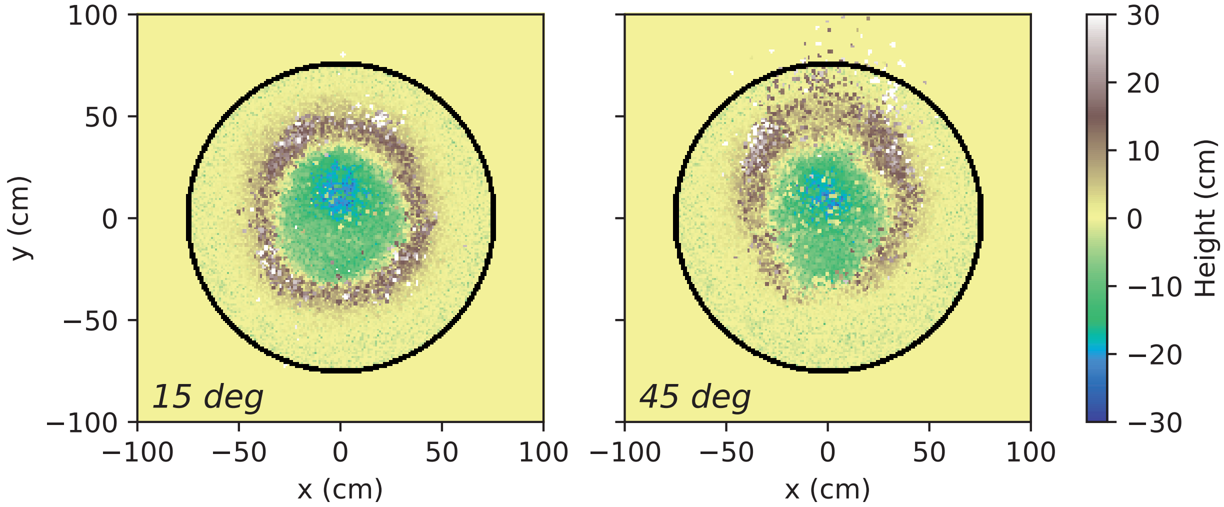

Fig. 6. Relief of the trace left by MASCOT on the regolith about 14 s after the impact for a moderate-friction regolith. The color bar represents the height of the regolith (bed and ejecta). MASCOT lands in the Back-Corner-First configuration with an impact angle of 15° (*left*) and at 45° (*right*). The regolith is 30 cm deep. For the 15° impact, MASCOT has not left the surface (its height corners are still under the surface level), whereas it did after 7.5 s for the 45° impact.

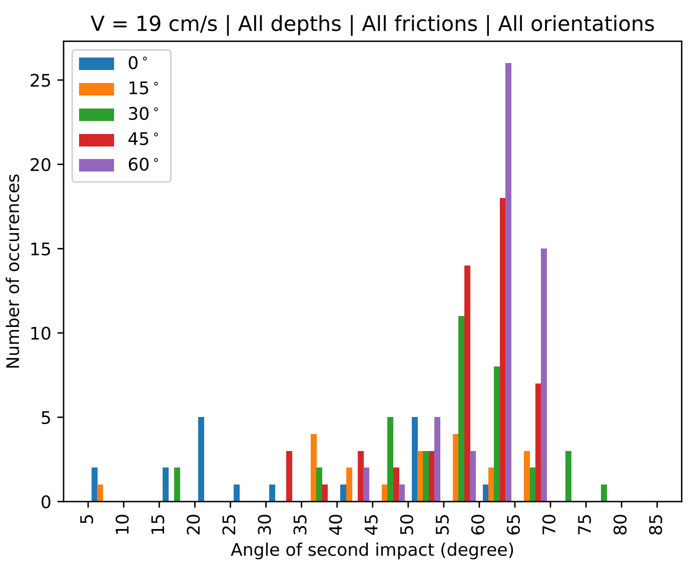

Fig. 7. Histogram of the second impact angle in the event of a second contact, for the five angles of impact considered in this article. The data represent the five angles of impact, the three bed depths, the three orientations, and the two friction properties (total of 270 simulations).

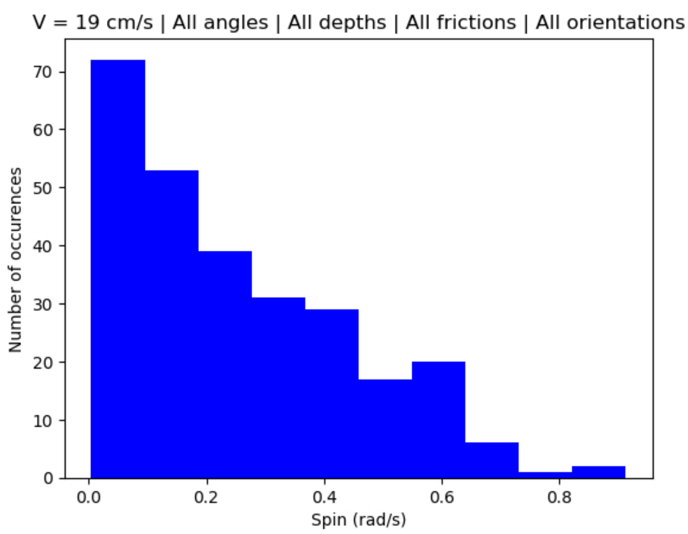

Fig. 8. Histogram of the final spin after the first impact. The data represent the five angles of impact, the three bed depths, the three orientations, and the two friction properties (total of 270 simulations).

first impact angle, the second impact angle is mostly around 60°. Indeed, when MASCOT bounces at the first impact, almost 45% of the simulations show a second impact angle between 55° and 65°, and more than 65% show one between 50° and 70°. Regolith friction, cylinder depth and MASCOT's orientation show no significant influence on the second impact angle directly.

The high value of the second impact angle may lead to a second bounce; we could assume that it would be weaker because of the smaller impact speed, but we also have to consider the role of the rotation after the first bounce. As we already indicated, spins of 0.1 rad s^{-1} have already been studied by Maurel et al. (2017). However, we do see in our simulations that the final spin of the lander can be greater than 0.1 rad s^{-1} (Fig. 8 shows that it can reach more than 0.8 rad s^{-1}) and more work remains to be done to understand whether a fast spin can influence the putative second impact. The resulting spin after the impact can lead to high total coefficients of restitution, as shown in Fig. 9. The four parameters (first impact angle, regolith friction, depth of the bed, and MASCOT's orientation) influence the spin, the total CoR, and the traveled distance equally. Therefore, considering the first impact angle, the more grazing the angle, the higher the spin and the total CoR, and the greater the traveled distance.

3.2. Influence of the regolith friction properties

The nature of the regolith, through its friction properties, also has an influence on the different output quantities. As shown in Fig. 2, the distance traveled by MASCOT after the first impact is greater with a gravel-like regolith bed than with a moderate-friction one, in particular for grazing impacts that lead to the greatest distances. Indeed, with a moderate-friction bed, the global resistance is weaker since particles are smoother, allowing the lander to penetrate deeper into the bed, losing more energy

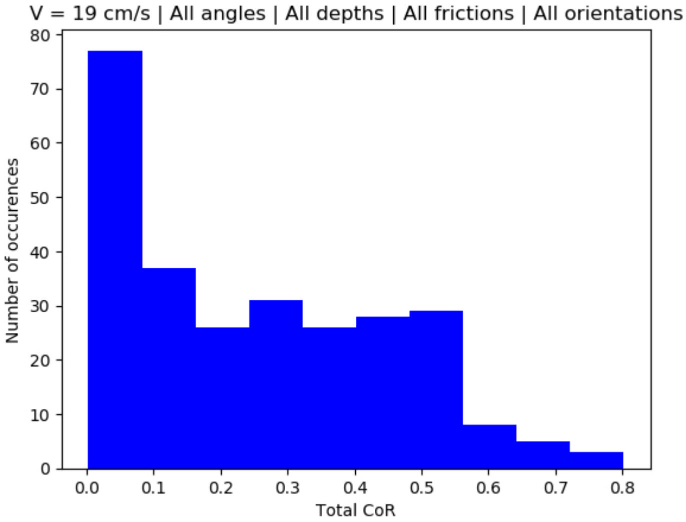

Fig. 9. Histogram of the total CoR (i.e., outgoing-to-incoming total energy ratio). The data represent the five angles of impact, the three bed depths, the three orientations, and the two friction properties (total of 270 simulations).

than it would in a gravel-like medium. Thus, more energy is lost at impact and the lander goes less far.

By looking at cross-sections of the bed during the impact, we can better understand the process governing the impact. Figure 10 shows cross-sections for the Back-Corner-First configuration and we see that, with a gravel-like regolith, the lander hits first with the back corner then pivots swiftly to hit with the front corner. Therefore, the bottom-back part of the lander still has a certain energy and, after its bottom-front part impacts the regolith, its inertia causes the whole body to spin. The bottom face of MASCOT cannot push the regolith particles downward, or at least not enough to penetrate deeply into the bed, because the gravel-like friction makes the bed somewhat rigid. There are in that case two holes in the bed after 30 s. Conversely, the moderate friction makes the penetration smoother, and the lander leaves only one hole. The smaller friction between the particles of the bed makes the bed more compliant, and then MASCOT pivots less but digs more into the regolith. Since the lander pivots more swiftly for a gravel-like regolith bed, the resulting spin after the impact is on average higher than for a moderate-friction bed. The spin and linear speed being higher, the total CoR is also higher.

The impact process described here is particularly true for the Back-Corner-First orientation. The process is similar for the two other configurations (Flat and FCF impacts), that are described in Sect. 3.4. For all the processes discussed in this article, the friction of the regolith bed has the same influence: the higher the friction, the higher the grains' resistance to MASCOT's penetration, and the greater the distance traveled. With gravel-like regolith, the distance is greater, the collision duration is shorter, and the penetration is shallower.

These differences in behavior between the two considered frictions are visible if we look at the characteristics of the traces left by MASCOT. Figures 11 and 12 show snapshots of the regolith bed seen from above, during the landing of MASCOT with an angle of impact of 45° on the back corner, for a gravel-like bed and for a moderate-friction bed, respectively. We notice that the impact of the lander in the gravel-like material bed leaves a two-hole crater, whereas the smoother regolith with moderate friction leads to a one-hole crater, as suggested by the cross-sections. We also notice that the volume of ejecta for the moderate-friction bed is much larger than that produced with a gravel-like bed because the lander gives more energy to the particles, and the particles dissipate less energy among themselves by friction. We find that the volume of ejecta for a moderate-friction bed is on average 80% larger than that for a gravel-like regolith bed when MASCOT impacts on the back corner, and 60% when it lands flat on the ground. Therefore, the images taken by the main spacecraft after impact can inform us indirectly, either from the volume of ejecta or from the crater's shape, of the properties of the regolith layer on Ryugu.

Since MASCOT leaves a two-hole crater in the ground for a gravel-like regolith, we can estimate in which direction MASCOT is traveling after the impact by looking at the alignment of the two holes, even if it is not obvious and there is scattering. In Figs. 11 and 12, the lander comes from the bottom and continues toward the top. Also, in the example of the moderate-friction case, the spatial distribution of ejecta informs us about the direction of the lander. Indeed, there's almost no ejecta in the direction MASCOT comes from, and the ejecta travels farther in the direction the lander is going.

After the lander bounces on a moderate-friction bed, since it loses more energy during the bouncing, the incoming speed for the second impact is smaller than that for a gravel-like regolith and therefore we can expect a smaller second bounce or no bounce at all.

In conclusion, the regolith friction has a direct impact on the distance traveled by the lander and on the traces left on the ground (crater size, ejecta volume) and by looking at the size of the crater we can extrapolate MASCOT's direction and distance (for details on the different cases, see Sect. 3.4). However, for scientific purposes, the shape of the traces can also give us precious information about the friction of the regolith, and therefore partially on its nature. Moreover, a posteriori, after we find the lander, its distance from the first impact site may also give us insight on the regolith friction. Obviously, this method cannot give us the exact composition of the regolith directly, but in the event of dysfunction of instruments on board MASCOT or combined with the measurements of these instruments, it can help to deduce the nature of the regolith.

3.3. *Influence of the depth of the regolith bed*

Since the depth of the regolith bed is difficult to measure from distant observations, we also analyzed its influence to determine whether we can infer it from the impact outcome. Table 4 shows averages of several characteristic output quantities over the different considered impact angles, orientations of MASCOT, and material types (each quantity is averaged over 90 simulations for each depth). We see that the shallower the bed, the greater the distance traveled by the lander after the first bounce, and the smaller the penetration depth. We also find that the differences in average impact characteristics are smaller for beds with depths of 30 cm and 40 cm, implying that the differences seen for the bed with a depth of 15 cm are largely due to boundary conditions, i.e., to the effect of the bottom of the cylinder. To confirm this, we used different coefficients of restitution for the bottom wall for the different bed depths. We noticed non-negligible variations in the output quantities only for the 15 cm bed. For a shallow bed, the wave provoked by the impact of the lander on the top of the bed is not damped yet when it reaches the bottom of the cylinder, and reflects off the bottom wall.

Figure 13 shows the root-mean-square (RMS) speed of the particles in each 5 cm layer forming the regolith bed. It can be

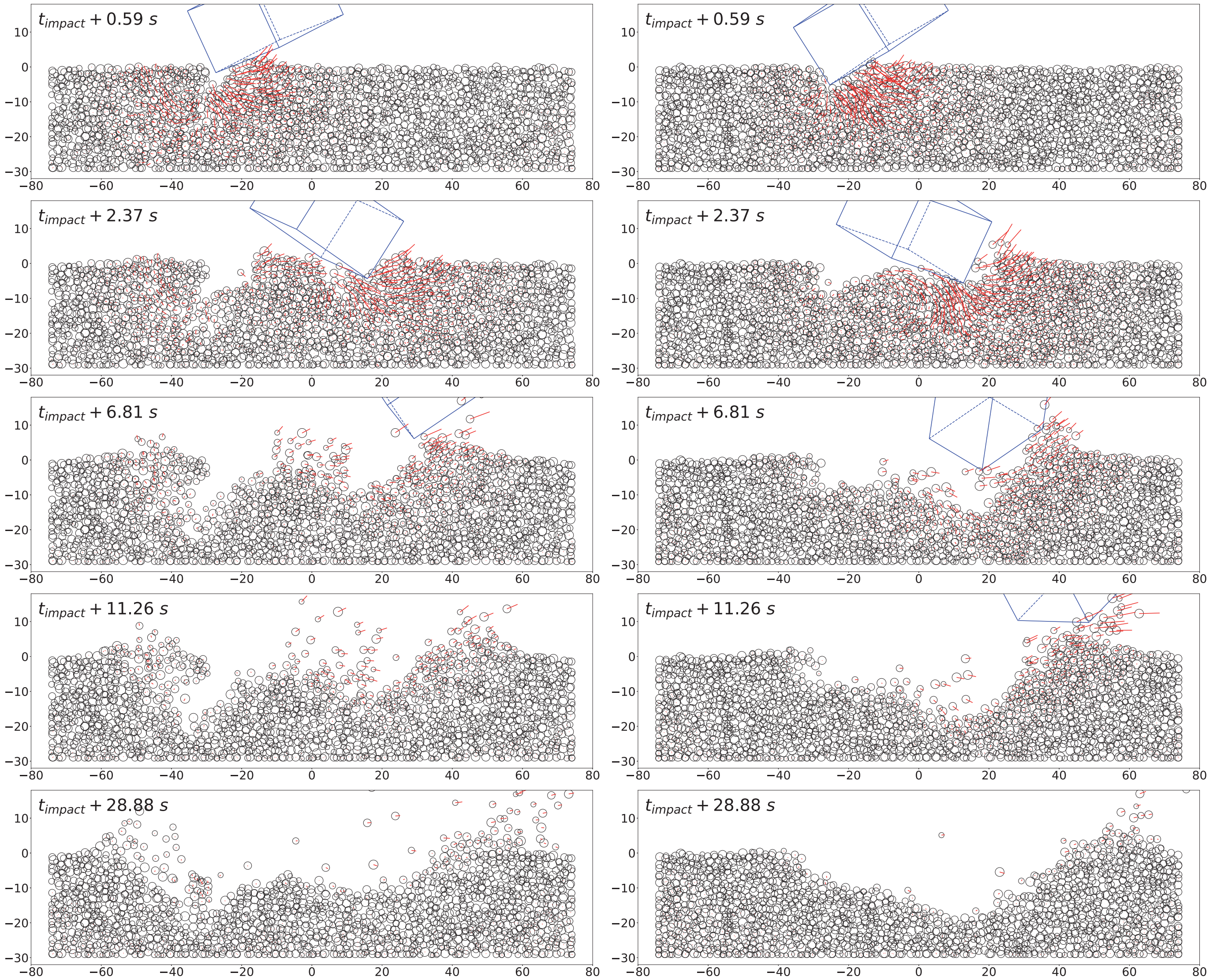

Fig. 10. Snapshots of MASCOT impact, represented in a cross-section of a gravel-like regolith bed (*left column*) and a moderate-friction regolith bed (*right column*) for different times. The blue cuboid represents MASCOT, and each red line indicates the projected 2D velocity of the corresponding particle. MASCOT lands in the Back-Corner-First configuration with an impact angle of 45°, and the regolith is 30 cm deep.

noticed that for a 40 cm bed, the wave almost does not reach the bottom, and therefore will not reflect off it, whereas for a 15 cm bed the particles at the bottom of the cylinder are submitted to relatively high velocities.

Considering the second bounce, as the regolith layer gets thicker, the speed at second impact decreases (Table 4) and the total expected number of lander bounces decreases. The after-impact spin and the total CoR also decrease when the regolith layer is deeper.

3.4. Influence of the orientation

As shown in Fig. 2, the distance traveled by MASCOT in the Back-Corner-First configuration is greater than that in the two other configurations. The way MASCOT hits the granular medium influences the dynamics of the lander. In the Back-Corner-First configuration, because the first contact point is behind MASCOT's center of gravity (in the direction of motion), the resulting rotation is in the same direction as the initial motion of MASCOT, and therefore the lander is only partly slowed down. On the other hand, for the Front-Corner-First configuration, MASCOT's center of gravity is behind the first contact point, which results in a greater slowdown and therefore a shorter traveled distance. The two configurations show very similar impact outcomes, but the BCF orientation has a first phase: when the back corner impacts the ground, MASCOT gains spin and momentum and therefore impacts in a second phase with its front corner with a higher momentum. With the FCF orientation, the front corner impacts the ground directly with no spin beforehand and the traveled distance is consequently shorter.

When MASCOT lands flat on the regolith bed, the process is the same as for the two other orientations. Since the ground is not completely flat, the lander cannot land exactly on its bottom side. It also cannot land perfectly on an edge, and either one of the back corners or the front corners will touch the bed first, leading to the previous cases but in a softer way. However, since the first contact with the ground may be close to a corner and not exactly on one of these, and since it is not oriented the same way as for BCF and FCF (i.e., back and front corners aligned with the tangential velocity) the distance traveled after MASCOT landed flat may even be smaller than with FCF orientation.

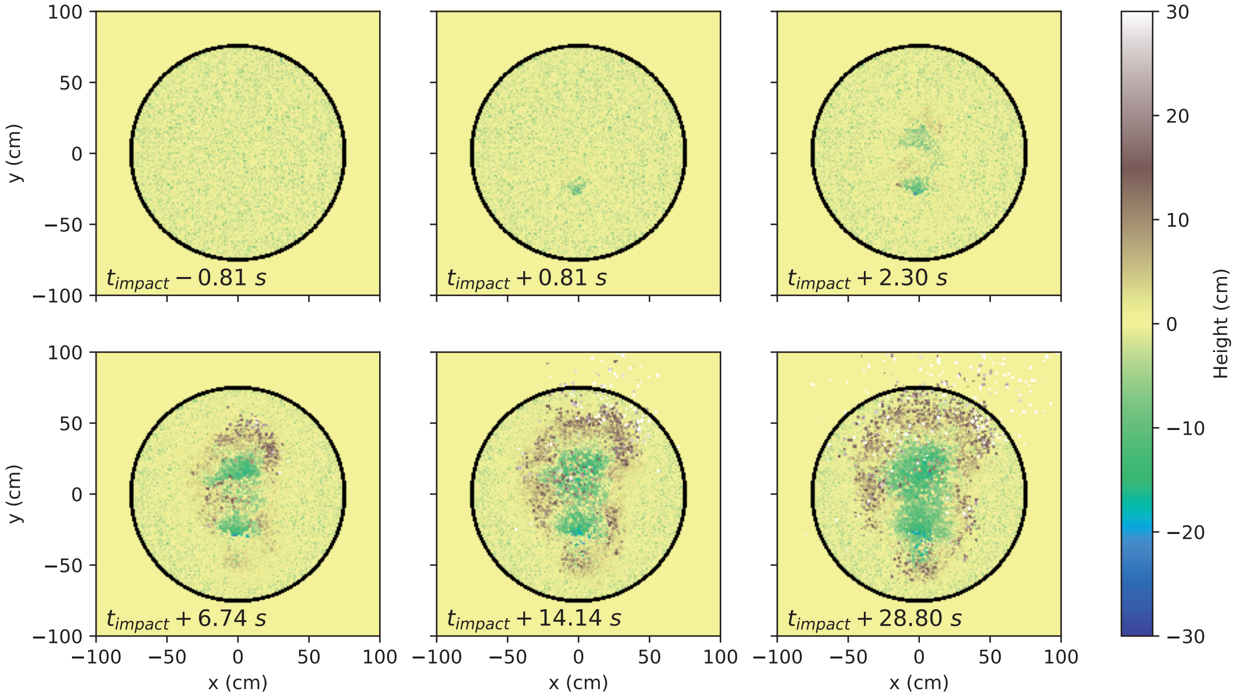

Fig. 11. Characteristics of the trace left by MASCOT on the regolith (in cm) at different times for a gravel-like regolith, where t_{impact} corresponds to the simulation time when MASCOT is for the first time in contact with the regolith. The color bar represents the height of the regolith (bed and ejecta). MASCOT lands in the Back-Corner-First configuration with an impact angle of 45° and has no spin before the impact, and the regolith is 30 cm deep.

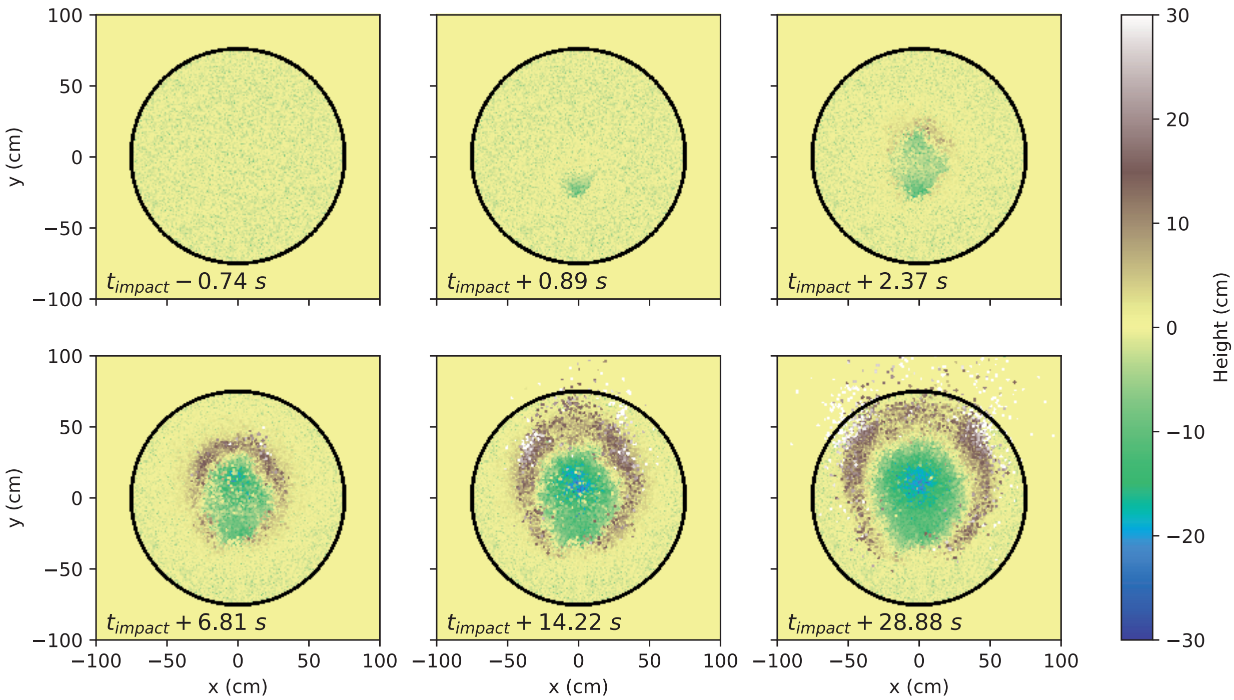

Fig. 12. Characteristics of the trace left by MASCOT on the regolith (in cm) at different times for a moderate-friction regolith, where t_{impact} corresponds to the simulation time when MASCOT is for the first time in contact with the regolith. The color bar represents the height of the regolith (bed and ejecta). MASCOT lands in the Back-Corner-First configuration with an impact angle of 45° and has no spin before the impact, and the regolith is 30 cm deep.

Table 4. Average impact characteristics for 90 simulations with five different angles of approach, two material types, and three orientations at impact for each of the three depths considered in our simulations.

Depth	Traveled distance	Time between impacts	$\frac{V_{\text{out}}}{V_{\text{in}}}$	$\frac{E_{\text{rot,out}}}{E_{\text{lin,in}}}$	$\frac{E_{\text{rot,out}}}{E_{\text{lin,out}}}$	Collision duration	Maximum penetration depth	Incoming angle before second impact	Speed before second impact
15 cm	12.2 m	252 s	27%	4.6%	111%	5.5 s	4.5 cm	53°	5.0 cm s^{-1}
30 cm	6.2 m	136 s	18%	3.6%	135%	9.1 s	8.5 cm	68°	3.2 cm s^{-1}
40 cm	5.4 m	122 s	16%	2.9%	149%	10.0 s	9.2 cm	69°	2.7 cm s^{-1}

Notes. V, E_{rot}, and E_{lin} correspond respectively to MASCOT's speed, rotational energy and linear energy, and *out* and *in* to outgoing and incoming values.

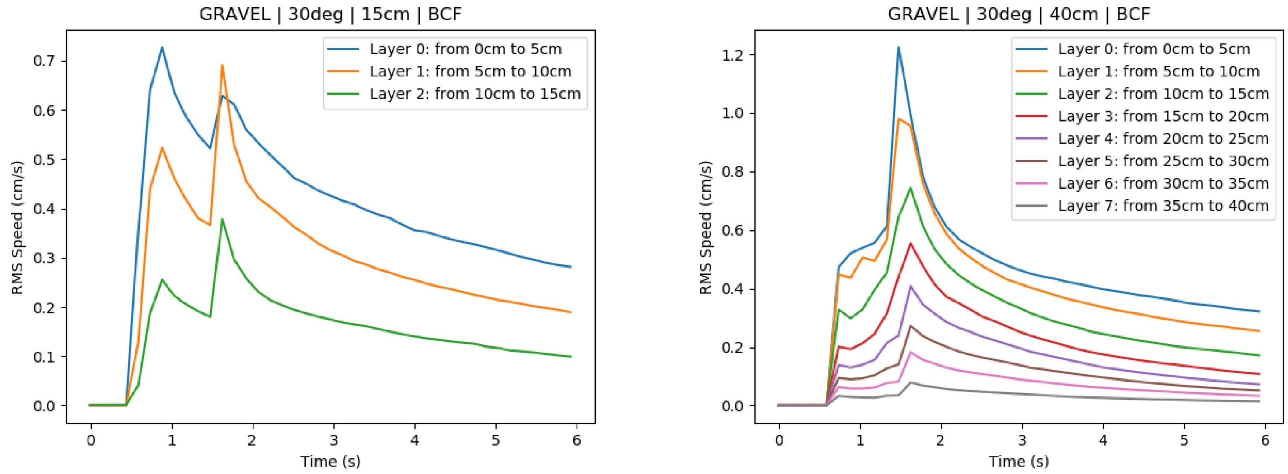

(a) 15 cm deep

(b) 40 cm deep

Fig. 13. Root-mean-square (RMS) speed of the particles located in different 5 cm layers of the cylinder as a function of time. MASCOT lands in the Back-Corner-First configuration with an impact angle of 30° on a gravel-like regolith. The bed is 15 cm deep in the left figure and 40 cm deep in the right figure.

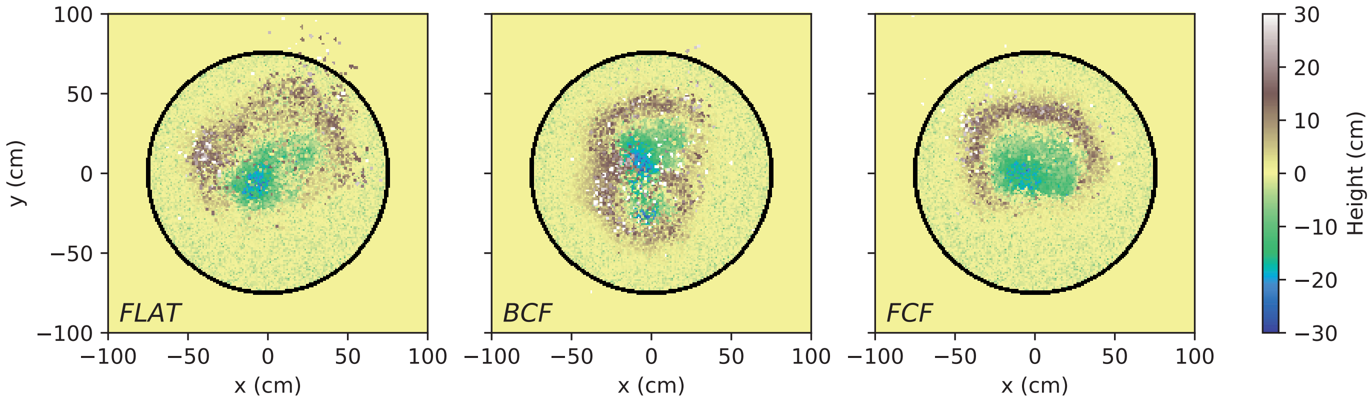

Fig. 14. Characteristics of the trace left by MASCOT on the regolith about 14 s after the impact for a gravel-like regolith. MASCOT lands with an impact angle of 30° and the regolith is 30 cm deep. For the BCF impact, MASCOT left the surface after 3 s, and after 6 s for the Flat impact, whereas it still has not left the surface for the FCF impact.

Figures 14 and 15 show the differences of traces depending on the orientation when MASCOT impacts the regolith bed for the two considered frictions considered. We find that the crater is shallower when MASCOT lands flat on the ground.

For a gravel-like friction (see Fig. 14), the three different orientations are discernible. In the case of MASCOT landing flat, we find a main hole and a secondary, shallower, hole. If the lander is close to horizontal, after the first corner hits the bed a second corner will impact the ground, but at a lower speed than the BCF orientation would generate, producing a second shallower hole. Since MASCOT's tangential velocity is not necessarily aligned with the first two impacting corners, the ejecta dispersion is not uniformly distributed around the two holes, and depends strongly on the corners, giving us information on the direction of MASCOT (mostly from the first hole to the second one). When the lander's orientation is no longer close to horizontal, we have either one clear deep hole (Front-Corner-First)

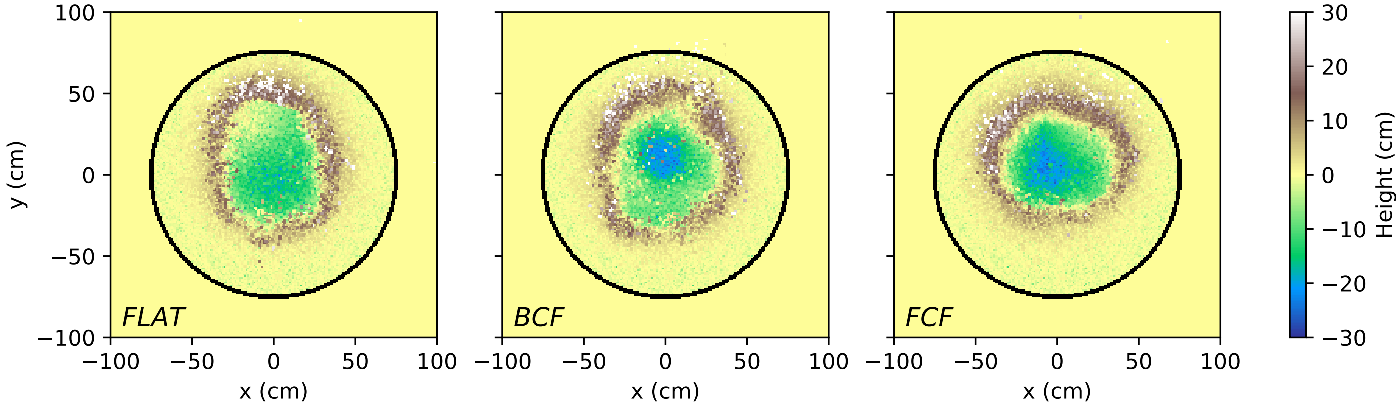

Fig. 15. Characteristics of the trace left by MASCOT on the regolith about 14 s after the impact for a moderate-friction regolith. MASCOT lands with an impact angle of 30° and the regolith is 30 cm deep. For the BCF impact, MASCOT left the surface after 11.5 s, whereas it still has not left the surface for the Flat and FCF impacts.

or two deep holes (Back-Corner-First). This process has already been described in Sect. 3.2.

With a moderate friction, the process is similar; however, since the regolith bed shows less resistance to the lander's penetration, MASCOT's bottom side also digs into the ground, leading to larger and more homogeneous traces. Moreover, whatever the orientation, the ejecta quantity is larger and goes in all directions, even if a slightly larger volume can be found in the direction MASCOT comes from. The direction MASCOT takes after the impact is within approximately ten degrees of the incoming direction. When MASCOT lands flat, it will leave on the ground a shallow and large hole. There will be a deep hole for both BCF and FCF orientations, but the traces still show different features. When MASCOT's front corner hits the ground first, it is barely stopped by the smooth regolith bed, and a large volume of ejecta is expelled, mostly in an ellipse whose semimajor axis is perpendicular to the direction of MASCOT. On the other hand, when the back corner first hits the bed, the bottom side drags particles, as explained in Sect. 3.2. Since the particles it hits and drags the most while pivoting are in the direction of the lander, the ellipsoidal ejecta ring will have a semimajor axis parallel to MASCOT's direction. By looking at the shape of the crater after the impact and the ejecta deposits, we can therefore deduce the orientation of MASCOT when it impacted and have a hint of the distance MASCOT travels after the first impact before impacting again.

Figure 16 confirms that the distance traveled is greatest when MASCOT lands on its back corner. Moreover, we find that the Flat configuration leads to less ejecta than the two other configurations. Indeed, when the lander hits the ground on one of its corners, it penetrates deeper into the bed and ejects a lot of particles. However, this trend is less visible for gravel-like regolith, and there is also no trend for a 15 cm deep bed with gravel-like friction. The post-impact spin is also higher on average when MASCOT lands on its back corner (Fig. 17). Since both speed and spin are mostly the highest with BCF, the total CoR is also the largest with this orientation.

3.5. Maximum values

To record the most extreme scenarios, we collected the maximum values found for each output quantity studied from all our simulations (Table 5). The maximum distances traveled (and therefore time of travel) are obtained for a 15 cm gravel-like bed, with an impact angle of 60° from the vertical, and for MASCOT

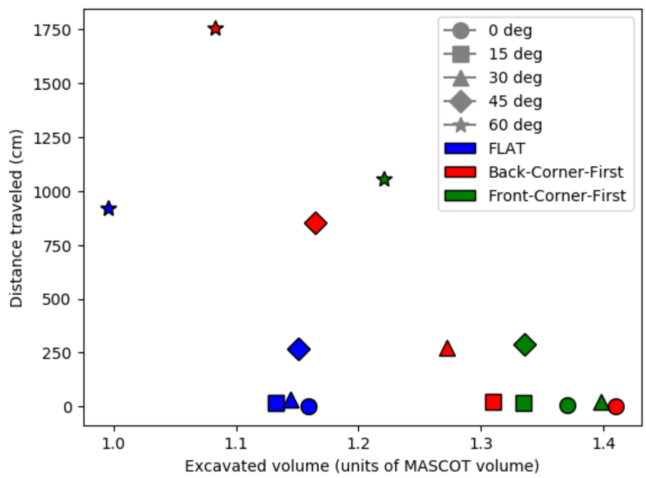

Fig. 16. Excavated volume vs. distance traveled by the lander between the first bounce and the second impact at the end of the simulation as functions of the orientation and the impact angle. MASCOT lands on a moderate-friction bed 40 cm in depth.

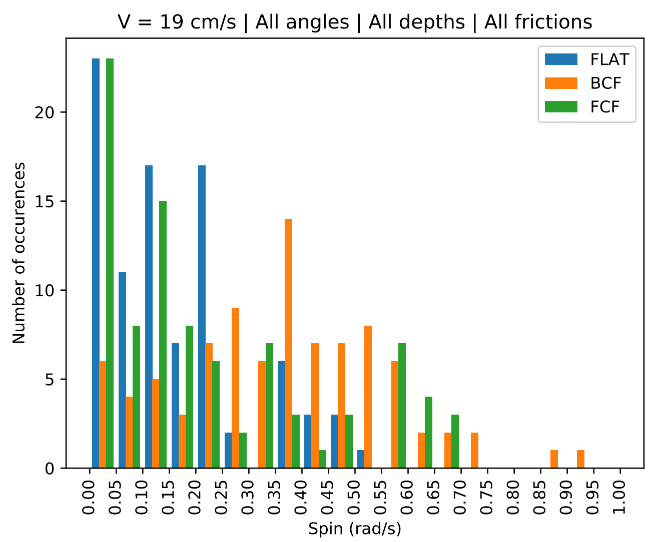

Fig. 17. Histogram of the second impact angle in the event of a second contact for the three orientations considered in this article. The data represent the five angles of impact, the three bed depths, the three orientations, and the two friction properties (total of 270 simulations).

Table 5. Maximum values of different impact characteristics and initial conditions of the corresponding simulations.

Characteristic	Value	Corresponding simulation			
		Friction	Angle of impact	Bed depth	Orientation
Distance between first and second impacts	7800 cm	Gravel	60°	15 cm	Back-Corner-First
Time between first and second impacts	810 s	Gravel	60°	15 cm	Back-Corner-First
Speed before second impact	14 cm s^{-1}	Gravel	60°	15 cm	Back-Corner-First
Maximum penetration	20.2 cm	Moderate	30°	30 cm	Front-Corner-First

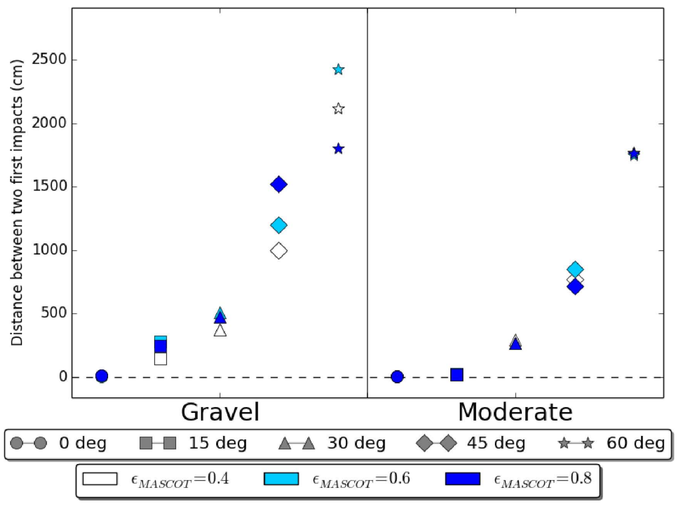

Fig. 18. Distance traveled by the lander between the first bounce and the second impact as a function of the impact angle (different marker shapes), the material type (as indicated on the plot), and the structural CoR of MASCOT (different colors). MASCOT lands in the Back-Corner-First configuration with no spin before the impact, and the regolith is 40 cm deep.

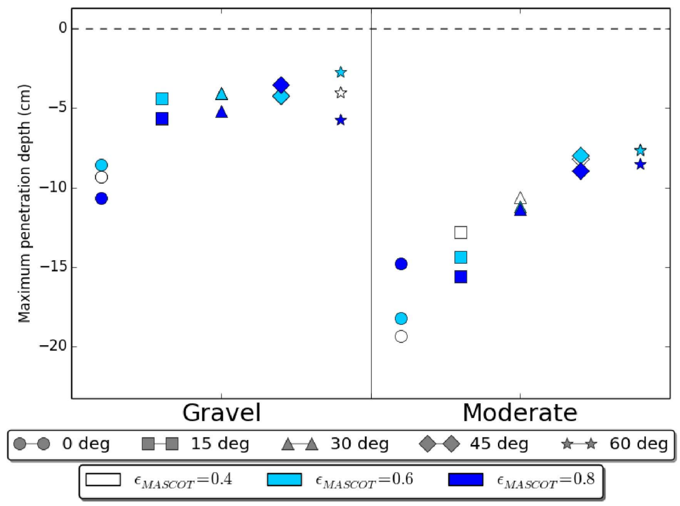

Fig. 19. Maximum penetration depth of the lander into the bed as a function of the impact angle (different marker shapes), the material type (as indicated on the plot), and the structural CoR of MASCOT (different colors). MASCOT lands in the Back-Corner-First configuration with no spin before the impact, and the regolith is 40 cm deep.

landing on its back corner. After its first contact with the ground, the lander can travel as far as 78 m from the impact point, over an interval of more than 13 minutes. The corresponding simulation confirms the trends we established previously. For such distances, the curvature of the asteroid can play a role, as can a non-uniform gravity field, but we did not take these effects into account because most of our results give smaller distances where curvature and non-uniform gravity play reduced roles. Moreover, the shape of the asteroid, its gravity field, and the surface topography are still very poorly known.

The speed before the second impact can reach 14 cm s^{-1}, from which we can expect a significant second bounce. Finding the lander may then become a challenge. However, we have seen that by looking at the crater's characteristics and the amount of ejecta during the tens of seconds following the impact, we can derive the value of the distance traveled by MASCOT within an order of magnitude and roughly guess the direction the lander took.

3.6. Influence of MASCOT's structural coefficients of restitution

We now analyze the influence of the coefficients of restitution, two parameters characterizing the energy dissipation. We studied separately the influence of MASCOT's coefficients of restitution and of those of the particles constituting the regolith bed.

MASCOT's normal and tangential structural CoR, due to damping inside the structure, have been measured by Biele et al. (2017) to be about 0.6. Since there is some uncertainty on these values, we ran a set of simulations with different values for the two structural CoRs and analyzed the results to check whether a small change in these values has a non-negligible effect on MASCOT's attitude during and after the impact. The significance of these CoRs was investigated for two different initial orientations (Flat and Back-Corner-First), and the three different bed depths (15, 30, and 40 cm), in addition to the usual five different angles of impact and two regolith friction values. The different values of structural CoRs considered here are 0.4, 0.6, and 0.8, with the same value for both the normal and tangential CoRs.

As shown in Fig. 18 (distance traveled), the results may differ slightly depending on MASCOT's CoRs. However, the differences are small, and the physics of the impact and the way MASCOT interacts with the particles do not change; we therefore consider for most of the simulations CoR values of 0.6. The slight disparities of values in the three configurations confirm the nature of the bounce of MASCOT, i.e., the pivot due to MASCOT's tangential velocity before the impact. The CoR of the corner that first impacts the soil has no major influence on the dynamics of the impact, and thus on the value of the traveled distance and on its evolution as a function of the angle of impact and of the regolith friction properties.

Figure 19 gives the maximum penetration depth for the three different structural CoRs. We can see that MASCOT's different structural CoRs do not yield significant variations, meaning that even if the structural CoR were measured with slight errors, this

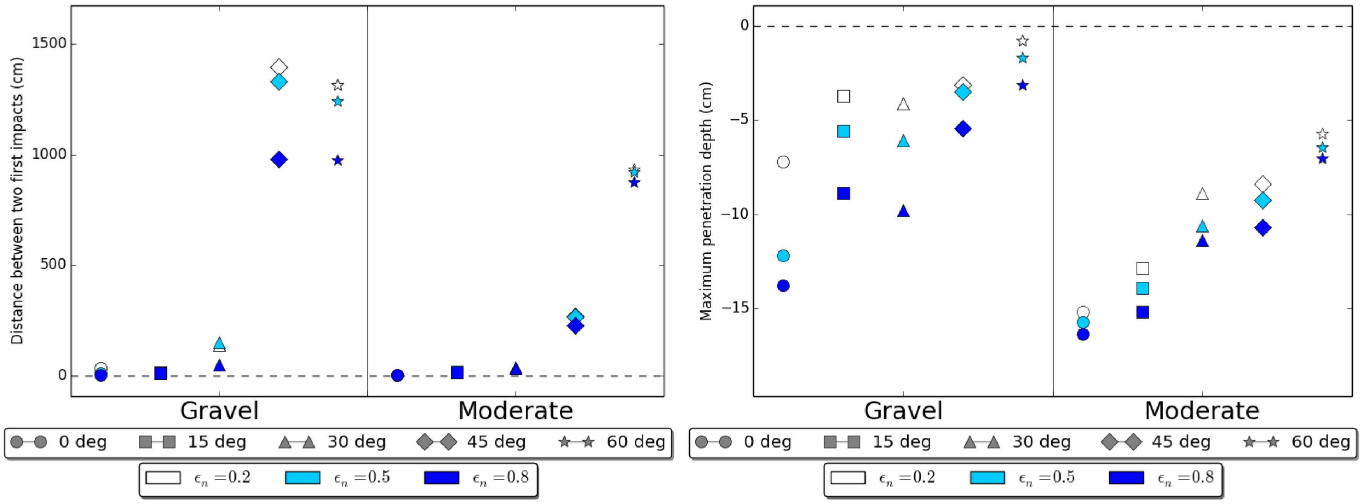

Fig. 20. Distance traveled by the lander between the first bounce and the second impact (*left plot*) and its maximum penetration depth into the bed (*right plot*) as a function of the impact angle (different marker shapes), the material type (indicated on the plots), and the normal CoR of the particles (different colors), with the tangential CoR equal to 0.5. MASCOT lands in the Flat configuration with no spin before the impact, and the regolith is 40 cm deep.

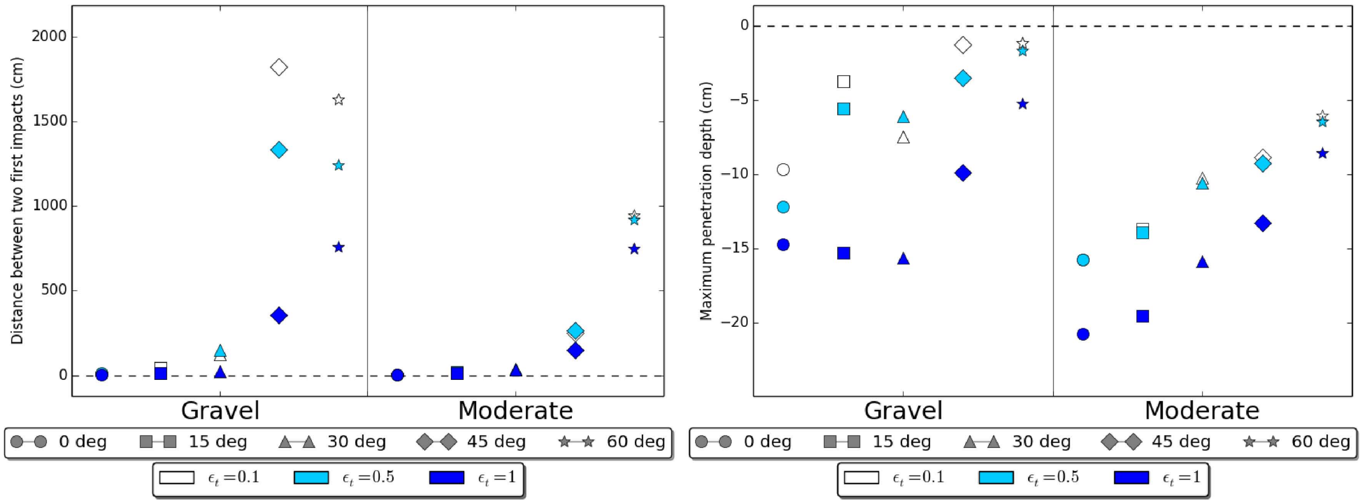

Fig. 21. Distance traveled by the lander between the first bounce and the second impact (*left plot*) and its maximum penetration depth into the bed (*right plot*) as a function of the impact angle (different marker shapes), the material type (indicated on the plots), and the tangential CoR of the particles (different colors), with the normal CoR equal to 0.5. MASCOT lands in the Flat configuration with no spin before the impact, and the regolith is 40 cm deep.

should not invalidate our predictions or strongly affect the values we obtained. The fact that we do not have a clear increase or decrease as a function of the structural CoR may be due to the complexity of the impact or to the stochasticity mentioned later.

3.7. Influence of the regolith grains' coefficients of restitution

Finally, we analyzed how the particles' CoR values affect the behavior of MASCOT during and after the impact, and how they affect the volume of particles ejected by the impact. For most of the simulations shown here we adopted $\varepsilon_n = \varepsilon_t = 0.5$ (see Table 1), which is a typical choice given the angle of repose of the material considered (Maurel et al. 2017). In order to make sure that the previously established trends do not depend on specific values of particle CoRs, we ran a set of simulations with the normal CoR ε_n varying from 0.2 to 0.8 and the tangential CoR ε_t from 0.1 to 1.

Figure 20 shows the distance traveled by MASCOT after the first impact and the maximum penetration depth for a tangential coefficient of restitution $\varepsilon_t = 0.5$ and different normal coefficients of restitution ε_n. A noticeable trend is that the higher the normal coefficient of restitution (for a given tangential coefficient of restitution of 0.5), the shorter the distance traveled and the deeper the penetration of the lander into the soil. Similarly, as shown in Fig. 21 with the same quantities but with a fixed normal CoR and different tangential CoR, the higher the coefficient, the shorter the distance and the deeper the penetration. Evidently, low coefficients of restitution for the particles make them conduct less energy between each other, and therefore the particles' speed initiated by the impact is damped in shallower layers of the regolith bed. Therefore, the bed behaves like a more rigid material, making MASCOT bounce farther, confirming the results of the simulations.

Figure 22 shows the different cases combined together for easier comparison. The plots show the results as a function of the normal CoR in the left figure and of the tangential CoR in the right one. These figures show that the higher the particles' tangential CoR, the shorter the distance traveled and the

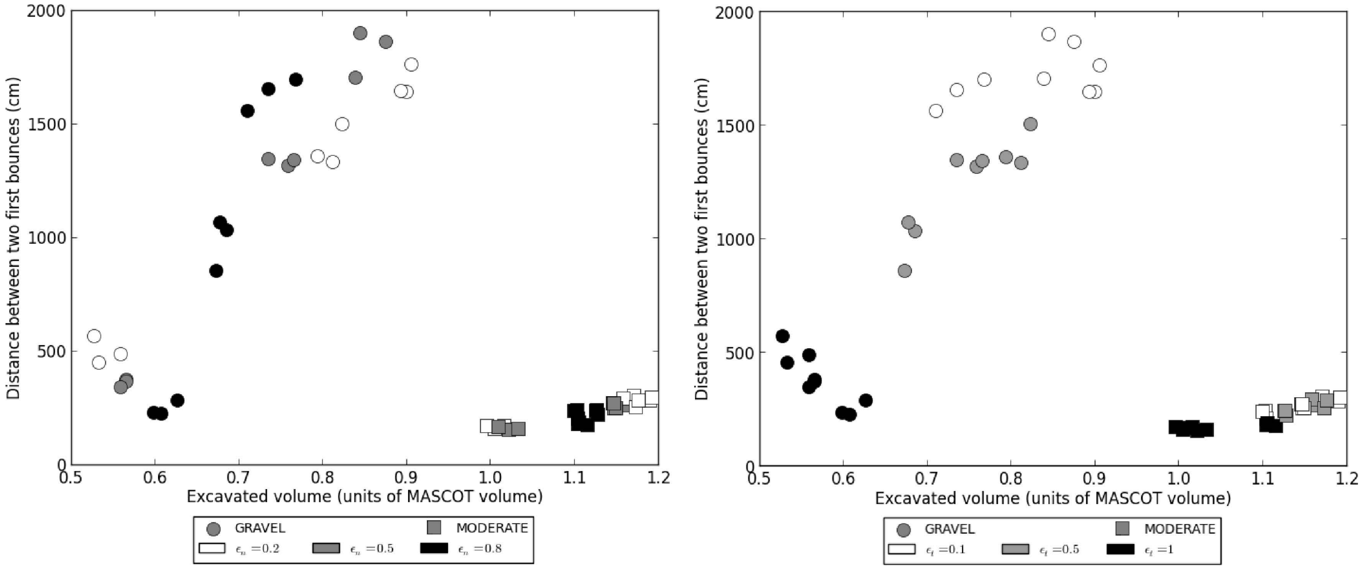

Fig. 22. Excavated volume vs. distance traveled by the lander between the first bounce and the second impact at the end of the simulation for 54 simulations for which MASCOT lands in the Flat configuration with an impact angle of 45° and no spin before the impact, and the regolith is 40 cm deep, for various values of normal CoR (0.2, 0.5, and 0.8) and tangential CoR (0.1, 0.5, and 1). The shade of gray denotes the value of the normal CoR (*left*) or of the tangential CoR (*right*) and the symbol shape denotes the material type.

smaller the excavated volume, as mentioned previously, and we can now see that this trend does not depend on the value of the normal CoR. For the latter, although we have the same trend for the traveled distance (a decrease with increasing coefficient), the volume of ejecta seems to depend on the value of the tangential CoR. Indeed, the excavated volume seems to decrease when the normal CoR increases for low tangential CoR, but increases for high tangential CoR. Thus, further investigations are needed to establish a clearer dependence on the normal CoR.

3.8. Stochasticity

The behavior of MASCOT is strongly influenced by the relative position of the protuberant MicrOmega sensors (for the Flat orientation) and of the impacting corner (for the two Corner-First orientations) with respect to the grains. For example, the outcome will be different if the sensors hit the top of a grain or if they hit the surface between two grains.

Depending on the number of CPU cores or their natures, we find that there is a certain level of chaos in the system, and that particles with exactly the same initial conditions can have a slightly different position at the impact point of the lander on the regolith bed. Along these lines, we ran three simulations with similar initial bed arrangements, friction coefficients, and angles of arrival, to check that the trends that we identified are not due to these stochastic effects, and then either considered the average of all the results or considered all of them individually.

The maximum differences in position of the same particles between simulations with the same initial conditions are shown in Fig. 23. These differences are due to the regolith bed being not completely at rest and to different CPU cores computing the interactions between these particles slightly differently (we used bi CPUs Intel Xeon Ivy Bridge E5-2670 v2). Even if the differences in position are very small, these differences have an influence on the impact outcomes. For example, we computed the standard deviations for the traveled distance for three simulations with similar initial conditions (Fig. 24). For most of the simulations, the standard deviation is low enough to validate

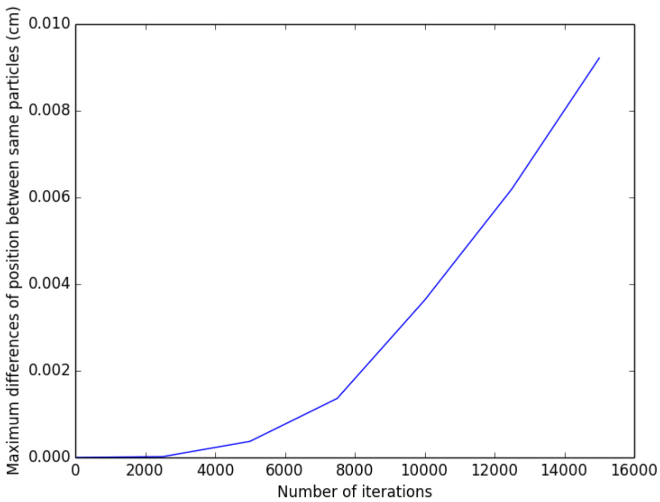

Fig. 23. Maximum differences of position for the same particles between simulations with same initial conditions as a function of time, represented by the number of iterations. These are the maxima for all the particles' differences of position of every configuration considered in this article (with $\epsilon_n = \epsilon_t = 0.5$). The 15 000 iterations correspond to about 0.44 s and occur just before the impact of the lander on the surface.

the trends. The standard deviation is particularly large for the simulations with a 15 cm bed and with grazing impacts because the traveled distances are greater. However, these larger standard deviations do not invalidate the trends described in the previous sections, as shown in Figure 2.

4. Conclusions

In this paper we presented our sets of numerical simulations of the low-speed impact of Hayabusa2 lander MASCOT on the surface of the asteroid Ryugu. We first investigated the influence of the depth and of two different sets of friction parameters of the regolith, as well as MASCOT's impact configuration

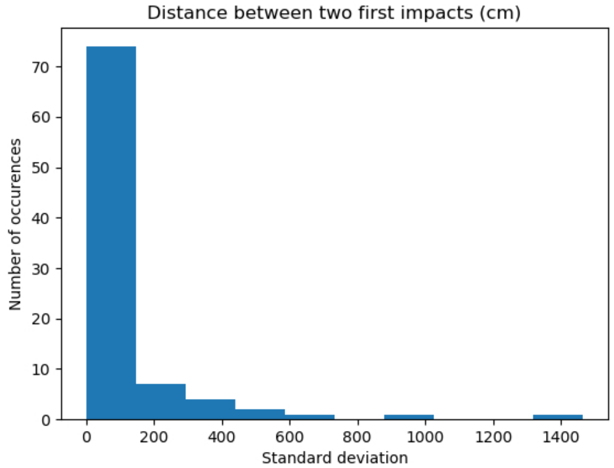

Fig. 24. Histogram of the standard deviations (in cm) of the traveled distance for every configuration considered in this article (with $\epsilon_n = \epsilon_t = 0.5$).

(orientation, impact angle), on the distance traveled by the lander and the traces left on the ground.

In general, for the considered impact speed of 19 cm s^{-1}, our simulations indicate that MASCOT is likely to bounce after its first impact. We then find that the greatest distances traveled by MASCOT after this first impact are obtained for the shallowest considered regolith bed, a gravel-like regolith, and the most-grazing impacts of the lander. The resulting spin and speed of the lander from the first impact suggest that a second bounce cannot be ruled out, but further work is needed to determine in greater detail the evolution of the lander after the second impact. However, our results can provide standard coefficients of restitution (MASCOT's outgoing-to-incoming speed ratio, for example) and traveled distances that can serve as a reference for other software to study the whole evolution of MASCOT.

We analyzed the traces left by MASCOT on Ryugu's surface after the first impact. We find that the signature left by MASCOT is very different for the two considered types of regolith. We also find that there is a relation between the traces left by MASCOT (crater shape and ejecta deposits), and the resulting travel distance and direction after the first impact. The instruments on board Hayabusa2 may be able to observe these impact traces, and in that case, the data will be extremely useful to give insight on both the nature of the regolith in terms of friction properties and the location of MASCOT on Ryugu's surface.

We studied the influence of the structural coefficients of restitution of MASCOT on its evolution, as these parameters are poorly constrained and may have an influence on MASCOT's behavior. The results indicate that the precise knowledge of these parameters is not essential in order to determine the processes governing the impact as they appear to have little influence on the general trends.

We looked at the influence of the two coefficients of restitutions (normal and tangential) of the regolith grains (in addition to their friction parameters). We find that the smallest values of the two coefficients of restitution result in a more rigid behavior of the regolith, and therefore result in shallower penetration into the bed as well as a greater distance traveled by the lander. Furthermore, an increase in the tangential coefficient of restitution roughly decreases the volume of ejecta, whereas a strong trend for the normal coefficient of restitution has not been found.

The actual properties of Ryugu's regolith are not known yet, and this study considered only a limited set of possibilities that already allowed us to determine general trends for MASCOT's behavior during the first impact. This can help both engineering and scientific teams of the Hayabusa2 mission in the search for the lander and in the determination of the regolith properties.

Further investigations will be devoted to other areas of the parameter space. In particular, the influence of the regolith packing, of a given level of cohesion between grains, and of the presence of a big boulder within the regolith or lying on it will be studied. Regarding MASCOT's impact conditions, it will also be important to consider the effect of the impact speed and other conditions within the range of possible conditions.

This study also contributes to the general understanding of the behavior of granular materials in the low-gravity environment of an asteroid's surface when experiencing an external action, here represented by the low-speed impact of a cuboid.

Acknowledgements. F.T. is supported by a PhD fellowship of the University of Nice-Sophia. P.M. and F.T. acknowledge funding support from the French space Agency CNES (BCU66), as well as from Academies of Excellence: Complex systems and Space, environment, risk, and resilience, part of the IDEX JEDI of the Université Côte d'Azur in connexion with its Center for Planetary. Simulations were performed at Mésocentre SIGAMM hosted at the Observatoire de la Côte d'Azur and on the Deepthought2 HPC cluster at the University of Maryland. E.T. and S.S. acknowledge support from the Japan Society for the Promotion of Science (JSPS) Core-to-Core program "International Network of Planetary Sciences".

References

Ballouz, R. 2017, PhD thesis, University of Maryland, College Park
Biele, J., Kesseler, L., Grimm, C., et al. 2017, ArXiv e-prints, [arXiv:1705.00701]
Binzel, R. P., Harris, A. W., Bus, S. J., & Burbine, T. H. 2001, Icarus, 151, 139
Boehnhardt, H., Bibring, J.-P., Apathy, I., et al. 2017, Phil. Trans. R. Soc. A, 375, 20160248
Delbo, M., Mueller, M., Emery, J. P., Rozitis, B., & Capria, M. T. 2015, in Asteroids IV, eds. P. Michel, F. E. DeMeo, & W. F. Bottke, 107
Goldman, D. I., & Umbanhowar, P. 2008, Phys. Rev. E, 77, 021308
Gundlach, B., & Blum, J. 2013, Icarus, 223, 479
Ho, T.-M., Baturkin, V., Grimm, C., et al. 2017, Space Sci. Rev., 208, 339
Kameda, S., Suzuki, H., Takamatsu, T., et al. 2017, Space Sci. Rev., 208, 17
Lauretta, D. S., Balram-Knutson, S. S., Beshore, E., et al. 2017, Space Sci. Rev., 212, 925
Maurel, C., Michel, P., Biele, J., Ballouz, R.-L., & Thuillet, F. 2017, Advances in Space Research, in press, 10.1016/j.asr.2017.05.029
Müller, T. G., Ďurech, J., Hasegawa, S., et al. 2011, A&A, 525, A145
Müller, T. G., Ďurech, J., Ishiguro, M., et al. 2017, A&A, 599, A103
Richardson, D., Quinn, T., Stadel, J., & Lake, G. 2000, Icarus, 143, 45
Richardson, D., Michel, P., Walsh, K., & Flynn, K. 2009, Planet. Space Sci., 57, 183
Richardson, D., Walsh, K., Murdoch, N., & Michel, P. 2011, Icarus, 212, 427
Schwartz, S., Richardson, D., & Michel, P. 2012, Granular Matter, 212, 363
Schwartz, S. R., Michel, P., Richardson, D. C., & Yano, H. 2014, Planet. Space Sci., 103, 174
Seguin, A., Bertho, Y., & Gondret, P. 2008, Phys. Rev. E, 78, 010301
Stadel, J. 2001, PhD thesis, University of Washington, USA
Suzuki, H., Yamada, M., Kouyama, T., et al. 2018, Icarus, 300, 341
Watanabe, S.-i., Tsuda, Y., Yoshikawa, M., et al. 2017, Space Sci. Rev., 208, 3
Yu, Y., Richardson, D. C., Michel, P., Schwartz, S. R., & Ballouz, R.-L. 2014, Icarus, 242, 82
Zhang, Y., Richardson, D., Barnouin, O., et al. 2017, Icarus, 294, 98

4.5 Article MASCOT II

Numerical modeling of lander interaction with a low-gravity asteroid regolith surface - II

Interpreting Hayabusa2 MASCOT successful landing

by

Florian Thuillet, Patrick Michel, Jens Biele, Shingo Kameda, Seiji Sugita, Eri Tatsumi, Stephen R. Schwartz, and Ronald-Louis Ballouz

2019, *A&A*, accepted under minor revisions

Abstract

JAXA asteroid sample return mission Hayabusa2 reached its target (162173) Ryugu in June 2018 and released European lander MASCOT in October 2018. MASCOT successfully landed on the surface and Hayabusa2 Optical Navigation Camera system has been able to image parts of MASCOT's trajectory. This work builds on our first study of interactions between a landing package and a granular material, in the context of MASCOT on Ryugu. The purpose is to expand our knowledge in this field, and to help constrain physical properties of surfaces, by considering observations of Ryugu from orbit and MASCOT's actual trajectory. We ran a new campaign of numerical simulations using the same N-body code pkdgrav, with the soft-sphere discrete element method, by expanding our parameter space. The surface is modeled as a granular medium, but we also considered the presence of a larger aggregate in the bed and a rigid wall. MASCOT is faithfully modeled as the actual one, and we considered different impact angles, speeds, or surface slopes. We were particularly interested in the outgoing-to-incoming speed ratio. We find that the presence of a boulder in the bed generally increases both the stochasticity of the outcomes and the speed ratio, and the closer the boulder, the larger the increases. We also find that a slope does not affect our previous results, and that the impact speed has no influence on the speed ratio for moderate-friction material. Finally, we find that a speed ratio as low as 0.3 can occur with a solid rock and not only with a soft surface, meaning that

inferring surface physical properties from outcomes such as the speed ratio must be done with caution.

Astronomy & Astrophysics manuscript no. output
July 31, 2019

Numerical modeling of lander interaction with a low-gravity asteroid regolith surface - II

Interpreting Hayabusa2 MASCOT successful landing

Florian Thuillet[1], Patrick Michel[1], Jens Biele[2], Shingo Kameda[3], Seiji Sugita[4,5], Eri Tatsumi[4,6], Stephen R. Schwartz[7], and Ronald-Louis Ballouz[7]

[1] Université Côte d'Azur, Observatoire de la Côte d'Azur, CNRS, Laboratoire Lagrange, Bd de l'Observatoire, CS 34229, 06304 Nice cedex 4, France
e-mail: fthuille@oca.eu

[2] DLR German Aerospace Center, Micro-Gravity User Support Center, 51147 Cologne, Germany

[3] Department of Physics, Rikkyo University, Tokyo, Japan

[4] Department of Earth and Planetary Science, University of Tokyo, 7-3-1 Hongo, Bunkyo-ku, Tokyo 113-0033, Japan

[5] Research Center for the Early Universe, University of Tokyo, 7-3-1 Hongo, Bunkyo-ku, Tokyo 113-0033, Japan

[6] Instituto de Astrofísica de Canarias (IAC), C/Vía Láctea s/n, 38205 La Laguna, Tenerife, Spain

[7] Lunar & Planetary Laboratory, University of Arizona, Tucson, AZ, USA

July 31, 2019

ABSTRACT

Context. JAXA asteroid sample return mission Hayabusa2 reached its target (162173) Ryugu in June 2018 and released European lander MASCOT in October 2018. MASCOT successfully landed on the surface and Hayabusa2 Optical Navigation Camera system has been able to image parts of MASCOT's trajectory.
Aims. This work builds on our first study of interactions between a landing package and a granular material, in the context of MASCOT on Ryugu. The purpose is to expand our knowledge in this field, and to help constrain physical properties of surfaces, by considering observations of Ryugu from orbit and MASCOT's actual trajectory.
Methods. We ran a new campaign of numerical simulations using the same N-body code `pkdgrav`, with the soft-sphere discrete element method, by expanding our parameter space. The surface is modeled as a granular medium, but we also considered the presence of a larger aggregate in the bed. MASCOT is faithfully modeled as the actual one, and we considered different impact angles, speeds, or surface slopes. We were particularly interested in the outgoing-to-incoming speed ratio.
Results. We find that the presence of a boulder in the bed generally increases both the stochasticity of the outcomes and the speed ratio, with larger increases when the boulder sits closer to the surface. We also find that a slope does not affect our previous results, and that the impact speed has no influence on the speed ratio for moderate-friction material. Finally, we find that a speed ratio as low as 0.3 can occur with a solid rock and not only with a soft surface, meaning that inferring surface physical properties from outcomes such as the speed ratio must be done with caution.

Key words. Minor planets, asteroids: individual: (162173) Ryugu – Methods: numerical

1. Introduction

Our knowledge of low-speed impacts into granular media has significantly increased during the last decade. Studies on granular material were initiated to better understand the behavior of this medium on Earth, with various industrial applications, but the discovery that the surface of asteroids is covered with granular material called regolith (which can appear in very different forms and does not necessarily blanket entire bodies), initiated a new area of research in planetary science devoted to the understanding of granular material dynamics on low-gravity bodies. In particular, the development and the proceedings of two sample return missions from asteroids, Hayabusa2 (Watanabe et al. 2017) and OSIRIS-REx (Lauretta et al. 2017), were two powerful motors for the activity in this field. A series of experiments have since been conducted to better understand the dynamics ruling low-speed impacts into such media.

Most of them were conducted under Earth gravity, for obvious reasons of feasibility. From these experiments can be extracted several characteristics of low-speed impacts in granular material, such as the drag-force law stopping the impactor (for example Katsuragi & Blum (2017) for dust aggregates, Katsuragi & Durian (2007) for glass beads, and Uehara et al. (2003) for several granular media), and properties of the crater formed by the impact (Uehara et al. 2003; Walsh et al. 2003; de Vet & de Bruyn 2007).

However, to better replicate an asteroidal environment, reduced-gravity experiments can be performed on Earth thanks to Atwood machines (Murdoch et al. 2017), or with parabolic flights (Colwell et al. 2008, 2015). With these methods can be reached gravities as low as 10^{-2} g. Another solution is to perform experiments in space, for example in the Space Shuttle (Colwell 2003), where the gravitational acceleration can go down to 10^{-4} g. From these experiments was shown that the behavior of an impactor can vary depending on the gravity, and that a smaller gravity incites bouncing (Brisset et al. 2018).

Numerical simulations can be a manner to bypass the gravity problem, as the gravitational field is usually a modifiable parameter. They first need to be validated by experiments but are a powerful tool to explore wider parameter spaces.

The purpose of this study is to expand our knowledge of low-speed impacts through numerical simulations. It consists of a direct application to Hayabusa2 lander MASCOT. Hayabusa2 is a JAXA asteroid sample return mission towards the C-type near-Earth asteroid (162173) Ryugu (Binzel et al. 2001; Wada et al. 2018). It arrived at Ryugu on June 27, 2018 (Watanabe et al. 2019), and successfully performed a first touch-down and sampling on February 21, 2019, with the goal of bringing asteroid material back to Earth in 2020.

Before the first touch-down, Hayabusa2 spacecraft released 2 mini-rovers MINERVA-II-1A/B in September 2018 (Van wal et al. 2018, 2019) and the CNES-DLR lander MASCOT (Ho et al. 2017) on October 3, 2018, which safely reached Ryugu's surface. MASCOT's purpose was to carry out in-situ measurements, thanks to an imaging spectrometer (Bibring et al. 2017), a camera (Jaumann et al. 2017), a radiometer (Grott et al. 2017), and a magnetometer (Herčík et al. 2017). MASCOT was safely found by Optical Navigation Camera Telescope (Kameda et al. 2017) on board the Hayabusa2 spacecraft, and data could be retrieved. In addition, supplementary information on Ryugu's surface properties can be obtained by reconstructing MASCOT's trajectory and in particular its bouncing on the asteroid's surface.

This study builds on Maurel et al. (2018); Thuillet et al. (2018), who modeled the landing of MASCOT on a regolith bed with a 19 cm s^{-1} speed, before the actual landing happened. Here, we perform new modeling aimed at understanding what actually happened during the actual landing and determining whether MASCOT's behavior can allow us to infer some properties of Ryugu's surface. We first remind the setup of our simulations in Section 2, and then we present our results obtained for different configurations that could represent what MASCOT experienced in Section 3.

2. Methodology

This study is the continuation of Maurel et al. (2018); Thuillet et al. (2018), and most of the parameters used in our simulations are identical. We use the N-body numerical code `pkdgrav` (Richardson et al. 2000; Stadel 2001; Richardson et al. 2009, 2011), with the implementation of the Soft-Sphere Discrete Element Method (SSDEM) (Schwartz et al. 2012) in order to better represent interactions between grains, such as friction and energy damping. The grain interactions were later improved by Zhang et al. (2017), by using spring-dashpot-slider models for the twisting and rolling frictions. `pkdgrav` was validated through several comparisons with experiments, such as hopper discharges (Schwartz et al. 2012), low-speed impacts (Schwartz et al. 2014; Ballouz 2017), and avalanches and angle-of-repose experiments (Yu et al. 2014; Maurel et al. 2018).

The setup is similar to Thuillet et al. (2018), i.e., a 150 cm-radius cylinder filled with grains and the lander MASCOT impacting it at 19 cm s^{-1} (except in Section 3.3). We generally consider a 30 cm high regolith bed, with a Gaussian size distribution (mean radius of 1 cm, standard deviation of 33%, and a cut-off at 1σ). The grain size distribution on Ryugu was actually measured to be a power law with an exponent of -2 to -2.5 (Sugita et al. 2019; Michikami et al. 2019). The resolution of ONC-T images at the actual MASCOT impact site is 30 cm pix^{-1}. Therefore, from these images it is difficult to determine the exact grain size of the region. The resolution near the impact site is 6 cm pix^{-1} as shown in Fig. S14B in Sugita et al. (2019). This shows that a large portion of the surface is covered with boulders with size comparable to or larger than MASCOT. But there are patches of regolith deposits with grains much smaller than MASCOT. In fact, the size distribution appears to continue down to 10 cm as shown in Fig. S14A (Sugita et al. 2019); however, there are regolith deposits with grain size smaller than 10 cm near MASCOT impact site. Since we do not know how the size distribution may change for 1 cm size grains, we assume a Gaussian distribution, which allows us to optimize the computation time of simulations and to cover a larger parameter space regarding other properties and impact conditions.

The different physical parameters used in our simulations are the same as the ones in Thuillet et al. (2018). The three friction parameters (static μ_s, rolling μ_r, and twisting μ_t), the shape parameter β, and the coefficients of restitution (the main source of energy dissipation) are shown in Table 1. The shape parameter β represents the angularity of the grains, even if the grains in our simulations are spherical, and it also plays a role in the angle of repose and the friction of the material. A description of the meaning of each coefficient can be found in Thuillet et al. (2018) and in Section 2 in Zhang et al. (2017). We chose two different materials, one with a high friction (gravel-like) and another with a moderate friction; these materials differ by the shape parameter, i.e., by the angularity of the grains. This results in different angles of repose: the highest angle of repose corresponds to the largest angularity.

As it was already done in Maurel et al. (2018); Thuillet et al. (2018), we use "walls", i.e., immobile surfaces, to model the cylinder containing the regolith bed. These walls have the same physical properties as the grains, except that we consider lower coefficients of restitution to avoid reflections of impact waves on the walls. We note that the boundary conditions do not seem to have an influence on the outcomes of the impact, particularly on the dynamics of MASCOT (Thuillet et al. 2018).

We model MASCOT as a 19.5 cm × 27.5 cm × 29 cm cuboid with a small prominence that represents the hyperspectral microscopic imager MicrOmega (Bibring et al. 2017). In our simulations, MASCOT is made of an assembly of "reactive" walls, i.e., walls that react with particles, and are therefore affected by the forces they apply on them. The assembly links the walls together, by having a center of gravity, a single matrix of inertia and three principal axes. The friction coefficients ruling the interactions between MASCOT and the grains are the same as the grain-grain coefficients. However, the coefficients of restitution of MASCOT correspond to the structural coefficient of restitution measured by Biele et al. (2017), i.e. 0.6, and their influence has been investigated in Thuillet et al. (2018).

In this study, we particularly looked at the outgoing-to-incoming speed ratio, as it is a general result that can be used in several environments and that was derived from images taken by the Hayabusa2 Optical Navigation Camera before and after the first bouncing. The speed ratio was also studied in Maurel

Table 1: Characteristics and properties of the two material types considered in our simulations. They are similar as Thuillet et al. (2018).

Material type	Angle of repose (°)	ε_n	ε_t	μ_s	μ_r	μ_t	β
Gravel-like friction	38.5	0.5	0.5	1.0	1.05	1.3	1.0
Moderate friction	28						0.2

et al. (2018); Thuillet et al. (2018), and therefore this enables direct comparisons with previous works. Moreover, since the asteroid surface is not flat, and the gravitational field we consider is only locally correct, the speed ratio is more convenient for comparisons with the actual landing.

3. Results

In this section we describe the different modifications that are operated on the setup, and the analyses of the results. First, because we cannot rule out this possibility when MASCOT bounced on Ryugu's surface, we introduce the notion of a boulder in the regolith bed, and study its influence on MASCOT's behavior. Then, we consider local variations of gravity, either with slopes or with the improved knowledge of Ryugu's gravity field, and then we consider a bounce on a wall representing a the vertical side of a high boulder, as suggested by Hayabusa2 Optical Navigation Cameras' images.

3.1. Presence of a boulder

We first analyzed the effect of a boulder buried in the regolith bed. In effect, we cannot rule out the possibility that a boulder was located just under the surface or deeper, and it would be totally undetectable from Hayabusa2's home position. Because of the Brazil-nut effect (Rosato et al. 1987; Maurel et al. 2017), we do not expect to have completely buried rocks in the regolith bed, but asteroids have already brought their fair share of surprises, Ryugu's images also showed that some boulders are at least partially buried (Sugita et al. 2019), and it is thus a possibility to consider.

Boulders, or aggregates, are modeled in `pkdgrav` as standard particles stuck together, meaning they behave as a rigid body. We considered ellipsoidal boulders with aspect ratios 1:0.74:0.43, corresponding to the ratios $\frac{a}{a}$, $\frac{b}{a}$ and $\frac{c}{a}$ of the semi-axes a, b and c. These ratios are close to the ones usually considered for products of catastrophic disruptions 2: $\sqrt{2}$:1, and to the mean aspect ratios experimentally observed on fragments resulting from high energy collisions by Fujiwara et al. (1978); Capaccioni et al. (1984, 1986); Durda et al. (2015); Michikami et al. (2016, 2018). These aspect ratios are very similar to the ones of boulders observed on (25143) Itokawa by Hayabusa (Michikami et al. 2016), and to the particles sampled by Hayabusa and brought to Earth from Itokawa (Tsuchiyama et al. 2014; Michikami et al. 2018).

Concerning the semi-major axis, 30 cm is a critical boulder length as it is a size comparable to the one of MASCOT, but cannot be detected from the Hayabusa2's home position. Thus, we took 30 cm as the longer dimension of the boulder. The second and third ones are coming directly out of the aspect ratios given before. As a result, the boulders we consider in our simulations consist of grains whose centers are located in a 30 cm × 22.2 cm × 12.9 cm ellipsoid. This is to be compared to the average particle radius of 1 cm. Boulders have a weight of about $5 - 5.6$ kg, and the same density as grains in the bed, i.e., about $1.1 - 1.3$ g cm^{-3}. They have the same friction coefficients and coefficients of restitution as individual grains, and react to grains and MASCOT.

We studied four vertical positions and three horizontal ones for the boulder aggregate. We looked at the influence of the boulder being at the bottom of the bed ("bottom"), in the middle of it ("midheight"), just under the surface ("top") or half buried ("surface"), as shown in Fig. 1.

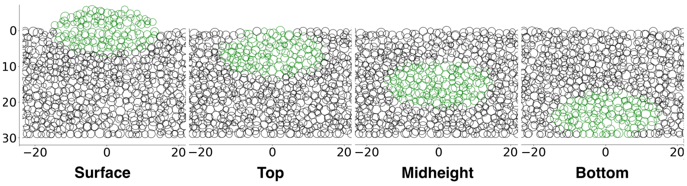

Fig. 1: Different vertical positions considered for the boulder. The average particle radius is 1 cm.

Concerning the influence of the boulder's vertical position, the speed ratio $\frac{V_{out}}{V_{in}}$ is shown on Fig. 2.

Firstly, as expected, we notice that the higher and the closer to the surface the boulder, the larger the differences with the "no boulder" case. We find that a boulder located on the bottom of the regolith bed has little to no influence on the speed ratio, and the disparities come more from the stochasticity of the impact than from the presence of a boulder at the bottom of the cylinder. Concerning midheight boulders, we find that in general, the speed ratios are higher than with no boulder or a bottom-located one. These differences can be as high as 0.2, corresponding to an outgoing speed difference of about 4 cm s^{-1}. For a moderate-friction material, as usual, differences are smaller, and stochasticity may have some role in these differences. We can also notice that on average the differences are more pronounced for a 30 cm bed than for a 40 cm one. This is due to the distance between the surface and the top of the boulder being logically shorter for a 30 cm bed.

If there is no boulder, the particles are mobile and when the lander impacts, the resulting transferred energy to particles in contact is propagated to others mobile particles, leading to ejecta and a reduction of the local porosity. However, if a boulder is present in the regolith bed, this compaction cannot operate. For a bottom boulder, it is located sufficiently far from the impact zone to have no influence, but in the case of a midheight or higher boulder, it can either be directly impacted by MASCOT or prevent compaction. On the other hand, as stated in Thuillet et al. (2018), for a back-corner-first impact, the outgoing energy partly comes from the rotation created at impact by the back corner of MASCOT encountering resistance, MASCOT pivoting until its front corner is also blocked by the regolith bed. The higher the resistance encountered, the higher the rotation rate and thus the higher the outgoing speed. Therefore, the presence of a boulder close enough to the impact location increases the outgoing-to-incoming speed ratio by increasing the resistance to penetration. Fig. 3 shows cross-section snapshots of MASCOT impacting the regolith bed containing a buried boulder.

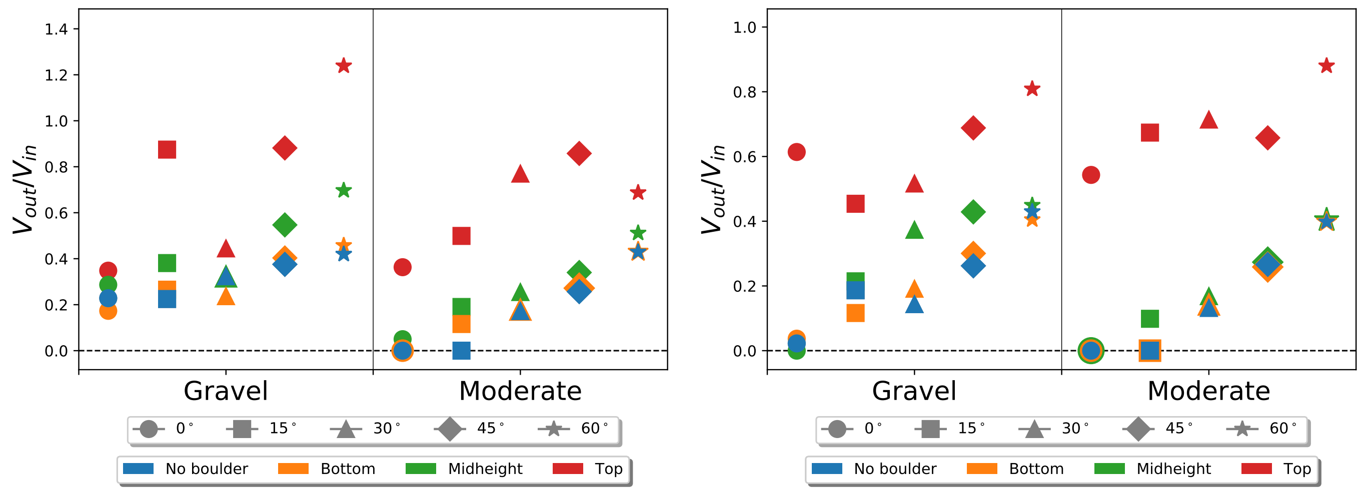

(a) 30 cm deep bed

(b) 40 cm deep bed

Fig. 2: Outgoing-to-incoming speed ratio of the lander as a function of the impact angle (“0° being a normal impact and larger angles corresponding to more grazing impacts), the material’s friction, and the position of the boulder, for a 30 cm bed (left) and a 40 cm bed (right). The columns represent the two frictions, the shapes of symbols represent the impact angle, and different positions of the boulder corresponds to the different colors. MASCOT lands on its back-corner first in these simulations.

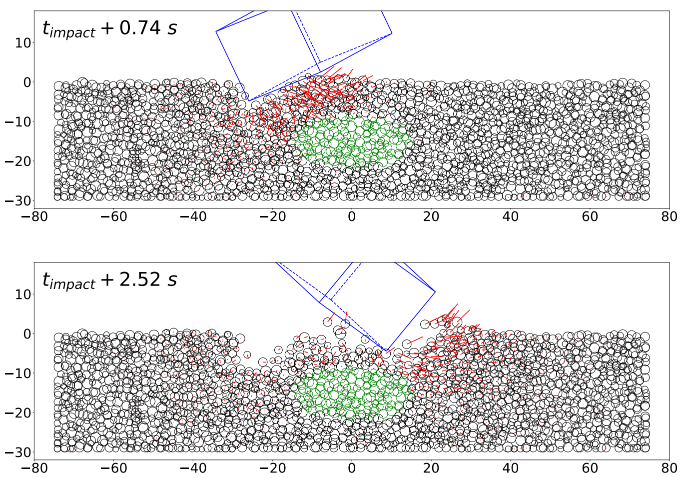

Fig. 3: Cross-section snapshots at two different times of MASCOT impacting the moderate-friction 30 cm regolith bed, with a buried boulder (in green), with an impact angle of 45°, on its back corner first. The blue cuboid represents MASCOT, and each red line indicates the projected 2-D velocity of the corresponding particle.

When the boulder is just under the surface (“top boulder”), we find that the outgoing speeds are much higher, for the same reasons as those previously stated. Moreover, the outcome is much more stochastic than for the other cases. Whereas we generally find that the speed ratio increases as a function of the angle, it is more erratic with a top boulder, as MASCOT comes directly in contact with the aggregate. In this case, we can even have speed ratios higher than 1. In our simulations, it only happens with a very grazing angle (60°), a 30 cm bed and a top boulder, and the outgoing angle is about 45°. Even in the worst case scenario, MASCOT’s vertical speed does not exceed Ryugu’s escape velocity, which is about 33 cm s^{-1} near the equator and about 36 cm s^{-1} near the poles. This was taken care of when designing MASCOT (structural coefficient of restitution lower than 1) and planning the release (low initial rotational energy that could be converted into translational energy, and initial translational velocity low enough to be half the escape velocity at impact). In addition, since MASCOT can impact different parts of the boulder according to its orientation, the results are very stochastic.

Concerning the penetration depth, we generally find smaller values with a boulder than without one. Moreover, the closer the boulder to the surface, the shallower the penetration, for the same reasons as for the speed ratio. While there is almost no difference between the speed ratios without boulder and with one located at the bottom of the bed, the penetration depth can differ from a few centimeters between these two cases.

With a surface boulder (a half-buried boulder), we find the same trends, i.e., a high stochasticity in the results depending on where MASCOT impacts the boulder, and potentially very high speed ratios. The different speed ratios obtained for the different vertical positions of the boulder are shown in Fig. 4, which confirms the trends we established earlier: the presence of a boulder on average increases the outgoing-to-incoming speed ratio as well as the stochasticity, and higher speed ratios are obtained with top or surface boulders. Figure 4 shows that, even if the highest speed ratios are obtained with a top boulder, just under the surface, the average speed ratios increase with the boulder’s height.

As the impact mechanism consists of MASCOT encountering resistance from the bed, pivoting and gaining rotational energy then partly transformed into translational energy, it is also interesting to look at MASCOT’s spin after the impact. It could be an indicator of the impact efficiency, and is also an important input for potential following bounces. Figure 5 shows the outgoing spin as a function of the speed ratio and the vertical position of the boulder. We notice that, in a general way, the higher the spin, the higher the speed ratio, and that we need a high speed ratio to lead to a high outgoing spin. Moreover, the stochasticity obtained with top and surface boulders is visible again. More generally, the higher the boulder in the bed, the larger the range of possible outcomes in terms of speed ratio and spin. If we de-

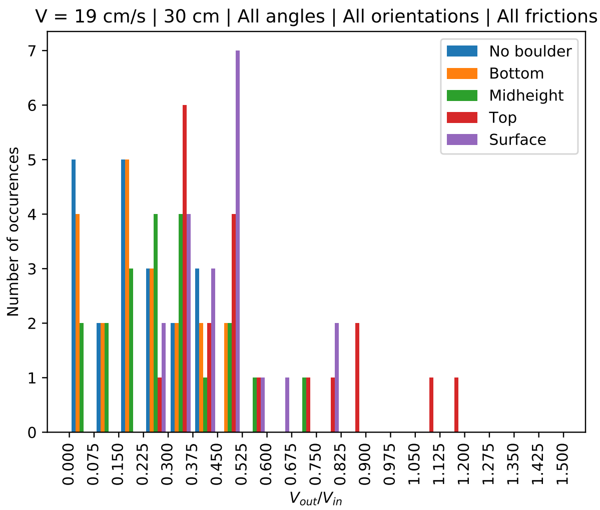

Fig. 4: Histogram of the outgoing-to-incoming speed ratio. Results were obtained with a 30 cm bed, two different frictions, five different angles, two different orientations and five boulder positions.

fine a cone of outcomes with its summit on the origin in Fig. 5, the higher the boulder, the larger the cone's angle. That is due to the large space of possibilities for MASCOT's behavior after the impact, when it comes in contact with a boulder.

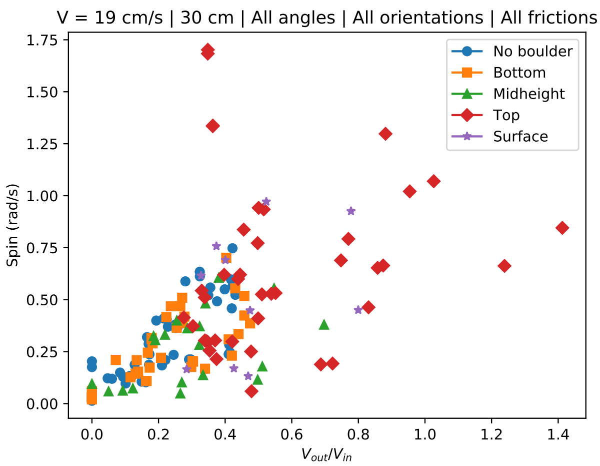

Fig. 5: MASCOT's spin as a function of the outgoing-to-incoming speed ratio for the five angles, two orientations, two frictions, and two depths considered in this study.

Furthermore, MASCOT directly impacting a boulder can lead to surprisingly low speed ratios, even with a hard (rigid and non-deformable) boulder like the one we considered. As shown in Fig. 4, for a surface boulder the speed ratios can reach values as low as 0.3 for several different configurations. This is due, in our simulations, not to a low restitution of energy after a single impact but to the accumulation of several contacts between MASCOT and the boulder. Indeed, the bounce can be decomposed in several contacts, for which each time a certain amount of energy is dissipated both in the boulder and MASCOT. The combination of these multiple contacts leads to a small overall speed ratio, even if each of them is a hard contact with a low energy dissipation.

Moreover, when MASCOT hits several times a boulder in a small amount of time, each contact generates a rotation opposed to the previous one, and therefore it prevents MASCOT from gaining a higher rotation rate. By successively changing the rotation axis or the direction of rotation, MASCOT cannot pivot as fast as it does for a standard back-corner-first landing on regolith (or when impacting a boulder in a different way), also leading to lower outgoing spin and/or speed.

In other words, measuring only the incoming and outgoing speed can be misleading regarding the surface softness and one needs to consider how many micro-bounces the lander may have experienced before moving to another location.

We also investigated the traces left after the impact in the presence of a boulder. Whereas in Thuillet et al. (2018), we showed that gravel-like and moderate friction surfaces reacted differently to the impact (deeper, more homogeneous and more circular with moderate friction than with gravel-like friction), a boulder has a significant effect on the traces, as it could be expected. Even if the boulder is buried under 8.5 cm of regolith (our equivalent of "midheight" with a 30 cm deep bed), it is visible in the traces. On Fig. 6 and 7, the boulder is discernible in the middle in the traces for moderate friction beds. For gravel-like friction beds, even if the boulder is not discernible, the differences between no boulder and a midheight one are still visible. For example, ejecta opposed to MASCOT's direction before impact are less abundant. While no boulder would enable MASCOT to dig more material and to go deeper, the aggregate restrains the particles from being pushed by the lander and remains in the crater after the impact. However, craters obtained with moderate friction regolith are still deeper and more homogeneous than the ones obtained with gravel-like grains. We recognize the no-boulder shapes with a midheight or lower boulder, apart from the boulder in the center. The boulder reduces the contrasts between the impact location and its vicinity, which complicates the task of finding MASCOT by looking at its traces, although hints of the impact can still be detected.

For a top boulder, if MASCOT touched the regolith bed before the boulder with one of its corners, a hole can be detected there, and its position and depth can be a proxy to understand how MASCOT bounced and where it is headed for. The hole is due to one of the corners digging into the ground, before experiencing hard resistance from the bed (due to the presence of the boulder that decreases the grains' mobility) or directly from the boulder. However, this state is only transitory: since the hole is deep but narrow, the bordering grains fall down the hole and fill it after MASCOT goes away, leaving few hints regarding the way MASCOT impacted.

We also looked at the influence of the horizontal position of the boulder, i.e., if it is located on the left or on the right of the landing point. We considered a midheight boulder located in the middle between the center of the cylinder and its edge, i.e. at a radius of 32.5 cm from the center (the cylinder's radius being 75 cm). Considering the size of MASCOT and the boulders, the closest edge of the boulder is from 1 to 5 cm from the edge of MASCOT (in the x-y plane). Fig. 8 shows that a "left" or "right" boulder has almost no influence on the speed ratio even if located on the top part of the packing (under the surface), contrarily to a midheight boulder below the impact point.

Therefore, we see that, for a boulder to have a significant influence on the impact outcome, it needs to be directly on MASCOT's trajectory or just below the impacted zone. As we saw that impacting a boulder adds a lot of stochasticity in the results, knowing that the 'zone of influence' of a boulder is reduced to the few dozens of centimeters above the boulder is reassuring for

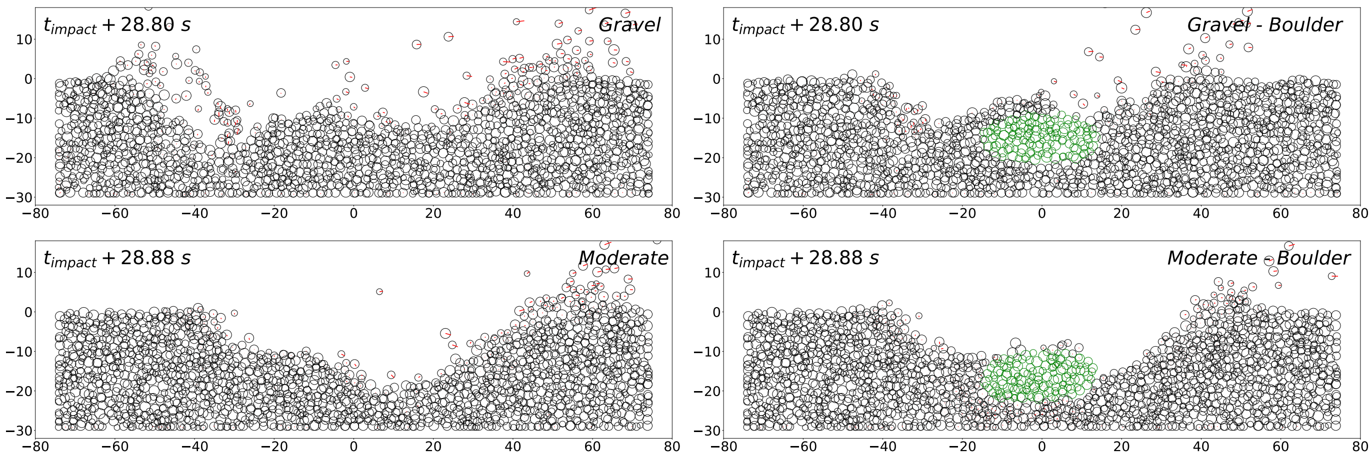

Fig. 6: Cross-section snapshots of MASCOT impacting different 30 cm regolith beds, with an impact angle of 45°, on its back corner first. The beds differ in friction (gravel-like and moderate) and the presence or not of a midheight boulder. The blue cuboid represents MASCOT, the green particles constitute the boulder, and each red line indicates the projected 2-D velocity of the corresponding particle. t_{impact} corresponds to the simulation time when MASCOT is for the first time in contact with the regolith.

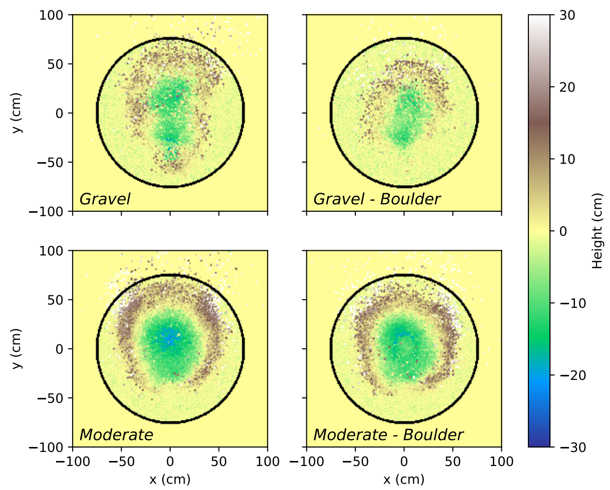

Fig. 7: Characteristics of the trace left by MASCOT about 29 s after having impacted different 30 cm regolith beds, with an impact angle of 45○, on its back corner first. t_{impact} corresponds to the simulation time when MASCOT is for the first time in contact with the regolith. The color bar represents the height of the regolith (boulder, bed and ejecta).

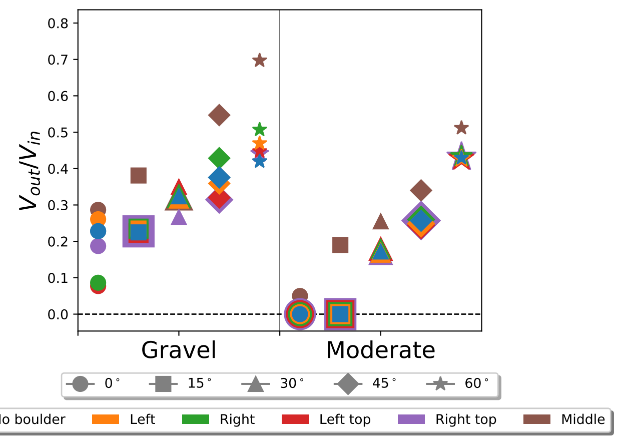

Fig. 8: Outgoing-to-incoming speed ratio of the lander as a function of the impact angle (0° being a normal impact and larger angles corresponding to more grazing impacts), the material's friction, and the position of the boulder, for a 30 cm bed. The columns represent the two frictions, the shapes of the symbols represent the impact angle, and their colors the position of the boulder. MASCOT lands on its back-corner first in these simulations.

MASCOT's or other landers' safety, as well as for understanding trajectories and determining surface properties from landing.

3.2. Gravity and slopes

Our first sets of simulations (Thuillet et al. 2018) were conducted with a gravity of $2.5 \cdot 10^{-4}$ m s^{-2}, which was Ryugu's gravity assumed before arrival computed by considering a simple rotating sphere approximation and the asteroid's radius measured from ground observations by Müller et al. (2011, 2017). Hayabusa2 measured accurately the gravity to be $1.2 \cdot 10^{-4}$ m s^{-2} for the landing site, a value lower than the one previously considered. We therefore checked if such a variation in the gravity field could lead to different impact outcomes.

We did not see any systematic variation in the different investigated outcomes, except for the traveled distance and the time of travel. The outgoing-to-incoming speed ratios are similar for the two gravity values considered here (see Fig. 9), and the outgoing angles are almost the same, thus leading to larger traveled distances and longer times for the lower gravity. Indeed, when we consider a ballistic trajectory (i.e., gravity being the only force), if the initial speed and angle are the same in both cases, half the gravity force corresponds to doubled traveled distance and time of travel. Therefore, these observed variations were expected. The non variation of impact characteristics such as the outgoing-to-incoming speed ratio or the penetration depth (see Fig. 10) may be due to the very low gravity field, as our simulations with slopes suggest.

All the simulations we conducted were run with a gravity field perpendicular to the surface. However, the surface will presumably not be totally flat, and for an asteroid of only about 870

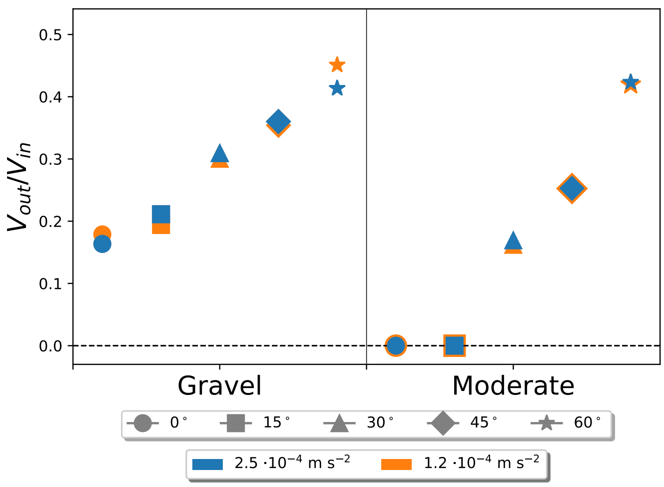

Fig. 9: Outgoing-to-incoming speed ratio of the lander as a function of the impact angle, the material's friction, and the position of the boulder, for a 30 cm bed. The columns represent the two frictions, the shapes of the symbol represent the impact angle, and their colors the gravity field. MASCOT lands on its back-corner first in these simulations.

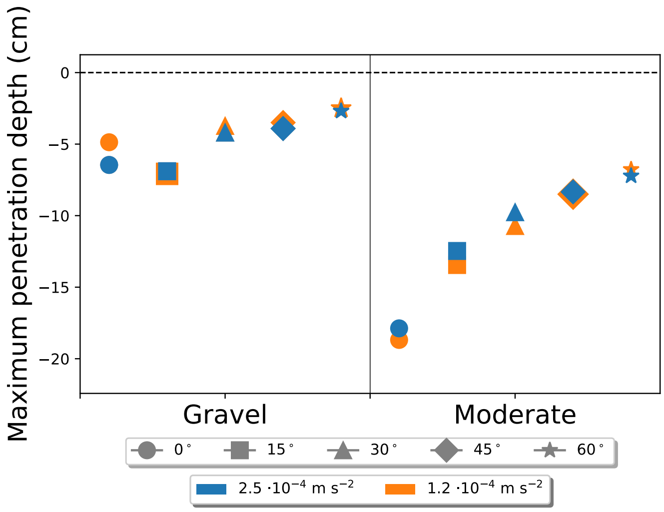

Fig. 10: Penetration depth of the lander as a function of the impact angle, the material's friction, and the position of the boulder, for a 30 cm bed. The columns represent the two frictions, the shapes of the symbol represent the impact angle, and their colors the gravity field. MASCOT lands on its back-corner first in these simulations.

m of diameter, we expect a lot of irregularities. Therefore, we want to be certain that the trends established in Thuillet et al. (2018) and in this article do not depend on the slope of the terrain. Ryugu's gravity is weak enough that it should not play any significant role in the mechanism governing the impact, but we nevertheless want to confirm the legitimacy of this assumption. For this purpose, we need to model slopes in our simulations. One of the solutions is to generate new packings with more particles on one side, elevating the walls of the cylinder to maintain them. However, having more particles leads to more time-consuming simulations, and creating such beds adds complexity. Another option is to remove enough particles from the bed to create a slope. the simulations then run even faster than previous ones, but a lower number of particles also means that it corresponds to shallower beds than it should have been, and direct comparisons are not straightforward anymore.

The solution we chose was to change the orientation of the gravity vector, keeping of course an angle smaller than the angle of repose of both considered materials. We consider four different angles: two positive ones (+15° and +25°) and two negative ones (−15° and −25°), as shown in Fig. 11.

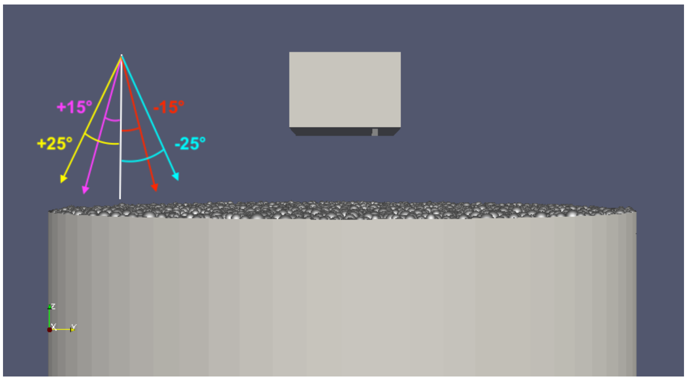

Fig. 11: Snapshot of MASCOT before impacting the regolith bed, with the description of the different gravity angles considered in this study to represent slopes.

The angles we considered are the rotation angles of gravity vectors around the x-axis, i.e. the axis normal to MASCOT's velocity before impact. Since in our simulations, MASCOT is impacting the bed from the negative part of the y-axis (from the right in Fig. 11 if the impact is not normal), if the angle is negative, that means that MASCOT is impacting the regolith bed on a downward slope. Respectively, if the gravity angle is positive, MASCOT is impacting an upward slope. These angles are smaller in absolute numbers than the angles of repose of both considered materials: gravel-like and moderate friction materials have respectively repose angles of 38.5° and 28°, which are higher than the highest considered slope of 25°. Therefore, we do not expect a perturbation of the bed when modifying the gravity. Yet, as a check, we ran simulations without MASCOT and observed the overall behavior of the particles forming the bed. Our expectations were confirmed as the bed remains in its equilibrium state.

The speed ratio, for a flat impact is shown in Fig. 12, for different impact angles, gravity angles, and material frictions. We see no significant influence of the gravity direction on the speed ratio, as well as on the post-impact velocity direction and on the other outputs, like for example the distance traveled and the penetration depth. We sometimes notice large differences between simulations for which only the gravity slope differs, but we believe these differences are mainly due to the stochasticity of the impact.

Firstly, we do not see any monotonic trend concerning the evolution of the speed ratio as a function of the slope; we could expect for example higher values for a downward slope or for an upward one, but the speed ratio does not seem to depend on the nature of the slope. The only exception is for a 15° impact angle and a gravel-like friction. In this case, downward slopes lead to higher speed ratios, and the steeper the slope, the more significant the effect. Unfortunately, we do not find this trend for other impact angles. However, even if this trend were to be true (and for example concealed here by the stochasticity of each impact), the variations are faint (less than 0.1 for the speed ratio) and therefore the influence of the slope angle is much weaker than that of other parameters such as the orientation, the impact angle, or other unknowns of the impact.

Secondly, the fact that the variations are almost non existent for a moderate friction bed while the gravity angle reaches values closer to the angle of repose falls in line with our statement that the variations are mainly due to the stochasticity or are very small. Indeed, for a moderate friction material, the stochasticity is always much smaller, as often said here and in (Thuillet et al. 2018), making the trends easier to identify.

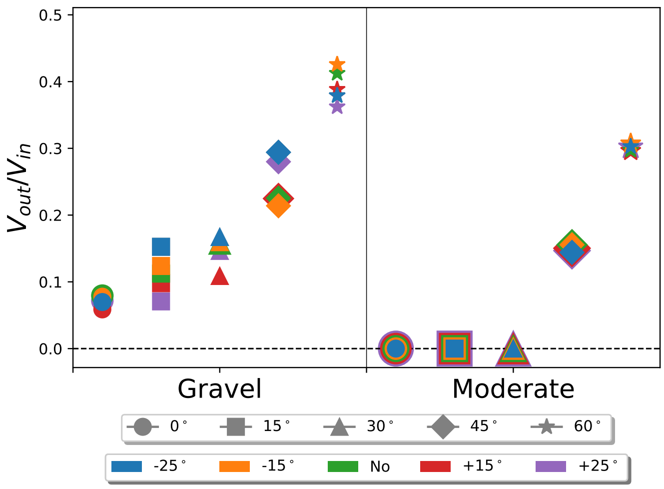

Fig. 12: Outgoing-to-incoming speed ratio of the lander as a function of the impact angle (0° being a normal impact and larger angles corresponding to more grazing impacts), the material's friction, and the gravity slope, for a 30 cm bed. The columns represent the two frictions, the shapes of the symbols represent the impact angle, and their colors the gravity slope. MASCOT lands flat in these simulations.

The negligible influence of the gravity angle on the results is mainly due to the very low gravity. Indeed, the gravity is about a hundred thousand times lower than the one we are used to on Earth (9.81 m s^{-2} compared to 1-2.5$\times 10^{-4}$ m s^{-2}), which makes a modification in the orientation of the gravity vector a very tiny variation in absolute numbers for the different components.

These simulations tend to show that the gravity slope has no significant effect on MASCOT's impact mechanisms (at least for slopes gentle enough, i.e., with angles lower than the angle of repose of the material), and therefore our results concerning speed ratios among others should still be valid if the lander impacts a non-horizontal terrain.

3.3. Impact speed

The impact speed is loosely constrained, because of the uncertainties on Ryugu's shape and mass prior to arrival, as well as on MASCOT's release. It is therefore important to check if the impact speed has a major influence on the various outcomes, like the outgoing-to-incoming speed ratio. Indeed, it is interesting to test the stability of our results when the impact speed changes, for example for the reconstruction of the trajectory or to learn about the surface physical properties by looking not only at the first-impact traces but also at the ones at the following impacts. Also, it is interesting to investigate the traveled distances and times of travel for the different possible impact speeds (first impact and/or following ones). Furthermore, it could be interesting to check if the penetration depth in our simulations increases with the speed as given in impact cratering scaling laws.

We ran simulations with different impact speeds, from 2 to 20 cm s^{-1}. In general, we do not expect impact speeds larger than 20 cm s^{-1}, and therefore we used this speed value as a maximum. Our simulations were also conducted for different impact angles to check if the incoming speed has any influence on the trends we previously established (Thuillet et al. 2018).

First of all, there is clearly a difference between gravel-like and moderate-friction simulations, even in the evolution of the investigated outcomes as a function of impact speed. For a moderate-friction bed, the trends are much easier to establish and identify than for other dependencies, like the impact angle and the bed depth. Concerning the outgoing-to-incoming speed ratio, the values obtained with both frictions are shown in Fig. 13 for the five considered impact angles, different speeds, and a back-corner-first orientation.

The outgoing speed is set to 0 if the lander does not bounce (if all of its height corners do not go higher than the initial surface level); this is the case for very slow impact speeds and therefore the lowest speed value in Fig. 13 has to be considered with caution. This may for example explain why the speed ratio drops to 0 in Fig. 13a for a 60° impact at about 2 cm s^{-1}, whereas it was much closer to 0.4 for all higher speeds.

Figure 13a shows that the speed ratio is almost constant for each impact speed considered. This means that the mechanism does not depend on the incoming speed. We can also notice that, as we previously stated, the speed ratio generally increases with the impact angle, and this seems to be true whatever the incoming speed (at least for speeds higher than 5 cm s^{-1}).

However, it is much more complicated to establish a trend for a gravel-like bed. As shown on Fig. 13b, when the particles making up the bed have a high friction, the speed ratio can be almost constant (45° impact), slightly increasing (60° impact), or showing peaks for specific speed values (like the 15° impact at about 14 cm s°). Once again, we see that tendencies are harder to establish for a gravel-like bed: the general higher friction represented by the higher β coefficient (meaning that particles behave less like spherical particles but more like angular ones) makes the bed very sensitive to each subtle change in the impact conditions. It is therefore difficult to claim that in a general way, the speed ratio does not depend on the impact speed from the gravel-like bed simulations.

4. Conclusion

In this paper we performed new simulations of the Hayabusa2 lander MASCOT begun in Maurel et al. (2018); Thuillet et al. (2018), by expanding the parameter space and considering new setups accounting for actual MASCOT landing observations. In general, these simulations allow improving our understanding of low-speed impacts of non-spherical objects on low gravity surfaces, accounting for different contexts and impact geometries. Their outcomes can thus also be directly used to study other phenomena than the landing of a lander, such as the low-speed impact of a non-spherical rock on an asteroid, and its consequences.

We first looked at the influence of a boulder in the regolith bed, and we found that if the boulder is buried about 15 cm under the surface, it has no influence on the outcomes of the impact. Otherwise, the higher the boulder, the larger the stochasticity, and in a general way the higher the outgoing-to-incoming speed ratios. If a boulder is located on the side of the impact point, it has little to no influence on the lander's bouncing behavior.

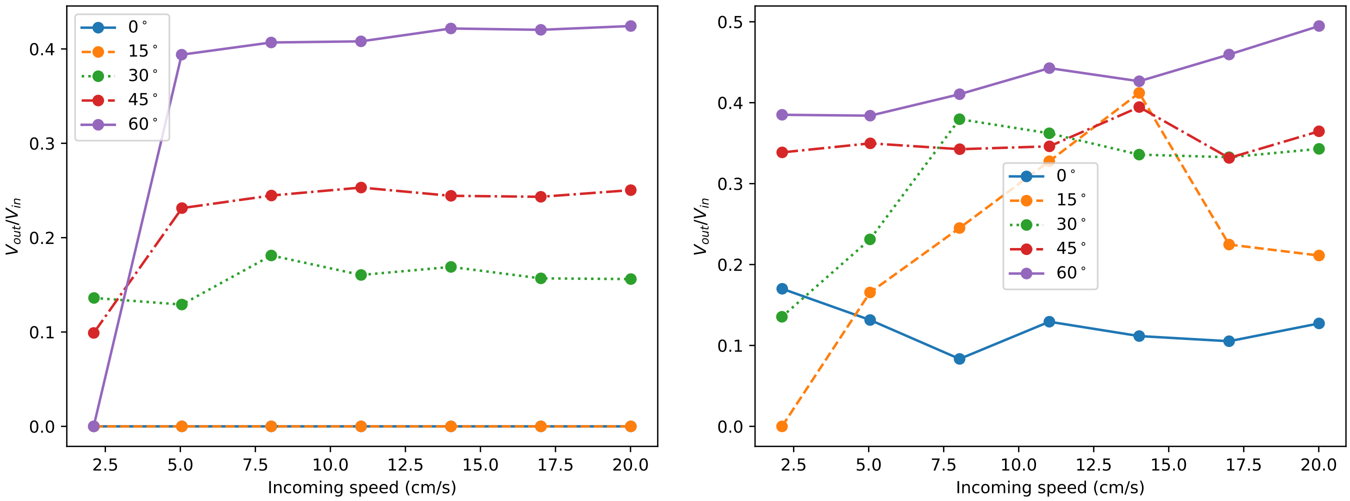

(a) Moderate-friction bed

(b) Gravel-like bed

Fig. 13: Outgoing-to-incoming speed ratio of the lander as a function of the impact speed and angle. MASCOT lands on a gravel-like bed (left) or a moderate-friction one (right) and on its back-corner-first in these simulations.

We also found that landing on a rigid boulder can result in speed ratios as low as 0.3.

Moreover, we considered the actual gravity of Ryugu measured by Hayabusa2 (about half the magnitude used in our former work) and noticed that results stay unchanged. When changing the slope (i.e., the gravity vector orientation), variations seem more due to stochasticity than to a real influence of the slope. This can be explained by the very low magnitude of the gravitational field.

Concerning the impact speed, for speeds high enough to allow bouncing, the speed ratio does not seem to depend on the impact speed, for a moderate-friction regolith bed. However, for a gravel-like regolith, a trend is much harder to define, even if a constant speed ratio is noticeable for several angles. Due to the increased stochasticity in the gravel-like case, it is difficult to be sure that the speed ratio is constant or if it increases with the impact speed.

These results and previous ones from Maurel et al. (2018); Thuillet et al. (2018) can help determine or constrain the physical properties of Ryugu and of other small bodies, from observations either of the trajectory of a natural or artificial impacting device with non-spherical shape or the traces left on the surface by a low-speed impact. Observed actual particle distribution on Ryugu may be different from our assumption, and in the future it would be interesting to consider different distributions than the Gaussian one. To improve even more the comparisons with the rocky surface of Ryugu, the implementation of breakable aggregates would be a significant step forward. However, setting up the value of the critical deformation leading to rupture can only be based on assumptions and a large range will need to be covered to explore its influence on the outcome.

Finally the finding that a speed ratio as low as 0.3 can happen even though the impact occurs on a solid rock has strong implications as it indicates that a low speed ratio does not necessarily implies a soft surface but can rather be due to the impact geometry and the accumulation of microbounces. Therefore interpreting the outcome of a low speed impact in terms of surface properties must be done with caution.

Acknowledgements. F.T. is supported by a PhD fellowship of the University of Nice-Sophia. P.M. and F.T. acknowledge funding support from the French space Agency CNES, as well as from Academies of Excellence: Complex systems and Space, environment, risk, and resilience, part of the IDEX JEDI of the Université Côte d'Azur in connection with its Center for Planetary Origins (C4PO). Simulations were performed at Mésocentre SIGAMM hosted at the Observatoire de la Côte d'Azur. This study was supported by the Japanese Society for Promotion of Science (JSPS) Core-to-Core program "International Network of Planetary Sciences.

References

Ballouz, R.-L. 2017, PhD thesis, University of Maryland, College Park
Bibring, J.-P., Hamm, V., Langevin, Y., et al. 2017, Space Science Reviews, 208, 401
Biele, J., Kesseler, L., Grimm, C. R., et al. 2017, arXiv e-prints, arXiv:1705.00701
Binzel, R. P., Harris, A. W., Bus, S. J., & Burbine, T. H. 2001, Icarus, 151, 139
Brisset, J., Colwell, J. E., Dove, A., et al. 2018, Progress in Earth and Planetary Science, 5, 73
Capaccioni, F., Cerroni, P., Coradini, M., et al. 1986, Icarus, 66, 487
Capaccioni, F., Cerroni, P., Coradini, M., et al. 1984, Nature, 308, 832
Colwell, J. E. 2003, Icarus, 164, 188
Colwell, J. E., Brisset, J., Dove, A., et al. 2015, European Planetary Science Congress, EPSC2015
Colwell, J. E., Sture, S., Cintala, M. J., et al. 2008, Icarus, 195, 908
de Vet, S. J. & de Bruyn, J. R. 2007, Physical Review E, 76, 041306
Durda, D. D., Campo Bagatin, A., Alemañ, R. A., et al. 2015, Planetary and Space Science, 107, 77
Fujiwara, A., Kamimoto, G., & Tsukamoto, A. 1978, Nature, 272, 602
Grott, M., Knollenberg, J., Borgs, B., et al. 2017, Space Science Reviews, 208, 413
Herčík, D., Auster, H.-U., Blum, J., et al. 2017, Space Science Reviews, 208, 433
Ho, T.-M., Baturkin, V., Grimm, C. R., et al. 2017, Space Science Reviews, 208, 339
Jaumann, R., Schmitz, N., Koncz, A., et al. 2017, Space Science Reviews, 208, 375
Kameda, S., Suzuki, H., Takamatsu, T., et al. 2017, Space Science Reviews, 208, 17
Katsuragi, H. & Blum, J. 2017, The Astrophysical Journal, 851, 23
Katsuragi, H. & Durian, D. J. 2007, Nature Physics, 3, 420
Lauretta, D. S., Balram-Knutson, S. S., Beshore, E., et al. 2017, Space Science Reviews, 212, 925
Maurel, C., Ballouz, R.-L., Richardson, D. C., Michel, P., & Schwartz, S. R. 2017, Monthly Notices of the Royal Astronomical Society, 464, 2866
Maurel, C., Michel, P., Biele, J., Ballouz, R.-L., & Thuillet, F. 2018, Advances in Space Research, 62, 2099
Michikami, T., Hagermann, A., Kadokawa, T., et al. 2016, Icarus, 264, 316
Michikami, T., Honda, C., Miyamoto, H., et al. 2019, Icarus, 331, 179
Michikami, T., Kadokawa, T., Tsuchiyama, A., et al. 2018, Icarus, 302, 109

Müller, T. G., Durech, J., Hasegawa, S., et al. 2011, Astronomy & Astrophysics, 525, A145
Müller, T. G., Durech, J., Ishiguro, M., et al. 2017, Astronomy & Astrophysics, 599, A103
Murdoch, N., Avila Martinez, I., Sunday, C., et al. 2017, Monthly Notices of the Royal Astronomical Society, 468, stw3391
Richardson, D. C., Michel, P., Walsh, K. J., & Flynn, K. W. 2009, Planetary and Space Science, 57, 183
Richardson, D. C., Quinn, T., Stadel, J., & Lake, G. 2000, Icarus, 143, 45
Richardson, D. C., Walsh, K. J., Murdoch, N., & Michel, P. 2011, Icarus, 212, 427
Rosato, A., Strandburg, K. J., Prinz, F., & Swendsen, R. H. 1987, Physical Review Letters, 58, 1038
Schwartz, S. R., Michel, P., Richardson, D. C., & Yano, H. 2014, Planetary and Space Science, 103, 174
Schwartz, S. R., Richardson, D. C., & Michel, P. 2012, Granular Matter, 14, 363
Stadel, J. 2001, PhD thesis, University of Washington
Sugita, S., Honda, R., Morota, T., et al. 2019, Science, 364, eaaw0422
Thuillet, F., Michel, P., Maurel, C., et al. 2018, Astronomy & Astrophysics, 615, A41
Tsuchiyama, A., Uesugi, M., Uesugi, K., et al. 2014, Meteoritics & Planetary Science, 49, 172
Uehara, J. S., Ambroso, M. A., Ojha, R. P., & Durian, D. J. 2003, Physical Review Letters, 90, 194301
Van wal, S., Tsuda, Y., Yoshikawa, K., et al. 2018, Journal of Spacecraft and Rockets, 55, 797
Van wal, S., Yoshikawa, K., & Tsuda, Y. 2019, AAS 19-243: Deployment Analysis and Trajectory Reconstruction of MINERVA-II Rovers on Asteroid Ryugu, Tech. rep., JAXA, Sagamihara
Wada, K., Grott, M., Michel, P., et al. 2018, Progress in Earth and Planetary Science, 5, 82
Walsh, A. M., Holloway, K. E., Habdas, P., & de Bruyn, J. R. 2003, Physical Review Letters, 91, 104301
Watanabe, S.-i., Hirabayashi, M., Hirata, N., et al. 2019, Science, 364, 268
Watanabe, S.-i., Tsuda, Y., Yoshikawa, M., et al. 2017, Space Science Reviews, 208, 3
Yu, Y., Richardson, D. C., Michel, P., Schwartz, S. R., & Ballouz, R.-L. 2014, Icarus, 242, 82
Zhang, Y., Richardson, D. C., Barnouin, O. S., et al. 2017, Icarus, 294, 98

Hayabusa2 Sampling Mechanism

5

> *I don't like sand. It's coarse and rough and irritating and it gets everywhere.*
>
> — **Hayabusa2 sampler**
> (which never asked for this job)

Contents

This chapter presents the concept of the Hayabusa2 sampling mechanism and my simulations of the sampling, which also contributed to a better general understanding of the impact in a low-gravity granular material.

5.1 Description of the Hayabusa2 Sampling Mechanism

5.1.1 Sampling mechanism

As stated in Watanabe et al. (2017), the most crucial part of the mission is to efficiently collect asteroid samples and to bring them back to Earth. It is also the most challenging one, as it was already tried once in the history of asteroid exploration by Hayabusa and the sampling mechanism did not work (even if some samples were eventually recovered in the capsule back on Earth). The main difficulty is that the topology of the surface is not known prior to the arrival at Ryugu, and therefore the sampling mechanism is designed so that it can handle a range of surface properties that seem compatible with the very limited data provided by observations from Earth (Kim et al., 2013; Müller et al., 2017; Perna et al., 2017) and past asteroid missions. The goal of Hayabusa2 is to collect at least 100 mg of surface materials, with the specificity that three surface samplings are planned (Watanabe et al., 2017; Sawada et al., 2017b), with one inside or in the vicinity of the crater potentially generated by the small carry-on impacter (Saiki et al., 2017).

Hayabusa2 sampling mechanism is very similar to the previous one on board Hayabusa (Fujiwara et al., 2005; Yano et al., 2006), with slight but useful modifications (Sawada et al., 2017b). It is principally composed of three units: the sampler storage and transfer mechanism, the sampler horn, and the projectors. The sampler storage and transfer mechanism are located inside the spacecraft, and their purpose is to collect particles that reached the top of the sampling mechanism and securely store them into one of the three chambers. The sampler horn is a deployable assembly of tapered cylinders, that, once ready for sampling, is 1007 mm-long and has a circular aperture with a diameter of 140 mm (Sawada et al., 2017b). Near the top of the horn is a filter that let only pass through particles smaller than 1 cm across. On the bottom of the horn have been added teeth in order to scoop up particles during the sampling and increasing the chances of bringing back samples. Projectors are located near the top of the horn and are designed to shoot 17 mm-diameter, 4.85 g tantalum projectiles. There are three projectors, each with a projectile, for the three planned samplings. Different shapes for the projectile (Makabe et al., 2008) and different sampling systems (Yano et al., 2009) were investigated to optimize the ejected volume, and it was found that a conical projectile was the best for Hayabusa2 sampling mechanism, for a regolith surface. However, it was eventually decided to keep the same design as Hayabusa sampling mechanism to take advantage of its high technology readiness level, and therefore reduce the risks. More details on the sampling mechanism can be found in Sawada et al. (2017b).

5.1.2 Touchdown site selection

The sampling operation was supposed to consist of a free fall to the surface (with an accuracy from the navigation guidance system of about 50 m), a contact with the ground detected by the bending of the sampler horn, followed almost instantaneously by the firing of a projectile at 300 m s^{-1}. Then the spacecraft would activate thrusters, quickly ascend and leave the surface, and once far enough, decelerate. The bottom scoop-up part could pull up particles on the surface when the spacecraft would go up (because of bouncing or spacecraft thrust) and the decelerating phase would enable the ejected material to go up into the sample storage and transfer mechanism, to be collected Sawada et al. (2017b).

In order to perform this operation, the choice of the sampling site is essential. The different steps that led to the sampling are detailed in JAXA Hayabusa2 Project (2019c), and are summarized here. A list of requirements to determine the sampling site was established just after arrival, in August 2018. Because of solar panels and antenna, the sampling site latitude had to be between $-30°$ and $30°$, and the inclination of the surface should not exceed $30°$. Also, the accuracy of the navigation guidance system being conservatively 50 m, the site had to be a flat surface of about 100 m in diameter, and should not contain boulders higher than 50 cm, both to reduce risks of damaging the spacecraft. Finally, to preserve most fragile equipment, the surface temperature had to be smaller than $97°$ C. From these conditions and the shape model of Ryugu were chosen 15 potential sites through a safety analysis, then narrowed down to 7 sites, from image evaluation, that are shown in Fig. 5.1.

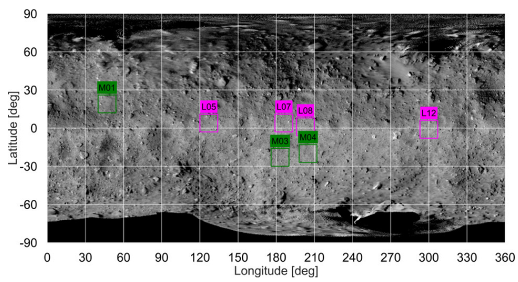

Fig. 5.1.: Seven selected sites for the first touchdown after first selections. M sites are , and L sites to Image credit: JAXA, University of Tokyo, Kochi University, Rikkyo University, Nagoya University, Chiba Institute of Technology, Meiji University, University of Aizu, AIST, CNES, DLR.

Images and measurements from orbit revealed that the critical criteria were the boulder distribution and heights. Indeed, Ryugu's rocky surface does not present large areas without any large boulder. One of the conditions had to be slightly relaxed to a maximum boulder height inferior to 70 cm, which was still considered as sufficiently safe since the horn is about 1 m-long. The low-latitude L08 site was finally chosen because of the lowest percentage of boulders, during the meetings held in mid-August in Tokyo, in which I had the honor to participate, and in which were also decided and validated MASCOT's and MINERVA II landing sites.

A series of operations called rehearsals were conducted to observe from closer distance the candidate site starting from September 2018. These operations revealed that the boulder distribution could jeopardize the mission safety, but inside L08 itself, smaller, safer, sites were observed. One of them, named L08-B, was chosen to perform a touchdown rehearsal on October 25, 2018, instead of the sampling itself, originally planned at this epoch, and the accuracy of the descent was confirmed to be improved to 15 m. However, it was not enough yet, as no safe area was as large as 30 m across.

Thus, another method was developed by taking advantage of the dropped target marker, called the "pinpoint touchdown" method, which enabled an accuracy of 2.7 m. Thanks to this advantageous method, a new touchdown site could be chosen inside L08, named L08-E1, with a diameter of 6 m and a boulder distribution that finally matches the initial requirements.

The touchdown operation was conducted from February 20 to 22, 2019, and, despite various issues, everything eventually worked as expected. The spacecraft was able to safely get back to its home position, and the high amount of ejecta observed by the publicly-founded camera on board the sampler suggests that material was collected.

5.1.3 Modeling the touchdown

Prior to the real operations, several ground-based tests were conducted with Hayabusa2 sampling mechanism. They were conducted with a copy that was stored in a similar environment on Earth to the actual one, and their purposes were to check if the sampler still worked more than a year after launch and to confront the sampler with a Ryugu-like material. From orbit, MINERVA, and MASCOT observations has been synthesized a Ryugu simulant, closer to gravel than fine dust. Trials with such simulant were positive and more than minimally required material was collected (Bartels, 2019). However, in order to also represent Ryugu's low-gravity environment, JAXA was interested into numerical simulations of the sampling, and provided us with the actual dimensions of the sampling mechanism. From these dimensions, we were able to model the sampler using the numerical code `pkdgrav`, presented in Section 2, using a setup very similar to the one we used for MASCOT (see Chapter 4).

We were confronted to a major problem: modeling a 300 m s^{-1} shot, and all the interactions between the projectile and the surface particles, requires a very low timestep. On the other hand, since we want to model a sampling and reduce the effects of boundary conditions on this sampling, we need particles small enough to be collected, and a bed whose cylinder is at least as large as the sampler's opening. However, the more particles there are, the longer the time the simulations take to run. Therefore, a compromise had to be reached to have realistic computation times and insightful simulations. We finally decided to consider a 15 cm-radius, 20 cm-deep, cylinder. With this radius, the cylinder is larger than twice the aperture of the sampler horn. Concerning the particle size, we used an average radius of 0.25 cm, half the size of what is allowed to pass the filter.

Concerning the simulation parameters, we had to define a spring constant k_n and a timestep Δ_t. These parameters are indeed hard to evaluate directly from physical characteristics of the process, at least if we want a timestep that is not too conservative and that therefore enables longer simulations. We found a suitable timestep and spring constant step by step, by first roughly determining a parameter space for which the simulations do not crash, and then refine this parameter space by looking at the maximum particle overlaps in the simulations. For example, if the spring constant is too low, the repulsive force is not strong enough for such an impact, and the overlap between particles becomes too large. On the other hand, if the spring constant is too high, particles repulse each other too strongly, and particles that were previously in contact end up too far from each other, making the simulation terminate. As we wanted our simulations to represent at least the first seconds after impact, we also tried to find the largest timestep with reasonable overlaps and not causing simulation crashes. For example, for the 300 m s^{-1} impact simulations, we chose a timestep of about $\Delta_t = 2.5 \cdot 10^{-7}$ s. The influence of these parameters is discussed in Section 5.3.

For the parameters ruling the physical properties of the material, we chose the same coefficients as for the gravel-like case of MASCOT (see Section 4). Since we ran simulations after arrival to Ryugu, we observed that the rough surface hinted at a high friction, and we only considered the gravel-like case. Chosen parameters are listed in Table 5.1.

Tab. 5.1.: Characteristics and properties of the two material types considered in our simulations

Material type	Angle of repose (°)	ε_n	ε_t	μ_s	μ_r	μ_t	β
Gravel-like friction	38.5	0.5	0.5	1.0	1.05	1.3	1.0

Generating the bed

Using the same method as for MASCOT, we decided to generate a regolith bed in a cylinder to represent Ryugu's surface. We first generated particles randomly inside and above the cylinder, respecting a Gaussian size distribution with a mean of $\overline{r} = 2.5$ cm, a standard deviation of $\sigma = 30\%$ and a cutoff at 1σ. We then let particles fall under Earth's gravity ($g_{\text{Earth}} = 9.81$ m s^{-2}). Using Earth's gravity for the fall allows us to gain non-negligible computation time. Once settled, before applying Ryugu's gravity, we remove every particle out of the cylinder, or above the top of the cylinder, and use two transitional gravities in order to ease the relaxation: $g_{\text{trans},1} = 10^{-2} g_{\text{Earth}}$ and $g_{\text{trans},2} = -2.55 \cdot 10^{-5} g_{\text{Earth}}$. Since we do not use the same timesteps and spring constants depending on the gravity, the transitional states prevent the simulation from crashing or particles from popping out of the bed. Finally, we set the simulation gravity to the considered Ryugu's gravity: $g_{\text{Ryugu}} = -0.01186$ cm s^{-2} $= 1.2 \cdot 10^{-5} g_{\text{Earth}}$, and let the bed finish relaxing.

At the end of the relaxation, when we consider the bed ready to be used for sampling simulations, the root-mean-square (RMS) speed of all particles constituting the bed is $v_{\text{rms}} = 0.030$ cm s^{-1}, and the maximum particle speed is $v_{\text{max}} = 0.79$ cm s^{-1}. Both are very small compared to the projectile speed (300 m s^{-1}), and we can therefore consider particles at rest during the simulation before the impact (which is almost instantaneous in our simulations). The perturbation triggered by the impact is much larger than the initial speed of the particles, and our bed can be considered as totally relaxed at the beginning of the sampling simulation.

At the end of the whole process to prepare the bed, we check that the size distribution of particles is still similar to the initial one, which means that there was no artificial selection in the sizes of the particles that were removed. The size distribution of the particles inside the bed is shown in Fig. 5.2a, with a minimum radius of about 0.175 cm, and a maximum one of 0.325 cm.

The particle distribution along the z-axis is shown in Fig. 5.2b. We see that the distribution is quite homogeneous, even on the edges of the cylinder. There are 101657 particles in the relaxed bed, with a grain density of 2.43 g cm^{-3}, the same as the one we took for MASCOT's simulations presented in Chapter 4. This leads to a bulk density for the cylinder of about 1.23 g cm^{-3}.

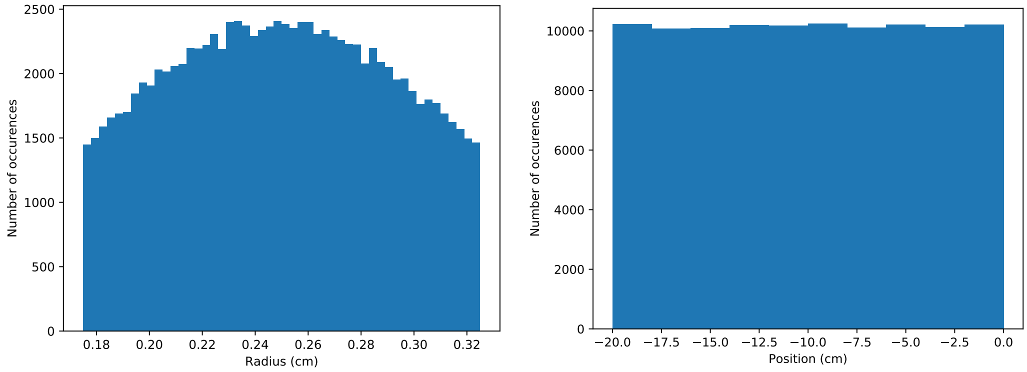

(a) Particle size distribution

(b) Particle distribution along z-axis

Fig. 5.2.: Histograms of the particle size distribution, supposed to be Gaussian, and of the particle distribution along the z-axis, for the bed used for sampling simulations.

Modeling the sampler

Thanks to the dimensions of the several parts of the sampler horn provided by JAXA, we were able to faithfully model the sampling mechanism. In `pkdgrav`, the tools at our disposal for modeling such shapes are walls. In the case of the sampling mechanism, we used tapered cylinders, also called conical frustums. Since it is an essential component of the sampler, we also modeled the filter. The whole sampling mechanism we considered in our simulations is shown in Fig. 5.3.

Unlike MASCOT, however, we did not use inertial walls for the sampler horn. To use a horn that reacts to the particle forces would require the knowledge of its exact moments of inertia, i.e., its inertia matrix and the principal axes. Since the horn is attached to the spacecraft, this would require the inertia matrix of the whole assembly, and make the modeling much more complex. Moreover, the horn is deformable (the bending of the horn triggers the projectors), and implementing deformable walls into `pkdgrav` would require a substantial amount of additional work. Therefore we considered a rigid horn, immobile in the bed cylinder's frame, and we do not take into account the scoop-up part of the sampling. Thus, in our simulations, collected particles come only from the impact of the projectile on the surface, and not from any contact between the bottom of the horn and the regolith bed.

We fix the sampler horn at 0.5 cm above the surface of the regolith bed, which represents the mean size of a particle. This way, we make sure that we do not miss too many particles that would be captured by the horn if its bottom were actually in contact with the surface.

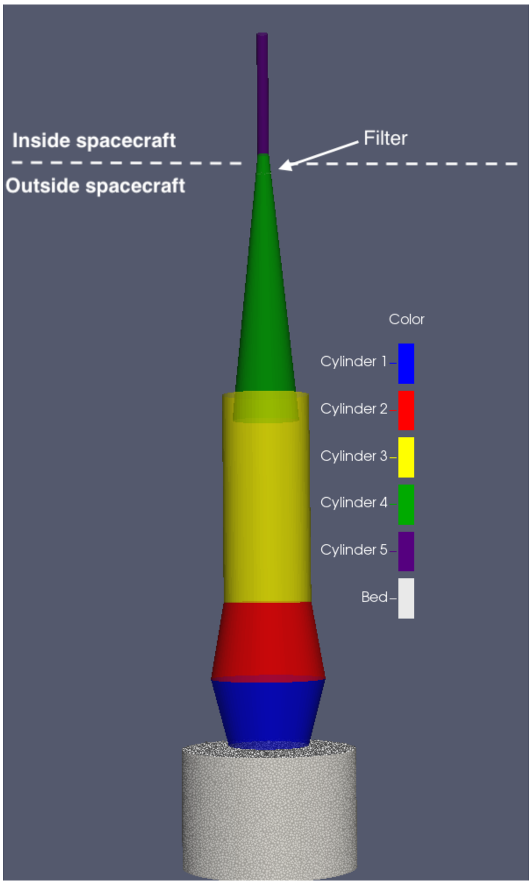

Fig. 5.3.: Model of the sampler with the bed, each color representing a cylinder and a part of the sampling mechanism.

5.1.4 Studying the cratering process

We also ran simulations without the sampler horn. This was the opportunity to characterize the impact and therefore link results we obtained with the sampler to what actually happens at the moment of impact, or to what it would lead to in term of crater formation. This was also a way to compare our results with previous papers about cratering processes, and check if our results look consistent with what had already been done.

Craters being the most frequently observed feature in the Solar System, a lot of work has already been done on crater formation. The purpose was to determine, either from the crater size and shape or the ejecta distribution, the physical properties of the surface. Moreover, counting craters is a proxy to the surface age (Tatsumi et al., 2018). In the case of asteroids, it can even lead to the age of the asteroid. Conferences, such as the Symposium on Planetary Cratering Mechanics (for example Roddy et al. (1977)), were held to discuss about these implications for planetary science and exchange new models or experimental results. Among this model was the Z-model proposed by Maxwell (1977), whose goal is to predict the streamlines inside an impacted target, depending only on one parameter Z. This model is discussed in Section 5.3, where we explain it and compare our results to it.

In "Impact Cratering. A Geologic Process.", Melosh (1989) gives a review of all the work that has been done in the previous years, and establish many analytical formulas for describing the physical mechanism at work. Holsapple (1993) also presented a review of the scaling of impact processes for a point source impact. Impacts are partitioned into two regimes: a "strength regime" and a "gravity regime". The strength regime is supposed to correspond to relatively-low-speed impacts and small craters, and the crater efficiency depends on the impact speed, and not on the gravity. On the other hand, the gravity regime is related to larger craters, and when the target's strength is small compared to the lithostatic pressure term, for example for large impactors. Usually, by necessity, experiments on Earth are limited to the strength, except when cohesionless granular materials are used.

A pair of scaling exponents are used in scaling rules, μ and ν, to respectively represent the influence of the impact speed and the mass density in far fields measurements. Depending on the value of μ, the kinetic energy or the momentum of the impactor can be the correct indicator of the outcomes of the impact. If we are in the momentum conservation mode, $\mu = \frac{1}{3}$, and if we have an energy scaling, $\mu = \frac{2}{3}$.

Since then, a lot of laboratory experiments and numerical simulations tried to confront the scaling theory to experimental data under Earth 1 g. Part of them were conducted with low-speed impacts, usually with objects falling into granular targets. In those experiments, the impact speed is generally smaller than 4.4 m s^{-1}, which corresponds to a free fall from a height of 1 m under Earth gravity. Some were more interested in the crater diameter and depth, as in general the crater diameter is the easiest dimension to measure and in theory the crater depth is assumed proportional to the diameter, with targets being either glass beads (Walsh et al., 2003; Vet et al., 2007), or various granular media (Uehara et al., 2003). The purpose is to discuss the coefficients ruling the dependency of the diameter and the depth on the projectile's properties and the impact speed. Others were more interested in the restraining drag force felt by the impactor, in dry granular media (Uehara et al., 2003; Katsuragi et al., 2007; Katsuragi et al., 2017), or glass beads immersed in a fluid (Nordstrom et al., 2013), in order to universalize a drag force and be able to predict the penetration depth of the impactor.

However, laboratory experiments were not restrained to free fall impacts, and medium-speed impacts up to 300 m s^{-1} can be reproduced thanks to spring-guns (Machii et al., 2013), light-gas guns (Yamamoto et al., 2005; Yamamoto et al., 2006; Yamamoto et al., 2009), or airsoft guns (Nakamura et al., 2013). From these experiments can be studied the transient crater growth (Yamamoto et al., 2006; Yamamoto et al., 2009), the ejecta characteristics and volume (Yamamoto et al., 2005; Makabe et al., 2008), penetration depth measurements (Nakamura et al., 2013), or threshold speeds to embed chondrules into matrices (Machii et al., 2013). The sampling mechanism of Hayabusa2 firing a 300 m s^{-1} projectile, this range of medium speeds is more suited for comparisons.

Numerical simulations were developed, inspired by the results of these experiments, and aiming for a much larger parameter space than what laboratory experiments allow (Mitani, 2003). Among them are DEM codes. By using such codes, Wada et al. (2006) looked at the crater formation and ejecta characteristics, and Schwartz et al. (2014) compared ejected volumes for different projectile shapes from experiments by Makabe et al. (2008). From previous analytic work like the Z-model (Maxwell, 1977) and the residual velocity (Melosh, 1985), new models also continued to be developed to better understand impact cratering mechanics and state predictive behaviors for numerical simulations (Kurosawa et al., 2019).

However, all the experiments and numerical modeling previously listed were conducted under Earth gravity, contrarily to crater formation on the surface of asteroids, or the impact of Hayabusa2 sampling. Cratering experiments in low-gravity or microgravity require appropriate equipment, and a considerable amount of time, either to build the experimental setup or to run them. Some experiments were made feasible thanks to the Space Shuttle, like COLLIDE (Colwell, 2003), parabolic flights, such as PRIME (Colwell et al., 2008; Colwell et al., 2015) or Nakamura et al. (2013), or drop towers like the Atwood machine described in Sunday et al. (2016) and used in Murdoch et al. (2017). Minimum gravitational acceleration reached for these experiments are about 10^{-2} g for the Atwood machine and parabolic flight experiments to 10^{-4} g for microgravity space experiments. Even if these considered gravities are still larger than the one of Ryugu, differences with 1 g experiments and modelings already appear, which motivates low-gravity studies. For example, Brisset et al. (2018) showed that under microgravity, impactor rebound happens even for low impact energies, and a higher mass of ejecta is produced.

Besides the difficulty of reaching Ryugu's gravity in experiments, another caveat is combining microgravity experiments and speeds as high as 300 m s^{-1}, which may not be considered as high speed for somebody familiar with hyper-velocity impacts, but are hard to reproduce in usually confined areas where microgravity is achieved. COLLIDE and PRIME only considered speeds lower than 2.3 m/s (Brisset et al., 2018), whereas Nakamura et al. (2013) could experiment with 70 m s^{-1} impacts. For both safety reasons and convenience, experimental studies of the Hayabusa2 sampling mechanism or similar impact speeds could not have been done before the actual sampling under Ryugu's environment conditions (vacuum, very low gravity, etc.).

It is therefore useful to take profit of numerical simulations of Hayabusa2 sampling mechanism to study the behavior of our granular bed during the impact, e.g., the ejecta characteristics and volume as well as the cratering process itself, without the sampler horn.

5.2 Simulation results

5.2.1 General results from simulations

The results of my simulations are presented in the article in Section 5.3. Concerning the crater formation, we find that predictions of the streamlines by the Z-model (Maxwell, 1977) fits well with our data, when we consider an instant not too soon after the impact (a stationary state as to be reached), and not too late, due to boundary conditions. We compared our work to previous experiments by Housen et al. (1983) and Yamamoto et al. (2006), and numerical simulations by Wada et al. (2006). We generally find similar processes for the crater formation, even if our gravity, much lower than the terrestrial gravity considered in previously mentioned studies, significantly increases the duration of the crater formation. Also, similarly to high-velocity impacts, we notice that less than 10% of the projectile's kinetic energy is usually converted into ejecta kinetic energy.

Concerning the ejecta, we find that doubling the impact speed halves the time needed to reach a certain amount of ejecta. If time is scaled with respect to the impact speed, volumes of ejected particles are similar for all impact speeds, which means impacting faster leads to the same excavation process happening faster, at least for the speed range considered (50 to 300 m s^{-1}). Cavity depths as functions of cavity radii are also very similar, which confirms that the impact formation should be the same for the several speeds considered. Moreover, most of particles are ejected with an angle between $48°$ and $54°$ from the horizontal for a 300 m s^{-1} impact, and the angle slightly decreases with a lower impact speed. Varying the normal coefficient of restitution of grains has an influence on the ejecta speed and angle, but not on the quantity. Moreover, with tilted angles, there are more high-speed ejecta, and their absolute velocity is higher. More details concerning the influence of the normal coefficient of restitution and the impact geometry can be found in the article in Section 5.3.

With the model of the sampler (see Section 5.1.3 and article in Section 5.3), we found that the mission goal to bring more than 100 mg is almost always reached after 1 s on the surface. In the actual sampling, more material is expected to be excavated, as the scoop-up part by the teeth at the bottom of the horn are present in the real case, and as the considered particles may be larger than actual ones. It was also found that no jamming is observed near the filter after 1 s, but it may happen with an expanded time on the surface. A second shot quickly after the first one, which could have been considered for the first touchdown, increases the ejecta volume, but not necessarily the collected volume, and could increase the probability of jamming.

Comparison with actual samplings

Before the return of Hayabusa2 to Earth, we do not have the possibility to directly measure whether particles were collected during the first touchdown. However, pictures of the first sampling were taken, and a comparison between our experiments and an actual picture from CAM-H on board Hayabusa2 is shown in Fig. 5.4.

On both images can be seen a lot of material ejected from the impact point. Material is ejected quickly after impact, in what also looks like a cone. Blocks larger than the size considered in the simulations are visible in the actual image, and by looking at the video we see aggregates breaking down into smaller pieces, which is a motivation for considering breakable aggregates in

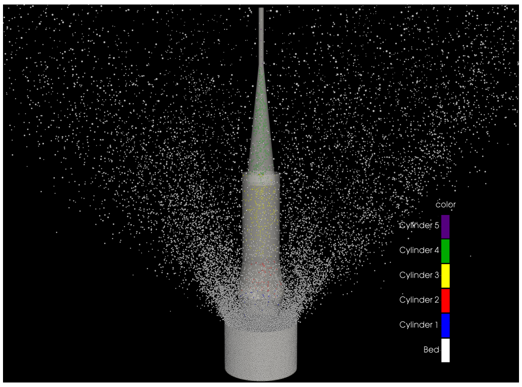

(a) Snapshot of a simulation of Hayabusa2 sampling 4.5 s after impact

(b) Image taken by CAM-H. Image credit: JAXA Hayabusa2 Project (2019a) in cooperation with Kimura lab., Tokyo University of Science

Fig. 5.4.: Comparison between numerical results and actual image from CAM-H of the first sampling.

future studies. However, smaller grains are also visible, and from the images we expect to have collected material.

The second sampling happened on July, 11 and aimed to collect particles near the impact crater formed by the Small Carry-On Impactor. It was once again successful, and images are shown in Fig. 5.5. These images also show small grains ejected either by the contact with the horn or by the projectile. These observations seem to confirm the presence of small grains on the surface, and show the ejection of lot of material, as was observed in our simulations.

However, these ejections of particles could also be due to the thruster firing, and it would be useful to try to determine by looking closely to the images, with the knowledge of the exact timings, when the thruster firing occur to try to differentiate the ejecta preceding and following the firing.

(a) Moment of touchdown

(b) 4 seconds after touchdown

Fig. 5.5.: Images taken by CAM-H of the second sampling. Image credit: JAXA Hayabusa2 Project (2019b) in cooperation with Kimura lab., Tokyo University of Science

5.3 Article Sampling Mechanism

Numerical modeling of medium-speed impact on a granular surface in a low-gravity environment

Application to Hayabusa2 sampling mechanism

by

Florian Thuillet, Patrick Michel, Shogo Tachibana, Ronald-Louis Ballouz, Stephen R. Schwartz

Submitted

Abstract

Even if craters are very common on Solar System body surfaces, crater formation in granular media such as the ones covering most of visited asteroids still needs to be better understood, above all in low-gravity environments. JAXA's sample return mission Hayabusa2, currently visiting asteroid (162173) Ryugu, is a perfect opportunity for studying medium-speed impacts into granular matter, since its sampling mechanism partly consists of a 300 m s^{-1} impact. In this paper, we look at medium-speed impacts, from 50 to 300 m s^{-1}, into a granular material bed, to better understand crater formation and ejecta characteristics. We then consider the sampler horn of Hayabusa2 sampling mechanism and monitor the distribution of particles inside the horn. We find that the cratering process is much longer under low gravity, and that the crater formation mechanism does not seem to depend on the impact speed, in the considered range. The Z-model seems to rightly represent our velocity field for a steady excavation state. From the impact, less than 10% is transmitted into the target, and grains are ejected mostly with angles between $48°$ and $54°$. Concerning the sampling mechanism, we find that for most of the simulations, the science goal of 100 mg is fulfilled, and that a second impact increases the number of ejecta but not necessarily the number of collected particles.

MNRAS **000**, 1–27 (2019) Preprint 7 October 2019 Compiled using MNRAS LATEX style file v3.0

Numerical modeling of medium-speed impacts on a granular surface in a low-gravity environment Application to Hayabusa2 sampling mechanism

Florian Thuillet,[1⋆] Patrick Michel,[1] Shogo Tachibana,[2,3] Ronald-L. Ballouz[4] and Stephen R. Schwartz[4]

[1] *Université Côte d'Azur, Observatoire de la Côte d'Azur, CNRS, Laboratoire Lagrange, Bd de l'Observatoire, CS 34229, 06304 Nice cedex 4, France*
[2] *UTOPS, University of Tokyo, Tokyo 113-0033, Japan*
[3] *Institute of Space and Astronautical Science (ISAS), Japan Aerospace Exploration Agency (JAXA), Sagamihara 252-5210, Japan*
[4] *Lunar & Planetary Laboratory, University of Arizona, Tucson, AZ, USA*

Accepted XXX. Received YYY; in original form ZZZ

ABSTRACT

Even if craters are very common on Solar System body surfaces, crater formation in granular media such as the ones covering most of visited asteroids still needs to be better understood, above all in low-gravity environments. JAXA's sample return mission Hayabusa2, currently visiting asteroid (162173) Ryugu, is a perfect opportunity for studying medium-speed impacts into granular matter, since its sampling mechanism partly consists of a 300 m s^{-1} impact. In this paper, we look at medium-speed impacts, from 50 to 300 m s^{-1}, into a granular material bed, to better understand crater formation and ejecta characteristics. We then consider the sampler horn of Hayabusa2 sampling mechanism and monitor the distribution of particles inside the horn. We find that the cratering process is much longer under low gravity, and that the crater formation mechanism does not seem to depend on the impact speed, in the considered range. The Z-model seems to rightly represent our velocity field for a steady excavation state. From the impact, less than 10% is transmitted into the target, and grains are ejected mostly with angles between 48° and 54°. Concerning the sampling mechanism, we find that for most of the simulations, the science goal of 100 mg is fulfilled, and that a second impact increases the number of ejecta but not necessarily the number of collected particles.

Key words: Minor planets, asteroids: individual: (162173) Ryugu – Methods: numerical

1 INTRODUCTION

Since the discovery of a fine-grained layer on the surface of asteroids (Robinson et al. 2002), termed regolith, understanding the dynamics of granular material in low-gravity environments has become crucial. This knowledge could help us better comprehend the outcomes of both low-speed and high-speed impacts on the surface of small bodies (Katsuragi 2016), and their surface evolutions and histories (Asphaug 2007; Melosh 2011). Moreover, the development and launch of two asteroid sample return missions, JAXA's Hayabusa2 (Watanabe et al. 2017) and NASA's OSIRIS-REx (Lauretta et al. 2017), further motivated research in this field. Indeed, understanding granular material serves a scientific purpose, but also an engineering one, particularly in the case of sample collection, where understanding and predicting the interactions with the surface is fundamental.

One of the main sources of information on Solar System bodies surface properties and histories are impact craters. Craters are the most frequently and easily observed surface features by space probes that performed a fly-by or a rendezvous to a small body. A planetary body's crater morphology and dimensions can help infer the physical properties of its surface and sub-surface. Furthermore, the size distribution of craters is a hint for the age of a surface, but craters have to be discriminated into categories to determine if they have been created by an exogenous impactor (primary craters) or by ejecta fallout (secondary craters). The correct interpretation of craters on the surface of asteroids requires a good understanding of crater formation

⋆ E-mail: florian.thuillet@oca.eu

on low-gravity surfaces made of regolith, for both low- and high-speed impacts (Hirata et al. 2009; Walsh et al. 2019).

Low-speed impacts on asteroids have also had a human origin, and are one of the chosen solutions for sampler return missions to collect material. JAXA chose for both Hayabusa and Hayabusa2 missions a sampling mechanism consisting of a projectile impacting the asteroid surface at 300 m s^{-1} (Sawada et al. 2017). Thus, increasing our knowledge on low-speed impacts on regolith material is also beneficial for the design of sampling mechanisms and for the interpretation of their outcome.

Analytical formulae have been derived from experiments to scale the cratering process in a general way, most often focusing on impacts that are equivalent to an explosion and for which a point source solution applies (Melosh 1989; Holsapple 1993). Some were more interested in very low speed impacts (less than 4 m s^{-1}), and among them different parts were emphasized, but always in the context of Earth's gravity, such as the restraining force (Katsuragi & Durian 2007; Katsuragi & Blum 2017) or the crater's shape and size (Uehara et al. 2003; Walsh et al. 2003; de Vet & de Bruyn 2007; Nordstrom et al. 2013). Others conducted experiments with much faster projectiles, closer to the speed used for the Hayabusa2 sampling mechanism: for example Yamamoto et al. (2005) looked at the velocity distribution of ejecta, Yamamoto et al. (2009) at the transient crater growth, and Nakamura et al. (2013) at the penetration depth of the impactor. Experiments have even been possible under low-gravity or microgravity, through the use of an Atwood machine (Murdoch et al. 2017) or parabolic flights (Nakamura et al. 2013; Brisset et al. 2018).

However, these experiments require a lot of time to set up, are limited by available material and equipment, and rarely achieve true micro-gravity conditions. In parallel to these experiments, numerical simulations could be developed and then compared to actual data. They enable an exploration of a wide parameter space and make it far easier to measure a system's physical properties that are otherwise difficult to collect. Comparisons between experiments and numerical simulations could then been done, for instance penetration depth measurements (Nakamura et al. 2013) and crater formation (Wada et al. 2006).

Before it was eventually decide that the Hayabusa2 sampling mechanism would adopt the same design as the Hayabusa mechanism with a semi-spherical projectile, experiments were done to study the influence of the projectile shape (Makabe & Yano 2008) on the amount of ejected mass. Numerical comparisons by Schwartz et al. (2014) were then done, but limited to experiments with impact speeds of 11 m s^{-1} in Earth gravity. Our study builds on an improved version of the code used by Schwartz et al. (2014) and considers the low-gravity environment of the Hayabusa2 target (162173) Ryugu (Binzel et al. 2001; Wada et al. 2018). Ryugu's surface is represented as a collection of grains with assumed physical and mechanical properties. We then develop numerical simulations of the Hayabusa2 sampling projectile impact with the surface to provide estimates of the amount of ejecta produced by the impact as well as the excavation and crater formation, as a function of assumed surface properties. We also compare our results to the numerical simulations of Wada et al. (2006) and the experiments of Housen et al. (1983); Yamamoto et al. (2003, 2005, 2006). Finally, we perform numerical simulations that include the exact geometry of Hayabusa2 sampling horn, in addition to the projectile, to monitor the amount of ejecta that may be captured in the different parts of the horn.

In Section 2, we describe the characteristics of our grains and briefly our method, and in Section 3 we present our results, without and with the sampling horn. In Section 4, we provide a discussion of these results and an outlook on future work.

2 METHOD

In this section, we describe the different choices we made to model Ryugu's surface, and the quantities we investigated and monitored.

2.1 Simulation parameters and setup

Our simulations were performed with the N-body gravity tree code `pkdgrav` (Richardson et al. 2000; Stadel 2001; Richardson et al. 2009, 2011). In order to model the interaction between regolith grains, we use the Soft-Sphere Discrete Element Method (SSDEM) version developed by Schwartz et al. (2012), improved with a new rotational resistance model for the grains (Zhang et al. 2017), and the addition of "reactive walls", i.e., inertial walls that react to particles' forces, contrarily to regular walls, (Maurel et al. 2018). The version used here is the same as the one used in Thuillet et al. (2018), and several comparisons with experiments have been run all along the development of the code to check the validity of the results, from silo discharges (Schwartz et al. 2012), to projectile penetrations (Schwartz et al. 2014) and measurements of the angle of repose for different materials (Yu et al. 2014; Maurel et al. 2018).

In order to represent the environment in which the Hayabusa2's sampling will be performed, we considered the low-gravity environment of the asteroid Ryugu, assuming a constant gravitational acceleration. We then investigate the sampling process only in a close area around the sampling system. The gravitational acceleration has been computed from the measurements done by Hayabusa2 (Watanabe et al. 2019) and from the approximate location of the sampling, leading to a value of $g = 1.19 \cdot 10^{-4}$ m s^{-2}.

We first ran simulations of the impact of the projectile without the sampling horn to study the characteristics of the impact, considering a regolith bed contained in a 15 cm radius and 20 cm deep cylinder. The projectile is modeled by a 5 g sphere with a radius of 0.4 cm. The real projectile is not exactly a sphere but the part impacting the regolith bed is spherical, and we assume that the response of the regolith is similar for an entirely spherical projectile. Schwartz et al. (2014) also used a spherical projectile in their comparisons between experiments and simulations with `pkdgrav`, and found good matches. We use a cylinder radius as a compromise between the computation time (a larger radius implying a much larger number of particles) and the long duration of the cratering process in low gravity. The bed is also defined to be larger than the bottom of the sampling horn (13.8 cm diameter).

Our bed is made of 101,657 particles, with a particle density of 2.43 g cm^{-3} as in Thuillet et al. (2018). The bulk density of the whole medium is about 1.23 g cm^{-3}, implying a macro-porosity of ~ 50%. The size distribution of our particles is assumed to be Gaussian, with a mean radius of 0.25 cm, a standard deviation σ of 30% and a cut-off at 1σ. The choice of particle size was motivated by the opening of Hayabusa2 sampler's filter, which prevents particles larger than 1 cm in diameter to be ingested. The compromise was to consider particles small enough to be able to go through the horn and filters (with considerations on the computation time), but not too small to determine whether the filter will be clogged by larger particles.

The bed was created by randomly generating particles inside and above the cylinder, and allowing them to free-fall under Earth gravity. Once the bed has begun to settle, we switch the gravity to that on Ryugu, and we let the bed relax until a very low average speed (RMS speed), less than $3 \cdot 10^{-4}$ m s^{-1}, is achieved. Particle interactions are defined in `pkdgrav` by several parameters that include various friction and energy dissipation coefficients (Schwartz et al. 2012; Thuillet et al. 2018). We took the same parameters as for the gravel-like material in Thuillet et al. (2018). Concerning friction coefficients, the chosen values are $\mu_s = 1.0$ for the static friction, $\mu_r = 1.0$ for the rolling friction, $\mu_t = 1.0$ for the twisting friction, and $\beta = 1.0$ for the shape factor, a parameter representing the fact that real particles are not perfectly spherical (Zhang et al. 2017). Concerning the energy dissipation, the normal and tangential coefficients of restitution ε_n and ε_t are both set to 0.5. Nevertheless, we study the influence of these coefficients in Section 3.3.1. More explanations concerning these coefficients can be found in Thuillet et al. (2018).

In order to increase the range of applications of our modeling work, we consider impact speeds ranging from 50 m s^{-1} to 300 m s^{-1}. Cross-section snapshots for 50 m s^{-1} and 300 m s^{-1} are shown as examples in Sect. 3.1.

The timestep was defined so that the contact between particles and possible overlaps are well resolved for the considered dynamics of the system. For instance for the 300 m s^{-1} impact simulations, we chose a timestep $\Delta_t \approx 2.5 \cdot 10^{-7}$ s. We look at the influence of these parameters in Section 3.1.

2.2 Analysis method

Our objective is to model Hayabusa2's sampling and check its efficiency for the considered regolith properties. Following Wada et al. (2006), we also examine several impact characteristics such as the ejecta volume, the ejecta speed and the evolution of the crater as a function of time. We also look at the energy distribution and the wave propagation during the first impact times, and look for potential links between the impact process and the outcome. Moreover, we compare our results to the Z-model theory (Maxwell 1977).

Concerning simulations that include the sampler itself (the horn surrounding the projectile), we measure the quantity of actual sampled material for cases where particles are collected. Also, we measure the volume of material going through each part of the sampler, to determine the effect of the sampler's geometry and of the filter.

3 RESULTS

In this section, we describe the different results of our simulations. First, we present cases without the sampling horn, covering a range of impact speeds, in order to provide more general results on the impact process and its outcome into a granular material in reduced gravity (here chosen as RyuguâĂŹs one). These cases allow us to study more general outcomes, such as the crater formation, the ejecta production and direction, and to compare them with those given by a theoretical model (Sect. 3.1). Then, we present cases where we include the sample horn in order to measure the amount of collected material (Sect. 3.2). Finally, we study the influence of material properties and impact geometry (Sec. 3.3.2).

3.1 Impact outcomes for several impact speeds

3.1.1 General results

The impact speeds considered here range from 50 m s^{-1} to 300 m s^{-1}, with a particular focus on 300 m s^{-1} impacts.

Cross-section snapshots of simulations at different times for the 300 m s^{-1} impact are shown on Fig. 1. The cross-sections are 1 cm wide, and represent the slice $x = \pm 0.5cm$ of the regolith bed, i.e., the directions we see are the y- and z-axes. The snapshots are representative of the three-dimensional cavity.

When the projectile hits the bed, the wave propagates through the medium and particles are ejected very quickly. Several particles located very close to the impact point, on the top of the surface, and which are not directly hit by the projectile, linger in free fall since particles below them have been pushed downwards or not in their directions. They have a very small speed due to friction with particles they were in contact with, but these speeds are negligible compared to the speeds of the other particles around them. Because the gravity field is weak, they fall very slowly, and we can see one of them in the last snapshot, after 1230 ms (see Fig. 1).

Another way to visualize the cratering process is to consider the whole cylinder instead of a slice, and to take advantage of its axial symmetry. Figure 2 shows the particle density of the regolith bed, for different radii and heights, and for the same times as in Fig. 1. For each cell representing a toroid, the number of particles is summed along the azimuth and then divided by the toroid's volume.

The crater formation is visible in Fig. 2, as well as the particles ejected from the bed. This is also a way to ensure that the crater dimensions observed in cross sections are the same for all directions, and not only along a preferred one.

We notice that the crater formation in our simulations is much longer than in previous studies such as Wada et al. (2006). It is mostly due to the very low value of the gravity acceleration, compared to the terrestrial one used in Wada et al. (2006). Also, we see that radial boundaries certainly play a role in the cratering process, as the radius of the crater is very close to the radius of the cylinder. However, similar processes can be observed in our setup and the one of Wada et al. (2006).

After the impact, particles are pushed away radially, at the same speed, leading to a hemispherical cavity, as can be seen in the top left panel of Fig. 1. This was observed in laboratory experiments (Yamamoto et al. 2003) and simulations

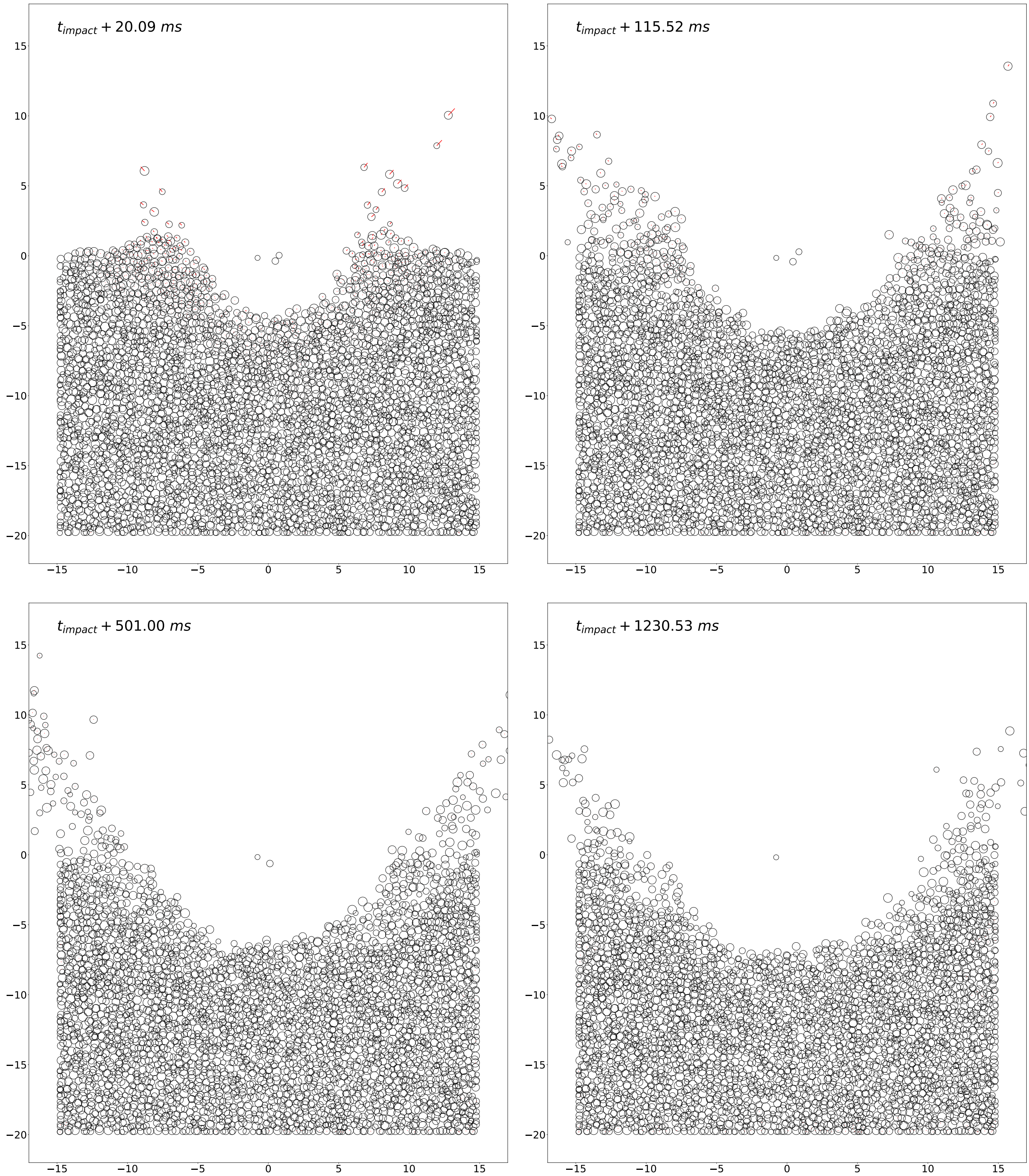

Figure 1. Cross-section snapshots of the projectile impacting the regolith bed, in the yz-plane. In red are represented the velocities of the different particles in this plane. The cross-section width is 1 cm and the impactor is not represented in this section.

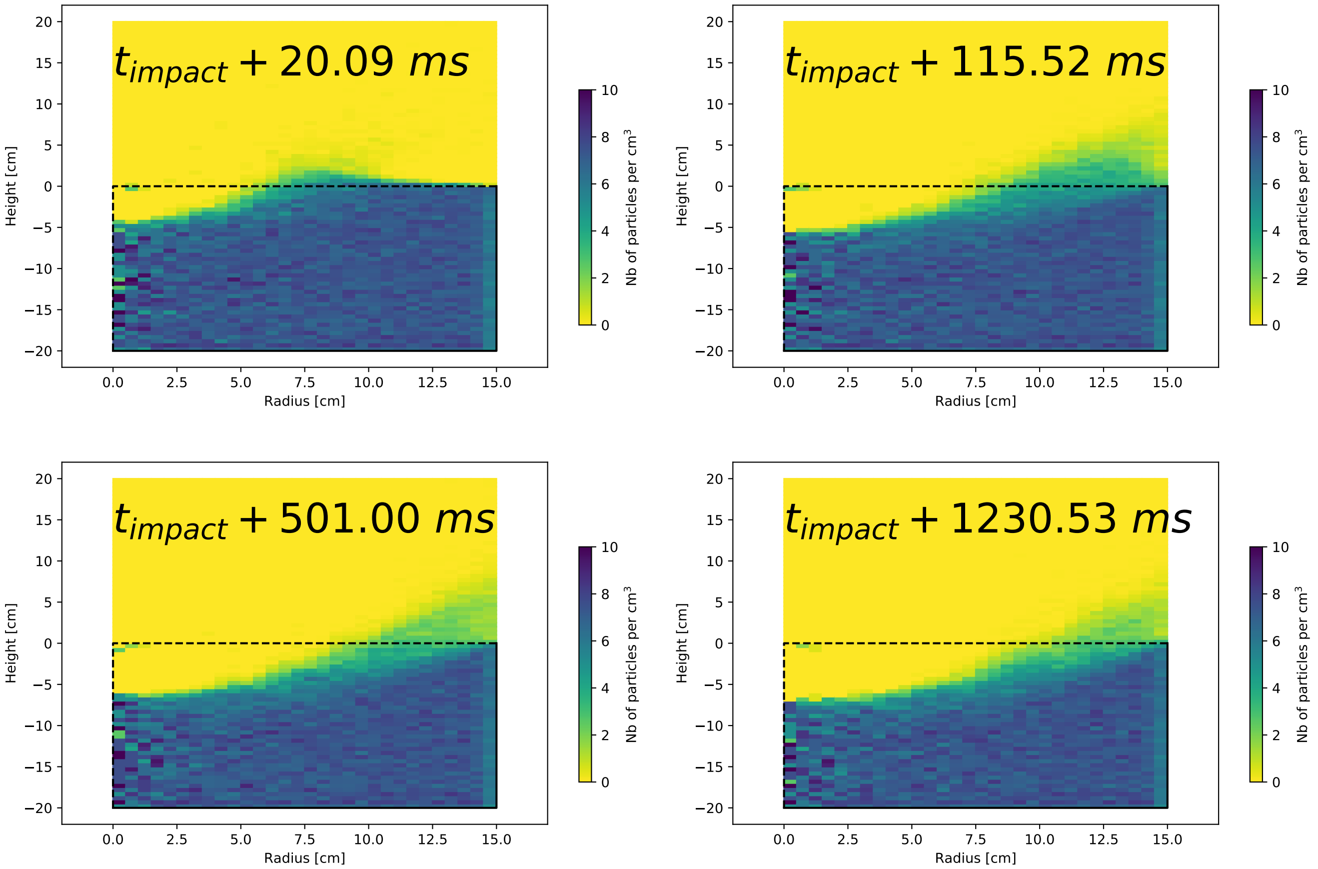

Figure 2. Particle density in the bed for different heights and radii, represented by toroids whose symmetry axes are the cylinder's symmetry axis, and whose sections are 0.5 cm-side squares. The color bar represents the number of particle centers per toroid, divided by the toroid's volume to consistently compare inner and outer regions. Maximum values are 12.73 particles per cm^3 for the four panels, but we took a maximum of 10 particles per cm^3 for the color bar to increase contrasts and better see ejected particles.

(O'Keefe & Ahrens 1999; Wada et al. 2006). However, about 30 ms after the impact, the cavity depth does not increase as fast as the cavity radius anymore. After about 300 ms, the cavity depth has almost reached its final value, meanwhile the cavity's radius keeps growing, as shown in Fig. 1. This was also observed in Earth-gravity laboratory experiments (Melosh 1989; Yamamoto et al. 2003), as well as in numerical simulations (Wada et al. 2006), and we can see that the phenomenon happens even under very weak gravity.

The cavity radius and depth as function of time are shown in Fig. 3. To calculate the cavity radius and depth, we counted the number of particles in different 1 mm layers, taking into account only the center of the cylinder and horizontal layers for the depth, and the surface and vertical layers for the radius. We then set a threshold of particle density to define the frontier between the cavity and regolith bed and determine the crater dimensions as a function of time.

During the first stage, particles are pushed radially away from the impact, both depth and radius increase at the same speed, and the depth as a function of the radius is close to the $y = x$ line. This stage is however very short and in a second stage, the cavity depth then increases more slowly. The cavity radius increase also slows down, as particles constituting the crater rim have lower speeds than the ones ejected from the center. The cavity depth stops increasing after about 1 s, whereas the lateral growth continues.

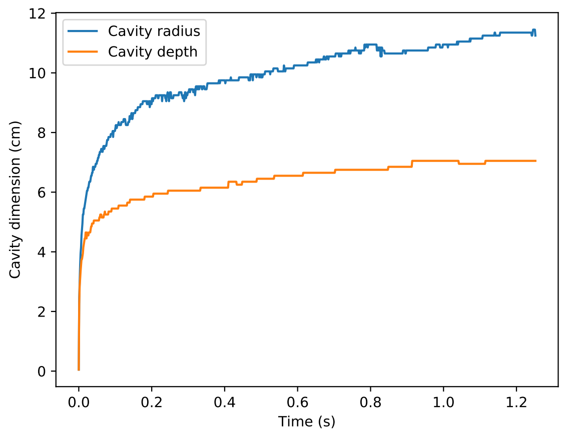

Figure 3. Cavity dimensions (depth and radius) as a function of time, for a 300 m s^{-1} impact.

We can also compute the cavity depth as a function of the cavity radius, as shown on Fig. 4, for four different speeds. The higher the impact speed, the faster the increase

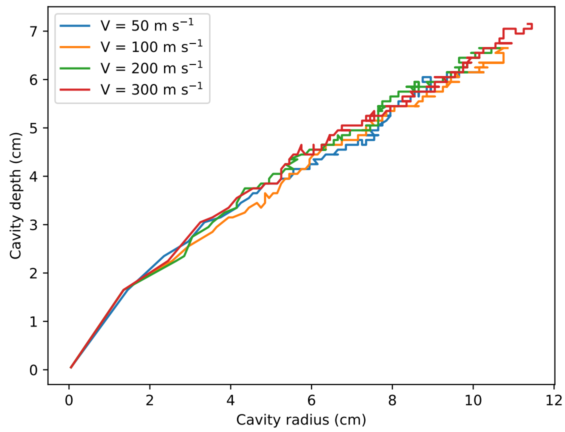

Figure 4. Cavity depth as a function of cavity radius for four different impact speeds.

in cavity dimensions. However, we observe that the evolution of the crater depth as a function of the crater radius is very similar regardless of the impact speed.

Yamamoto et al. (2006) and Wada et al. (2006) define the transient crater as the time when, the bowl-shaped cavity being formed and the cavity depth being stabilized, the crater rim starts collapsing and an uplift of the crater's bottom occurs. Our simulations do not last long enough to observe such an uplift and a collapse of the crater's walls. Moreover, the cylinder is too small to avoid boundary effects, and enlarging it and extending the duration would significantly increase the computation time. At the end of our simulations, which cannot be run until the transient crater is completely formed, we find a crater depth-to-radius ratio of about 0.6-0.65, which keeps slowly decreasing with time as the crater goes on expanding laterally, to be compared of the value of 0.52-0.54 observed in Yamamoto et al. (2006). The main difference between these experiments and our simulations, besides the fact that the transient crater is not reached yet in our simulations, is the gravity that is much weaker in our simulations. Therefore, particles can travel further away from the impact location, and therefore a crater should form with a lower depth-to-radius ratio. However, this effect is compensated by our boundary conditions. Moreover, the porosity, the internal friction, the grain size and the densities of both the projectile and the target also differ from the experiments, and Yamamoto et al. (2006) showed that these characteristics do not seem to affect very much the transient crater depth-to-radius ratio, even if they certainly affect the transient crater growth.

Our values (0.6-0.65) may seem very high compared to the depth-to-radius ratio of natural craters. For example, the largest craters observed on Ryugu had ratios between 0.28 and 0.4 (Sugita et al. 2019), and on Bennu the ratios were about 0.32 (Barnouin et al. 2019). However, these values correspond to final craters ratio and, as stated previously, our ratios correspond to transient craters. The transient crater ratio decreases with time, when the rim collapses and sometimes the floor lifts up. Yamamoto et al. (2006) found depth-to-radius ratios of about 0.52-0.54 for transient craters and 0.22-0.28 for final ones, showing that our simulations would certainly lead to much lower ratios than 0.6 if we could reach the final state of the crater formation. Moreover, for actual asteroids, meteorite impacts can induce seismicity, leading to crater relaxation and lower observed depth-to-radius ratios (Richardson et al. 2004).

We did not only explore the crater dimensions, but also the impact energetics by studying how the energy is distributed during the first instance after impact.

3.1.2 Energy distribution during the first impact instants

We computed the different energies present in the first instants of the simulations, for the different considered impact speeds between 50 m s^{-1} to 300 m s^{-1}, with a particular focus on the 300 m s^{-1} case.

In our simulations, there are four types of energy: the translational kinetic energy K, the rotational energy E_{rot}, the stored elastic energy E_{el}, and the gravitational potential energy. We studied these energies for both the impactor and the target (sum of all the particles forming the granular bed), as well as the total energy in the simulation. We found that the gravitational potential energy was always negligible and therefore is never included in the following figures.

The kinetic energies are computed as following:

$$K = \frac{1}{2}mv^2, \tag{1}$$

$$E_{\rm rot} = \frac{1}{2}I\omega^2 \tag{2}$$

where m is the mass, v the translational speed, I the moment of inertia, and ω the angular velocity.

The elastic energies stored in each particle/particle or particle/wall contact come from the repulsive restoring spring force defined by Hooke's law, which is the interaction model used in `pkdgrav` (Schwartz et al. 2012). The stored normal, tangential, rolling, and twisting elastic energies can be defined as :

$$E_{\rm el,\ norm} = \frac{1}{2}k_n d_{\rm overlap}^2, \tag{3}$$

$$E_{\rm el,\ tang} = \frac{1}{2}k_t x_{\rm tang}^2, \tag{4}$$

$$E_{\rm el,\ roll} = \frac{1}{2}k_n \beta^2 R_{\rm red}^2 \theta_{\rm roll}^2, \tag{5}$$

$$E_{\rm el,\ twist} = k_t \beta^2 R_{\rm red}^2 \theta_{\rm twist}^2 \tag{6}$$

where k_n is the normal spring constant (see Schwartz et al. (2012)), $d_{\rm overlap}$ the overlap length between the two considered particles, $k_t = \frac{2}{7}k_n$ the tangential spring constant, β the shape parameter, and $R_{\rm red}$ the reduced radius. $x_{\rm tang}$, $\theta_{\rm roll}$, and $\theta_{\rm twist}$ represent the distention/compression of the respective springs, the rolling and twisting springs being angular springs. Then, equations from 1 to 6 should be summed over all considered particles.

We considered that the energies were equally distributed between particles in contact, and therefore Eq. 3, which represents the stored normal elastic energy for a pair of particles in contact, has to be halved after being summed on all particles to consider contacts only once.

We normalized the different energies by dividing them by the impactor's initial translational kinetic energy, the largely predominant energy prior to the impact, in order to facilitate comparisons between various impact speeds involving different orders of magnitude of energies.

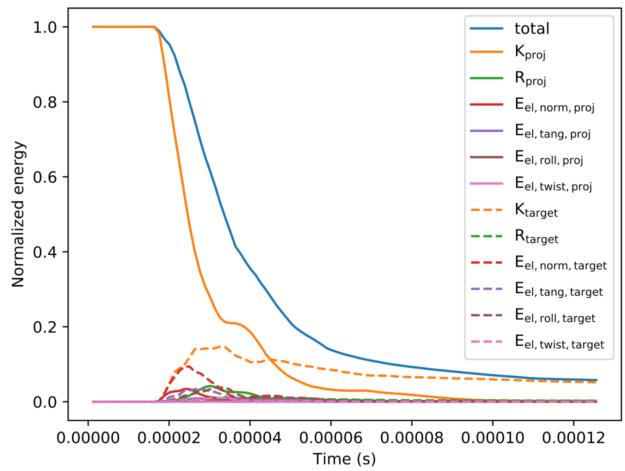

Figure 5. Different energies at stake for impact speeds of 300 m s^{-1}, as well as the total energy (sum of all other energies in the simulations) as function of time. Energies are normalized with the impactor's initial kinetic energy and are represented for the first instants of the impact. Timescales are different for both impacts, as well as the absolute energies.

The different energies as function of time are shown on Fig. 5. The timestep and spring constant, respectively Δ_t and k_n, have been scaled depending on the impact speed, i.e., the timestep used for the 300 m s^{-1} impact is six times shorter than the one used for the 50 m s^{-1}, and the spring constant is $6^2 = 36$ times higher. Indeed, we considered a timestep varying proportionally to the inverse of the impact speed, and according to Schwartz et al. (2012), the timestep is proportional to the inverse of the square root of the spring constant. These choices of timestep and spring constant allow us to keep the same constant value for $\Delta_t \cdot \sqrt{k_n}$, and to have access to longer durations for smaller speeds.

Impacts evolve similarly regardless of the impact speed. The major differences between cases with different impact speeds are the timescale and the absolute amounts of energy. As expected, the higher the impact speed, the faster the energy dissipation and transmission to the target, and the higher the energy at the end of the collision (when the projectile kinetic energy is negligible compared to other energies). However, the normalized energy profiles are very similar, with the same peaks and a little less than 10% energy left at the end (and still decreasing with time). The fact that the total amount of kinetic energy in the ejecta is less than 10% of the initial kinetic energy was also found by Colwell (2003) in microgravity impact experiments and in high-speed experiments (Davis et al. 2002).

Looking more closely at the evolution of the energy a a function of time, we can discern several steps. At first, the impactor's kinetic energy is by far the highest energy source (that is also an indicator that our bed is completely settled before the impact, as the sum of the kinetic energies of all particles forming the target is close to zero and negligible compared to the impactor's energy). Quickly, the projectile's kinetic energy is transformed into elastic energy as particle overlaps increase (for both the impactor and the target), and, simultaneously, part of this elastic energy is transformed back into target's kinetic energy. The impact wave propagates through the particles closest to the impact point, and overlaps between target's particles not in contact with the projectile increase, leading to a higher elastic energy for the target. The impact can also make the impactor spin, as it never impacts perfectly on the center of a particle. This spin is represented in Fig. 5 by the rotational energy. The target particles' rotational energies stay very low during the impact; even if particles have a non-zero rotation rate, their mass is much lower compared to the impactor's.

When the impactor penetrates into the bed, overlaps with target particles steadily increase, and this stored elastic energy is eventually transformed into kinetic energy. Therefore, the impactor is slowed down while particles are accelerated. Overlaps between the impactor and particles will therefore decrease, leading to a fall of target's elastic energy. During this short moment, particles almost do not stop the motion of the impactor anymore, which is represented by a little "bump" in the impactor's kinetic energy on Fig. 5.

After having reached its peak, the target's kinetic energy decreases with time because of dissipation through the impact wave. Energy dissipation in the medium comes from friction and damping (the coefficients of restitution are smaller than 1). After 10^{-4} s for a 300 m s^{-1} impact (see Fig. 5), most of the energy left in the simulation is contained in the target (the target's kinetic energy is predominant), and the projectile has been almost completely stopped. The energy will then slowly decrease due to friction and energy dissipation in grain interactions in the regolith bed.

These different phases are shown on Fig. 6 for the 300 m s^{-1} impact, only for particles close to the impact point. The representations are cross-sections along the vertical plane containing both the initial position of the projectile and the center of the first particle impacted, for different times. They aim at a better understanding of the energy distribution, by looking at the first contacts with the impactor and the bed. In Fig. 6a, we show the first projectile-target contact, corresponding to a time of about 0.018 ms in Fig. 5, when the impactor's kinetic energy starts decreasing. The kinetic energy decreases quickly, due to the increasing impactor-particle overlap and overlaps between particles, as shown in Fig. 6b. After about 0.33 ms, the first particle to be impacted has pushed away other particles, among them the particle under the second particle to be in contact with the impactor, which enables particles to find less resistance in their path (and have speeds comparable to the impactor), and therefore the impactor can push them more easily and lose less kinetic energy (Fig. 6c). However, the impactor comes quickly in contact with a new particle (about $9 \cdot 10^{-6}$ s later), and therefore it is slowed down again, as shown in Fig. 6d.

We can also analyze the number of particles the projectile collides with during its penetration. Fig. 7 shows the number of particles that are in contact at least once with the projectile during this short simulation.

In Fig. 7, we see a first overlap between a particle (n°8860) and the projectile, corresponding to the steep decrease of the target's kinetic energy. Then, the overlap decreases because n°8860 has gained speed, and this corresponds to the "bump" in Fig. 5. The second drop in the projectile's kinetic energy happens when projectile forms new contacts with target particles (in this case it forms four simultaneously). The projectile cannot transfer as much en-

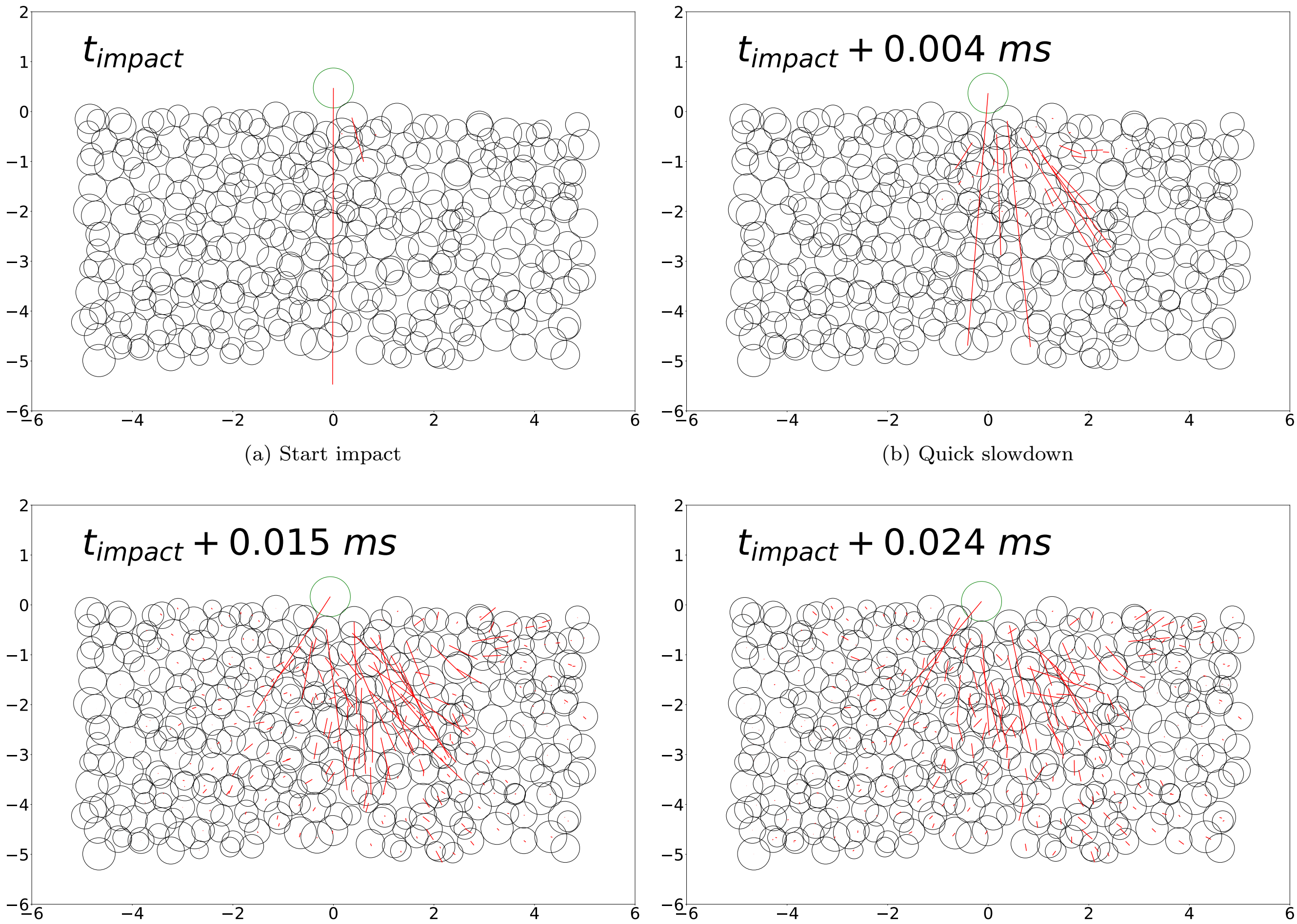

(a) Start impact

(b) Quick slowdown

(c) Start of small resistance phase

(d) Start of second slowdown

Figure 6. Zoomed-in cross-section representations of the projectile impacting the regolith bed, in the vertical plane containing both the initial position of the impactor and the first particle in contact, and for different times. The impactor is in green, and in red are represented the velocities of the different particles and impactor in this plane. The impact speed is 300 m s^{-1}, and the cross-section width is 1 cm. Distances are in centimeters.

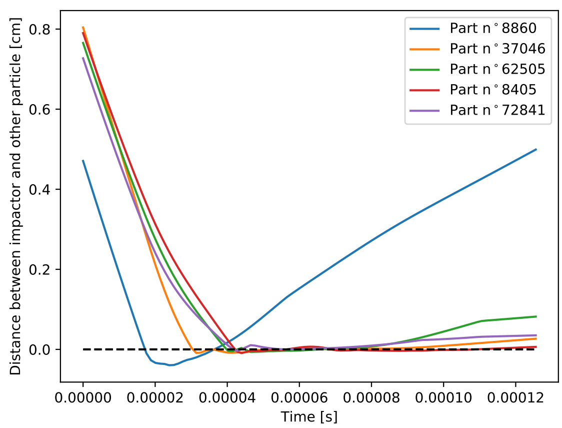

Figure 7. Overlaps between impactor and different particles in contact with it during the simulation, for a 300 m s^{-1} impact.

ergy as before, and therefore the contacts last longer and the projectile's kinetic energy drops although overlaps are small.

Since we ran simulations with lower impact speeds with scaled timestep and spring constant, one can wonder the influence of these parameters, and the changes in the impact process if these are kept the same for every speed. Here we consider a 50 m s^{-1} impact, with $\Delta_{t_0} = 1.5 \cdot 10^{-6}$ s and $k_{n_0} = 5.47 \cdot 10^9$ kg s^{-2}, i.e., the timestep and spring constant we used for the previous simulations. The considered range of timestep and spring constant is relatively small, and do not change the packing before impact. For example, for the simulations presented in Fig. 8a and 8b, there are respectively 65 and 390 iterations before the impact, and the maximum displacement per iteration is $6 \cdot 10^{-6}$ cm, leading to less than $2.5 \cdot 10^{-3}$ cm in total from the beginning of the simulation to the impact.

If we decrease the spring constant from k_{n_0} to $0.58\, k_{n_0}$, the impactor keeps being slowed down by particles, as shown on Fig. 8a, contrarily to what was observed in Fig. 5. Thus, its kinetic energy decreases much faster. Since the spring constant is smaller, the spring repulsive forces are slightly weaker and particles experience longer contacts, leading to higher elastic energies for both the impactor and the target. We particularly notice that the tangential and rolling elastic energies are noticeably higher.

When particles initially pushed by the impactor encounter other particles, they are slowed down, and since in this case the impactor stays in contact, the slowing down increases the impactor-particles overlap and the former feels a higher, upward-directed, spring repulsive force than with a higher spring constant. This force is strong enough to change its trajectory, and the impactor bounces on the surface. However, the energy contained in the ejecta and the total energy are similar to the ones obtained with k_{n_0}. Since we are more interested in the amount of ejecta than in the fate of the impactor, a lower spring constant can be considered for further simulations.

Figure 9 shows the overlaps between the impactor and the five particles which are in contact with it at one moment of the simulation. It confirms that overlaps are larger and last longer in this case, i.e., when the spring constant is smaller. The difference is even clearer for the contact with the second particle (particle n°37046).

If we look more closely at the moment that was just before the phase with less resistance and compare what happens for the two different spring constants, we notice that the contact between the second particle and the impactor is slightly different in both cases (see Fig. 10).

Indeed, the velocity of the second particle (the one below the impactor) does not have the same orientation, due to the deeper penetration of the impactor into the first particle. Since granular media are usually anisotropic, the bed does not answer in the same way if pushed in one direction or another, and this answer depends on the structure or preparation of the medium. For each contact, the target particle does not have the same mobility freedom in every direction, and this has to be taken into account for each particle along the created force chain. In Fig. 10b, the particle encounters more resistance along the direction of its velocity, and cannot move as well as in Fig. 10a, leading to the impactor bouncing away from the bed.

We explained how we scaled the timestep and the spring constant depending on the impact speed, and found very similar profiles. However, we also tried to compare different speeds with the same parameters. For this purpose, for simulations with impact speeds from 50 to 300 m s^{-1}, we harmonized timesteps and spring constants to respectively the lowest and highest ones, i.e., the ones of the 300 m s^{-1} impact. For example, for the 50 m s^{-1}, this leads to $\Delta_t = \frac{\Delta_{t_0}}{6}$ and $k_n = 36\, k_{n_0}$. The energy distribution for these parameters is shown on Fig. 8b. In this case, with a higher spring constant, the first impactor-particles contact pushes particles away quicker, and elastic energy increases very fast. Also, the repulsive force from particles is higher and the impactor's kinetic energy falls as fast as the elastic energy increases.

However, since the impactor and particles are pushed away from one another efficiently, the impactor-particles overlaps also shorten soon. The same phenomenon happens as it does with a spring constant of Δ_{t_0}, where the impactor-particles spring forces become weaker as they move away, except this time the higher spring constant implies a longer time for the impactor to encounter low to no resistance from the bed. Where it does again, we can see once again the two phases "quick slow down" and "free penetration", softened because of a lower speed and a medium becoming more dense. At the end, the kinetic energy of the target and the total energy are almost exactly the same as for other simulations. We therefore expect a similar behavior for the target in a larger point of view, for example the cavity dimensions as we have seen in Section 3.1.1, or the amount of ejecta (see Section 3.1.5).

3.1.3 Wave propagation at the first impact instants

We stated in 3.1.1 that, just after the impact, the impact wave propagates through the medium. This is shown for the 300 m s^{-1} impact on Fig. 11, where we represent the speed of particles as a function of their distance from the impact point. Only particles located under the impact point, within a 60° half-apex-angle downward cone, are considered in this figure, to avoid taking into account ejecta and to capture only the propagation of the wave inside the granular medium.

In Fig. 11, we see that particles far from the impact point have smaller speeds and are more numerous than close particles. This is due to the wave propagating through the medium, and being attenuated by it. In every contact, energy is lost due to friction and dissipation, leading to the decrease of particle speed with distance. Also, we can see the propagation of the wave in Fig. 11b, since particles further from 0.1 m have been significantly accelerated, and fastest particles, close to the impact point, have shared their energy with their neighbours and slowed down.

Shock propagation theories (Melosh 1989) state that particle speed decreases with distance following a power law, and that the power-law exponent is contained between −1 (for the energy conservation mode) and −2 (for the momentum conservation mode). The particle speed decrease with distance is best seen in Fig. 11b for t = 0.08 ms, and the power-law exponent can be estimated from a fit on the fastest particles for a range of distances. We consider a range of distances with enough particles to be representative of the wave propagation, but not too far from the impact point to consider only particles directly set in motion by the wave. We find a slope of about −1.91; therefore, in our simulations, the impact wave propagation mostly exists within the momentum conservation regime. Wada et al. (2006), in their SSDEM simulations with similar impact speeds, found that their impacts belonged to the same regime.

We find similar results with smaller impact speeds, although the particle speeds are obviously slower with smaller impact speeds. Power-law exponents are also found to be very close to −2, and indicate a pressure wave propagation in the momentum conservation mode.

3.1.4 Comparison with Z-model

We also compared the first instants of our simulations to the Z-model, which is an analytical model that represents the ejecta velocity field with streamlines after a vertical impact (Maxwell 1977). If we assume that the material is incompressible, the geometry of the streamline can be expressed

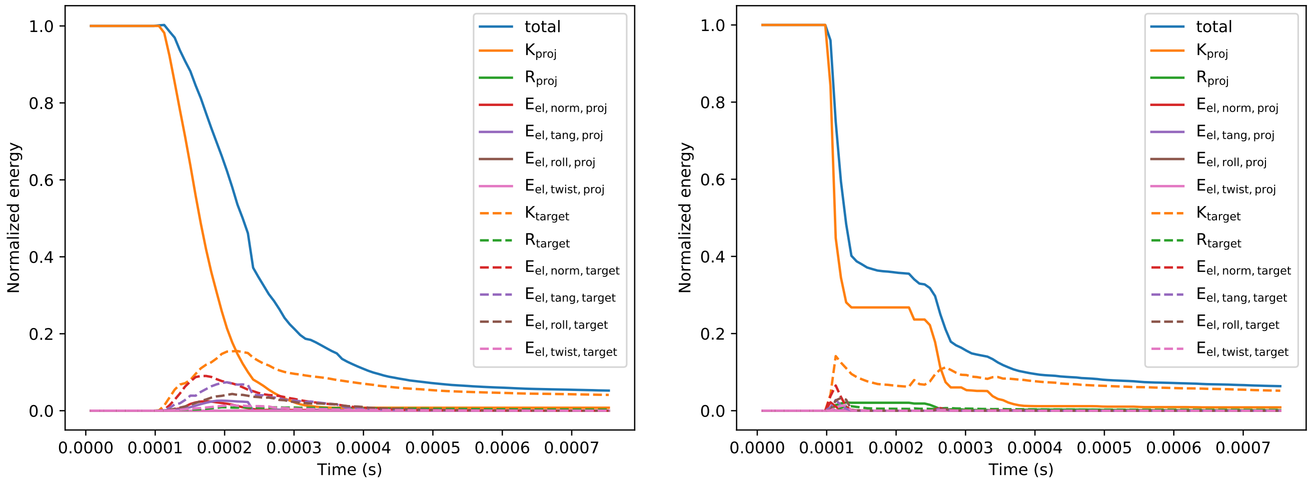

(a) $\Delta_t = \Delta_{t_0}$, $k_n = 0.58\,k_{n_0}$ (b) $\Delta_t = \frac{\Delta_{t_0}}{6}$, $k_n = 36\,k_{n_0}$

Figure 8. Different energies at stake for 50 m s^{-1} impacts with different timescales and spring constants. Energies are normalized with the impactor's initial kinetic energy and are represented for the first instants of the impact.

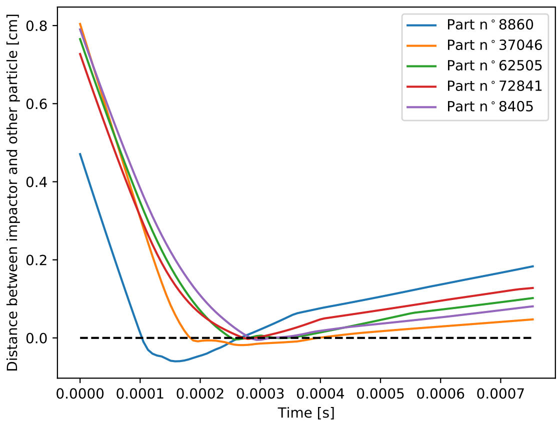

Figure 9. Overlaps between impactor and different particles in contact with it during the simulation, for a 50 m s^{-1} impact, for $k_n = 0.58\,k_{n_0}$.

in two dimensions (taking advantage of the axial symmetry) by a simple equation, in polar coordinates (r, θ), where the center of the coordinates system is the impact point, and $\theta = 0$ corresponds to the downward vertical direction. The equation of a given streamline is:

$$r = R(1 - \cos\theta)^{\frac{1}{Z-2}}, \tag{7}$$

where R is the horizontal distance from the impact point to the intersection between the considered streamline and the surface, and Z the main parameter of the Z-model, a decay parameter that defines the curvature of the streamlines. An example of streamlines is shown in Fig. 12, with the ejection angles.

From Eq. 7, the ejection angle of particles θ_e can be determined. This ejection angle is supposed to be the same whatever the horizontal distance R, and equal to:

$$\theta_e = \arctan(Z - 2), \tag{8}$$

With the same method used for Fig. 2, we considered toroids with 0.25 cm-side square sections and looked at the average particle velocity in each of these toroids. We were more interested by the velocity direction than the magnitude, and for a clear figure, we divided the velocity vectors by their norm to look only at their orientation.

In order to find the corresponding Z for the beginning of our simulation, we consider the ejection angles assumed to not be influenced by the boundary conditions. We also do not account for the vicinity of the center where there are very few particles and therefore where variations in the ejection angles are much larger. Thus we consider ejected particles in a region that is at a distance from the center from 4 to 10 cm and in the upper layer (height from −0.25 to 0 cm). This gives us an average ejection angle of about 44°, and $Z = 2.966$. However, with such a value for Z, data do not seem to match the streamlines defined by the Z-model in deeper layers.

To improve our determination of Z, we do not consider only the uppermost layer but also deeper ones (from about −6.5 to 0 cm). From Eq. 7, the velocity angle θ_v (with the horizontal) for any point in the bed along a streamline can be determined:

$$\theta_v = \arctan\left(\frac{(Z-2)\sin\theta - (Z-1)\sin\theta\cos\theta}{1 + (Z-2)\cos\theta - (Z-1)\cos^2\theta}\right). \tag{9}$$

If we consider the ejection angle, i.e., $\theta = \frac{\pi}{2}$, we find that Eq. 9 is compatible with Eq. 8, namely $\theta_v(\theta = \frac{\pi}{2}) = \theta_e$.

From Eq. 9, we can compare each average velocity angle per section in the considered area to the theoretical ones given by the Z-model. We determine the corresponding R and θ for each center of the areas from Eq. 10 and 11, and compare the velocity angle in our simulation with the theoretical one for a varying Z. We choose the Z value on the basis of the minimum root-mean-square of the differences

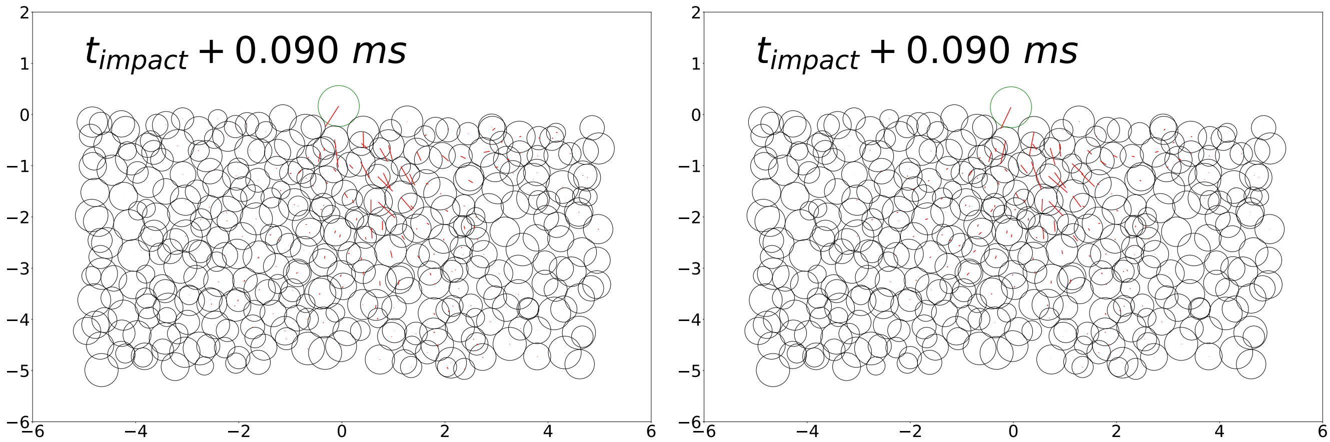

(a) $k_n = k_{n_0}$ (b) $k_n = 0.58\,k_{n_0}$

Figure 10. Zoomed-in cross-section representations of the projectile impacting the regolith bed, in the vertical plane containing both the initial position of the impactor and the first particle in contact, for different spring constants and a same time after impact. The impactor is in green, and in red are represented the velocities of the different particles and impactor in this plane. The cross-section width is 1 cm. Distances are in centimeters.

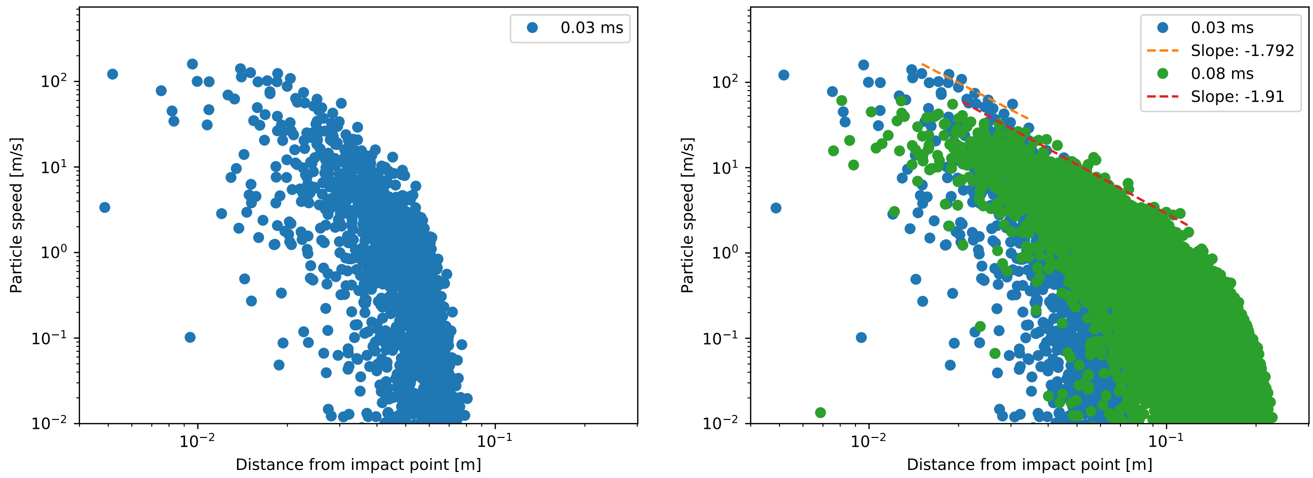

(a) 0.012 ms after impact (b) 0.012 ms and 0.062 ms after impact

Figure 11. Particle speed as function of the distance from the impact point for a 300 m s^{-1} impact, and for two different times, 0.012 ms after impact on the left, and 0.062 ms after impact on the right, corresponding respectively to $t = 0.03$ and $t = 0.08$ ms after the start of the simulation. The dotted lines represent the slope of the fastest particles for different distances, in orange for $t = 0.03$ ms, and in red for $t = 0.08$ ms. The orange slope has a value of -1.792 and the red one -1.91. We only consider particles within the vertical 60° half-apex-angle cone under the impact point.

between theoretical velocity angles and numerical ones.

$$\theta = \arctan\left(\frac{x_{\text{area}}}{-z_{\text{area}}}\right), \tag{10}$$

$$R = \frac{\sqrt{x_{\text{area}}^2 + z_{\text{area}}^2}}{(1-\cos\theta)^{\frac{1}{Z-2}}} \tag{11}$$

where $(x_{\text{area}}, z_{\text{area}})$ are the coordinates of the center of each 0.25 cm square area, in the plane (x_{area} corresponding to the distance from the cylinder central axis, and z_{area} to the height).

This leads to $Z = 2.675$, with an average angle error of 8.9° and a standard deviation of 6.8°. The streamlines and the velocity angles are shown in Fig. 13 for the computed Z.

We see that the deeper and the further from the impact point, the larger the angle differences. Since the Z-model is supposed to be for a stationary state, we looked at other instants much further in time, $1.25 \cdot 10^{-3}$ s and $1.25 \cdot 10^{-2}$ s after impact, and try to associate a Z to those instants. The further in time we consider, the greater the influence of the boundary conditions on the velocity distribution, as the cavity expands.

For $1.25 \cdot 10^{-3}$ s after the impact, the Z-model works better than just after the impact, and for the area considered, we find that the best match is for $Z = 2.836$, with an

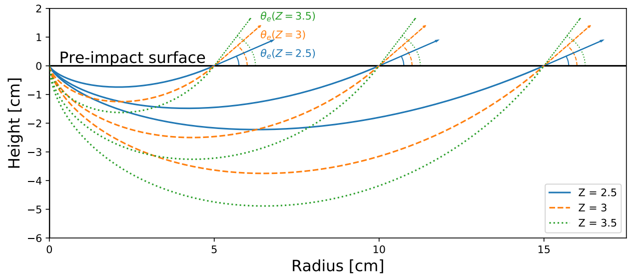

Figure 12. Examples of streamlines (for R = 5, R = 10, and R = 15 cm) defined by the Z-model, with several values for the parameter Z. The ejection angle θ_e is also shown at the surface for the considered Z.

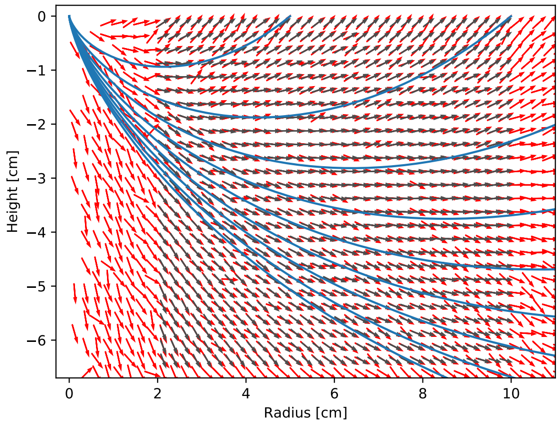

Figure 13. View of the average normalized velocities in the bed as function of their distance from the center of the cylinder and the height, at time $t = 4.52 \cdot 10^{-5}$ s after the impact. Only a part of the cylinder is shown here. Each red arrow corresponds to the average normalized velocity for particles inside the corresponding 0.25 cm-side square section toroid. Blue lines correspond to the streamlines associated with Z = 2.675 (see text) for different R separated from each other by 5 cm, and grey arrows correspond to the normalized velocities associated with these streamlines, in the center of the toroids.

average angle difference between the model and our data of $3.6 \pm 3.2°$ (see Fig. 14).

When we try to fit our data to the Z-model further in time, i.e., for $1.25 \cdot 10^{-2}$ s, we see that the discrepancies increase. The best fit is for $Z = 3.388$, with an average angle difference of $9.8 \pm 8.7°$, which is much larger than the previous one (see Fig. 15).

The change in Z as a function of time can be explained by the fact that an almost stationary state as assumed in the Z-model is only reached near $1.25 \cdot 10^{-3}$ s after impact. The angle errors are indeed much higher (more than twice) if we consider a time after impact that is too short (stationary state not reached yet) or too long (effects of boundary conditions). This implies that the Z parameter associated with our impact is close to 2.836. According to Housen et al. (1983), momentum conservation is associated to a Z of 3, whereas energy conservation corresponds to Z = 2. In our simulations, Z is much closer to 3, and therefore to the momentum conservation regime, than to 2. This is consistent

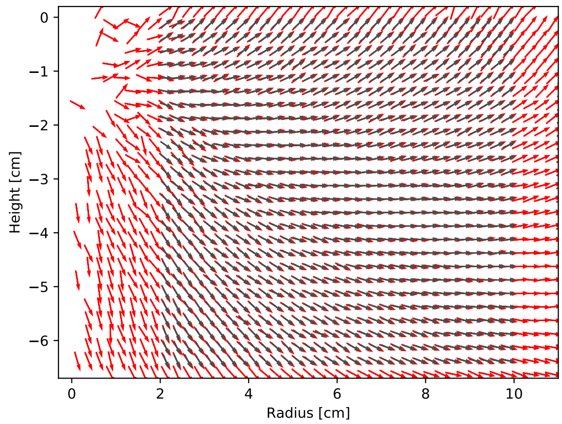

Figure 14. View of the average normalized velocities in the bed as function of their distance from the center of the cylinder and the height, at time $t = 1.25 \cdot 10^{-3}$ s after the impact. Only a part of the cylinder is shown here. Each red arrow corresponds to the average normalized velocity for particles inside the corresponding 0.25 cm-side square section toroid. Blue lines correspond to the streamlines associated with Z = 2.836 (see text for explanation) for different R separated from each other by 5 cm, and grey arrows correspond to the normalized velocities associated with these streamlines, in the center of the toroids.

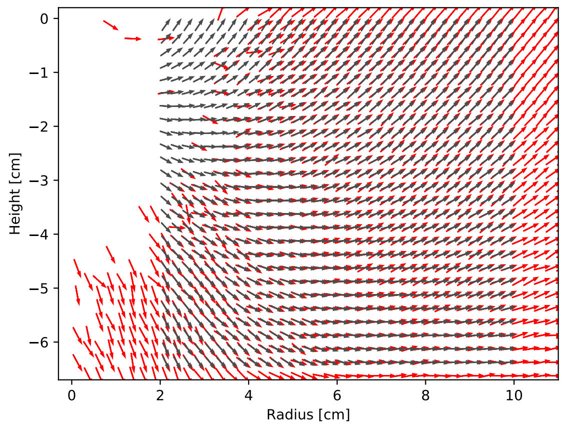

Figure 15. View of the average normalized velocities in the bed as function of their distance from the center of the cylinder and the height, at time $t = 1.25 \cdot 10^{-2}$ s after the impact. Only a part of the cylinder is shown here. Each red arrow corresponds to the average normalized velocity for particles inside the corresponding 0.25 cm-side square section toroid. Blue lines correspond to the streamlines associated with Z = 3.388 (see text for explanation) for different R separated from each other by 5 cm, and grey arrows correspond to the normalized velocities associated with these streamlines, in the center of the toroids.

with the regime we deduced previously from the application of the shock propagation theory to the particle speed in the bed.

We also notice that the best fit for Z increases with time. An increasing Z with time for a normal impact was previously observed in other numerical models (Austin et al. 1981). Studies from Cintala et al. (1999) and Anderson et al. (2002) also suggested, from the change of ejection angles and positions with time, that either the value of Z or the depth of

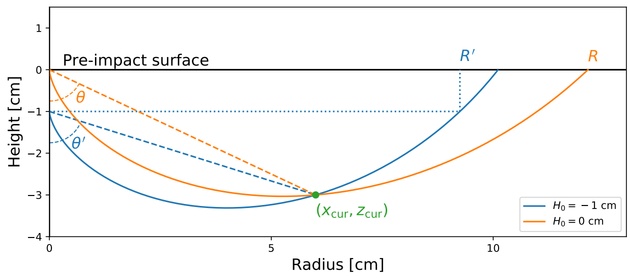

Figure 16. Examples of streamlines going through (x_{cur}, z_{cur}) defined by the Z-model, with several values for the height of the flow-field center H_0. Regular θ and R are shown, as well as θ' and R', the equivalent values for a flow-field center not at the surface.

the flow-field center (starting point of all streamlines) should change over time during the cratering process.

A migrating flow-field center was observed in numerical models (Thomsen et al. 1979; Austin et al. 1980) and generalized in Croft (1980). With a flow-field center not at the impact point, the ejection velocity depends on the horizontal distance R. Eq. 10 and 11 need to be changed into Eq. 12 and 13:

$$\theta' = \arctan\left(\frac{x_{\text{area}}}{H_0 - z_{\text{area}}}\right), \tag{12}$$

$$R' = \frac{\sqrt{x_{\text{area}}^2 + (H_0 - z_{\text{area}})^2}}{(1 - \cos\theta')^{\frac{1}{Z-2}}} \tag{13}$$

where θ' and R' correspond to previously defined θ and R but from the vertically translated flow-field center, as shown in Fig. 16. Therefore, R' corresponds to the horizontal distance for the intersection between the streamline and $y = H_0$. By replacing R and θ into R' and θ' in Eq. 9, we can determine the velocity angle in $((x_{\text{area}}, z_{\text{area}})$, and use the same method as before to find the best matches for H_0 and Z.

With the new addition of a migrating flow-field center, we look at $1.25 \cdot 10^{-3}$ s after impact, when we had the best fit of the three considered instants. We find that the best fit is $Z = 2.857$ and $H_0 = 0.05$ cm. H_0 is very low and we can consider that the best fit was in fact obtained for a flow-field center at the impact point. When we try to fit (Z, H_0) for $1.25 \cdot 10^{-2}$ s after impact, we find that Z should be higher than 5, which, according to Kurosawa & Takada (2019) should be the upper limit for Z. This means that the Z-model is not adapted to the geometry of the streamlines that we find for this impact instant. As previously stated, this may be due to the crater not being in the stationary excavation flow phase anymore, and this is potentially due to boundary condition effects. This may also be due to the complexities of a granular medium.

3.1.5 Ejecta speed, volume, and direction

After having described the cavity formation and characterized the impact by its first instants, we look at the ejecta, i.e., particles ejected from the regolith bed. In this study, we consider as ejecta target's particles whose heights are higher than the maximum height of surface particles before the impact.

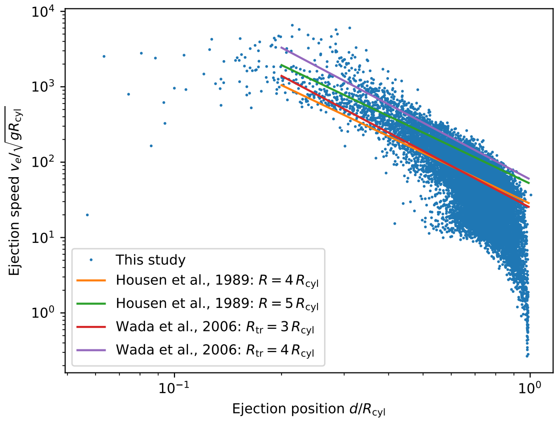

Figure 17. Normalized ejection speed as a function of normalized ejection distance, i.e., distance between impact point and position from where the particle is ejected, divided by the cylinder's radius, after a time of about 1.25 s, corresponding to the end of the cavity depth main increase. Our simulation data are compared to Housen et al. (1983) and Wada et al. (2006) by respectively considering different final crater and transient crater radii.

Concerning the ejecta speed, we analyze their dependency on the ejection position, i.e., the distance between the impact point and the position from where the particle is ejected. According to Housen et al. (1983), from dimensional analysis and laboratory experiments, Equation 14 links the normalized ejection speed and the normalized ejection position:

$$\frac{v_e}{\sqrt{gR}} = 0.62\left(\frac{d}{R}\right)^{-2.55} \tag{14}$$

where v_e is the ejection speed, d the ejection position, R the crater radius, and g the gravitational acceleration. Wada et al. (2006) also derived such a law from numerical simulations, but using the transient crater radius and not the final one:

$$\frac{v_e}{\sqrt{gR}} = 0.923\left(\frac{d}{R_{\text{tr}}}\right)^{-2.50} \tag{15}$$

where R_{tr} is the transient crater radius.

In our simulations, we reach neither the transient crater nor the final one. To normalize the ejection speed and distance, we use instead a characteristic length of our simulation, i.e., the cylinder's radius $R_{\text{cyl}} = 15$ cm, which leads to Fig. 17. We used the data at time about 1.25 s after impact because it corresponds to the end of the main increase of the cavity depth. Later than 1.25 s after impact, the cavity bottom is more or less stabilized, and the depth is roughly constant.

We see in Fig. 17 that there are several particles with relatively small speed and very close to the impact point. These are particles near the surface, not directly hit by the impactor but barely in contact with other ejected particles, which felt a very small upward acceleration and are therefore considered as ejecta. We also see that the further from the impact point, the slower the ejecta, as expected. We also see that in our simulations, the ejecta do not behave as predicted by Housen et al. (1983) and Wada et al. (2006). There are much more low-speed particles far from the impact point than predicted with a power law like Eq. 14 and 15. This may be due to the earliness of the crater formation, to the boundary conditions, or to the material properties. Furthermore, although the gravitational acceleration is taken into account in the normalization of the ejection speed, since power laws from Housen et al. (1983) and Wada et al. (2006) come both from Earth's gravity environment, the significant difference in the value of g may also be an explanation for these dissimilarities.

However, despite these variations, data from this study are not so far from previous data. We can try to derive a final crater radius, or a transient crater radius, from our data. As shown in Fig. 17, if the power laws from Wada et al. (2006) and Housen et al. (1983) are applied to our simulations, we expect a transient crater of about $3-3.5R_{\rm cyl}$ and a final crater of about $4-4.5R_{\rm cyl}$. This confirms that boundary conditions certainly play a role in our simulations for the crater dimensions, at least when the cavity radius gets close to the cylinder radius.

We observe similar behaviors for lower speeds, leading to smaller crater radius equivalences. The slower the impact, the smaller the final crater, at least from our equivalences explained previously. We find that our data for 50, 100, and 200 m s^{-1} correspond to final crater radii of respectively $2.5-3R_{\rm cyl}$, $3-3.5R_{\rm cyl}$, and $4R_{\rm cyl}$.

We also study the amount of ejecta as a function of time, still without considering the presence of the sampling horn. The ejecta volume as a function of time is shown on Fig. 18a for four different impact speeds. We ran these simulations for scaled timesteps and spring constants proportional to impact speeds, as well as with the same timesteps and spring constants for all of them to be sure that the choice has no big influence on the outcome. We comfirm the absence of significant influence (in the short range we covered), as expected from Sec. 3.1.2. The ejecta volume clearly depends on the impact speed: a higher speed leads to more ejecta, if we look at a certain time after impact, or same amounts of ejecta are reached sooner for a higher impact speed. This is what was expected, as higher speeds mean higher incoming energies to be distributed to the target.

By scaling the time with the impact speed (see Fig. 18b), we notice that the relation previously indicated is now directly a proportionality. If the impact speed is twice higher, it takes half the time to reach the same amount of ejecta. Indeed, if we remove this time difference, we have very similar amounts of ejecta. This could be expected when we scale the timesteps and the spring constants with the impact speed, since the main force on the bed is the impactor's penetration force, but we also have this result when we set the same timesteps and spring constants for all speeds. This is particularly due to the very low gravity, allowing particles with even small speeds to escape from the bed. Indeed, we expect particles to have higher ejection speeds with a 300 m s^{-1} impact than a 50 m s−1, but a great amount of particles in both cases is ejected in this low-gravity environment.

The ejected volume can also be expressed as a function of the ejection speed. Here we consider the total volume of all particles faster than a given speed, normalized by a characteristic length, as a function of the normalized ejection speed. Due to the transient crater not being reached and the boundary condition effects (a too small cylinder), we are missing ejecta. Therefore, we do not expect to have as much ejecta volume as in Housen et al. (1983) and Wada et al. (2006), even more since the ejected volume in Housen et al. (1983) comes from measurements of ejecta blankets, and therefore corresponds to a porous global volume and not a volume computed from the sum of grains. However, by using the equivalent final crater radii given previously in this section, we can at least check the agreement of the slope, shown in Fig. 19. Since we saw that it takes twice the time to have the same amount of ejecta for an impact with half the speed, we considered each simulation at different times, scaled according to the impact speed in order to represent the same stage in the crater formation.

We observe in Fig. 19 similarities with Wada et al. (2006), i.e., a depletion of low-volume particles, certainly due to the too small number of grains in our simulations, and a decrease of volume with an increasing ejection speed. We also notice that Wada et al. (2006) had a higher volume of slow ejecta but a much lower amount of fast ejecta. This may be due to the difference in the material properties, as the energy is not necessarily transmitted with the same efficiency through the bed in both simulations.

According to Housen et al. (1983), the power law that should apply to the normalized volume of ejecta faster than a given speed is:

$$\frac{V(>v_e)}{R^3} = 0.32\left(\frac{v_e}{\sqrt{gR}}\right)^{-1.22} \tag{16}$$

where V is the volume, v_e is the ejection speed, R the crater radius, and g the gravitational acceleration. This power law is shown in Fig. 19 and is as expected higher than for our data. Also, the section we obtain with a clear slope is for particles faster than the ones used for deriving the power law in Eq. 16. Nevertheless, our slope is very close to the theoretical one.

Finally, to conclude this study on the ejecta, we analyze the ejecta velocity directions. The prediction of the ejection direction of particles can be useful for a spacecraft shooting on a low-gravity surface, both for risk minimization or sampling efficiency.

For different times, we compute the direction of the velocity of each ejecta. We can then deduce the preferred direction of ejection. Since the setup shows axial symmetry, directions are represented by angles ranging from 0° (horizontal plane) to 90°. The ejecta velocity directions for a 300 m s^{-1} impact are shown on Fig. 20, for a duration up to 1 s. Since there is gravity, even if low, the velocity considered for computing the angle is the original one when leaving the bed, and not the current one. This means that variations with time are due to new particles being ejected, and not to gravity affecting the ejecta speed directions. The ejecta velocity angle therefore corresponds to an ejection angle.

During the whole simulation, most particles are ejected with an angle of about 50°, and in majority between 48° and 54°. This means that a spacecraft located above for example 70° should be safe from any ejecta, or that, in the opposite case when the spacecraft wants to capture particles, it needs to cover angles higher than about 45° to increase its chances of sampling. As a comparison, Wada et al. (2006) also found a majority of ejecta having an ejection angle around 45 and 50°, with a same impact speed and a projectile slightly smaller (radius of 3 mm instead of 4 mm).

We also studied the ejection angles for lower impact speeds down to 50 m s^{-1} and found that the preferred direc-

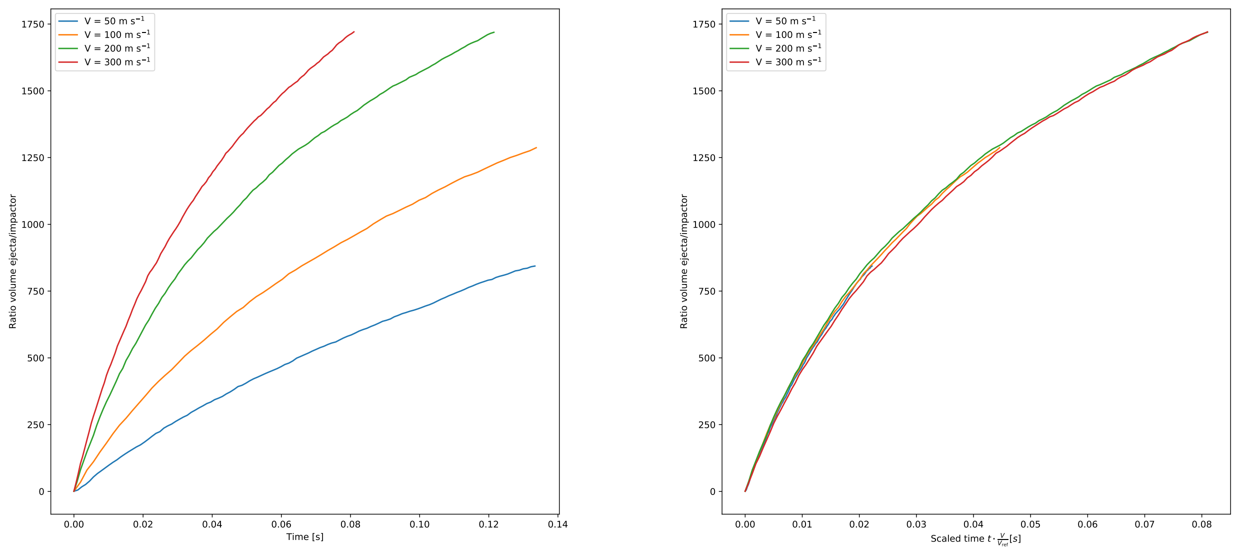

(a) Regular timescale (b) Adapted timescale

Figure 18. Ejecta volume as a function of time for four different impact speeds, with a regular timescale and an adapted one.

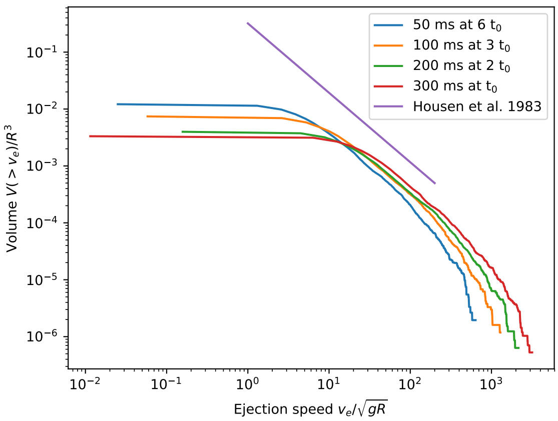

Figure 19. Normalized total ejecta volume of particles whose speed is larger than a given speed as a function of normalized ejection speed, where R is the radius of the equivalent final crater (see text for details). We considered $R_{50\mathrm{m/s}} = 2.75R_{\mathrm{cyl}}$, $R_{100\mathrm{m/s}} = 3.25R_{\mathrm{cyl}}$, $R_{200\mathrm{m/s}} = 4R_{\mathrm{cyl}}$, and $R_{300\mathrm{m/s}} = 4.25R_{\mathrm{cyl}}$. The data correspond to different times depending on the impact speed to reach the same crater phase, as shown in the legend, in which $t_0 = 0.6$ s. The line labeled Housen et al. 1983 comes from Eq. 16.

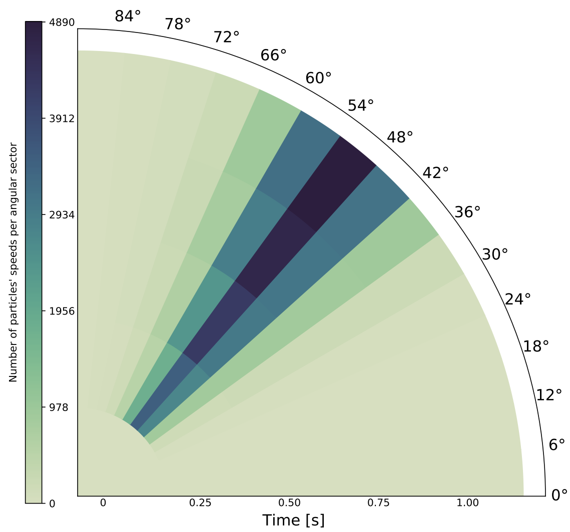

Figure 20. Ejecta velocity angles from the horizontal as function of time, for a 300 m s^{-1} impact. Each ring represents an instant, and the quarter circle is divided into several 6° angular sectors.

tions seem to be similar whatever the impact speed. However, by looking closely at the results, the preferred ejection angle slightly increases with the impact speed. For example, for a 50 m s^{-1} impact, there are much more particles ejected with angles between 42° and 48°, even if the majority is still in the previous angular section. This is due to the impactor penetrating deeper into the bed for higher impact speeds, and therefore ejecting particles with higher angles.

Now that we have characterized the impact, from the cavity's dimensions to the ejecta volume, we add the sampling horn in our simulations to apply these results to Hayabusa2 sampling.

3.2 Application to Hayabusa2 sampling

The sampler of Hayabusa2 is composed of a long horn with a non uniform radius, a filter located near the top of the horn, and a narrow path to the sample return capsule. Its geometry is described in Sawada et al. (2017). We modeled the horn and a part of the sampler storage and transfer mechanism (that we incorporate to the horn for more simplicity in this study) thanks to five circular frustums, i.e., cylinders with tapered radii, or truncated cones. The four pieces of the filter were also modeled faithfully to the original one, and prevent particles with a diameter larger than 1 cm to go through, in order to avoid any jamming upstream from the sample return capsule. The bottom of the horn is supposed to come in contact with the surface, and the projectile is fired immediately after the contact with the surface. However, to model the contact between the horn and the surface would require the knowledge of all moments of inertia, including the spacecraft, and to implement the reaction of the whole system to the surface. In order to simplify, we consider the spacecraft and the sampling mechanism as hovering motionless 0.5 cm above the surface, and we are more interested in particles ejected from the projectile's impact than due to the contact between the horn and the surface.

In the actual sampling mechanism, particles in the top cylinder (later called Cylinder 5) are transferred to the storage area, located at the same height as the cylinder but not represented here for more clarity. We did not seal the top of the sampler in order to avoid jamming inside Cylinder 5, where there would not be any in reality. However, when we consider the mass collected, we take into account particles that went through the top of Cylinder 5 as well as particles still inside it.

3.2.1 General results

First, we consider a simulation of the 300 m s^{-1} impact, with a nominal timestep of dt_{norm} = and a nominal spring constant of k_n, i.e., the same ones we took for our 300 m s^{-1} impacts in Section 3.1. A snapshot of the simulation is shown in Fig. 21a, where each color represents a different cylinder, i.e., a different part of the sampler. Since the sampler is supposed to stay about 1 s at the surface before activating thrusters and leaving the asteroid's surface, we represent here the state of our simulation 1 s after the impact.

In order to check what could happen if we stay longer on the surface or what could be seen from the spacecraft, we ran some simulations with a larger timestep, for which we adapted the spring constant with the rule proposed by Schwartz et al. (2012) as explained in Section 3.1.2. This allows us to simulate the sampling up to 4.5 s, as shown on 21b. We observe that, even if we have a bed limited in size, we already have a lot of ejecta that can also be seen from the spacecraft as they are flying outside the sampling horn. That was indeed observed by Hayabusa2 on-board small monitor camera (CAM-H) right after the sampling. We also see that particles all along the simulations tend to gather together inside what we called Cylinder 4, i.e., the frustum that contains the filter. It is due to a combined effect of the filter and the bottleneck-like geometry of this part of the sampling horn.

This is confirmed by a representation of the packing fraction inside the sampling horn, as shown in Fig. 22, also for 1 and 4.5 s after the impact. The packing fraction is defined here, for each 0.1 cm horizontal slice of the sampling horn and the bed, as the volume occupied by particles divided by the volume of the slice. We see that the packing fraction increases with time near the filter, as particles accumulate. However, we see that the packing fraction does not exceed 0.3, which implies that the part upstream the filter is still not jammed after 4.5 s. Indeed, we see peaks of packing fraction inside the upper cylinder on both panels of Fig. 22, as well as particles in Cylinder 5 in Fig. 21. We also see in Fig. 22 that the packing fraction in the bed drops off as particles are ejected and the crater forms.

There is stochasticity in our simulations. Even with exact same initial conditions, a very slight change in a calculation at the moment of impact can have consequences on the direction of the ejecta, and thus on the direction they impact the walls of the sampling horn. These errors can accumulate and lead to different particles density in the cylinders. Naturally, in the highest cylinders, the particle density is smaller, and a slight difference at impact can imply a particle not going through the bottleneck or the filter. Therefore, the number of particles collected can vary from one simulation to the other. The relatively low number of particles and associated large particular size in our simulations consequently also leads to a low number of particles that go through the filter, which emphasizes this effect. We did not consider very small particles, which would be ejected faster by the impact, and would have more chances to go through the filter. Therefore, if smaller grains are present on Ryugu, our simulations could represent a worse case scenario since from them, we should expect to collect less particles than the actual sampling. What Nevertheless, our simulations can help to determine the expected ratio of particles between the different cylinders.

We used data from two different simulations with different timesteps and spring constants for Fig. 21 and Fig. 22, and we saw in Sec. 3.1.2 that the energy distribution differs depending on these parameters. However, there is no noticeable influence on the ejecta volume (see Sec. 3.1.5). In order to confirm the lack of influence on the sampling, we ran several simulations with different $\Delta t/k_n$ pairs, and we show the distribution of particles in each cylinder in Fig. 23. This is also a way to reduce the stochasticity by running more simulations.

First, we see that the $\Delta t/k_n$ pairs have no major influence on the outcomes of the simulation, as long as they stay in an appropriate domain where the simulations do not crash and that the first contact between the projectile and the surface lasts enough iterations. There are dissimilarities between the simulations, but there are as large between different $\Delta t/k_n$ pairs as they are for same pairs, and are therefore due to stochasticity. Nevertheless, even in Cylinder 4, the number of particles in all simulations is almost equivalent. The largest discrepancies appear for Cylinder 5, the one where particles are collected, where the number of particles is the smallest, and therefore where every particle matters.

We see that the peak of particle number moves with time among the cylinders as particles go up in the sampling horn, and that the bed does not replenish the lower cylinders with particles during the whole simulation. However, we see that after 4.5 s, Cylinder 2 still contains a huge amount of particles, almost a hundred, and this is a reminder of the low-gravity environment, where gravity has a very slow influence on ejected particles.

For almost all of the simulations, at least one particle would be collected after 1 s, i.e., has penetrated into the final cylinder. The collected mass after 1 s can go up to 0.4

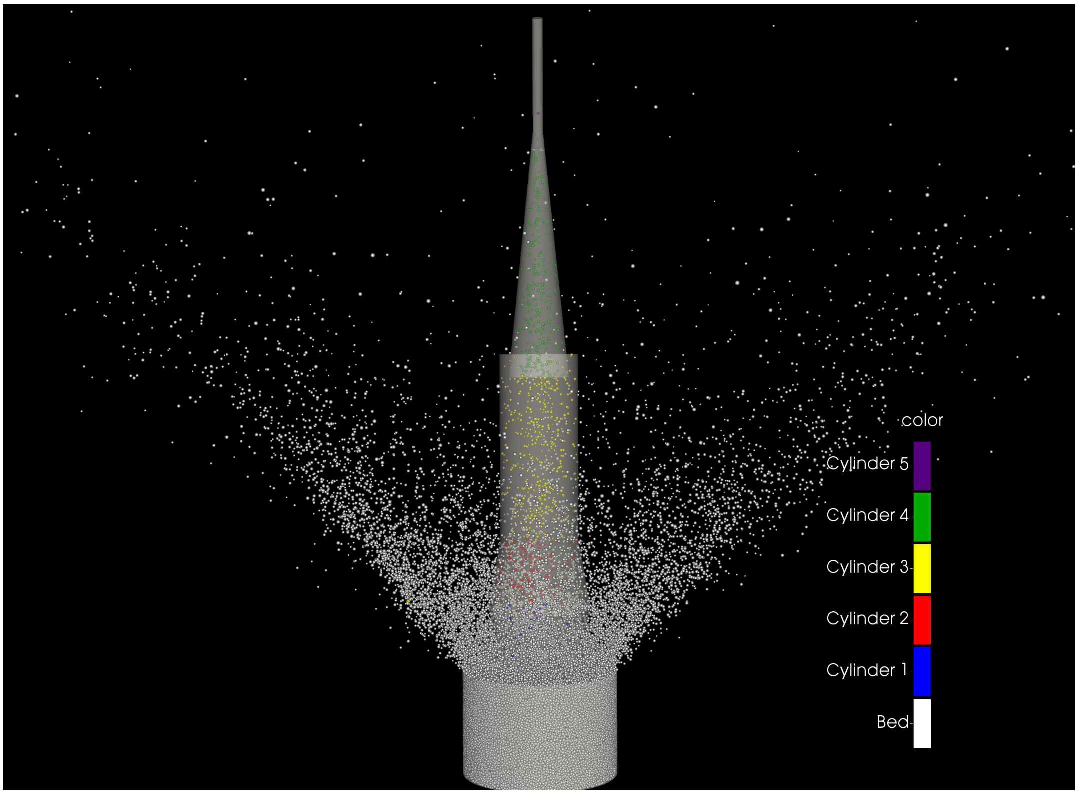

(a) 1 s after impact

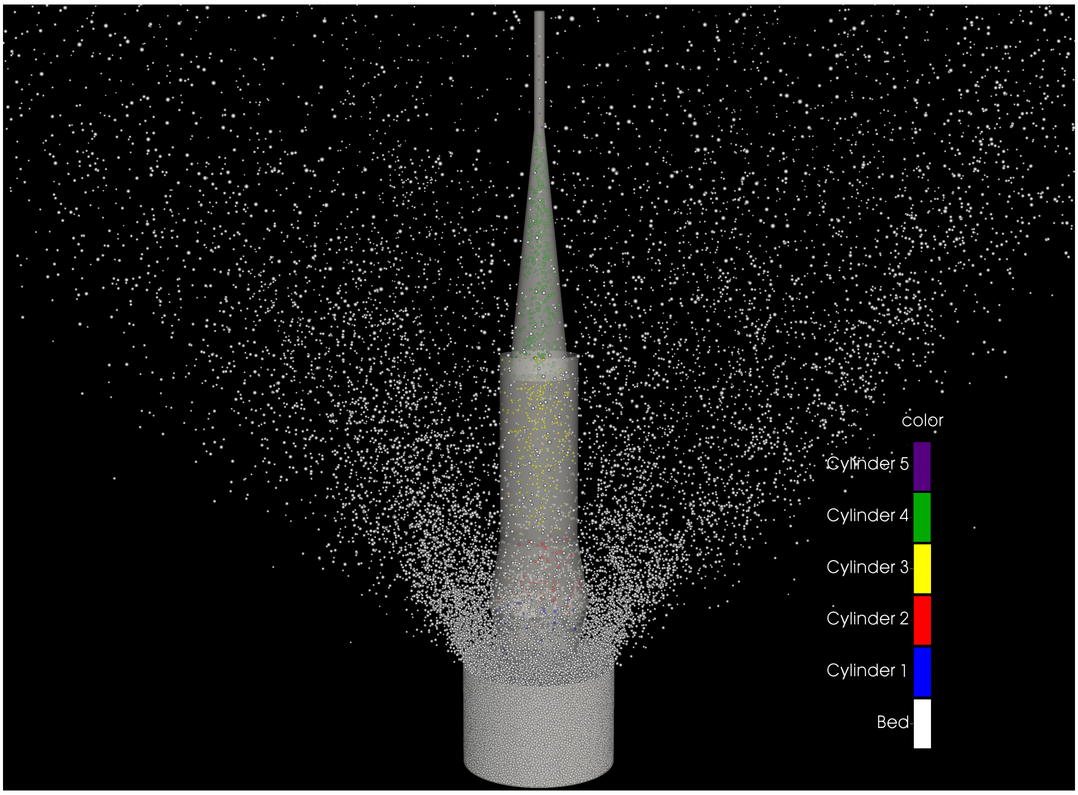

(b) 4.5 s after impact

Figure 21. Snapshots of simulations of the sampler and the regolith bed about 1 s and 4.5 s after the projectile has been fired. The colors correspond to the different tapered cylinders composing the sampling horn, where the smallest value corresponds to the lowest cylinder. The filter can be seen near the top of Cylinder 4.

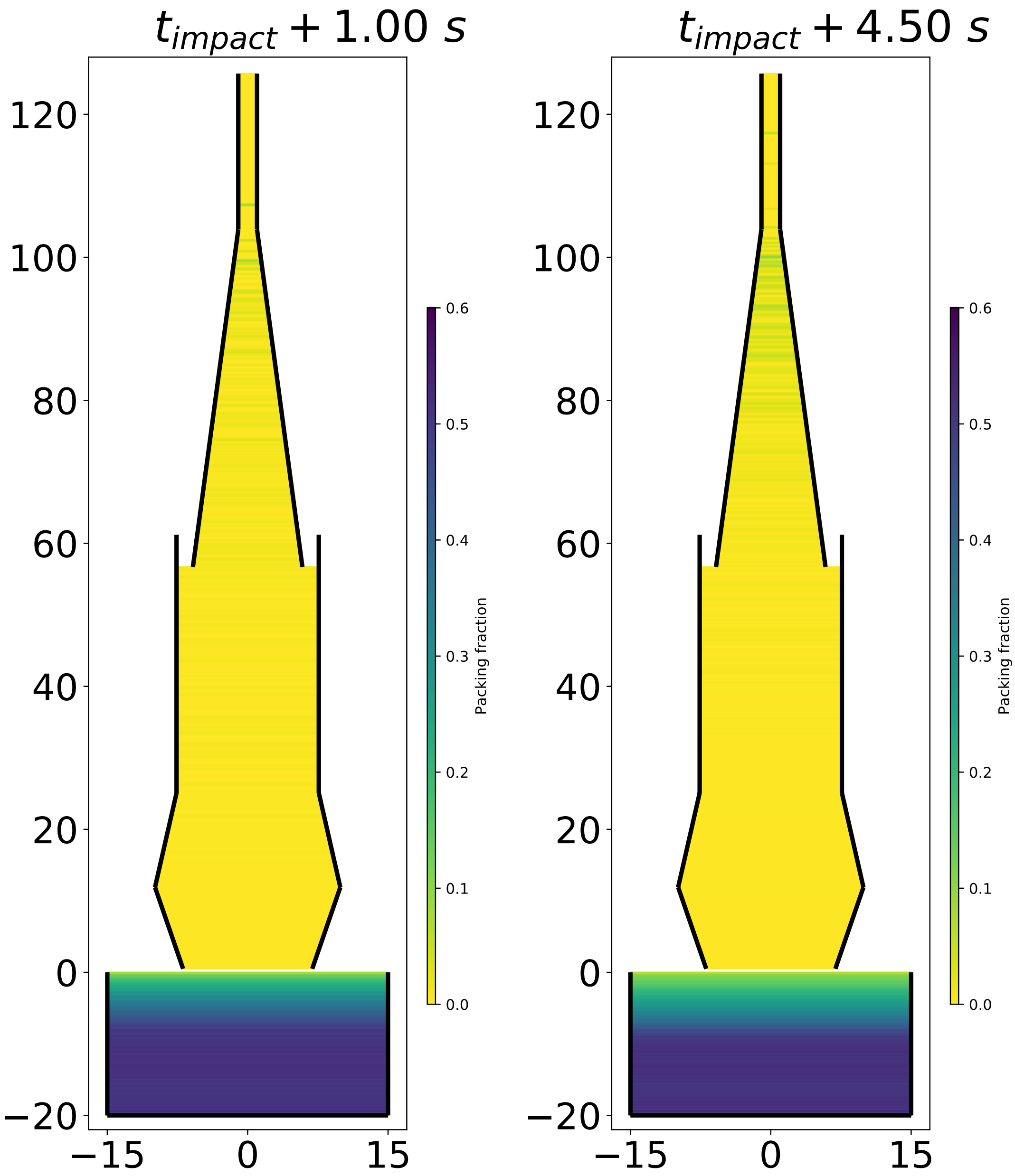

Figure 22. Packing fraction inside the sampling horn for each 0.1 cm slice inside the bed cylinder and the sampling horn, for 1 s and 4.5 s after impact. Distances are in centimeters.

g, which is higher than 100 mg, the scientific objective of Hayabusa2 (Sawada et al. 2017). The density of particles in our simulations being 2.43 g cm^{-3}, one particle with a radius larger than 0.215 cm or two particles with any sizes are enough to fulfill the scientific requirements. The mean radius in our particle distribution is 0.25 cm, and since we get more than one particle in most of the simulations, the scientific goal is usually fulfilled.

After 1 s, the density is still increasing in Cylinder 4, upstream to the filter, meaning that a longer time eventually leads to more collected particles, if a jamming does not occur. As we previously said, the number of particles collected in our simulations is not necessarily representative of the actual one, as smaller particles would be ejected with a higher speed. Also, the contact between the surface and the toothed bottom of the horn could also increase the volume of ejected material. Despite these dissimilarities, we still have collected particles for most of the simulations, which is auspicious for the actual sampling.

In order to continue the comparison with lower speeds as it was done in Sec. 3.1, we did simulations with 50 m s^{-1} impact speed. As it can be expected, the ejecta take much more time to reach the highest cylinders, and by 1.5 there are less than 50 particles in Cylinder 3 (and none has reached Cylinder 4), whereas for 300 m s^{-1} impacts, we have more than 300 particles. We saw in Sec. 3.1.5 that a six times lower speed implies a six times larger duration to reach the same amount of ejecta. We interestingly find the same correlation

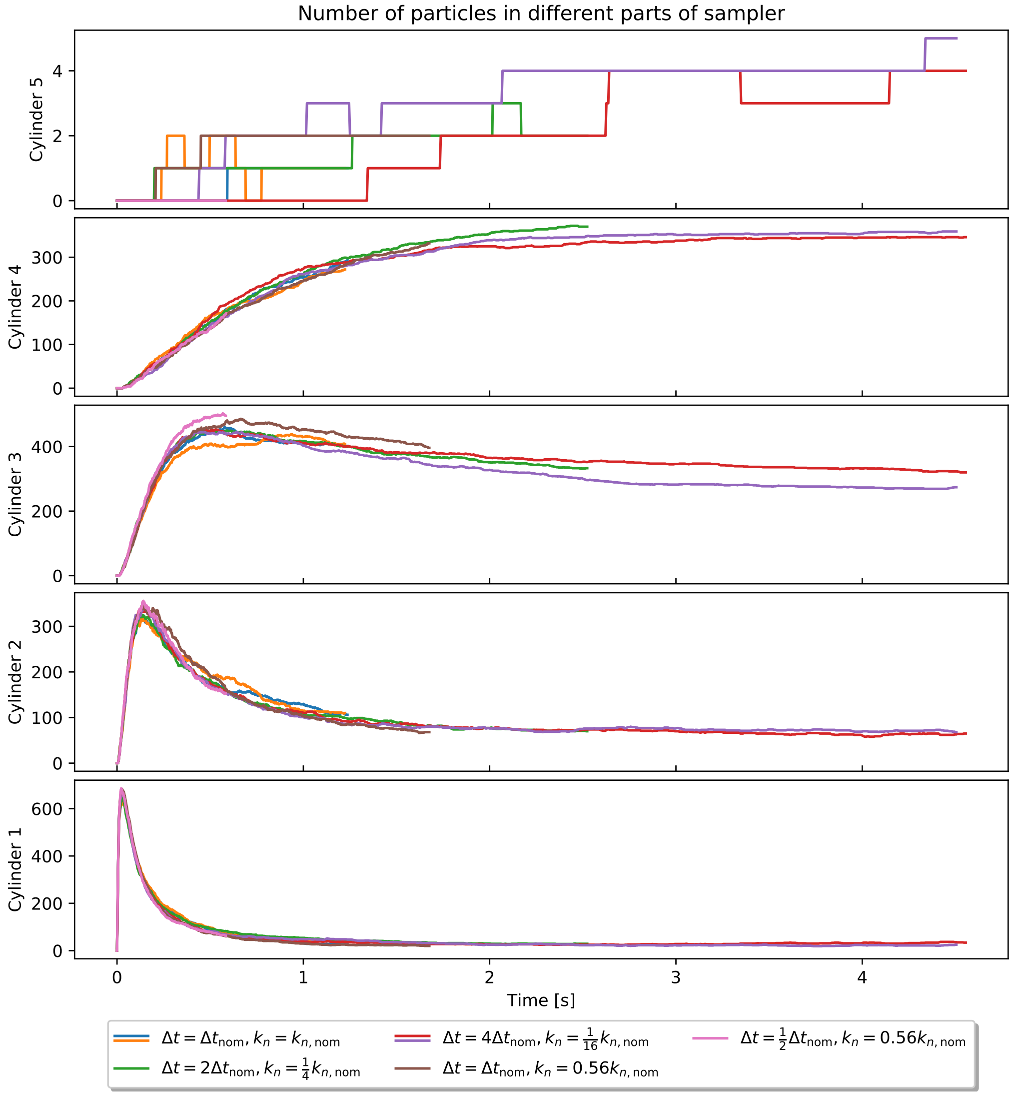

Figure 23. Number of particles in different cylinders of the sampler. Cylinder 1 is the lowest tapered cylinder and Cylinder 5 the highest one. Each color represents a simulation. Different $\Delta t/k_n$ pairs were chosen to run these simulations, and are indicated in the legend.

in each cylinder (at least before Cylinder 5, in which the number of particles is too stochastic). Indeed, if we look at the amount of ejecta for the 50 m s^{-1} impact in Cylinder 4 after 1.2 s for example, it is close to the amount of particles in the same cylinder for the 300 m s^{-1} impact after 0.2 s. Peaks of population also follow this rule in lower cylinders. The volume of particles inside the cylinders seems to scale linearly with the impact speed.

3.2.2 Second projectile

Since Hayabusa2 spacecraft has three projectiles at its disposal (Sawada et al. 2017), it is interesting to check if firing the second projectile a short moment after the first one during the same sampling could significantly increase the number of ejecta and collected particles, or if the changes would stay marginal. In order to investigate this, we model the impact of a second impactor 0.2 s after the first one. The projectile is fired from the bottom of Cylinder 4.

The number of particles per cylinder for simulations with and without a second shot is shown in Fig. 24.

As expected, firing a second impactor increases even more stochasticity. In effect, discrepancies between simulations increase as the second projectile does not hit the same surface for each simulation, and can even hit ejecta before impacting the surface. In all simulations, firing a second projectile significantly increases the ejecta volume in lower cylinders. However, for upper cylinders, beginning with Cylinder 3, a second shot can have the effect of reducing the number of particles or at least delaying its growth.

Also, it is noticeable that increasing the particle volume in Cylinder 4 does not necessarily increase the number

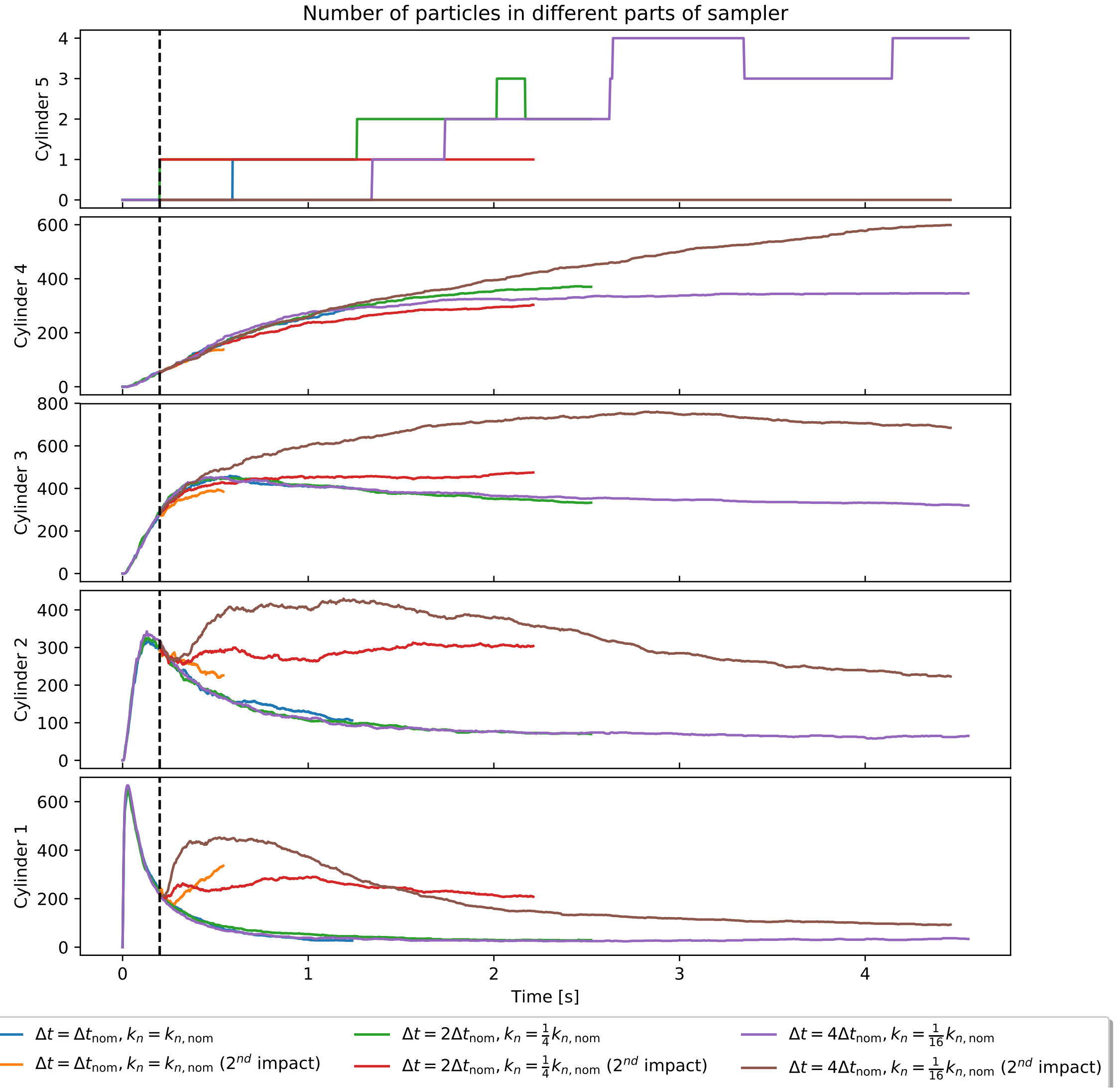

Figure 24. Number of particles in different cylinders of the sampler. Cylinder 1 is the lowest tapered cylinder and Cylinder 5 the highest one. Each color represents a simulation. Different $\Delta t/k_n$ pairs were chosen to run these simulations, and are indicated in the legend. In the legend is also indicated simulations with a second fired projectile after 0.2 s. The black dotted line represents the moment of second firing for the relevant simulations.

of particles in Cylinder 5, and therefore the number of particles collected. Increasing the ejecta number also increases collisions between particles, and therefore can reduce the speeds of particles or change their directions.

Now that we have characterized the impact, and looked at the outcomes for such an impact in the context of Hayabusa2 sampling, we try to expand the parameter space to see if some of the parameters we initially chose have a significant influence on results of Sec. 3.1 and 3.2.

3.3 Expansion of the parameter space

3.3.1 *Influence of the normal and tangential coefficients of restitution ε_n and ε_t*

In this section, we investigate the influence of the target's normal and tangential coefficients of restitution ε_n and ε_t on the impact and the sampling. We begin with the influence of ε_n on the energy distribution during the first instants. The influence of this coefficient has already been studied in Thuillet et al. (2018) concerning the interaction of the Hayabusa2 French-German (CNES-DLR)landing package MASCOT with Ryugu's modeled surface. It was found that a lower ε_n leads to a harder surface and therefore to a higher outgoing-to-incoming speed ratio for MASCOT.

First, we noticed that the spring constant had to be lowered for simulations with a very low normal coefficient of restitution. Otherwise, the simulation would crash because particles went too far from each other in a too short duration, i.e., they would reject each other too strongly. However, one could think that decreasing the normal coefficient of restitution would be not equivalent but at least similar to decreasing the spring constant. Indeed, according to Schwartz et al. (2012), the oscillation half-period of an isolated two-particle collision τ_{overlap} in `pkdgrav` can be computed with Eq. 17.

$$\tau_{\text{overlap}} = \frac{\pi}{\omega_{0n}\sqrt{1-\xi^2}} \tag{17}$$

where $\omega_{0n} = \sqrt{\frac{k_n}{\mu}}$ is the undamped harmonic frequency, μ is the reduced mass of the colliding pair, and ξ is the damping coefficient that can be computed from the normal coefficient of restitution ε_n thanks to Eq. 18.

$$\xi = \frac{-\ln \varepsilon_n}{\sqrt{\pi^2 + (\ln \varepsilon_n)^2}} \tag{18}$$

Equations 17 and 18 lead to the expression of τ_{overlap} as a function of k_n and ε_n shown in Fig. 19.

$$\tau_{\text{overlap}} = \sqrt{\frac{\mu\left(\pi^2 + (\ln \varepsilon_n)^2\right)}{k_n}} \tag{19}$$

In Eq. 19, if ε_n decreases, since $0 < \varepsilon_n < 1$, $(\ln \varepsilon_n)^2$ increases, and we could expect overlap durations to increase, and to find a similar behaviour as if k_n would decrease.

However, this is only true for a single contact, and it is much more complex for a bed composed of thousands of particles. For example, we do not see a 121% increase of overlap duration as predicted when changing ε_n from 0.5 to 0.1, even if we see slight differences in the overlaps between particles. If we look at the energy distribution at the first impact instants as we did in Sec. 3.1.2, when ε_n reaches very small values like 0.1, we see a very high amount of energy, much higher than for any other parameters. The amount of energy in the projectile stays more or less the same but the target's rotational energy can reach very high values, and the energy after $1.2 \cdot 10^{-4}$ s is about 3.75 times the one for $\varepsilon_n \geqslant 0.2$. If $0.2 \geqslant \varepsilon_n \geqslant 0.5$, or $0.5 \geqslant \varepsilon_n \geqslant 0.9$, we do not see any significant difference in the energy distribution. We find that this energy surge effect for very low ε_n disappears for smaller timesteps, for example with a timestep two times smaller. This phenomenon is nonetheless interesting because, from Eq. 19, a decrease in ε_n should increase the overlap durations, and therefore the timestep could be increased. On the contrary, it has to be decreased to faithfully represent the impact mechanism. Once again, we find an unexpected behavior for the normal coefficient of restitution.

Once the timestep is small enough, we find that the distributions are very similar whatever ε_n. The main differences are that the higher ε_n, the higher the peak of target's kinetic energy and the higher this kinetic energy after $1.2 \cdot 10^{-4}$ s. If we look at the target's kinetic energy after $1.2 \cdot 10^{-4}$ s for $\varepsilon_n = 0.1$ and $\varepsilon_n = 0.9$, these variations account for about 6% of the initial total energy, which can seem low, but represents a change from 4.3% to 10.4% of the total initial energy,

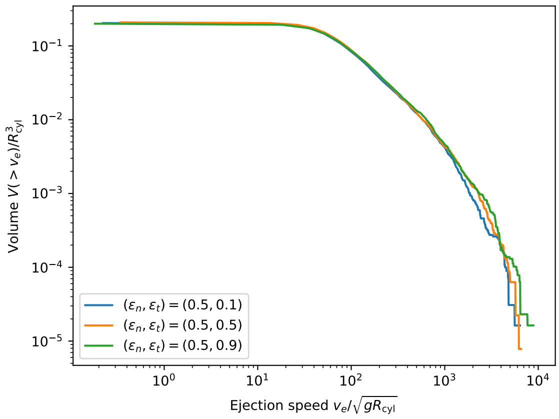

Figure 25. Normalized total ejecta volume of particles faster than a given speed as a function of normalized ejection speed, where R_{cyl} is the radius of the cylinder. The data correspond to different ε_n, 0.25 s after the impact.

and therefore this energy more than doubles from a very low ε_n to a high one.

The amount of ejecta does not seem to depend on ε_n. By looking at the number of particles located at higher levels than the initial surface like we did in Sec. 3.1.5, we find the same amounts for ε_n equal to 0.1, 0.5, and 0.9. Therefore, even if a higher normal coefficient of restitution leads to slightly larger target's kinetic energy, this does not affect the ejecta amount. This is true only if the timestep is small enough, otherwise we find that the amount of ejecta is much larger for $\varepsilon = 0.1$.

Concerning the direction of the velocities of these ejecta, the higher ε_n, the smaller the ejection angle (between the horizontal and the velocity vector). Most particles are ejected with an angle between 48 and 54° for $\varepsilon_n = 0.1$, whereas for $\varepsilon_n = 0.9$ most ejecta velocity angles are in the range between 42 and 48°.

With a higher ε_n, particles are also ejected with higher speeds, as it is shown in Fig. 25. We see that the volume of ejecta for very low ejection speeds are very similar in all cases, but with high ε_n, we have a slightly higher number of high-speed particles. Therefore, even if we saw no direct correlation between the amount of ejecta and the energy distribution during the first instants, we see that the higher target's kinetic energy comes from the fastest ejecta.

When ε_n is higher, the impact wave feels less damping and spread more easily inside the regolith bed. This leads to particles ejected with a higher speed. However, not only ejected particles get a higher speed, but also particles inside the bed, and this implies a visible difference in the cratering process. Indeed, both the lateral and vertical growths of the crater are faster with high ε_n, as shown in Fig. 26. If we look at the depth-to-radius ratio, it is almost the same for $\varepsilon_n = 0.1$ and $\varepsilon_n = 0.5$, i.e., about 0.68 after 0.25 s, but is much higher for $\varepsilon_n = 0.9$ and is about 0.78 at the same time. Yamamoto et al. (2006) found that cratering depends on, among others, internal friction, and our results also provide information on how cratering depends on the physical properties of the target medium.

Concerning the tangential coefficient of restitution ε_t, we see higher target's kinetic energies as well with higher ε_t,

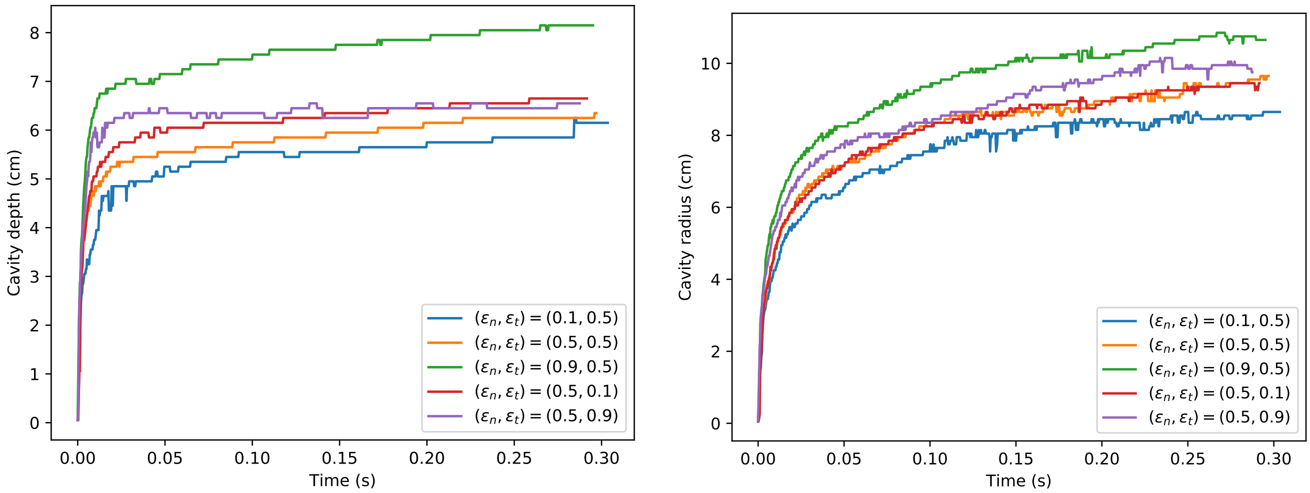

Figure 26. Cavity dimensions (depth and radius) in cm as a function of time for various simulations, differing from each other in their coefficients of restitution ε_n and ε_t. All represent a 300 m s^{-1} impact.

but these do not have the same outcomes as for ε_n. Indeed, ejecta volumes and ejecta speeds are very similar whatever ε_t. Also, as shown in Fig. 26, the relation between ε_t and cavity radius or depth is not as simple as it is with ε_n. Even if the cavity does grow faster with higher ε_t at the beginning of the impact (which was expected from mapping the energy distribution at the first instants), it changes with time and for example after about 0.15 s, a low ε_t can lead to a deeper cavity than found with a high one. Therefore, the relation between ε_t, crater dimensions, ejecta volume, and ejecta speed is a more complex one than for ε_n, and no clear trend can be established.

We also checked the influence of the normal coefficient of restitution ε_n on the sampling (see Fig. 27. We saw that a lower ε_n implies higher ejection angles but particles are ejected with smaller speeds. In Fig. 27, we observe that $\varepsilon_n = 0.9$ leads to high particle densities in Cylinders 1 to 4 for the first tenths of seconds, due to higher ejecta speeds and to a high coefficient of restitution on the walls constituting the sampler horn. With a very low coefficient of restitution ($\varepsilon_n = 0.1$), particles are ejected more slowly and therefore the particle density inside the cylinders takes more time to increase. However, since the ejection angle is higher, the particle density increases more than for higher ε_n in lower cylinders. Because of the low coefficient of restitution on the walls, it is more difficult for particles to reach the highest cylinders. With a small ε_n, particles that succeed in reaching Cylinders 4 and 5 are ejected with higher angles and bounce less against the sampler's walls than with a high ε_n. We find the same results with a 50 m s^{-1} impact, which confirms that particles are ejected faster with a high coefficient of restitution but that ejecta inside the horn are less numerous in total.

Since the amount of ejecta seemed to be the same for all ε_n, the low number of ejecta with high ε_n inside the horn is certainly due to the crater forming faster, and therefore the cavity's boundaries quickly go over the mouth of the sampler horn. Hence, particles are still ejected but outside of the horn.

3.3.2 *Influence of the impact geometry*

Since the regolith bed cannot be perfectly flat, being composed of grains, it is interesting to look at the influence of the impact position with respect to the surface grains on the energy distribution, the crater formation, and the sampling.

First, we look at the energy distribution in the case of a slight shift along the x-axis. Since the average particle radius is 0.25 cm, we chose this value for the shifts, in order to be sure to have a different layout at the impact location than the one already tried. If we call x_0 the regular impact location along the x-axis (the cylinder's axis is located at $x = x_0$ and $y = y_0$), the energy distribution and impactor-particles overlaps for shifts of $x = x_0 \pm 0.25$ cm are shown on Fig. 29 and 28.

We see that the energy distribution at the first instants of the impact depends on the impact location. On Fig. 28, we see that the projectile comes in contact with three particles at the same time, i.e., it goes into a "hole" in the middle of these particles. That is why the impact happens later than for the other simulations, because the impact location height is lower. Also, since it is stopped by three particles at the same time, we see that the overlaps are shallower and the projectile's kinetic energy decreases very fast. In this case, we do not have two phases as in the regular impact location. Nonetheless, the target's kinetic energy after $1.2 \cdot 10^{-4}$ s is very similar in both cases.

With a -0.25 cm shift (see Fig. 29), the projectile hits the same top particle as with the regular location but deeper, and this time there are no other very close particles. Because of that, the projectile's kinetic energy does not decrease as fast as with previous impact locations. The projectile eventually hits other particles and slows down. The elastic energies and the overlaps show that the first contact is longer than for example the +0.25 cm case. We see that, even if the energy distribution depends on the geometry of the surface where the impact happens, there is always a fast decrease of target's energy, peaks in elastic energies and target's kinetic energy. Moreover, the kinetic energy contained in the grains after $1.2 \cdot 10^{-4}$ s is of the same order of magnitude.

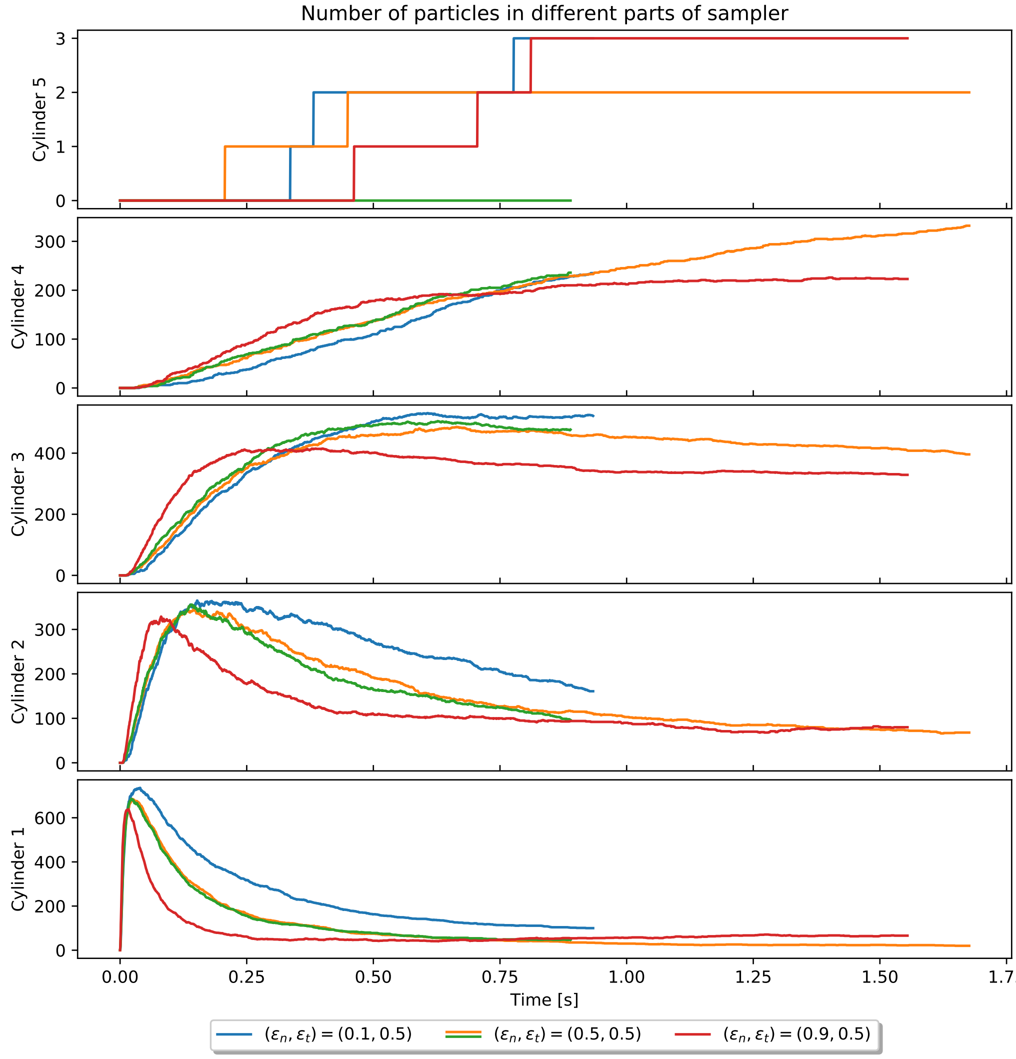

Figure 27. Number of particles in different cylinders of the sampler. Cylinder 1 is the lowest tapered cylinder and Cylinder 5 the highest one. Each color represents a simulation. Different normal coefficients of restitution were chosen to run these simulations, and are indicated in the legend.

Concerning the whole crater formation, the cavity depth and radius do not seem to depend on the impact location, and the small disparities are more due to stochasticity than to actual differences in the formation mechanisms (see Fig. 30). When we look at the ejecta volume as a function of the distance from the impact point, the shift in the impact point seems to have no influence. We can see some dissimilarities when looking at the ejecta volume as a function of the ejection speed, but these faint variations do not correspond to faster cavity growths, and are therefore not as noticeable as they were for ε_n in Sec. 3.3.1.

Because the impact may not be perfectly vertical to the surface (and will certainly not be as the projectors are not parallel to the horn central axis), we also study the influence of a tilted impact, with an angle of −25° or +25° from the vertical in the x-z plane. Whereas the evolution of the cavity radius is very similar whatever the geometry of the impact, the cavity is significantly shallower in the case of a +25° tilted impact (see Fig. 30). When we also look at the amount of ejected particles, we see that a +25° tilted impact generates much fewer ejecta than the other geometries. A −25° tilted impact also produces less ejecta than a normal impact during the first instants but the volume increases faster than for other geometries, and the volume of ejecta becomes equal for all geometries except the +25° case at about 0.8 s after the impact. This shows that the regolith bed is anisotropic, and this is certainly due to the layout of the grains and to the force chains in the bed itself. In the vertical direction, particles are subject to very different constraints depending on the particle layout, and it

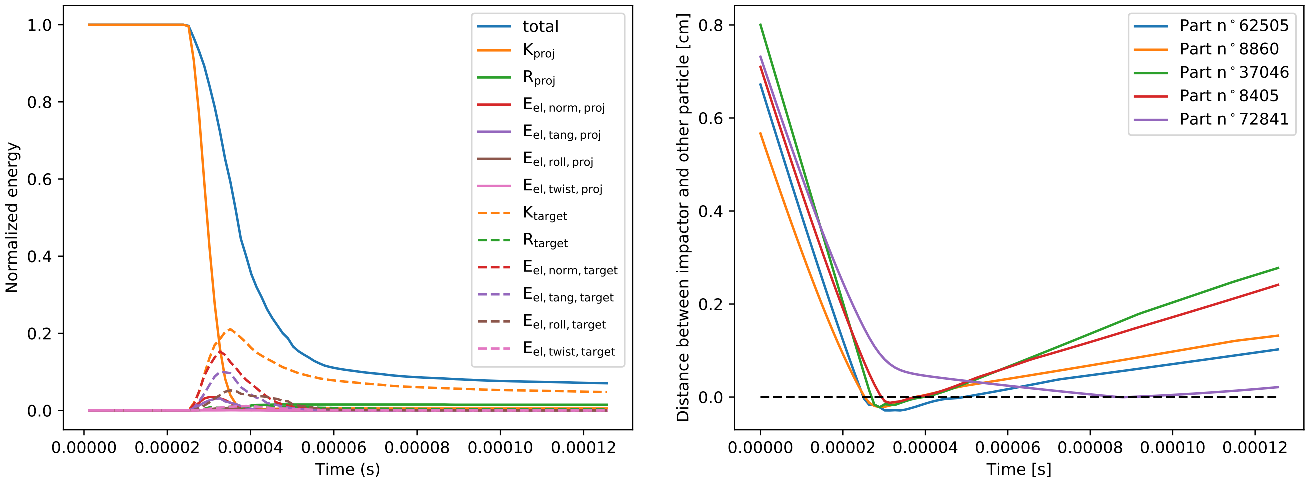

Figure 28. Energy distribution (left) and impactor-particles overlaps (right) for a 300 m s^{-1} impact as function of time, with an impact shift of $x = x_0 + 0.25$ cm.

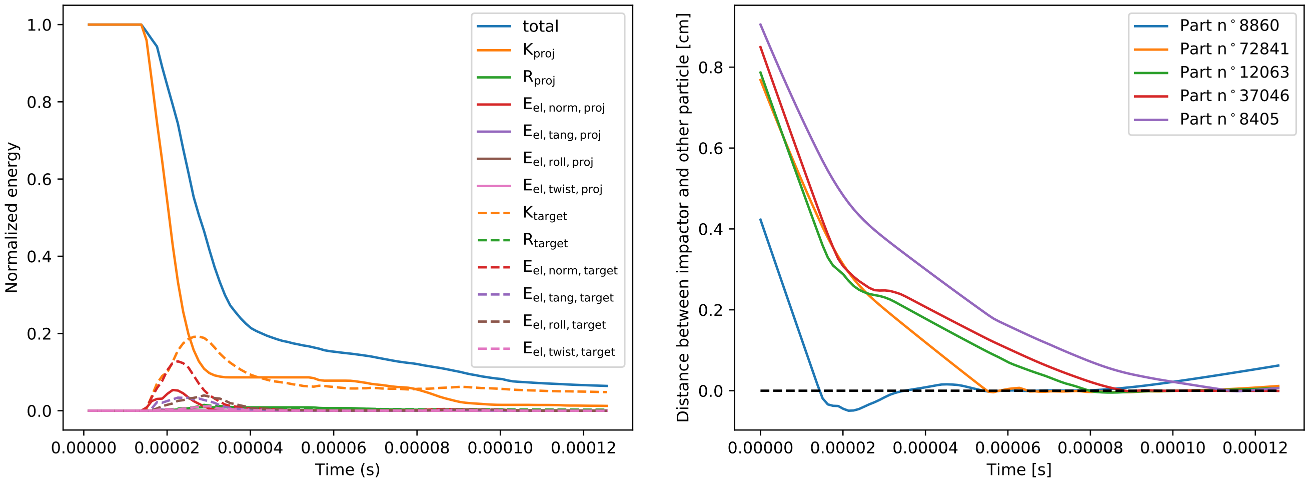

Figure 29. Energy distribution (left) and impactor-particles overlaps (right) for a 300 m s^{-1} impact as functions of time, with an impact shift of $x = x_0 - 0.25$ cm.

can be easier or harder for them to move down, whereas in the horizontal direction, the constraints are weaker due to the surface, and therefore these variations of constraints are fainter. We also find that the directions of ejection do not depend on the impact angle within the considered range, and that most of the particles are ejected with an angle between 48° and 54° whatever the impact angle.

Looking at the high-speed ejecta, we see that they are faster and more numerous from a tilted impact than from a vertical one (see Fig. 31). Indeed, for both simulations with a tilted impact, we find a larger population of ejecta with an ejection speed higher than 10 m s^{-1}. This is in agreement with Yamamoto et al. (2005), who also find an increase in high-velocity ejecta with an increasing impact angle (from the vertical).

Simulations including the sampling horn show a shortage of ejecta observed for the +25° tilted impact, which has an influence on the particle density in Cylinders 1 to 4, as shown in Fig. 32. Surprisingly, more particles go through the filter and into Cylinder 5. This is certainly due to the high stochasticity of the particle number in Cylinder 5; the fact that a particle penetrates or not into Cylinder 5 depends on very slight differences in the particle direction. It may also be due to the lower particle density in lower cylinders, and therefore fewer collisions between particles. More particles can then reach Cylinder 5 without experiencing any collision with other ejecta. We also observe a temporary shortage of ejecta at the beginning of simulations of the −25° tilted impact. In summary, tilted impacts produce less ejecta during the first instants, which can be seen in the lowest cylinders. However, that does not mean in our case that the number of collected particles is smaller. The medium appears to be anisotropic and the direction of impact can lead to a different number of ejecta.

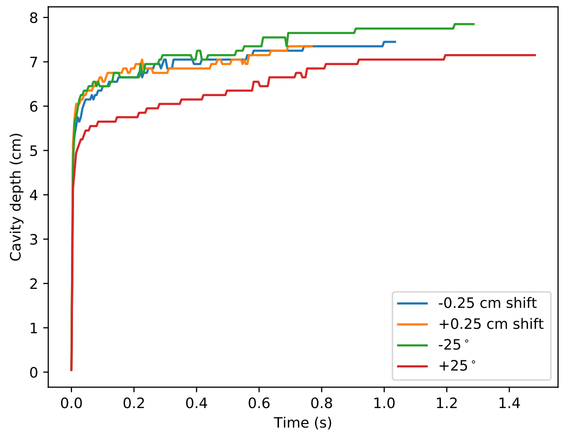

Figure 30. Cavity radius in cm as a function of time for various simulations, differing from each other in the impact geometry. All represent a 300 m s^{-1} impact. In the legend, degrees are from the vertical, in the x-z plane.

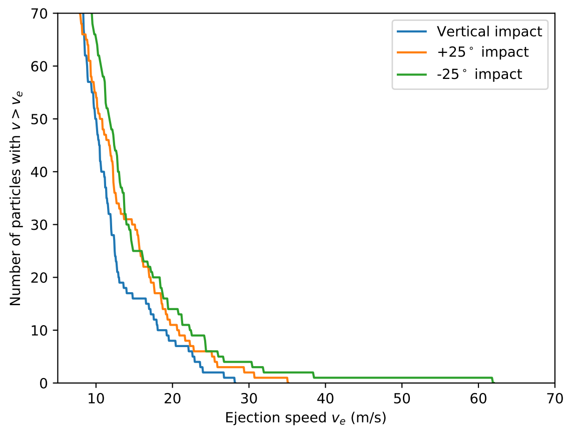

Figure 31. Number of ejected particles whose ejection speed is larger than a given speed as a function of the ejection speed, for different impact angles. On this figure is only considered a speed range from about 10 m s^{-1} to 70 m s^{-1}.

We notice that the impact location has a small influence on the sampling. For a −0.25 cm shifted impact, particles ejected with a high speed are less numerous, leading to more particles in the lowest cylinders and less in the highest ones soon after the impact, but the particle density in these cylinders then increases with time as particles have time to go up. The impact location has therefore more influence on the ejecta speed than on the ejecta volume.

4 CONCLUSIONS

In this paper, we presented the results of our simulations of 300 m s^{-1} impacts into a regolith bed, under the low-gravity environment of Ryugu. We also considered for comparison impacts speeds of 50, 100, and 200 m s^{-1}. We first presented our simulations without the sampler horn, to characterize the impact and the reaction of our bed, without adding the complexity and influence of the sampling mechanism.

We found that the cratering process is much longer under Ryugu's low gravity than for 1 g simulations and experiments. At first, we see a hemispherical growth, then the depth increase slows down, leading to a mainly lateral growth phase. Higher impact speeds lead to larger cavities, but the evolutions of the cavity depth as a function of the cavity radius are very similar. We also studied the energy distribution during the first instants after impact, and we find that less than 10% of the initial kinetic energy is transmitted into the ejecta kinetic energy, which is consistent with what is typically assumed in collisional evolution models (e.g. Davis et al. 2002).

Confronting our simulations to the shock propagation theory, we find that the impact shows characteristics of the momentum conservation mode. Moreover, by applying the Z-model to our simulations, we find that it matches very well only for a certain time, when we have a stationary excavation state. When it matches, we find again that we are in the momentum conservation regime. From the three considered instants, Z seems to increase with time, but the flow-field center appears to be located at the impact point.

We also studied the particles ejected from the bed. Based on ejecta charcteristics, we can expect a transient crater between 3 and 5 cylinder radii, decreasing with the impact speed. Most of particles are ejected with an angle between 48 and 54°.

When we consider the sampling horn of the Hayabusa2 sampling mechanisms, we observe some stochasticity as similar impacts can give different results, due to the high number of interactions between the projectile, the particles, and the horn. However, for most of the simulations, the scientific goal of 100 mg is almost always fulfilled after 1 s, even without taking into account the interaction between the horn and the surface, and the scoop-up part. Generally, we see that a higher number of ejecta in the lower parts of the horn does not mean a higher density in the upper part. As an example of this observation, a second shot 0.2 s after the first one would increase the initial amount of ejecta but not necessarily the portion that goes in the upper parts of the horn, due to a rising probability of collisions between grains.

Finally, we looked at the influence of the physical parameter ε_n and of the impact geometry on our results. The influence of ε_n is not as straightforward as basic equations could let us think, as we had to decrease the timestep for low ε_n. The amount of ejecta does not seem to depend on this coefficient, but the ejection angle and speed do. With the sampling horn, we find that there are less particles in upper cylinders for a high ε_n but they reach them more quickly. Our study on the impact geometry, with slightly translated and tilted impacts, shows that the regolith bed is anisotropic, and that the outcome of the impact depends more on the impact angle than on the exact location of the impact. With tilted impacts, high-speed ejecta are more numerous and faster, but in the first instants the total amount of ejected particles is usually smaller.

To conclude, this study provides many results concerning the outcome of impacts in a low-gravity environment, under conditions that are hard to reproduce on Earth. Our results are in agreement with many previous studies, even if we sometimes find discrepancies due to our relatively restraining boundary conditions.

This study is based on several assumptions (e.g., the size of the cylinder containing the bed, the grain sizes, the fric-

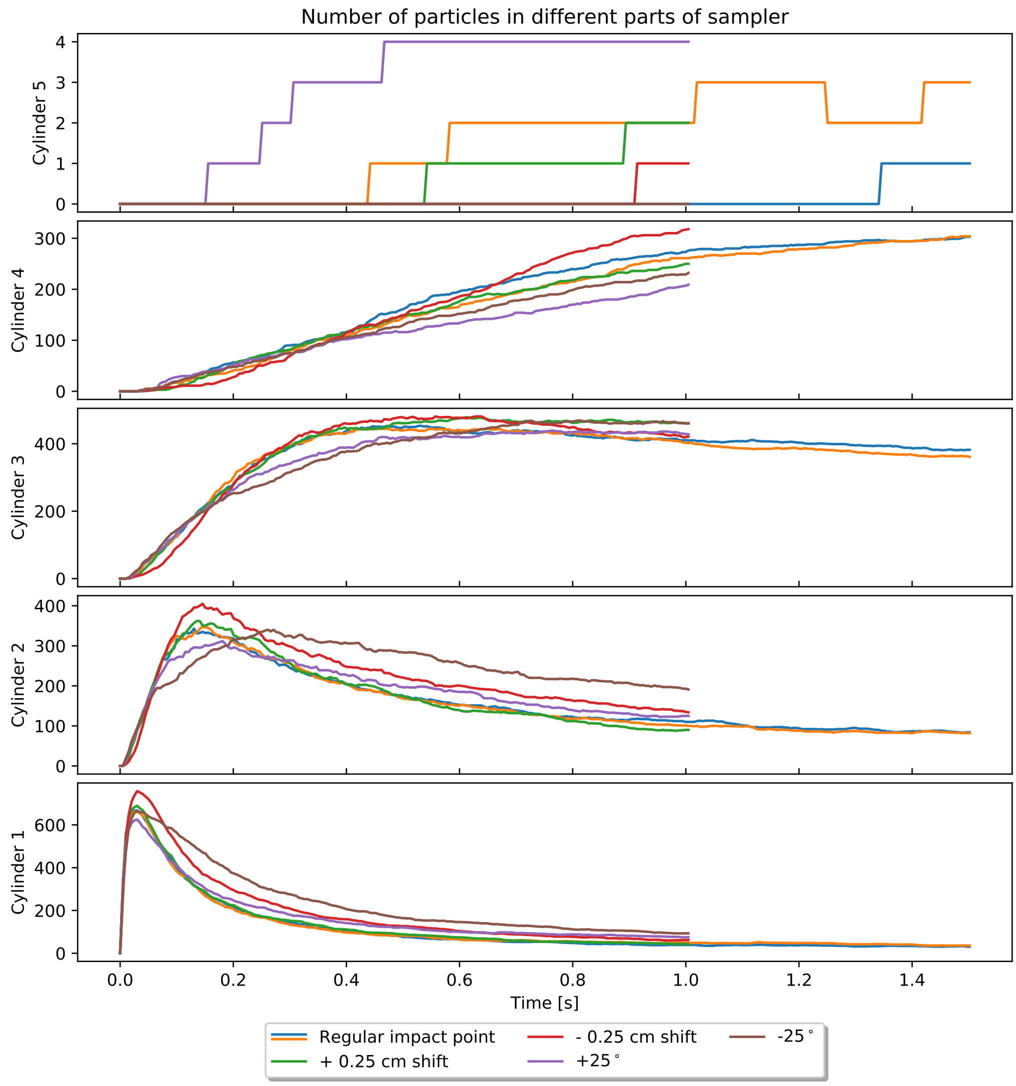

Figure 32. Number of particles in different cylinders of the sampler. Cylinder 1 is the lowest tapered cylinder and Cylinder 5 the highest one. Each color represents a simulation. Different impact angles and locations were chosen to run these simulations, and are indicated in the legend. In the legend, degrees are from the vertical, in the x-z plane.

tion coefficients etc.) and in order to better understand the cratering process under low gravity, future numerical simulations should be done, for instance, with a larger cylinder to avoid boundary effects and enable the cavity to grow freely. To do so, solutions have to be found to decrease the computation time, or a large amount of time should be dedicated to run these simulations, because increasing the cylinder radius has a significant effect on computation time. Moreover, to better represent the actual rocky surface of Ryugu, grains could be represented as aggregates of smaller particles, that break when submitted to strong forces. Finally, the bottom teeth could be modeled, as well as the interaction of the horn with the surface, taking into account the inertia of the whole spacecraft, and making much more complex the simulations. This is something we will consider in future studies so that we full understanding of such a sampling mechanism efficiency can be assessed over a wide range of parameters and gravity conditions than can be achieved with experiments.

ACKNOWLEDGEMENTS

F.T. is supported by a PhD fellowship of the University of Nice-Sophia. P.M. and F.T. acknowledge funding support from the French space Agency CNES, as well as from Academies of Excellence: Complex systems and Space, environment, risk, and resilience, part of the IDEX JEDI of the Université Côte d'Azur in connection with its Center for Planetary Origins (C4PO). Simulations were performed at

Mésocentre SIGAMM hosted at the Observatoire de la Côte d'Azur.

REFERENCES

Anderson J. L. B., Schultz P. H., Heineck J. T., 2002, Lunar and Planetary Science Conference, p. 1762

Asphaug E., 2007, Science (New York, N.Y.), 316, 993

Austin M. G., Thomsen J. M., Ruhl S. F., Orphal D. L., Schultz P. H., 1980, in Lunar and Planetary Science Conference Proceedings. p. 2325, https://ui.adsabs.harvard.edu/abs/1980LPSC...11.2325A/abstract

Austin M. G., Thomsen J. M., Ruhl S. F., Orphal D. L., Borden W. F., Larson S. A., Schultz P. H., 1981, in Multi-ring basins: Formation and Evolution. p. 197, https://ui.adsabs.harvard.edu/abs/1981mrbf.conf..197A/abstract

Barnouin O. S., et al., 2019, Nature Geoscience, 12, 247

Binzel R., Harris A. W., Bus S. J., Burbine T. H., 2001, Icarus, 151, 139

Brisset J., Colwell J., Dove A., Abukhalil S., Cox C., Mohammed N., 2018, Progress in Earth and Planetary Science, 5, 73

Cintala M. J., Berthoud L., Hörz F., 1999, Meteoritics & Planetary Science, 34, 605

Colwell J. E., 2003, Icarus, 164, 188

Croft S. K., 1980, in Lunar and Planetary Science Conference. p. 180, https://ui.adsabs.harvard.edu/abs/1980LPI....11..180C/abstract

Davis D. R., Durda D. D., Marzari F., Campo Bagatin A., Gil-Hutton R., 2002, in , Asteroids III. University of Arizona Press, p. 545, https://ui.adsabs.harvard.edu/abs/2002aste.book..545D/abstract

Hirata N., et al., 2009, Icarus, 200, 486

Holsapple K. A., 1993, Annual Review of Earth and Planetary Sciences, 21, 333

Housen K. R., Schmidt R. M., Holsapple K. A., 1983, Journal of Geophysical Research, 88, 2485

Katsuragi H., 2016, Physics of Soft Impact and Cratering. Lecture Notes in Physics Vol. 910, Springer Japan, Tokyo, doi:10.1007/978-4-431-55648-0, http://link.springer.com/10.1007/978-4-431-55648-0

Katsuragi H., Blum J., 2017, The Astrophysical Journal, 851, 23

Katsuragi H., Durian D. J., 2007, Nature Physics, 3, 420

Kurosawa K., Takada S., 2019, Icarus, 317, 135

Lauretta D. S., et al., 2017, Space Science Reviews, 212, 925

Makabe T., Yano H., 2008, in 26th International Conference on Space Technology and Science (ISTS), 2008-k-08. ISTS Web Paper Archives, Hamamatsu, https://archive.ists.or.jp/upload{_}pdf/2008-k-08.pdf

Maurel C., Michel P., Biele J., Ballouz R.-L., Thuillet F., 2018, Advances in Space Research, 62, 2099

Maxwell D. E., 1977, in Impact and Explosion Cratering: Planetary and Terrestrial Implications. pp 1003–1008, https://ui.adsabs.harvard.edu/abs/1977iecp.symp.1003M/abstract

Melosh H. J., 1989, Impact Cratering : A Geologic Process. Oxford University Press, https://ui.adsabs.harvard.edu/abs/1989icgp.book.....M/abstract

Melosh H. J., 2011, Planetary Surface Processes. Cambridge University Press, Cambridge, doi:10.1017/CBO9780511977848, http://ebooks.cambridge.org/ref/id/CBO9780511977848

Murdoch N., Avila Martinez I., Sunday C., Zenou E., Cherrier O., Cadu A., Gourinat Y., 2017, Monthly Notices of the Royal Astronomical Society, 468, stw3391

Nakamura A. M., Setoh M., Wada K., Yamashita Y., Sangen K., 2013, Icarus, 223, 222

Nordstrom K., Lim E., Harrington M., Losert W., 2013, APS March Meeting Abstracts, 2013, N29.013

O'Keefe J. D., Ahrens T. J., 1999, Journal of Geophysical Research: Planets, 104, 27091

Richardson D., Quinn T., Stadel J., Lake G., 2000, Icarus, 143, 45

Richardson J. E., Melosh H. J., Greenberg R., 2004, Science, 306, 1526

Richardson D., Michel P., Walsh K., Flynn K., 2009, Planetary and Space Science, 57, 183

Richardson D. C., Walsh K. J., Murdoch N., Michel P., 2011, Icarus, 212, 427

Robinson M. S., Thomas P. C., Veverka J., Murchie S. L., Wilcox B. B., 2002, Meteoritics & Planetary Science, 37, 1651

Sawada H., et al., 2017, Space Science Reviews, 208, 81

Schwartz S. R., Richardson D. C., Michel P., 2012, Granular Matter, 14, 363

Schwartz S. R., Michel P., Richardson D. C., Yano H., 2014, Planetary and Space Science, 103, 174

Stadel J. G., 2001, PhD thesis, University of Washington, https://ui.adsabs.harvard.edu/{#}abs/2001PhDT.......21S/abstract

Sugita S., et al., 2019, Science, 364, eaaw0422

Thomsen J. M., Austin M. G., Ruhl S. F., Schultz P. H., Orphal D. L., 1979, in Lunar and Planetary Science Conference Proceedings. p. 2741, https://ui.adsabs.harvard.edu/abs/1979LPSC...10.2741T/abstract

Thuillet F., et al., 2018, Astronomy & Astrophysics, 615, A41

Uehara J. S., Ambroso M. A., Ojha R. P., Durian D. J., 2003, Physical Review Letters, 90, 194301

Wada K., Senshu H., Matsui T., 2006, Icarus, 180, 528

Wada K., et al., 2018, Progress in Earth and Planetary Science, 5, 82

Walsh A. M., Holloway K. E., Habdas P., de Bruyn J. R., 2003, Physical Review Letters, 91, 104301

Walsh K. J., et al., 2019, Nature Geoscience, 12, 242

Watanabe S.-i., Tsuda Y., Yoshikawa M., Tanaka S., Saiki T., Nakazawa S., 2017, Space Science Reviews, 208, 3

Watanabe S., et al., 2019, Science, 364, 268

Yamamoto S., Wada K., Matsui T., 2003, in Proceedings of the 36th ISAS Lunar and Planetary Symposium. Institute of Space and Astronautical Science, Japan Aerospace Exploration Agency (JAXA/ISAS)

Yamamoto S., Kadono T., Sugita S., Matsui T., 2005, Icarus, 178, 264

Yamamoto S., Wada K., Okabe N., Matsui T., 2006, Icarus, 183, 215

Yamamoto S., Barnouin-Jha O. S., Toriumi T., Sugita S., Matsui T., 2009, Icarus, 203, 310

Yu Y., Richardson D. C., Michel P., Schwartz S. R., Ballouz R.-L., 2014, Icarus, 242, 82

Zhang Y., et al., 2017, Icarus, 294, 98

de Vet S. J., de Bruyn J. R., 2007, Physical Review E, 76, 041306

This paper has been typeset from a TEX/LATEX file prepared by the author.

OSIRIS-REx and (101955) Bennu

6

> *I know this place.*
>
> — **Hayabusa2 team**
> (looking at first images of Bennu)

Contents

In the previous chapters, I presented the numerical code `pkdgrav` and my work in relation with Hayabusa2 and Ryugu. During my PhD, I was also a member of the OSIRIS-REx science team, and attended to the science meetings. In this chapter, I first briefly introduce Bennu and then I present a small analysis of the paper published in the journal Nature Geosciences in which I am a co-author, about our interpretations of the geology of (101955) Bennu. I particularly emphasizes the parts concerning the granular material on the surface, in order to show the potential applicability to Bennu of the previous studies I presented. Finally the paper itself is reproduced in its integrality: Walsh et al. (2019).

6.1 OSIRIS-REx

The NASA mission OSIRIS-REx (Origins, Spectral Interpretation, Resource Identification and Security-Regolith Explorer), the third mission of the New Frontiers program (Lauretta et al., 2017), is also a sample return mission to a primitive asteroid. As its Japanese counterpart, it is aimed to visit a NEA, here (101955) Bennu, collect samples from its surface and bring them back to Earth. It was launched on September 8, 2016 from Cape Canaveral in Florida, USA, and was aimed at reaching its asteroid target in November 2018.

OSIRIS-REx's plan consists of a two-year close-observation sequence and an attempt of sample collection with the Touch And Go Sample Acquisition Mechanism (TAGSAM). A minimum of 60 g of material is necessary for the mission to be considered as a success (Lauretta et al., 2017).

In order to investigate Bennu's properties, the spacecraft is equipped with a broad set of instruments. These include the OSIRIS-REx Camera Suite (OCAMS) (Rizk et al., 2018), the OSIRIS-REx Laser Altimeter (OLA) (Daly et al., 2017), the OSIRIS-REx Visible and InfraRed Spectrometer (OVIRS) (Reuter et al., 2018), the OSIRIS-REx Thermal Emission Spectrometer (OTES) (Christensen et al., 2018), the student-experiment REgolith X-Ray Imaging Spectrometer (REXIS) (Masterson et al., 2018), a radio transmitter coupled with the Deep Space Network (McMahon et al., 2018), and the Touch And Go CAMera System (TAGCAMS) (Bos et al., 2018). During the two-year investigation around Bennu, the set of instruments previously listed focused on four criteria in order to determine a sampling site on the surface of the asteroid: two from scientific teams, the science value and the sampleability (regarding TAGSAM and regolith properties), and two from engineering teams, the safety and the deliverability (concerning flight dynamics and navigation).

Prior to arrival, we had more information about asteroid Bennu than about Ryugu. (101955) Bennu was discovered in 1999 by the LINEAR survey, like Ryugu. Bennu is also a C-complex asteroid but, contrarily to Ryugu, it is a B-type asteroid. Its visible and infrared spectra have been extensively observed (Clark et al., 2011; Müller et al., 2012b; Emery et al., 2014; Binzel et al., 2015) as well as its shape and spin state through ground-based radar (Nolan et al., 2013). It is one of the most dangerous detected PHAs (Chesley et al., 2014). Its orbit semi-major axis is 1.13 AU with a perihelion of 0.897 AU, and thus Bennu belongs to the Apollo family. The observations have enabled a precise knowledge of the rotational period (4.2978 hours) and an estimate of its the bulk density (1260 ± 70 kg m^{-3}). Its shape was believed to be a spheroid, more precisely a "spinning top", i.e., an oblate spheroid with an equatorial ridge, with dimensions about $565 \pm 10 \times 535 \pm 10 \times 508 \pm 52$ m (Lauretta et al., 2015).

OSIRIS-REx started its approach phase in August 2018 and arrived at Bennu in December 2018. Its global properties are described in (Lauretta et al., 2019), and other observations and interpretations can be found in a series of 2019 Nature Geoscience and Astronomy papers. Among them, Barnouin et al.

(2019b) analyzed the shape and global features, and Walsh et al. (2019), to which I contributed, looked at craters, boulders, and regolith.

6.2 Bennu

6.2.1 General properties

Bennu's spinning-top shape and B-type taxonomy were confirmed by first images from OSIRIS-REx, as well as other global properties, and is believed to be linked to CM carbonaceous chondrites (Lauretta et al., 2019). Bennu's average diameter is 490.06 ± 0.16 m, and has a volume 3.5 times larger than Itokawa's and 6 times smaller than Ryugu's. (Barnouin et al., 2019b). Its density was determined as 1.190 ± 0.013 g cm^{-3}, very similar to the one of Ryugu (see Chapter 3), and its total porosity is estimated to $50 - 60\%$ depending on the meteorite material considered (CI or CM) (Barnouin et al., 2019b). Thus, Bennu is believed to be a rubble pile.

A model of Bennu's surface is shown in Fig. 6.1, showing that the poles are topographic highs whereas the equator is a low. Bennu's shape is different from Ryugu's one, as the equatorial ridge is not as pronounced (with only several isolated high points), and four major longitudinal ridges give Bennu a shape closer to the one of a diamond (see views from poles in Fig. 6.1). These ridges have heights up to 25 m and lengths from 400 to 780 m.

An analysis of Bennu's surface is presented in the article in Section 6.3. Here, as I did for Ryugu in Chapter 3, I concentrate on the evidence of regolith material on the surface.

6.2.2 Regolith on the surface

Bennu's surface is at first sight similar to the one of Ryugu. Numerous boulders cover the surface, and craters can be identified, as well as an equatorial ridge and grooves.

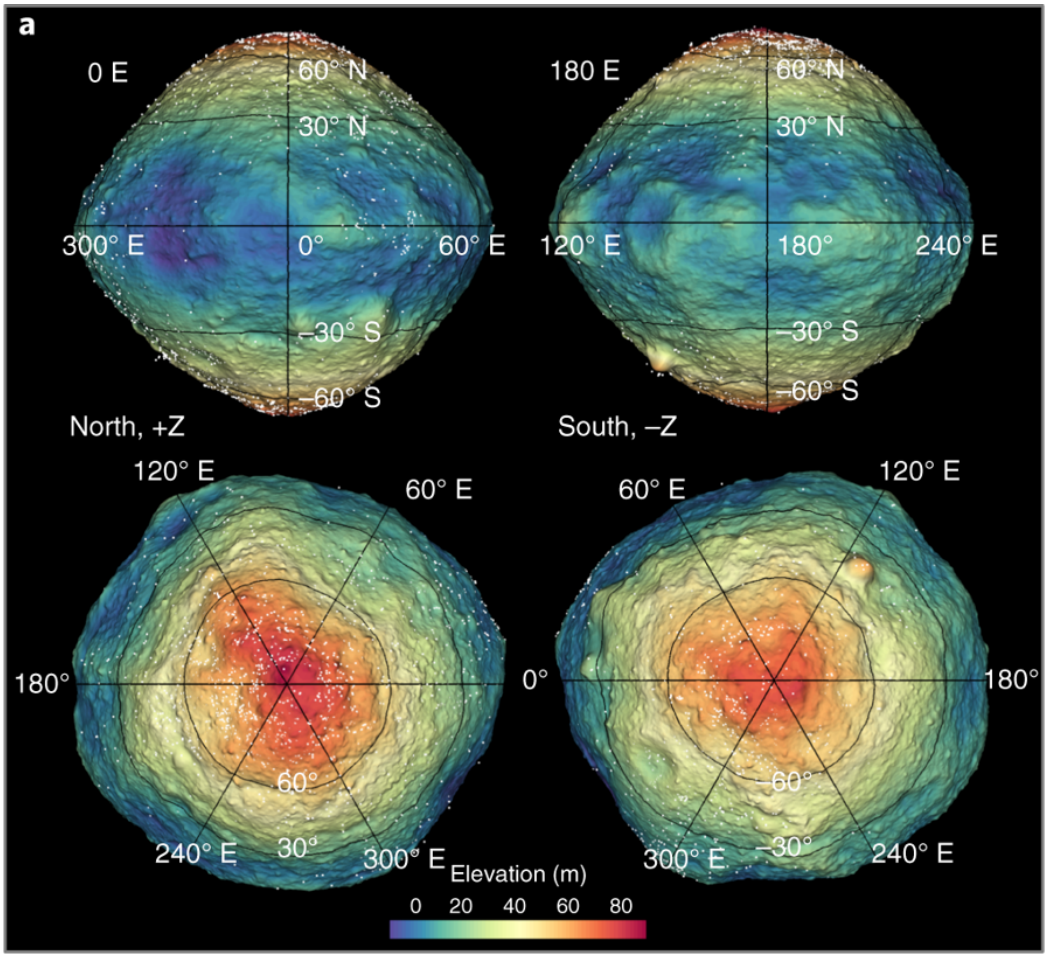

Fig. 6.1.: Views of the global digital terrain model of Bennu, colorized by elevation. In white are indicated locations of OLA returns used to verify the accuracy of the model. Image credit: Barnouin et al. (2019b)

Boulders

Boulders are ubiquitous on the surface, even if there are areas with higher concentration than others. For example, high concentrations of boulders where identified in local topographic lows, which suggest mass wasting and movement of unconsolidated material. Moreover, some boulders appear to be partially buried. They could have been dug out by granular processes such as the Brazil-nut effect, or could also have been exhumed by regolith motion.

Fractured boulders are also present on Bennu's surface; some fractures are linear and others are not (Fig. 1c,d&e in the article in Section 6.3). The origin of these fractures could be impacts (large-scale or meteoroid) or thermal fatigue, and these processes are among the most probable causes of regolith creation (Delbo et al., 2014).

Craters

Several tens of candidate impact craters were identified on Bennu's surface. Some candidates are shallow, with no distinct rims and no clear textural contrast between boulders inside and outside the depressions. This could be explained by a degradation of the craters with time, for example due to impact-induced seismic shaking, and would indicate motion of unconsolidated material on the slopes of the depressions. Moreover, elevation profiles of the largest candidate crater (shown in Fig. 4 in the article) show mass movement on the slopes.

This theory is reinforced by the shortage of small craters in the range observable from orbit (from about 10 m to 50 m). This shortage could be due to armoring, since boulders are numerous on the surface, but it could also be caused by the erasure of small craters by motion of material on the surface and/or seismic shaking.

Small candidate craters observed on Bennu are not filled with large boulders, and could therefore be filled with fine grains.

Thermal inertia and color

The thermal inertia measured by OSIRIS-REx suggests the presence of centimeter-sized particles on the surface (DellaGiustina et al., 2019). However, as stated in Chapter 3 about Ryugu, and because no large "smooth" areas were identified on images, the low thermal inertia could be due to the porosity of boulders rather than to the small sizes of particles, and we need to be cautious when deriving the particle size from the thermal inertia.

The presence of dust (or micrometer-sized particles) has also been inferred from the phase reddening observed on MapCam images (DellaGiustina et al., 2019). On the other hand, the thermal emission spectra measured by OTES advocate for a surface dominated by particles larger than 125 μm.

Differences of albedo and color were observed on some boulders, which could mean that these boulders are impact breccias, like on Ryugu, or that dust or fine particles could partially cover them. However, large albedo variations were also observed in very small regions (a few meters) without any visible boulder. These variations could be explained by the presence of unresolved submeter particles.

Cohesion

According to Barnouin et al. (2019b), if we consider that Bennu is made of cohesionless granular material, this material needs an angle of internal friction higher than $18°$ to explain Bennu's shape. As stated in Section 1.3.4, without cohesion, the angle of internal friction is equal to the angle of repose. The average surface slope on Bennu has been estimated to be $17 \pm 2°$ (Scheeres et al., 2019), close to the minimum angle of repose required for Bennu to maintain its shape.

If we consider a cohesionless Bennu, the same calculation as for Ryugu in Section 3.2.2 can be done and the minimum particle size can be computed. We consider as in Section 3.2.2 that cohesive forces are dominated by Van der Waals forces, that can be written as:

$$F_c = \frac{AS^2}{48\Omega^2}\frac{r}{2} = 1.99 \cdot 10^{-2} S^2 r, \tag{6.1}$$

where the Hamaker coefficient is equal to the lunar one, and the interparticle distance Ω is $1.5 \cdot 10^{-10}$ m.

Bennu is smaller than Ryugu, thus its surface gravitational acceleration is smaller. Bennu's mass is estimated to be $7.329 \pm 0.009 \cdot 10^{10}$ kg (Lauretta et al., 2019). Thus, the gravitational acceleration on the equator is roughly $6.47 \cdot 10^{-5}$ m s^{-2}, and $7.87 \cdot 10^{-5}$ m s^{-2} on the poles. By taking into account Bennu's rotation (Hergenrother et al., 2019; Lauretta et al., 2019), we can compute the rotation rate $\omega = 4.06 \cdot 10^{-4}$ rad s^{-1}, and find the net surface gravitational acceleration on the equator, $g_A = 1.93 \cdot 10^{-5}$ m s^{-2}. We notice that the higher rotation rate of Bennu and its smaller size contributes to a much higher influence of the rotation on the equatorial surface gravitational acceleration than on Ryugu.

The closest meteorite analogues to Bennu are CM chondrites (Lauretta et al., 2019), I therefore consider a grain density equal to $\rho_g = 2,920$ kg m^{-3} (Macke et al., 2011).

All these assumptions lead to a cohesive bond number of:

$$B_c = \frac{F_c}{F_g} = 1.63 \cdot 10^{-6} \frac{S^2}{g_A r^2}. \tag{6.2}$$

If we decide like in Section 3.2.2 that a weak cohesion means a bond number smaller than 1, the smallest grain radius on the equator is equal to 0.29 m for a cleanliness ratio $S = 1$, and 2.9 cm for $S = 0.1$. On the poles, the smallest grain radius would be 0.14 m for $S = 1$ and 1.4 cm for $S = 0.1$. These values are higher than the ones found for Ryugu, and this could mean that either the average grain size on Bennu is larger than on Ryugu, or that cohesion plays a larger role on Bennu. If we consider asperities on grains, we find for example that for $S = 0.1$, the smallest grain size for a bond number smaller than 1 would be 2.9 mm on the equator.

These results should be taken with caution, as they rely on many assumptions (as explained in Section 3.2.2). However, depending on the possibly observed presence of small particles on the surface, they can give an idea of the importance of cohesion on Bennu.

As a comparison, bond numbers for self-gravity are equal to:

$$B_{\text{sg,equator}} = 1.06 \cdot 10^{-2} r, \tag{6.3}$$

$$B_{\text{sg,poles}} = 2.59 \cdot 10^{-3} r. \tag{6.4}$$

Even if self-gravity on Bennu plays a larger role than on Ryugu, it is still negligible for centimeter-sized or millimeter-sized grains.

6.3 Article Bennu

Craters, boulders and regolith of (101955) Bennu indicative of an old and dynamic surface

by

K. J. Walsh, E. R. Jawin, R.-L. Ballouz, . . . , F. Thuillet et al.

2019, *Nature Geoscience*, **12**, pp. 242-246

Abstract

Small, kilometre-sized near-Earth asteroids are expected to have young and frequently refreshed surfaces for two reasons: collisional disruptions are frequent in the main asteroid belt where they originate, and thermal or tidal processes act on them once they become near-Earth asteroids. Here we present early measurements of numerous large candidate impact craters on near-Earth asteroid (101955) Bennu by the OSIRIS-REx (Origins, Spectral Interpretation, Resource Identification, and Security-Regolith Explorer) mission, which indicate a surface that is between 100 million and 1 billion years old, predating Bennu's expected duration as a near-Earth asteroid. We also observe many fractured boulders, the morphology of which suggests an influence of impact or thermal processes over a considerable amount of time since the boulders were exposed at the surface. However, the surface also shows signs of more recent mass movement: clusters of boulders at topographic lows, a deficiency of small craters and infill of large craters. The oldest features likely record events from Bennu's time in the main asteroid belt.

ARTICLES
https://doi.org/10.1038/s41561-019-0326-6

nature geoscience

Corrected: Publisher Correction

Craters, boulders and regolith of (101955) Bennu indicative of an old and dynamic surface

K. J. Walsh[1*], E. R. Jawin[2], R.-L. Ballouz[3], O. S. Barnouin[4], E. B. Bierhaus[5], H. C. Connolly Jr.[6], J. L. Molaro[7], T. J. McCoy[2], M. Delbo'[8], C. M. Hartzell[9], M. Pajola[10], S. R. Schwartz[3], D. Trang[11], E. Asphaug[3], K. J. Becker[3], C. B. Beddingfield[12], C. A. Bennett[3], W. F. Bottke[1], K. N. Burke[3], B. C. Clark[13], M. G. Daly[14], D. N. DellaGiustina[3], J. P. Dworkin[15], C. M. Elder[16], D. R. Golish[3], A. R. Hildebrand[17], R. Malhotra[3], J. Marshall[12], P. Michel[8], M. C. Nolan[3], M. E. Perry[4], B. Rizk[3], A. Ryan[8], S. A. Sandford[18], D. J. Scheeres[19], H. C. M. Susorney[20], F. Thuillet[8], D. S. Lauretta[3] and The OSIRIS-REx Team[21]

Small, kilometre-sized near-Earth asteroids are expected to have young and frequently refreshed surfaces for two reasons: collisional disruptions are frequent in the main asteroid belt where they originate, and thermal or tidal processes act on them once they become near-Earth asteroids. Here we present early measurements of numerous large candidate impact craters on near-Earth asteroid (101955) Bennu by the OSIRIS-REx (Origins, Spectral Interpretation, Resource Identification, and Security-Regolith Explorer) mission, which indicate a surface that is between 100 million and 1 billion years old, predating Bennu's expected duration as a near-Earth asteroid. We also observe many fractured boulders, the morphology of which suggests an influence of impact or thermal processes over a considerable amount of time since the boulders were exposed at the surface. However, the surface also shows signs of more recent mass movement: clusters of boulders at topographic lows, a deficiency of small craters and infill of large craters. The oldest features likely record events from Bennu's time in the main asteroid belt.

NASA's OSIRIS-REx (Origins, Spectral Interpretation, Resource Identification, and Security-Regolith Explorer) asteroid sample return mission arrived at near-Earth asteroid (NEA) (101955) Bennu on 3 December 2018. An imaging campaign during the Approach phase of the mission collected panchromatic images with the OSIRIS-REx Camera Suite (OCAMS) PolyCam imager[1–3]. Images collected by the OCAMS MapCam imager[1] during the Preliminary Survey phase of the mission were combined with approach-phase imaging to produce a three-dimensional shape model of the asteroid, revealing a spheroidal spinning-top shape with a diameter of 492 ± 20 m (ref. [4]), as predicted by radar observations[5].

Over the past three decades, ground-based and spacecraft observations of asteroids, combined with theoretical and computational advances, have transformed our understanding of small NEAs (diameters $<\sim 10$ km). Observations of NEA shapes, spins and sizes combined with theoretical analyses that have provided insight into their interior properties suggest that NEAs with diameters $>\sim 200$ m are 'rubble piles': gravitationally bound, unconsolidated fragments with very low bulk tensile strength[6,7].

Rubble-pile asteroids originate from the main asteroid belt, where catastrophic collisions between larger objects create a population of gravitationally reaccumulated remnants[8]. Small asteroids have limited collisional lifetimes in the main belt (~0.1 to 1 billion years), and their residence time in the main belt can be shorter than the age of the Solar System due to Yarkovsky drift-induced ejection[9]. After departing the main belt, NEAs are subject to further evolutionary processes, such as rotational spin-up due to thermal torques or tidal effects caused by close planetary flybys[7]. These processes can alter their global and surface morphologies. Studies of the rubble-pile NEA (25143) Itokawa found large boulders exposed on its surface, seemingly rapid degradation of impact craters and evidence of substantial movement of surface material[10]. This suggests that Itokawa has undergone dynamical events[10–12] that operate on timescales shorter than its expected residence time in near-Earth space (~10 million years)[7].

Detailed study of Bennu's surface geology, particularly the abundance of its craters and morphology of its boulders, provides constraints on the surface age, which is important to disentangle evolutionary processes that operated in near-Earth space from those that operated in the main belt.

Rubble-pile nature of Bennu

The measured density of $1{,}190\,\mathrm{kg\,m^{-3}}$ and inferred high bulk porosity of Bennu[4,13] and the lack of either high surface slopes or

[1]Southwest Research Institute, Boulder, CO, USA. [2]Smithsonian Institution National Museum of Natural History, Washington, DC, USA. [3]Lunar and Planetary Laboratory, University of Arizona, Tucson, AZ, USA. [4]The Johns Hopkins University Applied Physics Laboratory, Laurel, MD, USA. [5]Lockheed Martin Space, Littleton, CO, USA. [6]Department of Geology, Rowan University, Glassboro, NJ, USA. [7]Planetary Science Institute, Tucson, AZ, USA. [8]Université Côte d'Azur, Observatoire de la Côte d'Azur, CNRS, Laboratoire Lagrange, Nice, France. [9]Department of Aerospace Engineering, University of Maryland, College Park, MD, USA. [10]INAF–Osservatorio Astronomico di Padova, Padova, Italy. [11]Hawai'i Institute of Geophysics and Planetology, University of Hawai'i at Mānoa, Honolulu, HI, USA. [12]SETI Institute, Mountain View, CA, USA. [13]Space Science Institute, Boulder, CO, USA. [14]The Centre for Research in Earth and Space Science, York University, Toronto, Ontario, Canada. [15]NASA Goddard Space Flight Center, Greenbelt, MD, USA. [16]Jet Propulsion Laboratory, California Institute of Technology, Pasadena, CA, USA. [17]Department of Geoscience, University of Calgary, Calgary, AB, Canada. [18]NASA Ames Research Center, Moffett Field, CA, USA. [19]Smead Department of Aerospace Engineering, University of Colorado, Boulder, CO, USA. [20]Department of Earth, Ocean and Atmospheric Sciences, University of British Columbia, Vancouver, British Columbia, Canada. [21]A list of participants and their affiliations appears in the online version of the paper. *e-mail: kwalsh@boulder.swri.edu

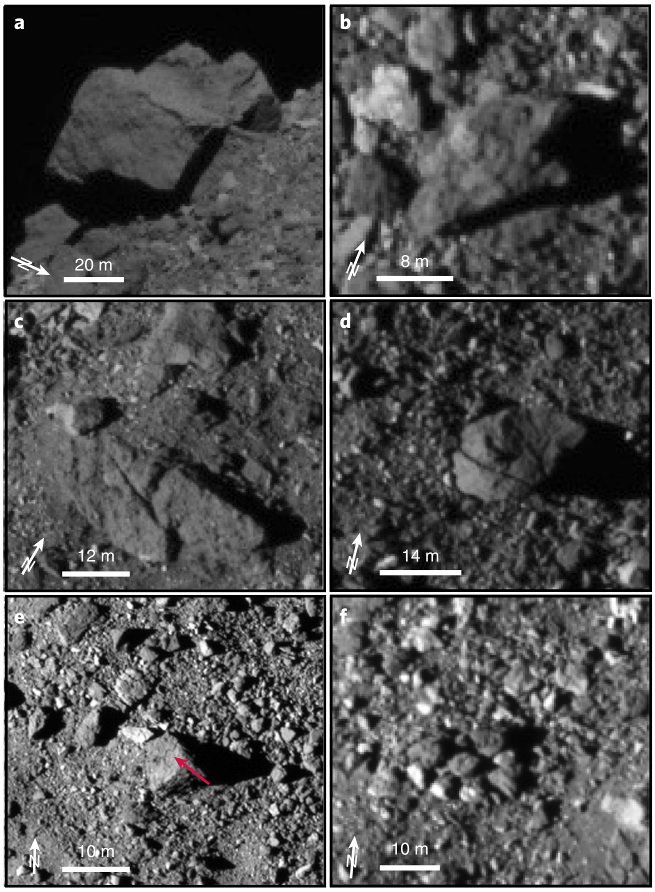

Fig. 1 | The boulders of Bennu can be large and are sometimes fractured or brecciated. a, A boulder located at 48° S and 125° E with a diameter of approximately 56 m and height of over 20 m relative to the surrounding surface of Bennu. **b**, A brecciated boulder located at 6° S and 247° E that is approximately 21 m in diameter with large constituent pieces showing measurable geometric albedo differences[1]. **c**, A boulder with a diameter of approximately 40 m located at 42° N and 129° E that shows a complex web of large fractures. **d**, A boulder with a diameter of approximately 20 m located at 11° S and 258° E with a single linear fracture. **e**, A boulder with a diameter of approximately 10 m located at 5° N and 310° E with a nonlinear fracture (red arrow). **f**, A cluster of metre-sized boulders centred at 44° N and 111° E. Images taken on: **a**, 1 December 2018 from a spacecraft distance of 31.5 km; **b**,**d**, 2 December 2018 from a distance of 24.0 km; **c**, 2 December 2018 from a distance of 23.8 km; **e**, 2 December 2018 from a distance of 24.2 km; **f**, 2 December 2018 from a distance of 23.6 km.

substantial topographic relief indicate that Bennu is a rubble pile. Bennu's density requires 25–50% macroporosity if it is constructed primarily of CI (bulk density of 1,570 kg m^{-3}) or CM (bulk density of 2,200 kg m^{-3}) chondrite-like material[14]. If the microporosity present in these meteorite classes is also considered[15], the total porosity of Bennu may be as high as 60%. In addition, the slope at each point on the surface of Bennu—determined from the combination of the shape, mass and spin state—shows a relaxed distribution with values averaging approximately 17°, and almost entirely below typical angles of approximately 30° allowed by the angle of repose of terrestrial materials and found on other similarly sized NEAs[13,16].

Boulders dominate the local topography of Bennu, some with heights >20 m (Fig. 1a). The most prominent boulder on Bennu was first detected with ground-based radar and estimated to be 10 to 20 m in diameter[2]. This same boulder is apparent in PolyCam images and measures approximately 56 m in its longest dimension (Fig. 1a). There are three identified boulders with long axes exceeding 40 m and more than 200 boulders larger than 10 m (ref. [2]). Boulders in the tens-of-metres size range are larger than plausible ejecta from any of the large crater candidates on Bennu[17], and also unlikely to be meteorites that Bennu could have accreted in its current orbit, suggesting instead that their origins trace back to the formation of Bennu in the asteroid belt.

Boulders on Bennu have albedo and colour diversity[1], with some showing these differences within distinct metre-sized clasts in an otherwise unfragmented rock. We interpret such assemblages as impact breccias (Fig. 1b). Processes capable of creating breccias spanning tens of metres with metre-sized clasts imply energetic events that far exceed what Bennu can support[18,19].

The possible inherited origin of Bennu's largest boulders supports the idea that rubble piles form as reaccumulated remnants of disruptive collisions of larger asteroids in the main asteroid belt[8]. Furthermore, the existence of breccias suggests that they are a record of the parent body's accretion, that they formed during impact regolith gardening on the surface of that parent body or that they originated during the catastrophic disruption event that formed Bennu. The noted albedo and colour diversity of the boulders, and the distinct metre-scale components visible in some of them, may point to the compositional diversity of Bennu's parent body and/or its catastrophic impactor.

Boulder geology of Bennu

The spatial distribution of boulders on the surface of Bennu is not uniform. We find concentrations of boulders in some local topographic lows[4] (tens-of-metres elevation differences relative to the surrounding terrain), with boulder abundances up to an order of magnitude greater than the global average (Fig. 2). These collections of boulders stand in contrast to topographic lows on Itokawa, which are distinct for their lack of large boulders and collections of small grains[11].

The boulders on Bennu's surface also exhibit diversity in size, geologic context and morphology. To date, boulders >8 m in diameter have been adequately resolved with PolyCam images, for which we have measured a size-frequency distribution best fit with a power-law index of -2.9 ± 0.3 (ref. [2]). Many of these boulders appear to be resting on top of the surface, while some are partially buried, pointing to active burial and/or exhumation processes. Several examples of imbricated boulders have been identified, although these locations are smaller in extent than the imbricated regions observed on Itokawa[11], with no obvious correlation between imbrication and fine-grained deposits. Both rounded and angular boulders are present on the surface, which may suggest a variety of formation mechanisms, compositions and/or boulder evolutionary processes.

We observe fractured boulders exhibiting multiple fracture types. Some of the most dramatic examples include large, linear fractures that appear to split boulders into two or more pieces (Fig. 1c,d). These occur at all resolvable scales and within some of the largest boulders on the surface. In contrast, other boulders exhibit nonlinear fractures that suggest some interaction between the fracture-driving mechanisms and the rock bulk structure (Fig. 1e). We also found examples of discrete, yet tightly clustered metre-scale boulders that appear to have fractured in situ, and remain in clusters with minimal displacement (Fig. 1f). Complex networks of fractures also occur in some boulders (Fig. 1c,d), with many deep fractures crossing each other at various angles, although some are clearly linear. These numerous and morphologically varied fractures may be produced by one or a combination of processes, such as large-scale impact events, micrometeoroid impacts and thermal fatigue. The latter two processes may also be responsible for the shallow fractures and surficial features observed on visibly textured boulders, which indicate exfoliation, near-surface disaggregation or regolith production processes (for example, refs. [20–22]).

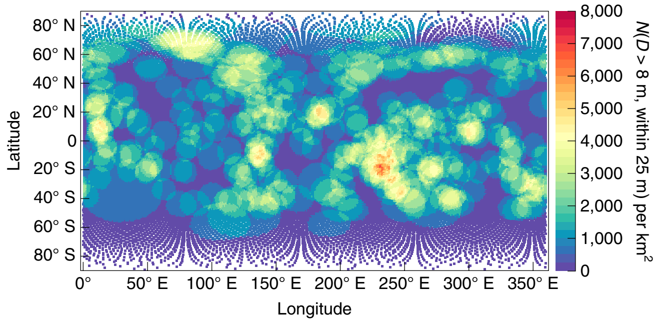

Fig. 2 | Boulder abundance map of the surface of Bennu. The abundance of boulders for each location on the surface of Bennu based on a 49,152-facet shape model of the surface, where the boulder abundance (N) is calculated by counting the number of boulders larger than 8 m within a radius of 25 m in each facet and then normalized to square kilometre.

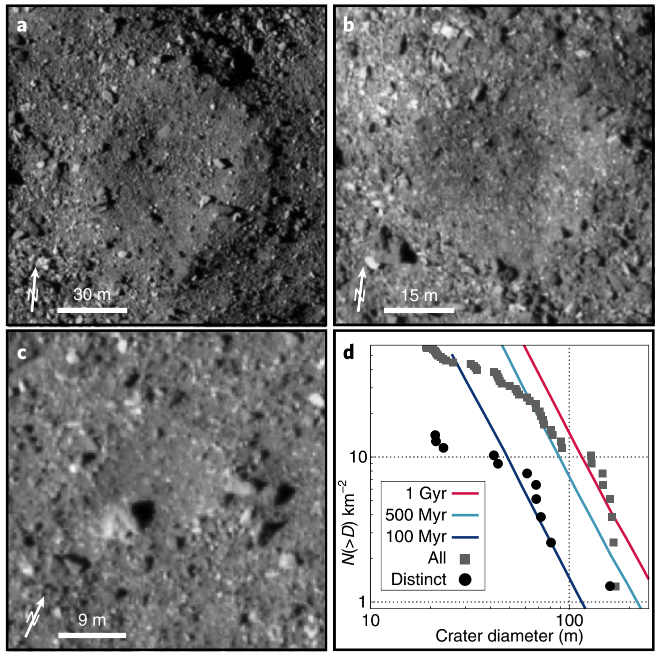

Fig. 3 | Examples of Bennu's craters. a, A feature on Bennu's surface that meets all of the criteria to be considered a distinct candidate crater, including clear topography associated with its rim. This candidate crater is centred at 3° S and 152° E and has a diameter of 81 m. **b**, A distinct candidate crater located at 5° S and 126° E with diameter of 44 m differs in texture between the inside and outside of its rim and shows a distinct lack of boulders. **c**, Example of a less-distinct candidate crater located at 54° N and 68° E, with some textural differences between the inside and outside of the circular feature, but that shows only hints of a circular shape with no clear topography. **d**, The established 'distinct' candidate craters provide a lower bound on age by comparing their distributions to the expected crater production function (see Methods), and we use the entire population of less-distinct candidate craters to estimate an upper bound. In both groups, the change in size-frequency distribution appears around $D = 50$ m. Images taken on: **a**,**b**, 2 December 2018 from a distance of 23.7 km; **c**, 2 December 2018 from a distance of 23.5 km.

Although boulder fracture could potentially represent past processing on Bennu's parent body, the abundance of fractured boulders and some cases where boulders appear to have disaggregated in situ points to surface processes active in Bennu's recent geologic history, since it evolved to a near-Earth orbit. However, these fracture formation mechanisms need time to operate, suggesting that the surface has not been dynamically refreshed since Bennu's transition from the main belt to its near-Earth orbit, where a typical NEA's dynamical lifetime is on the order of 10 million years[23]. Breakdown due to micrometeoroid bombardment and thermal fatigue is predicted to be faster and slower, respectively, in the main belt than in near-Earth space[20,22,24]. However, the relative efficiencies of these and other active processes are not well constrained, making it difficult to use fractures to assess absolute surface age. Some processes also act over multiple timescales, such as thermal fatigue, which may generate fractures over different spatial scales owing to diurnal and annual thermal cycles.

Craters of Bennu

Bennu has experienced a number of impacts that have transformed its surface. We have identified several tens of candidate impact craters, which range in size from approximately 10 m to more than 150 m in diameter. The characteristics of distinct candidate impact craters include circular features with raised rims and depressed floors, and/or clear textural differences (apparent concentration or lack of boulders) between the interior and exterior of the crater. Less-distinct candidate craters have subdued rims or an absence of raised rims, shallow interiors, and lack of contrast between the interior and exterior boulder populations. Based on current image data, we have identified 12 distinct, and at least 40 less-distinct, candidate craters. Notably, several large distinct craters are located on Bennu's equatorial ridge, suggesting that the ridge is an old feature (Fig. 3).

We used the population of large distinct candidate craters (diameter $D > 50$ m) to estimate the age of Bennu's surface. Assuming that the craters record impact events, they are primarily a record of Bennu's history in the main asteroid belt[25]. Crater scaling laws can convert impact parameters to crater diameters, although for small rubble-pile bodies there is added uncertainty due to their microgravity regime[26,27]. By applying Bennu's physical properties to these scaling relationships (for example, a crater scaling law for dry soil with a strength of 0.18 MPa (ref. [26])), we can estimate the ratio of crater to projectile diameters. The size-frequency distribution of main-belt projectiles striking Bennu is assumed to follow the collisional evolution results[25], while the intrinsic collision probability of Bennu with a main-belt projectile is assumed to be fairly similar to Gaspra, a relatively low inclination asteroid residing in the innermost region of the main belt (where the intrinsic collisional probability is $P_i = 2.8 \times 10^{-18}\,\mathrm{km^{-2}\,yr^{-1}}$)[28]. These components, when combined with Bennu's cross-section[28], can be fit to Bennu's $D > 50$ m craters. We find that it would take between 100 million and 1 billion years to explain the origin of Bennu's largest crater candidates (Fig. 3d).

However, cratering into low-strength material under low-gravity conditions may lead to larger crater diameters, which in turn could lead to younger age estimates[27]. Conversely, cratering into high-porosity material may lead to reduced diameters and older age estimates[29]. It is possible that determining the surface exposure age of the returned sample will quantitatively constrain Bennu's crater retention age and provide a better understanding of which aspects play dominant roles in crater formation on Bennu and other high-porosity, low-strength targets.

The imaging and topographic data allowed identification of craters approximately 10 m and larger. The observations show a depletion of small craters (~$10\,\mathrm{m} < D < 50\,\mathrm{m}$) relative to expectations based on the production rate of large craters (Fig. 3d). The depletion of small craters has also been found on other NEAs including Itokawa and Eros[30,31]. The prevalence of boulders on the surface can potentially stifle the formation of small craters, whereby impactors strike and break boulders rather than making craters[32]. Conversely, the depletion of small craters may reflect,

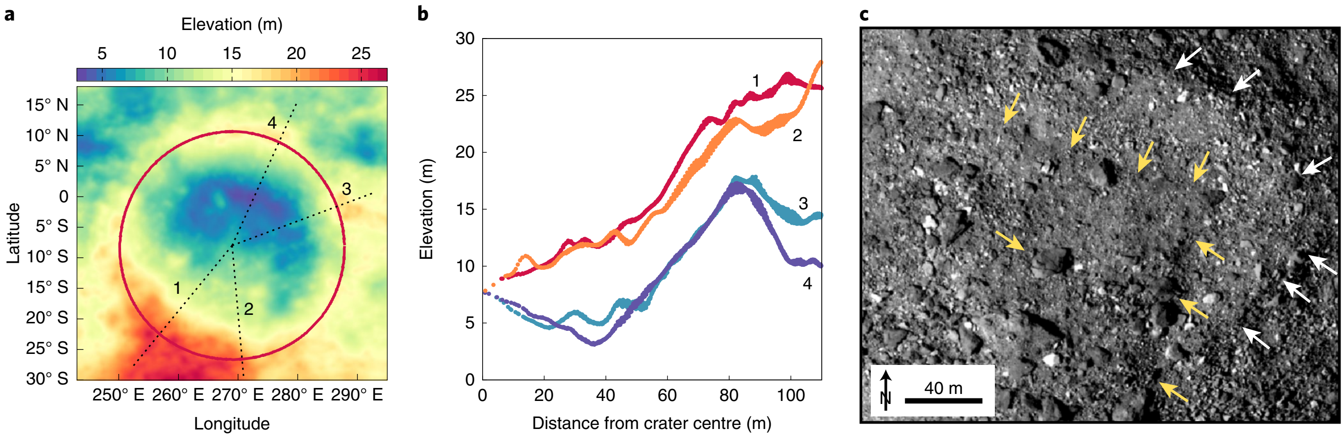

Fig. 4 | Flow of material into a $D = 160$ m candidate crater. a, A large candidate crater is centred near the equator at 8° S and 269° E, and initial measurements indicate a diameter of 160 m. The drawn circle outlines the crater rim and four dotted lines indicate profiles along which elevation was extracted radially from the centre of the crater outward. **b**, The elevation profiles for the different regions of the crater, where the profiles 1 and 2 show that the southwest region of the crater is elevated relative to the rest of the crater shown with profiles 3 and 4. The mass movement appears to have overtopped the crater rim and covered parts of the crater with metres of material. **c**, Image showing the relationship between the material flow and the candidate crater. White arrows indicate the crater rim, and yellow arrows indicate the edge of the flow which has entered the crater from the west (the flow correlates with the elevated portion of topographic profiles 1 and 2). Stratigraphic relationships show that the flow occurred after the formation of the crater. Leftmost yellow arrow indicates additional material movement that has partly buried the westernmost portion of a larger boulder (which is also shown in Fig. 1c). Image used for **c** was taken on 1 December 2018 from a distance of 31.8 km.

as previously postulated, crater erasure due to surface material movement and/or seismic shaking[33,34]. There are clear examples on some large candidate craters on Bennu of material movement and crater infill, where the thickness of the fill layer is comparable to the depth of small craters (Fig. 4)[4].

Regolith of Bennu

The interiors of many small candidate impact craters ($D < 20$ m) are largely devoid of resolvable boulders (Fig. 3). These locations may be reservoirs for smaller particles produced or exposed during the crater formation process. Similarly, boulder-fracturing processes or abrasion and mechanical erosion between boulders during surface material movement could each contribute to the production of fine grains more widely across the surface of Bennu.

There is some evidence that fine-grained material (of the centimetre-scale sizes that are ingestible by the OSIRIS-REx sample mechanism[35] and of smaller, micrometre-scale sizes) is present despite not being resolved with current imaging. The measured thermal inertia is consistent with a population of centimetre-sized particles[2]. The phase reddening observed with the MapCam images suggest some photometric contribution by micrometre-sized particles[2]. Thermal emission spectra[14] exhibit evidence of a surface dominated by particles greater than 125 µm at spatial scales of approximately 80 m, but these data cannot provide more specific information on the range of particle sizes greater than 125 µm or rule out the presence of a small fraction of particles smaller than 125 µm.

Finally, certain regions only a few metres in size have large albedo differences and lack observable boulders, suggesting that they are dominated by unresolved (<1 m) particles[1]. Other fine-particulate patches appear as surficial layers indiscriminately draped over boulder and inter-boulder areas alike[2]. However, low-albedo deposits do not mask the outlines of boulders. The dark material comprising these patches may be dust or fine particles.

History of Bennu

The large boulders on the surface of Bennu may provide information about the composition and geology of its parent body, as well as the collision that disrupted it. The observed impact breccias may have formed during the evolution of its parent body, through repeated impact events on its surface over most of Solar System history, or during the large impact event that resulted in the formation of Bennu. Alternatively, these breccias may even date to the accretion of the original parent body in the protoplanetary disk.

The retention of large craters on Bennu's equatorial ridge requires that the surface age predates the expected approximately 10-million-year duration as a NEA. There is no clear geologic indication of the process that formed the ridge, and given its relation to the large craters it could be a feature preserved from the formation of Bennu[36], which would make it the oldest feature on its surface[4,13,31]. Bennu's surface therefore also recorded processes from its time in the main belt; the formation timescales of the largest craters suggest that Bennu recorded hundreds of millions of years of history during this period.

Bennu retains very old craters despite evidence of continued and varied surface evolution. The processes that have removed small craters may be size limited or spatially localized and therefore cannot efficiently erase larger craters. The crater infill observed on the largest distinct crater has deposited an approximately 5-m-thick layer of material inside the crater and has partially degraded a large swath of the crater rim (Fig. 4). If surface material movement of this scale were to act widely and frequently, it could contribute to large-scale resurfacing of the asteroid. However, the old age of the surface of Bennu indicates that this type of event may either be localized, or of low frequency, possibly occurring only during its time as an NEA.

Resurfacing and surface movement will have influenced and resorted the fine-grained surface material that is the final target of the OSIRIS-REx mission[37]. The returned sample of this material will tell us about processes that occurred since Bennu has been a NEA, while Bennu was in the main belt, and likely processes that occurred on its original parent body and in the solar nebula long before Bennu formed.

Online content

Any methods, additional references, Nature Research reporting summaries, source data, statements of data availability and associated accession codes are available at https://doi.org/10.1038/s41561-019-0326-6.

Received: 28 January 2019; Accepted: 11 February 2019;
Published online: 19 March 2019

References

1. Lauretta, D. S. et al. The unexpected surface of asteroid (101955) Bennu. *Nature* https://doi.org/10.1038/s41586-019-1033-6 (2019).
2. DellaGiustina, D. N. et al. Properties of rubble-pile asteroid (101955) Bennu from OSIRIS-REx imaging and thermal analysis. *Nat. Astron.* https://doi.org/10.1038/s41550-019-0731-1 (2019).
3. Rizk, B. et al. OCAMS: the OSIRIS-REx camera suite. *Space Sci. Rev.* **214**, 26 (2018).
4. Barnouin, O. S. et al. Shape of (101955) Bennu indicative of a rubble pile with internal stiffness. *Nat. Geosci.* https://doi.org/10.1038/s41561-019-0330-x (2019).
5. Nolan, M. C. et al. Shape model and surface properties of the OSIRIS-REx target asteroid (101955) Bennu from radar and lightcurve observations. *Icarus* **226**, 629–640 (2013).
6. Richardson, D. C., Leinhardt, Z. M., Melosh, H. J., Bottke, W. F. & Asphaug, E. in *Asteroids III* (eds Bottke, W. F. Jr, Cellino, A., Paolicchi, P. & Binzel, R. P.) 501–515 (Univ. Arizona Press, 2002).
7. Walsh, K. J. Rubble pile asteroids. *Annu. Rev. Astron. Astrophys.* **56**, 593–624 (2018).
8. Michel, P., Benz, W., Tanga, P. & Richardson, D. C. Collisions and gravitational reaccumulation: forming asteroid families and satellites. *Science* **294**, 1696–1700 (2001).
9. Bottke, W. F. et al. Dynamical spreading of asteroid families by the Yarkovsky effect. *Science* **294**, 1693–1696 (2001).
10. Fujiwara, A. et al. The rubble-pile asteroid Itokawa as observed by Hayabusa. *Science* **312**, 1330 (2006).
11. Miyamoto, H. et al. Regolith migration and sorting on asteroid Itokawa. *Science* **316**, 1011–1014 (2007).
12. Hirata, N. et al. A survey of possible impact structures on 25143 Itokawa. *Icarus* **200**, 486 (2009).
13. Scheeres, D. N. et al. The dynamic geophysical environment of (101955) Bennu based on OSIRIS-REx measurements. *Nat. Astron.* https://doi.org/10.1038/s41550-019-0721-3 (2019).
14. Hamilton, V. E. et al. Evidence for widespread hydrated minerals on asteroid (101955) Bennu. *Nat. Astron.* https://doi.org/10.1038/s41550-019-0722-2 (2019).
15. Macke, R. J., Consolmagno, G. J. & Britt, D. T. Density, porosity, and magnetic susceptibility of carbonaceous chondrites. *Meteorit. Planet. Sci.* **46**, 1842–1862 (2011).
16. Ostro, S. J. et al. Radar imaging of binary near-Earth asteroid (66391) 1999 KW4. *Nature* **314**, 1276–1280 (2006).
17. Bart, G. D. & Melosh, H. J. Using lunar boulders to distinguish primary from distant secondary impact craters. *Geophys. Res. Lett.* **34**, L07203 (2007).
18. Bischoff, A., Edward, R. D. S., Metzler, K. & Goodrich, C. A. in *Meteorites and the Early Solar System II* (eds Lauretta, D. S. & McSween H. Y. Jr) 679–712 (Univ. Arizona Press, 2006).
19. Noguchi, T. et al. Surface morphological features of boulders on Asteroid 25143 Itokawa. *Icarus* **206**, 319–326 (2010).
20. Molaro, J. L., Byrne, S. & Le, J. L. Thermally induced stresses in boulders on airless body surfaces, and implications for rock breakdown. *Icarus* **294**, 247–261 (2017).
21. Delbo', M. et al. Thermal fatigue as the origin of regolith on small asteroids. *Nature* **508**, 233–236 (2014).
22. Basilevsky, A. T., Head, J. W., Horz, F. & Ramsley, K. Survival times of meter-sized rock boulders on the surface of airless bodies. *Planet. Space Sci.* **117**, 312–328 (2015).
23. Gladman, B., Michel, P. & Froeschlé, C. The near-Earth object population. *Icarus* **146**, 176–189 (2000).
24. Graves, K. J., Minton, D. A., Molaro, J. L. & Hirabayashi, M. Resurfacing asteroids from thermally induced surface degradation. *Icarus* **322**, 1–12 (2019).
25. Bottke, W. F. et al. The fossilized size distribution of the main asteroid belt. *Icarus* **175**, 111–140 (2005).
26. Holsapple, K. A. The scaling of impact processes in planetary sciences. *Ann. Rev. Earth Planet. Sci.* **21**, 333–373 (1993).
27. Holsapple, K. A. & Housen, K. R. A crater and its ejecta: an interpretation of Deep Impact. *Icarus* **187**, 345–356 (2007).
28. Bottke, W. F., Nolan, M. C., Greenberg, R. & Kolvoord, R. A. Velocity distributions among colliding asteroids. *Icarus* **107**, 255–268 (1994).
29. Prieur, N. C. et al. The effect of target properties on transient crater scaling for simple craters. *J. Geophys. Res. Planets* **122**, 1704–1726 (2017).
30. Thomas, P. C. & Robinson, M. S. Seismic resurfacing by a single impact on the asteroid 433 Eros. *Nature* **436**, 366–369 (2005).
31. Michel, P., O'Brien, D. P., Abe, S. & Hirata, N. Itokawa's cratering record as observed by Hayabusa: implications for its age and collisional history. *Icarus* **200**, 503–513 (2009).
32. Tatsumi, E. & Sugita, S. Cratering efficiency on coarse-grain targets: Implications for the dynamical evolution of asteroid 25143 Itokawa. *Icarus* **300**, 227–248 (2017).
33. Richardson, J. E., Melosh, H. J., Greenberg, R. J. & O'Brien, D. P. The global effects of impact-induced seismic activity on fractured asteroid surface morphology. *Icarus* **179**, 325–349 (2005).
34. Asphaug, E. Critical crater diameter and asteroid impact seismology. *Meteorit. Planet. Sci.* **43**, 1075–1084 (2008).
35. Bierhaus, E. B. et al. The OSIRIS-REx spacecraft and the touch-and-go sample acquisition mechanism (TAGSAM). *Space Sci. Rev.* **214**, 107 (2018).
36. Michel, P. et al. Disruption and reaccumulation as the possible origins of Ryugu and Bennu top shapes. In *Lunar Planetary Sci. Conf. 50* abstr. 1659 (2019).
37. Lauretta, D. S. et al. OSIRIS-REx: sample return from asteroid (101955) Bennu. *Space Sci. Rev.* **212**, 925–984 (2017).

Acknowledgements

This material is based on work supported by NASA under contracts NNM10AA11C and NNH09ZDA007O issued through the New Frontiers Program. M.P. was supported for this research by the Italian Space Agency (ASI) under the ASI-INAF agreement no. 2017–37-H.0. M.D., P.M., and A.R. would like to acknowledge the French space agency CNES. M.D., A.R., P.M. and S.R.S acknowledge support from the Academies of Excellence on Complex Systems and Space, Environment, Risk and Resilience of the Initiative d'EXcellence 'Joint, Excellent, and Dynamic Initiative' (IDEX JEDI) of the Université Côte d'Azur. Part of this work was performed at the Jet Propulsion Laboratory, California Institute of Technology, under contract with the National Aeronautics and Space Administration.

Author contributions

K.J.W. led the mapping, analysis and manuscript writing. E.R.J., R.-L.B., O.S.B., E.B.B., H.C.C., J.L.M. and T.J.M. contributed to the mapping, analysis and writing of the manuscript. D.S.L. leads the mission and contributed to analysis and writing. M.D., C.M.H., M.P., S.R.S. and D.T. contributed to mapping and manuscript writing. E.A., K.J.B., C.B.B., W.F.B., C.A.B., K.N.B., B.C.C., M.G.D., D.N.D., J.P.D., C.M.E., D.R.G., A.R.H., R.M., J.M., P.M., M.C.N., M.E.P., B.R., A.R., D.J.S., H.C.C., S.A.S., H.C.M.S. and F.T. all contributed to the mapping, analysis or manuscript writing. The entire OSIRIS-REx Team made the Bennu encounter possible.

Competing interests

The authors declare no competing interests.

Additional information

Reprints and permissions information is available at www.nature.com/reprints.

Correspondence and requests for materials should be addressed to K.J.W.

Publisher's note: Springer Nature remains neutral with regard to jurisdictional claims in published maps and institutional affiliations.

Methods

Initial boulder identification was carried out following the methods outlined in ref. [2]. Subsequent detailed mapping and geologic analyses of boulders were performed by a visual analysis of PolyCam and MapCam data using the Small Body Mapping Tool (SBMT), which projects spacecraft images onto a shape model[38]. Boulders were mapped by drawing an ellipse around the resolved boulder margins; this method allows for the analysis of both long and intermediate axis lengths, as well as boulder orientation. Boulders were viewed under a range of viewing geometries including various phase angles and illumination angles. Detailed boulder morphology was assessed using a combination of unprojected images which facilitated fine-scale analyses, and projected images within SBMT, which provides geologic context. Boulder abundance (Fig. 2) was calculated using a 49,152-facet shape model[4], where the boulder abundance was calculated by counting the number of boulders larger than 8 m within a 25 m radius in each facet and then normalizing to 1 km^2. Image for Fig. 1a is ocams20181201t055746s307_pol_iofl2pan_63551 taken on 1 December 2018 from a spacecraft distance of 31.5 km. Fig. 1b,d is from image ocams20181202t072303s706_pol_iofl2pan_63785 taken on 2 Decemeber 2018 with a spacecraft distance 24.0 km. Fig. 1c is taken from image ocams20181202t082747s619_pol_iofl2pan_63714 taken on 2 December 2018 with a spacecraft distance of 23.8 km. Fig. 1e is taken from image 20181202T064001S485_pol_iofL2pan taken on 2 December 2018 with a spacecraft distance of 24.2 km. Fig. 1f is taken from image20181202T084918S806_pol_iofL2pan taken on 2 December 2018 with a spacecraft distance of 23.6 km.

Crater identification and measurement was performed using a combination of projected and unprojected PolyCam and MapCam images, as well as stereophotoclinometry-derived topography data[4]. All mapping was carried out in SBMT by mapping ellipses around the maximum extent of the resolvable crater rim. Multiple members of the team mapped the surface for craters and only those mapped by multiple members as distinct crater candidates were counted in the 'distinct' category for the purposes of analysis. All mapped individual craters were included in the 'non-distinct' group. To calculate surface age, we used the largest craters to estimate a range of possible surface ages based on the impactor size distribution found in the main belt, an average main-belt impact probability and impact velocity ($P_{\mathrm{i}} = 2.8\times10^{-18}\,\mathrm{km}^{-2}\,\mathrm{yr}^{-1}$ and $v_i = 5.3\,\mathrm{km\,s}^{-1}$)[25,39], and a crater scaling law for dry soil with a strength of 0.18 MPa (ref. [26]). The clearly established 'distinct' candidate craters, normalized to one square kilometre, provide a lower bound on age, and we use the entire population of less-distinct candidate craters to estimate an upper bound. In both groups, the change in size-frequency distribution appears around $D = 50$ m. Image ocams20181202t083822s735_pol_iofl2pan_64172 was used for Fig. 3a,b and was taken on 2 December 2018 from a spacecraft range of 23.7 km. Image for Fig. 3c was ocams20181202t091159s321_pol_iofl2pan_64104 and was taken on 2 December 2018 from a spacecraft range of 23.5 km. Image ocams20181201t051455s588_pol_iofl2pan_63071 was used for Fig. 4c and was taken on 1 December 2018 from a spacecraft distance of 31.8 km.

Many of the geologic assessments relied on elevation, which was derived from shape model v14. The construction of the shape model, and different versions of the shape model, and calculation of elevation is described in detail in a companion paper[4].

Data availability

Raw through to calibrated datasets will be available via the Planetary Data System (PDS) (https://sbn.psi.edu/pds/resource/orex/). Data are delivered to the PDS according to the OSIRIS-REx Data Management Plan available in the OSIRIS-REx PDS archive. Higher-level products, for example, global mosaics and elevation maps, will be available in the PDS one year after departure from the asteroid.

References

38. Ernst, C. M., Barnouin, O. S. & Daly, R. T. The Small Body Mapping Tool (SBMT) for accessing, visualizing, and analyzing spacecraft data in three dimensions. In *Lunar Planetary Sci. Conf. 49* abstr. 1043 (2018).
39. Marchi et al. The cratering history of (2867) Steins. *Planet. Space Sci.* **58**, 1116–1123 (2010).

7 Applications to Bennu

> *Never tell me the odds!*
>
> — **OSIRIS-REx Team**
> (discovering ejected particles)

Contents

In this section, I treat the applications of other studies previously presented in this thesis to Bennu, and particularly to two phenomena observed by NASA's OSIRIS-REx spacecraft: particle ejection and terraces.

7.1 Particle ejection on Bennu

On January 6, 2019 was detected the first particle ejection from Bennu in OSIRIS-REx optical navigation data. It was a tremendous discovery as no particle ejection had never been closely observed before on an asteroid. This discovery makes Bennu belong to the restricted (as we know of) group of active asteroids.

7.1.1 Active asteroids

The line between comets and asteroids can be very thin. Usually, three criteria define the nature of small bodies. First of all, the observation of an unbound atmosphere (called *coma*) is generally the signature of a comet. However, the detection of the coma can depend on the resolution of the images (depending for example on the instrument or on the observing conditions).

Secondly, a dynamical criterion can settle the uncertainty: the Tisserand parameter with respect to Jupiter T_J (Kresak, 1982; Kosai, 1992), defined by:

$$T_J = \frac{a_J}{a} + 2\left[\left(1 - e^2\right)\frac{a}{a_J}\right]^{\frac{1}{2}} \cos i, \tag{7.1}$$

where a, e, and i are the semi-major axis, the eccentricity, and the inclination (relative to Jupiter's orbit plane) of the small body's orbit, and a_J is the semi-major axis of Jupiter's orbit. $T_J < 3$ corresponds to comets, whereas $T_J > 3$ defines dynamical asteroids. Yet, because the Tisserand parameter relies on a simplified representation of the Solar System, when T_J is close to 3, this criterion may not be as deciding as it may seem.

Thirdly, comets are supposed to be rich in ice and are believed to be formed beyond the snow-line, contrarily to the ice-free asteroids formed inside it. The main issue with this criterion is the difficulty to detect the presence of ice on the surface or subsurface.

From these criteria, we already see that the line between comets and asteroids is not as clear as one would think. There are several types of comets and of asteroids, and objects that share some attributes of both. The first two criteria (visible coma or not, and value of T_J) define several small body populations in the Solar System, defined in Jewitt et al. (2015). For example, "classic" asteroids do not have a coma and have $T_J > 3$, whereas "classic" comets (either from Jupiter, Long period or Halley families) present a coma and have $T_J < 3$. However, there are small bodies that show a coma, with $T_J > 3$. These small bodies are active asteroids. They were previously called main-belt comets, but some of them being discovered out of the main belt and the origin of the mass-loss activity being unknown, they are now rather called active asteroids. They are thoroughly described in Jewitt (2012) and Jewitt et al. (2015).

Several mechanisms have been proposed to explain the loss of mass, and are presented in Jewitt et al. (2015). The activity can be due to rotational instability, for example because of the YORP effect increasing the rotation rate of an asteroid beyond the limit for which the asteroid remains completely gravitationally bound. This is the preferred explanation for the activity of asteroids 311P and P/2013 R3, as well as recently for (6478) Gault (Kleyna et al., 2019).

Another explanation for mass loss could be impacts. It was shown in Jewitt et al. (2015), using results from Housen et al. (2011), that relatively small projectiles (for example meter-sized) with impact speeds of about 5 km s^{-1} (average impact speed in the main belt) should create observable events, and could therefore be at the origin of the activity detected on some asteroids.

Moreover, mass loss could also be due to thermal fracturing and disintegration. Thermal fatigue has already been evoked several time in Chapter 1 as a possible source of regolith (Delbo et al., 2014). It can also be a source of mass loss on small asteroids, where small grains can be ejected by thermal fracturing with speeds larger than the asteroid escape speed (Jewitt, 2012).

Other explanations can be at the origin of asteroid activity, such as the sublimation of ice on the surface (when the asteroid gets closer to the Sun or depending on the incidence of solar rays on the surface), or dust lofting due to electrostatic forces or radiation pressure.

The first confirmed active asteroid was 133P/(7968) Elst-Pizarro, in the main asteroid belt, in 1996. By 2015, 18 active asteroids had been detected and, as of mid-2019, this number is already as high as 30 and keeps increasing.

Among the two target asteroids, Ryugu was the candidate as an active asteroid. Indeed, before Hayabusa2 arrived at the asteroid, a subtle scattering of light and unusual reflectance spectra were observed (Busarev et al., 2018). However, direct observation of mass loss was observed not on Ryugu but on Bennu, for which there was no suspicion of activity. This confirms that our knowledge about active asteroids, and the size of their population, is biased by the limitations of Earth-base observations.

7.1.2 Discovery of particle ejection on Bennu and possible origin

As previously stated, particle ejection was discovered on Bennu on January 6, 2019. In the optical navigation data, several particles were detected where were only expected several visible stars and the dark background of space. This was not an isolated event, as no fewer than 11 events were detected, with 3 of them being substantial ones with more than 60 particles detected. An article by Lauretta et al. in *Science*, to which I contributed, is currently under review, and describes the particle detections and discusses the possible explanations and the implications for Bennu.

A view of Bennu ejecting particles on January 19, 2019, is shown in Fig. 7.1. This view corresponds to the second large ejection event and was made by combining a short-exposure (1.4 ms) image of Bennu and a long-exposure (5 s) image showing the particles, plus several other image-processing techniques.

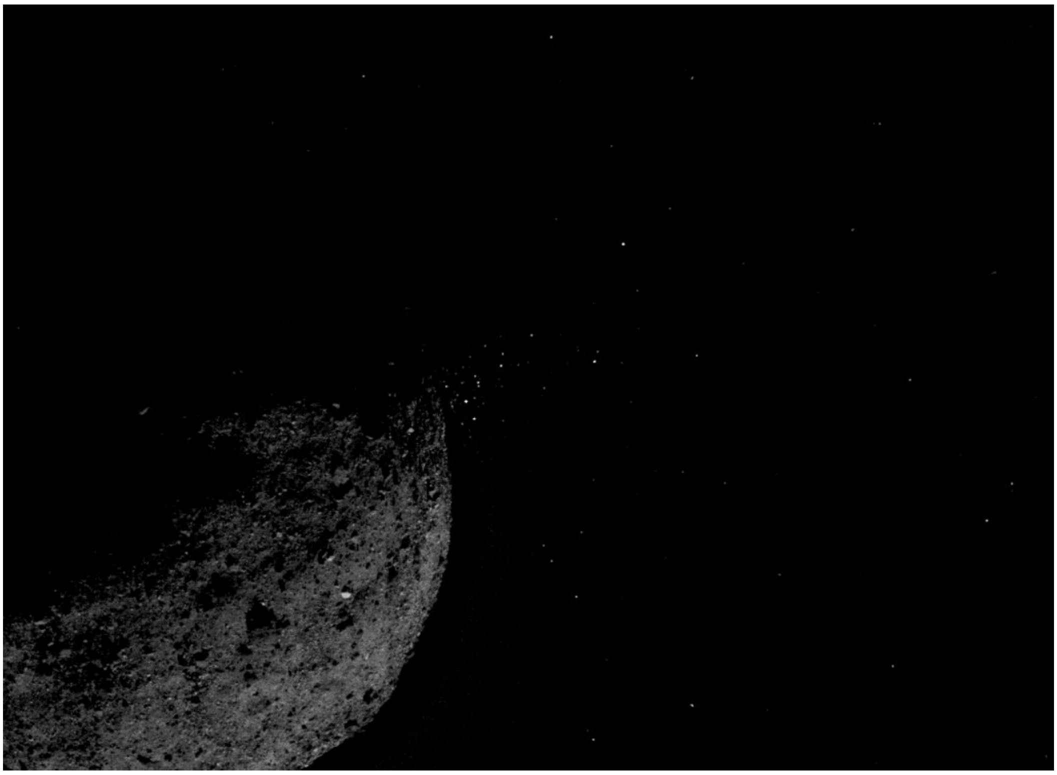

Fig. 7.1.: Bennu particle ejection event on January 19, 2019 observed by OSIRIS-REx's spacecraft. Image credit: NASA/Goddard/University of Arizona/Lockheed Martin

Using the results I presented in Chapter 4, we found, with Ronald-Louis Ballouz, Kevin Walsh, and Patrick Michel, that a possible origin of the minor ejection events could be re-impacts. The results of simulations presented in Chapter 4 of MASCOT landing on a fine-grain medium can also be used to represent the slow re-impacts of large ejecta (with possible irregular shapes) released by large ejection events on Bennu. Dynamical calculations were done for the article, showing that ejected particles can re-impact Bennu's surface days after their ejection. Therefore, the multiple minor events observed between the major ones could be due to slow re-impacts of material released in major ejection events.

Even if my simulations consider Ryugu's gravity, which is slightly larger than Bennu's one, and not a real ejected particle but MASCOT, a 10 kg 19.5 cm $\times$ 27.5 cm $\times$ 29 cm cuboid, the distribution of ejecta can still give us valuable information concerning the possibility of observing ejecta faster than the escape speed, from first-released-ejecta re-impacts. In order to study that, I collected ejecta data from MASCOT simulations, and computed the average values and the standard deviations of ejecta speeds, sizes, and directions for each simulation.

In Fig. 7.2 is shown the maximum ejecta speeds for each simulation in a stacked histogram. We notice that there are simulations for which at least one particle has a speed faster than Bennu's escape velocity on the equator, estimated to be about 18.9 cm s^{-1}, with $GM = 4.892$ m^3 s^{-2} and an average radius on the equator of about 275 m (Lauretta et al., 2019). For comparison, the escape velocity on the poles is about 19.8 cm s-1.

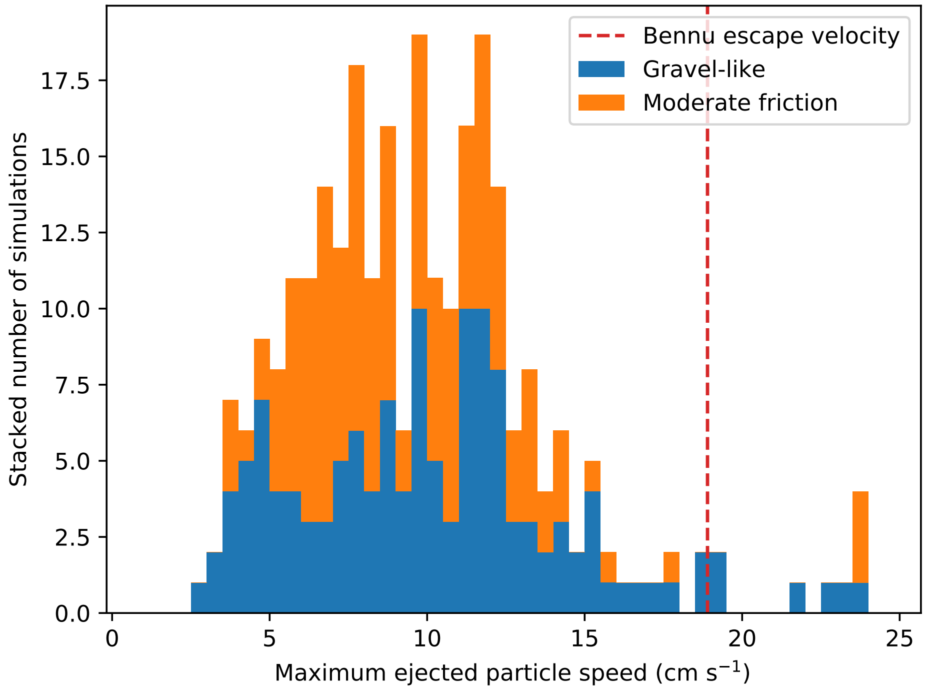

Fig. 7.2.: Stacked histogram of MASCOT simulations as a function of the maximum speed of all ejecta. Bennu's equatorial escape velocity (18.9 cm s^{-1}) is indicated, as well as the material type.

This means that particles observed on OSIRIS-REx images could be due to such re-impacts: large particles can be ejected in big events, that would eventually re-impact the surface. Such a large ejected particle has not been observed yet, and therefore remains still one of the possible explanations for the minor ejection events, but such particles/boulders at the origin of re-impacts could have not ascended high enough to be detected in current images.

Since Bennu is covered with boulders, I also considered the cases with boulders, presented as well in Chapter 4. The corresponding histogram is presented in Fig. 7.3. The definition of the boulder position is given in my second article about MASCOT, in Section 4.5. They are ordered from the lowest boulder to the higher one in the regolith bed. We see that even when we consider boulders, we can see the ejection of particles faster than the escape velocity, and therefore that re-impacts stay a possible source of minor ejection events. For a “top” boulder, probabilities of ejecting particles faster than the escape velocity are even increased, compared to a regolith without boulder.

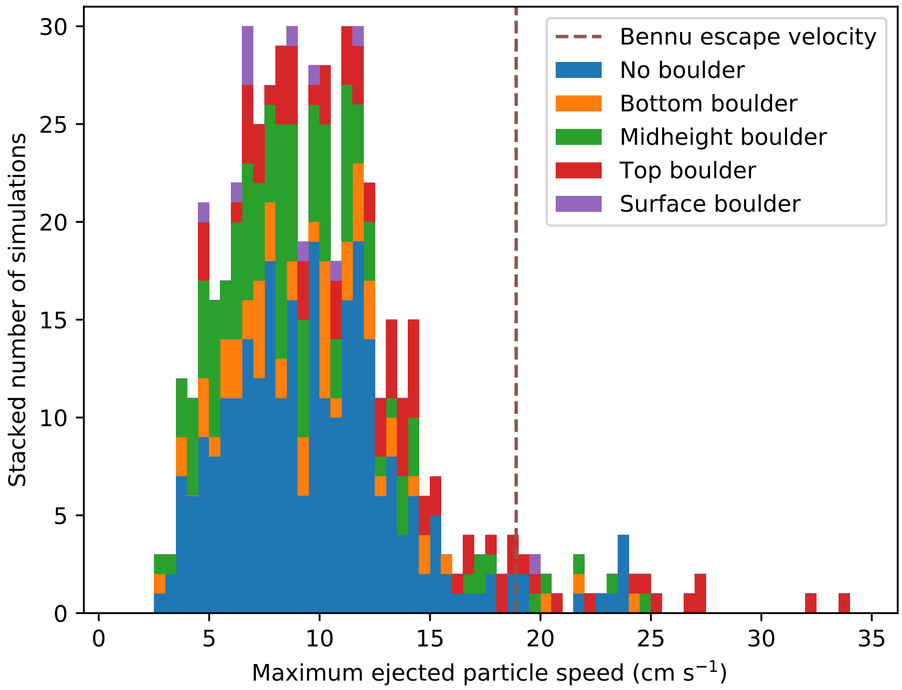

Fig. 7.3.: Stacked histogram of MASCOT simulations as a function of the maximum speed of all ejecta. Bennu’s equatorial escape velocity (18.9 cm s^{-1}) is indicated, as well as the presence or not of a boulder, and its height. The boulder height is described in Section 4.5, but the legend is ordered from the lowest boulder to the highest one.

Even if there are differences between the setup and the environment of MASCOT simulations and Bennu’s surface, this is an example of application of a previous study that shows that investigating low-velocity impacts on granular medium and, more generally, interactions with a granular surface under a low gravity, can result in insightful information with a wider range of applications than initially anticipated. This is still a preliminary study that can be improved. For example, the data from my simulations can help

Ronald-Louis Ballouz build a Monte-Carlo model of kinetic particle ejections to better understand the potential results of those possible re-impacts.

7.2 Terraces on Bennu

7.2.1 Observations on Bennu and experiments

Latitudinal scarps or terraces were observed on Bennu by OSIRIS-REx (Barnouin et al., 2019b). After arrival, a global digital terrain model was developed thanks to images collected by the OSIRIS-REx Camera Suite (OCAMS). The model is shown in Chapter 6 in Fig. 6.1.

Terraces are detected by latitudinal variations of the slope, and were detected mainly near Bennu's north pole. These variations are much larger in latitude than in longitude, as shown in Fig. 7.4.

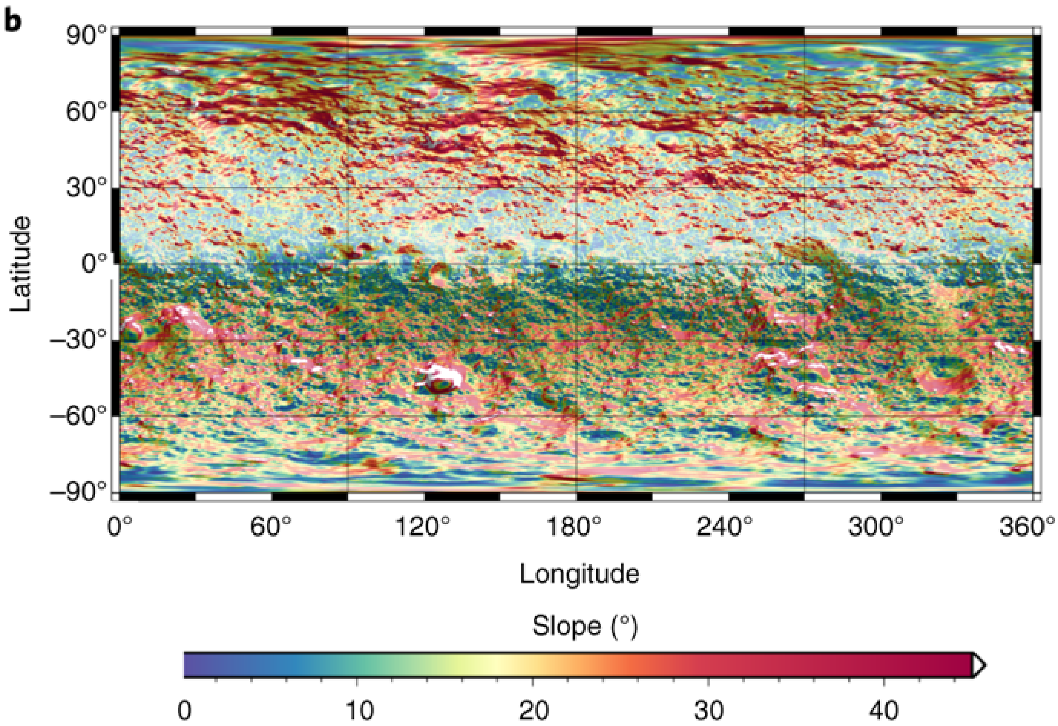

Fig. 7.4.: Shaded relief of the global digital terrain model of Bennu. The GDTM has a resolution of about 0.8 m per facet and 1.5 million facets. Image credit: Barnouin et al. (2019b)

As proposed by Olivier S. Barnouin et al., a possible origin of terraces on Bennu is surface mass wasting, i.e., mass movement along slopes (Barnouin et al., 2019a). They conducted laboratory experiments of boxes filled with a gravel mixture (with diameters of about 0.2 cm, 0.5 cm, and 1 cm), with a significant number of large grains to represent the numerous boulders on Bennu. They steadily and slowly inclined the bed and observed the mass movements. Mass wasting first appeared on the surface, as individual particles (usually the largest ones) fall down the slope. Then, they observed regional failures that produced local topographies very similar to the ones observed on Bennu.

Therefore, the formation of terraces due to regional failures seems to be a probable scenario. In order to check if we could observe similar results with `pkdgrav`, I conducted simulations using the same setting as the experiments mentioned above. This consists only of a preliminary study, and I present here my first results and the tools I implemented to analyze the data.

7.2.2 Numerical simulations

As for the inclined plane simulations presented in Section 2.3, I used a non-vertical gravity vector to reproduce the increasing slope. In `pkdgrav`, it is possible to use as input a file describing the gravity vector as a function of time, and I used this feature to change the inclination of the gravity vector with time. The magnitude of the gravity vector was chosen to be similar to the one on Bennu, i.e., $10^{-5}g$.

For my first simulations, I considered meter-sized grains in a box with dimensions of 80 m $\times$ 60 m $\times$ 15 m, where the largest dimension is the downhill one. Grains have gravel-like properties described in Chapter 2 and used in Chapters 4 and 5 for MASCOT and sampling simulations. The size distribution is a Gaussian distribution with a mean radius of 50 cm, a standard deviation σ of 30% and a cut-off at 1σ.

To generate this bed, I let grains fall under a normal gravity of $10^{-2}g$ to accelerate the processus, let the bed relax, and switched the gravity to $10^{-5}g$. Once again I waited for the bed to relax, flattened the surface by removing some grains, and then inclined the gravity up to 30°. Since I used a gravel-like material, 30° was well under the critical angle of repose. The relaxed bed, with an inclination of 30°, is shown in Fig. 7.5.

I increased the inclination angle up to 60° and first observed grains on the surface falling downhill, then the whole bed collapsed. The inclination is increased by half a degree every $100,000$ iterations, i.e., about every 630 s, or 10.5 min.

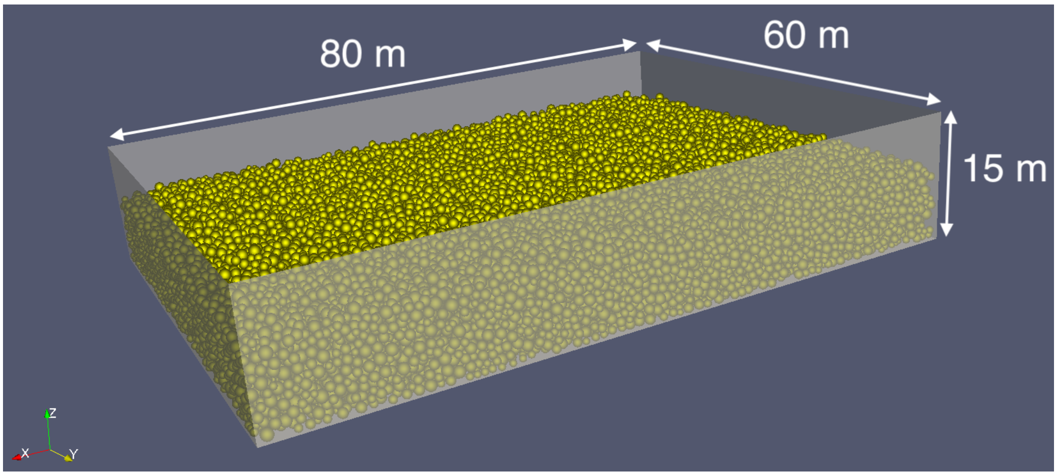

Fig. 7.5.: Setup of terraces simulation. The dimensions of the box are indicated on the figure, and the mean diameter of grains is 1 m. There are about $40,000$ grains in the bed.

After about 7 h and an inclination of $50°$, we begin to see individual grains falling downhill. Afterwards, failures happen in the bed and it collapses.

In order to analyze the intermediary states when displacements of individual particles occur on the surface, I considered different angles between $43°$ and $52°$ from the first simulation, and stopped increasing the inclination angle. For angles larger than $45 - 46°$, we identify displacements of grains on the surface, and the packing fraction at the top of the box increases, whereas it decreases in underneath layers, meaning that the bed begins to collapse. However, for some simulations such as for $45 - 47°$, particles on the top move less and less, indicating that, after a regional failure, the bed could come back to an immobile state. To be totally sure that it does not collapse very slowly, it is necessary to continue these simulations.

I computed the average displacements between each simulation output (about 63 s) for each horizontal layer, as well as the packing fraction, and they are shown in Fig. 7.7 for a $46°$ inclination angle, and in Fig. 7.8 for a $50°$ angle. We can see that the higher the inclination angle, the faster the failure of the upper layers, and the deeper the decrease in packing fraction.

Finally, I also developed a routine in Python to visualize the bed from above. By generating movies from these images, we can see the upper particles move on the bed, much faster than the lower layers. Such visualizations for a $48°$ inclination angle are shown in Fig. 7.9 by considering the whole bed from 0 to 10 m, and in Fig. 7.10 by only considering the upper layers from 8 to 10 m.

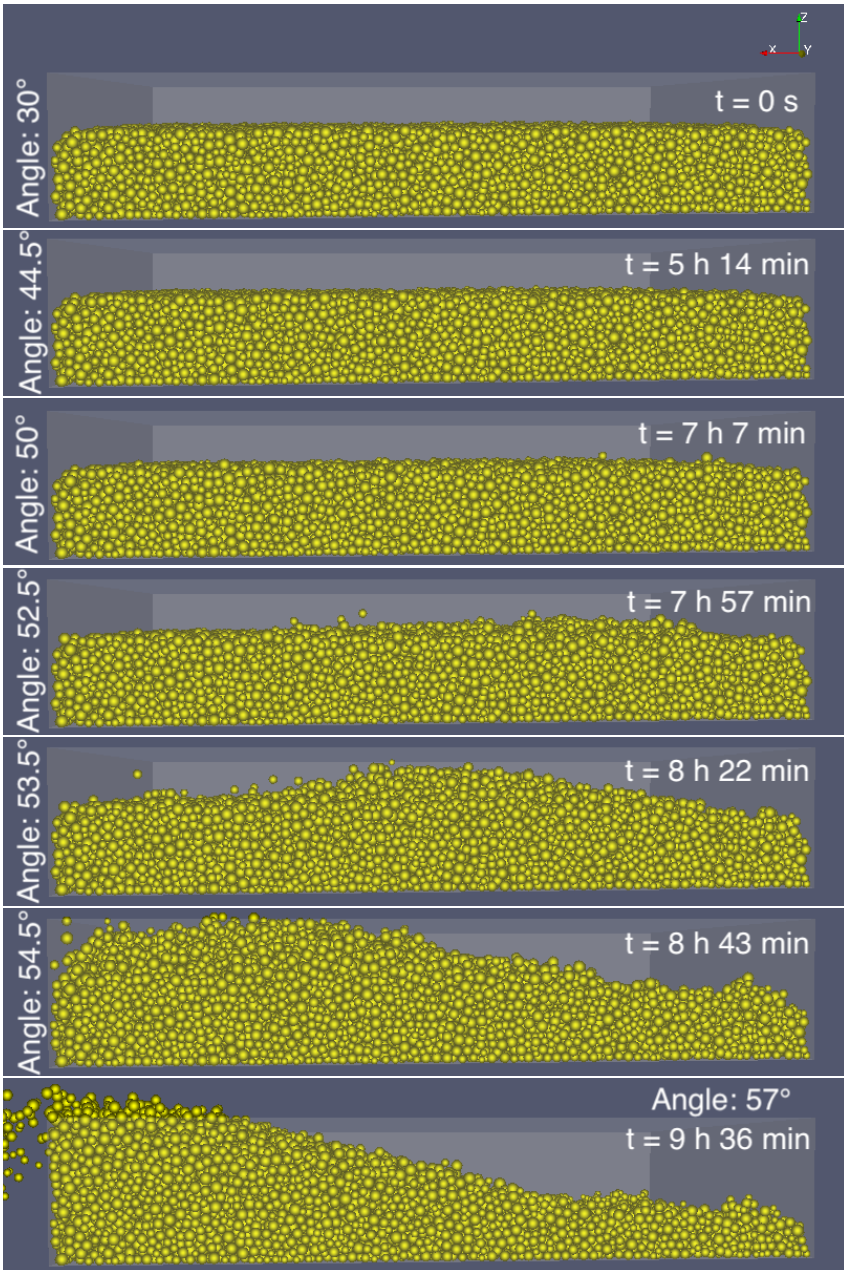

Fig. 7.6.: Snapshots of a simulation when the gravity vector is inclined by an additional half degree every 10.5 min. Inclination angles and durations since the beginning of the simulation at $30°$ are indicated in each figure.

In my simulations, I identified behaviors similar to the ones observed in laboratory experiments, such as individual grains toppling over and regional failures that could possibly stop with time, if the inclination angle stops increasing. I also developed visualisation tools to observe the evolution of the bed. Even if it is a preliminary study and more work is required to draw final conclusions, it is encouraging. A possible alternative is not to consider a Gaussian size distribution but a bidisperse distribution to reproduce the

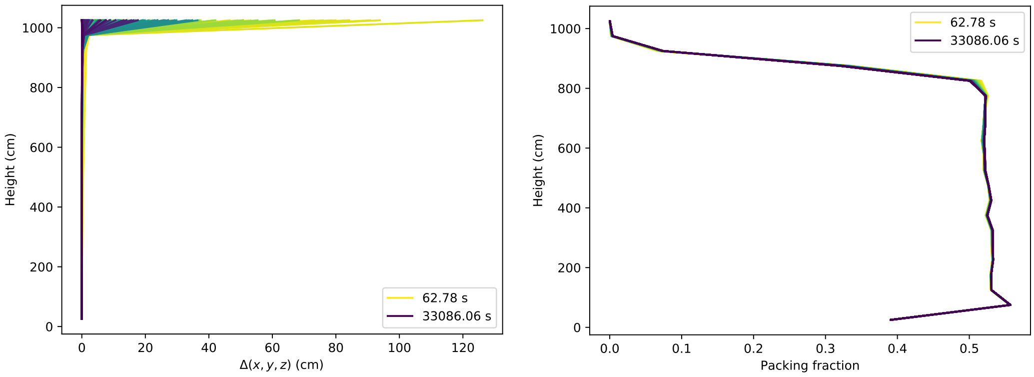

Fig. 7.7.: Average displacements and packing fractions as a function of the height, for a constant inclination angle of $46°$. Horizontal layers have a width of 50 cm.

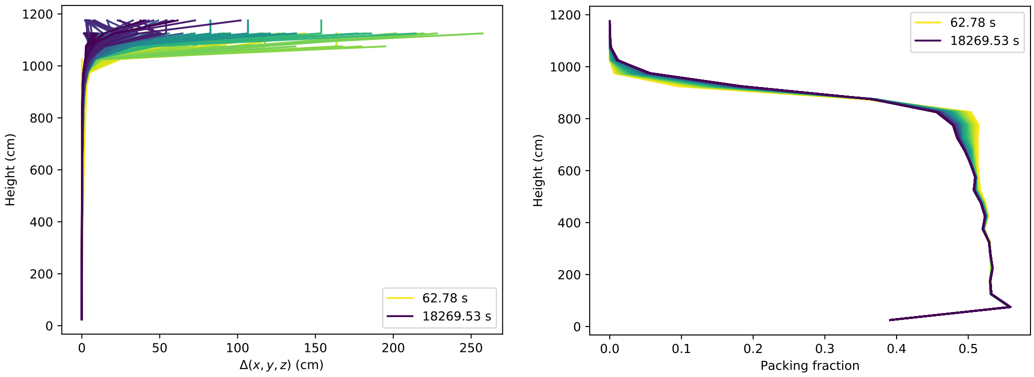

Fig. 7.8.: Average displacements and packing fractions as a function of the height, for a constant inclination angle of $50°$. Horizontal layers have a width of 50 cm.

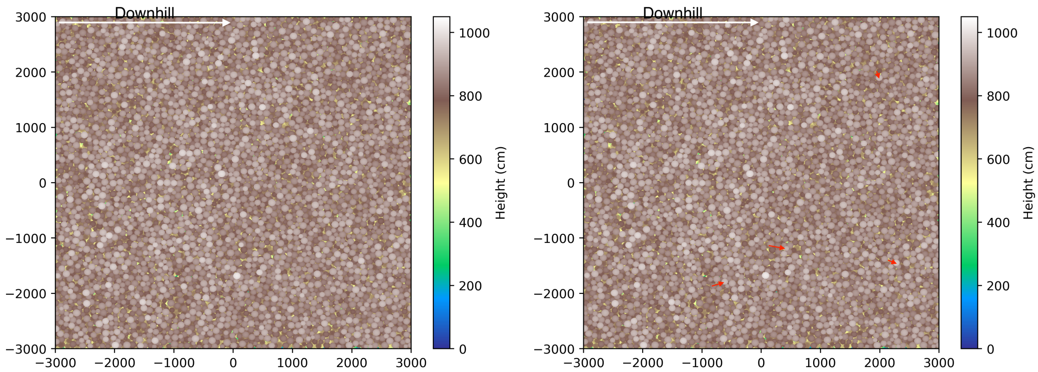

Fig. 7.9.: Visualizations of the whole bed from above for a $48°$ inclination separated by about 2 min. Four displacements (among others) are indicated by red arrows on the right panel, as well as the downhill direction.

presence of large boulders on the surface. I am considering it and am currently conducting simulations with this type of distribution.

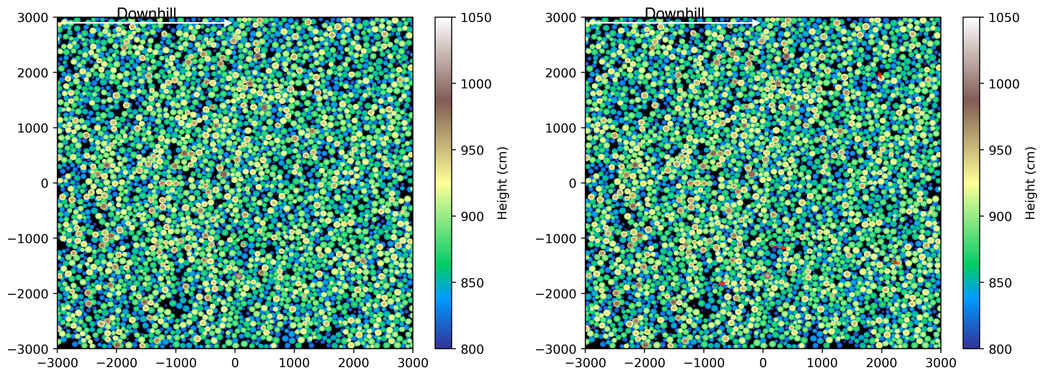

Fig. 7.10.: Visualizations of the upper layers of the bed from above for a $48°$ inclination separated by about 2 min. Four displacements (among others) are indicated by red arrows on the right panel, as well as the downhill direction.

8 Conclusion and perspectives

I will finish what you started.

— **My future padawan**

During my PhD, I aimed at a better understanding of the dynamics of granular material adapted to asteroid surfaces. The purpose was to improve our scientific understanding of this problem but also to provide decision support results to engineering and scientific teams of both Hayabusa2 and OSIRIS-REx teams, and to help to interpret data and observations. To this end, I conducted numerical simulations of diverse interactions with granular material in appropriate gravity conditions, by adapting the SSDEM numerical code `pkdgrav`.

Firstly are synthesized the main results of the different subjects I treated in this thesis, as well as a general conclusion. Then are announced perspectives of future research projects and applications of my results to other contexts.

8.1 Main results

After having introduced the SSDEM numerical code `pkdgrav`, I performed comparisons with actual experiments to validate the actual version of the code for low-velocity impacts. I thus conducted numerical simulations with the exact same setup (same bed dimensions, grain size, and impactor) as the experiments realized by Nguyen et al. (2019). Experiments and simulations were done with 5 mm and 1 cm glass beads and, in both cases, results proved to be very similar, validating the use of `pkdgrav` for this type of application. Comparing our numerical and experimental results, I found behaviors that are different from other experiments in glass beads (Katsuragi et al., 2007). By considering the acceleration, I possibly identified the form of the Coulomb force, namely the force due to friction opposing the penetration, in our results. This form, compared to previous studies, seems to be characterized by a trend: depending on the size of the grain, or on the impactor-grain size ratio, the linear Coulomb force could go from constant to proportional to the penetration.

An issue with SSDEM codes such as `pkdgrav` is usually the large computation time. In order to bypass this, a project is to merge the SSDEM method with the much faster continuum approach using a constitutive law relating the friction parameter and inertial number $\mu(I)$. Alternating between both methods, when appropriate, during a same simulation would drastically reduce the computation time. For this purpose, relations between parameters of both methods have to be established. In a preliminary study, I performed inclined plane simulations with `pkdgrav` to find the parameters related to two material types, a gravel-like one and a moderate one. I found that velocity profiles correspond to the ones predicted by the $\mu(I)$ rheology but only for a moderate friction, and in this case, the best parameters are roughly $\mu_s = 0.51$, $\mu_2 = 0.82 - 0.83$, and $I = 0.26 - 0.33$. When the friction is too high, the discrepancies may be due to the high dilution of the flow. However, as long as the inclination angle does not exceed critical values, the moderate-friction material profiles match the predictions, and I proposed potential corresponding $\mu(I)$ parameters.

After these general results, I then presented my work related to the Hayabusa2 mission. Firstly, I proposed a brief analysis of the paper by Sugita et al. (2019), investigating Ryugu geophysics, followed by the paper itself. I show that, from a simple calculation of the cohesion force, a negligible cohesion would mean particles on the surface should be larger than millimeter-sized. In this mission, I particularly worked on the lander MASCOT and on the sampling mechanism, in order to support operations that took place during the PhD and interpret observations.

Based on Earth-based observations of Ryugu to define realistic assumptions for my simulations, pre-arrival simulations were conducted whose results and analyses can be found in Thuillet et al. (2018), following Maurel et al. (2018). Stochasticity was identified in the simulation outcomes, particularly due to MASCOT's irregular shape. Nevertheless, general trends could be established. For example, greatest distances after impact are obtained with the shallowest beds, the most-grazing impacts, the highest-friction material, and with MASCOT landing on its back corner. Moreover, it was found that depending on the attitude at impact and on the friction properties of the surface material, the traces left by MASCOT on the ground after the impact are different. This means that the shape of the traces could give hints on the distance traveled by MASCOT, or on the nature of the material, which has therefore applications for both engineering and scientific teams.

As a continuation of the first article, the parameter space was extended, to look at the influence of slopes and of the impact speed. For a moderate-friction regolith, it was found that the outgoing-to-incoming speed ratio does not seem to depend on the impact speed. For a higher-friction material, the trend is more difficult to establish and would require a more advanced investigation. Moreover, close-up observations revealed the presence of numerous boulders on Ryugu's surface. Adding a boulder in the simulations increased the stochasticity in the outcomes, and the higher the boulder in the bed, the larger the stochasticity. It was also found that landing on a rigid boulder can result in outgoing-to-incoming speed ratios as low as 0.3, due to a succession of microbounces, each of them dissipating energy. This leads to the conclusion that interpreting the surface properties from the sole outgoing-to-incoming speed ratio has to be done with caution with a nonspherical body such as MASCOT. All these results can be found in an article accepted under minor revision, inserted in this thesis.

I then studied Hayabusa2 sampling and for this purpose conducted simulations of $50 - 300$ m s^{-1} impacts under Ryugu's gravity. Firstly, I did not include the sampler horn to characterize the impact itself. It was found that the cratering process is much longer under such a low gravity. However, a hemispherical growth followed by a mainly lateral growth were observed as for previous 1 g simulations and experiments. Numerical results were also compared to the Z-model (Maxwell, 1977), a predictive analytical model for the streamlines inside the bed during an impact, and great agreements were found during the excavation state. More results (for example on ejecta and crater dimensions) are presented in the submitted article inserted in this thesis. After having added the horn and monitored the number of grains in each part of the sampler, we found that most simulations fulfill the scientific objective of collecting at least 100 mg after 1 s, even without taking into account the scoop-up part of the sampler. Moreover, a second shot 0.2 s after the first one seems to increase the total mass of ejecta but not necessarily the collected mass. These results and additional ones with tilted angles and different coefficients of restitution can be found in the article.

Finally, I also worked on the OSIRIS-REx mission, and contributed to the analysis of the surface in the article by Walsh et al. (2019). After the discovery of particle ejection on Bennu, we proposed an explanation for minor ejection events by applying my MASCOT simulations to this different context. Large ejected irregular particles could re-impact the surface days after their ejection, which could be well represented by MASCOT simulations, where an irregular body of a few tenths of cm in size impacts at low speed a granular bed. Even if simulations were conducted with Ryugu's gravity, our preliminary results adapted to Bennu are worth being further investigated. Terraces were also observed on Bennu, and in a preliminary study, I performed several simulations by inclining a box filled with grains and observed the collapse. I observed similarities with laboratory experiments, such as the displacement on the surface of individual grains before the global collapse. Moreover, it seems that some simulations present regional collapses that eventually stop, which could lead to the formation of terraces. However, this needs to be verified with longer simulations.

To conclude, I performed a large range of simulations to better understand the impact mechanisms in granular materials, in order to apply them to Hayabusa2 and OSIRIS-REx, two missions I had the privilege to be a member of, and which taught me a lot about the functioning of space missions. For Hayabusa2 in particular, I had the opportunity to interact with both scientific and engineering teams, and support the operations. Even if numerical models cannot fully represent the reality and always have limitations, they can bring insightful information, otherwise very difficult to obtain on Earth. The low gravity and vacuum are for example a major advantage of simulations. Concerning `pkdgrav`, I dedicated part of my PhD to improve its reliability, to have a comparison that can serve as a reference for low-speed impacts, because numerical modeling is a powerful tool but first needs to be validated.

8.2 Perspectives

The code `pkdgrav` is under permanent improvement. For example, a cohesion model is currently implemented in the code, and I conducted MASCOT simulations to see the effect of cohesion on the impact, and the critical cohesion for which we observe a notable difference. However, no validation has been done with the code for low-speed impacts with cohesion, and this could be a next step.

Moreover, we have to find a solution to simulate the contact between an assembly of inertial walls, such as MASCOT, and a static, rigid, wall. Our solution of sticking particles on the wall, because contacts between walls are not treated, proved to create an excess of energy in the bounce. Therefore, this solution has to be fixed, or another solution should be investigated. Treating contacts between two walls is not the first purpose of `pkdgrav`, as it is a SSDEM code; nonetheless, we see that such an ability could reveal to be very useful when modeling a nonspherical impactor bouncing on both non-granular and granular surfaces. MASCOT's trajectory reconstruction is a perfect example of this kind of motivation.

Because many boulders were observed on Ryugu and Bennu, and these boulders would break if under a too high pressure, it could be interesting to investigate the influence of using breakable aggregates in our simulations. It has already been implemented in `pkdgrav` with springs but still need to be applied to such low-impact speed simulations. Aggregates would break off if the forces on grains forming them exceed a threshold. One of the major difficulties with breakable aggregates is to define this threshold for materials we do not have in laboratories, and this adds a new free parameter. However, comparisons with returned samples or simulants created on Earth could give insightful hints concerning the value of the threshold.

Concerning the near future, comparisons with low-speed experiments are planned to be expanded for low gravities, to check the evolution with gravity of the different conclusions I drawn. The results presented in this thesis and possibly these new results should be submitted soon. As I already stated, this potential paper could be a reference for the validity of `pkdgrav` for low-speed experiments, and therefore its publication remains a priority. The continuation of our work on particle ejection and the formation of terraces is also planned.

Furthermore, with potential future missions such as MMX (Martians Moon eXploration) (Kuramoto et al., 2018) and AIDA (Michel et al., 2018; Cheng et al., 2018), understanding the interactions between rovers, landers, or impactors with the surface is essential. The simulations I conducted participated to this effort, but there is still a lot to be done. For example, studying the flow of fine regolith around rover's wheels could bring a significant amount of information on the properties of the surface. On Phobos, MMX's rover, in the framework of a CNES-DLR cooperation, should be able to observe such a flow, and being able to interpret it could lead to potential breakthroughs for the field.

Moreover, landers usually have nonspherical shapes whereas most of the analytical and experimental work addresses spherical or ogive-like impactors.

Irregular shapes add a lot of stochasticity, as MASCOT simulations showed, thus one could doubt of the utility of conducting simulations modeling the impact. However, general trends can still be defined and, more importantly, nonspherical shapes can be at the origin of counterintuitive results, such as our finding that MASCOT bouncing on a rigid boulder can lead to low speed ratios. Without simulations or experiments with these nonspherical shapes, interpreting raw data could lead to wrong conclusions.

In a more distant future, the interest of private companies in asteroid mining will require a great understanding of the interactions between the surface and any man-made extraction systems. Whether these extractions are brought back to Earth or used for refueling space vehicles, numerical simulations will enable pre-arrival tests in low-gravity environments otherwise very difficult to obtain on Earth.

A Volume of intersection between a sphere and a cube

Concerning the analysis of my terraces simulations (see Section 7.2), I wanted to show the packing fraction from the y-axis, and therefore in the 2D x-z-plane, by considering the whole y-length and check the evolution as a function of x and z. Each cell would therefore represent the packing fraction in a rectangular cuboid whose visible faces from the y-axis would be squares, and its length the length of the box along the y-axis, i.e., 60 m. To compute the exact packing fraction in the bed for such cells, it is necessary to compute the volume of the intersection between a cuboid and a sphere, which is not a trivial problem. To generalize the problem, I considered an intersection between a cube and a sphere of radius R. We can see this intersection as the intersection between the sphere and 6 half-spaces. Such an intersection space can be written as:

$$C = \{(x, y, z) \in \mathbb{R} : x^2 + y^2 + z^2 \leq R^2, x_0 < x < x_1, y_0 < y < y_1, z_0 < z < z_1\}, \tag{A.1}$$

if we consider that the center of the sphere is the origin, and where (x_0, x_1), (y_0, y_1), and (z_0, z_1) are the coordinates of the planes that cut the sphere. For a cube with a center (x_c, y_c, z_c) and edge length $2a$, we have for example $x_0 = x_c - a$, and $x_1 = x_c + a$.

Analyzing the definition of the space presented in Eq. A.1, I found that the volume can be computed as:

$$V_{\text{inter}} = \int_{\max(x_0, -\sqrt{R^2-y_L^2-z_L^2})}^{\min(x_1, \sqrt{R^2-y_L^2-z_L^2})} \int_{\max(y_0, -\sqrt{R^2-\alpha^2-z_L^2})}^{\min(y_1, \sqrt{R^2-\alpha^2-z_L^2})} \int_{\min(z_0, -\sqrt{R^2-\alpha^2-\beta^2})}^{\min(z_1, \sqrt{R^2-\alpha^2-\beta^2})} \mathrm{d}\gamma \mathrm{d}\beta \mathrm{d}\alpha \tag{A.2}$$

by considering the limiting coordinates $y_L = \max(y_0, -y_1, 0)$ and $z_L = \max(z_0, -z_1, 0)$. This double integral (if we compute analytically the inner integral as just a subtraction of both limits), can be computed thanks to the routine `from scipy.integrate.dblquad`.

In order to check Eq. A.2, I compared the results from integration with the analytical formula of a spherical cap for a first validation. The volume of a spherical cap, defined by Fig. A.1, can be computed as $V_{\text{cap}} = \frac{\pi h^2}{3}(3R - h)$, where h is the height of the cap and a radius R. In this equation, h can be larger than the radius.

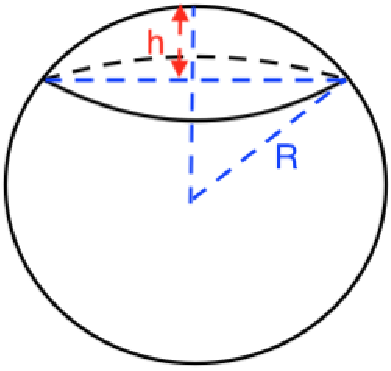

Fig. A.1.: Spherical cap of a sphere, with the height of the cap h and the radius R.

I compared the results for a sphere without one spherical cap ($x_0 < x$) and without two spherical caps ($x_0 < x < x_0 + 0.5$), and they are shown in Fig. A.2 for $R = 1$. I also plotted the volume computed from the integral for $x_0 < x$ and $z_0 < z$ with $z_0 \in \{-0.5, 1, 1.5\}$ to show an example with two different directions. I found that the computation with integration could be considered as exact, and the difference between numerical integration and analytical was smaller than 10^{-14} cm^3.

However, the issue for the moment is that, even if one volume computation is rather fast, when used for the computation of porosity with about $40,000$ grains, I did not managed yet to make the computation time acceptable. This could be a subject of future work, whether by reducing the computation time of one call to the function, or by optimizing the number of calls. Such a function to rightly compute porosity in a grid could be useful in the future.

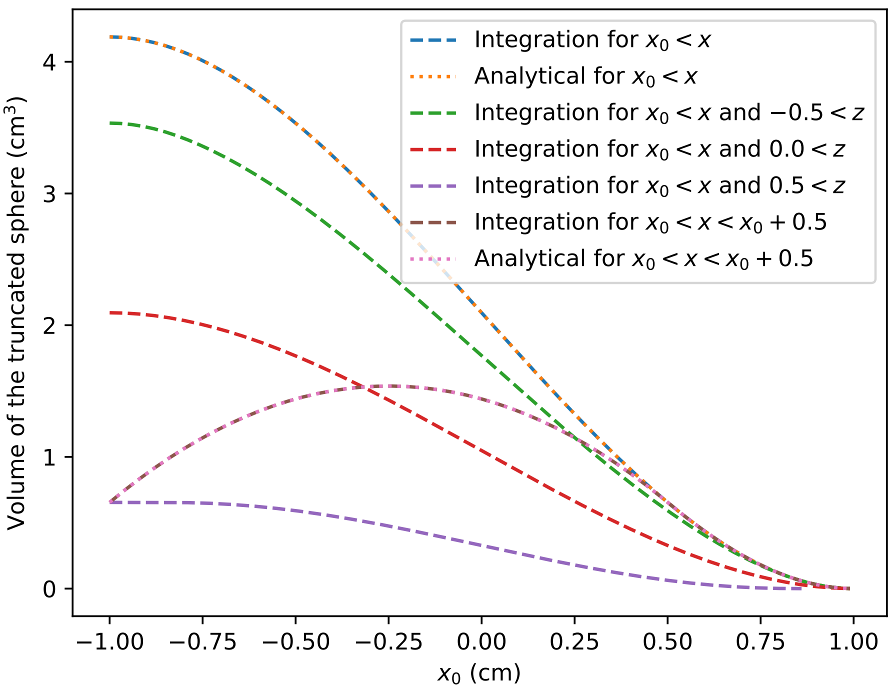

Fig. A.2.: Comparison of volumes of truncated spheres (R=1) computed from numerical integration and analytical formulas.

Bibliography

Abell, P. A. et al. (2015). “Human Exploration of Near-Earth Asteroids”. In: *Asteroids IV*. University of Arizona Press, p. 855. arXiv: 1306.2418 (cit. on p. 7).

Ai, J. et al. (2011). “Assessment of rolling resistance models in discrete element simulations”. In: *Powder Technology* 206.3, pp. 269–282 (cit. on p. 53).

Altshuler, E. et al. (2014). “Settling into dry granular media in different gravities”. In: *Geophysical Research Letters* 41.9, pp. 3032–3037 (cit. on p. 57).

Ambroso, M. A. et al. (2005). “Penetration depth for shallow impact cratering”. In: *Physical Review E* 71.5, p. 051305. arXiv: 0411231 [cond-mat] (cit. on p. 61).

Ancey, C. et al. (1999). “A theoretical framework for granular suspensions in a steady simple shear flow”. In: *Journal of Rheology* 43.6, pp. 1673–1699 (cit. on p. 81).

Andreotti, B. et al. (2013). *Granular Media*. Cambridge: Cambridge University Press (cit. on p. 24).

Arai, T. et al. (2017). “Thermal Imaging Performance of TIR Onboard the Hayabusa2 Spacecraft”. In: *Space Science Reviews* 208.1-4, pp. 239–254 (cit. on pp. 98, 105).

Asphaug, E. (2007). “Planetary science. The shifting sands of asteroids.” In: *Science (New York, N.Y.)* 316.5827, pp. 993–4 (cit. on p. 21).

Ballouz, R.-L. (2017). “Numerical Simulations of Granular Physics in the Solar System”. PhD thesis. University of Maryland, College Park (cit. on pp. 46, 51, 56, 57, 59).

Barlow, Nadine G. (2008). *Mars: an introduction to its interior, surface and atmosphere*. Cambridge University Press, p. 264 (cit. on p. 27).

Barnouin, O. S. et al. (2019a). “On the possible origin of terraces on Bennu”. In: *EPSC Abstracts*. 13. Geneva: EPSC-DPS 2019, pp. 2019–255–1 (cit. on p. 235).

Barnouin, O. S. et al. (2019b). “Shape of (101955) Bennu indicative of a rubble pile with internal stiffness”. In: *Nature Geoscience* 12.4, p. 247 (cit. on pp. 214–216, 218, 235).

Barnouin-Jha, O. S. et al. (2001). “Preliminary Impact Crater Dimensions on 433 Eros from the NEAR Laser Rangefinder and Imager”. In: *32nd Annual Lunar and Planetary Science Conference*. Houston: LPSC (cit. on p. 16).

Barnouin-Jha, O. S. et al. (2008). “Small-scale topography of 25143 Itokawa from the Hayabusa laser altimeter”. In: *Icarus* 198.1, pp. 108–124 (cit. on pp. 20, 21).

Barucci, M. A. et al. (2015). “The Flybys of Asteroids 2867 Steins, 21 Lutetia, and 4179 Toutatis”. In: *Asteroids IV*. University of Arizona Press, p. 433 (cit. on p. 11).

Beitz, E. et al. (2011). “Low-velocity Collisions of Centimeter-sized Dust Aggregates”. In: *The Astrophysical Journal* 736.1, p. 34 (cit. on p. 41).

Belton, M. J. S. et al. (1996). “Galileo’s Encounter with 243 Ida: An Overview of the Imaging Experiment”. In: *Icarus* 120.1, pp. 1–19 (cit. on p. 9).

Benner, L. A. M. et al. (2002). “Radar observations of asteroid 1999 JM8”. In: *Meteoritics & Planetary Science* 37.6, pp. 779–792 (cit. on p. 8).

Benz, W. et al. (1994). “Numerical simulations of catastrophic disruption: recent results”. In: *Planetary and Space Science* 42.12, pp. 1053–1066 (cit. on p. 43).

Beuzit, J.-L. et al. (2008). “SPHERE: a ’Planet Finder’ instrument for the VLT”. In: *Ground-based and Airborne Instrumentation for Astronomy II*. Ed. by Ian S. McLean et al. Vol. 7014, p. 701418 (cit. on p. 4).

Bibring, J.-P. et al. (2017). “The MicrOmega Investigation Onboard Hayabusa2”. In: *Space Science Reviews* 208.1-4, pp. 401–412 (cit. on p. 124).

Biele, J. et al. (2017). “Experimental Determination of the Structural Coefficient of Restitution of a Bouncing Asteroid Lander”. In: *arXiv e-prints*, arXiv:1705.00701 (cit. on p. 125).

Binzel, R. P. et al. (1989). *Asteroids II* (cit. on p. 9).

Binzel, R. P. et al. (2001). “Spectral Properties of Near-Earth Objects: Palomar and IRTF Results for 48 Objects Including Spacecraft Targets (9969) Braille and (10302) 1989 ML”. In: *Icarus* 151.2, pp. 139–149 (cit. on p. 98).

Binzel, R. P. et al. (2002). “Physical Properties of Near-Earth Objects”. In: *Asteroids III*, p. 255 (cit. on p. 6).

Binzel, R. P. et al. (2015). “Spectral slope variations for OSIRIS-REx target Asteroid (101955) Bennu: Possible evidence for a fine-grained regolith equatorial ridge”. In: *Icarus* 256, pp. 22–29 (cit. on p. 214).

Bos, B. J. et al. (2018). “Touch And Go Camera System (TAGCAMS) for the OSIRIS-REx Asteroid Sample Return Mission”. In: *Space Science Reviews* 214.1, p. 37 (cit. on p. 214).

Bottke, W. F. et al. (2002a). *Asteroids III* (cit. on p. 9).

Bottke, W. F. et al. (2002b). “The Effect of Yarkovsky Thermal Forces on the Dynamical Evolution of Asteroids and Meteoroids”. In: *Asteroids III*, p. 395 (cit. on pp. 5, 6).

Bottke, W. F. et al. (2006). “The Yarkovsky and YORP Effects: Implications for Asteroid Dynamics”. In: *Annual Review of Earth and Planetary Sciences* 34.1, pp. 157–191 (cit. on p. 5).

Bouvier, A. et al. (2010). “The age of the Solar System redefined by the oldest Pb-Pb age of a meteoritic inclusion”. In: *Nature Geoscience* 3.9, pp. 637–641 (cit. on p. 5).

Bridgwater, J. (1976). “Fundamental powder mixing mechanisms”. In: *Powder Technology* 15.2, pp. 215–236 (cit. on p. 40).

Brisset, J. et al. (2018). “Regolith behavior under asteroid-level gravity conditions: low-velocity impact experiments”. In: *Progress in Earth and Planetary Science* 5.1, p. 73 (cit. on pp. 131, 181).

Buczkowski, D. L. et al. (2008). “433 Eros lineaments: Global mapping and analysis”. In: *Icarus* 193.1, pp. 39–52 (cit. on p. 15).

Buratti, B. J. et al. (1996). “The Lunar Opposition Surge: Observations by Clementine”. In: *Icarus* 124.2, pp. 490–499 (cit. on p. 10).

Buratti, B. J. et al. (2004). “9969 Braille: Deep Space 1 infrared spectroscopy, geometric albedo, and classification”. In: *Icarus* 167.1, pp. 129–135 (cit. on p. 12).

Burns, J. A. (1992). *Contradictory clues as to the origin of the Martian moons*. University of Arizona Press, p. 1283 (cit. on p. 27).

Bus, S. J. et al. (2002). “Phase II of the Small Main-Belt Asteroid Spectroscopic Survey A Feature-Based Taxonomy”. In: *Icarus* 158.1, pp. 146–177 (cit. on p. 5).

Busarev, V. V. et al. (2018). “New candidates for active asteroids: Main-belt (145) Adeona, (704) Interamnia, (779) Nina, (1474) Beira, and near-Earth (162,173) Ryugu”. In: *Icarus* 304, pp. 83–94 (cit. on p. 231).

Busch, M. W. et al. (2008). “Physical properties of near-Earth Asteroid (33342) 1998 WT24”. In: *Icarus* 195.2, pp. 614–621 (cit. on p. 8).

Carr, M. H. et al. (1994). “The Geology of Gaspra”. In: *Icarus* 107.1, pp. 61–71 (cit. on p. 12).

Carrigy, M. A. (1970). “Experiments on the Angles of Repose of Granular Materials 1”. In: *Sedimentology* 14.3-4, pp. 147–158 (cit. on p. 33).

Carvano, J. M. et al. (2010). “SDSS-based taxonomic classification and orbital distribution of main belt asteroids”. In: *Astronomy and Astrophysics* 510, A43 (cit. on p. 2).

Castellanos, A. (2005). “The relationship between attractive interparticle forces and bulk behaviour in dry and uncharged fine powders”. In: *Advances in Physics* 54.4, pp. 263–376 (cit. on pp. 34, 35, 104).

Chapman, C. R. (1976). “Asteroids as meteorite parent-bodies: the astronomical perspective”. In: *Geochimica et Cosmochimica Acta* 40.7, pp. 701–719 (cit. on p. 9).

Charnoz, S. et al. (2010). “The recent formation of Saturn’s moonlets from viscous spreading of the main rings”. In: *Nature* 465.7299, pp. 752–754 (cit. on p. 27).

Charnoz, S. et al. (2011). “Accretion of Saturn’s mid-sized moons during the viscous spreading of young massive rings: Solving the paradox of silicate-poor rings versus silicate-rich moons”. In: *Icarus* 216.2, pp. 535–550 (cit. on p. 27).

Chau, K.T. et al. (2002). “Coefficient of restitution and rotational motions of rockfall impacts”. In: *International Journal of Rock Mechanics and Mining Sciences* 39.1, pp. 69–77 (cit. on p. 54).

Cheng, A. F. (2002). “Near Earth Asteroid Rendezvous: Mission Summary”. In: *Asteroids III*, p. 351 (cit. on pp. 12, 15, 18).

Cheng, A. F. et al. (1997). “Near-Earth Asteroid Rendezvous: Mission overview”. In: *Journal of Geophysical Research: Planets* 102.E10, pp. 23695–23708 (cit. on pp. 12, 15).

Cheng, A. F. et al. (2007). “Fundamentally distinct outcomes of asteroid collisional evolution: Itokawa and Eros”. In: *Geophysical Research Letters* 34.9, p. L09201 (cit. on p. 21).

Cheng, A. F. et al. (2018). “AIDA DART asteroid deflection test: Planetary defense and science objectives”. In: *Planetary and Space Science* 157, pp. 104–115 (cit. on pp. 7, 245).

Cheng, B. et al. (2019). “Numerical simulations of the controlled motion of a hopping asteroid lander on the regolith surface”. In: *Monthly Notices of the Royal Astronomical Society* 485.3, pp. 3088–3096 (cit. on p. 46).

Chesley, S. R. et al. (2014). “Orbit and bulk density of the OSIRIS-REx target Asteroid (101955) Bennu”. In: *Icarus* 235, pp. 5–22 (cit. on p. 214).

Christensen, P. R. et al. (2018). “The OSIRIS-REx Thermal Emission Spectrometer (OTES) Instrument”. In: *Space Science Reviews* 214.5, p. 87 (cit. on p. 214).

Clark, A. H. et al. (2013). “Granular impact model as an energy-depth relation”. In: *EPL (Europhysics Letters)* 101.6, p. 64001 (cit. on pp. 62, 75, 77, 79, 80).

Clark, B. E. et al. (2011). “Asteroid (101955) 1999 RQ36: Spectroscopy from 0.4 to 2.4μm and meteorite analogs”. In: *Icarus* 216.2, pp. 462–475 (cit. on p. 214).

Colwell, J. E. (2003). “Low velocity impacts into dust: results from the COLLIDE-2 microgravity experiment”. In: *Icarus* 164.1, pp. 188–196 (cit. on pp. 42, 180).

Colwell, J. E. et al. (2005). “Dust transport in photoelectron layers and the formation of dust ponds on Eros”. In: *Icarus* 175.1, pp. 159–169 (cit. on p. 36).

Colwell, J. E. et al. (2008). “Ejecta from impacts at 0.2-2.3 m/s in low gravity”. In: *Icarus* 195.2, pp. 908–917 (cit. on pp. 42, 180).

Colwell, J. E. et al. (2015). “PRIME: Studying Low-Velocity Impacts in Microgravity”. In: *European Planetary Science Congress*, EPSC2015–766 (cit. on pp. 42, 180).

Coulomb, C.-A. (1776). *Essai sur une application des règles de maximis & minimis à quelques problèmes de statique, relatifs à l’architecture*. Paris: De l’Imprimerie Royale (cit. on p. 32).

Coupez, T. et al. (2013). “Solution of high-Reynolds incompressible flow with stabilized finite element and adaptive anisotropic meshing”. In: *Computer Methods in Applied Mechanics and Engineering* 267, pp. 65–85 (cit. on pp. 43, 49, 83).

Cruz, F. da et al. (2005). “Rheophysics of dense granular materials: Discrete simulation of plane shear flows”. In: *Physical Review E* 72.2, p. 021309 (cit. on p. 81).

Cundall, P. A. et al. (1979). “A discrete numerical model for granular assemblies”. In: *Géotechnique* 29.1, pp. 47–65 (cit. on pp. 45, 50).

Daly, M. G. et al. (2017). “The OSIRIS-REx Laser Altimeter (OLA) Investigation and Instrument”. In: *Space Science Reviews* 212.1-2, pp. 899–924 (cit. on p. 214).

Delbo, M. et al. (2014). “Thermal fatigue as the origin of regolith on small asteroids”. In: *Nature* 508.7495, pp. 233–236 (cit. on pp. 30, 105, 216, 231).

DellaGiustina, D. N. et al. (2019). “Properties of rubble-pile asteroid (101955) Bennu from OSIRIS-REx imaging and thermal analysis”. In: *Nature Astronomy* 3, p. 341 (cit. on p. 217).

DeMeo, F. E. et al. (2009). “An extension of the Bus asteroid taxonomy into the near-infrared”. In: *Icarus* 202.1, pp. 160–180 (cit. on p. 5).

DeMeo, F. E. et al. (2015). “The Compositional Structure of the Asteroid Belt”. In: *Asteroids IV*. University of Arizona Press, p. 13 (cit. on p. 5).

Derjaguin, B. V. et al. (1975). “Effect of contact deformations on the adhesion of particles”. In: *Journal of Colloid and Interface Science* 53.2, pp. 314–326 (cit. on p. 34).

Dove, A. et al. (2013). “Investigations of charged particle motion on the surfaces of dusty, airless solar system bodies (Invited)”. In: *AGU Fall Meeting Abstracts* 2013, P53F–01 (cit. on p. 42).

Duran, J. (2000). *Sands, Powders, and Grains : An Introduction to the Physics of Granular Materials*. Springer, p. 214 (cit. on p. 22).

Durda, D. D. et al. (2013). “Laboratory Investigation of Asteroid Regolith Properties”. In: *European Planetary Science Congress*, EPSC2013–1050 (cit. on p. 36).

Emery, J. P. et al. (2014). “Thermal infrared observations and thermophysical characterization of OSIRIS-REx target asteroid (101955) Bennu”. In: *Icarus* 234, pp. 17–35 (cit. on p. 214).

Falco, S. et al. (2017). “Generation of 3D polycrystalline microstructures with a conditioned Laguerre-Voronoi tessellation technique”. In: *Computational Materials Science* 136, pp. 20–28 (cit. on p. 129).

Ferrari, F. et al. (2018). “A code for the study of gravitational aggregates with non-spherical particles”. In: *European Planetary Science Congress*. Berlin: EPSC 2018 (cit. on p. 44).

Fétick, R. J.-L. et al. (2019). “Closing the gap between Earth-based and interplanetary mission observations: Vesta seen by VLT/SPHERE”. In: *Astronomy & Astrophysics*. arXiv: 1902.01287 (cit. on p. 4).

Forterre, Y. et al. (2008). “Flows of Dense Granular Media”. In: *Annual Review of Fluid Mechanics* 40.1, pp. 1–24 (cit. on pp. 24, 25).

French, R. et al. (2000). “Saturn’s Rings II Particle Sizes Inferred from Stellar Occultation Data”. In: *Icarus* 145.2, pp. 502–523 (cit. on p. 27).

Fujiwara, A. et al. (2005). “HAYABUSA Mission to Asteroid Itokawa: In-Situ Observation and Sample Return”. In: *Dust in Planetary Systems* 1280, p. 50 (cit. on p. 172).

Fujiwara, A. et al. (2006). “The Rubble-Pile Asteroid Itokawa as Observed by Hayabusa”. In: *Science* 312.5778, pp. 1330–1334 (cit. on pp. 9, 19, 21).

Fuse, T. et al. (2008). “Searching satellites of asteroid Itokawa by imaging observation with Hayabusa spacecraft”. In: *Earth, Planets and Space* 60.1, pp. 33–37 (cit. on p. 19).

Garcia, R. F. et al. (2015). “Micro-meteoroid seismic uplift and regolith concentration on kilometric scale asteroids”. In: *Icarus* 253, pp. 159–168 (cit. on p. 39).

Gault, Donald E et al. (1963). *Spray Ejected from the Lunar Surface by Meteoroid Impact*. Tech. rep. Washington, D.C.: NASA-TN-D-1767 (cit. on p. 20).

Gehrels, T. (1956). “Photometric Studies of Asteroids. V. The Light-Curve and Phase Function of 20 Massalia.” In: *The Astrophysical Journal* 123, p. 331 (cit. on p. 10).

– (1979). *Asteroids* (cit. on p. 9).

Geissler, P. et al. (1996). “Erosion and Ejecta Reaccretion on 243 Ida and Its Moon”. In: *Icarus* 120.1, pp. 140–157 (cit. on p. 13).

Gladman, B. J. et al. (1997). “Dynamical Lifetimes of Objects Injected into Asteroid Belt Resonances”. In: *Science* 277.5323, pp. 197–201 (cit. on pp. 2, 6).

Granvik, M. et al. (2018). “Debiased orbit and absolute-magnitude distributions for near-Earth objects”. In: *Icarus* 312, pp. 181–207. arXiv: 1804.10265 (cit. on p. 2).

Gray, J. M. N. T. et al. (2005). “A theory for particle size segregation in shallow granular free-surface flows”. In: *Proceedings of the Royal Society A: Mathematical, Physical and Engineering Sciences* 461.2057, pp. 1447–1473 (cit. on p. 40).

Gray, J. M. N. T. et al. (2006). “Particle-size segregation and diffusive remixing in shallow granular avalanches”. In: *Journal of Fluid Mechanics* 569, p. 365 (cit. on p. 40).

Grott, M. et al. (2017). “The MASCOT Radiometer MARA for the Hayabusa 2 Mission”. In: *Space Science Reviews* 208.1-4, pp. 413–431 (cit. on p. 124).

Güttler, C. et al. (2013). “Granular convection and the Brazil nut effect in reduced gravity”. In: *Physical Review E* 87.4, p. 044201 (cit. on pp. 40, 42).

Hapke, B. et al. (1963). “Photometric studies of complex surfaces, with applications to the Moon”. In: *Journal of Geophysical Research* 68.15, pp. 4545–4570 (cit. on p. 35).

Heide, F. et al. (1995). *Meteorites : Messengers from Space*. Springer Berlin Heidelberg, p. 233 (cit. on p. 5).

Heiken, G. et al. (1991). *Lunar sourcebook : a user’s guide to the moon*. Cambridge University Press, p. 736 (cit. on p. 27).

Heim, L.-O. et al. (1999). “Adhesion and Friction Forces between Spherical Micrometer-Sized Particles”. In: *Physical Review Letters* 83.16, pp. 3328–3331 (cit. on p. 34).

Herčík, D. et al. (2017). “The MASCOT Magnetometer”. In: *Space Science Reviews* 208.1-4, pp. 433–449 (cit. on p. 124).

Hergenrother, C. W. et al. (2019). “The operational environment and rotational acceleration of asteroid (101955) Bennu from OSIRIS-REx observations”. In: *Nature Communications* 10.1, p. 1291 (cit. on p. 218).

Hertz, H. (1896). *Miscellaneous papers*. London, New York: Macmillan and co. (cit. on p. 34).

Hildebrand, A. R. et al. (1991). “Chicxulub Crater: A possible Cretaceous/Tertiary boundary impact crater on the Yucatán Peninsula, Mexico”. In: *Geology* 19.9, p. 867 (cit. on p. 7).

Hillier, J. K. et al. (2011). “Photometric modeling of Asteroid 5535 Annefrank from Stardust observations”. In: *Icarus* 211.1, pp. 546–552 (cit. on p. 12).

Hirabayashi, M. (2014). “Structural failure of two-density-layer cohesionless biaxial ellipsoids”. In: *Icarus* 236, pp. 178–180 (cit. on p. 36).

Hirabayashi, M. et al. (2014). “Constraints on the Physical Properties of Main Belt Comet P/2013 R3 from its Breakup Event”. In: *The Astrophysical Journal* 789.1, p. L12. arXiv: 1406.0804 (cit. on p. 36).

Hitti, K. et al. (2013). “Optimized Dropping and Rolling (ODR) method for packing of poly-disperse spheres”. In: *Applied Mathematical Modelling* 37.8, pp. 5715–5722 (cit. on p. 128).

Ho, T.-M. et al. (2017). “MASCOT — The Mobile Asteroid Surface Scout Onboard the Hayabusa2 Mission”. In: *Space Science Reviews* 208.1-4, pp. 339–374 (cit. on pp. 98, 124).

Hofmeister, P. G. et al. (2009). “The Flow Of Granular Matter Under Reduced-Gravity Conditions”. In: *AIP Conference Proceedings*. Vol. 1145. AIP, pp. 71–74 (cit. on p. 41).

Holsapple, K. A. (1993). “The Scaling of Impact Processes in Planetary Sciences”. In: *Annual Review of Earth and Planetary Sciences* 21.1, pp. 333–373 (cit. on pp. 43, 179).

Holsapple, K. A. et al. (2006). “Tidal disruptions: A continuum theory for solid bodies”. In: *Icarus* 183.2, pp. 331–348 (cit. on p. 25).

Housen, K. R. et al. (1983). “Crater ejecta scaling laws: Fundamental forms based on dimensional analysis”. In: *Journal of Geophysical Research* 88.B3, p. 2485 (cit. on p. 181).

Housen, K. R. et al. (2011). “Ejecta from impact craters”. In: *Icarus* 211.1, pp. 856–875 (cit. on p. 230).

Huang, J. et al. (2013). “The Ginger-shaped Asteroid 4179 Toutatis: New Observations from a Successful Flyby of Chang’e-2”. In: *Scientific Reports* 3.1, p. 3411 (cit. on pp. 8, 14).

Hudson, R. S. et al. (2003). “High-resolution model of Asteroid 4179 Toutatis”. In: *Icarus* 161.2, pp. 346–355 (cit. on pp. 8, 14).

Hughes, A. L. H. et al. (2008). “Electrostatic dust transport on Eros: 3-D simulations of pond formation”. In: *Icarus* 195.2, pp. 630–648 (cit. on p. 36).

Ionescu, I. R. et al. (2015). “Viscoplastic modeling of granular column collapse with pressure-dependent rheology”. In: *Journal of Non-Newtonian Fluid Mechanics* 219, pp. 1–18 (cit. on p. 83).

Ishibashi, K. et al. (2017). “Performance of Hayabusa2 DCAM3-D Camera for Short-Range Imaging of SCI and Ejecta Curtain Generated from the Artificial Impact Crater Formed on Asteroid 162137 Ryugu (1999 JU3)”. In: *Space Science Reviews* 208.1-4, pp. 213–238 (cit. on p. 98).

Israelachvili, J. N. (2011). “Van der Waals Forces”. In: *Intermolecular and Surface Forces*. Academic Press, pp. 107–132 (cit. on p. 34).

Ivezić, Ž. et al. (2001). “Solar System Objects Observed in the Sloan Digital Sky Survey Commissioning Data”. In: *The Astronomical Journal* 122.5, pp. 2749–2784 (cit. on p. 2).

Ivezić, Ž. et al. (2007). “LSST Survey Strategy”. In: *American Astronomical Society Meeting Abstracts*. Vol. 211, p. 137.02 (cit. on p. 4).

Iwata, T. et al. (2017). “NIRS3: The Near Infrared Spectrometer on Hayabusa2”. In: *Space Science Reviews* 208.1-4, pp. 317–337 (cit. on p. 98).

Jaeger, H. M. et al. (1996). “Granular solids, liquids, and gases”. In: *Reviews of Modern Physics* 68.4, pp. 1259–1273 (cit. on pp. 22, 23, 39).

Jaumann, R. et al. (2017). “The Camera of the MASCOT Asteroid Lander on Board Hayabusa 2”. In: *Space Science Reviews* 208.1-4, pp. 375–400 (cit. on p. 124).

JAXA Hayabusa2 Project (2019b). *Asteroid explorer, Hayabusa2, reporter briefing: March 5, 2019*. Tech. rep. JAXA (cit. on p. 183).

Jeffreys, H. (1952). *The Earth: Its Origin, History and Physical Constitution*. Cambridge University Press (cit. on p. 31).

Jenkins, J. T. et al. (2002). “Kinetic theory for identical, frictional, nearly elastic spheres”. In: *Physics of Fluids* 14.3, pp. 1228–1235 (cit. on p. 25).

Jewitt, D. (2012). “The Active Asteroids”. In: *The Astronomical Journal* 143.3, p. 66. arXiv: 1112.5220 (cit. on pp. 230, 231).

Jewitt, D. et al. (2015). “The Active Asteroids”. In: *Asteroids IV*. University of Arizona Press, p. 221 (cit. on p. 230).

Jiang, M. et al. (2013). “Microscopic contact model of lunar regolith for high efficiency discrete element analyses”. In: *Computers and Geotechnics* 54, pp. 104–116 (cit. on p. 134).

Jiang, M. et al. (2015a). “A novel three-dimensional contact model for granulates incorporating rolling and twisting resistances”. In: *Computers and Geotechnics* 65, pp. 147–163 (cit. on p. 134).

Jiang, Y. et al. (2015b). “Boulders on asteroid Toutatis as observed by Chang’e-2”. In: *Scientific Reports* 5.1, p. 16029 (cit. on p. 106).

Johnson, K. L. et al. (1971). “Surface Energy and the Contact of Elastic Solids”. In: *Proceedings of the Royal Society A: Mathematical, Physical and Engineering Sciences* 324.1558, pp. 301–313 (cit. on p. 34).

Jones, R. L. et al. (2009). “Solar System Science with LSST”. In: *Earth, Moon, and Planets* 105.2-4, pp. 101–105 (cit. on p. 4).

Jop, P. et al. (2006). “A constitutive law for dense granular flows”. In: *Nature* 441.7094, pp. 727–730 (cit. on pp. 43, 49, 81, 82, 84, 92).

Jutzi, M. (2015). “SPH calculations of asteroid disruptions: The role of pressure dependent failure models”. In: *Planetary and Space Science* 107, pp. 3–9. arXiv: 1502.01860 (cit. on p. 44).

Jutzi, M. et al. (2008). “Numerical simulations of impacts involving porous bodies”. In: *Icarus* 198.1, pp. 242–255. arXiv: 0807.1264 (cit. on p. 44).

Jutzi, M. et al. (2013). “The structure of the asteroid 4 Vesta as revealed by models of planet-scale collisions”. In: *Nature* 494.7436, pp. 207–210 (cit. on p. 44).

Kaasalainen, M. et al. (2002). “Asteroid Models from Disk-integrated Data”. In: *Asteroids III*, p. 139 (cit. on p. 4).

Kameda, S. et al. (2017). “Preflight Calibration Test Results for Optical Navigation Camera Telescope (ONC-T) Onboard the Hayabusa2 Spacecraft”. In: *Space Science Reviews* 208.1-4, pp. 17–31 (cit. on p. 98).

Katsuragi, H. et al. (2007). “Unified force law for granular impact cratering”. In: *Nature Physics* 3.6, pp. 420–423 (cit. on pp. 61, 62, 70, 74, 78–80, 179, 241).

– (2013). “Drag force scaling for penetration into granular media”. In: *Physical Review E* 87.5, p. 052208 (cit. on p. 79).

Katsuragi, H. et al. (2017). “The Physics of Protoplanetesimal Dust Agglomerates. IX. Mechanical Properties of Dust Aggregates Probed by a Solid-projectile Impact”. In: *The Astrophysical Journal* 851.1, p. 23 (cit. on p. 179).

Kawaguchi, J. et al. (2004). “The Ion Engines Cruise Operation and the Earth Swingby of ’Hayabusa’ (MUSES-C)”. In: *55th International Astronautical Congress of the International Astronautical Federation, the International Academy of Astronautics, and the International Institute of Space Law*. Vancouver (cit. on p. 18).

Kawaguchi, J. et al. (2010). “Hayabusa Reentry and Recovery of Its Capsule -Quick Report”. In: *38th COSPAR Scientific Assembly*. Vol. 38, p. 4 (cit. on p. 19).

Keller, H. U. et al. (2010). “E-Type Asteroid (2867) Steins as Imaged by OSIRIS on Board Rosetta”. In: *Science* 327.5962, pp. 190–193 (cit. on p. 13).

Kim, M.-J. et al. (2013). “Optical observations of NEA 162173 (1999 JU3) during the 2011-2012 apparition”. In: *Astronomy & Astrophysics* 550, p. L11 (cit. on pp. 99, 172).

Kimura, H. et al. (2014). “Electrostatic lofting of dust aggregates near the terminator of airless bodies and its implication for the formation of exozodiacal disks”. In: *Planetary and Space Science* 100, pp. 64–72 (cit. on pp. 21, 36).

Kirkwood, D. (1867). “Meteoric astronomy: a treatise on shooting-stars, fireballs, and aerolites.” In: *Philadelphia* (cit. on p. 2).

Kitazato, K. et al. (2019). “The surface composition of asteroid 162173 Ryugu from Hayabusa2 near-infrared spectroscopy”. In: *Science* 364.6437, eaav7432 (cit. on p. 99).

Kleinhans, M. G. et al. (2011). “Static and dynamic angles of repose in loose granular materials under reduced gravity”. In: *Journal of Geophysical Research* 116.E11, E11004 (cit. on p. 33).

Kleyna, J. T. et al. (2019). “The Sporadic Activity of (6478) Gault: A YORP-driven Event?” In: *The Astrophysical Journal* 874.2, p. L20 (cit. on p. 230).

Knight, J. B. et al. (1993). “Vibration-induced size separation in granular media: The convection connection”. In: *Physical Review Letters* 70.24, pp. 3728–3731 (cit. on p. 40).

Kosai, H. (1992). “Short-period comets and apollo-amor-aten type asteroids in view of tisserand invariant”. In: *Celestial Mechanics and Dynamical Astronomy* 54.1-3, pp. 237–240 (cit. on p. 230).

Krasinsky, G et al. (2002). “Hidden Mass in the Asteroid Belt”. In: *Icarus* 158.1, pp. 98–105 (cit. on p. 2).

Krause, M. et al. (2004). “Growth and Form of Planetary Seedlings: Results from a Sounding Rocket Microgravity Aggregation Experiment”. In: *Physical Review Letters* 93.2, p. 021103 (cit. on p. 42).

Kresak, L. (1982). “On the Similarity of Orbits of Associated Comets”. In: *Bulletin of the Astronomical Institute of Czechoslovakia* 33, p. 104 (cit. on p. 230).

Kudrolli, A. (2004). “Size separation in vibrated granular matter”. In: *Reports on Progress in Physics* 67.3, pp. 209–247 (cit. on p. 40).

Kuramoto, K. et al. (2018). “Martian Moons eXploration (MMX) : an overview of its science”. In: *European Planetary Science Congress*. Vol. 12. EPSC 2018, EPSC2018–1036 (cit. on pp. 28, 245).

Kurosawa, K. et al. (2019). “Impact cratering mechanics: A forward approach to predicting ejecta velocity distribution and transient crater radii”. In: *Icarus* 317, pp. 135–147 (cit. on p. 180).

Lacaze, L. et al. (2009). “Axisymmetric Granular Collapse: A Transient 3D Flow Test of Viscoplasticity”. In: *Physical Review Letters* 102.10, p. 108305 (cit. on p. 83).

Lagrée, P.-Y. et al. (2011). “The granular column collapse as a continuum: validity of a two-dimensional Navier-Stokes model with a μ(I)-rheology”. In: *Journal of Fluid Mechanics* 686, pp. 378–408 (cit. on p. 83).

Lambe, T. W. et al. (1969). *Soil Mechanics*. SI Edition. Wiley, New York, p. 553 (cit. on p. 39).

Lauretta, D. S. et al. (2015). “The OSIRIS-REx target asteroid (101955) Bennu: Constraints on its physical, geological, and dynamical nature from astronomical observations”. In: *Meteoritics & Planetary Science* 50.4, pp. 834–849 (cit. on pp. 8, 214).

Lauretta, D. S. et al. (2017). “OSIRIS-REx: Sample Return from Asteroid (101955) Bennu”. In: *Space Science Reviews* 212.1-2, pp. 925–984 (cit. on pp. 8, 213, 214).

Lauretta, D. S. et al. (2019). “The unexpected surface of asteroid (101955) Bennu”. In: *Nature* 568.7750, pp. 55–60 (cit. on pp. 214, 215, 218, 233).

Lay, T. et al. (1995). *Modern global seismology*. Academic Press, p. 521 (cit. on p. 38).

Lee, P. (1996). “Dust Levitation on Asteroids”. In: *Icarus* 124.1, pp. 181–194 (cit. on p. 21).

Lee, P. et al. (1996). “Ejecta Blocks on 243 Ida and on Other Asteroids”. In: *Icarus* 120.1, pp. 87–105 (cit. on p. 20).

Lorda, L. et al. (2017). *Mascot: Analyses of the Descent and Bouncing Trajectories to Support the Landing Site Selection*. Tech. rep. (cit. on pp. 124–126).

Machii, N. et al. (2011). “Experimental study on static and impact strength of sintered agglomerates”. In: *Icarus* 211.1, pp. 885–893 (cit. on p. 56).

Machii, N. et al. (2013). “Collision of a chondrule with matrix: Relation between static strength of matrix and impact pressure”. In: *Icarus* 226.1, pp. 111–118 (cit. on p. 180).

Macke, R. J. et al. (2011). “Density, porosity, and magnetic susceptibility of carbonaceous chondrites”. In: *Meteoritics & Planetary Science* 46.12, pp. 1842–1862 (cit. on pp. 103, 218).

Makabe, T. et al. (2008). “The effective projectile shape for asteroid impact sampling”. In: *26th International Conference on Space Technology and Science (ISTS), 2008-k-08*. Hamamatsu: ISTS Web Paper Archives (cit. on pp. 56, 172, 180).

Mantz, A. et al. (2004). “Regolith transport in craters on Eros”. In: *Icarus* 167.1, pp. 197–203 (cit. on p. 17).

Marchi, S. et al. (2015). “Cratering on Asteroids”. In: *Asteroids IV*. University of Arizona Press, p. 725 (cit. on p. 101).

Marouf, E. A. et al. (1983). “Particle size distributions in Saturn’s rings from voyager 1 radio occultation”. In: *Icarus* 54.2, pp. 189–211 (cit. on p. 27).

Masiero, J. R. et al. (2009). “The Effect of the Dust Size Distribution on Asteroid Polarization”. In: *The Astronomical Journal* 138.6, pp. 1557–1562 (cit. on p. 30).

Massironi, M. et al. (2012). “Geological map and stratigraphy of asteroid 21 Lutetia”. In: *Planetary and Space Science* 66.1, pp. 125–136 (cit. on p. 13).

Masterson, R. A. et al. (2018). “Regolith X-Ray Imaging Spectrometer (REXIS) Aboard the OSIRIS-REx Asteroid Sample Return Mission”. In: *Space Science Reviews* 214.1, p. 48 (cit. on p. 214).

Matsumura, S. et al. (2014). “The Brazil nut effect and its application to asteroids”. In: *Monthly Notices of the Royal Astronomical Society* 443.4, pp. 3368–3380 (cit. on pp. 40, 46).

Maurel, C. et al. (2017). “Numerical simulations of oscillation-driven regolith motion: Brazil-nut effect”. In: *Monthly Notices of the Royal Astronomical Society* 464.3, pp. 2866–2881 (cit. on pp. 40, 46).

Maurel, C. et al. (2018). “Numerical simulations of the contact between the lander MASCOT and a regolith-covered surface”. In: *Advances in Space Research* 62.8, pp. 2099–2124 (cit. on pp. 51, 52, 54, 55, 57, 60, 131, 242).

Maxwell, D. E. (1977). “Simple Z model for cratering, ejection, and the overturned flap.” In: *Impact and Explosion Cratering: Planetary and Terrestrial Implications*, pp. 1003–1008 (cit. on pp. 179–181, 243).

Mazrouei, S. et al. (2014). “Block distributions on Itokawa”. In: *Icarus* 229, pp. 181–189 (cit. on p. 106).

McGlaun, J. M. et al. (1990). “CTH: A three-dimensional shock wave physics code”. In: *International Journal of Impact Engineering* 10.1-4, pp. 351–360 (cit. on p. 43).

McMahon, J. W. et al. (2018). “The OSIRIS-REx Radio Science Experiment at Bennu”. In: *Space Science Reviews* 214.1, p. 43 (cit. on p. 214).

McNaught, A. D. et al. (1997). *IUPAC Compendium of chemical terminology: The Gold Book, Second Edition*. Blackwell Science, p. 450 (cit. on p. 34).

Melosh, H. J. (1985). “Impact cratering mechanics: Relationship between the shock wave and excavation flow”. In: *Icarus* 62.2, pp. 339–343 (cit. on p. 180).

– (1989). *Impact Cratering : A Geologic Process*. Oxford University Press (cit. on p. 179).

– (2011). *Planetary Surface Processes*. Cambridge: Cambridge University Press (cit. on pp. 29, 32, 33).

Mériaux, C. et al. (2008). “Scaling the final deposits of dry cohesive granular columns after collapse and quasi-static fall”. In: *Physics of Fluids* 20.3, p. 033301 (cit. on p. 36).

Michel, P. et al. (2001). “Collisions and Gravitational Reaccumulation: Forming Asteroid Families and Satellites”. In: *Science* 294.5547, pp. 1696–1700 (cit. on p. 20).

Michel, P. et al. (2009). “Itokawa’s cratering record as observed by Hayabusa: Implications for its age and collisional history”. In: *Icarus* 200.2, pp. 503–513 (cit. on pp. 21, 37, 101).

Michel, P. et al. (2013). “Collision and gravitational reaccumulation: Possible formation mechanism of the asteroid Itokawa”. In: *Astronomy & Astrophysics* 554, p. L1 (cit. on p. 45).

Michel, P. et al. (2015a). *Asteroids IV*. Ed. by Patrick Michel et al. University of Arizona Press (cit. on p. 9).

Michel, P. et al. (2015b). “Selective sampling during catastrophic disruption: Mapping the location of reaccumulated fragments in the original parent body”. In: *Planetary and Space Science* 107, pp. 24–28 (cit. on p. 107).

Michel, P. et al. (2018). “European component of the AIDA mission to a binary asteroid: Characterization and interpretation of the impact of the DART mission”. In: *Advances in Space Research* 62.8, pp. 2261–2272 (cit. on pp. 7, 245).

Michikami, T. et al. (2008). “Size-frequency statistics of boulders on global surface of asteroid 25143 Itokawa”. In: *Earth, Planets and Space* 60.1, pp. 13–20 (cit. on p. 20).

Michikami, T. et al. (2016). “Fragment shapes in impact experiments ranging from cratering to catastrophic disruption”. In: *Icarus* 264, pp. 316–330 (cit. on p. 136).

Michikami, T. et al. (2018). “Influence of petrographic textures on the shapes of impact experiment fine fragments measuring several tens of microns: Comparison with Itokawa regolith particles”. In: *Icarus* 302, pp. 109–125 (cit. on p. 136).

Midi, Gdr (2004). “On dense granular flows”. In: *The European Physical Journal E* 14.4, pp. 341–365 (cit. on p. 83).

Mignard, F. et al. (2007). “The Gaia Mission: Expected Applications to Asteroid Science”. In: *Earth, Moon, and Planets* 101.3-4, pp. 97–125 (cit. on p. 4).

Mitani, N. K. (2003). “Numerical simulations of shock attenuation in solids and reevaluation of scaling law”. In: *Journal of Geophysical Research* 108.E1, p. 5003 (cit. on p. 180).

Miyamoto, H. et al. (2007). “Regolith Migration and Sorting on Asteroid Itokawa”. In: *Science* 316.5827, pp. 1011–1014 (cit. on pp. 21, 37).

Mizuno, T. et al. (2017). “Development of the Laser Altimeter (LIDAR) for Hayabusa2”. In: *Space Science Reviews* 208.1-4, pp. 33–47 (cit. on p. 98).

Monaghan, J. J. (1988). “An introduction to SPH”. In: *Computer Physics Communications* 48.1, pp. 89–96 (cit. on p. 44).

– (2012). “Smoothed Particle Hydrodynamics and Its Diverse Applications”. In: *Annual Review of Fluid Mechanics* 44.1, pp. 323–346 (cit. on p. 44).

Morbidelli, A. et al. (2002). “Origin and Evolution of Near-Earth Objects”. In: *Asteroids III*, p. 409 (cit. on p. 6).

Morbidelli, A. et al. (2015). “The Dynamical Evolution of the Asteroid Belt”. In: *Asteroids IV*. University of Arizona Press, p. 493 (cit. on p. 6).

Muinonen, K. et al. (2002). “Asteroid Photometric and Polarimetric Phase Effects”. In: *Asteroids III*, p. 123 (cit. on p. 10).

Müller, P. et al. (2012a). “Oblique impact of frictionless spheres: on the limitations of hard sphere models for granular dynamics”. In: *Granular Matter* 14.2, pp. 115–120 (cit. on p. 50).

– (2013). “Event-driven molecular dynamics of soft particles”. In: *Physical Review E* 87.3, p. 033301 (cit. on p. 50).

Müller, T. G. et al. (2005). “Thermal infrared observations of the Hayabusa spacecraft target asteroid 25143 Itokawa”. In: *Astronomy & Astrophysics* 443.1, pp. 347–355 (cit. on p. 19).

Müller, T. G. et al. (2011). “Thermo-physical properties of 162173 (1999 JU3), a potential flyby and rendezvous target for interplanetary missions”. In: *Astronomy & Astrophysics* 525, A145 (cit. on p. 128).

Müller, T. G. et al. (2012b). “Physical properties of OSIRIS-REx target asteroid (101955) 1999 RQ 36”. In: *Astronomy & Astrophysics* 548, A36 (cit. on p. 214).

Müller, T. G. et al. (2017). “Hayabusa-2 mission target asteroid 162173 Ryugu (1999 JU$_3$): Searching for the object’s spin-axis orientation”. In: *Astronomy & Astrophysics* 599, A103 (cit. on pp. 99, 172).

Murdoch, N. et al. (2012). “Numerical simulations of granular dynamics II: Particle dynamics in a shaken granular material”. In: *Icarus* 219.1, pp. 321–335. arXiv: `1306.1799` (cit. on p. 45).

Murdoch, N. et al. (2013a). “Granular Convection in Microgravity”. In: *Physical Review Letters* 110.1, p. 018307 (cit. on pp. 40, 42).

Murdoch, N. et al. (2013b). “Granular shear flow in varying gravitational environments”. In: *Granular Matter* 15.2, pp. 129–137 (cit. on p. 42).

Murdoch, N. et al. (2015). “Asteroid Surface Geophysics”. In: *Asteroids IV*. University of Arizona Press, p. 767 (cit. on pp. 11, 15, 45, 51).

Murdoch, N. et al. (2017). “An experimental study of low-velocity impacts into granular material in reduced gravity”. In: *Monthly Notices of the Royal Astronomical Society* 468.2, stw3391 (cit. on pp. 41, 58, 180).

Naidu, S. P. et al. (2015). “Radar Imaging and Characterization of the Binary Near-Earth Asteroid (185851) 2000 DP107”. In: *The Astronomical Journal* 150.2, p. 54 (cit. on p. 8).

Nakamura, A. M. et al. (1994). “Velocity of finer fragments from impact”. In: *Planetary and Space Science* 42.12, pp. 1043–1052 (cit. on p. 21).

Nakamura, A. M. et al. (2013). “Impact and intrusion experiments on the deceleration of low-velocity impactors by small-body regolith”. In: *Icarus* 223.1, pp. 222–233 (cit. on pp. 57, 180, 181).

Nesvorný, D. et al. (2002). “Regular and Chaotic Dynamics in the Mean-Motion Resonances: Implications for the Structure and Evolution of the Asteroid Belt”. In: *Asteroids III*, p. 379 (cit. on p. 5).

Nesvorný, D. et al. (2005). “Evidence for asteroid space weathering from the Sloan Digital Sky Survey”. In: *Icarus* 173.1, pp. 132–152 (cit. on p. 2).

Nguyen, G. et al. (2019). “Low-velocity and shallow impacts into granular material: application to small-body landing”. In: *MNRAS* submitted (cit. on pp. 58–61, 63–75, 77, 78, 80, 241).

Nichol, K. et al. (2010). “Flow-Induced Agitations Create a Granular Fluid”. In: *Physical Review Letters* 104.7, p. 078302 (cit. on p. 23).

Nicholson, P. D. et al. (2008). “A close look at Saturn’s rings with Cassini VIMS”. In: *Icarus* 193.1, pp. 182–212 (cit. on p. 27).

Nolan, M. C. et al. (2013). “Shape model and surface properties of the OSIRIS-REx target Asteroid (101955) Bennu from radar and lightcurve observations”. In: *Icarus* 226.1, pp. 629–640 (cit. on p. 214).

Nordstrom, K. et al. (2013). “Granular Dynamics during Impact”. In: *APS March Meeting Abstracts* 2013, N29.013 (cit. on p. 180).

Ogawa, K. et al. (2017). “System Configuration and Operation Plan of Hayabusa2 DCAM3-D Camera System for Scientific Observation During SCI Impact Experiment”. In: *Space Science Reviews* 208.1-4, pp. 125–142 (cit. on p. 98).

Okada, T. et al. (2017). “Thermal Infrared Imaging Experiments of C-Type Asteroid 162173 Ryugu on Hayabusa2”. In: *Space Science Reviews* 208.1-4, pp. 255–286 (cit. on pp. 98, 105).

Ostro, S. J. et al. (2004). "Radar observations of asteroid 25143 Itokawa (1998 SF36)". In: *Meteoritics & Planetary Science* 39.3, pp. 407–424 (cit. on p. 19).

Pater, I. de et al. (2015). *Planetary Sciences*. Cambridge: Cambridge University Press (cit. on pp. 6, 9, 12).

Perko, H. A. et al. (2001). "Surface Cleanliness Effect on Lunar Soil Shear Strength". In: *Journal of Geotechnical and Geoenvironmental Engineering* 127.4, pp. 371–383 (cit. on pp. 34, 35, 103).

Perna, D. et al. (2017). "Spectral and rotational properties of near-Earth asteroid (162173) Ryugu, target of the Hayabusa2 sample return mission". In: *Astronomy & Astrophysics* 599, p. L1 (cit. on pp. 99, 172).

Pohlman, N. A. et al. (2006). "Surface roughness effects in granular matter: Influence on angle of repose and the absence of segregation". In: *Physical Review E* 73.3, p. 031304 (cit. on p. 33).

Prockter, L. et al. (2002). "Surface Expressions of Structural Features on Eros". In: *Icarus* 155.1, pp. 75–93 (cit. on pp. 15, 18).

Radjaï, F. et al. (2011). *Discrete-element modeling of granular materials*. ISTE-Wiley, p. 425 (cit. on p. 45).

Renne, P. R. et al. (2013). "Time Scales of Critical Events Around the Cretaceous-Paleogene Boundary". In: *Science* 339.6120, pp. 684–687 (cit. on p. 7).

Rennilson, J. J. et al. (1974). "Surveyor observations of lunar horizon-glow". In: *The Moon* 10.2, pp. 121–142 (cit. on p. 36).

Reuter, D. C. et al. (2018). "The OSIRIS-REx Visible and InfraRed Spectrometer (OVIRS): Spectral Maps of the Asteroid Bennu". In: *Space Science Reviews* 214.2, p. 54 (cit. on p. 214).

Richard, P. et al. (2005). "Slow relaxation and compaction of granular systems". In: *Nature Materials* 4.2, pp. 121–128 (cit. on pp. 22, 25).

Richardson Jr., J. E. et al. (2005). "The global effects of impact-induced seismic activity on fractured asteroid surface morphology". In: *Icarus* 179.2, pp. 325–349 (cit. on pp. 37, 39, 101).

Richardson, D. C. (1994). "Tree code simulations of planetary rings". In: *Monthly Notices of the Royal Astronomical Society* 269.2, pp. 493–511 (cit. on p. 44).

– (1995). "A Self-Consistent Numerical Treatment of Fractal Aggregate Dynamics". In: *Icarus* 115.2, pp. 320–335 (cit. on p. 44).

Richardson, D. C. et al. (1998). "Tidal Distortion and Disruption of Earth-Crossing Asteroids". In: *Icarus* 134.1, pp. 47–76 (cit. on p. 45).

Richardson, D. C. et al. (2000). "Direct Large-Scale N-Body Simulations of Planetesimal Dynamics". In: *Icarus* 143.1, pp. 45–59 (cit. on p. 50).

Richardson, D. C. et al. (2009). "Numerical simulations of asteroids modelled as gravitational aggregates with cohesion". In: *Planetary and Space Science* 57.2, pp. 183–192 (cit. on p. 50).

Richardson, D. C. et al. (2011). “Numerical simulations of granular dynamics: I. Hard-sphere discrete element method and tests”. In: *Icarus* 212.1, pp. 427–437 (cit. on pp. 45, 50).

Richardson, D. C. et al. (2012). “Comparison of Discrete Element Methods for Simulating Low-Speed Rubble Pile Collisions: First Results”. In: *Lunar and Planetary Science Conference*. 1659, p. 2195 (cit. on p. 51).

Richardson, J. E. et al. (2004). “Impact-Induced Seismic Activity on Asteroid 433 Eros: A Surface Modification Process”. In: *Science* 306.5701, pp. 1526–1529 (cit. on pp. 21, 37, 101).

Rizk, B. et al. (2018). “OCAMS: The OSIRIS-REx Camera Suite”. In: *Space Science Reviews* 214.1, p. 26 (cit. on p. 214).

Robinson, M. S. et al. (2001). “The nature of ponded deposits on Eros”. In: *Nature* 413.6854, pp. 396–400 (cit. on p. 36).

Robinson, M. S. et al. (2002). “The geology of 433 Eros”. In: *Meteoritics & Planetary Science* 37.12, pp. 1651–1684 (cit. on pp. 9, 10, 15, 16, 18, 101).

Roddy, D. J. et al. (1977). “Impact and explosion cratering: Planetary and terrestrial implications; Proceedings of the Symposium on Planetary Cratering Mechanics, Flagstaff, Ariz., September 13-17, 1976”. In: *Symposium sponsored by the Lunar and Planetary Institute New York, Pergamon Press, Inc., 1977. 1315 p (For individual items see A78-44031 to A78-44087)* (cit. on p. 178).

Rognon, P. G. et al. (2008). “Dense flows of cohesive granular materials”. In: *Journal of Fluid Mechanics* 596, pp. 21–47 (cit. on p. 34).

Rosato, A. et al. (1987). “Why the Brazil nuts are on top: Size segregation of particulate matter by shaking”. In: *Physical Review Letters* 58.10, pp. 1038–1040 (cit. on pp. 26, 40).

Rozitis, B. et al. (2014). “Cohesive forces prevent the rotational breakup of rubble-pile asteroid (29075) 1950 DA”. In: *Nature* 512.7513, pp. 174–176 (cit. on p. 36).

Russell, C. T. et al. (2013). “Dawn completes its mission at 4 Vesta”. In: *Meteoritics & Planetary Science* 48.11, pp. 2076–2089 (cit. on p. 11).

Russell, C. T. et al. (2016). “Dawn arrives at Ceres: Exploration of a small, volatile-rich world”. In: *Science* 353.6303, pp. 1008–1010 (cit. on p. 11).

Rycroft, C. H. (2001). “Multiscale Modeling in Granular Flow”. PhD thesis (cit. on p. 129).

Saiki, T. et al. (2017). “The Small Carry-on Impactor (SCI) and the Hayabusa2 Impact Experiment”. In: *Space Science Reviews* 208.1-4, pp. 165–186 (cit. on pp. 98, 172).

Saito, J. et al. (2006). “Detailed Images of Asteroid 25143 Itokawa from Hayabusa”. In: *Science* 312.5778, pp. 1341–1344 (cit. on pp. 20, 21).

Sakatani, N. et al. (2017). “Thermal conductivity model for powdered materials under vacuum based on experimental studies”. In: *AIP Advances* 7.1, p. 015310 (cit. on p. 105).

Sánchez, P. et al. (2014). “The strength of regolith and rubble pile asteroids”. In: *Meteoritics & Planetary Science* 49.5, pp. 788–811 (cit. on pp. 36, 134).

– (2016). “Disruption patterns of rotating self-gravitating aggregates: A survey on angle of friction and tensile strength”. In: *Icarus* 271, pp. 453–471 (cit. on p. 134).

Sardo, L. et al. (2018). “Low Impact Cratering on Granular Beds Under Low Gravity”. In: *WCCM XIII, PANACM II*. New York: WCCM XIII, PANACM II, Abstracts Q–T, 146 (cit. on p. 83).

Savage, Stuart B. (1984). “The Mechanics of Rapid Granular Flows”. In: *Advances in Applied Mechanics* 24, pp. 289–366 (cit. on p. 81).

Sawada, H. et al. (2017a). “Deployable Camera (DCAM3) System for Observation of Hayabusa2 Impact Experiment”. In: *Space Science Reviews* 208.1-4, pp. 143–164 (cit. on p. 98).

Sawada, H. et al. (2017b). “Hayabusa2 Sampler: Collection of Asteroidal Surface Material”. In: *Space Science Reviews* 208.1-4, pp. 81–106 (cit. on pp. 98, 172, 173).

Scheeres, D. J. (2014). “Sandcastles in space”. In: *Nature* 512.7513, pp. 139–140 (cit. on p. 36).

Scheeres, D. J. et al. (2010). “Scaling forces to asteroid surfaces: The role of cohesion”. In: *Icarus* 210.2, pp. 968–984 (cit. on pp. 30, 34–37, 103, 104).

Scheeres, D. J. et al. (2015). “Asteroid Interiors and Morphology”. In: *Asteroids IV*. University of Arizona Press, p. 745 (cit. on p. 30).

Scheeres, D. J. et al. (2019). “The dynamic geophysical environment of (101955) Bennu based on OSIRIS-REx measurements”. In: *Nature Astronomy* 3, p. 352 (cit. on pp. 30, 218).

Schenk, P. et al. (2011). “The Snows of Enceladus”. In: *EPSC-DPS Joint Meeting 2011* 2011, p. 1358 (cit. on p. 27).

Schmid, H.-M. et al. (2018). “SPHERE/ZIMPOL high resolution polarimetric imager. I. System overview, PSF parameters, coronagraphy, and polarimetry”. In: *Astronomy & Astrophysics* 619, A9 (cit. on p. 4).

Schräpler, R. et al. (2012). “The Physics of Protoplanetesimal Dust Agglomerates. VII. The Low-velocity Collision Behavior of Large Dust Agglomerates”. In: *The Astrophysical Journal* 758.1, p. 35 (cit. on p. 41).

Schulte, P. et al. (2010). “The Chicxulub Asteroid Impact and Mass Extinction at the Cretaceous-Paleogene Boundary”. In: *Science* 327.5970, pp. 1214–1218 (cit. on p. 7).

Schwartz, S. R. et al. (2012). “An implementation of the soft-sphere discrete element method in a high-performance parallel gravity tree-code”. In: *Granular Matter* 14.3, pp. 363–380 (cit. on pp. 23, 46, 50–53, 56).

Schwartz, S. R. et al. (2013). “Numerically simulating impact disruptions of cohesive glass bead agglomerates using the soft-sphere discrete element method”. In: *Icarus* 226.1, pp. 67–76 (cit. on p. 56).

Schwartz, S. R. et al. (2014). “Low-speed impact simulations into regolith in support of asteroid sampling mechanism design I: Comparison with 1-g experiments”. In: *Planetary and Space Science* 103, pp. 174–183 (cit. on pp. 46, 52, 56, 57, 59, 180).

Schwartz, S. R. et al. (2018). “An Ultra-Low-Gravity Centrifuge in Low-Earth Orbit”. In: *European Planetary Science Congress*. Berlin: EPSC 2018 (cit. on p. 42).

Sekiguchi, T. et al. (2003). “Thermal observations of MUSES-C mission target (25143) 1998 SF$_{36}$”. In: *Astronomy & Astrophysics* 397.1, pp. 325–328 (cit. on p. 19).

Senshu, H. et al. (2017). “Dust Detection Mode of the Hayabusa2 LIDAR”. In: *Space Science Reviews* 208.1-4, pp. 65–79 (cit. on p. 98).

Shoemaker, E. M. et al. (1967). “Surveyor V: Television Pictures”. In: *Science* 158.3801, pp. 642–652 (cit. on pp. 9, 26).

– (1969). “Observations of the lunar regolith and the Earth from the television camera on Surveyor 7”. In: *Journal of Geophysical Research* 74.25, pp. 6081–6119 (cit. on p. 9).

Shoemaker, E. M. et al. (1979). “Earth crossing asteroids: orbital classes, collision rates with earth, and origin.” In: *Asteroids*, p. 253 (cit. on p. 6).

Sierks, H. et al. (2011). “Images of Asteroid 21 Lutetia: A Remnant Planetesimal from the Early Solar System”. In: *Science* 334.6055, pp. 487–490 (cit. on pp. 13, 14).

Sirono, S.-i. (2004). “Conditions for collisional growth of a grain aggregate”. In: *Icarus* 167.2, pp. 431–452 (cit. on p. 44).

Stadel, J. (2001). “Cosmological N-body simulations and their analysis”. PhD thesis. University of Washington, p. 3657 (cit. on p. 50).

Sugita, S. et al. (2019). “The geomorphology, color, and thermal properties of Ryugu: Implications for parent-body processes”. In: *Science* 364.6437, eaaw0422 (cit. on pp. 97, 99, 102, 107, 242).

Sullivan, R. J. et al. (1996). “Geology of 243 Ida”. In: *Icarus* 120.1, pp. 119–139 (cit. on p. 12).

Sullivan, R. J. et al. (2002). “Asteroid Geology from Galileo and NEAR Shoemaker Data”. In: *Asteroids III*, p. 331 (cit. on p. 9).

Sunday, C. et al. (2016). “A novel facility for reduced-gravity testing: A setup for studying low-velocity collisions into granular surfaces”. In: *Review of Scientific Instruments* 87.8, p. 084504 (cit. on pp. 41, 180).

Suzuki, H. et al. (2018). “Initial inflight calibration for Hayabusa2 optical navigation camera (ONC) for science observations of asteroid Ryugu”. In: *Icarus* 300, pp. 341–359 (cit. on p. 98).

Szabó, Gy. M. et al. (2004). “Colour variability of asteroids in the Sloan Digital Sky Survey Moving Object Catalog”. In: *Monthly Notices of the Royal Astronomical Society* 348.3, pp. 987–998 (cit. on p. 2).

Tancredi, G. et al. (2012). “Granular physics in low-gravity environments using discrete element method”. In: *Monthly Notices of the Royal Astronomical Society* 420.4, pp. 3368–3380 (cit. on pp. 40, 46).

Tardivel, S. et al. (2014). “Contact Motion on Surface of Asteroid”. In: *Journal of Spacecraft and Rockets* 51.6, pp. 1857–1871 (cit. on p. 125).

Tatsumi, E. et al. (2018). “Cratering efficiency on coarse-grain targets: Implications for the dynamical evolution of asteroid 25143 Itokawa”. In: *Icarus* 300, pp. 227–248 (cit. on p. 178).

Thomas, N. et al. (2012). “The geomorphology of (21) Lutetia: Results from the OSIRIS imaging system onboard ESA’s Rosetta spacecraft”. In: *Planetary and Space Science* 66.1, pp. 96–124 (cit. on p. 13).

Thomas, P. C. (1993). “Gravity, Tides, and Topography on Small Satellites and Asteroids: Application to Surface Features of the Martian Satellites”. In: *Icarus* 105.2, pp. 326–344 (cit. on p. 27).

Thomas, P. C. et al. (2000). “Phobos: Regolith and ejecta blocks investigated with Mars Orbiter Camera images”. In: *Journal of Geophysical Research: Planets* 105.E6, pp. 15091–15106 (cit. on p. 40).

Thomas, P. C. et al. (2001). “Shoemaker crater as the source of most ejecta blocks on the asteroid 433 Eros”. In: *Nature* 413.6854, pp. 394–396 (cit. on pp. 20, 106).

Thomas, P. C. et al. (2002). “Eros: Shape, Topography, and Slope Processes”. In: *Icarus* 155.1, pp. 18–37 (cit. on pp. 15–18).

Thomas, P. C. et al. (2005). “Seismic resurfacing by a single impact on the asteroid 433 Eros”. In: *Nature* 436.7049, pp. 366–369 (cit. on p. 37).

Thomas, P. C. et al. (2010). “Tectonics of small bodies”. In: *Planetary Tectonics*. Ed. by Thomas R. Watters et al. Cambridge University Press, pp. 233–263 (cit. on p. 11).

Thuillet, F. et al. (2018). “Numerical modeling of lander interaction with a low-gravity asteroid regolith surface”. In: *Astronomy & Astrophysics* 615, A41 (cit. on pp. 60, 123, 138, 242).

Tsimring, L. S. et al. (2005). “Modeling of impact cratering in granular media”. In: *Powders and Grains*. Ed. by R. Garcia-Rojo et al. Rotterdam: A.A. Balkema, pp. 1215–1223 (cit. on p. 62).

Tsuchiyama, A. et al. (2011). “Three-Dimensional Structure of Hayabusa Samples: Origin and Evolution of Itokawa Regolith”. In: *Science* 333.6046, pp. 1125–1128 (cit. on pp. 19, 21, 29, 30, 36, 104).

Tsuchiyama, A. et al. (2014). “Three-dimensional microstructure of samples recovered from asteroid 25143 Itokawa: Comparison with LL5 and LL6 chondrite particles”. In: *Meteoritics & Planetary Science* 49.2, pp. 172–187 (cit. on p. 136).

Tsuda, Y. et al. (2013). “System design of the Hayabusa 2 - Asteroid sample return mission to 1999 JU3”. In: *Acta Astronautica* 91, pp. 356–362 (cit. on p. 98).

Tsuji, D. et al. (2018). “Relaxation Dynamics of a Granular Pile on a Vertically Vibrating Plate”. In: *Physical Review Letters* 120.12, p. 128001 (cit. on p. 38).

Uehara, J. S. et al. (2003). “Low-Speed Impact Craters in Loose Granular Media”. In: *Physical Review Letters* 90.19, p. 194301 (cit. on pp. 61, 179).

Valette, R. et al. (2017). “Quantitative predictions of the μ(I) rheology in 2D and 3D granular column collapse: scaling laws and quasi-static vs. inertial regimes”. In: *EPJ Web of Conferences* 140. Ed. by F. Radjai et al., p. 11005 (cit. on p. 83).

Valette, R. et al. (2019). “The effect of viscosity, yield stress, and surface tension on the deformation and breakup profiles of fluid filaments stretched at very high velocities”. In: *Journal of Non-Newtonian Fluid Mechanics* 263, pp. 130–139 (cit. on p. 43).

Vet, S. J. de et al. (2007). “Shape of impact craters in granular media”. In: *Physical Review E* 76.4, p. 041306 (cit. on p. 179).

Veverka, J. et al. (1994). “Galileo’s Encounter with 951 Gaspra: Overview”. In: *Icarus* 107.1, pp. 2–17 (cit. on p. 9).

Veverka, J. et al. (1999). “NEAR Encounter with Asteroid 253 Mathilde: Overview”. In: *Icarus* 140.1, pp. 3–16 (cit. on p. 12).

Veverka, J. et al. (2000). “NEAR at Eros: Imaging and Spectral Results”. In: *Science* 289.5487, pp. 2088–2097 (cit. on pp. 15–18).

Veverka, J. et al. (2001a). “Imaging of Small-Scale Features on 433 Eros from NEAR: Evidence for a Complex Regolith”. In: *Science* 292.5516, pp. 484–488 (cit. on pp. 15, 16, 101).

Veverka, J. et al. (2001b). “The landing of the NEAR-Shoemaker spacecraft on asteroid 433 Eros”. In: *Nature* 413.6854, pp. 390–393 (cit. on pp. 15, 17, 18).

Vincent, J.-B. et al. (2012). “Physical properties of craters on asteroid (21) Lutetia”. In: *Planetary and Space Science* 66.1, pp. 79–86 (cit. on p. 13).

VonNeumann, J. et al. (1950). “A Method for the Numerical Calculation of Hydrodynamic Shocks”. In: *Journal of Applied Physics* 21.3, pp. 232–237 (cit. on p. 43).

Wada, K. et al. (2006). “Numerical simulation of impact cratering on granular material”. In: *Icarus* 180.2, pp. 528–545 (cit. on pp. 46, 131, 180, 181).

Walsh, A. M. et al. (2003). “Morphology and Scaling of Impact Craters in Granular Media”. In: *Physical Review Letters* 91.10, p. 104301 (cit. on p. 179).

Walsh, K. J. (2018). “Rubble Pile Asteroids”. In: *Annual Review of Astronomy and Astrophysics* 56.1, pp. 593–624 (cit. on p. 9).

Walsh, K. J. et al. (2008). “Rotational breakup as the origin of small binary asteroids”. In: *Nature* 454.7201, pp. 188–191 (cit. on p. 45).

– (2012). “Spin-up of rubble-pile asteroids: Disruption, satellite formation, and equilibrium shapes”. In: *Icarus* 220.2, pp. 514–529 (cit. on p. 45).

Walsh, K. J. et al. (2019). “Craters, boulders and regolith of (101955) Bennu indicative of an old and dynamic surface”. In: *Nature Geoscience* 12.4, p. 242 (cit. on pp. 213, 215, 243).

Watanabe, S.-i. et al. (2017). “Hayabusa2 Mission Overview”. In: *Space Science Reviews* 208.1-4, pp. 3–16 (cit. on pp. 98, 99, 171, 172).

Watanabe, S.-i. et al. (2019). “Hayabusa2 arrives at the carbonaceous asteroid 162173 Ryugu - A spinning top-shaped rubble pile”. In: *Science* 364.6437, pp. 268–272 (cit. on pp. 30, 99, 100, 103).

Williams, J. C. (1976). “The segregation of particulate materials. A review”. In: *Powder Technology* 15.2, pp. 245–251 (cit. on p. 40).

Yamada, R. et al. (2017). “Albedo Observation by Hayabusa2 LIDAR: Instrument Performance and Error Evaluation”. In: *Space Science Reviews* 208.1-4, pp. 49–64 (cit. on p. 98).

Yamada, T. M. et al. (2016). “Timescale of asteroid resurfacing by regolith convection resulting from the impact-induced global seismic shaking”. In: *Icarus* 272, pp. 165–177 (cit. on p. 40).

Yamamoto, S. et al. (2005). “Velocity distributions of high-velocity ejecta from regolith targets”. In: *Icarus* 178.1, pp. 264–273 (cit. on p. 180).

Yamamoto, S. et al. (2006). “Transient crater growth in granular targets: An experimental study of low velocity impacts into glass sphere targets”. In: *Icarus* 183.1, pp. 215–224 (cit. on pp. 180, 181).

Yamamoto, S. et al. (2009). “An empirical model for transient crater growth in granular targets based on direct observations”. In: *Icarus* 203.1, pp. 310–319 (cit. on p. 180).

Yano, H. et al. (2006). “Touchdown of the Hayabusa Spacecraft at the Muses Sea on Itokawa”. In: *Science* 312.5778, pp. 1350–1353 (cit. on pp. 21, 36, 172).

Yano, H. et al. (2009). “Development of Sampling Systems for Small Solar System Bodies onboard the Hayabusa Follow-on Missions”. In: *27th International Symposium on Space Technology and Science (ISTS), 2009-k-11*. Tsukuba: ISTS Web Paper Archives (cit. on p. 172).

Yeomans, D. K. et al. (2000). “Radio Science Results During the NEAR-Shoemaker Spacecraft Rendezvous with Eros”. In: *Science* 289.5487, pp. 2085–2088 (cit. on pp. 15, 16).

Yoshikawa, M. et al. (2015). “Hayabusa Sample Return Mission”. In: *Asteroids IV*. University of Arizona Press, p. 397 (cit. on pp. 18–20, 30).

Yoshimitsu, T. et al. (2006). “The opearation and scientific data of MINERVA rover in Hayabusa mission”. In: *36th COSPAR Scientific Assembly*. Vol. 36, p. 2987 (cit. on p. 98).

Yu, Y. et al. (2014). “Numerical predictions of surface effects during the 2029 close approach of Asteroid 99942 Apophis”. In: *Icarus* 242, pp. 82–96 (cit. on pp. 46, 57, 59).

Zhang, J. et al. (2008). “Force chains in a two-dimensional granular pure shear experiment”. In: *Chaos: An Interdisciplinary Journal of Nonlinear Science* 18.4, p. 041107 (cit. on p. 23).

Zhang, Y. et al. (2017). “Creep stability of the proposed AIDA mission target 65803 Didymos: I. Discrete cohesionless granular physics model”. In: *Icarus* 294, pp. 98–123 (cit. on pp. 44, 46, 51–53, 57).

Zhang, Y. et al. (2018). “Rotational Failure of Rubble-pile Bodies: Influences of Shear and Cohesive Strengths”. In: *The Astrophysical Journal* 857.1, p. 15 (cit. on p. 134).

Zhu, M.-H. et al. (2014). “Morphology of asteroid (4179) Toutatis as imaged by Chang’E-2 spacecraft”. In: *Geophysical Research Letters* 41.2, pp. 328–333 (cit. on pp. 14, 15).

Websites

Bartels, M. (2019). *Japan Just Shot a Fake Asteroid with a Space Bullet . . . for Science*. URL: `https://www.space.com/hayabusa2-team-shoots-fake-asteroid-practice-ryugu.html` (visited on July 14, 2019) (cit. on p. 174).

ESO (2019). *ESO - The European ELT*. URL: `https://www.eso.org/sci/facilities/eelt/` (visited on Feb. 12, 2019) (cit. on p. 4).

IAU Minor Planet Center (2019). *Latest Published Data*. URL: `https://www.minorplanetcenter.net/mpc/summary` (visited on Feb. 2, 2019) (cit. on p. 2).

JAXA Hayabusa2 Project (2019a). *2nd touchdown image bulletin*. URL: `http://www.hayabusa2.jaxa.jp/en/topics/20190711e%7B%5C_%7DPPTD%7B%5C_%7DImageBulletin/` (visited on July 27, 2019) (cit. on p. 183).

– (2019c). *The touchdown site*. URL: `http://www.hayabusa2.jaxa.jp/en/topics/20190220e%7B%5C_%7DTDPoint/` (visited on Apr. 29, 2019) (cit. on p. 173).

JAXA et al. (2019). *Ryugu at an altitude of 1 km*. URL: http://www.hayabusa2.jaxa.jp/en/topics/20180807e/index.html (visited on Feb. 2, 2019) (cit. on p. 136).

List of Figures

List of Tables

Colophon

This thesis was typeset with $\LaTeX\,2_\varepsilon$. It uses the *Clean Thesis* style developed by Ricardo Langner. The design of the *Clean Thesis* style is inspired by user guide documents from Apple Inc.

Download the *Clean Thesis* style at `http://cleanthesis.der-ric.de/`.